UNIVERSIDADE DE LISBOA

INSTITUTO SUPERIOR TÉCNICO

Probing the Interplay between Calcitonins and Islet Amyloid Polypeptides with Membranes using Advanced Fluorescence Methodologies

Joana Catarina Ribeiro Ricardo

Supervisor: Doctor Ana Isabel Abrantes Coutinho

Co-Supervisor: Doctor Manuel José Estevez Prieto

Thesis approved in public session to obtain the PhD Degree in Chemistry

Jury final classification: *Pass with Distinction*

2019

UNIVERSIDADE DE LISBOA

INSTITUTO SUPERIOR TÉCNICO

Probing the Interplay between Calcitonins and Islet Amyloid Polypeptides with Membranes using Advanced Fluorescence Methodologies

Joana Catarina Ribeiro Ricardo

Supervisor: Doctor Ana Isabel Abrantes Coutinho
Co-Supervisor: Doctor Manuel José Estevez Prieto

Thesis approved in public session to obtain the PhD Degree in Chemistry

Jury final classification: *Pass with Distinction*

Jury

Chairperson: Doctor Maria Matilde Soares Duarte Marques, Instituto Superior Técnico, Universidade de Lisboa

Members of the Committee:

Doctor Margarida Maria Henriques Mesquita Bastos, Faculdade de Ciências, Universidade do Porto;

Doctor Luís Miguel Santos Loura, Faculdade de Farmácia, Universidade de Coimbra;

Doctor Ana Isabel Abrantes Coutinho, Faculdade de Ciências, Universidade de Lisboa;

Doctor Ana Margarida Nunes da Mata Pires de Azevedo, Instituto Superior Técnico, Universade de Lisboa.

Funding Institutions

Fundação para a Ciência e Tecnologia

2019

Table of contents

Acknowledgments

I would like to start by thanking *Fundação para a Ciência e Tecnologia* (FCT) from *Ministério da Ciência, Tecnologia e Ensino Superior* (MCTES) for the financial support of my research work (PhD fellowship SFRH/BD/95856/2013). Also, I want to express my gratitude to the Portuguese Biochemical Society and Portuguese Biophysical Society, to the European Biophysical Societies' Association and Federation of European Biochemical Societies for sponsoring my participation in national and international scientific meetings and courses that allowed me to present part of this work and enrich my scientific background.

I want to thank *Centro de Química-Física Molecular* / Institute for Bioengeneering and Biotechnology at *Instituto Superior Técnico* (CQFM/IBB at IST) for receiving me and providing the working conditions to carry out this project and to all the present and past colleagues that went through it. To Prof. Manuel Prieto for letting me be a part of the Biological Fluorescence group, 8 years ago – that in the meanwhile evolved to group III – and for the dedication, knowledge and enthusiasm in this work. I would also like to thank Sandra Pinto and Fábio Fernandes, for the kind words and the incentives over the years.

I want specially and mostly to thank Prof. Ana Coutinho. I fulfilled the dream of working with her. Thank you for the supervision and all that came with it, for the inspiration, the sharing and the companionship through these years. It's the end of an era. The little ruminator squirrel is going to miss the office 535.

To my 'juniors', Luís, Tânia Santos, Ester, Patrícia, Clara, Alexandre and Tiago, I will be your President Forever! It would have been a lot less fun without you. A special word goes for Lourdes Renart, impeccable person and colleague, and for my partner in crime, Paulo Caldas. Not only for dividing the load of work but for the incredible person you are. We have missed you both greatly.

To Tânia 'Xuxu' Patrícia, words can probably not describe our journey. Started together, struggled together, and (almost) finished together. I made a friend for life. The students 80104 and 80105 can finally rest and enjoy.

To my "godmother" Maria João, there is a common, mostly good, denominator in most of my adult life, and part of it was thanks to you. Let's go, *Portugália* is waiting for us.

I thank to the friends down the hall, Tiago Palmeira, Inês Mariz and Tânia Ribeiro. Especially, I would like to acknowledge all the times Inês stopped working to help me in the microscope. Thank you for the patience and for all the kind words you always have to offer.

I thank Gu for the Brazilian fun in those very fleeting months you were here.

“Team Portugal” rocked in every congress we were! Paulo, Marcelo, Bárbara, Mário, Ana, Tiago, I thank you for all the nice journeys we made together. To Nuno Santos, I thank his permission to use the resources in *Instituto de Medicina Molecular* but especially for the great memories outside work.

To Mariana, I thank not only the past life-saving advices regarding work, but also, and mostly, for the recent friendship. To Martin for the cheerful attitude and for the opportunity.

I thank my parents, Lourdes and Álvaro who are such nice people and work so hard they probably deserved much more than what life brought to them. I hope this gives them one more reason to smile. I thank my big sisters, for the door that is always open and for the unconditional love. To my brother’s in law, Flávio e Fernando, who watch me grow and to my 6 noisy, lovely and by now too big nieces and nephews, João, Natacha, Rafael, Rodrigo, Carolina and Isaac, that always put a smile in my face. I love you all. Also to my other half, the Faustino family. Especially Joana and Hugo, I thank you for being always a great company and I wish you two all the best!

I owe a word to the oldest friends for never letting that friendship feeling pass, even if we only get together twice a year.

To my beloved friends in solving board game crimes and so, so much more, Luís, Vasco and my “godchildren” Mário e Inês, thanks for the hours of support and laughter. The crime WAS in the office, you just didn’t know it! I also thank Teresa, Luciano, Inês and Tiago; I love how simple things are when I am with you.

And finally, a very special acknowledgment goes to André. Most of the time you were the reason I got out of the bed in the morning, to be a better person for you. And for the hard times coming, Thank you. Again. For everything.

Resumo

A conversão de péptidos/proteínas do seu estado nativo solúvel em depósitos fibrilhares ricos em folhas β é uma característica de várias doenças humanas. As membranas biológicas podem modular este processo in vivo, aumentando a sua complexidade. Neste trabalho, a calcitonina (CT) e o polipéptido amilóide dos ilhéus pancreáticos (IAPP) foram usados como modelos para se obter informação mecanística sobre a influência das membranas lipídicas aniónicas nas suas vias de fibrilhação. De modo a se obter informação estrutural e dinâmica sobre os intermediários oligoméricos formados, realizou-se um estudo biofísico comparado da agregação de uma variante humana amiloidogénica (hCT e hIAPP, respectivamente) e de um péptido controlo não-amiloidogénico (as sequências de salmão (sCT) e de ratinho (rIAPP), respectivamente). A conjugação dos péptidos com sondas fluorescentes permitiu ainda aplicar metodologias de fluorescência avançadas.

Inicialmente, realizou-se um estudo fotofísico comparado da sonda HL488 livre e das CTs conjugadas em meio homogéneo. Os decaimentos de anisotropia de fluorescência permitiram monitorizar detalhadamente as alterações conformacionais sofridas pelo HL488-hCT e HL488-sCT em misturas binárias trifluoroetanol/água. O período de latência da agregação da hCT em solução era proporcional à sua concentração, apoiando a ocorrência de um mecanismo de fibrilhação não canónico. A partição da sCT, mas não da hCT, para vesículas lipídicas aniónicas é maioritariamente controlada por interações electroestáticas. Foi ainda possível identificar um mecanismo de partição-oligomerização da sCT e detectar a formação de agregados do tipo H pela HL488-sCT.

As membranas aniónicas catalisam a fibrilhação do hIAPP na direcção da solução. Pelo contrário, a oligomerização do rIAPP está confinada à superfície das membranas. A saturação progressiva da interface membranar por rIAPP é acompanhada por uma diminuição do diâmetro médio das vesículas lipídicas. Estudos de TRES da sonda Laurdan revelaram que este efeito provavelmente é causado por uma desidratação/aumento da rigidez da interface causada pelo rIAPP.

Palavras-chave

Péptidos amiloidogénicos e não-amiloidogénicos; Fibrilhas amilóides; Membranas lipídicas aniónicas; Interação lípido-péptido; Espectroscopia e Microscopia de Fluorescência.

Abstract

The conversion of peptides/proteins from their native soluble states into β-sheet-rich fibrillar assemblies is the hallmark of several human diseases. Biological membranes can modulate amyloid fibril formation in vivo, increasing its complexity. Here, calcitonin (CT) and islet amyloid polypeptide (IAPP) were used as model polypeptides to obtain a mechanistic understanding of how anionic lipid membranes influence their fibrillation pathways. Comparative biophysical studies of the self-assembly of the human amyloidogenic (hCT and hIAPP, respectively) and a control non-amyloidogenic variant of each peptide (salmon (sCT) and rat (rIAPP) sequences, respectively) were performed to elucidate the structural and dynamic features of the oligomeric intermediates formed in each case. Fluorescent conjugates of the peptides were used to increase the scope of the applied advanced fluorescence techniques.

A comparative photophysical study of free HL488 dye and of the fluorescently-labelled CTs was first performed in homogeneous solution. The fluorescence anisotropy decays allowed tracking the one- and two-step α-helical folding transitions of HL488-sCT and HL488-hCT in trifluoroethanol/buffer binary mixtures, respectively. The lag time of hCT aggregation was proportional to the peptide concentration supporting the recent proposal that its fibrillation pathway follows a non-canonical mechanism. The partition of sCT towards anionic liposomes was mainly driven by electrostatic interactions, at variance with hCT. HL488-sCT formed membrane-bound H-type aggregates that can be related with sCT annular oligomers previously described.

The membrane-catalyzed fibrillation of hIAPP resulted in fibril growth into the solution. However, the membrane-mediated self-assembly of rIAPP was confined to the lipid bilayer. This process was accompanied by a remodeling of the lipid membranes since the progressive membrane saturation with rIAPP produced a reduction of the average size of the anionic liposomes. This effect is probably related with an increased rigidity/membrane surface dehydration caused by rIAPP binding and oligomerization on the membranes as revealed by a TRES study of Laurdan.

Keywords

Amyloidogenic and non-amyloidogenic peptides; Amyloid fibrils; Anionic lipid membranes; Lipid-peptide interaction; Fluorescence spectroscopy and microscopy.

Abbreviations

The acronyms used are expanded on first usage and whenever seemed necessary to improve clarity. For reasons of text economy very common acronyms, scientific or not (such as “RNA” or “USA”), are not expanded nor described. Amino acid residues and sequences are indicated using the one or three-letter code.

1PE: One-photon excitation
2PE: Two-photon excitation
A488: Alexa Fluor 488 carboxylic acid, succinimidyl ester
AC: Autocorrelation
AD: Alzheimer’s disease
AFM: Atomic force microscopy
AH: amphipathic helix
APD: Avalanche photodiode
Atto488: Atto488 NHS Ester
Atto488-hIAPP: fluorescently labeled human IAPP with Atto488
Atto488-rIAPP: fluorescently labeled rat IAPP with Atto488
Au: arbitrary units
Aβ peptide: Amyloid β peptide
Aβ40: Amyloid β peptide with 40 residues
Aβ42: Amyloid β peptide with 42 residues
bCT: bovine calcitonin
BLM: Black lipid bilayer membranes
BSA: Bovine serum albumin
CD: Circular dichroism
Chol: cholesterol
CLSM: Confocal laser scanning microscopy
CGRP: calcitonin gene-related peptide
CT: calcitonin
CTR: CT receptor
DLS: Dynamic light scattering
DHPC: 1,2-dihexanoyl-sn-glycero-3-phosphocholine
DMPC: 1,2-dimyristoyl-sn-glycero-3-phosphocholine
DMPG: 1,2-Dimyristoyl-sn-glycero-3-phosphorylglycerol
DMSO: Dimethyl sulfoxide
DOPC: 1,2-dioleoyl-sn-glycero-3-phosphocholine
DOPG: 1,2-dioleoyl-sn-glycero-3-phosphoglycerol
DOPS: 1,2-dioleoyl-sn-glycero-3-phosphoserine
DPC: Dodecylphosphocholine
DPPC: 1,2-dipalmitoyl-sn-glycero-3-phosphocholine
DPPG: 1,2-Dipalmitoyl-sn-glycero-3-phosphoglycerol
EDTA: ethylenediamine-N,N,N’,N’-tetraacetic acid
eCT: eel calcitonin
E_{FRET}: FRET efficiency
EM: Electron microscopy
EPR: Electron paramagnetic resonance
FA: Fluorescence anisotropy
FAIM: Fluorescence anisotropy imaging microscopy
FCS: Fluorescence correlation spectroscopy
FLIM: Fluorescence Lifetime Imaging Microscopy
FRET: Förster resonance energy transfer
FWHM: Full width at half-maximum
GFP: Green fluorescent protein
GM1: Monosialoganglioside GM1
GP: Generalized polarization
GUVs: Giant unilamellar vesicles
hCT: human calcitonin
HEPES: 4-(2-hydroxyethyl)-1-piperazineethanesulfonic acid
HFIP: 1,1,1,3,3,3-hexafluoro-2-propanol
hIAPP: Human islet amyloid polypeptide
HL488: HiLyte ™Fluor 488
HL488-hCT: fluorescently labeled human calcitonin with HL488
HL488-sCT: fluorescently labeled salmon calcitonin with HL488
HTV: High tension voltage

IAPP: islet amyloid polypeptide
IC: internal conversion
IDPs: Intrinsically disordered proteins
IR: Infrared spectroscopy
IRF: Instrument response function
L/P: Lipid-to-peptide/protein molar ratio
Laurdan: 6-dodecanoyl-2-dimethylaminonaphthalene
LDS 751: 6-(dimethylamino)-2-[4-[4-(dimethylamino)phenyl]-1,3-butadienyl]-1-ethyl, perchlorate
LPB: low-protein binding
LUVs: Large unilamellar vesicles
MD: Molecular dynamics
MHKS: Mark–Houwink–Kuhn–Sakurada
MP: Multiphoton
MS: Mass spectrometry
MW: Molecular weight
NA: numerical aperture
NAYA: *N*-acetyl-*L*-tyrosinamide
NIBS: non-invasive backscatter detection
NMR: Nuclear magnetic resonance
PBS: Double polarizing beam splitter
PC/PhC: Phosphatidylcholine
PDB (ID): Protein Data Bank (identification)
pCT: porcine calcitonin
PdI: Polydispersity index
PE: phosphoethanolamine
PET: photon-induced electron transfer
PFG-NMR: Pulsed-field gradient-nuclear magnetic resonance
PG: phosphorylglycerol
PI: phosphatidylinositol
PMT: photomultiplier
POPC: 1-palmitoyl-2-oleoyl-sn-glycero-3-phosphocholine
POPE: 1-palmitoyl-2-oleoyl-sn-glycero-3-phosphoethanolamine
POPG: 1-palmitoyl-2-oleoyl-sn-glycero-3-phosphoglycerol
POPS: 1-palmitoyl-2-oleoyl-sn-glycero-3-phosphoserine
PS: phosphatidylserine
PTA: phosphotungstic acid
PTH: Parathyroid hormone
RAMPs: receptor activity-modifying proteins
RCF: Raw correlation function
RhodB: Rhodamine B
Rhod110: Rhodamine 110
Rhod6G: Rhodamine 6G
Rhod-DOPE: 1,2-dioleoyl-sn-glycero-3-phosphoethanolamine-N-(lissamine rhodamine-B-sulfonyl)
rIAPP: rat islet amyloid polypeptide
RP-HPLC: reversed-phase high performance liquid chromatography
RT: room temperature
S/N: signal-to-noise ratio
sCT: salmon calcitonin
SD: standard deviation
SDS: Sodium dodecyl sulfate
SE: Succinimidyl ester
SLBs: Supported lipid bilayers
SLD: scattering length density
SM: Sphingomyelin
SOPC: 1-stearoyl-2-oleoyl-sn-glycero-3-phosphocholine
SR: solvent relaxation
SR 101: Sulforhodamine 101
ssFA: steady-state fluorescence anisotropy
SUVs: Small unilamellar vesicles
T2DM: Type II diabetes mellitus
TCSPC: Time-Correlated Single-Photon Counting technique
TDFS: time-dependent fluorescence shifts
TEM: Transmission electron microscopy
TFE: 2,2,2-Trifluoroethanol
ThT: Thioflavin T
TRES: time-resolved emission spectra
UCSF – University of California, San Francisco (USA)
UV – Ultraviolet

Outline

The main goal of this work was to use model polypeptides to study the modulation of amyloid pathologies by accessory cellular components, namely lipid membranes. Several studies have shown that membrane surfaces can act as catalysts that promote the aggregation of membrane-bound amyloidogenic polypeptides. On the other hand, accumulated evidence supports the hypothesis that cell membranes are also a target of the cytotoxic species formed. Prefibrillar intermediates assembled along the polypeptide fibrillation pathway, rather than the final mature amyloid fibrils themselves, seem to be the primary species responsible for triggering the pathological processes that lead to disease due a disruption of the membrane structural integrity. However, the exact mechanism (pore formation, carpeting or detergent-like effect) by which these amyloidogenic polypeptides induce membrane permeabilization is not yet fully understood. To address this question, human calcitonin (CT) and islet amyloid polypeptide (IAPP) were chosen as models peptides to examine the possible influence that anionic lipid membranes exert on their self-assembly pathways. In each case, a non-amyloidogenic variant (salmon CT and rat IAPP, respectively) was studied in parallel to the amyloidogenic human sequence since they are mechanistically-informative as their membrane-bound oligomers do not progress to fibrils. Using a multi-probe fluorescence approach, in combination with a complementary set of biophysical techniques, we aimed to obtain detailed structural and dynamic information about the membrane-induced oligomerization/ amyloid fiber formation pathways of these peptides, and their ability to perturb membrane organization.

This dissertation is divided in 5 chapters. The first chapter includes an overview of the amyloidogenesis thematic, including a general description of protein fibrillation kinetics and amyloid fibril structure. The second part of this chapter focuses on the dual role played by lipid membranes on amyloidogenesis, as they act both as a template and a target of the cytotoxic intermediates formed along the protein/peptide fibrillation pathway, with minor notes on other accessory cellular components. Chapter 2 presents the implementation and calibration of a recently installed two-photon fluorescence anisotropy imaging (FAIM) setup in the host lab, which was used in the characterization of some of the systems studied in Chapter 4. The experimental studies performed with the selected CT and IAPP variants are presented in detail in Chapters 3 and 4, respectively. Each of these chapters begins with a brief introduction to the amyloidogenic/non-amyloidogenic pair of peptides to be studied, including information on their structures and their tendency to fibrillate and interact with lipid

membranes. In the final chapter, an overall conclusion of the developed work is presented, together with suggestions of further testable hypotheses and future perspectives.

The work presented in this thesis was supported by FCT/MCTES *via* grant SFRH/BD/95856/2013 and projects PTDC/BBB-BQB/2661/2012 and FAPESP - FCT (FAPESP/20107/2014). The work was carried mainly at CQFM/IBB in IST under the joint supervision of Prof. Ana Coutinho and Prof. Manuel Prieto. The individual credits to others investigators that contributed to the development of this work are detailed in the Overview section at the beginning of each chapter.

1. General introduction

1.1. Protein Folding and Amyloidogenesis

All proteins begin their existence on a ribosome as a linear sequence of amino acid residues (Figure 1.1). Polypeptides fold during and following its synthesis to acquire a specific three-dimensional native conformation via the establishment of intramolecular contacts and, thus, acquire its function. It is believed that the information for the tertiary structure of proteins is contained in its amino acid sequence, since each amino acid has a certain propensity to take up a specific secondary structure, like α-helices or β-sheets (Nelson and Cox, 2005). Protein folding is a complex process that does not follow a specific pathway but presents different routes consisting of a series of sequential steps between increasingly native-like conformations, until the final native structure is adopted (Figure 1.1). The global free energy of the system progressively decreases with the adoption of a more ordered structure until it reaches an energy minimum in the native three-dimensional conformation (Turoverov *et al.*, 2010). The possible factors that modulate the features of the protein free energy landscape are the amino acid sequence, post-translational modifications, chaperons, ligands, cofactors and environmental conditions (Nelson and Cox, 2005; Knowles *et al.*, 2014).

Nevertheless, a range of proteins are considerably unstructured in their native state and are described as intrinsically disordered proteins/peptides (IDPs) (Lee *et al.*, 2014). Several studies revealed that some proteins are capable of fulfilling their specific functions without a defined globular structure. This lack of a more ordered structure makes possible the establishment of diverse interactions with numerous binding partners (Turoverov *et al.*, 2010) with some of them folding to more ordered structures after these interactions. Unlike globular proteins, the energy landscapes of IDPs do not show one deep local minimum but are much shallower, with many minima without intrinsic large energy barriers (Uversky, 2013). Thus, these proteins can easily sample many conformations depending on its ligands and environmental conditions.

All states available to a peptide/protein are controlled by a series of sophisticated cellular quality control mechanisms. Although the environment in which these polypeptides function and their amino acid sequence evolved to maintain them in a functional soluble state, in some circumstances they might turn into oligomeric/aggregated toxic species. Intra- or extracellularly, misfolding can occur if a specific peptide or protein fails to adopt or maintain its native functional conformational state (Dobson, 1999).

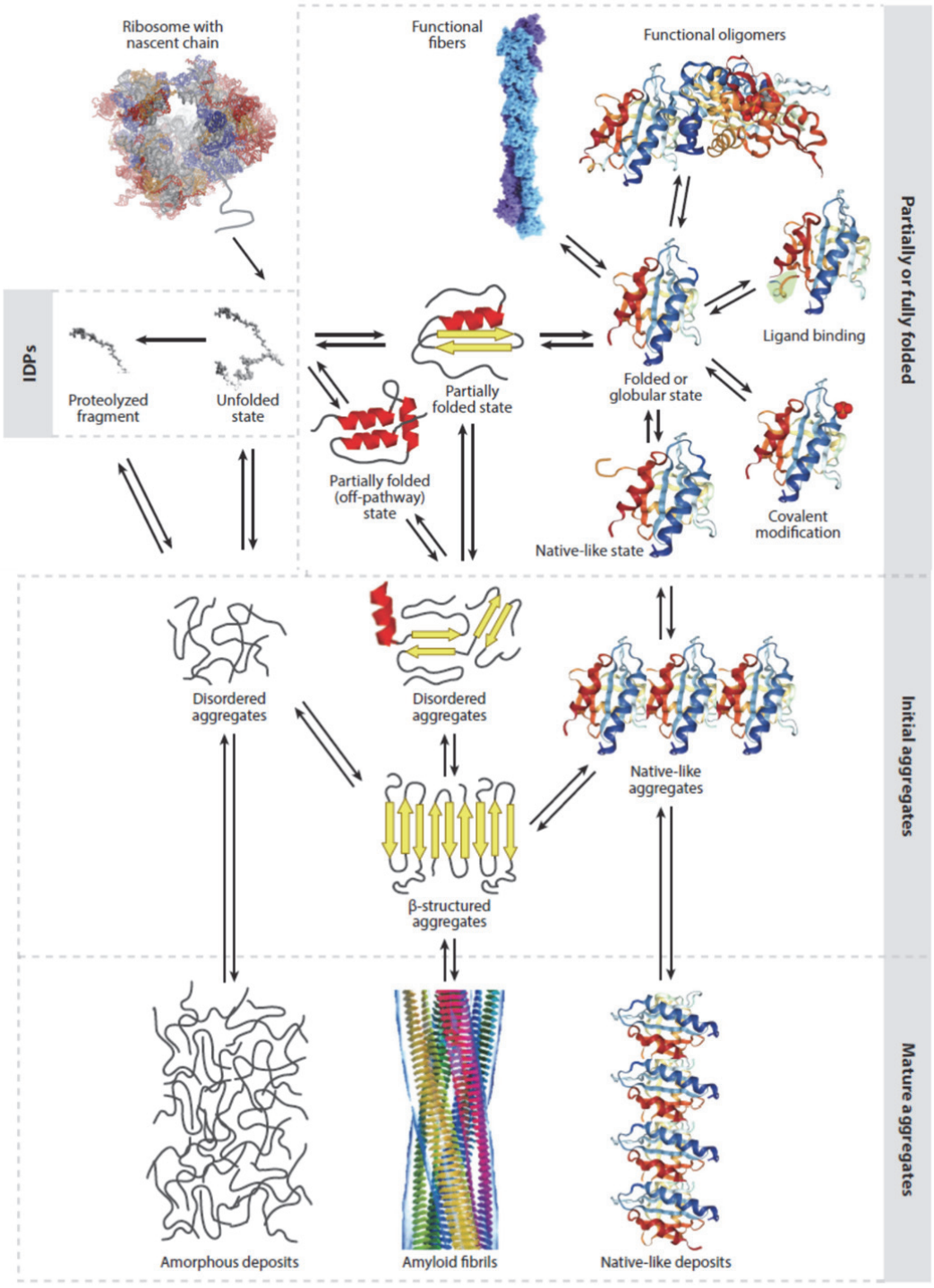

Figure 1.1 - Schematic illustration of the multiplicity of conformational states that can be adopted by a polypeptide chain following its biosynthesis and the possible transitions between the different states. Boxes include intrinsically disordered proteins (IDPs), partially or fully folded proteins, initial aggregates, and mature aggregates, respectively. All these conformational states and their interconversions are carefully regulated in the biological environment by means of the proteostasis network. Protein aggregation can result in the formation of amyloid fibrils (bottom, center), native-like deposits (bottom, right), or amorphous deposits (bottom, left), all of which are associated with pathological states when they are formed in an uncontrolled manner. Adapted from (Chiti and Dobson, 2017).

A variety of pathological conditions in humans (Table 1.1) are associated with a diminishing availability of the protein to play its normal role or with the conversion of specific peptides/proteins into aggregates (Chiti and Dobson, 2006). In this last case, the misfolding events can often result in a gain of toxicity. No curative treatment is yet available for these amyloid diseases. Most approaches act to control the symptoms and are drug- or immunotherapy-based (Briggs *et al.*, 2016; Valera and Masliah, 2016; Valera *et al.*, 2016).

IDPs are a class of particular interest regarding protein deposition disorders with examples such as Amyloid-β (Aβ) peptides, involved in Alzheimer's disease (AD), islet amyloid polypeptide (IAPP) in Type II diabetes mellitus (T2DM) and α-synuclein in Parkinson's disease. In contrast to globular proteins, IDPs are intrinsically ready for intermolecular interactions that might lead to aggregation, whereas the former need to partially unfold prior to self-assembly (Turoverov *et al.*, 2010; Relini *et al.*, 2013; Knowles *et al.*, 2014). The species formed in the initial steps of aggregation are relatively small (i.e. constituted by a few peptide/protein monomers), unstable and with weak interactions, probably remaining in equilibrium with soluble species. As aggregation proceeds, depending on the pathway, the aggregates may become amorphous deposits, ordered filamentous structures, or native-like deposits (Figure 1.1, bottom panel).

Table 1.1 – Human diseases associated with the formation of extracellular amyloid deposits or intracellular inclusions with amyloid-like characteristics. Adapted from (Chiti and Dobson, 2006).

Disease	Aggregating protein or peptide	Number of residues[a]	Native structure of protein or peptide[b]
Alzheimer's disease[c]	Amyloid-β peptide	40 or 42	Natively unfolded
Parkinson's disease[c]	α-synuclein	140	Natively unfolded
Lysozyme amyloidosis[d]	Mutants of lysozyme	130	α+β, lysozyme fold
Type II diabetes mellitus[c]	Islet amyloid polypeptide	37	Natively unfolded
Medullary carcinoma of the thyroid[c]	Calcitonin	32	Natively unfolded

[a] Number of residues of the processed polypeptide chains that deposit into aggregates.
[b] According to Structural Classification of Proteins.
[c] Predominantly sporadic, although in some cases hereditary forms associated with specific mutations are well documented.
[d] Predominantly hereditary, although in some cases sporadic forms are documented.

Amyloidosis is by definition any pathological state associated with the formation of extracellular amyloid deposits. This definition, and also the term “amyloid”, have been generalized to include some intracellular inclusions, morphologically and structurally related to the fibrils, associated with Parkinson’s and Alzheimer’s diseases, like the Lewy bodies or the neurofibrillary tangles, respectively. It has also been further extended to include synthetically obtained protein fibrils with some amyloid properties (Chiti and Dobson, 2006; Sipe *et al.*, 2010).

However, being disordered or aggregated is not necessarily a synonym of disease. Living systems evolved and apparently some fibrillar assemblies are physiologically useful. The first example of a functional amyloid fiber was demonstrated in *E. coli* and other Gram-negative bacteria, that produce a functional amyloid fiber called curli (Hammer *et al.*, 2008; Maji *et al.*, 2009). Others have been found in yeast, fungus and even some human structures, like the p-mel organization in melanosomes. Also, the polypeptide hormones organization when stored in secretory vesicles seem to have an amyloid fibril structure (Chiti and Dobson, 2006; Hammer *et al.*, 2008; Sipe *et al.*, 2010).

There are accumulating evidences which support the hypothesis that structural transformation of a polypeptide chain into a partially folded conformation, with some structural flexibility, is a critical prerequisite for fibril formation (Kelly, 1998; Rochet and Lansbury, 2000; Gorbenko and Kinnunen, 2006), but this process can also occur from native-like conformations (Chiti and Dobson, 2009). To date, there are 37 peptides or proteins that have been found to form amyloid deposits in human pathologies (Chiti and Dobson, 2017) with a third of them having a defined fold in the native state and a third being IDPs. These diseases are normally grouped in three major classes, depending on where the accumulation of fibrils take place: (i) neurodegenerative diseases, where the formation of amyloid occurs in the brain e.g. AD; (ii) non-neuropathic localized amyloidosis, in which the aggregation occurs in other type of tissue rather than the brain e.g. T2DM, deposition of IAPP in the pancreas; and (iii) systemic amyloidosis, in which aggregates are found in a range of tissues, including kidney, liver, spleen and heart e.g. a series of systemic amyloidosis caused by the accumulation of Apolipoproteins A or C, or fragments of those proteins (Chiti and Dobson, 2017).

Protein aggregation is not promoted by the least ordered regions but by particular aggregation-prone sequences, such as those having a high hydrophobicity (Relini *et al.*, 2013). There are particular short (4–10 residues) segments of proteins which are capable of forming amyloid-like fibrils (Balbirnie *et al.*, 2001; Nelson *et al.*, 2005). An experiment performed by Goldschmidt and co-workers observed that the sequence is more important that residue composition in determining propensity for formation of amyloid-like fibrils. This

means that when the sequence of a fibrillating segment is shuffled, the rearranged sequence loses its tendency to form fibrils. Conversely, when the sequence of a non-fibrillating segment is rearranged to one with a higher tendency for fibrillation, it can convert to a fibril (Goldschmidt *et al.*, 2010). Also, the predisposition to form ordered aggregates is not just associated with disease-causing proteins but to almost any protein when subjected to the appropriate environmental conditions, e.g. temperature, ionic strength, pH, etc (Chiti *et al.*, 1999; Gorbenko and Kinnunen, 2006; Aso *et al.*, 2007), especially the ones that favor non-covalent interactions within the polypeptide chain, in particular hydrogen bonding.

1.2. Protein fibrillation kinetics and amyloid fibril structure

Protein fibrillation is an extremely complex process, commonly involving kinetic competition between formation of amorphous aggregates and fibrillar species, a variety of intermediates, multiple conformational states, and a number of filamentous forms (Knowles *et al.*, 2014). The experimentally observed sigmoidal profile characteristic of a fibrillogenesis kinetics is usually interpreted as a Nucleation-Dependent Polymerization model (Figure 1.2 A), in which protein assembling into fibrillar structures can be divided in three stages: (i) the initial slow nucleation (*lag phase*) where the monomers associate into a critical oligomeric nucleus, being the highest energy state and thus the thermodynamically unfavorable species along the polymerization pathway, followed by (ii) an *elongation phase*, where the elongation of the nucleus via the attachment of additional monomers becomes energetically favorable, thereby resulting in exponential fibril growth, leading to a (iii) a *plateau phase*, dominated by mature and large amyloid fibrils (Gorbenko and Kinnunen, 2006; Butterfield and Lashuel, 2010) (Figure 1.2 B). In vivo, this last theoretical situation would never occur, since the cells would keep producing the peptide in question and new molecules would be added to existing deposits or new sites of amyloid formation would be created (Raleigh *et al.*, 2017). The process is time-dependent and proceeds through the formation of dimers, trimers, tetramers and different kinds of proto-fibrils until reaching the final insoluble fibrillar structure. The rate of amyloid formation was found to be promoted by the addition of preformed fibrils for several amyloid proteins (seeding experiments) (Hamada and Dobson, 2002), a finding indicative of a nucleation-dependent process.

Secondary processes are also important for the kinetics of protein aggregation, such as the fragmentation of a growing fiber or secondary nucleation, with the surface of a forming fiber acting as nuclei and catalyzing the formation of new clusters of monomers (Padrick and Miranker, 2002; Knowles *et al.*, 2014; Chiti and Dobson, 2017). These two processes can be dominant in contributing to the rapid fibril growth during the elongation phase (Knowles *et al.*, 2009; Arosio *et al.*, 2015).

Independently of amino acid sequence, one of the striking characteristics of the amyloid fibrils is that they are structurally very similar. Normally, each filament is displayed in a way that the polypeptide chain forms β-sheets that are perpendicular to the long axis of the fibril (Figure 1.2 B) (Rochet and Lansbury, 2000; Dumoulin *et al.*, 2005; Biancalana and Koide, 2010; Groenning, 2010). On the other hand, backbone hydrogen bonds are parallel to the axis and stabilize the overall structure. Fibrils will adopt the structure that is of lowest free energy and/or the most kinetically accessible. These structures are very stable and are typically protease resistant, which contributes to the difficulty presented by cells in eliminating these deposits (Chiti and Dobson, 2006). They are also detergent-insoluble and can bind some molecular probes such as the classical markers Thioflavin T and Congo Red, which are largely used to study amyloid fibril formation. Still, even before molecular structures of amyloid fibrils started to emerge, the idea that there was a significant morphological variation between fibrils formed by the same peptide or protein had already been accepted. These variations may be linked to different arrangements in the position and orientation of the proteins within the fibrils (Chiti and Dobson, 2006; Knowles *et al.*, 2014).

Several 3D and structural models have been obtained for amyloid fibrils from different sources, from techniques such as Transmission Electron Microscopy (TEM) or cryo-electron microscopy (Schmidt *et al.*, 2009), nuclear magnetic resonance (NMR) (Tycko, 2011) and X-ray crystallography (Nelson *et al.*, 2005).

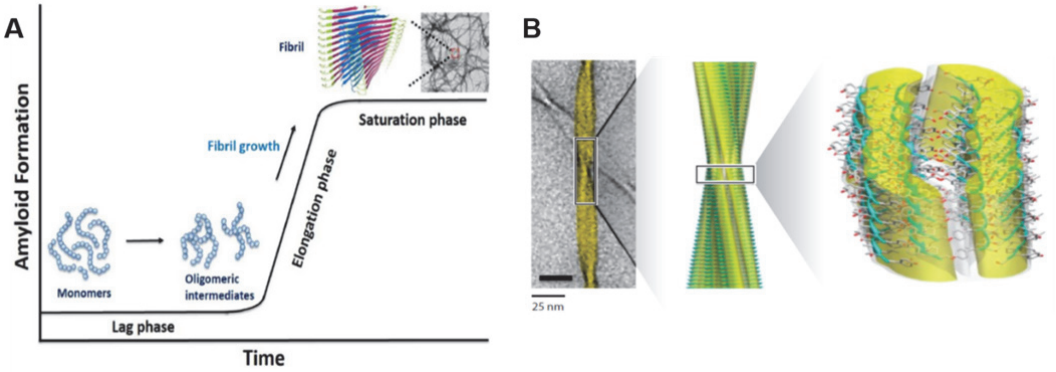

Figure 1.2 – Experimentally observed sigmoidal profile characteristic of a fibrillogenesis kinetics and the resulting fibrils. (**A**) Schematic diagram of a Nucleation-Dependent Polymerization model to describe fibril formation, with the lag, elongation and saturation phase. For more details see the text. (**B**) Representative structure of a six-protofilament fibril described for a peptide corresponding to residues 105-115 of transthyretin. Adapted from Fitzpatrick *et al.*, 2013 and Raleigh *et al.*, 2017.

The full knowledge of the amyloid formation pathway is far from being totally understood, as this would require structural elucidation of every species and the determination of the kinetics of interconversion of all species on the reaction pathway. It is difficult to achieve this goal due to the expected large variety of intermediates that are formed transiently and in small quantities that are often too difficult to be detected by the techniques available. This can be really challenging, especially since there is a variety of proteins causative of conformational diseases that may not facilitate or allow the development of a general methodology to isolate and/or to study all the intermediates, independently of their nature. It is still unclear which conformational species is a direct precursor of fibril formation, but it has been accepted that there must be the involvement of partially folded structures that successively accumulate in solution (Lundberg *et al.*, 1997; Raffen *et al.*, 1999; Blackley *et al.*, 2000).

There are increasing evidences that the unfolded, metastable intermediates or oligomers, which exist transiently in the protein aggregation/folding pathways are the likely origins of pathological behavior rather than the mature amyloid fibrils (Aisenbrey *et al.*, 2008; Hebda and Miranker, 2009; Kinnunen, 2009; Butterfield and Lashuel, 2010), probably because they interact with biological membranes, as it will be discussed later on. It has been proved that oligomers and/or pre-fibrillar amyloid assemblies of different amyloid proteins (e.g. Aβ peptides, α-synuclein and huntingtin) are either cytotoxic or neurotoxic. They share a surprising structural and functional similarity which might suggest that a shared structural feature is at the basis of their toxicity (Conway *et al.*, 2000; Poirier *et al.*, 2002; Relini *et al.*, 2004; Cleary *et al.*, 2005; Chimon *et al.*, 2007; Ono *et al.*, 2009; Ahmed *et al.*, 2010). Mature amyloid fibrils however cannot be considered completely inert, as they can act as a catalyst for generating new toxic oligomers through secondary nucleation and their accumulation in non-neuropathic amyloidosis affect organ integrity (Chiti and Dobson, 2017). One astonishing finding came from the study of Martins and co-workers, where Aβ42 mature amyloid fibrils were reversed to soluble toxic species towards primary cultures of neurons after incubation with biological relevant lipids, including lipid extracts from a cow brain (Martins *et al.*, 2008). The lipids tested included pure 1,2-dioleoyl-sn-glycero-3-phosphocholine (DOPC), and mixtures of DOPC, 1,2-Dimyristoyl-sn-glycero-3-phosphorylglycerol (DMPG), cholesterol (Chol), sphingomyelin (SM), monosialoganglioside GM1 (GM1) and the brain total extract. They found similar features in terms of biophysical, cell biological and behavioral assays for these “backward” protofibrils when compared to the “forward” protofibrils. This study strongly suggests that amyloid plaques should not be considered inert in the amyloid process.

1.3. The role of lipidic membranes on amyloidogenesis

In vitro fibrillation kinetic studies of peptides/proteins are a simplified model of the biological process that occurs in vivo. However, there are more and more indications that accessory cellular components play a crucial role in the facilitation and/or induction of the adoption of unfolded and metastable intermediates that initiate amyloidogenesis. The deposits found in patients that suffer from any amyloid disease are not only composed by the specific proteins which normally forms the core of the deposit but also by other components such as collagen, apolipoprotein E, serum amyloid P component, metal ions, glycosaminoglycans (GAGs) or specific lipids. This has already been demonstrated for different types of amyloidosis, namely serum amyloid A amyloidosis, transthyretin amyloidosis, λ light chain amyloidosis, κ light chain amyloidosis and in the prion protein-dependent amyloidosis (Klein *et al.*, 1998; Kyle, 2001; Alexandrescu, 2005; Gellermann *et al.*, 2005; Chiti and Dobson, 2006; Ryan *et al.*, 2008). These findings lead to an extensive line of research dedicated to study how biological factors like lipid membranes modulate amyloid polypeptides assembly into cytotoxic species (Gorbenko and Kinnunen, 2006; Aisenbrey *et al.*, 2008; Hebda and Miranker, 2009; Kinnunen, 2009; Butterfield and Lashuel, 2010).

The composition of the cellular membrane is extremely complex (Figure 1.3). There is a wide variety of membrane proteins, glycosaminoglycans on the surface of cells or in the extracellular matrix of multicellular organisms, either covalently linked to the protein core of proteoglycans or as free macromolecules, and hundreds of different lipids species with differing head groups and unsaturation of the acyl chains that can be found in different cells (García-Sáez and Schwille, 2010; Lopez and Koch, 2017). Cellular membranes have both functional and structural roles and must be stable enough to maintain a permeability barrier while being sufficiently fluid to sustain changes in shape or volume, which allows the different cellular processes to occur.

Interactions between lipids and proteins play a key role in a multiplicity of cellular processes including energy conversion in the cell, control of membrane fusion, viral fusion processes, signal transduction, antimicrobial defense, hormone-receptor interactions and drug bioavailability across the blood-brain barrier (Gorbenko and Kinnunen, 2006; Kinnunen, 2009; Galdiero *et al.*, 2013). The chemical nature of the bilayer components and structural characteristics of the proteins/peptides in question are likely to be determinant in the mode and extent of the membrane binding of proteins. This will affect the structure, the dynamics, the orientation and position of peptides in lipid bilayer and their effects on surrounding lipids.

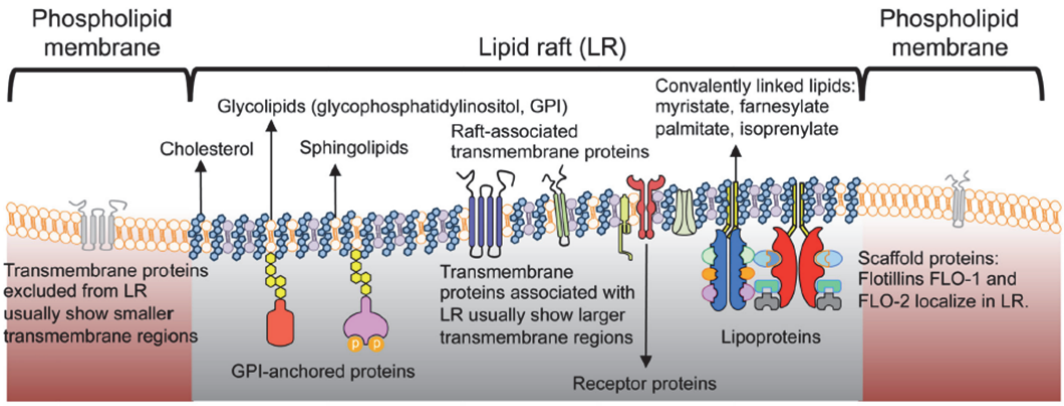

Figure 1.3 - Illustration of a membrane of a eukaryotic cell. Cell membranes are composed of very different lipids, regarding their lengths, charge and composition, as well as receptor proteins, which play a role in signaling pathways, lipoproteins and transmembrane proteins. Lipid rafts are characterized by being cholesterol and sphingolipid-enriched microdomains, and eventually other components, that may exist transiently or permanently in cell membranes. Adapted from Lopez and Koch, 2017.

1.3.1. Lipids as the targets of toxic intermediates

Lipid membranes have a dual role in amyloidogenesis: they can serve as a catalyst that favors the formation of intermediates in the fibrillation pathway of a peptide/protein and be themselves the target of the toxic intermediates produced during this process. The cytotoxicity of these intermediates has been related to the permeabilization and/or disruption of membrane integrity and leakiness of cell membranes (Figure 1.4) allowing an uncontrolled flow of ions into the cell (particularly Ca^{2+}). These effects are not exclusive of amyloidogenic peptides, being intimately related with the action of antimicrobial peptides, cell-penetrating peptides or viral peptides (Domanov and Kinnunen, 2006; Butterfield and Lashuel, 2010; Nielsen and Otzen, 2010; Berthelot *et al.*, 2013). The influx of Ca^{2+} may be sufficient to trigger the permeability transition of the mitochondrial membrane, which leads to the generation of reactive oxygen species and the releasing of cytochrome *c*, which activates apoptotic signals that lead cells to death (Quist *et al.*, 2005; Hebda and Miranker, 2009; Kinnunen, 2009).

Membrane damage can represent a unifying explanation for all the cytotoxicity related with amyloid diseases, but finding a unique model that explains all the results is usually hampered by different peptide preparation protocols and experimental conditions used in each study. Different models have been proposed for the mechanism by which intermediates make the membranes permeable and it is likely that different mechanisms take action concurrently within the disruption of membranes (Williams and Serpell, 2011). The modes of action include the formation of membrane channels or pores, the carpeting effect, a detergent-like process and the raft model (Figure 1.4). In the first case, it has been

hypothesized that a subpopulation of doughnut-shaped oligomers or nonselective amyloid pores may explain the amyloid toxicity. The formation of membrane pores is also a common feature of amphipathic cationic peptides (Yandek *et al.*, 2007; Fuertes *et al.*, 2010). Small annular rings with a central pore have been identified by electron microscopy (EM), atomic force microscopy (AFM), among other techniques, in the fibrillation pathway of different proteins and peptides, namely for Aβ (Lin *et al.*, 2001; Inoue, 2008), calcitonin (Diociaiuti *et al.*, 2006) or IAPP (Zhao *et al.*, 2014). Quist and co-workers described the conformational changes undergone by Aβ40, α-synuclein, IAPP and others in the presence of reconstituted bilayer membranes. The peptides formed those ion-channel-like structures with ion-channel activity with slight structural differences between them, due to the intrinsic differences among peptides. These channels would weaken the selective permeability of cells and induce cell pathophysiology and degeneration in amyloid diseases (Quist *et al.*, 2005). Yoshiike and co-workers found a shared structural and functional homology between amyloid oligomers and pore-forming bacterial toxin, alpha-hemolysin and human perforin from cytotoxic T lymphocytes, which supports the idea that this mode of membrane destabilization is not exclusive of amyloidogenic peptides (Yoshiike *et al.*, 2007).

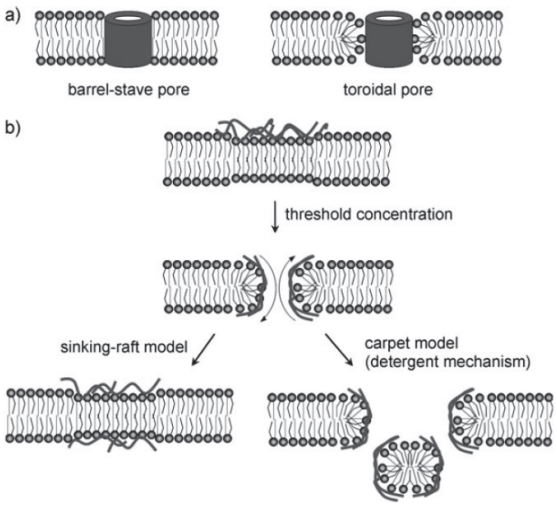

Figure 1.4 - Various models that may explain membrane destabilization and toxicity upon the interaction of intermediates of the fibrillation pathway or mature amyloids with membranes. a) Models for barrel-stave and toroidal pores. **b**) Representation of sinking-raft and carpet model associated with detergent mechanism. Adapted from Butterfield and Lashuel, 2010.

With the accumulation of peptide at the surface of the membrane, oligomeric species have been proposed to create two structural arrangements of pores (Figure 1.4 a). In a barrel-stave pore, it is considered that hydrophobic clusters from the peptides interact with the acyl chains of the lipids, while the hydrophilic ends of the peptides are oriented outwards of the

membranes. This causes leakage into and out of the membrane with minimal interference for the membrane architecture. For the metastable toroidal pores, the hydrophilic ends of the peptides remain in contact with the hydrophilic head of the phospholipids, leading to an induction of curvature of the membrane and eventually a collapse through the sinking-raft model or a detergent mechanism (Figure 1.4 B). In the first case, the pore splits and the bilayer is resealed, leaving peptides in the inner and outer sides of the membrane. In the latter, the membrane gets disintegrated in a detergent-like mechanism and lipids can be incorporated in aggregates/fibrils (Hebda and Miranker, 2009; Butterfield and Lashuel, 2010; Relini *et al.*, 2013).

The carpeting model is alternatively explained by the binding of oligomers or prefibrillar states to one leaflet of the membrane, normally oriented parallel to the surface, which causes an asymmetric pressure between the two leaflets. At lower peptide surface concentration this leads to the leakage of small molecules (Yandek *et al.*, 2007). At some critical threshold concentration, they cause the vesicle to disintegrate. This then might lead to a detergent-like effect, where again the amyloid precursor uptakes lipids from the membrane, leading to a membrane thinning or a possible total disruption of the vesicle or cell. Sparr and co-workers showed this effect for hIAPP: upon its interaction with DOPC giant unilamellar vesicles (GUVs), the vesicles were completely disrupted and lipids were incorporated into the emerging fibril (Sparr *et al.*, 2004). There are also reports of hIAPP fibrils lining up on the surface of vesicles. This distorts the structure of the vesicle, affecting the curvature and weakening the lipid packing, enabling leakage of the vesicle (Engel *et al.*, 2008). The fact that most of these different mechanisms appear to be at some point overlapped with others reveals very thin frontiers between the different mechanism and a difficulty in clearly defining a boundary among them (Hebda and Miranker, 2009).

1.3.2. Membranes as a 2D surface for peptide aggregation

In the context of amyloid diseases, the interaction of peptides/proteins with membranes is a key step in the adoption of protein conformations that might be aggregation-prone. Amyloid fibril formation can be extensively modulated by lipid-peptide/protein interactions by decreasing the energy barrier for protein unfolding, since the nucleation phase of amyloid fibril formation is thermodynamically unfavorable (Zhao *et al.*, 2004; Gorbenko and Kinnunen, 2006). In fact, in vitro studies have demonstrated that surfaces in general have an aggregation-inducing action and a direct role on the kinetics of aggregation. Membranes can act as an effective two-dimensional surface for the pathological conversion of amyloidogenic proteins/peptides into toxic intermediates and eventually amyloid fibrils (Zhao *et al.*, 2004; Bellotti and Chiti, 2008; Butterfield and Lashuel, 2010; Relini *et al.*,

2013). The principal factors responsible for the enhanced formation of fibrils when amyloidogenic proteins/peptides interact with membranes appear to be:

(i) stabilization by membranes of partially folded and flexible aggregation-prone protein confirmations;

(ii) increase, in a restricted volume, of the local concentration of the protein in the membrane, which favors not only the interactions among proteins and the conformational switching to β-sheet but also protein aggregation;

(iii) spatial restrictions allied to the promotion of particular disposition of the aggregating species relative to a lipid-water interface and;

(iv) variation in the depth of bilayer penetration that affects the nucleation propensity of the protein associated with the membrane (Gorbenko and Kinnunen, 2006; Aisenbrey *et al.*, 2008; Hebda and Miranker, 2009).

The changes in composition and physicochemical properties of lipid bilayer associated with aging or other physiological or pathological processes may increase the binding of proteins to membranes, setting off amyloidogenesis in vivo (Gorbenko and Kinnunen, 2006). The chemical characteristics of membranes are determinant for this catalysis. The lipid composition of membranes, including the length and degree of unsaturation of its phospholipid acyl chains, influences their lipid lateral packing density, bilayer curvature, degree of hydration and the net surface charge of the lipid bilayer (Hebda and Miranker, 2009). This largely affects the interaction between peptides/proteins and the membranes, ultimately shaping all the processes described above.

1.3.3. The importance of negatively-charged lipids

The anchoring of the aggregation-prone peptides to the anionic membrane is a shared feature among proteins/peptides and suggests a common mechanism for membrane-mediated misfolding and their subsequent self-assembly. The in vitro conversion from a disorder monomeric peptide to highly ordered amyloid fibrils has been extensively studied for IAPP, α-synuclein and Aβ peptides, providing substantial evidences for the importance of anionic lipids in the amyloidogenesis catalyzed by cellular membranes (Nath and Rhoades, 2013). Negatively-charged phospholipids have been implicated in the enhancement of amyloid fibril formation by amyloidogenic proteins and peptides, usually mixed with other phospholipids like phosphatidylcholine (PC) and phosphatidylethanolamine (PE).

Much of the basis for the importance of anionic lipids is that amyloidogenic peptides are normally positively charged. In general, the interaction of those peptides with the lipid

membrane is initiated by an electrostatic attraction to the anionic membranes. This will normally significantly increase the concentration of the peptide near the membrane surface, in a confined space. Upon reaching a critical surface coverage, hydrophobic interaction between aggregation-prone conformations are promoted and accelerate the cooperative formation of amyloid fibrils rich in a cross-β-sheet structure (Seelig, 2004). Peptides are usually in a random coil conformation in solution and will adopt an α-helical conformation upon their association with the lipid membranes. The adoption of secondary structure and thus the induction of α-helix when in contact with the membrane might arise from the need of the peptide backbone to form hydrogen bonds since the dielectric constant of the membrane is significantly lower than it is in solution (Jayasinghe and Langen, 2007). Membrane partitioning and self-assembly of the peptides are two coupled equilibria, greatly influenced by the lipid-to-protein/peptide molar ratio (L/P). These ratios govern the fractional population of aqueous and membrane-bound monomeric and oligomeric species present in the system. At high L/P ratios, it is likely that the intermediate α-helices formed are stabilized and inhibit the formation of β-sheet, in the absence of intermolecular contacts. At low L/P, where the concentration of peptides is exceedingly high in a confined space, the interactions among different peptides are favored and the conversion to β-sheet rich structure is boosted (Butterfield and Lashuel, 2010; Melo *et al.*, 2013; Fernandes *et al.*, 2015).

Specific lipids can also be relevant for the process of amyloidogenesis. Depending on the membrane composition, groups of specific lipids may aggregate into patches with physical properties distinct from those of other membrane domains, like lipid rafts. Rafts are liquid-ordered microdomains that have been associated with many biological processes including membrane traffic and signaling, endocytosis and exocytosis, viral assembly and budding, among others (Simons and Ikonen, 1997; Wakabayashi and Matsuzaki, 2009).

These domains are highly dynamic and enriched in sterols such as Chol and sphingolipids, like SM (Simons and Sampaio, 2011). The depletion of these components frequently leads to a loss of membrane organization and protein function as a consequence of the destruction of lipid rafts. Chol is a versatile molecule that is universally present in large amounts (30-40%) in the plasma membrane of eukaryotic cells (Tong *et al.*, 2009). It determines the biophysical properties of cellular membranes, having the unique ability to increase lipid order in fluid membranes, while maintaining fluidity and diffusion rates (Mouritsen and Zuckermann, 2004).

The influence of Chol and SM in amyloid formation is controversial since one can find in literature authors claiming that it has a protective role against fibrillation, while others present results towards these lipids promoting peptide/protein fibrillation, leading to

impairment in the membranes (Gorbenko and Kinnunen, 2006; Kinnunen, 2009; Caillon *et al.*, 2013). Any alteration in Chol homeostasis has been pointed as a primary cause of several neurodegenerative diseases (Kakio *et al.*, 2003). The relation between cholesterol content, the formation of aggregates and cytotoxicity requires more extensive research. Nevertheless, the data presently available indicate that, in general, the presence of Chol in the cell membrane may have an impact on conformational changes of determined proteins/peptides and that an increased cholesterol content, which rigidifies the membrane, may protect the cell membranes from the interaction with intermediates and reduce the perturbation of membrane integrity, diminishing the toxicity (Stefani, 2012).

Both human calcitonin (hCT) and human IAPP (hIAPP) are IDPs, potentially amyloidogenic and involved in human diseases. These peptides have variants from different species that are non-amyloidogenic. This feature makes them suitable for (i) investigating the differences among variants that cause their aggregation/ fibrillation in solution and (ii) to directly assess the influence of mimetics of the biological environment in this process.

2. Implementation of a two-photon fluorescence anisotropy imaging setup

2.1. Overview

Fluorescence anisotropy imaging microscopy (FAIM) is an increasingly expanding powerful tool that combines anisotropy measurements to fluorescence microcopy, providing spatial resolution to an additional contrasting readout of the system under study. Herein, we describe the implementation and calibration of a two-photon excitation FAIM setup which was performed in the scope of the discipline “Técnicas (e Metodologias) Experimentais Avançadas “, as a part of the PhD program.

The need to take into account the fluorescence depolarization that results from the use of high numerical aperture objectives was first addressed by performing calibration measurements with a set of Rhodamine B aqueous glycerol solutions. Steady-state fluorescence anisotropy (ssFA) images for the fluorescent dye free in solutions of variable viscosity were calculated on a pixel-by-pixel basis using a customized MATLAB script. The ability of ssFA imaging to resolve spectrally similar particles was then confirmed using the 2.5 μm Inspeck™ Microscope Image Intensity Calibration beads. The 10, 30 and 100% reference fluorescent microspheres used present similar emission spectra but distinct values of FA each due to an efficient homo-FRET process among the encapsulated dye. Overall, the FAIM setup were considered operational at the imaging level since the averages of the steady-state anisotropy distributions retrieved from each field of view were close to the experimental values obtained in control cuvette measurements performed in a spectrofluorometer.

The installation of the system was made by Dr. Aleksander Fedorov and Dr. Maria João Sarmento, which was also involved in an initial optimization and calibration of the system. The experimental design and data analysis was shared by me and Prof. Ana Coutinho. The laboratory work was performed by me. The MATLAB script used to analyze the FAIM images was written by Dr. Fábio Fernandes.

Prof. Ana Coutinho and Prof. Manuel Prieto supervised the work.

2.2. Introduction

Fluorescence anisotropy (FA) measurements are based on the principle of photoselective excitation of fluorophores by linearly polarized light. Photoselection is the process by which fluorophores are preferentially excited if their absorption transition dipole moment is more parallel to the electric vector of the polarized excitation light source. For a random distribution of molecules, the transition moment of each fluorophore has a defined orientation with respect to the molecular axis. The probability of absorption is dependent on a directional distribution function, f_i, proportional to the $\cos^{2i}\theta$, where θ is the angle between the plane of polarization of excitation and the absorption transition dipole moment, and i describes the use of one (1PE) and two-photon excitation (2PE) (Lakowicz, 2006). Accordingly, most of the excited fluorophores are aligned close to the z-axis (parallel to the vertically polarized excitation light) and very few have their transition moments oriented close to the x-y plane (Figure 2.1).

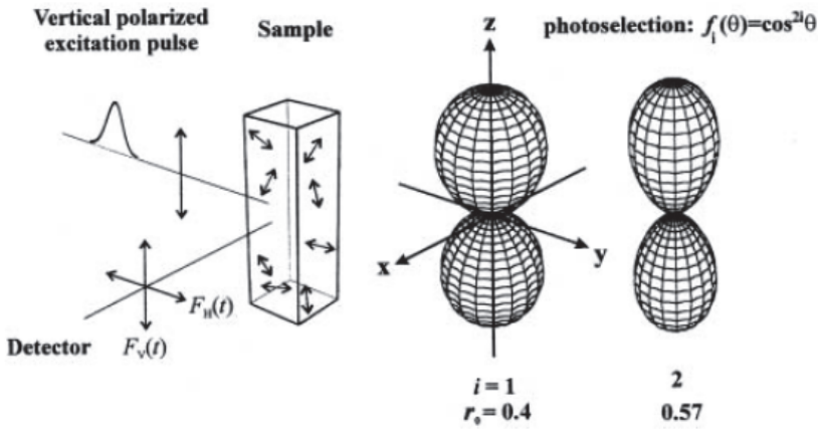

Figure 2.1 - Orientational distribution function $f_i(\theta)$ of excited molecules for i = 1 and 2 photon absorption. Adapted from (Birch, 2001).

One important difference between 1PE and 2PE relies on the higher degree of molecular orientation photoselected, with an associated increase in the fundamental anisotropy r_{0i} of the fluorophore when using polarized multiphoton excitation. The increasing degree of photoselection with *i* can be expressed as:

$$r_{0i} = \frac{2i}{2i+3}\left[\frac{3}{2}cos^2\beta - \frac{1}{2}\right] \qquad \textbf{Eq. 2.1}$$

where *β* is the angle between the absorption and emission transition dipole moments of the fluorophore. Eq. 2.1 describes the maximum dynamic range of anisotropy measurement which, in the collinear (*β*=0) case, is 2/5= 0.400 for 1PE and 4/7=0.571 for 2PE. This increase in the fundamental anisotropy can be very convenient when solving complex

rotational kinetics (i.e. more than one rotational correlation time) as compared to the simple case of a free isotropic rotor.

FA is a parameter used to quantify the degree of fluorescence depolarization after excitation with a plane of polarized light. The depolarization of fluorescence emission mainly occurs due to rotational movement of the excited fluorescent molecule (Jameson and Ross, 2010) and/or non-radiative Förster resonance energy transfer (FRET) between identical fluorophores, a phenomenon known as homo-FRET (Chan *et al.*, 2011). Depolarization by rotational diffusion of spherical rotors is described by the Perrin equation:

$$\langle r \rangle = \frac{r_0}{1 + \frac{\tau}{\varphi}} \qquad \textbf{Eq. 2.2}$$

which depends on the lifetime of the fluorophore τ, the fundamental anisotropy, r_0, and the rotational correlation time, φ. The rotational correlation time depends on the apparent hydrodynamic volume of the rotating species, $V_{\mathrm{h}}^{\mathrm{app}}$, the Boltzman constant, k_B, and the environment characteristics, such as viscosity, η, and temperature, T:

$$\varphi = \frac{\eta \,.\, V_{\mathrm{h}}^{\mathrm{app}}}{k_B \,.\, T} \qquad \textbf{Eq. 2.3}$$

According to the Perrin equation, if the correlation time of a fluorophore is much longer than its lifetime (φ >> τ), the measured anisotropy is equal to the fundamental anisotropy. Special conditions like the use of extremely low temperatures and very viscous solvents as the ones that form a clear glass at low temperature (e.g. propylene glycol or glycerol) are normally used to determine r_0 since the fluorophore remains immobile during the lifetime of the excited state. In this case, FA will only reflect the relative orientation of the transition dipole moments of the molecule (angle *β*, Eq. 2.1). If, on the other hand, the molecule is free to rotate, then the anisotropy value will not only be influenced by its fundamental anisotropy but also by the extent of rotation of the fluorophore, which will lead to a depolarization of the fluorescence emission. The time for this rotation to occur is limited by the lifetime of the fluorescent species. A larger molecule or fluorophore will rotate slower than a small one, hence resulting in a longer rotational correlation time and FA (Jameson and Ross, 2010). Consequently, FA measurements can reveal changes in environmental conditions and interactions between molecules, from ligand binding or immunoassays, which will be reflected in the higher anisotropy value measured due to the increase in the volume of the rotating species (Ghosh *et al.*, 2012).

The other possible depolarization factor that has to be taken into account is homo-FRET. When fluorophores are relatively close together, in the nanometer range, homo-FRET can take place between identical fluorophores, if the fluorophores have a significant overlap

between their absorption and emission spectrum (Figure 2.2 A). This will allow energy migration over a large angular distribution of acceptor fluorophores resulting in a strong depolarization of the fluorescence emitted. Because FRET is usually an extremely fast process compared to the lifetime of the fluorophore, measuring the time-resolved anisotropy decays provides information about the probability of FRET, thus directly reporting on the distances between fluorophores. Therefore, measurement of steady-state anisotropy and the time-resolved decays provide information both about the fraction of fluorophores undergoing FRET and the distance between fluorophores, respectively.

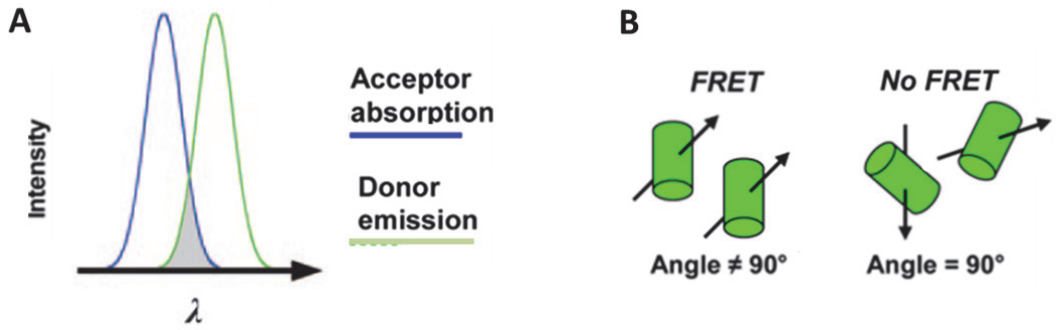

Figure 2.2 – Requirements for the occurrence of homo-FRET. Besides the close proximity among equal fluorophores (in the range of 1 to 10 nm), (**A**) homo-FRET requires a spectral overlap between absorption and emission spectra of the fluorophore and also (**B**) depends on the relative orientation of the donor emission dipole moment and the acceptor absorption dipole moment.

In summary, FA measurements can yield information on the properties of a sample that cannot be extracted by simple intensity and lifetime methods, regarding the rotational motion of the molecule in solution and its ability to participate in homo-FRET processes (Levitt *et al.*, 2009). These characteristics make FA a powerful tool to study biological systems, especially if one adds the spatial resolution given by coupling anisotropy measurements to fluorescence microscopy. Measurements of rotational mobility of fluorophores in the microscope have been used to monitor changes in nuclear morphology (Rao *et al.*, 2007), membrane fluidity (Li *et al.*, 2007) and digestion of DNA by nucleases (Cao *et al.*, 2006) while measurements of energy migration have been used to determine cluster sizes of GFP-labelled lipid markers (Bader *et al.*, 2007), oligomerization states/degree of oligomerization (Yeow and Clayton, 2007) and heterogeneity of lipid order on nanoscale in plasma membrane (Sharma *et al.*, 2004). More recently, Warren and co-workers have discussed the potential of homo-FRET based biosensors for monitoring the spatio-temporal correlation of signaling pathways within a single live cell, demonstrating that the homo-FRET between pleckstrin homology domains of Akt labelled with mCherry may be used to monitor 3′-phosphoinositide accumulation in live cells (Warren *et al.*, 2015). Others

created an Apollo sensor for $NADP^+$ that exploits $NADP^+$-dependent homodimerization of enzymatically inactive glucose-6-phosphate dehydrogenase, exploring these genetically encoded sensors based on ssFA homo-FRET to measure NADPH/$NADP^+$ redox states in β-cells responding to oxidative stress (Cameron *et al.*, 2016).

From a methodological point of view, FA measurements have been increasingly extended to different optical microscopy imaging modalities in order to spatially and temporally resolve several biological processes in living cells (Ghosh *et al*., 2012). FA has, for example, been coupled with wide-field time-resolved fluorescence imaging system to measure standard multi-well plate samples of rhodamine 6G dissolved in methanol, ethylene glycol, trimethylene glycol, and glycerol (Siegel *et al.*, 2003). More complex applications demonstrated how selective plane illumination microscopy can be utilized for 3D FA imaging of live cells, examining the formation of focal adhesions by 3D time lapse anisotropy imaging of CHO-K1 cells expressing an EGFP-paxillin fusion protein (Hedde *et al.*, 2015). Devauges and co-workers combined total internal reflection fluorescence microscopy anisotropy measurements with measurement of steady-state acceptor FA in order to perform live cell FRET imaging at the plasma membrane (Devauges *et al.*, 2014). The multiple imaging modalities open interesting possibilities to investigate molecular and physical organization in live cells at the molecular scale. In this regard, multiphoton (MP) microscopy has several benefits when compared to conventional confocal microscopy. MP microscopy has a higher axial resolution, higher contrast and the advantage that all the fluorescence from the focal point is collected by the detector. Since the excitation light has a longer wavelength, less excitation light is lost to scattering and consequently there is an increased penetration depth in the samples. In addition, there is a reduced photobleaching of marker dyes and less damage to living tissues, associated with an increase in the cell viability (Birch, 2001).

In this work, the recently installed 2PE FAIM setup was further optimized and calibrated. We were able to record 2PE FA images of discrete objects (the 2.5 μm Inspeck™ Microscope Image Intensity Calibration beads), after optimizing both data acquisition and treatment with homogeneous Rhodamine B solutions with different viscosities. Our system was able to measure FAs similar to the ones measured in the spectrofluorometer.

2.3. Materials and methods

2.3.1. Calibrators

Rhodamine B (RhodB, Sigma Chemical Co., St. Louis, MO) stock solution was prepared in UVASOL grade ethanol (Merck, Darmstadt, Germany) and its exact concentration was determined spectrophotometrically using $\varepsilon_{542\ \mathrm{nm}}^{\mathrm{RhodB}}$= 106 000 $M^{-1}cm^{-1}$ (Haugland, 2005). Water/glycerol solutions were prepared gravimetrically with a glycerol (Sigma Chemical Co) content ranging from 0 to 100% (V/V). RhodB was added to these aqueous glycerol solutions at a final concentration of 1 µM. The solutions were left stirring overnight before performing their steady-state fluorescence characterization. The fluorescent probe Alexa Fluor 488 carboxylic acid, succinimidyl ester (mixed isomers, dilithium salt) (A488) was obtained from Molecular Probes, Invitrogen (Eugene, OR, USA). Typically, the final concentration of A488 in 20 mM HEPES-KOH, 1 mM EDTA, pH 7.4 buffer was 0.5 µM, determined spectrophotometrically using $\varepsilon_{494\ \mathrm{nm}}^{\mathrm{A488}}$= 73 000 $M^{-1}cm^{-1}$ (Haugland, 2005). A set of 2.5 µm Inspeck™ Microscope Image Intensity fluorescent beads (InSpeck Green, Molecular Probes) designed for intensity calibration in flow cytometry (Lidke *et al*., 2005) were also used to test our 2PE FAIM setup. The steady-state fluorescence properties of these calibration beads were first characterized using a 10x diluted solution in water of each batch of fluorescent microspheres (with 1, 3, 10, 30 and 100% relative fluorescence intensity). The stock solutions of beads were always sonicated for 30 s in a bath sonicator and vortexed prior to the dilutions. For the 2PE FAIM measurements, a 5 µL drop of the concentrated 10, 30 or 100% fluorescent beads was directly applied on a glass bottom 8-well Ibidi chamber (Ibidi, Munich, Germany) and covered with a drop of mounting media (Molecular Probes).

2.3.2. UV-visible Spectroscopy

UV-visible absorption measurements were carried out at room temperature (RT) using a Shimadzu MPC-3100 spectrophotometer (Shimadzu Corp., Kyoto, Japan) or a double-beam V-660 Jasco spectrophotometer (Jasco Corp., Tokyo, Japan). Typically, the absorption spectra of samples were taken from 250-700 nm in 0.5 x 0.5 or 1.0 x 0.2 cm path length quartz cuvettes (Hellma Analytics, Müllheim, Germany) using a bandwidth and sampling interval of 1 nm after a buffer *versus* buffer or air *versus* air baseline.

2.3.3. Steady-state fluorescence measurements

Fluorescence measurements of RhodB aqueous glycerol solutions were performed in a SLM-AMINCO 8100 spectrofluorometer (SLM Instruments Inc., Rochester, NY) with double excitation and emission monochromators. This apparatus, which also contains automated rotating Glan-Thompson polarizers, was operated in photon-counting mode. The light source was a 450-watt Xe arc lamp and the reference was a RhodB quantum counter solution. The sample temperature was controlled at 20 ºC with a water circulating bath from Julabo (model F25). The excitation and emission wavelengths employed were 560 nm and 580 nm, respectively. The fluorescence measurements of the reference fluorescent microspheres, 10x diluted, were performed in a HORIBA Jobin Yvon Fluorolog-3-21 spectrofluorometer (New Jersey, USA). This apparatus, which has double excitation and emission monochromators, is fitted with automated rotating Glan-Thompson polarizers and was operated in "photon counting" mode. The light source was a 450-watt Xe lamp, the reference was a silicon diode and it contains a R928P photomultiplier tube detector which provides sensitive spectral characterization in the UV through the visible range of wavelengths. The excitation and emission wavelengths employed were 470 nm and 510 nm, respectively. This apparatus is equipped with a FI-3751 thermoelectric temperature controller (Wavelength Electronics) and the temperature was set to 20 ºC. For both spectrofluorometers, the measurements were usually performed using 0.5 x 0.5 cm width quartz cuvettes at RT in right-angle geometry and background intensities were always taken into account and subtracted from the measured sample intensities. The ssFA, $\langle r \rangle$, is defined by:

$$\langle r \rangle = \frac{I_{\mathrm{VV}} - G \cdot I_{\mathrm{VH}}}{I_{\mathrm{VV}} + 2\,G \cdot I_{\mathrm{VH}}} \qquad \textbf{Eq. 2.4}$$

and was obtained by measuring the vertically (parallel, I_{VV}) and horizontally (perpendicular, I_{VH}) polarized components of the fluorescence emission with the excitation polarized vertically. The *G*-factor is an instrumental factor that takes into account the different transmissivity of the monochromators and sensitivity of the detection system to each polarized component of the radiation:

$$G = \frac{I_{\mathrm{HV}}}{I_{\mathrm{HH}}} \qquad \textbf{Eq. 2.5}$$

I_{HV} and I_{HH} are the vertically and horizontally polarized components of the fluorescence emission when the excitation is polarized horizontally, respectively.

2.3.4. Fluorescence anisotropy imaging microscopy

The optical setup used for the FAIM measurements is based on a custom-modified Leica TCS SP5 (Leica Microsystems CMS GmbH, Mannheim, Germany) confocal laser scanning microscope (CLSM) system equipped with an inverted DMI6000 confocal microscope. This system, which is illustrated schematically in Figure 2.3, is coupled to a fluorescence lifetime imaging microscopy (FLIM) setup from Becker & Hickl that operates according to the time-correlated single-photon counting (TCSPC) technique. Briefly, 2PE was accomplished with a mode-locked, femtosecond-pulsed Ti:Sapphire laser (Mai Tai BB Spectra-Physics, 710−990 nm) operating at a repetition rate of 80 MHz. A Glan-Thompson polarizer (Newport, USA) and a half-wave plate (Thorlabs, USA) allowed controlling the output power of the laser. The excitation light, transmitted along a polarization preserving optical fiber, was then delivered to the sample through the objective and the resulting fluorescence emission was collected by the same objective (epi-collection mode) – either a Zeiss 10x 0.4 numerical aperture (NA) (without immersion) or a Zeiss 63x 1.2 NA (water immersion) objective was used. A SP700 Near-IR/UV block-visible shortpass filter (filter F1 in Figure 2.3) was used to prevent any excitation light from reaching the detector, and the fluorescence emission from each sample was spectrally filtered using an adequate band-pass filter (filter F2 in Figure 2.3). Fluorescence emission was separated in two orthogonal linearly polarized states (parallel, par and perpendicular, per, components, respectively) through the use of a double polarizing beam splitter (PBS) cube. The use of a double PBS system allows for a two-fold selection of each polarization component, improving the quality of the signal. The two orthogonal linearly polarized light components were then focused and detected by two separate photomultiplier tubes (PMTs). Simultaneous acquisition of the par and per polarized decay components is recommended to avoid severe anisotropy artifacts induced by intensity fluctuations over time. Each polarized component had to be focused onto the respective PMC-100-4 cooled high speed PMT detector head for photon counting (Becker & Hickl), which were placed equidistant from the PBS cube. Both single-point decays and images were acquired using the Becker & Hickl SPC 830 module. The Ti:sapphire laser was tuned at 760 nm and the fluorescence emitted was detected using a 500–550 nm band pass filter for A488/Inspeck beads while for RhodB aqueous glycerol solutions, the laser was tuned at 820 nm, using a 535-585 nm band-pass filter for the detection (see Figure 2.3). Typically, the laser power was controlled by setting the filter wheel to 12.5% and the gain between 40% and 70% in order to minimize photobleaching problems and heating up of the samples. Pulse pile-up effects were avoided during the measurements by keeping the recorded counting rates lower than 10^6cps (< 1% of the excitation frequency of the laser). For single-point acquisition of the two orthogonal linearly polarized decays from each sample, a time window of 1024 channels (9.77 ps/channel) was

used. Image acquisition with a frame size of 128 × 128 pixels required the use of 256 time channels, with a time scale of 39.1 ps/channel. All measurements were performed in glass bottom 8-well Ibidi chambers (Ibidi, Martinsried, Germany) at RT ((20±1)ºC).

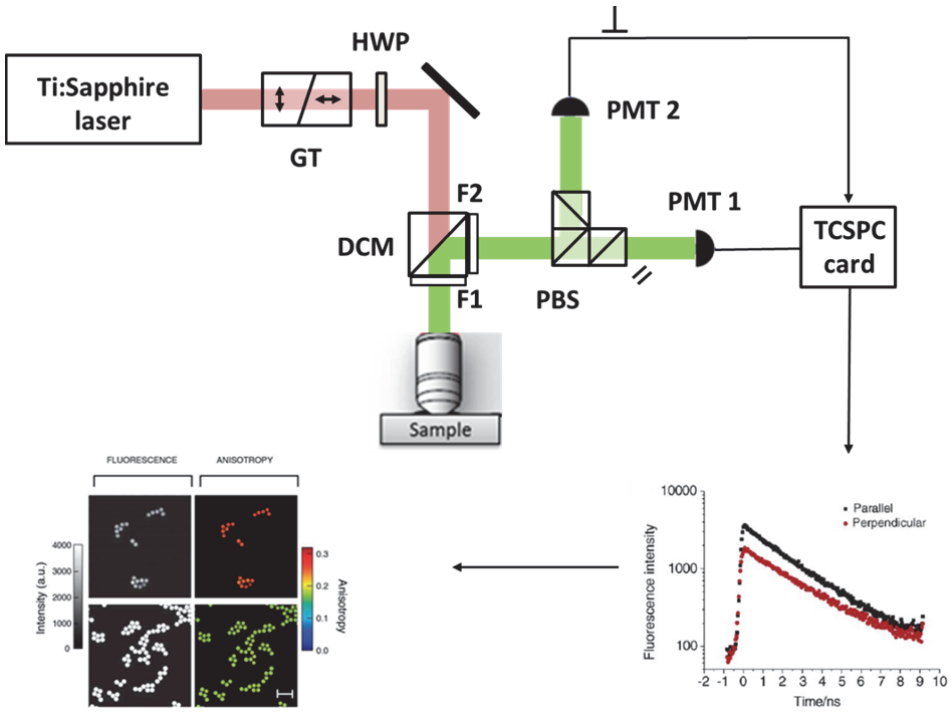

Figure 2.3 - Schematic representation of the experimental 2PE FAIM setup. A Ti:Sapphire laser is used to excite the sample with linearly polarized pulsed light. After traversing a Glan-Thompson polarizer (GT) and a half-wave plate (HWP), the polarized excitation beam reaches the sample passing through a dichroic mirror (DCM) and the objective. Fluorescence emission is epi-collected through a SP700 filter (filter F1). A second band-pass filter (filter F2) is then used to selectively collect the fluorescence emission from the sample (500-550 nm for A488/ Inspeck beads and 535-585 nm for the aqueous solutions of RhodB). The two orthogonal linearly polarized components of the emitted light are then separated using a double polarization beam splitter (PBS) cube. Simultaneous detection of both fluorescence components is accomplished using the TCSPC technique through photomultipliers 1 (PMT 1) and 2 (PMT 2). Polarization-resolved images are then processed to result in 2PE FA images. Adapted from Dubach *et al*., 2014.

Equal voltages were first applied to both detectors. However, due to the different ages of the two PMTs used in our apparatus, the *G*-factor of the FAIM setup was very high and highly variable on a daily basis (*G*-factor~5–7). In addition, the parallel and perpendicular fluorescence decays obtained for each sample were fairly temporally misaligned. This situation was successfully optimized by slightly increasing the applied voltage to the per PMT (93%) compared to the par detector (90%). In this way, the sensitivity of the per PMT was maximized, greatly improving the reproducibility of the apparatus *G*-factor (*G*-factor~ 2 for both objectives) and causing the temporal alignment of both decay components. Acquisition times for the images varied between 8 and 30 minutes depending on the

sample, the main controlling factors being the brightness of the sample and the low detection efficiency of the per PMT.

2.3.5. Image processing

Data analysis was performed using MATLAB with a script written by Dr. Fábio Fernandes. It was necessary to perform several steps before calculating the 2PE ssFA from the two acquired images. First of all, the *G*-factor of our 2PE FAIM apparatus had to be determined on a daily basis. This was accomplished by measuring the two orthogonally polarized fluorescence decays for either RhodB or A488 in water, and determining the *G*-factor either on a single-point or on a pixel-by-pixel basis:

***G*-factor – single-point analysis**

1.1. open and read each image file by creating a (x, y, z) matrix with 128x128x256 dimensions. The first and second dimension of the matrix correspond to x (row) and y (column) pixel position in each image; the z corresponds to the time dimension within each pixel x,y, since a fluorescence decay (either par or per polarized) was acquired in each pixel using a time window of 256 channels, ($I_{\mathrm{par}}^{\mathrm{pixel\ i,j}}(t)$ and $I_{\mathrm{per}}^{\mathrm{pixel\ i,j}}(t)$, respectively). The matrix was then reduced to 127x125x256, since 1 and 3 pixels in the x and y dimensions, respectively, had always 0 counts due to an unidentified option in the measurement setup;

1.2. the equivalent to single-point par and per fluorescence decay ($I_{\mathrm{par}}(t)$ and $I_{\mathrm{per}}(t)$,) respectively) were then calculated from each of the two acquired images in order to increase the signal-to-noise (S/N) ratio of the data. This involved summing the photon counts obtained at a given time channel z from all pixels x,y of each image:

$$I_{\mathrm{par}}(t) = \sum_i \sum_j I_{\mathrm{par}}^{\mathrm{pixel}\ i,j}(t) \qquad \textbf{Eq. 2.6}$$

$$I_{\mathrm{per}}(t) = \sum_i \sum_j I_{\mathrm{per}}^{\mathrm{pixel}\ i,j}(t) \qquad \textbf{Eq. 2.7}$$

1.3. these two decays were then plotted, aligned and the channels to be used in background calculation, as well as the end channel of the analysis, were identified;

1.4. after subtracting an average background from each aligned fluorescence decay, $I_{\mathrm{par}}^{\mathrm{c}}(t)/I_{\mathrm{per}}^{\mathrm{c}}(t)$ was plotted and the channels to be used in the *G*-factor calculation were selected by identifying the channel range that gave an approximately constant

$I^{c}_{par}(t)/I^{c}_{per}(t)$ ratio over time. The single-point *G*-factor corresponded to the average *G* value calculated from this selected channel interval.

G-factor – pixel-by-pixel analysis

The G-factor was also calculated on a pixel-by-pixel basis in order to test its uniformity over a given field-of-view:

2.1. using the background channels and the end channel of the analysis previously identified on the single-point analysis (step 1.3), step 1.4 was now repeated for the two orthogonally fluorescence decays obtained on a pixel-by-pixel basis,

2.2. a *G*-factor was then obtained for each pixel x,y, $G-\mathrm{factor}_{\mathrm{pixel}\ i,j}$, by repeating the calculations described on step 1.4. but now on a pixel-by-pixel basis.

2PE fluorescence anisotropy – pixel-by-pixel analysis

The following steps were then used to calculate the 2PE ssFA images:

3.1. the previously aligned and background-corrected parallel and perpendicular fluorescence decays were integrated over time on a pixel-by-pixel basis:

$$I^{\mathrm{pixel}\ i,j}_{\mathrm{par}} = \sum_{t} I^{\mathrm{cor,pixel}\ i,j}_{\mathrm{par}}(t) \qquad \textbf{Eq. 2.8}$$

$$I^{\mathrm{pixel}\ i,j}_{\mathrm{per}} = \sum_{t} I^{\mathrm{cor,pixel}\ i,j}_{\mathrm{per}}(t) \qquad \textbf{Eq. 2.9}$$

3.2. the 2PE ssFA was then calculated for each pixel using a constant *G*-factor for all the image pixels (the *G*-factor obtained previously from the single-point analysis (steps 1.1. to 1.4.) and the x_{NA} factor adequate for the objective used in each set of measurements (see section 2.4.2):

$$\langle r\rangle_{\mathrm{pixel}\ i,j} = \frac{I^{\mathrm{pixel}\ i,j}_{\mathrm{par}} - G\cdot I^{\mathrm{pixel}\ i,j}_{\mathrm{per}}}{I^{\mathrm{pixel}\ i,j}_{\mathrm{par}} + x_{\mathrm{NA}} G\cdot I^{\mathrm{pixel}\ i,j}_{\mathrm{per}}} \qquad \textbf{Eq. 2.10}$$

3.3. when the measurement resulted in relatively low photon counts in each pixel, a threshold was applied to the calculation of $\langle r\rangle_{\mathrm{pixel}\ i,j}$. Typically, $\langle r\rangle_{\mathrm{pixel}\ i,j}$ was considered valid only when $I^{\mathrm{pixel}\ i,j}_{\mathrm{per}}$ > 20 – 50 photon counts.

3.4. to visualize the data obtained, the FA maps were plotted using a color scale, and a frequency histogram was obtained from each data set.

2.4. Results and discussion

In this work, we describe the optimization and calibration of the recently installed 2PE FAIM setup in order to be able to measure FA with spatial and temporal resolution. This first required validating the microscope FA measurements using a set of RhodB aqueous glycerol solutions. The ability to map discrete objects and to resolve spectrally similar particles using FA as the spectroscopic readout was then confirmed using the 2.5 μm Inspeck™ Green calibration beads.

2.4.1. G-factor correction

The *G*-factor used in the calculation of FA (Eq. 2.4) corrects for the different transmission and detection efficiencies of the instrument setup for the two polarization components. This is particularly important in the implemented FAIM setup because different PMTs are used to detect the parallel and perpendicular polarized components of the fluorescence emitted by each sample. *G*-factor determination requires the use of a small fluorophore in solution that presents a rotational correlation time much shorter than its fluorescence lifetime to rapidly depolarize the fluorescence signal within the time window of the measurement. The fluorescent calibrator dye should be freely rotating in a uniform environment (such as water), ideally with a monoexponential fluorescence decay kinetics, in order to avoid artifacts associated with hindered rotations found in complex samples. It is also important that the calibrator fluorophore shares the spectral emission characteristics with the sample under study, since the *G*-factor is usually wavelength-dependent (Suhling *et al.*, 2014). In our case, freely diffusing RhodB in water was used when studying the series of RhodB aqueous glycerol solutions, and A488 was employed when performing measurements with the Inspeck™ Calibration beads. The normalized one-photon absorption and emission spectra and two-photon absorption cross-section of RhodB and A488 in aqueous solution are presented in Figure S 2.1 A and B, respectively. The fluorescence from both these calibrators decayed monoexponentially in aqueous solution with a fluorescence lifetime of 1.82 ns and 4.1 ns, respectively (Haugland, 2005). In addition, their rotational correlation times were very short due to their small hydrodynamic volume, as previously determined (0.22 ns (Sahoo *et al.*, 2009) and 0.15 ns (Schröder *et al.*, 2005), respectively). The *G*-factor was first calculated by a single-point analysis as it is explained in detail in Section 2.3.5 and illustrated in Figure 2.4 for the objective 63x, NA 1.2 using A488 as the calibrator dye. Due to the limited number of detected photons per pixel, the S/N ratio of this calculation is greatly improved by summing the photon counts obtained at a given time channel z from all pixels x,y of each image ($I_{\mathrm{par}}(t)$ and $I_{\mathrm{per}}(t)$). After aligning the two single-point decays, these were background-corrected by subtracting the average count

number obtained typically between 0.5 and 1.5 ns. The *G*-factor was then calculated by the tail-matching method, where the corrected parallel polarized signal was divided by the corrected perpendicular polarized signal at each time *t* ($I^c_{\mathrm{par}}(t)/I^c_{\mathrm{per}}(t)$) as it is exemplified in Figure 2.4. The average limiting value of the resulting decay at long times is the single-point *G*-factor. This value should be close to 1 in an optimized system. The *G*-factor of the implemented setup was found to be *G*= 2.1 ± 0.1, independently of the excitation wavelength and objective used. This is mainly due to the different sensitivity of the detectors for the par and per polarized components, but the slightly variable position of the PBS cube (which had to be removed occasionally from the setup) may also contribute to this variability. Since the exact *G*-factor value has a large impact on the results, it was determined on a daily basis and used to check if the FAIM system was operational.

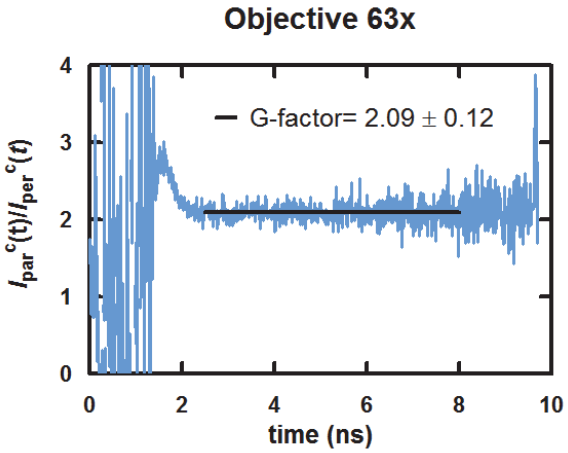

Figure 2.4 – Determination of the *G*-factor for the implemented FAIM setup with a 63x objective and using Alexa 488 as the calibrator dye by the tail matching method The average *G*-factor obtained between 2.5 and 8 ns was 2.09 ± 0.12. At longer times, the individual polarized decays have very low fluorescence counts which increase the error in the determination of the *G*-factor. The total acquisition time of each polarized image was 120 s with a scan rate of 200 Hz (λ_{exc}= 760 nm).

The next question was whether the *G*-factor was position-dependent, i.e. whether there was a spatially dependent sensitivity of different detector pixels. To address this question, the *G*-factor was calculated on a pixel-by-pixel basis and mapped for FAIM measurements carried out with either the 10x, NA 0.4 or the 63x, NA 1.2 objective. This is illustrated in Figure 2.5 for the objective 63x, NA 1.2 using again A488 as the calibrator dye. Although there was some intensity differences at the edges of both images (Figure 2.5 A and B) probably caused by galvo scanning the sample during their acquisition (Dubach *et al.*, 2014), the *G*-factor map obtained is not only fairly homogeneous throughout the image but its average value (*G*= 2.17 ± 0.20) is also very close to the corresponding single-point calculation made for the same sample (*G*=2.09 ± 0.12). Similar results were obtained with the other objective.

Therefore, a constant *G*-factor for all the image pixels was used in the calculation of FA on a pixel-by-pixel basis, namely the *G*-factor obtained from the single-point analysis of the calibrator.

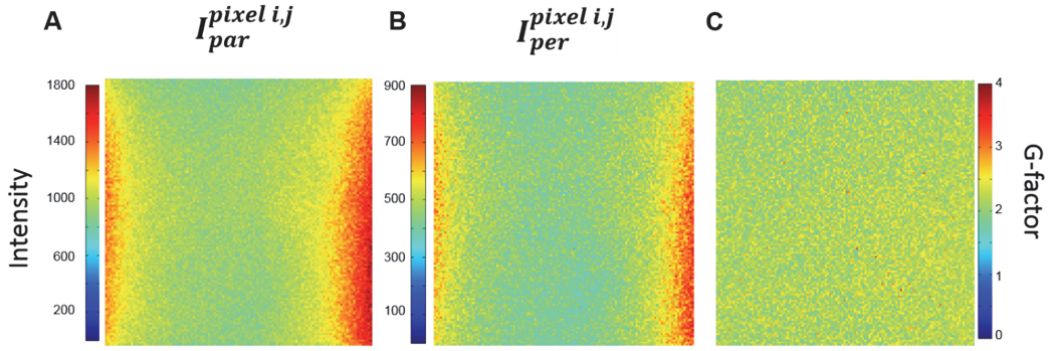

Figure 2.5 - Integrated (A) parallel and (B) perpendicular polarized fluorescence intensity images and (C) *G*-factor map obtained for the 63x, NA 1.2 objective using Alexa488 as the calibrator dye. The intensity images have some brighter areas at the edges. Nevertheless, the *G*-factor calculated by the tail-matching method on a pixel-by-pixel basis is fairly homogenous throughout the image. The images were made using MATLAB using a false color-coded scale ($\lambda_{\mathbf{exc}}$ = 760 nm).

2.4.2. Objective-induced depolarization correction

An additional consideration has to be made when using high NA objectives to collect the fluorescence, a situation that is very common in biological studies. Among other effects, the original polarization of the excitation light is distorted near the focal point due to strong condensation by the high NA objective lens (Figure 2.6) and also, fluorescence is collected by the same objective lens at a large solid angle. Both these factors result in an additional depolarization factor in the excitation and detection pathways of each sample. This objective-induced depolarization can be accounted for empirically, by replacing the factor "2" in Eq. 2.4 with a factor x_{NA} ≤ 2 (Koshioka *et al.*, 1995; Devauges *et al.*, 2012), resulting in:

$$\langle r \rangle = \frac{I_{\mathrm{VV}} - G \cdot I_{\mathrm{VH}}}{I_{\mathrm{VV}} + x_{\mathrm{NA}}\, G \cdot I_{\mathrm{VH}}} \qquad \textbf{Eq. 2.11}$$

This correction factor can be determined experimentally by measuring the single-point FA of a set of aqueous glycerol RhodB solutions under the microscope with a given objective and then by comparing these values with reference measurements made in a conventional spectrofluorometer. The ssFA values measured in the spectrofluorometer for the RhodB solutions prepared with variable glycerol content are summarized in Table S 2.1.

These experimental values were converted to the ones expected if 2PE instead of 1PE (as is the spectrofluorometer) was used. This conversion takes into account the intrinsic difference between the fundamental anisotropy when fluorophores are excited with 1PE (r_0= 0.400) and 2PE (r_0 = 0.571). The conversion factor is thus 0.571/0.400 = 1.428.

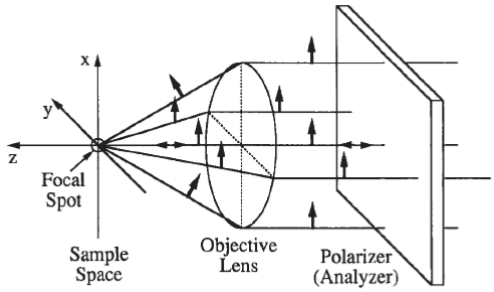

Figure 2.6 – Schematic diagram of the objective-induced depolarization of the excitation light. There is a condensation by the lenses that compose the objectives that changes the polarization orientation, so the sample is not only excited by the original exciting polarization, but also by other different aligned polarized light. Adapted from Koshioka *et al*., 1995.

As expected, the ssFA of RhodB increased with the glycerol content of the solution mainly due to the concomitant increase in the solution viscosity (Table S 2.1.). The single-point FA data measured in the microscope for the same set of solutions resulted in lower anisotropy values than the ones obtained in the spectrofluorometer, particularly when the 63x, NA 1.2 objective was used (Figure 2.7), as a consequence of the depolarization-induced by the objective, an effect discussed above.

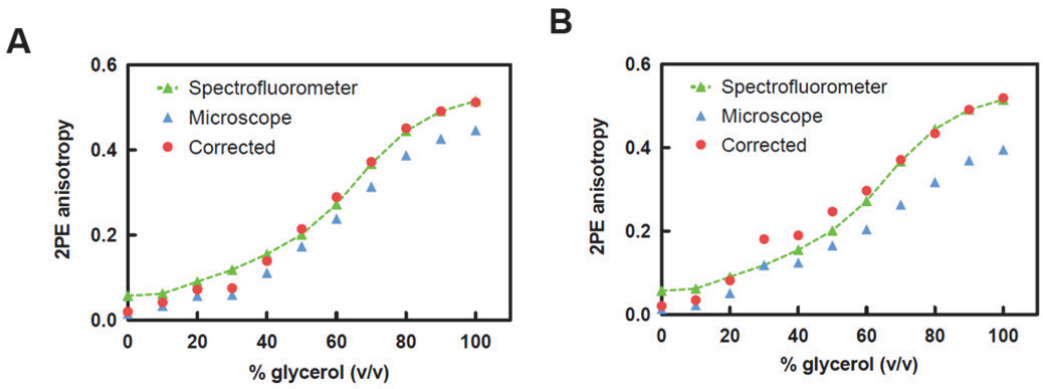

Figure 2.7 – Determination of the empirical factor x_{NA} for each objective used in the FAIM setup. The FA of RhodB in aqueous glycerol solutions of distinct glycerol content was measured both in a spectrofluorometer (green triangles) and in the microscope (single-point calculations (blue triangles)) using a (**A**) 10x, NA 0.4 or (**B**) 63x, NA 1.2 objective (T= 20 ± 1°C). The best fitting x_{NA} values that allowed correcting the microscopy data (red circles) were (**A**) x_{NA}= 1.309 and (**B**) x_{NA}=0.814, respectively. Note that the spectrofluorometer FA values are already corrected for 2PE instead of 1PE.

Finally, the microscope FA measurements were validated on a pixel-by-pixel basis using a small set of the prepared RhodB aqueous glycerol solutions, namely the ones containing 0, 20, 60 and 90% glycerol (v/v). Figure 2.8 A shows the corresponding 2PE FA colored maps obtained using the 10x, air objective, which were found to be rather uniform throughout the images. This result was further confirmed by the frequency distributions of the FA values obtained using either the 10x or 63x objective (Figure 2.8 B and C, respectively). A Gaussian distribution was successfully fitted to these data, with rather narrow standard deviations (Table S 2.1) confirming the ability of the implemented FAIM setup to image the 2PE FAs from highly fluorescent homogeneous solutions.

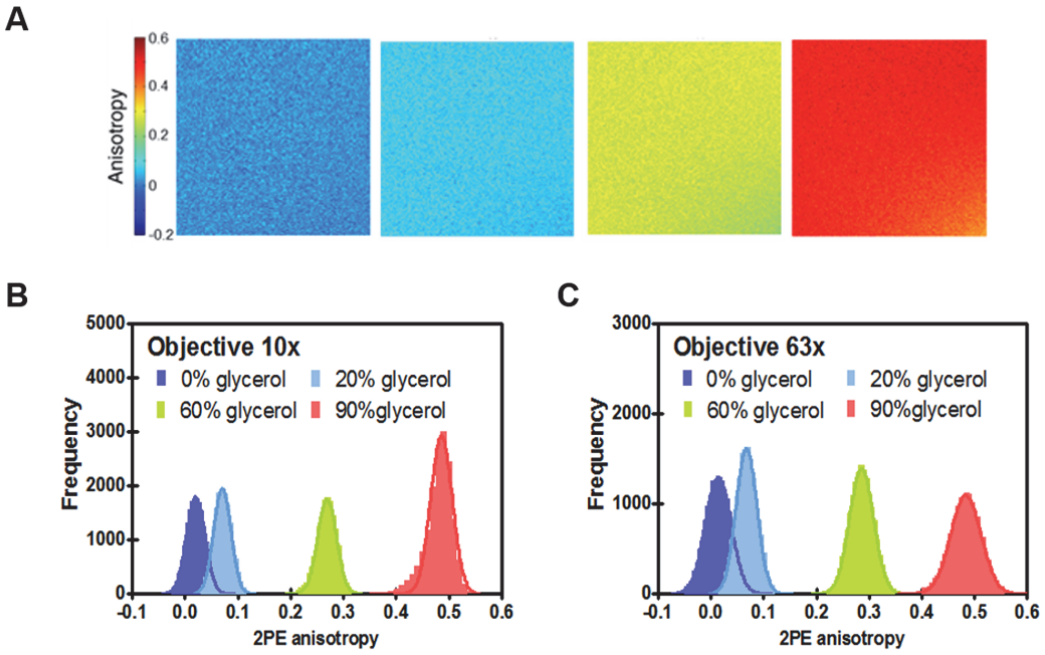

Figure 2.8 – (A) The 2PE FA maps of four wells filled with RhodB in different aqueous glycerol solutions are uniform throughout the images. The FAIM measurements were carried out using the 10x air objective. The pixel-by-pixel calculated FA is represented in a color scale from blue (-0.2) to red (0.6). The increase of 2PE FA with solvent viscosity is evident and can also be seen in the corresponding histograms obtained for the **(B)** 10x, NA 0.4 and **(C)** 63x, NA 1.2 objective. A Gaussian distribution was successfully fitted to these histograms (full curves), the average and standard deviation of these fits are in Table S 2.1.Image processing for obtaining the histograms was performed using MATLAB.

2.4.3. Characterization of the Inspeck™ Green calibration beads

The next step of this work consisted in testing the ability of the FAIM setup to map the 2PE FA of discrete fluorescent objects. The 2.5 μm commercial Inspeck™ Green microscope image intensity calibration beads were chosen for this purpose. These beads are internally labelled with different amounts of Molecular Probes´s proprietary dye, giving rise to distinct fluorescence intensities, namely 1, 3, 10, 30 and 100% relatively to the more intense sample. The normalized fluorescence excitation and emission spectra of the 10-fold diluted

aqueous solutions of 10, 30 and 100% intensity fluorescent beads are presented in Figure 2.9 A.

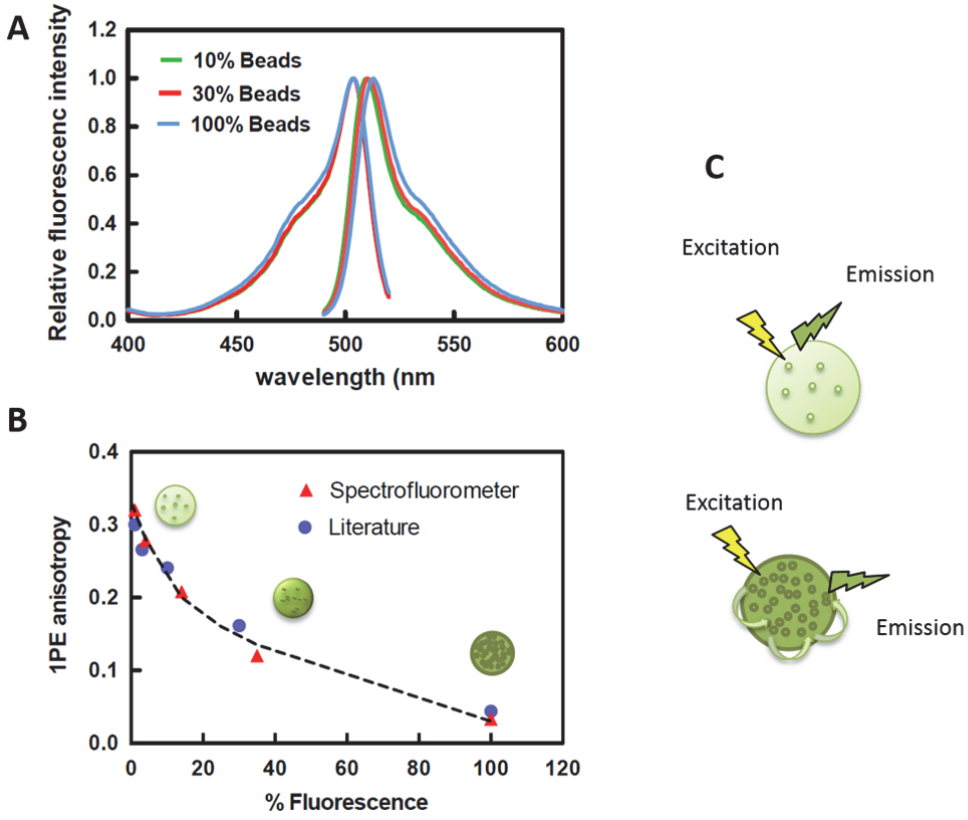

Figure 2.9 – (A) Normalized excitation and emission spectra and (B) 1PE FA measurements for the 2.5 μm Inspeck™ Microscope Image Intensity Calibration beads. Each stock sample was 10-fold diluted in aqueous solution and measured at 20°C. The literature data was obtained from Lidke *et al*., 2005 (**C**) The excitation and emission fluorescence spectra of the beads have a considerable overlap which allows for an efficient homo-FRET process to occur among the encapsulated dyes: (**C**, upper panel) for a low % of internally labeling of the beads, the average separating distance between the dyes is so large that the depolarization of the fluorescence emission due to homo-FRET is negligible; (**C**, lower panel) upon increasing the concentration of the encapsulated dye, the fluorophores become much closer to each other, which results in a very efficient energy migration process (strong fluorescence depolarization), and hence the very low FA values measured for these beads. Dashed line is just a guide to the eye.

The spectra obtained were essentially independent of the type of bead used. However, the 1PE FA of the samples progressively decreased from 0.33 to 0.03 upon increasing their relative fluorescence intensity, as it is displayed in Figure 2.9 B and summarized in Table S 2.2 in agreement with the literature (Lidke *et al.*, 2005; Dubach *et al.*, 2014). This result can be assigned to a very efficient homo-FRET process among the encapsulated dyes (Lidke *et al*., 2005; Dubach *et al*., 2014). In fact, the absorption and emission spectra of the fluorescent dye present a significant overlap (small Stokes shit) (Figure 2.9 A) allowing for a strong depolarization of the fluorescence due to energy migration when the encapsulated dyes are very close to each other in the more concentrated solutions (Figure 2.9 C). The

possibility that the fluorescence lifetime of these fluorescent beads was controlling their FA values was ruled out by performing time-resolved fluorescence measurements. The mean fluorescence lifetime of the 10, 30 and 100% fluorescent microspheres varied between 4.0 and 4.4 ns (data not shown) which, according to the Perrin equation (Eq. 2.2) cannot account for the sharp drop in their FA value.

2.4.4. Imaging the Inspeck™ Green calibration beads

The following step of the calibration of the FAIM setup involved imaging discrete fluorescent objects and for that we used the 2.5 μm reference beads characterized previously. It was necessary to add a drop of the very viscous mounting medium to each sample to prevent a significant translational diffusion of the beads during the rather long times necessary to acquire the images. Although the microspheres were fairly homogeneously distributed in each image, they only accounted for a small fraction of the total image pixels (15875 pixels in total), i.e. normally less than 10% of the 127x125 pixels (Figure 2.11 and Figure S 2.2). The only exceptions were the 30% and 100% microspheres measured with the 63x water immersion objective, where between 4000 and 5000 pixels presented fairly good signals (Figure 2.11). These signals were nonetheless much lower than the average integrated pixel counts obtained with the RhodB aqueous glycerol solutions. In fact, for 2PE, the number of photons measured by the PMTs during image acquisition of the fluorescent beads ranged between tens to a few thousands. Therefore, it was necessary to establish an analysis threshold when processing the images in order to get meaningful 2PE FA values, as it is illustrated in detail in Figure 2.10. After aligning and background-correcting the par and per fluorescence decays, they were integrated over time for each pixel of the two images. The resulting integrated fluorescence intensities were then plotted one against the other in order to evaluate the range of values obtained and to check for the adequacy of the background correction made on a pixel-by-pixel basis (Figure 2.10 A). The 2PE FAs were then calculated (step 3.4) and plotted against the integrated perpendicular intensity of each pixel. As can be seen in Figure 2.10 B, for low intensity values the basis of the 2PE FA histogram is very widespread because there is a large error associated to the calculation of the FA for those pixels. These must therefore be removed by establishing an adequate threshold value during data analysis, which was typically set at $I_{\mathrm{per}}^{\mathrm{pixel}\,i,j}$> 20 - 50. The resulting histogram of 2PE FA became much narrower, as expected (Figure 2.10 C).

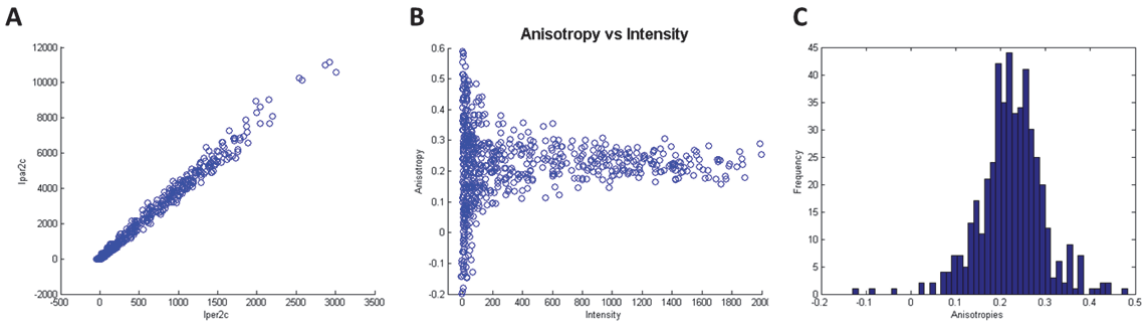

Figure 2.10 – Example of data analysis for the 30% microspheres imaged with a 10x, air objective. (**A**) The integrated par and per polarized components are plotted against each other to test for an adequate background correction, which was made on pixel-by-pixel basis. (**B**) The 2PE FA is then calculated according to Eq. 2.11 and plotted against the integrated per intensity. Due to very low counts obtained in some pixels, the base of this histogram is very broad. (**C**) After removing these pixels from data analysis by setting an analysis threshold for the integrated per component, the resulting histogram becomes much narrower. Image processing for obtaining the histograms was performed using MATLAB.

The 2PE FA maps and their respective histograms obtained for the 10, 30 and 100% fluorescent microspheres with the 63x water immersion and 10x air objectives are presented in Figure 2.11 and Table S 2.1. Interestingly, the centers of these distributions were very close to the 2PE-corrected FAs measured in the spectrofluorometer, although these values were obtained in water. This indicates that the major factor responsible for the depolarization of the fluorescence emitted by the rather large beads (with a diameter of 2.5 μm) is an intra-bead homo-FRET process and not the rotational diffusion of the microspheres in solution during their excited state lifetime.

One of the advantages of the implemented FAIM setup is the possibility of using 2PE FA as the contrasting readout in a measurement, i.e. the identification of different rotating/oligomerization species in an image that share the same spectral characteristics but present very different FAs. In this way, the last test performed with our setup was to measure the 2PE FA of an 8:2 mixture of 10% and 100% fluorescent beads. The 2PE FA color-coded map obtained clearly allows identifying two highly homogeneous populations of green-fluorescent beads with distinct anisotropy values (yellow and blue, respectively), as it is shown in Figure 2.12.

The corresponding histogram was now bimodal, and a sum of two Gaussian distributions with relative amplitudes of 59 and 41% was necessary for the data to be properly fitted ($\langle r \rangle_1$= 0.022 ± 0.044, $\langle r \rangle_2$= 0.270 ± 0.096; n= 907 corresponding to the 100% and 10% fluorescently labeled microspheres, respectively).

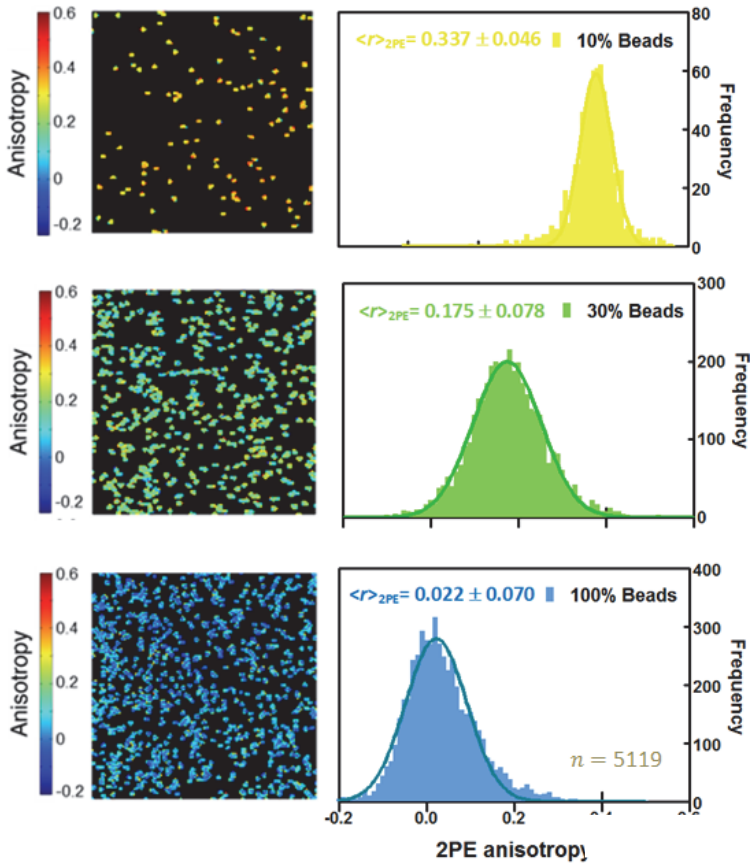

Figure 2.11 – 2PE FA colored maps (left panels) and histograms (right panels) obtained for the 10, 30 and 100% fluorescent microspheres with the 63x water immersion objective. A Gaussian distribution was successfully fitted to each of these histograms (full curves), the average and standard deviation of these fits being presented in Table S 2.2 (the number of pixels processed were n= 742, n= 4034 and n= 5119 for the top, middle and bottom histograms, respectively). Image processing for obtaining the histograms were performed using MATLAB.

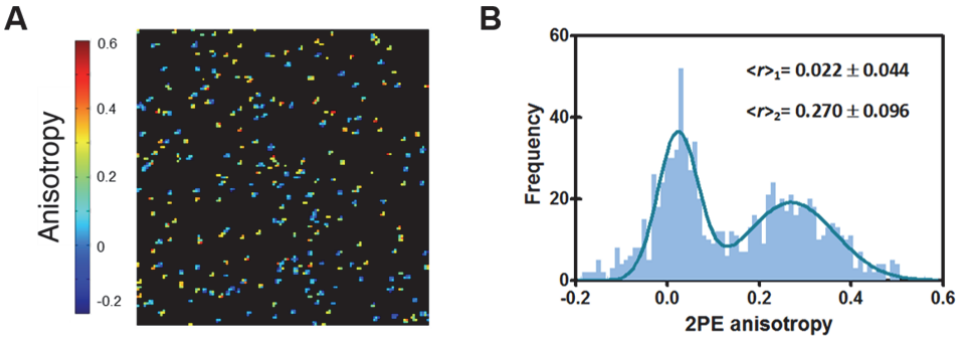

Figure 2.12 – Resolving spectrally similar objects using 2PE FA. (**A**) 2PE FA colored map and (**B**) histogram obtained for a 8:2 mixture of 10 and 100% green fluorescent microspheres with a 10x air objective. A bimodal Gaussian distribution with relative amplitudes of 59 and 41% was successfully fitted to the histogram (full curve). The population with low fluorescence intensity had a high FA ($\langle r \rangle_2$= 0.270 ± 0.096), while the population with high fluorescence intensity presented a low FA $\langle r \rangle_1$= 0.022 ± 0.044), average ± SD. The number of pixels processed were n= 907. Image processing for obtaining the histogram was performed using MATLAB.

2.5. Conclusions and perspectives

There were considerable advances made in the optimization and calibration of the FAIM setup that was previously implemented at CQFM/IBB at IST. The system is now fully operational at the imaging and not only at the single-point level, allowing the acquisition of 2PE FA colored maps of the samples under study. The ability of our apparatus to resolve spectrally similar particles using FA as the contrasting readout was also established. A major improvement in the quality of the data resulted from slightly adjusting the voltages of the two PMT detectors used which greatly simplified data analysis because the polarized fluorescence components became almost ideally temporally aligned. In addition, the *G*-factor of the instrumentation was also greatly improved. However, the measuring times used here were relatively long, taking into account that the ultimate goal of this setup is to image biological samples expressing fluorescent proteins. In fact, these are usually less bright, transiently expressed at relatively low concentrations and much less photostable than the reference fluorescent probes and calibration beads used in this study. Therefore, it would be extremely beneficial to re-equip the implemented FAIM setup in a near future with a pair of matched detectors with much improved detection sensitivity (e.g. hybrid detectors). This would be essential to minimize the acquisition times of more complex biological systems without compromising the number of photons detected per pixel, which ultimately control the resolution of anisotropy imaging. Furthermore, it would be also possible to fully exploit all the information contained in the time-resolved polarized fluorescence measurements that the system is acquiring at the pixel level, and which is lost upon integration of both polarized decays.

2.6. Supplementary information

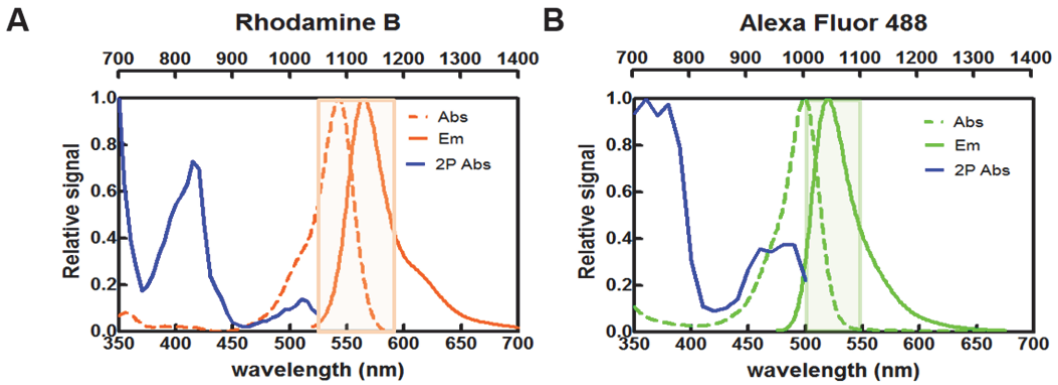

Figure S 2.1 - Normalized one-photon absorption and fluorescence emission spectra and two-photon absorption cross-section of (A) RhodB and (B) Alexa488 aqueous solutions. The normalized one-photon absorption and emission spectra are presented in (**A**) orange and (**B**) green dashed and solid lines, respectively. The normalized two-photon absorption cross-sections are presented in blue in both panels and use the upper wavelength scale in nm for better visualization. The shadowed rectangles represent the band-pass filters used in the 2PE FAIM measurements: RhodB: λ_{exc}= 820 nm; λ_{em}= 535-585 nm; A488: λ_{exc}= 760 nm; λ_{em}= 500-550 nm. Adapted from http://www.spectra.arizona.edu/.

Table S 2.1 – Steady-state fluorescence anisotropies obtained for RhodB in aqueous glycerol solutions of distinct viscosities, η, in a conventional spectrofluorometer and in the implemented FAIM setup, corrected for the depolarization induced by the objective (Microscope). FAIM measurements were performed using two different objectives: 10x, NA 0.4 air (10x) and 63x, NA 1.2 water immersion (63x) (T= 20 ± 1°C).

		Steady-state Fluorescence Anisotropy					
% glycerol (V/V)	η (cP)	Spectrofluorometer		Microscope			
		Cuvette (1PE)	Cuvette[1] (2PE)	10x[2]	63x[2]	Image 10x[3]	Image 63x[3]
0	1.0	0.040	0.057	0.020	0.004	0.021 ± 0.018	0.014 ± 0.024
10	1.3	0.043	0.062	0.042	0.018		
20	1.8	0.063	0.090	0.072	0.064	0.071 ± 0.016	0.068 ± 0.020
30	2.5	0.083	0.118	0.075	0.164		
40	3.7	0.109	0.155	0.139	0.173		
50	6.0	0.141	0.201	0.214	0.230		
60	10.8	0.190	0.272	0.289	0.282	0.268 ± 0.019	0.286 ± 0.023
70	22.5	0.257	0.367	0.372	0.356		
80	60.0	0.311	0.444	0.451	0.420		
90	219	0.344	0.491	0.491	0.479	0.481 ± 0.025	0.482 ± 0.030
100	1412	0.361	0.515	0.512	0.507		

[1] The ssFAs obtained in the spectrofluorometer (λ_{exc}= 560 nm, λ_{em}= 580 nm) were converted to the expected values if 2PE instead of 1PE was used. The conversion factor is 0.571/0.400=1.428.
[2] Single-point FA (λ_{exc}^{2PE} = 820 nm).
[3] Gaussian fits (average ± standard deviation) to the histograms obtained from the FA maps calculated on a pixel-by-pixel basis from the 127x125 pixels image.

Table S 2.2 – Steady-state fluorescence anisotropies obtained for the Inspeck™ Microscope Image Intensity Calibration beads in a conventional spectrofluorometer and in the implemented FAIM setup (Microscope). Spectrofluorometer and FAIM measurements used 10-fold diluted aqueous solutions and samples of the calibration beads prepared with mounting media, respectively. FAIM measurements were performed using two different objectives: 10x, NA 0.4 air (10x) and 63x, NA 1.2 water immersion (63x) (T= 20 ± 1°C). n.d. - not determined.

	Steady-state Fluorescence Anisotropy					
Relative fluorescence intensity	Spectrofluorometer		Microscope			
	Cuvette (1PE)	Cuvette[1] (2PE)	10x[2]	63x[2]	Image 10x[3]	Image 63x[3]
1	0.330	0.471	-	-	-	-
3	0.297	0.425	-	-	-	-
10	0.220	0.315	0.304	0.329	0.327 ± 0.088	0.337 ± 0.046
30	0.119	0.171	n.d.	0.161	0.224 ± 0.071	0.175 ± 0.078
100	0.031	0.044	n.d.	0.033	0.053 ± 0.088	0.022 ± 0.070

[1] The ssFAs obtained in the spectrofluorometer (λ_{exc}= 470 nm, λ_{em}= 510 nm) were converted to the expected values if 2PE instead of 1PE was used. The conversion factor is 0.571/0.400=1.428.
[2] Single-point FA (λ_{exc}= 760 nm)
[3] Gaussian fits (average ± standard deviation) to the histograms obtained from the FA maps calculated on a pixel-by-pixel basis from the 127x125 pixels image.

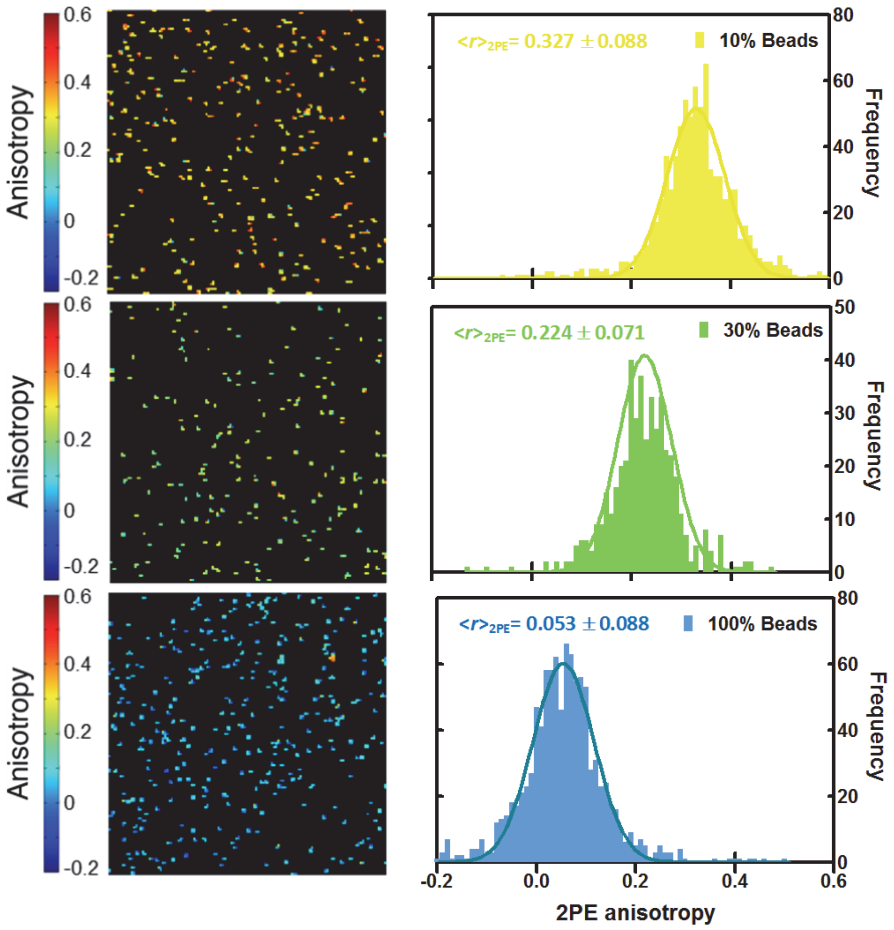

Figure S 2.2 - 2PE FA maps (left panels) and histograms (right panels) obtained for the 10, 30 and 100% fluorescent microspheres with the 10x air objective. A Gaussian distribution was successfully fitted to each of these histograms (full curves), the average and standard deviation of these fits being presented in Table S 2.2. The number of pixels processed were n= 816, n= 471 and n= 1003 for the top, middle and bottom images, respectively. Images and the raw data for the histograms were obtained using MATLAB.

3. Calcitonin

3.1. Overview

It is well established that many biological factors are susceptible to modulate amyloid fibril formation in vivo, including biological membranes. These can induce the pathological conversion of amyloidogenic proteins/peptides into toxic aggregates by providing a soft surface that can promote their misfolding and self-assembly. In this chapter, both human and salmon calcitonins (hCT and sCT, respectively) were used as model peptides to study their fibrillation in solution and the possible role that negatively-charged lipid membranes can play in the modulaton of their aggregation pathway. Using a combination of far-UV circular dichroism (CD) and steady-state and time-resolved fluorescence measurements, we structurally and kinetically characterized the properties of both unmodified and fluorescently-labeled hCT and sCT in homogeneous solution and in interaction with large unilamellar vesicles prepared with a variable lipid composition..

This part of the work is divided in 3 sections. In the **first section**, a detailed characterization of the photophysical properties of the recently commercialized dye HiLyte™ Fluor 488 (HL488) was carried out in homogeneous solution since this topic had not yet been comprehensively addressed in the literature. This preliminary study was essential to provide an interpretation framework for the spectroscopic data obtained later with the fluorescently-labeled peptides in more complex systems, like in interaction with lipid membranes. The fluorescent dye HL488, positioned at the N-terminal of the peptides, was a sensitive reporter of the conformational transitions undergone by both peptides upon increasing the 2,2,2-trifluoroethanol (TFE) content of the binary solvent mixtures. In agreement with the data obtained from parallel far-UV CD studies, a two-step α-helical folding was detected for hCT over the whole TFE/buffer range, whereas sCT displayed a single conformational transition, with the α-helical structure promoted almost completely in a single step at 0-30% TFE.

In the **second section**, we aimed to define reproducible and feasible conditions to study the kinetics of CT amyloid fibril formation in solution using the extrinsic amyloid dye Thioflavin T and by taking advantage of the fluorescence properties of tracer amounts of the HL488-labeled peptides. Preliminary results indicate that the aggregation lag times and the peptide concentrations used in the hCT fibrillation kinetics do not have a canonical relationship, in agreement with a recent study (Kamgar-Parsi *et al.*, 2017). However, at this point we were not yet able to implement a reproducible microplate reader fluorescent assay of hCT fibrillation in solution.

Finally, in the **third section** of this chapter, the interaction of both HL488-labelled calcitonin variants with 1-palmitoyl-2-oleoyl-sn-glycero-3-phosphocholine (POPC) liposomes prepared with a variable content of 1-palmitoyl-2-oleoyl-sn-glycero-3-phosphoserine (POPS) was

examined by performing a multi-parametric steady-state and time-resolved fluorescence intensity/anisotropy study. The partition coefficient of monomeric sCT/HL488-sCT varied exponentially with the anionic lipid content of the vesicles containing more than 10 mol% of POPS confirming the importance of electrostatic interactions in sCT binding to the lipid vesicles. On the contrary, no spectroscopic evidence was obtained for hCT/HL488-hCT binding to liposomes prepared with a wide range of lipid compositions, at variance with the literature. A more detailed study of the interaction between higher concentrations of HL488-sCT and POPC:POPS 80:20 LUVs was also carried out. The excitonic band detected in the absorption spectra of HL488-sCT at a low L/P molar ratio (at low phospholipid concentrations) revealed the formation of membrane-bound parallel (H-type) dimers/oligomers between the HL488 chromophores covalently linked to sCT, which were non-fluorescent. Accordingly, the biphasic changes detected in the fluorescence intensity/mean lifetime of HL488-sCT as function of its membrane surface concentration were interpreted in relation to a coupled partition/oligomerization model of HL488-sCT.

The experimental design was shared by me, M.Sc. Paulo Caldas and Prof. Ana Coutinho while the laboratory work and data analysis was performed by me with the following exceptions:

- all the time-resolved fluorescence measurements were performed by Dr. Aleksander Fedorov (CQFM/IBB, IST, Universidade de Lisboa (UL), Portugal). Their analysis was shared by me and M.Sc. Paulo Caldas;
- part of the laboratory work and data analysis related to the characterization of the interaction of CT variants with anionic liposomes was performed by M.Sc. Paulo Caldas;
- the far-UV CD measurements were performed at Nuno C. Santos Lab (*Instituto de Medicina Molecular* (IMM), UL, Portugal) with the aid of Dr. André Faustino (both in laboratory work and data analysis), to whom we are much thankful. Dr. André Faustino also aided with the global analysis of TFE-induced folding of CT peptides.

Prof. Ana Coutinho and Prof. Manuel Prieto supervised the work.

3.2. Introduction

3.2.1. The calcitonin peptide family

The calcitonin peptide family consists of calcitonin (CT), amylin or IAPP, calcitonin gene-related peptide (CGRP), adrenomedullin and intermedin (Naot and Cornish, 2008; Barwell et al., 2012; Cope et al., 2013). These are structurally related peptide hormones, with sequence homology ranging between 20% and 50%. All members of this family contain a functional disulfide bond that confers a short ring-like structure to the N-terminal of the peptide (with the exception of adrenomedullin, in which the disulfide is located between residues 16 and 21) and a C-terminal amidated residue (Figure 3.1). The sequence of this region is similar among CT family members (Cope et al., 2013).

Figure 3.1 - Members of the calcitonin family of peptides share common features in their sequence. All members contain a disulfide bond in the N-terminal region and a C-terminal amide residue. Adapted from (Naot and Cornish, 2008).

3.2.2. Biosynthesis and primary sequence of calcitonin

CT is a hormone produced by the C-parafollicular cells of the thyroid glands in mammals thas was discovered in 1962 by Copp and Cheney (Copp and Cheney, 1962) and plays an important role in calcium metabolism. CT and CGRP are encoded by the same gene, which is present in the short arm of chromosome 11. Translation and production of either peptide is tissue-dependent and is a result of alternative splicing of the primary RNA transcripts. In humans CT is synthesized as a preprohormone with 141 residues. The leader sequence is cleaved during the transport into the endoplasmatic reticulum, resulting in the procalcitonin with 116 residues, which is further proteolytically cleaved and amidated before secretion, originating CT and katacalcin, the latter with 21 residues (Jacobs *et al.*, 1981; Rosenfeld *et al.*, 1983; Wimalawansa, 1997).

CT is also present in other organisms as it was found to be synthesized by the ultimobranchial glands of birds, fishes, reptiles and amphibians (Motta *et al.*, 1998; Li *et al.*, 2009). The isolation and sequence determination of several variants of this peptide

hormone was achieved by isolating the peptide from either ultimobranchial bodies or isolated thyroid tissues. For example, from normal thyroid for porcine (pCT) (Potts *et al.*, 1967) and bovine (bCT) (Brewer and Ronan, 1970) and for sCT from ultimobranchial bodies (Niall *et al.*, 1969). However, since the human thyroid is a poor source of calcitonin whereas thyroid medullary carcinoma contains a high concentration of the hormone, hCT was isolated in pure form from a mass of medullary carcinoma (Neher *et al.*, 1968; Byfield *et al.*, 1969). The normal range of hCT in the blood is <10 pg/mL (~2.93 pM) and a serum CT value >100 pg/mL should be considered suspicious for medullary cancer. In cases of nodal metastases (metastases in lymph nodes near the primary tumor), the basal CT levels can be in the range of 10 – 40 pg/mL, whereas distant metastases are typically associated with a level >150 pg/mL and often >1,000 pg/mL (Roy *et al.*, 2013).

CT consists of 32 amino acids residues with an N-terminal disulfide bridge between cysteines in positions 1 and 7 and a C-terminal proline amide residue (Figure 3.3). Only eight residues are common to all species studied so far, and these are clustered at the two ends of the molecule – residues 4 to 7 and positions 1, 9, 28 and 32 (Motta *et al.*, 1998; Zaidi *et al.*, 2002; Chang *et al.*, 2004). Nevertheless, there is some similarity in the properties of the different amionacids e.g. one amino acid in the two sequences is different but both are hydrophobic. The process of maintaining the calcium homeostasis seems to be of greater importance in non-mammalian animals, as it was well reviewed by Hirsch and Baruch (2003) and Davey and Findlay (2013). This might explain why some variants, like fish CTs (salmon and eel (eCT)), are much more potent - about 40-fold – than, for example, human or porcine. Normally, modifications of thyroidal calcitonins that increase the homology with the sCT sequence increase their biological activity (Zaidi *et al.*, 2002).

3.2.3. Biological activities of calcitonin

The major physiological role of CT is its inhibitory action on osteoclast activity which has been shown both in vivo, in organ culture of bone, and in vitro, in isolated osteoclasts (Davey and Findlay, 2013). The peptide is secreted in response to increased serum calcium levels, having a regulatory function in calcium-phosphorus metabolism, inhibition of osteoclast bone resorption (process by which osteoclasts break down bone resulting in a transfer of calcium from bone fluid to the blood), decreasing calcium absorption in the intestine and kidney tubular reabsorption (Brown, 2013; Davey and Findlay, 2013). CT production is inhibited when the calcium concentration is decreased beyond normal levels, which then results in the secretion of the parathyroid hormone (PTH), which promotes the contrary reaction to CT in the body. The normal concentration of calcium in the bloodstream in maintained by the action of these two hormones (Figure 3.2).

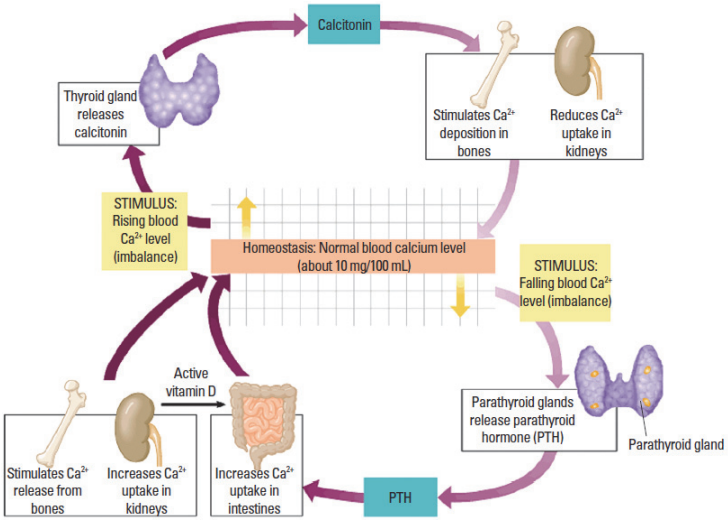

Figure 3.2 - Calcium Homeostasis. CT reduces the amount of calcium excreted by the bone, inhibiting the osteoclast activity and decreasing bone resorption. In response to a decline in serum calcium, the parathyroid glands secrete parathyroid hormone (PTH). PTH stimulates the release of Ca^{2+} from bone, increasing bone resorption. Therefore, these two hormones act to maintain a normal concentration of calcium in the bloodstream. Adapted from (Yi *et al.*, 2011).

The density of CT receptors (CTRs) in osteoclasts, a type of bone cell that resorbs bone tissue and the main cellular target of this hormone, is about one million per cell. CT binds with extreme affinity to the calcitonin receptors, while other peptides from the calcitonin family, like IAPP and CRGP, can also bind them but with low affinity. CT can cause changes in osteoclast adhesion, by affecting integrin engagement, the actin cytoskeleton and a number of components of the cell adhesion apparatus. It also inhibits osteoclastic motility and spreading (Breimer *et al.*, 1988; Fattore *et al.*, 2008). CT does not seem to affect osteoclast apoptosis or the expression of genes and transcription factors important for osteoclast differentiation and activity, although it has been reported that it can alter enzyme activity or ion transporter distribution (Fattore *et al.*, 2008). Another putative action of CT might be related to pregnancy and lactation; circulating CT levels are elevated during these conditions, supporting the concept that CT can protect the maternal skeleton from excessive resorption during lactation via its inhibitory actions on osteoclasts (Hirsch and Baruch, 2003). The CTR belongs to the subfamily B of G-protein coupled receptors. CTR can form complexes with members of the membrane protein family called receptor activity-modifying proteins (RAMPs). The association of CTR with the different RAMPs creates multiple receptor phenotypes with different specificities for the different members of the CT family (Sexton *et al.*, 2009; Davey and Findlay, 2013).

3.2.4. Therapeutic applications of calcitonins

Due to its ability in limiting bone resorption, CT has been actively used to treat bone disorders such as osteoporosis and Paget's disease. CTs exhibit low specificity which allows animal calcitonins to be used for the treatment of human diseases. The salmon variant has been used as a replacement for the human variant, which has a high tendency to self-associate and form amyloid fibrils in aqueous solution (Arvinte *et al.*, 1993; Kanaori and Nosaka, 1996; Motta *et al.*, 1998; Itoh-Watanabe *et al.*, 2013). hCT also self-assembles into fibrils in vivo in patients with medullar carcinoma of the thyroid (Khurana *et al.*, 2004). The high potency of sCT and lower tendency to self-associate made it a more suitable target for drug development for treatment of disorders of bone and mineral metabolism as an alternative to hCT. In addition, it is a suitable tool to be used in the study of molecular mechanisms of amyloid formation with particular attention to the early stages of aggregation. Still, long-term application of animal CTs leads to a sharp activity decrease in clinical use due to the accumulation of antibodies against these heterologous CTs (Li *et al.*, 2009) and also causes side effects such as anorexia and vomiting (Motta *et al.*, 1998; Fowler *et al.*, 2005; Li *et al.*, 2009). Both salmon and human calcitonins were indicated for the treatment of hypercalcemic emergency and Paget's disease, but only sCT was indicated for the treatment of osteoporosis. However, it has also been discouraged recently since it was determined that the potential risks of sCT outweigh its benefits (Honig *et al.*, 2013).

3.2.5. Structural and conformational features of calcitonin bioactivity

The primary structure of CTs is intrinsically related to their biological function. Structure-activity relationships studies have shown that several of the common structural features described above for this class of peptide hormones are very important for their in vivo bioactivity and receptor binding and/or signal transduction. The molecular determinants at the primary sequence level that have been found to be essential for in vivo hypocalcemic activity of CTs include the presence of a C-terminal proline residue in amidated form and the presence of the ring structure between Cys1 and Cys7 in hCT and pCT but not sCT. Receptor binding and adenylate cyclase activation studies have further shown that the highly conserved N-terminal region between residues 1 and 7 contains the structural requirements for adenylate cyclase activation, i.e. the agonist character of the CTs (Feyen *et al.*, 1992). Further studies conducted with chimeric constructs between sequences of hCT and glucagon (Stroop *et al.*, 1995) and PTH and CT (Bergwitz *et al.*, 1996) have suggested the presence of two physically dissociable CT interaction sites in the CTR that most likely cooperate in complexing CT with the receptor (Stroop *et al.*, 1995). These works led to the proposal that the N-terminal sequence (residues 1–11) interacts with the

membrane-embedded domain of its receptor and the associated loops, whereas the C-terminal CT sequence (between residues 12 and 32) binds to the N-extracellular terminal domain of the receptor, which has previously been suggested to be responsible for ligand binding. In the central region, CTs have a pattern of hydrophobic amino acids at every three or four residues, a typical feature of amphipathic α-helices (AH) that can bind to lipids (Epand *et al.*, 1983; Moriarty *et al.*, 1998; Schmidt *et al.*, 1998) (exemplified in Figure 3.3 B for hCT and sCT). This variable middle portion may produce variations in its potency and duration of action. This region has been suggested to act as an immunogen when exposed to antibody-producing cells in vivo (Breimer *et al.*, 1988; Azria, 1989), although more recently it has been questioned whether the development of CT antibodies in response to its administration is of clinical relevance This observation is related to the fact that the bioavailability of CT in the different preparations used for clinical uses - nasal spray and parenteral – might result in different antibody level production, with variable therapeutic outcomes (Chesnut *et al.*, 2008).

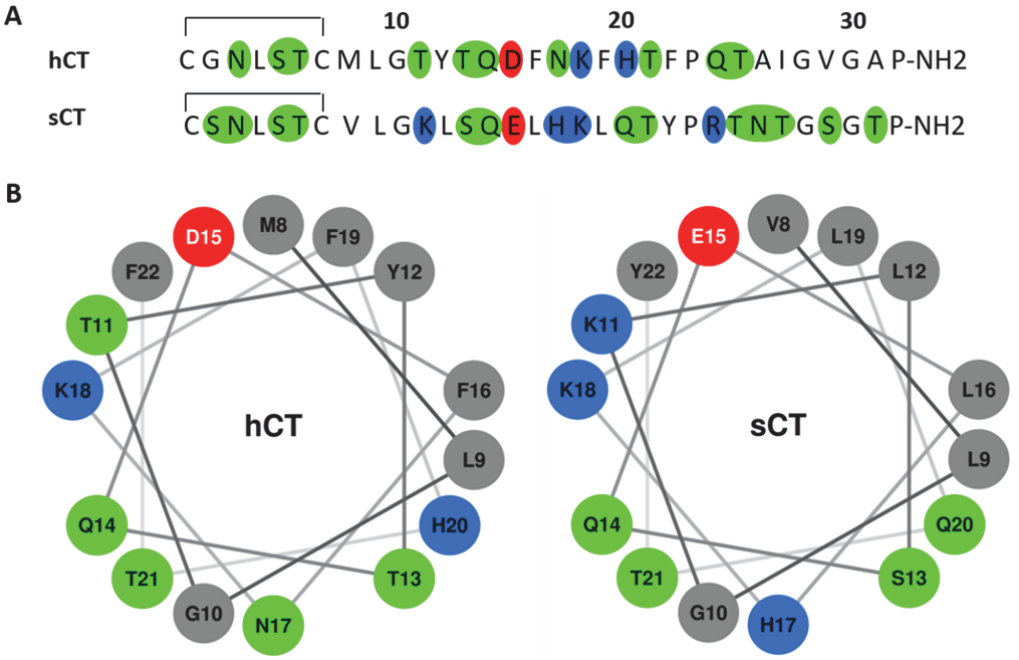

Figure 3.3 – Comparison between the (A) primary sequences and (B) helical wheels of human (hCT) and salmon (sCT) CT. (**A**) CT contains a disulfide bridge between Cys1 and Cys7 and a C-terminal amidated residue. (**B**) The N-terminal of these peptides can form an amphipathic helix as illustrated by the helical wheel from residues 8 to 22. Residues in blue, red and green are, respectively, positively charged, negatively charged and polar (solvent/headgroup accessible); grey residues are hydrophobic (tailgroup of phospholipids accessible).

Secondary structure predictions have proposed early on that a potential AH in the central region of teleost CTs might be associated with their bioactivity (Merle *et al.*, 1979), as compared to the CTs from other species, including hCT (α-helix hypothesis). This putative amphipathic α-helical structure of CTs was also suggested to be important for peptide binding to the cell membrane (Epand *et al.*, 1985; Stroop *et al.*, 1996; Hilton *et al.*, 2000). In the early 80s, Kaiser and co-workers systematically studied this hypothesis by testing sCT analogs designed to have a minimum homology with the putative α-helical region of the native sCT sequence while, at the same time, a maximum AH forming potential was maintained (Moe *et al.*, 1983; Moe and Kaiser, 1985; Green *et al.*, 1987). These analogs appeared to have α-helical contents similar to that of sCT and were close in potency to sCT, supporting the role of the amphiphilic α-helical propensity in controlling sCT bioactivity. The α-helix hypothesis was further tested using a series of α-helical and/or non-α-helical CT analogs (Epand *et al.*, 1983, 1985, 1986, 1988; Findlay *et al.*, 1985; Twery *et al.*, 1988; Nakamuta *et al.*, 1990; Houssami *et al.*, 1995). These studies revealed that, in addition to the putative α-helical conformation in the middle region of CT, other factors are also involved in determining bioactivity, like the conformational flexibility of the peptide and long-range interactions between the N- and C-terminal parts of CT (Epand *et al.*, 1986, 1988).

3.2.6. CD and NMR studies on calcitonins

Understanding the structural and conformational features of CTs is a fundamental prerequisite for the elucidation of their molecular mechanism of action and is the basis for the rational design of potent agonists and antagonists of their physiological effects (Kapurniotu, 2004). As the elucidation of the hormone-receptor complex is extremely challenging, the secondary and 3D structure of the CTs in solution and, in particular, the conformational features of sCT as compared to hCT and other species, have been extensively studied over the past 50 years using primarily CD and NMR spectroscopies (Motta, Temussi, *et al.*, 1991; Motta *et al.*, 1998; Amodeo *et al.*, 1999; Kamihira-Ishijima *et al.*, 2000; Ogawa *et al.*, 2006; Huang *et al.*, 2012). The majority of the spectroscopic studies have been performed in non-α-helix-inducing (e.g. aqueous solutions and dimethyl sulfoxide (DMSO)/water mixtures) and α-helix-inducing (e.g. methanol (MeOH) and TFE) solvent conditions, as well as in the presence of membrane-mimic systems (e.g. sodium dodecyl sulfate (SDS) micelles).

CD spectroscopy has been extensively employed to characterize the influence of different solvents or membrane-mimicking systems on the molecular conformations adopted by several natively occurring CT sequences from different species and deletion and substitution synthetic analogs of CTs (Epand *et al.*, 1983; Arvinte and Drake, 1993; Ogawa

et al., 1994; Kazantzis *et al.*, 2002; Andreotti and Motta, 2004; Wang *et al.*, 2005a; b; Andreotti *et al.*, 2006; Kamgar-Parsi *et al.*, 2017). Early CD studies revealed that pCT, hCT and sCT were predominantly in a random coil conformation in various buffer solutions (Epand *et al.*, 1983; Arvinte and Drake, 1993; Siligardi *et al.*, 1994). These authors also explored the effect of adding TFE or aliphatic alcohols, on the conformational equilibria of these peptides. The secondary structure of both hCT and sCT underwent pronounced alterations with the increasing content of TFE/MeOH in the binary mixtures prepared with water as reported by their CD spectra. The ordering of the Cys1-Cys7 disulfide bond, detected at 290 nm, was similar for hCT and sCT, being completed below 11 mol% TFE/H_2O. At low TFE concentration, the dihedral angle of the S-S bond adopts a preferred conformation that correlates with the initiation of the α-helix (Arvinte and Drake, 1993). On the other hand, there was a sharp increase in sCT α-helix content up to 6 mol% of TFE while the first backbone folding step for hCT was completed at 11 mol% TFE. With the increase in TFE mol% there was an increase in the signal at 220 nm, indicating that the % α-helix was increasing in both peptides. In pure TFE, hCT acquired up to 57% of α-helix and sCT 42% (Arvinte and Drake, 1993). This revealed that sCT forms more readily α-helical conformation than hCT, although in pure solvent, the main helical conformation is more extended in hCT than in sCT (Arvinte and Drake, 1993; Siligardi *et al.*, 1994).

Similar CD studies were also conducted using SDS micelles and liposomes (Epand *et al.*, 1983, 1986; Orlowski *et al.*, 1987; Motta, Pastore, *et al.*, 1991; Siligardi *et al.*, 1994). Overall, these studies revealed the ability of several CT variants in adopting a helical structure in these environments. Siligardi and co-workers argued that the conformational properties of ultimobranchial and thyroidal CTs were quite different, after detecting 3 – 4 helical turns in sCT *versus* one helical turn in hCT when in interaction with SDS micelles (Siligardi *et al.*, 1994). Others showed that the degree of α-helix in the presence of SDS was much larger for sCT (Epand *et al.*, 1986; Orlowski *et al.*, 1987) than for hCT but smaller than the % of α-helix of sCT in 90% MeOH (Orlowski *et al.*, 1987). These results were related with the CD measurements performed to study the interaction of CTs (pCT, hCT and sCT) with liposomes prepared with variable mixtures of zwitterionic and anionic phospholipids, which suggested the formation of an AH between residues 8 and 22 with the increase in negatively charged lipids (Epand *et al.*, 1983).

The solution structures of several CT variants were also explored using 2D NMR techniques complemented with molecular modeling. In non-α-helix-inducing solvent conditions, both peptides have been found to adopt partially folded structures. A NMR study of sCT at in a 90% $DMSO_{d6}$-10% H_2O (v/v) mixture showed that the dominant feature was an extended conformation but with clear indications for a short double-stranded antiparallel β-sheet

regions in the central region comprising residues 12-18, connected by a three-residue hairpin loop formed by residues 14-16. Two tight turns, made by residues 6-9 and 25-28, were also identified, but no evidence was found for the presence of a regular helical segment (Motta *et al.*, 1989). The structure of hCT was also characterized in pure $DMSO_{d6}$ or 85% $DMSO_{d6}$ -15% water mixtures (Motta, Temussi, *et al.*, 1991). Again, it was found that the DMSO-water mixture rigidifies the polypeptide chain, favoring an ordered, extended conformation. A short double-stranded antiparallel β-sheet was now detected between residues 16-21, with a hairpin loop connection made by two residues, Lys18 and Phe19. Two tight β-turns in the N- and C-terminal, comprising residues 3 to 6 and 28 to 31, respectively, were also identified. More recently, high-resolution structures of hCT at concentrations of 0.3 mM and 1 mM in phosphate buffer (pH 2.9, 7% D_2O and 50 mM NaCl) have been elucidated using NMR spectroscopy (Huang *et al.*, 2012). At a peptide concentration of 0.3 mM, hCT adopted a flexible and extended structure (Figure 3.4 B, top panel). However, when the measurement was performed with 1 mM of peptide, the peptide undergoes a conformational transition from an extended structure to a β-hairpin in the central region (Tyr12-Phe19) that occurred concomitantly to its oligomerization in solution as detected by diffusion-ordered NMR (Figure 3.4 B, bottom panel). This structural rearrangement was stabilized by intermolecular $\pi - \pi$ stacking interactions between the aromatic side chains of Tyr12 and Phe16. These interactions were proposed to be critical for peptide association and fibrillation in aqueous solution (Huang *et al.*, 2012).

In α-helix-inducing solvent conditions, monomeric hCT prepared in a mixture of 40%TFE-60% H_2O with 0.05 M deuterated acetic acid at a concentration of 2 mM showed a α-helical segment from Leu4 to His20 (Figure 3.4 A, green helix, and C) (Ogawa *et al.*, 2006). On the other hand, Meadows and co-workers (Meadows *et al.*, 1991) found that monomeric sCT prepared in 90% MeOH-10% H_2O at a concentration of 6 mM assumes a α-helical segment from Val8 to Tyr22 (Figure 3.5 A, green helix, and B). An identical segment was proposed for sCT in 9:1 deuterated TFE/H_2O mixture and pure TFE, with the Cys1-Cys7 ring well defined and in close association with the helix, while the C-terminal decapepeptide folds back towards the core, forming a loose loop (Meyer *et al.*, 1991).

Several NMR studies of CTs were also conducted in the presence of SDS micelles. The first reports were from Motta and co-workers which elucidated the structure hCT (Motta *et al.*, 1998) and sCT (Motta, Temussi, *et al.*, 1991; Morelli *et al.*, 1992) in this membrane-mimicking environment. hCT in interaction with the detergent micelles takes up an AH between residues 9 and 16 (Figure 3.4 A, blue helix), with residues 16 to 19 forming a type-I β-turn acting as end capping to stabilize the C-terminus of the helix. From residue 20 onwards, the rest of the structure is extended with no interactions with the helix observed (Motta *et al.*, 1998). In contrast, sCT was shown to take up a unique backbone fold (helical

structure) between residues 6 and 22 (Figure 3.5 A, blue helix), which contains the segment 8-22 found in TFE (Meyer *et al.*, 1991) and MeOH (Meadows *et al.*, 1991). The C-terminal Pro23-Pro32 decapeptide was found in close association with the helix (Figure 3.5 C). Morelli and co-workers compared the conformational flexibility of hCT and sCT in interaction with SDS micelles at a CT:SDS ratio of ca. 1:120 at both pH 4.1 and 7.2 by conjugating NMR measurements with molecular dynamics (MD) simulations in MeOH (Amodeo *et al.*, 1999). Compared to sCT (Figure 3.5 C), the authors confirmed that hCT had a shorter helix length and no helix-tail interactions (Figure 3.4 D).

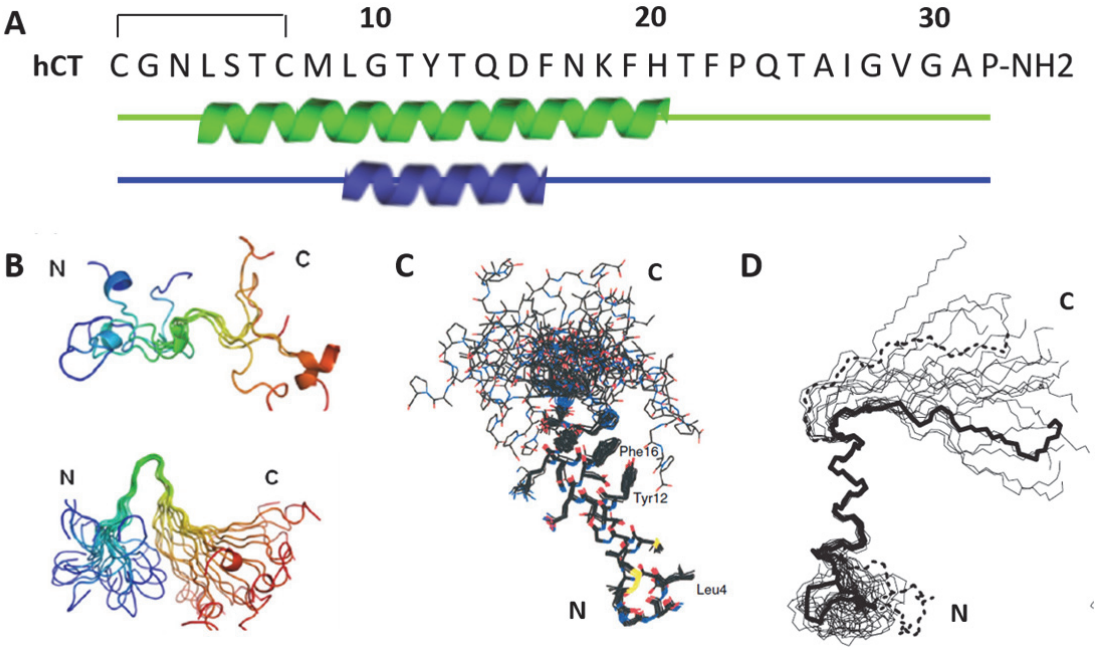

Figure 3.4 - Summary of conformational preferences for hCT measured using NMR spectroscopy. (A) Amino acid sequence of hCT and the length of its central amphipathic α-helix in different solvent environments: 40%TFE-60% H_2O with 0.05 M deuterated acetic acid - green helix (Leu4-His20) (Ogawa *et al*., 2006); SDS micelles – blue (Leu9-Phe16) (Motta *et al*., 1998 and Andreotti et al, 2006). **(B)** A conformational change in hCT accompanies peptide association and oligomerization in aqueous solution. Superimposition of 5 and 20 energy-minimized structures of hCT at peptide concentrations of 0.3 mM and 1 mM in phosphate buffer (pH 2.9, 7% D_2O and 50 mM NaCl) (top and bottom panels, respectively). For the 0.3 mM sample, hCT is largely unstructured. In the 1 mM sample, a well-defined β-hairpin structure is present in the central region of the peptide from Tyr12 to Phe19. The peptide chains are labeled with gradient colors from blue to red throughout the sequence from *N*-terminus to *C*-terminus (adapted from Huang *et al*., 2012). **(C)** Monomeric hCT prepared in a mixture of 40%TFE-60% H_2O with 0.05 M deuterated acetic acid showed a α-helical segment from Leu4 to His20 (overlay of 20 minimum energy structures, adapted from Ogawa *et al*., 2006). **(D)** Monomeric hCT stabilized by SDS micelles at a 1:120 hCT:SDS ratio adopts a α-helical segment from residues 13-21 with a constant helical region in the range 13-19, with no helix-tail interaction (best fit superposition of 22 frames of the 1.1 ns unrestrained MD simulation, adapted from Amodeo *et al*., 1999).

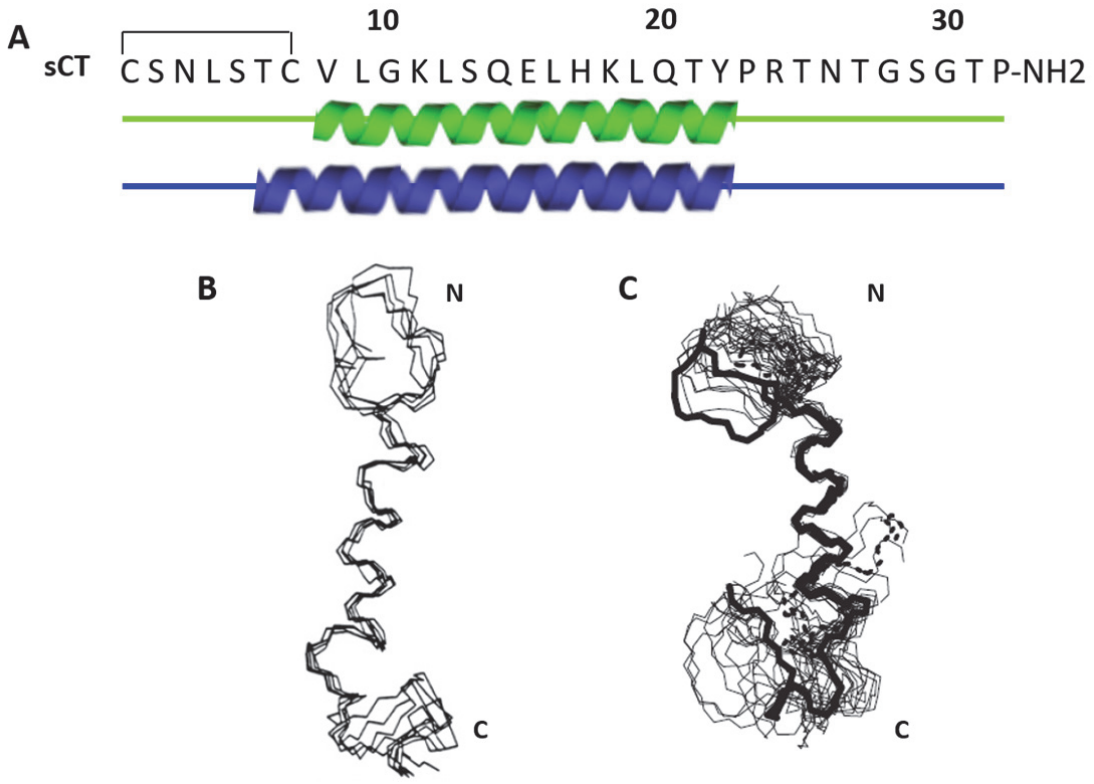

Figure 3.5 - Summary of conformational preferences for sCT measured using NMR spectroscopy. (A) Amino acid sequence of sCT and the length of its central α-helix in different solvent environments: 90% MeOH-10% H_2O (Meadows *et al*., 1991), 90%TFE-10% water and pure TFE (Meyer *et al*., 1991) – green helix (Val8-Tyr22); SDS micelles – blue helix (Thr6-Tyr22) (Andreotti *et al*., 2006). **(B)** Monomeric sCT prepared in 90% MeOH-10% H_2O showed a α-helical segment from Val8 to Tyr22 (adapted from Meadows *et al*., 1991). **(C)** Monomeric sCT stabilized by SDS micelles at a 1:120 sCT:SDS ratio adopts a similar middle α-helix spanning 9-19, with the C-terminal decapeptide folding back towards the helix (best fit superposition of 22 frames of the 1.1 ns unrestrained MD simulation) (adapted from Amodeo *et al*., 1999).

Interestingly, for hCT the flexibility was extended over the whole polypeptide chain, whereas the presence of three domains was apparent in the sCT structure with flexible loops connecting the head and the helix and the helix and tail regions (Figure 3.5 A, blue helix, and C). An important feature of the C-terminal region of sCT is the absence of large fluctuations up to the last residue, which confirms the influence of long range helix-tail interactions in the stabilization of the overall peptide folding. Motta and co-workers related the different aggregation propensity of hCT and sCT with the differences in their 3D structure. Although the predominant conformational feature of both CTs is an AH, the C-terminal decapeptide of sCT forms a loop folded back towards the helix, which could prevent sCT molecular association (Amodeo *et al.*, 1999) . For hCT, on the other hand, the hydrophobic side of the helix remains unhindered (Motta *et al.*, 1998), a feature also assumed to be important for the proper interaction with the receptor (Andreotti and Motta, 2004). Interestingly, sCT, but not hCT, was also shown to be able to dimerize in aqueous

solution via the hydrophobic phase of the AH (formation of an antiparallel α-helical dimer), and that Leu-Leu interactions stabilized the aggregate, thus preventing fibril maturation (Andreotti and Motta, 2004).

The structure activity studies performed by Kazantzis and co-workers with hCT and hCT analogs suggested that a type I β-turn/β-sheet conformation in the region 17-21 may be important for hCT bioactivity. Also, the conformation and topological features of the side chains of amino acids residues 18 and 19 are strongly associated with hCT self-assembly state and to the human receptor binding affinity (Kazantzis *et al.*, 2002).

The relation between helical length and the biological activity is not straightforward. The relative biological activities among the different variants of CT are known, assuming the potency of therapy for hypercalcaemia of hCT as one (Azria, 1989). hCT with Leu substitutions (positions 12, 16 and 19) takes up a helical structure between the residues 4–20 (17 residues) and has a potency of 15–20 (Maier *et al.*, 1976), eCT takes up the same helical conformation and has 40 of potency, similar to sCT which has a AH between residues 8 and 22 (15 residues) (Ogawa *et al.*, 2006).

3.2.7. Calcitonin has a tendency to aggregate and form fibrils

hCT tendency to aggregate and form fibrils in aqueous solution has been reported for long with the first studies performed in 1970 by Sieber and co-workers (Sieber *et al.*, 1970). hCT has also been associated with medullary thyroid carcinoma, being unequivocally demonstrated that this peptide is indeed the sole constituent of the amyloid deposits in that disease (Khurana *et al.*, 2004).

The hCT fibrillation kinetics was first proposed to follow a double nucleation mechanism by Arvinte and co-workers based on their EM studies. Briefly, the fibrillation starts with a homogeneous nucleation step in which spherical aggregates (“nodules”) and the first fibrils are formed from monomeric peptides; from these initial aggregates, multiple fibrils would then radiate in the second heterogeneous nucleation step. CD and infrared (IR) spectroscopy studies further revealed that hCT in its fibrillated state contains both α-helical and β-sheet components; the β-sheet component was proposed to be formed intermolecularly by the tail residues 23-32. Already at that time, electrostatic interactions between the monomers of hCT were considered to play an important role in its initial aggregation step (Arvinte *et al.*, 1993). At pH 7.4, the net charge of each CT variant is significantly different since hCT has an overall positive charge of one, whereas pCT and sCT have two and three positive net charges, respectively. In 1995, based on a ^{1}H-NMR study, Kanaori and Nosaka proposed that the molecular association of hCT is initiated by intermolecular hydrophobic contacts in the N-terminal (Cys1-Cys7) and central (Met8-

Pro23) regions, the C-terminal region (Gln24-Pro32) being subsequently involved in the fibrillation (Kanaori and Nosaka, 1995). On the same year, Bauer and collaborators systematically investigated the in vitro aggregation products of hCT using TEM. The concentration and history of the aggregated hCT solutions impacted the relative frequency of the supramolecular assemblies formed, which revealed distinct helical symmetries at their different levels of aggregation (Bauer *et al.*, 1995).

Several studies of the assembly process of hCT using multiple biophysical techniques confirmed later on that the fibrillogenesis of hCT is a pH-dependent process (Kamihira-Ishijima *et al.*, 2000, 2003; Naito *et al.*, 2004). Comparative studies performed at pH 7.5 and pH 3.3 revealed that under neutral conditions, hCT readily associates into fibrils, whereas the peptide slowly self-assembles under acidic conditions (Kamihira-Ishijima *et al.*, 2000). Using high-resolution solid-state ^{13}C NMR, it was directly observed that a local conformational transition from an α-helix to a β-sheet occurs in the central region of hCT in the process of fibril formation and that the conformation of the fibrils is pH dependent, due to changes in molecular interactions among charged side chains. While at pH 3.3 Lys18 and His20 are expected to be positively charged but located almost on opposite sides in the AH (Epand *et al.*, 1983), Asp15 is neutral. This causes unfavorable electrostatic interactions between positively charged side chains, leading to the formation of a mixture of parallel β-sheets in the entire region and antiparallel β-sheets in the central region. At pH 7.5, Lys18 has a positive charge while Asp15 has a negative charge, which enables the formation of homogeneous fibril with an antiparallel β-sheet conformation in the central region and a random coil in the *C*-terminus region (Figure 3.6) (Kamihira-Ishijima *et al.*, 2000).

This view was confirmed by studying the influence of the negatively-charged Asp15 residue in determining the structure and orientation of the hCT molecules in the fibril (Kamihira-Ishijima *et al.*, 2003). The authors demonstrated by using D15N-hCT that the absence of the negatively charged group in hCT lead to the fibril structure as a mixture of parallel and antiparallel β-sheets, confirming the importance of favorable electrostatic interaction among the charged side chains of hCT in controlling the preferable direction of molecular association.

The important role of aromatic residues in hCT in the stabilization of amyloid fibrils was also confirmed by Itoh-Watanabe and collaborators. The authors found that fibril formation rates of hCT were significantly reduced when aromatic residues (Tyr12, Phe16 and Phe19) were replaced with Leu residues (as in sCT), although their fibril structures were similar. Finally, the initial stage of hCT fibrillation was also examined in detail in HEPES solution (20 mM, pH 5.6) since these conditions were found to slow down the kinetics. Highly spherical

intermediates were clearly observed in TEM experiments that progressively converted into protofibrils (Itoh-Watanabe *et al*, 2013).

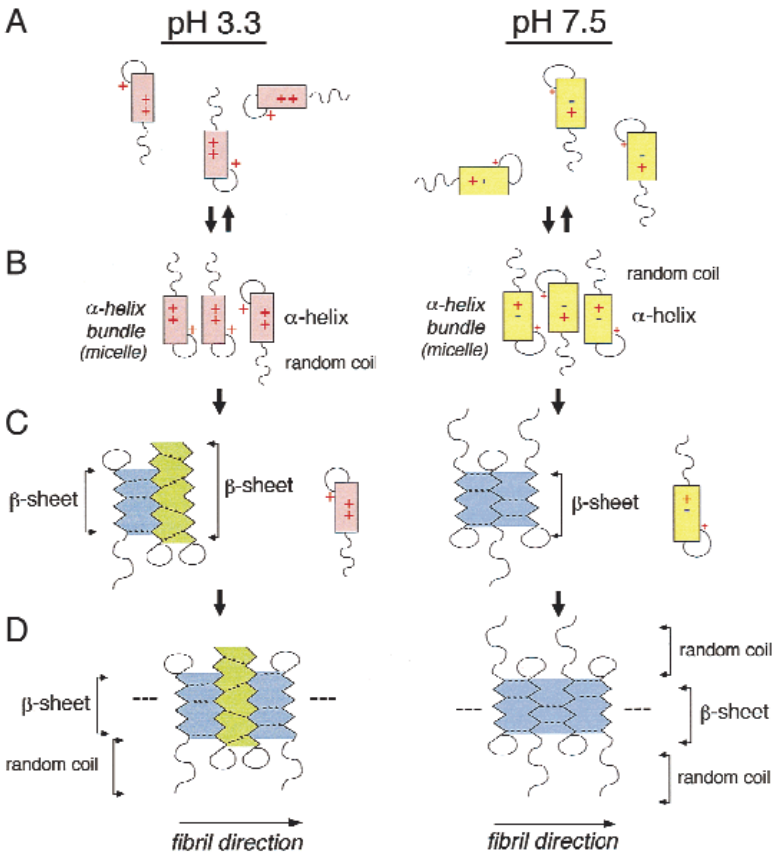

Figure 3.6 - Schematic representation of hCT fibrillation mechanism at pH 3.3. and pH 7.5. (A) hCT monomers in solution; **(B)** a homogeneous association to form the α-helical bundle (micelle); **(C)** a homogeneous nucleation process to form the β-sheet and heterogeneous associating process; (**D**) a heterogeneous fibrillation process to grow a large fibril. The alignment of the β-sheets is dependent on the pH due to the variable charges of the amino acid residues Asp15, Lys18 and His20 at the different pHs. Adapted from (Kamihira-Ishijima *et al.*, 2000).

The residues in the central region of hCT are sufficient for fibril formation, as a truncated peptide fragment of hCT as short as a pentapeptide - from Asp15 to Phe20 (DFNKF) - forms fibrils, similar to those formed by the intact peptide. The authors remarked that the formation of amyloid fibrils by this rather hydrophilic peptide was quite notable (Reches *et al.*, 2002), reinforcing the importance of aromatic interactions in the process of amyloid fibril formation (Azriel and Gazit, 2001), which was later confirmed experimentally by Shtainfeld and collaborators (Shtainfeld *et al.*, 2010). A MD simulation study implied that DFNKF might form a parallel stranded single β-sheet stabilized by electrostatic and hydrophobic interactions and by hydrogen bonds with π-stacking (Haspel *et al.*, 2005). The importance of the π-π stacking interactions between the aromatic residues in hCT was confirmed by X-ray

crystallography (Bertolani *et al.*, 2017). A note of caution should be introduced here, however, because it has been shown that the DFNKF peptide represents only partially the full-length CT behavior, since the residues flanking the amyloidogenic peptide seems to contribute to the stabilization of the experimentally observed antiparallel β-sheet packing in hCT (Rigoldi *et al.*, 2017).

An aggregation-prone sequence, consisting of residues 6-11 of hCT, TCMLGT, was predicted using a prediction algorithm called AMYLPRED. An analog of this peptide, TAMLGT, also predicted as an "aggregation-prone" peptide, was tested experimentally and showed to form amyloid fibrils, with a typical cross-β structure with a structural repeat of 4.57 Å along the fiber axis (corresponding to the spacing of adjacent β-strands). It was also observed that the peptide spontaneously assembled into supramolecular spherical structures named spherulites, with a diameter ranging from 10 to 200 μm. These structures have been found in other amyloid fibril forming proteins, namely insulin and Aβ42 (Krebs *et al.*, 2004; Exley *et al.*, 2010) leading the authors to propose that in several cases the pre-fibrillar amyloid intermediates, normally pathogenic, might be these spherulitic structures (Iconomidou *et al.*, 2013).

Attempts were made to rationally design an aggregation-resistant bioactive calcitonin (Fowler et al, 2005), and also to convert the highly amyloidogenic hCT into a powerful fibril inhibitor by 3D structure homology with the non-amyloidogenic sCT (Andreotti et al, 2011).

3.2.8. Objectives and chapter organization

The high potency of sCT and lower tendency to self-associate made it a more suitable target than hCT for drug development related to treatment of disorders of bone and mineral metabolism. Therefore, both hCT and sCT are suitable tools to be used in the study (i) of molecular mechanisms of CT amyloid formation, with particular attention to the early stages of their aggregation pathways, and (ii) the possible modulatory role played by lipid membranes in this process. Both unmodified and HL488-conjugated hCT and sCT were used in these studies.

This part of the work is divided in 3 subsections:
- in the **first section**, a detailed solvatochromic and photophysical study of the free HL488 dye and both HL488-labelled CT variants was performed in homogeneous medium. In addition to buffer, a set of aliphatic alcohols (methanol, ethanol, 2-propanol and 2-butanol) was also explored since they are often considered simple mimicking models of the interfacial effects exerted by biological membranes. Furthermore, a detailed photophysical and structural study of the TFE-induced conformational changes in hCT and sCT and the

corresponding conjugated peptides was performed using a combination of far-UV CD and steady-state and time-resolved fluorescence measurements. This preliminary study helped interpreting the spectroscopic data obtained with the fluorescently-labelled peptides in more complex systems, like in interaction with lipid membranes;

- in the **second section**, we aimed to (i) establish reproducible and feasible conditions to study the kinetics of calcitonin amyloid fibril formation using a microplate reader, and (ii) to obtain mechanistic information by studying the effect of peptide concentration on the kinetics of hCT fibril formation, using both the extrinsic amyloid dye Thioflavin T and the fluorescence properties of tracer amounts of HL488-labeled peptides. The ultimate goal here was to apply these optimized assay conditions to investigate in detail the possible role of accessory cellular components, like lipid membranes, in the modulation of CT fibril formation kinetics under high-throughput conditions;

- finally, the main goals of the **third section** were to (i) study and compare the interaction of sCT and hCT with liposomes prepared with different lipid compositions, particularly with a variable anionic phospholipid content, at infinite dilute conditions, and (ii) gain detailed structural and dynamic information about the membrane-induced oligomerization of these peptides by using a set complementary biophysical methods, namely far-UV CD measurements combined with steady-state and time-resolved fluorescence intensity and anisotropy measurements.

3.3. Materials and Methods

3.3.1. Reagents

Synthetic unlabeled hCT and sCT were obtained from AnaSpec (Fremont, CA, USA). Human and salmon calcitonin conjugated to HiLyte^{TM} Fluor 488 at their *N*-terminus - HL488-hCT and HL488-sCT, respectively - were also prepared by AnaSpec (Figure 3.7). The relative molecular mass and peptide purity (reported to be ≥95% for all peptide batches used in this work) was evaluated by the manufacturer using mass spectrometry (MS) and reversed-phase high-performance liquid chromatography (RP-HPLC), respectively (Table 3.1). Both the unlabeled and fluorescently-labeled peptides were kept frozen at -20°C protected from light and used without further purification. Insulin from bovine pancreas was obtained from Merck KgaA (Darmstadt, Germany).

Figure 3.7 - Sequence of calcitonins fluorescently-labeled with HL488. Human (top) and salmon (bottom) calcitonins were labeled by the manufacturer at their *N*-terminus. A disulfide bridge is present between Cys1 and Cys7 and the peptides have an amidated *C*-terminus. The amino acids colored are: acidic (red), basic (blue), polar (green) and hydrophobic (black).

The most used lipids in this section were 1-Palmitoyl-2-oleoyl-*sn*-glycero-3-phosphocholine (POPC) and 1-palmitoyl-2-oleoyl-*sn*-glycero-3-phosphoserine (POPS) (Figure 3.8 A and B, respectively). Additionally, 1,2-dioleoyl-sn-glycero-3-phosphocholine (DOPC), 1-palmitoyl-2-oleoyl-sn-glycero-3-phosphoethanolamine (POPE), 1-palmitoyl-2-oleoyl-sn-glycero-3-phosphoglycerol (POPG), monosialoganglioside GM1 (GM1) and sphingomyelin (SM) were also used. All these lipids were obtained from Avanti Polar Lipids (Alabaster, AL, USA). Cholesterol (chol) was obtained from Merck KgaA.

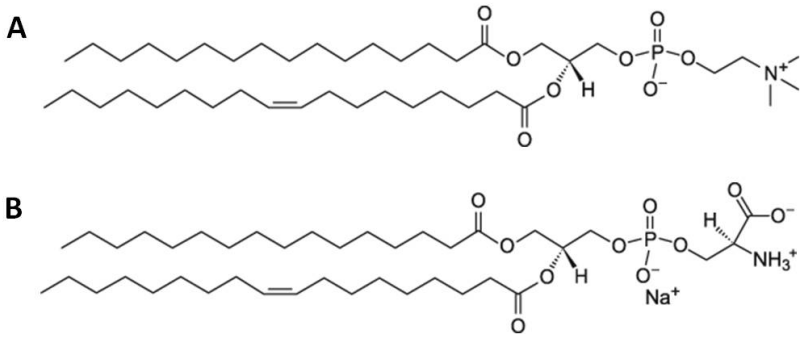

Figure 3.8 - Molecular structures of the most used phospholipids in this section: (A) 1-palmitoyl-2-oleoyl-sn-glycero-3-phosphocholine (POPC) and (B) 1-palmitoyl-2-oleoyl-sn-glycero-3-phosphoserine (POPS). Adapted from avantilipids.com [accessed March 2018].

Table 3.1 - Chemical properties of the synthetic full-length human and salmon CT variants (hCT and sCT, respectively) and the correspondingly fluorescently-conjugated peptides. All peptides were obtained from AnaSpec as trifluoroacetate salts**.**

Peptide	Catalog No.	$[M+H^+]$ (g mol^{-1})			
		Theoretical [1]	Determined by MS	Purity [1]	Net Charge at pH 7.0 [2]
hCT	AS-20673	3418.1	3419.2	> 95%	+1
sCT	AS-20677	3432.9	3431.5	> 95%	+3
HL488-hCT	custom synthesis	3774.4	3774.3	> 95%	+1
HL488-sCT	custom synthesis	3788.4	3790.0	>95%	+3

[1] determined by % peak area in RP-HPLC analysis

[2] by considering that the overall charge of the dye HL488 is +1 (private communication))

The fluorescent dyes A488, fluorescein, Rhodamine 110 (Rhod110), Sulforhodamine 101 (SR 101) and 6-(dimethylamino)-2-[4-[4-(dimethylamino)phenyl]-1,3-butadienyl]-1-ethyl, perchlorate (LDS 751) were obtained from Thermo Fisher Scientific (Waltham, MA, USA), whereas HiLyte^{TM} Fluor 488 acid, succinimidyl ester (HL488), TFA salt was purchased from

AnaSpec. Tryptophan, quinine sulfate and Thioflavin T (ThT) were obtained from Merck KgaA. The chemical structures of the more relevant used fluorescent probes are presented in Figure 3.9. The fluorescent dyes were quantified spectrophotometrically using the molar absorption coefficients obtained from the literature (Table 3.2). A488 and HL488 were kept frozen at -20 ºC protected from light, while the others were left at RT, protected from light, according to the manufacturer instructions. The stock solutions were prepared with the appropriate concentration and appropriate solvent and kept at 4 ºC, protected from light, until further use.

The organic solvents chloroform, methanol (MeOH, C1), ethanol (EtOH, C2), 2-propanol (PrOH, C3) and 2-butanol (BuOH, C4), glycerol, DMSO, 2,2,2-trifluorehtanol (TFE) were obtained from Merck KgaA. 1,1,1,3,3,3-hexafluoro-2-propanol (HFIP) (Ref 293410100, 99.9% for spectroscopy) was purchased from ACROS Organics, Thermo Fisher Scientific; all the other brands of HFIP tested had fluorescent impurities that hampered the use of the intrinsic fluorescence of peptides. All solvents were of spectroscopic Uvasol® grade unless otherwise stated.

Potassium hydroxide, ethylenediamine-*N,N,N',N'*-tetraacetic acid (EDTA), HEPES (4-(2-hydroxyethyl)-1-piperazineethanesulfonic acid) and *N*-acetyl-*L*-tyrosinamide (NAYA) were obtained from Merck KgaA. Unless otherwise stated, all other chemicals were purchased from Merck KgaA and used as provided.

Table 3.2 - Additional information for the fluorescent probes.

Fluorescent probe	Catalog number	Molecular mass (g. mol^{-1})	Solvent of the stock solution	Spectrophotometric quantification	
				λ (nm)	ε x 10^4 ($M^{-1}cm^{-1}$)
A488 SE	A20000	643.41	Ultra-pure water	494	7.3[1]
Fluorescein	F1300	332.31	0.1 M NaOH	490	9.3[1]
HL488 SE	81161	698.60	Ethanol	502	7.0[2]
Rhod110	D250	353.55	Ethanol	499	8.2[1]
ThT	T3516	318.86	Ultra-pure water	412	3.6[3]

[1] (Haugland, 2005)

[2] AnaSpec Catalog

[3] (Foderà *et al.*, 2009)

The main buffer system used in this work was 20 mM HEPES-KOH, 1 mM EDTA, pH 7.4 (HEPES-KOH buffer, pH 7.4). The buffer solution was prepared using ultrapure water produced using a Milli-Q system (>18 MΩ·cm) (Q-Gard® 1, Millipore, MA, USA) and was always filtered with 0.22 μm cellulose acetate filters (Millipore) prior to use. The exceptions

were *a*) the buffer 20 mM HEPES-KOH, 150 mM NaCl, 1 mM EDTA, pH 7.4 (HEPES-KOH buffer, 150 mM NaCl, pH 7.4) was used for some of the samples prepared in the study of the interaction of HL488-hCT with liposomes with a wide range of lipid compositions (section 3.4.3.2) and *b*) the buffer 5 mM HEPES-NaOH, 1 mM EDTA pH 7.4 was used for the CD studies to minimize interferences with the measurements.

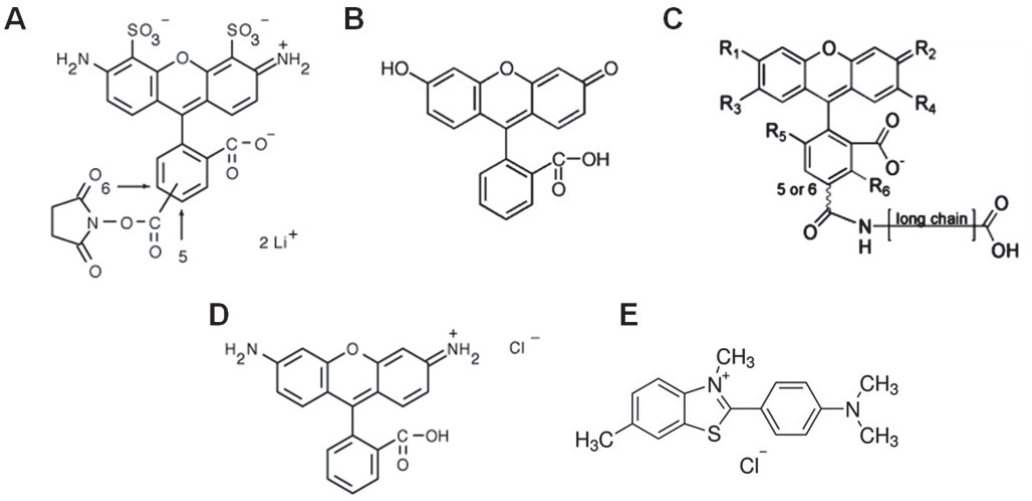

Figure 3.9 – Chemical structures of the fluorescent probes used. (A) Alexa Fluor 488, succinimidyl ester (A488), **(B)** Fluorescein, **(C)** HiLyte^{TM} Fluor 488 acid, succinimidyl ester (HL488), **(D)** Rhodamine 110 (Rhod110) and (**E**) Thioflavin T (ThT). The chemical structure of HL488 has not been fully disclosed. The chemical structure presented in (**C**) was adapted from (Jungbauer *et al.*, 2009). The others chemical structures were obtained from the internet site of the respective manufacturer [accessed March 2018].

3.3.2. Preparation of large unilamellar vesicles

Large unilamellar vesicles (LUVs) used were prepared by the extrusion technique (Mayer *et al.*, 1986). The stock solutions of all lipids were prepared in chloroform and stored at -20 ºC. The exact concentration of these solutions was determined using phosphate analysis (McClare, 1971) except for Chol, which concentration was determined by gravimetry (Mettler Toledo UMT2). Adequate volumes of each phospholipid stock solution were mixed in a round-bottom flask or Eppendorfs® (Eppendorf®, Hamburg, Germany) in order to prepare the appropriate lipid mixtures. A thin lipid film was formed first by evaporating the solvent using a gentle N_2 flow and then by maintaining the samples under vacuum for 4 -5 h using an oil pump. The lipid mixtures were hydrated with the appropriate buffer depending on the experiment (see previous section) and repeatedly vortexed until all lipid was removed from the flask/Eppendorf® wall. The resulting lipid dispersions were equilibrated by performing 10 freeze-thaw cycles using liquid nitrogen and a water or dry bath at 50 ºC. Finally, the lipid suspensions where extruded 21 times through 100 nm pore size

polycarbonate membranes (Whatman, Maidstone, UK) using a mini extruder device (Avestin Inc, Ottawa, Canada) and Gastight 1700 Series syringes (Hamilton, Reno, NV, USA). The resulting liposome solutions were either immediately used or stored overnight at 4 °C until use.

3.3.3. Preparation of peptide and dye samples

The stock solutions of unlabeled and fluorescently-labeled CTs were prepared by directly dissolving 1 mg of the lyophilized powder in an appropriate volume of pure HFIP to a final concentration of about 1 mM and stored at -20 ^{o}C protected from light. The stock of the control free HL488 was prepared by dissolving the appropriate amount of dye in ethanol. Before each experiment, the stock solutions of peptides and/or dye were allowed to thermally stabilize at RT for 10 min. The peptide solutions were then briefly sonicated for 1 min using a bath sonicator (Branson, CT, USA). The peptide and free dye samples were then prepared in Low-Protein Binding (LPB) Eppendorfs® by one of the two following methods:

Method I – samples prepared in the presence of a maximum of 1% (v/v) HFIP

After the initial steps, an intermediate working peptide solution was obtained by adding the peptide stock solution to an adequate volume of HEPES-KOH buffer, pH 7.4 in a LPB Eppendorf®. After a brief vortexing step, this intermediate solution was directly diluted with buffer in order to obtain samples containing variable final peptide concentrations, prepared individually.

Method II – samples prepared without HFIP

In this case, the appropriate volume of the adequate stock solution was added to the LPB Eppendorfs® and the organic solvent was evaporated with a nitrogen flow. The peptide/dye films were then resuspended in the appropriate volume of 20 mM HEPES-KOH, 1 mM EDTA buffer (pH 7.4) or the chosen organic solvent/binary solvent mixture. Finally, the peptides and free dye-containing samples were sonicated for approximately 1 min using a bath sonicator. Control spectrophotometric measurements of fluorescently-labeled CTs showed that ~90% of the peptide was recovered after solvent evaporation and peptide resuspension in buffer (data not shown).

3.3.3.1. Preparation of samples in solvents or binary solvent mixtures

The preparation of the samples with solvents or binary solvent mixtures was done by Method II, essentially as described in the previous section. The samples were prepared to a final peptide and free HL488 concentrations of 0.8 and 1 μM (unless otherwise stated), respectively. The free HL488 sample in glycerol was prepared gravimetrically by adding a

small volume of the HL488 stock solution in ethanol to glycerol in order to get a final dye concentration of 1 μM. The solution was then left stirring overnight at RT to guarantee complete homogeneity before performing the characterization of its steady-state fluorescence properties. The TFE/buffer mixtures were prepared by mixing the appropriate volume of buffer and TFE for the different desired % (vol/vol) prior to resuspending the peptide. The final concentration of the fluorescently-labeled peptides was evaluated spectrophotometrically (Table 3.2). The chemical-physical properties of the solvents used are summarized in the following tables.

Table 3.3 – Chemical and physical parameters for water, aliphatic alcohols and fluoroalcohols used in this study. Dielectric constant, ε, viscosity, η, and density ρ of the solvents used in this work (T= 25ºC).

Solvent	Molecular formula	Molecular mass (g mol^{-1})	Dipole moment (D)	ε	ρ (g cm^{-3})	η (mPa·s^{-1}) [3]
water	H_2O	18.02	1.84	78.54[1]	0.997	0.887
methanol	CH_3OH	32.04	1.69	32.63[1]	0.792	0.553
ethanol	CH_3CH_2OH	46.07	1.69	24.30[1]	0.789	1.105
2-propanol	$(CH3)_2CHOH$	60.10	1.66	18.30[1]	0.786	2.098
2-butanol	$CH_3CHOHCH_2CH_3$	74.12	1.41	16.6 [2]	0.808	3.115
TFE	CF_3CH_2OH	100.04	2.52	26.7	1.371	1.737
HFIP	$(CF3)_2CHOH$	168.04	2.05	17.8	1.596	1.650

[1] (Magde *et al* 1999)

[2] (Gilani *et al.*, 2011)

[3] (Canosa *et al.*, 1998)

Table 3.4 – Dipolarity/polarizability (SPP), solvent basicity (SB) and solvent acidity (SA) scales for pure solvents.

Solvent	SPP [2]	SB [1]	SA [1]
water	0.962	0.025	1.062
metanol	0.857 [3]	0.545	0.605
ethanol	0.853 [3]	0.658	0.400
2-propanol	0.848	0.830	0.283
2-butanol	0.842	0.888	0.221
TFE	0.908	0.107	0.893
HFIP	1.007	0.014 [4]	1.011 [5]

[1] (Catalán, 2009)
[2] (Catalán, López, and Pérez, 1995)
[3] (Catalán, López, Pérez, *et al.*, 1995)
[4] (Catalán *et al.*, 1996)
[5] (Catalán and Díaz, 1999)

Table 3.5 – Density, ρ and viscosity, η, of binary TFE/buffer mixtures at 25 ºC. Data adapted from (Palepu and Clarke, 1989).

%TFE (vol/vol)	ρ (g cm^{-3})	η (mPa·s^{-1})
0.0	0.997	0.890
9.7	1.043	1.152
17.6	1.078	1.358
24.7	1.111	1.528
30.6	1.136	1.634
50.0	1.221	1.882
63.6	1.264	1.876
73.0	1.296	1.819
80.3	1.321	1.757
85.8	1.338	1.713
88.2	1.347	1.656
94.3	1.364	1.651
97.4	1.372	1.673
100.0	1.371	1.737

Table 3.6 - Influence of temperature on the density, ρ and viscosity, η, of TFE. Data adapted from (Palepu and Clarke, 1989)

Temperature (ºC)	ρ (g cm^{-3})	η (mPa·s^{-1})
20	1.392	2.11
25	1.383	1.84
30	1.375	1.62
35	1.366	1.43
40	1.357	1.27
45	1.349	1.13
50	1.339	1.02
55	1.330	0.925
60	1.321	0.824

3.3.3.2. **Calcitonin fibrillation studies**

The kinetics of CT amyloid fibril formation was measured in HEPES-KOH pH 7.4 buffer by monitoring the changes over time of the fluorescence emission intensity of the amyloid specific dye ThT upon its binding to the CT amyloid fibrils using a microplate reader. The ThT stock solution was prepared at a concentration of approximately 0.75 mM and was stored at 4 ºC protected from light; the stock solution was always filtered using 0.22 μm cellulose acetate filters prior to its use. The samples were prepared using the two methods described in Section 3.3.3. For the samples prepared using Method I, the intermediate solution was directly diluted with buffer in order to obtain samples containing a variable final peptide concentration of 0, 1, 5, 10, 15 or 20 μM. An adequate volume of the stock ThT solution was then added to these samples in order to obtain a constant molar ratio of 1:0.75

peptide:ThT (Avidan-Shpalter and Gazit, 2006). The final volume of HFIP in each well was kept fixed at 1% (v/v) by the addition of pure HFIP when necessary. For the samples prepared using Method II, after solvent evaporation, a working solution was prepared with an intermediate concentration, sonicated for about 1 min, briefly vortexed, and used to prepare peptide samples containing a final peptide concentration within the range 0 - 20 μM by direct dilution with buffer on a microplate. Again, an adequate volume of the stock ThT solution was added to obtain a constant molar ratio of 1:0.75 peptide:ThT. Alternatively, the experimental readout of some fibrillation assays was the steady-state fluorescence anisotropy (ssFA) of a tracer amount of HL488-labelled CT in the presence of an excess of the correspondingly unlabeled peptide. Both methods I and II were again used to prepare the samples which now included a fixed concentration of the fluorescently-labelled peptide (0.2 μM) and a varying concentration of the corresponding unlabeled peptide, while keeping the total peptide concentration at 0-20 μM. The final labeling ratios of the samples therefore ranged from 20% to 1% for 1 to 20 μM of total peptide concentration in solution, respectively. The content of every well prepared was mixed by pipette aspiration prior to starting the measurements.

The fibrillation assays were run on a POLARstar OPTIMA microplate reader (BMG Labtech, Germany) using 96-well Greiner Bio-One non-binding black microplates (Ref 655906 Greiner Bio-One, Austria). The peptide samples were freshly prepared in triplicate or quintuplicate immediately prior to data acquisition at 25 ºC. Adequate blank controls (samples without peptide) were prepared in each case and the corresponding signals were always subtracted from the peptide-containing samples. The final sample volumes were either 150 or 300 μL/well, although 250 μL/well was also occasionally tested. The kinetics were performed either without shaking or using 30 or 300 s of orbital shaking at 600 rpm prior to data acquisition at each time point of the kinetics. The fluorescence intensity of ThT was bottom read using an excitation wavelength of 440 nm and an emission wavelength of 480 nm (both filters with a 10 nm bandwidth). The vertical and parallel polarized components of HL488-conjugated peptides were acquired simultaneously (top reading) during the kinetic assays using an excitation wavelength of 485 nm (filters with a 12 nm bandwidth) and an emission wavelength of 520 nm (10 nm bandwidth).

The ssFA of the samples was calculated using Eq. 2.4. The denominator of the previous equation is proportional to the total fluorescence intensity of a sample measured at the magic angle, I_{54} (Lakowicz, 2006). The *G*-factor of our microplate reader (Eq. 2.5) was calibrated using a highly fluorescent solution of free A488 in buffer solution – the gains of the microplate reader for detecting the I_{VV} and I_{VH} components were automatically adjusted in order that the ssFA measured in the microplate reader was identical to the value obtained in a spectrofluorometer using the same excitation and emission wavelengths. The *G*-factor

was found to be ca. 1 as the optimized gains for the two detection channels of the microplate reader were essentially identical. Complementary time-resolved fluorescence intensity and anisotropy measurements were also performed at the end stage of some kinetic assays to characterize the fluorescence properties of the end products of the kinetics.

Data analysis

Under certain conditions, the kinetics of CT fibril formation could be described as a sigmoidal curve defined by an initial lag phase, where minimal change in the fluorescence intensity or ssFA is observed, a subsequent sigmoidal growth phase in which the fluorescence parameter under study increased due to the growth of CT fibrils, and a final plateau level, where the fluorescence parameter stabilized over time indicating the end of fibril formation (Figure 3.10).

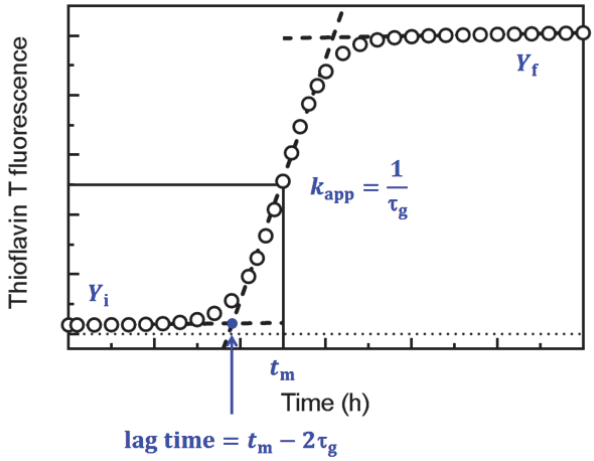

Figure 3.10- Schematic illustration of the sigmoidal increase in Thioflavin T fluorescence upon peptide/protein amyloid fibril formation and the parameters considered for a quantitative analysis. Adapted from (Nielsen *et al.*, 2001).

For a quantitative description and easy comparison of the kinetic curves obtained under distinct experimental conditions, ThT fluorescence intensity or the ssFA of HL488-conjugated peptides were plotted as a function of time and fitted by an empirical sigmoidal curve described by the following equation using OriginPro8:

$$Y = Y_i + m_i t + \frac{Y_f + m_f t}{1 + e^{-[(t - t_m)/\tau_g]}} \qquad \textbf{Eq. 3.1}$$

where Y is the fluorescence parameter under study measured at time t and t_m is the time at which 50% of maximal fluorescence intensity/ssFA is reached. The initial and final baselines prior and after the growth phase are described by $Y_i + m_i t$ and $Y_f + m_f t$, respectively. The

apparent rate constant for the growth/elongation of fibrils, k_{app}, is given by $1/\tau_{\mathrm{g}}$ and the lag time (τ_{lag}) is calculated as $t_{\mathrm{m}} - 2\tau_{\mathrm{g}}$ (Figure 3.10).

3.3.3.3. **Calcitonin partition studies**

The partition coefficient of the unlabeled and labeled CT peptides was determined by monitoring the changes in the ssFA or the far-UV CD mean molar residue ellipticity at 222 nm ($[\theta_{222\mathrm{nm}}]$) in the presence of POPC LUVS prepared with variable mol% of POPS (0 to 50 mol%). A constant concentration of either IAPP variant, normally from 0.2 μM to 20 μM, was added to LUVs suspensions prepared independently ranging, normally, from 0 to 2 mM accessible phospholipid concentration. After an incubation time of at least 30 min at RT, the ssFA measurements were performed using the wavelengths described in Table 3.7 or the conditions described in Section 3.3.5.2. Adequate controls were prepared in parallel and their fluorescence intensities or background CD spectra (see section 3.3.5.2 for details) were subtracted from the corresponding peptide-containing sample.

For the samples where the intrinsic fluorescence of the peptides was used, another correction was necessary due to the scattering of the LUVs. Briefly, the same experimental design as a partition study was employed but with POPC vesicles and a fixed bovine insulin concentration of 25 μM. Insulin has a negative net charge at neutral pH-values and is not expected to interact strongly with these zwitterionic membranes (Jeworrek *et al.*, 2009). Thus, the observed variations in its ssFA anisotropy can be attributed to the scattering effect of the liposome suspensions (Figure 3.11 B). The relative decrease in the ssFA of insulin measured for each phospholipid concentration was added to the respective value measured for the calcitonin-containing sample, considering an equivalent scattering contribution at the excitation wavelength used.

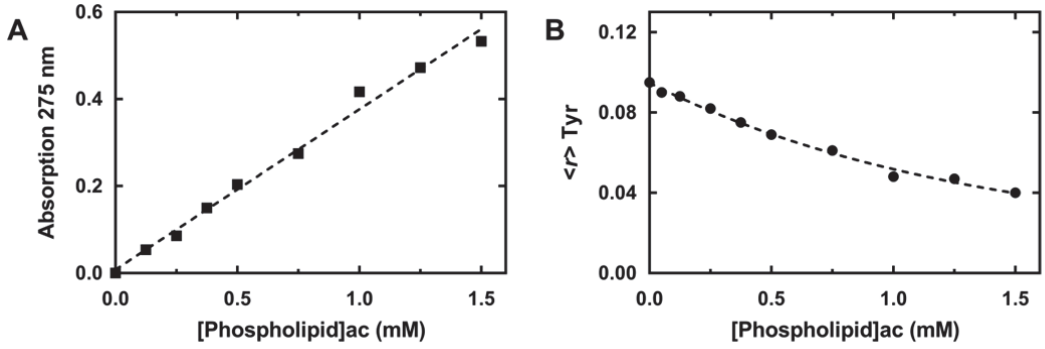

Figure 3.11 – Influence of the scattering contribution of LUVs to the ssFA measurements of insulin, a tyrosine-containing peptide. Typical results obtained for the variation of (**A**) the pseudo-absorbance at 275 nm and (**B**) the steady-state fluorescence anisotropy, $\langle r \rangle_{\mathrm{Y20}}^{275/300\mathrm{nm}}$, of 25 μM insulin with the accessible phospholipid concentration in solution using POPC LUVs.

The mole-fraction membrane-water partition coefficient, K_{p}, if a peptide is an equilibrium constant described as:

$$K_{\mathrm{p}} = \frac{\frac{n_{\mathrm{CT,L}}}{n_{\mathrm{L}} + n_{\mathrm{CT,L}}}}{\frac{n_{\mathrm{CT,W}}}{n_{\mathrm{W}} + n_{\mathrm{CT,W}}}} \qquad \textbf{Eq. 3.2}$$

where n_{W} and $n_{\mathrm{L}}$are the moles of water and lipid, and $n_{\mathrm{CT,i}}$ are the moles of CT present in each phase (i= W, aqueous phase; i= L, lipid phase). However, since in most experimental conditions $n_{\mathrm{W}} \gg n_{\mathrm{CT,W}}$ and $n_{\mathrm{L}} \gg n_{\mathrm{CT,L}}$ (to avoid deviations from ideal behavior), the definition is simplified to:

$$K_{\mathrm{p}} = \frac{\frac{n_{\mathrm{CT,L}}}{n_{\mathrm{L}}}}{\frac{n_{\mathrm{CT,W}}}{n_{\mathrm{W}}}} \qquad \textbf{Eq. 3.3}$$

Considering the mass balance $[\mathrm{CT}]_{\mathrm{T}} = [\mathrm{CT}]_{\mathrm{W}} + [\mathrm{CT}]_{\mathrm{L}}$ and Eq. 3.3, the membrane-bound CT mole fraction x_{L} can be derived as a function of the phospholipid concentration [L]:

$$x_{\mathrm{L}} = \frac{K_p[L]}{[W] + K_p[L]} \qquad \textbf{Eq. 3.4}$$

Anisotropy is an additive parameter (Lakowicz, 2006; Valeur and Berberan-Santos, 2012) so in the presence of liposomes, the ssFA of a peptide can be written as:

$$\langle r \rangle = \sum f_{\mathrm{i}} r_{\mathrm{i}} = f_{\mathrm{W}} r_{\mathrm{W}} + f_{\mathrm{L}} r_{\mathrm{L}} = \frac{\varepsilon_{\mathrm{W}} \Phi_{\mathrm{W}} x_{\mathrm{W}}}{\varepsilon_{\mathrm{W}} \Phi_{\mathrm{W}} x_{\mathrm{W}} + \varepsilon_{\mathrm{L}} \Phi_{\mathrm{L}} x_{\mathrm{L}}} r_{\mathrm{W}} + \frac{\varepsilon_{\mathrm{L}} \Phi_{\mathrm{L}} x_{\mathrm{L}}}{\varepsilon_{\mathrm{W}} \Phi_{\mathrm{W}} x_{\mathrm{W}} + \varepsilon_{\mathrm{L}} \Phi_{\mathrm{L}} x_{\mathrm{L}}} r_{\mathrm{L}} \qquad \textbf{Eq. 3.5}$$

where f_{i} is the fraction of light emitted by the peptide and x_i is its molar fraction in each phase. ε_{i}, Φ_{i} and r_{i} are the molar absorption coefficient, the fluorescence quantum yield and the ssFA of the peptide in each phase, respectively. Taken together Eq. 3.4 and Eq. 3.5, the FA of the peptide can be described as a function of [*L*] by Eq. 3.6, where $Q = \varepsilon_{\mathrm{L}} \Phi_{\mathrm{L}} / \varepsilon_{\mathrm{W}} \Phi_{\mathrm{W}}$. Further assuming that the molar absorption coefficient of the peptide is invariant with the environment, the Q parameter simplifies to $\Phi_{\mathrm{L}}/\Phi_{\mathrm{W}}$. A non-linear regression fit is made considering the accessible phospholipid concentration, $[L]_{\mathrm{ac}}$ (half of the total lipid concentration (Melo *et al.*, 2013)). With this fit, the values of K_p and r_{L} were obtained.

$$\langle r \rangle = \frac{r_{\mathrm{W}}[W] + K_p[L]_{\mathrm{ac}}\, r_{\mathrm{L}} Q}{[W] + K_p[L]_{\mathrm{ac}} Q} \qquad \textbf{Eq. 3.6}$$

The same equation was used with the data of $[\theta_{222\mathrm{nm}}]$, considering Q as 1, the signal of the peptide in water $[\theta_{222\mathrm{nm}}]_{\mathrm{W}}$, the signal of the peptide in the membrane as the maximum variation of mean molar residue ellipticity at 222 nm, $\Delta[\theta_{222\mathrm{nm}}]_{\mathrm{max}}$.

3.3.4. UV-visible absorption Spectroscopy

UV-visible absorption measurements were carried out at RT using a Shimadzu MPC-3100 spectrophotometer or using a double-beam V-660 Jasco spectrophotometer, described in Section 2.3.2.

Data analysis

In the measurements performed in the presence of increasing phospholipid concentrations, it was usually observed that the absorption spectrum of the control samples (liposomes at the different concentration) did not overlap the spectrum obtained for the respective peptide containing sample (liposomes + peptide) (Figure 3.12). For this reason, a "pseudo-background" spectrum was obtained for each sample of liposomes and peptide by performing a non-linear regression fitting of an empirical power law (Eq. 3.7, (Castanho *et al.*, 1997) to the absorption spectra in a wavelength range where significant absorption does not occur, i.e. for the unlabeled calcitonins 450-800 nm and for the HL488-labeled peptides 350-400 nm and 550-700 nm.

$$Abs = a + b\,\lambda^{-k} \qquad \textbf{Eq. 3.7}$$

The empirical fitting parameters obtained, a, b, and k, were used to extrapolate Eq. 3.7 to all wavelength values, resulting in an "pseudo-background" baseline that was subtracted from each sample, producing a corrected absorption spectrum (Figure 3.12 B).

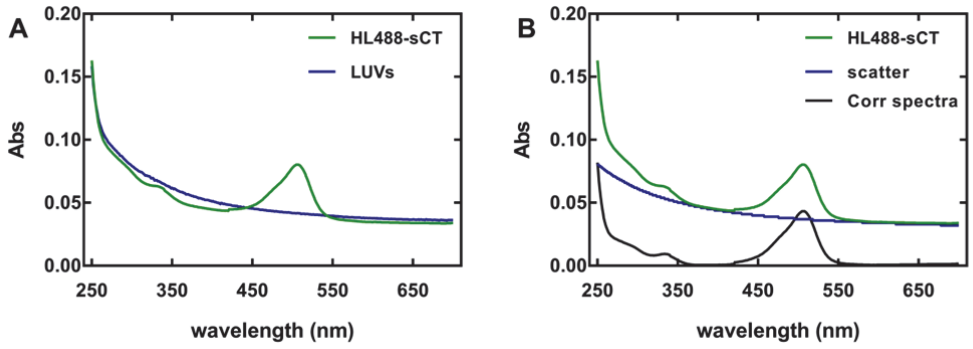

Figure 3.12 – Illustrative correction of the absorption spectrum measured in the presence of liposomes (**A**) Pseudo-absorption spectra obtained for 200 μM POPC:POPS 80:20 LUVs in the absence (blue curve) and in the presence of 1 μM of HL488-sCT (green curve). (**B**) Corrected absorption spectrum (black curve) resulting from the subtraction of the extrapolated "pseudo-background" baseline (blue curve) from the sample absorption spectrum (green curve) according to Eq. 3.7. See the text for more details.

3.3.5. Circular Dichroism

3.3.5.1. **Principles**

Circular dichroism (CD) spectroscopy has been used for several years for the analysis of protein secondary structure. It is based on the different absorption of left, Abs_{L}, and right, Abs_{R}, circularly polarized light by proteins and polypeptides which are chiral molecules:

$$\Delta Abs = Abs_{\mathrm{L}} - Abs_{\mathrm{R}} = (\varepsilon_{\mathrm{L}} - \varepsilon_{\mathrm{R}}) \cdot c \cdot \ell = \Delta\varepsilon \cdot c \cdot \ell \qquad \textbf{Eq. 3.8}$$

where ℓ is the path length (cm or mm), $\Delta\varepsilon$ is the difference in molar absorption coefficient ($M^{-1}cm^{-1}$) and c is its molar concentration (mol L^{-1}). The CD spectra are usually reported as ellipticity, θ, which is related to $\Delta\varepsilon$ by a factor of 3298.2:

$$\theta = 3298.2\ \Delta\varepsilon \qquad \textbf{Eq. 3.9}$$

The units of ellipticity are degrees or millidegrees (mdeg or m^{o}) (Kelly and Price, 2000). A CD signal will only arise where there is absorption of radiation. In polypeptides or proteins absorption bellow 240 nm ("far-UV") is of interest because it corresponds to the absorption region of the peptide bond. This region is dominated by $n \rightarrow \pi^*$ and $\pi \rightarrow \pi^*$ transitions of amide groups and distinct structural features of a molecule will give different spectral bands, as each one will absorb radiation in a different way. The peptide bond restricts the spatial arrangement of amino acid residues, namely the diehedral angles ϕ and ψ that they can adopt, and this prohibits some photo-excitation transitions of the peptide bond. The CD spectra are than a reflection of the different types of secondary structure adopted by the polypeptide chains: α-helices give negative bands at 222 nm and 208 nm and a positive band at 193 nm; β-sheets are negative at 218 nm and have a positive band at 196 nm, whereas random coil has a low ellipticity above 210 nm and negative bands near 195 nm. Measurements in the "near-UV" (250-320 nm) can be sensitive to the tertiary structure of proteins (Kelly *et al.*, 2005; Greenfield, 2007b; Ranjbar and Gill, 2009). In order to be able to compare different data sets, the ellipticity, θ, is often converted to molar ellipticity, $[\theta]$, which, for historical reasons, has units of $deg \cdot cm^2 \cdot dmol^{-1}$:

$$[\theta] = \frac{\theta}{10\ c \cdot \ell} = \frac{MW \cdot 100 \cdot \theta}{C \cdot \ell} \qquad \textbf{Eq. 3.10}$$

where MW is the molecular weight of the molecule ($g.mol^{-1}$) and C is the sample concentration ($g.L^{-1}$). The CD data is usually normalized to the repeating unit of the molecule (peptide bond in polypeptides). The mean molar residue ellipticity, $[\theta]_{\mathrm{MRE}}$, (with units $deg \cdot cm^2 \cdot dmol^{-1} \cdot res^{-1}$) is then given by:

$$[\theta]_{\mathrm{MRE}} = \frac{\theta}{10\ c_r \ell} \qquad \textbf{Eq. 3.11}$$

where c_r is the mean residue molar concentration:

$$c_r = n_{\mathrm{pb}} \cdot c \qquad \textbf{Eq. 3.12}$$

and n_{pb} is the number of peptide bonds in the protein or peptide ($n_{\mathrm{pb}} = n - 1$, n being the number of amino acid residues in the sequence). CD spectra are preferably acquired in quartz cuvettes with a very short path length (as 0.1 cm) (Greenfield, 2006). One crucial aspect to take into consideration is the High Tension Voltage (HTV) applied to the PMT. The sensitivity of the detector is amplified by applying HTV to the PMT. This HTV increases if there are not enough photons reaching the detector and it also increases for shorter wavelengths as less light is available. Above a certain threshold of HTV, one can consider that not enough photons are being sampled by the PMT to measure a reliable CD signal, and the data should be disregarded. Allied to the concentration of the sample and the path lengths of the cuvette, the solvent used is also a crucial aspect in CD measurements as any optically active material affects the total absorbance of the sample and might hamper the measurement of CD, especially at lower wavelengths (Kelly and Price, 2000; Kelly *et al*., 2005).

The methods used to obtain an estimation of the protein secondary structure from CD measurements give better results for helical secondary structures because these tend to be very consistent, with very regular ϕ and ψ angles and produce similar spectra with very intense CD signals. On the contrary, β-sheets have a considerable variance in their angles and can have a parallel or antiparallel orientation of adjacent strands, causing variable CD results with normally less intense signals (Whitmore and Wallace, 2008).

3.3.5.2. **Experimental measurements**

CD measurements were carried out at 25 ºC using a JASCO J-815 spectropolarimeter (Ishikawa, Tokyo, Japan). The far-UV CD spectra of the CT peptides prepared at 20 μM were obtained in either 5 mM HEPES-NaOH, 1 mM EDTA buffer (pH 7.4) or in binary mixtures prepared with variable % (v/v) of this aqueous buffer and TFE. Spectral scans from 195 to 260 nm were recorded using quartz cuvettes with 0.1 cm path length, step size of 0.2 nm, bandwidth 1 nm, scan speed of 50 nm/min and a data integration time of 1 s. At least 3 scans were acquired and averaged per sample to improve the S/N of the data. Background CD spectra of the appropriate buffer/solvent mixture (solvent baseline) were also recorded and subtracted from the peptide spectra. In addition to blank subtraction, experimental instrument-related baseline drift was corrected by subtracting to all spectra the average of

the signal between 250 and 260 nm. Spectra are plotted either as $[\theta]_{\mathrm{MRE}}$ (deg·cm^2·dmol^{-1}·res^{-1}) as a function of wavelength or $[\theta]_{222\mathrm{nm}}$ as a function of $[L]_{\mathrm{ac}}$.

Data analysis

The helical content of each peptide (% helicity) was calculated on the basis of the following equations:

$$\%\ \text{helicity} = \frac{[\theta]_{222\ \mathrm{nm}}}{[\theta]_{222\ \mathrm{nm,max}}} \times 100 \qquad \textbf{Eq. 3.13}$$

$$[\theta]_{222\ \mathrm{nm,max}} = \frac{(n - 4.6)(-40\ 000)}{n} \qquad \textbf{Eq. 3.14}$$

where $[\theta]_{222\ \mathrm{nm}}$ is the mean molar residue ellipticity at 222 nm, $[\theta]_{222\ \mathrm{nm,max}}$, is the theoretical maximal mean molar residue ellipticity of the peptide (i.e., the value expected for a peptide in a 100% helical conformation), and n is the number of amino acids residues in the peptide. The $[\theta]_{222\ \mathrm{nm,max}}$ of a 32-residue peptide is calculated to be −34 250 deg·cm^2·dmol^{-1}·res^{-1}.

3.3.6. Fluorescence spectroscopy

3.3.6.1. Steady-state fluorescence measurements

Principles

Fluorescence is the emission of light that occurs from an electronically excited state after the absorption of light by a fluorophore. A simplified Jablonski diagram (Figure 3.13) illustrates the processes that occur between the absorption and emission of light (Lakowicz, 2006). Before excitation, fluorophores are in the lowest vibrational states of the ground state (S_0). Upon excitation with light, which is extremely fast and occurs in the range of femtoseconds (10^{-15} s), the fluorophore absorbs photons which have the energy to cause an electron to be transferred to a different orbital, occurring a transition from S_0 to the first (S_1) excited singlet state. Normally, the energy absorbed is greater than the necessary to transition from the lowest vibrational state of S_0 to the lowest vibrational state of S_1, so the fluorophore is usually excited to some higher vibrational state of S_1. It can also absorb enough energy to be excited to a higher electronic orbital (S_2). Since fluorescence emission occurs from the lowest level of S_1, the excess energy absorbed is quickly dissipated by internal conversion and vibrational relaxation, processes that occur in picoseconds (10^{-12} s).

The consequent emission occurs within nanoseconds (10^{-9} s) with energy lower than the one of absorption, which explains why fluorescence is normally observed at higher wavelengths, an effect known as the Stokes shift. This shift can be further enhanced by the interaction of the fluorophore and its environment (Valeur and Berberan-Santos, 2012). The molar extinction coefficient (ε) measures how efficiently a particle absorbs light at a particular wavelength, per molar concentration ($M^{-1}cm^{-1}$).

Some properties are extremely important in fluorescence studies. The fluorescence quantum yield, Φ, is a ratio between the number of photons emitted and the number of photons absorbed. The brightest fluorophores have quantum yields close to unity. Both radiative and non-radiative processes can depopulate the excited state. The fraction of fluorophores that decay through the emission of fluorescence is given by

$$\Phi_{\mathrm{F}} = \frac{k_{\mathrm{f}}}{k_{\mathrm{f}} + k_{\mathrm{nr}}} \qquad \textbf{Eq. 3.15}$$

where k_{f} and k_{nr} are the decay rate constants for fluorescence and for non-radiative processes, respectively (Lakowicz, 2006). For convenience, all non-radiative decay processes are grouped in a single rate constant k_{nr}.

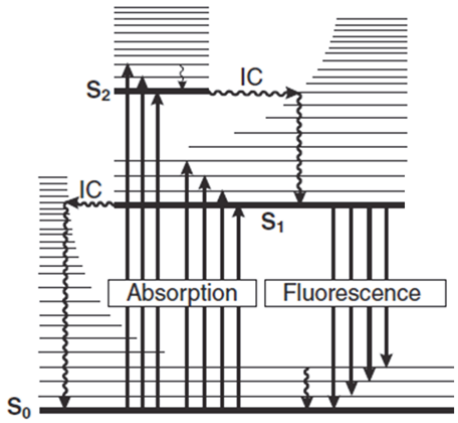

Figure 3.13 – Simplified Jablonski diagram. Light absorbed by a fluorophore causes an electron to move to a different orbital and leads to a change from the ground state (S_0) of energy to the first (S_1) or second (S_2) singlet electron state. If the energy of the photon is not exactly enough to cause a direct change from the lowest energy level of $S_0 \rightarrow S_1$, the excess energy is dissipated by vibrational relaxation. A fluorophore excited to S_2 will usually relax to S_1 prior to emission by internal conversion (IC) and vibrational relaxation. Upon reaching the lowest energy level of S_1, the energy is released as emission of light – fluorescence – and the fluorophore returns to its ground state. Adapted from Valeur and Berberan-Santos, 2012.

Experimental measurements

Intrinsic fluorescence measurements for unlabeled peptides were performed in the HORIBA Jobin Yvon Fluorolog-3-21 spectrofluorometer, described in section 2.3.3. The quantum yield of the tyrosine residue present in unlabeled peptides is very low and this is the most

sensitive apparatus available in the laboratory. Fluorescence measurements for the free dyes and N-terminally labeled peptides were either performed on the before mentioned HORIBA or on a SLM-AMINCO 8100 spectrofluorometer, described in section 2.3.3. The excitation and emission wavelengths employed in the experiments, unless otherwise stated, were used as presented in Table 3.7. The ssFA, $\langle r \rangle$, is defined by Eq. 2.4 described earlier.

Table 3.7 – Excitation and emission wavelengths used in the steady-state and time-resolved fluorescence measurements performed throughout this chapter.

Samples	Fluorescence emission spectra		Steady-state anisotropy measurements		Time-resolved fluorescence measurements	
	λ_{exc} (nm)	λ_{em} (nm)	λ_{exc} (nm)	λ_{em} (nm)	λ_{exc} (nm)	λ_{em} (nm)
Y22(sCT) and Y12(hCT)	275	280 – 380	275	300	280	300
HL488 and HL488-labeled peptides	480	485 – 680	480	525	335	525
Thioflavin T	450	470 – 600	-	-	-	-

The fluorescence quantum yield, Φ_{F}, of the unlabeled and HL488-fluorescently labeled peptides in buffer, several organic solvents and in the binary aqueous/TFE mixtures was evaluated using a relative method (Valeur and Berberan-Santos, 2012). The calculations were made relatively to a standard with a known quantum yield, Φ_{FS}, using Eq. 3.16 where Abs_i is the absorption of a diluted solution of each compound at the excitation wavelength selected, F_i is the integrated area under the corrected emission curve and n_i is the refractive index of the solvent used. The subscripts i= S and i= X refer to the standard and to the peptide species, respectively.

$$\frac{\Phi_{\mathrm{F}}}{\Phi_{\mathrm{FS}}} = \left(\frac{1-10^{-Abs_{\mathrm{S}}}}{1-10^{-Abs_{\mathrm{X}}}}\right)\left(\frac{F_{\mathrm{X}}}{F_{\mathrm{S}}}\right)\left(\frac{n_{\mathrm{X}}^2}{n_{\mathrm{S}}^2}\right) \qquad \textbf{Eq. 3.16}$$

The standard selected should have absorption and emission bands close to those of the fluorophore under study as both compounds need to be excited at the same wavelength (Valeur and Berberan-Santos, 2012). In our study, *N*-acetyl-*L*-tyrosinamide (NAYA) was chosen as a standard in the determination of the fluorescence quantum yield of the unlabeled peptides (Φ_{FS} = 0.049 (Noronha *et al.*, 2007)) and fluorescein was used as a standard for the HL488-fluorescently labeled peptides (Φ_{FS}= 0.95 $\pm$ 0.03 in 0.1 M NaOH (Valeur and Berberan-Santos, 2012). The measurements were performed at 25 °C using the experimental conditions described in Table 3.7.

For the determination of fluorescence quantum yields, it is necessary to obtain the instrument corrections factors. The monochromators and the photomultiplier of the spectrofluorometer do not have the same efficiency for all the wavelengths. This might introduce some deviation for what should be expected if this efficiency was independent of the wavelength. For this, there are published emission spectra for accepted standards which cover a large range of wavelengths. The instrument correction factors are calculated by determining the difference between the experimentally measured and the published spectra. For the different wavelengths, different standards were used (Table 3.8). They are usually overlapped in the extremities of the spectra so the one with higher fluorescence intensity in those particular wavelengths was normally used. Later on the corrected emission spectra was also used for the determination of Forster radius between Rhod-POPS LUVs and labeled hIAPP (Section 4.4.7) and in the determination of the corrected steady-state emission spectra for Time-Resolved Emission Spectra (TRES) (Section 4.4.9).

The fluorescence spectral center of mass (intensity-weighted average emission wavelength, $\langle\lambda\rangle$) was calculated according to:

$$\langle\lambda\rangle = \sum_i I_i \cdot \lambda_i \Big/ \sum_i I_i \qquad \textbf{Eq. 3.17}$$

where I_i is the fluorescence intensity measured at each wavelength λ_i (Lopes *et al.*, 2004). This method is more reliable for detecting spectral shifts than just determining the maximum emission wavelength of a fluorophore because it arises from a calculation involving the entire emission spectrum. Therefore, it reflects not only changes in its maximum position but also in the shape of the spectrum; in addition, this parameter is much less sensitive to the S/N ratio of the measurement.

Table 3.8 - Fluorescence standards used for the determination of the instrument correction factor, respective solvents and fluorescence range. Information obtained from Lakowicz, 2006 and Valeur and Berberan-Santos, 2012.

Fluorescence standard	Catalogue number	Solvent	Excitation (nm)	Emission (nm)
Tryptophan	108374	water	280	290-450
Quinine sulfate	22640	0.1 M sulfuric acid	345	360-600
Fluorescein	F1300	0.1 M NaOH	470	480-650
SR 101	S359	Ethanol	540	550-750
LDS 751	L7595	Methanol	550	645-845

3.3.6.2. **Time-resolved fluorescence measurements**

Experimental measurements

Time-resolved fluorescence intensity measurements with picosecond resolution were obtained by the TCSPC technique (Lakowicz, 2006; Valeur and Berberan-Santos, 2012). Excitation was accomplished by a cavity-dumped dye laser (701-2, Coherent, delivering 5-6 ps pulses with ~40 nJ/pulse at 3.4 MHz) working with Rhodamine 6G (Rhod6G) (560-620 nm) or DCM (620-700 nm). The DCM laser emission is doubled in a BBO crystal to deliver the pulses in 310-350 nm spectral range while Rhod6G laser is 280-320 nm. The experimental fluorescence intensity decays, $I_{\exp}(t)$, were measured with an emission polarizer set at the magic angle (54.7º) relative to the vertically polarized excitation beam. This condition is used to avoid the effects of rotational diffusion and/or anisotropy on the intensity decay (Lakowicz, 2006). The fluorescence was detected by a Hamamatsu R-2809U microchannel plate PMT at the desired wavelength that was selected using a Jobin-Yvon HR320 monochromator in combination with an adequate cut-off filter to avoid interference from Rayleigh-scattered light. The instrument response function (IRF), $IRF(t)$, was recorded as excitation light scattered by a Ludox solution (silica, colloidal water solution from Merck KgaA). The data were collected in a multichannel analyzer with a time window of 1024 channels, at typically 16 – 24.4 ps/channel and up to 50 000 and 20 000 counts in the peak channel of the IRF and decay curves, respectively. In some cases, the two polarized components of the fluorescence, parallel, $I_{\mathrm{VV}}(t)$ and perpendicular, $I_{\mathrm{VV}}(t)$, to the plane of polarization of the excitation beam, were recorded sequentially by alternating the orientation of the emission polarizer every 15, 30 or 60 s. For our setup system, the instrumental *G* factor is expected to be 1 because the polarized fluorescence light components were depolarized before the entrance slit of the monochromator. The excitation and emission wavelengths employed in the experiments are presented in Table 3.7.

Data analysis

- *Fluorescence intensity decays*

The lifetime of a fluorophore is the average time a fluorophore remains in the excited state following excitation, determining its availability to interact with the surrounding media. It is the inverse of the total decay rate:

$$\tau = \frac{1}{k_{\mathrm{f}} + k_{\mathrm{nr}}} \qquad \textbf{Eq. 3.18}$$

The fluorescence intensity decay curves, $I(t)$, of free fluorophores in solution will normally decay with a mono-exponential decay, while in interaction with other molecules and/or

depending on its closest environment can be described by a sum of discrete exponential terms (Lakowicz, 2006):

$$I(t) = \sum_{i=1}^{n} \alpha_i \cdot \exp(-t/\tau_i) \qquad \textbf{Eq. 3.19}$$

where α_i and τ_i are, respectively, the amplitude and the lifetime of the *i*th decay component of fluorescence. Briefly, the kinetic parameters describing each curve (α_i and τ_i) were obtained by iteratively convoluting the empirical function above with $IRF(t)$:

$$I_{\text{calc}}(t) = I_{\text{exp}}(t) \otimes IRF(t) \qquad \textbf{Eq. 3.20}$$

and fitting $I_{\text{calc}}(t)$ to $I_{\text{exp}}(t)$, using an iterative non-linear least squares regression method. The usual statistical criteria, namely a reduced χ^2_G value < 1.3 and a random distribution of weighted residuals and autocorrelation plots, were used to evaluate the goodness of the fits (Lakowicz, 2006). The amplitude-weighted mean fluorescence lifetime, $\langle\tau\rangle_1$, which is proportional to the area under de decay curve (and consequently to the fluorescence quantum yield of the fluorophore in the absence of static quenching), was calculated according to:

$$\langle\tau\rangle_1 = \int_0^{\infty} I(t)\,\mathrm{d}t = \sum_{i=1}^{n} \alpha_i \cdot \tau_i \qquad \textbf{Eq. 3.21}$$

The intensity-weighted mean fluorescence lifetime, $\langle\tau\rangle_2$, which reflects the average time that a fluorophore spends in its excited state, was obtained using:

$$\langle\tau\rangle_2 = \frac{\int_0^{\infty} t \cdot I(t)\,\mathrm{d}t}{\int_0^{\infty} I(t)\,\mathrm{d}t} = \frac{\sum_{i=1}^{n} \alpha_i . {\tau_i}^2}{\sum_{i=1}^{n} \alpha_i \cdot \tau_i} \qquad \textbf{Eq. 3.22}$$

The fractional contribution, f_i, of each decay time i to the steady-state fluorescence intensity was calculated according to:

$$f_i = \frac{\int_0^{\infty} I_i(t)\,\mathrm{d}t}{\int_0^{\infty} I(t)\,\mathrm{d}t} = \frac{\alpha_i \cdot \tau_i}{\sum_{i=1}^{n} \alpha_i \cdot \tau_i} \qquad \textbf{Eq. 3.23}$$

and therefore,

$$\langle\tau\rangle_2 = \sum_{i=1}^{n} f_i \cdot \tau_i \qquad \textbf{Eq. 3.24}$$

- *Fluorescence anisotropy decays*

The anisotropy decay functions, $r\,(t)$, were described by:

$$r\,(t) = \sum_{i=1}^{n} \beta_i \cdot exp\,(-t/\phi_i) + r_\infty \qquad \textbf{Eq. 3.25}$$

where β_i and ϕ_i are the initial anisotropy or normalized amplitude and the rotational correlation time of the *i*th decay component of anisotropy, respectively, and r_∞ is the residual or limiting anisotropy, containing information about the restriction of the depolarizing processes. The following condition should always be met:

$$r\,(0) = \sum_{i=1}^{n} \beta_i + r_\infty \leq r_0 \qquad \textbf{Eq. 3.26}$$

where $r(0)$ is the initial anisotropy of the system and r_0 is the fundamental anisotropy of the fluorophore at the excitation and emission wavelengths used in the measurements. This condition is met normally because, apart from instrumental or operational factors, torsional vibrations of the fluorophores about their equilibrium orientation and/or librational motions of the fluorophores in the solvent shell result in a fast depolarization component of the fluorescence emitted by the excited molecule (Valeur and Berberan-Santos, 2012). r_0 is the theoretical anisotropy of a molecule in the absence of any motion (Valeur and Berberan-Santos, 2012) and its given by Eq. 2.1. Since the orientation of the absorption dipole differs for each absorption band, the angle β varies with the excitation wavelength (Valeur and Berberan-Santos, 2012). When the absorption and emission transition moments are parallel, r_0 = 0.4. This is usually the case when the molecules are excited to the first singlet state since absorption and emission involving the same electronic transition have nearly collinear moments. Lower r_0 values are obtained upon excitation into higher electronic states, which are generally not the states responsible for fluorescence emission due to fast IC and relaxation processes. The anisotropy spectrum is a plot of the anisotropy *versus* the excitation wavelength for a fluorophore in a dilute rigid environment; this spectrum thus provides information about the angle between the absorption and emission transition moments. Due to instrumentation problems, the anisotropy decays of the fluorescently-labeled peptides were obtained upon excitation of the HL488 fluorophores to the second singlet state; this reduced the dynamic range of the time-resolved anisotropy measurements due to a decrease in the r_0 value of the fluorophore as explained above; however, each anisotropy decay itself can still be used to retrieve information about the local/global rotational dynamics of the HL488-CT peptides as both the IC and vibrational relaxation processes occur on a time scale that is much faster than fluorescence emission.

The time-resolved anisotropy decays were globally analyzed using a two-step procedure to increase its robustness, i.e. to minimize cross-correlation problems among the many fitting parameters to a single anisotropy decay curve. Briefly, the fluorescence decay parameters

(amplitudes, α_i and lifetimes, τ_i) were first obtained by iterative convolution of Eq. 3.19 with the IRF and fitting to the experimental data calculated as:

$$I_m(t) = I_{\mathrm{VV}}(t) + 2 \cdot G \cdot I_{\mathrm{VH}}(t) \qquad \textbf{Eq. 3.27}$$

using a nonlinear least-squares regression methods as previously described. After fixing the fluorescence lifetime components obtained in this analysis, the anisotropy decay parameters were then determined by simultaneous iterative convolution of $I_{\mathrm{VV}}(t)$ and $I_{\mathrm{VH}}(t)$:

$$I_{\mathrm{VV}}(t) = \frac{I(t)}{3}[1 + 2 \cdot r(t)] \qquad \textbf{Eq. 3.28}$$

$$I_{\mathrm{VH}}(t) = \frac{I(t)}{3}[1 - r(t)] \qquad \textbf{Eq. 3.29}$$

with the IRF and globally fitting to the experimental parallel and perpendicular polarized components of the fluorescence, $I_{\mathrm{VV}}^{\exp}(t)$ and $I_{\mathrm{VH}}^{\exp}(t)$, respectively (Lakowicz, 2006). The steady-state fluorescence anisotropy, $\langle r \rangle$, was used to check the time-resolved data by calculating a *G* factor according to Lakowicz (2006):

$$G = \left(\frac{1 - \langle r \rangle}{1 + 2\langle r \rangle}\right) \cdot \frac{\int_0^\infty I_{\mathrm{VV}}^{\exp}(t) \cdot dt}{\int_0^\infty I_{\mathrm{VH}}^{\exp}(t) \cdot dt} \qquad \textbf{Eq. 3.30}$$

As expected from the presence of a depolarizer prior to the detection system, the *G* factors obtained were always very close to 1. The analysis of the fluorescence intensity and anisotropy decays was performed using the TRFA Data Processing Package (Scientific Software Technologies Centre, Belarusian State University) which allows calculating automatically the confidence interval corresponding to one standard deviation for each fitted parameter (Lakowicz, 2006). At first, the quality of the fits to the fluorescence decays was often greatly improved by including an extra very short-lived lifetime component (typically fixed at 5 ps) in the analysis that allowed taking into account the detection of any scattered excitation light. This correction was no longer necessary when an updated version of the fitting software (TRFA Data Processing Package version 1.4) was used in the analysis of the time-resolved fluorescence data obtained more recently.

3.3.7. Fluorescence Correlation Spectroscopy

3.3.7.1. Principles of Confocal Laser Scanning Microscopy (CLSM)

In a basic fluorescent microscope, the excitation light from a mercury or xenon high-pressure bulb passes through the excitation filter into a dichroic mirror that reflects this excitation beam into the sample through a low or high NA objective. Most fluorescence

microscopes are operated in an epi-illumination mode, i.e. the light source and the detector are positioned in the same side of the sample plane to decrease the amount of excitation light that reaches the detector (Murphy, 2001). The fluorescence emitted by the sample can be directly observed by eye or recorded with a camera. Wide-field microscopy is commonly used since it is simple and low cost. All the parts of the sample are viewed simultaneously which gives an image with spatial resolution but high background fluorescence. Usually the excitation intensity is low which results in less photobleaching. The disadvantages are mostly related with low contrast and spatial resolution, as both diffraction-limited optics and out-of-focus light can cause shading artifacts and hamper the image resolution. Fluorescently-labeled structures very close to each other would result in a fluorescent blur rather than discrete structures (Murphy, 2001; Sanderson *et al.*, 2014).

A confocal fluorescence microscope comprises a series of components designed to obtain highly resolved images using fluorescence. The basis of a CLSM is a fluorescence microscope, equipped with laser light sources, appropriate excitation and emission filters, dichroic mirrors, a sequential scanning method of the point source and the appropriate optical and electronic equipment to translate the photons emitted excited fluorophores into a 2D or 3D image (Valeur and Berberan, 2012; Sanderson *et al.*, 2014). Confocal microscopy emerged with the introduction of the pinhole aperture to eliminate out-of-focus light. The fluorescence emitted by the sample passes the emission filter and is imaged onto a pinhole, which filters the out-of-focus light, significantly increasing the resolution since only fluorescence from the point in the sample where the excitation light was focused is seen. Optical sectioning of thick samples is also possible, since the CLSM also provides axial resolution. The photons emitted by the excited fluorophores pass through the objective and the emission filter and are collected by a PMT. The computer receives a continuously change in voltage signal from the PMT and translates it into a fluorescence-based image. For scanning the sample, the laser and pinhole remain stationary, but the focus point is optically moved across the sample by mirrors and the intensity is detected pixel-by-pixel (Renz, 2013; Sanderson *et al.*, 2014). Optical microscopes have an intrinsic limitation in spatial resolution because of image contrast and the effect of light diffraction. The best optics with one-photon excitation still limits the lateral resolution to approximately 200 nm and the axial resolution to 500 nm, which cannot resolve more fine cellular structures or specific events (Hell, 2003; Leung and Chou, 2011).

3.3.7.2. **Principles of Fluorescence Correlation Spectroscopy**

Fluorescence correlation spectroscopy (FCS) is a fluorescence technique based on the measurement of temporal fluctuations in intensity from a reduced number of fluorescent

molecules in a very small detection volume (Figure 3.14). Therefore, any process that affects these fluctuations, e.g. translational diffusion and/or a chemical reaction that results in a change in fluorescence intensity (conformational transitions, triplet dynamics and excited state reactions) can be detected from FCS data (Widengren *et al.*, 1995; Widengren and Rigler, 1998; Bulseco and Wolf, 2007; Al-Soufi *et al.*, 2008). The basic principles of this technique are analogous to what happens in dynamic light scattering (DLS), a technique based on fluctuations of laser light scattered by particles (see Section 4.3.7), that preceded and inspired FCS (Valeur and Berberan-Santos, 2012).

The fluctuations in intensity will vary with time and a normalized autocorrelation (AC) function, $G'(\tau)$, of the fluorescence intensity can be defined as the product of its intensity at time t, $I(t)$ and after a delay time τ, $I(t+\tau)$, averaged over a large number of measurements (Haustein and Schwille, 2007; Valeur and Berberan-Santos, 2012):

$$G'(\tau) = \frac{\langle I(t) \cdot I(t+\tau) \rangle}{\langle I(t) \rangle^2} \qquad \textbf{Eq. 3.31}$$

where $\delta I(t)$ are the temporal fluctuations of the fluorescence intensity around a mean value, $\langle I(t) \rangle$:

$$\delta I(t) = I(t) - \langle I(t) \rangle \qquad \textbf{Eq. 3.32}$$

The angular brackets refer to time averaging. Therefore, the AC function is a measure of the self-similarity of the fluorescence signal at time t and after a given delay time τ.

To simplify the mathematical expressions, the AC function of fluorescence fluctuations, $G(\tau)$, is often used instead (Hess and Webb, 2002; Lakowicz, 2006; Haustein and Schwille, 2007; Al-Soufi *et al.*, 2008):

$$G(\tau) = \frac{\langle \delta I(t) \cdot \delta I(t+\tau) \rangle}{\langle I(t) \rangle^2} = G'(\tau) - 1 \qquad \textbf{Eq. 3.33}$$

This function equals zero in the absence of correlation, whereas $G'(\tau)$ converges to 1 at long correlation times (Figure 3.14, d).

The information related with translational diffusion comes from the fluctuations in fluorescence intensity caused by each particle randomly entering and leaving the focus volume, so it is easier to detect these fluctuations if there are only a few particles (small *N*) in the observation volume. When the number of molecules inside the excitation volume increases, it becomes harder to perceive the individual fluctuations in the signal. As an example, for an average number of fluorescent molecules *N* = 100, the relative fluctuation drops to 1% compared to 100% for *N* = 1. Ideally, the focus volume is in the order of 1 fL = 1 μm^3 so the concentrations used in FCS measurements typically are within the nanomolar range (Bulseco and Wolf, 2007; Haustein and Schwille, 2007; Betaneli and Schwille, 2013).

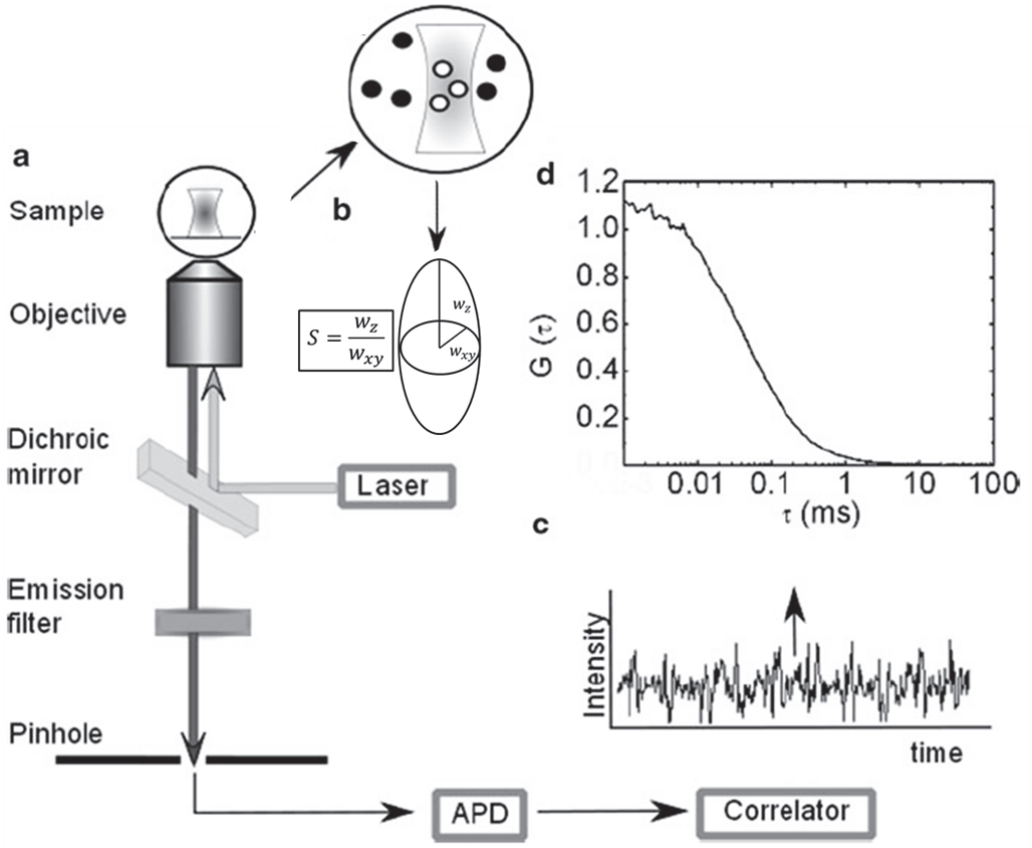

Figure 3.14 – General FCS setup. (**a**) in a confocal fluorescence microscope, the incident excitation light is reflected by a dichroic mirror and focused on the sample through a high NA objective. (**b**) The focus is estimated to have an ellipsoid shape with two equal lateral axes $\boldsymbol{w_{xy}}$ and axial $\boldsymbol{w_z}$ dimensions, and is in the order of 1 fL (10^{-15} L). The fluorescent molecules will be detected only if they diffuse through the confocal volume. The emitted fluorescence passes the emission filter and is imaged onto a pinhole, which filters the out-of-focus light, and is detected by a fast detector, normally an avalanche photodiode (APD). The APD produces an electrical pulse for each single photon detected which is counted and processed by a computer. (**c**) This gives rise to a fluctuating intensity signal which is correlated with itself at a later time ($\boldsymbol{t+\tau}$) to obtain the autocorrelation function (**d**). Adapted from (Betaneli and Schwille, 2013).

3D translational diffusion

The most common application of the FCS technique is to measure the translational diffusion coefficient, D_t, of a fluorescent species under extremely diluted conditions. The rate of diffusion depends on the size and shape of the diffusing molecule and its possible interactions with itself (self-assembly) or other molecules so these measurements are ideally suited to detect the oligomerization or binding interactions of the fluorescent species under study with different partners, including lipid vesicles (Hess and Webb, 2002; Rusu *et al.*, 2004; Takahashi *et al.*, 2007; Melo *et al.*, 2011; Bag *et al.*, 2013; Gehne *et al.*, 2013).

For a single fluorescent species undergoing Brownian motion with D_t, the AC function, $G_D(\tau)$, can be written as:

$$G_{\mathrm{D}}(\tau) = \frac{1}{N} \cdot \left(1 + \frac{\tau}{\tau_{\mathrm{D}}}\right)^{-1} \cdot \left(1 + \frac{\tau}{S^2 \tau_{\mathrm{D}}}\right)^{-1/2} \qquad \textbf{Eq. 3.34}$$

where N is the average number of fluorescent molecules in the laser focus, τ_{D} is the correlation time of the diffusing particle, i.e. the characteristic average diffusion time of the molecule through the observation ellipsoidal confocal volume with axial ω_{z} and lateral ω_{xy} dimensions and an aspect ratio $S = \omega_{\mathrm{z}} / \omega_{\mathrm{xy}}$ (Lakowicz, 2006). As mentioned above, another source of fluctuations in the fluorescence intensity is the possibility that the fluorophore undergoes intersystem crossing to its first excited triplet state. The AC function of the triplet state dynamics, $G_{\mathrm{T}}(\tau)$, is described by:

$$G_{\mathrm{T}}(\tau) = 1 + \frac{T}{1-T} \exp\left(-\frac{\tau}{\tau_{\mathrm{T}}}\right) \qquad \textbf{Eq. 3.35}$$

where T is the average fraction of fluorophores in the triplet state and τ_{T} is the characteristic relaxation time of the triplet state. The combined AC function for translational diffusion and triplet dynamics is then:

$$G(\tau) = \frac{1}{N} \cdot \left(1 + \frac{T}{1-T} \exp\left(-\frac{\tau}{\tau_{\mathrm{T}}}\right)\right) \cdot \left(1 + \frac{\tau}{\tau_{\mathrm{D}}}\right)^{-1} \cdot \left(1 + \frac{\tau}{S^2 \tau_{\mathrm{D}}}\right)^{-1/2} \qquad \textbf{Eq. 3.36}$$

The diffusion coefficient of the species can be calculated using the Einstein relation:

$$\tau_{\mathrm{D}} = {\omega_{\mathrm{xy}}}^2 / 4D_{\mathrm{t}} \qquad \textbf{Eq. 3.37}$$

Experimental measurements

FCS measurements were carried out on a FCS setup based on a dual channel ISS Alba fluorescence correlation detector with APDs connected to a Leica TCS SP5 confocal inverted microscope. The 488 nm line provided by an Argon laser was focused into the sample by the apochromatic water immersion objective (63x, NA 1.2 water immersion objective with a correction ring). The emission was detected confocally after passing through a 500–550 nm band-pass filter. A 111.44 µm diameter pinhole in the image plane blocked out-of-focus signals.

Each measurement consisted of 5 or 10 AC curves of 20 s each, acquired with a sampling frequency of 500 kHz. To correct for the variable thickness of each observation chamber, the correction collar of the objective was adjusted by focusing the reflection image generated at the transition of the coverslip/aqueous solution prior to each set of measurements. The laser power used was adjusted in order that the triplet fraction was never higher than 20%, as recommended in the FCS Vista user manual. Particular attention was also always paid to possible photobleaching artefacts in the FCS measurements by

confirming that the diffusion correlation times of the molecules were independent of the laser power used during the optimization of FCS data acquisition. FCS measurements were carried out at RT (T = 21±1 ºC) and the samples were measured in 8-well Ibidi chambers coated with BSA 1%. 300 µL of a 1% solution of BSA was placed in every well, left for at least 1h and then washed carefully at least 3 times with buffer. Samples were prepared as follows:

- a 10 nM Rhod110 solution (calibrator) was prepared by serial dilution from a concentrated stock solution in ethanol using filtered (0.22 µm cellulose acetate filters) ultrapure water obtained from a Milli-Q system;

- a 5 nM working solution of the free dyes A488 and HL488 where prepared by serial dilution from a stock solution using HEPES-KOH pH 7.4 buffer filtered with 0.22 µm cellulose acetate filters;

- samples of HL488-sCT and HL488-hCT were prepared by evaporating an appropriate amount of the stock solutions in HFIP in LPB Eppendorfs ® as previously described (Section 3.3.3). These intermediate solutions with approximately 4-8 µM was quantified spectrophotometrically using the molar absorption coefficients (Table 3.2) and filtered using a Vivaspin 5 KDa (Sartorius, Göttingen, Germany), centrifuged 8000 *g* for 22 min, accordingly to manufacturer instructions. The sample was again quantified spectrophotometrically (70 to 90% of the peptide was recovered) and the final samples of peptide, ranging from 15 to 90 nM, were prepared by dilution of this intermediate solution with filtered buffer.

Data analysis

Data analysis of the experimental AC curves was performed using the ISS Vista software (version 3.7). This program uses a Marquardt–Levenberg nonlinear least-squares fitting routine and the goodness of the fittings can be judged by the recovered χ^2_G and random distribution of the weighted residuals. A 3D Gaussian model was selected in the software for describing the laser point spread function with an effective volume $V_{\mathrm{eff}} = \pi^{3/2}\,{\omega_{\mathrm{xy}}}^2\omega_{\mathrm{z}}$.

A two-step analysis of the FCS data was implemented:

(*i*) calibration of the structural parameter S

Rhod110 was chosen as the calibrator of the FCS setup since it is a very bright reference dye with a high solubility in aqueous solution and a known diffusion coefficient, $D_{\mathrm{reference}} =$ 440 µm^2 s^{-1} (Gendron *et al.*, 2008). Eq. 3.36 was globally fitted to the experimental data obtained by linking the τ_{T}, T, its diffusing time, $\tau_{\mathrm{D\ reference}}$, and the structural parameter S

across all the AC curves obtained for this sample in order to help constraining the fitting parameters during the analysis. The S factor obtained was then held fixed for the other samples measured in the same chamber slide. With a good alignment of the system, the structural parameter ranges from 4 to 6 (Bacia and Schwille, 2007).

(*ii*) determination of D_{t}

Eq. 3.36 was globally fitted to the experimental FCS data obtained for the sample under study by linking τ_{T}, T, and its diffusing time, $\tau_{\mathrm{D\ sample}}$, across all the AC curves, while fixing S obtained in the calibration procedure. A relative method was then used to calculate the diffusion coefficient of the sample, D_{sample}:

$$D_{\mathrm{sample}} = \frac{\tau_{\mathrm{D\ reference}}}{\tau_{\mathrm{D\ sample}}} . D_{\mathrm{reference}} \qquad \textbf{Eq. 3.38}$$

Finally, the experimental $\boldsymbol{D_t}$ measured for the conjugated CT peptides were compared to predictions obtained from empirical power laws describing their dependence with the molecular weight, *MW*, and molecular shape of the protein/peptide, according to the Mark–Houwink–Kuhn–Sakurada (MHKS) model from polymer science (Harding, 1997; Creighton, 1999; Mark, 2007):

$$D_t = K{\cdot}MW^{-\varepsilon}\ (m^2 s^{-1}) \qquad \textbf{Eq. 3.39}$$

The value $\varepsilon_{\mathrm{sphere}}$= 0.333 describes the behavior expected for globular macromolecules with an overall spherical shape (Creighton, 1999). Assuming that the protein density, ρ, is 1.35 g.cm^{-3}, and that the temperature and water viscosity are 25 °C and 0.000891 kg.ms^{-1}, one gets K_{sphere}= 3.68·10^{-10} m^2/s (Loman, 2010). On the other hand, for random coil polypeptides $\varepsilon_{\mathrm{coil}}$= 0.51 and K_{coil}= 11·10^{-5} m^2/s (the polypeptide chain is modeled by the freely-jointed chain model of polymer chains assuming a random-chain segment length of 0.279 nm and an average molecular weight for an amino acid of 131 Da (Loman, 2010). In addition, the experimental FCS data were also compared to the D_t measured by Danielson and co-workers (Danielsson *et al.*, 2002) for Aβ-40 peptide and also for a series of fragments of this peptide using pulsed-field gradient-nuclear magnetic resonance (PFG-NMR) methods at 25 °C and physiological pH in aqueous solution. Using their data, Danielson and co-workers proposed the following empirical scale law:

$$D_t = (6.06\ \pm 0.01){\cdot}10^{-9}\ MW^{-(0.44\ \pm 0.02)}\ (m^2 s^{-1}) \qquad \textbf{Eq. 3.40}$$

and estimated the relation between the measured hydrodynamic radius, $\boldsymbol{R_h}$ (in Å) and the *MW* in Da of the polypeptide chain as:

$$R_{\mathrm{h}} = 0.27\, MW^{-0.50}$$ **Eq. 3.41**

3.3.8. Global analysis of TFE-induced folding of calcitonin peptides

The free energy of unfolding/folding of a peptide or protein as a function of solvent composition or denaturants can be determined by following the changes in any spectroscopic signal concomitant to the conformational transition (Greenfield, 2007a; Latypov *et al.*, 2007; Boehm *et al.*, 2008; Schneider *et al.*, 2017). In the case of the CT peptides, the increase in TFE concentration leads to the conversion of the peptides from a disordered state to a more folded state with a noticeable increase in $[\theta]_{222\,\mathrm{nm}}$ of the CTs, measured by CD, and the mean fluorescence lifetime of either fluorescently-labeled CT variant. The variation in the composition of the binary aqueous TFE/buffer mixture was also accompanied by an increase in the apparent hydrodynamic volume of the peptide, $V_{\mathrm{h}}^{\mathrm{app}}$, as evaluated from time-resolved fluorescence anisotropy measurements. The TFE-induced folding transitions of sCT and hCT were analyzed according to a two-state or three-state model, respectively.

- Two-state model

In this case, it was considered that upon increasing the %TFE (v/v) in solution the peptides can undergo a single cooperative transition whereupon the peptide converts from an unfolded (U) to a more folded (F) state:

$$\mathrm{U} \leftrightarrow \mathrm{F}$$ **Eq. 3.42**

The equilibrium folding constant, K_{F}, for this transition is:

$$K_{\mathrm{F}} = [\mathrm{F}]/\,[\mathrm{U}]$$ **Eq. 3.43**

where $[\mathrm{F}]$ and $[\mathrm{U}]$ are the concentrations of folded and unfolded peptide, respectively. The spectroscopic signal determined at each solvent composition (%TFE), S_{obs}, was assumed to be a linear combination of the fractional contribution from each species:

$$S_{\mathrm{obs}} = x_{\mathrm{U}} \cdot S_{\mathrm{U}} + x_{\mathrm{F}} \cdot S_{\mathrm{F}}$$ **Eq. 3.44**

where S_{U} and S_{F} are the signal for the unfolded and folded states and x_{U} and x_{F} are their respective molar fractions ($x_{\mathrm{U}} + x_{\mathrm{F}}$ = 1):

$$x_{\mathrm{U}} = \frac{1}{1 + K_{\mathrm{F}}}$$ **Eq. 3.45**

$$x_{\mathrm{F}} = \frac{K_{\mathrm{F}}}{1 + K_{\mathrm{F}}}$$ **Eq. 3.46**

Regarding the experimental data obtained for sCT, it was necessary to further take into account a post-transition dependence of the spectroscopic signal with the solvent composition:

$$S_{\mathrm{F}} = S_{\mathrm{F}}^{\mathrm{o}} + m \cdot \%\mathrm{TFE} \qquad \textbf{Eq. 3.47}$$

where $S_{\mathrm{F}}^{\mathrm{o}}$ and m are the intercept and slope of the final baseline, respectively. This probably results from the interaction of TFE with the α-helix formed or is due to a change in the physicochemical properties of the binary mixture used rather than from additional conformational changes (Greenfield, 2007a).

The standard free energy of folding, $\Delta G_{\mathrm{F}}^{\mathrm{o}}$ is related to K_{F} through the following equation:

$$\Delta G_{\mathrm{F}}^{\mathrm{o}} = -RT \ln K_{\mathrm{F}} \Leftrightarrow K_{\mathrm{F}} = \exp\left(-\frac{\Delta G_{\mathrm{F}}^{\mathrm{o}}}{RT}\right) \qquad \textbf{Eq. 3.48}$$

and, here, $\Delta G_{\mathrm{F}}^{\mathrm{o}}$ is assumed to show a linear relationship with %TFE in the binary mixture:

$$\Delta G_{\mathrm{F}}^{\mathrm{o}} = \Delta G_{\mathrm{F}}^{\mathrm{o}}(\mathrm{H_2O}) - m_{\mathrm{F}} \cdot \%\mathrm{TFE} \qquad \textbf{Eq. 3.49}$$

where m_{F} is related to the TFE dependence (or slope) of the transition, $\Delta G_{\mathrm{F}}^{\mathrm{o}}(\mathrm{H_2O})$ is the standard free energy of folding in the absence of TFE, *R* is the gas constant and *T* is the absolute temperature. It is useful to rearrange the previous equation using the mid-point of the cooperative transition, $\%\mathrm{TFE}_{1/2}$, since it has a low inherent error as it can be easily determined graphically. The mid-point of the transition occurs when $x_{\mathrm{U}} = x_{\mathrm{F}}$ and so K_{F}= 1, hence:

$$\Delta G_{\mathrm{F}}^{\mathrm{o}}(\mathrm{H_2O}) = m_{\mathrm{F}} \cdot \%\mathrm{TFE}_{1/2} \qquad \textbf{Eq. 3.50}$$

and

$$\Delta G_{\mathrm{F}}^{\mathrm{o}} = m_{\mathrm{F}}\,(\%\mathrm{TFE}_{1/2} - \%\mathrm{TFE}) \qquad \textbf{Eq. 3.51}$$

Eq. 3.44 can be re-written as:

$$S_{\mathrm{obs}} = \frac{S_{\mathrm{U}} + K_{\mathrm{F}}\left(S_{\mathrm{F}}^{\mathrm{o}} + m \cdot \%\mathrm{TFE}_{1/2}\right)}{1 + K_{\mathrm{F}}} \qquad \textbf{Eq. 3.52}$$

Eq. 3.52 was globally fitted to the experimental data of $[\theta]_{222\mathrm{nm}}$, $\langle\tau\rangle_1$ and $V_{\mathrm{h}}^{\mathrm{app}}$ as function of %TFE (v/v) to obtain eight unknown parameters after substituting for x_{U} and x_{F} in terms of m_{F} and $\%\mathrm{TFE}_{1/2}$ (which were globally linked between the three experimental curves) using equations Eq. 3.48 and Eq. 3.51. The parameters are the sets of S_{U} and S_{F} characteristic of each technique, m_{F} and $\%\mathrm{TFE}_{1/2}$.

- Three-state model

A sequential three-state model was considered for hCT: upon increasing the %TFE (v/v) of the binary solvent mixtures and starting from the unfolded state, U, the peptide first populates an equilibrium intermediate state, I, before adopting a final partial folded state, F:

$$\mathrm{U} \leftrightarrow \mathrm{I} \leftrightarrow \mathrm{F} \qquad \textbf{Eq. 3.53}$$

The equilibrium folding constants for each of these conformational transitions are K_{UI} and K_{IF}, respectively:

$$K_{\mathrm{UI}} = [\mathrm{I}]/\,[\mathrm{U}] \qquad \textbf{Eq. 3.54}$$

$$K_{\mathrm{IF}} = [\mathrm{F}]/\,[\mathrm{I}] \qquad \textbf{Eq. 3.55}$$

where $[\mathrm{U}]$, $[\mathrm{I}]$ and $[\mathrm{F}]$ are the concentrations of unfolded, intermediate and folded peptide, respectively. Each spectroscopic signal observed as a function of %TFE is considered to be the sum of the signals of the three pure states, the unfolded state, S_{U}, the intermediate state, S_{I} and the folded state S_{F}, weighted by their respective molar fractions, x_{U}, x_{I} and x_{F}, respectively (Figure 3.15):

$$S_{\mathrm{obs}} = x_{\mathrm{U}} \cdot S_{\mathrm{U}} + x_{\mathrm{I}} \cdot S_{\mathrm{I}} + x_{\mathrm{F}} \cdot S_{\mathrm{F}} \qquad \textbf{Eq. 3.56}$$

where

$$x_{\mathrm{U}} = \frac{1}{1 + K_{\mathrm{UI}}\,(1 + K_{\mathrm{IF}})} \qquad \textbf{Eq. 3.57}$$

$$x_{\mathrm{I}} = \frac{K_{UI}}{1 + K_{\mathrm{UI}}\,(1 + K_{\mathrm{IF}})} \qquad \textbf{Eq. 3.58}$$

and

$$x_{\mathrm{F}} = \frac{K_{\mathrm{UI}} \cdot K_{\mathrm{IF}}}{1 + K_{\mathrm{UI}}\,(1 + K_{IF})} \qquad \textbf{Eq. 3.59}$$

The equilibrium constants are defined by the following equations:

$$K_{\mathrm{UI}} = \exp\left(-\frac{\Delta G^{\mathrm{o}}_{\mathrm{UI}}}{RT}\right) \qquad \textbf{Eq. 3.60}$$

$$K_{\mathrm{IF}} = \exp\left(-\frac{\Delta G^{\mathrm{o}}_{\mathrm{IF}}}{RT}\right) \qquad \textbf{Eq. 3.61}$$

where the standard free energies $\Delta G^{\mathrm{o}}_{\mathrm{UI}}(\mathrm{H_2O})$ and $\Delta G^{\mathrm{o}}_{\mathrm{IF}}(\mathrm{H_2O})$ are assumed to be a linear function of the %TFE used:

$$\Delta G^{o}_{UI} = \Delta G^{o}_{UI}(H_2O) - m_1 \cdot \%TFE \quad \textbf{Eq. 3.62}$$

$$\Delta G^{o}_{IF} = \Delta G^{o}_{IF}(H_2O) - m_2 \cdot \%TFE \quad \textbf{Eq. 3.63}$$

As described above, for the mid-point of each transition:

$$\Delta G^{o}_{UI}(H_2O) = m_1 \cdot \%TFE^{1}_{1/2} \quad \textbf{Eq. 3.64}$$

$$\Delta G^{o}_{IF}(H_2O) = m_2 \cdot \%TFE^{2}_{1/2} \quad \textbf{Eq. 3.65}$$

and therefore:

$$\Delta G^{o}_{UI} = m_1 \, (\%TFE^{1}_{1/2} - \%TFE) \quad \textbf{Eq. 3.66}$$

$$\Delta G^{o}_{IF} = m_2 \, (\%TFE^{2}_{1/2} - \%TFE) \quad \textbf{Eq. 3.67}$$

Eq. 3.56 can be re-written as:

$$S_{obs} = \frac{S_U + K_{UI}(S_I + K_{IF} \cdot S_F)}{1 + K_{UI}\,(1 + K_{IF})} \quad \textbf{Eq. 3.68}$$

Using equations Eq. 3.61, Eq. 3.62, Eq. 3.67 and Eq. 3.68, the equation above (Eq. 3.69) was globally fitted to the experimental data of $[\theta]_{222nm}$, $\langle\tau\rangle_1$ and V_h^{app} as function of %TFE (v/v) to obtain thirteen unknown parameters: m_1 , $\%TFE^{1}_{1/2}$, m_2 and $\%TFE^{2}_{1/2}$ (which were globally linked between the three experimental curves) and S_U, S_I and S_F (each set of spectroscopic signals was allowed to vary for each experimental observable used in the global analysis).

The global fittings of the two-state and three-state models to the experimental data obtained for sCT and hCT, respectively, were performed by non-linear regression using the GraphPad Prism 7 software.

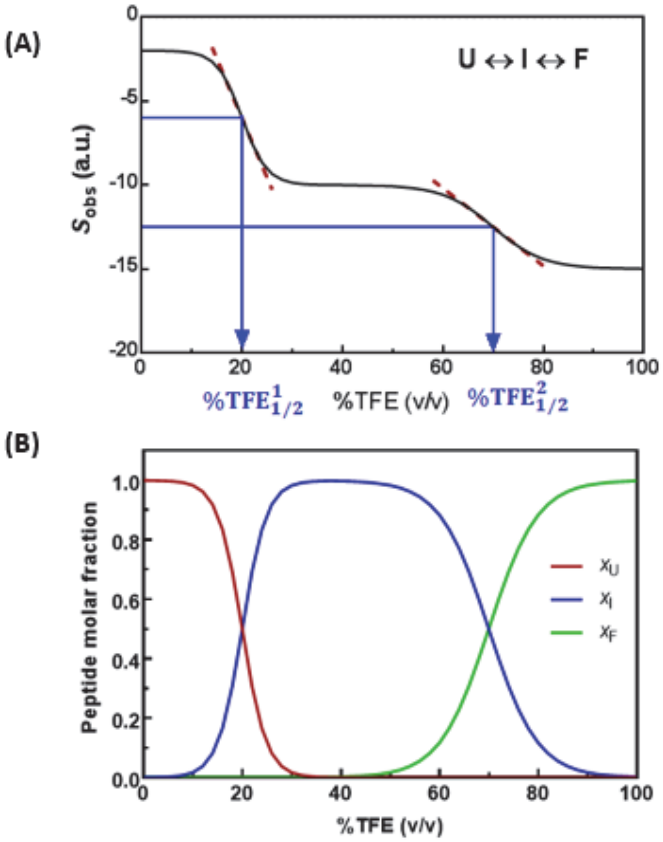

Figure 3.15- Schematic illustration of a sequential three-state TFE-induced peptide folding. (A) The data simulated was obtained considering $\boldsymbol{S_U = -2, S_I = -10}$ and $\boldsymbol{S_F = -15}$ (arbitrary units); $\boldsymbol{m_1 = 1000\%}$ (v/v)$^{-1}$, $\boldsymbol{m_2 = 500\%}$ (v/v)$^{-1}$; $\boldsymbol{\%TFE_{1/2}^{1} = 20\%}$ (v/v) and $\boldsymbol{\%TFE_{1/2}^{2} = 70\%}$ (v/v), respectively (*T*= 298 K). $\boldsymbol{m_1}$ and $\boldsymbol{m_2}$ define the TFE dependence (slope) of the first and second transitions, whereas $\boldsymbol{\%TFE_{1/2}^{1}}$ and $\boldsymbol{\%TFE_{1/2}^{2}}$ are the %TFE corresponding to the mid-point of transition 1: U ↔ I and transition 2: I ↔ F, respectively. (**B**) The corresponding peptide molar fractions are plotted as a function of %TFE (v/v) included in the binary solvent mixture (unfolded, $\boldsymbol{x_U}$ (red curve), intermediate, $\boldsymbol{x_I}$ (blue curve) and folded, $\boldsymbol{x_F}$ (green curve) peptide molar fractions, respectively). See the text for more details.

3.4. Results and Discussion

3.4.1. Conformational plasticity of calcitonin peptides in homogeneous solution: a fluorescence study

We first set out to perform a detailed solvatochromic and photophysical study of the free HL488 dye and both HL488-labelled CT variants in homogeneous medium. In addition to buffer, a set of alcohols with aliphatic chains of increasing length (methanol, ethanol, 2-propanol and 2-butanol) was used since alcohols are frequently considered minimal models for mimicking proximity to biological membranes, as they simulate the impact of a local decrease in the dielectric constant near the membrane surface on the structure of peptides/proteins (Meadows *et al.*, 1991; Arvinte and Drake, 1993; Munishkina *et al.*, 2003). Alcohols are also known to induce partially folded intermediates of peptides/proteins. In this regard, TFE is a popular fluoroalcohol that is known to have strong effects on peptide/protein conformation (Buck, 1998). TFE also has a low absorbance in the far-UV region, allowing the performance of complementary far-UV CD measurements that are extremely useful to probe for the concomitant TFE-induced alterations in the secondary structure of the peptides/proteins under study (Kelly *et al.*, 2005). This preliminary fluorescence study was essential to provide an interpretation framework for the spectroscopic data obtained later with the fluorescently-labelled peptides in more complex systems, i.e. in interaction with lipid membranes.

3.4.1.1. **Free HiLyte Fluor 488 (HL488)**

- Homogeneous solvents

The free HL488 probe presents a maximum absorption wavelength, $\lambda_{\max}^{\mathrm{Abs}}$, at 501 nm and an intensity-averaged emission wavelength, $\langle\lambda\rangle$, at 534.1 nm in HEPES-KOH buffer, pH 7.4 as it is displayed in Figure 3.16 A and B, respectively, and summarized in Table 3.9.

The solutions of the free dye dissolved in aliphatic alcohols of increasing aliphatic chain length presented batochromic shifts in both its absorption and fluorescence emission spectra, which were more noticeable in BuOH (Figure 3.16 A and B, dark blue, respectively and Table 3.9). The results obtained in this solvatochromic study do not conform to the general solvent effects theory. The interactions between the solvent and fluorophore will affect the energy difference between the ground and excited states and the Lippert-Mataga equation is an approximation to describe this energy difference. However, there is only a reasonable correlation between the observed and calculated energy losses in solvents that do not contain hydroxyl groups or other groups capable of hydrogen bonding (Lakowicz, 2006; Valeur and Berberan-Santos, 2012), which are the solvents used here. The data

obtained suggests that specific solvent effects such as hydrogen bonding must be at play due to the pronounced 8 – 9 nm and 13 – 16 nm hypsochromic shifts detected in both the absorption and emission spectra of HL488 in the fluoroalcohols TFE and HFIP, respectively (Table 3.9 and Figure 3.16 A and B, TFE red curve). With the exception of the dye dissolved in 2-butanol, the fluorescence emission decay kinetics of HL488 was always monoexponential as illustrated in Figure 3.1 C for buffer and TFE, and a radiative rate constant, k_F= (2.00 ± 0.06)×10^8 s^{-1} (n= 7) was obtained according to Eq. 3.15 and Eq. 3.18 (Table 3.9). In 2-butanol the dye presented a double exponential decay, although the long lifetime component obtained represented 99% of the decay (Table 3.9). Additionally, the fluorescence lifetime of the free probe was found to be critically dependent on the solvent acidity of the aliphatic/ fluoroalcohol used as illustrated in Figure 3.16 D.

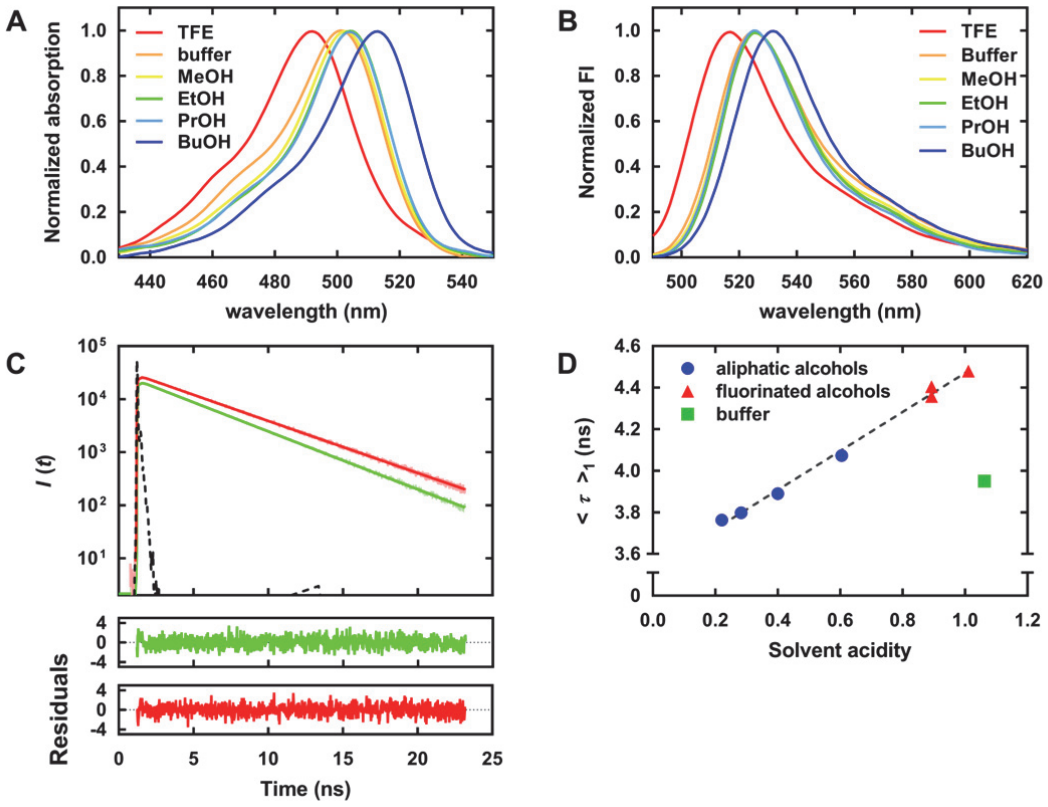

Figure 3.16 - Solvatochromic and photophysical studies of the free probe HL488 in buffer, aliphatic and fluorinated alcohols at 25 ºC. Representative normalized (**A**) absorption and (**B**) fluorescence emission spectra ((λ_{exc}= 480 nm) of 1 μM HL488 in TFE (red), buffer (orange), methanol (MeOH, yellow), ethanol (EtOH, green), 2-propanol (PrOH, light blue) and 2-butanol (BuOH, dark blue). (**C**) HL488 decays monoexponentially in homogeneous solution as it is exemplified here for the fluorescence intensity decays obtained in buffer (green curve) and TFE (red curve) (λ_{exc}= 335 nm; λ_{em}= 525 nm). The solid lines are the best fits of Eq. 3.19 to the experimental data and the bottom panels correspond to the residuals of the fit. The dashed line is the IRF. (**D**) The fluorescence lifetime, $\langle\tau\rangle_1$, of free HL488 is linearly dependent on the solvent acidity for aliphatic and fluoroalcohols (hydrogen-bond donor solvents), with the exception of buffer (green square) (r^2= 0.9947). See Table 3.9 for additional experimental details and the obtained parameters.

The rotational dynamics of the free HL488 probe in homogeneous solution was also studied. The excitation anisotropy spectrum obtained for this probe in glycerol at *T*= 8 ºC is presented in Figure 3.17 A. The fundamental anisotropy of HL488 at 335 nm and between 440-520 nm is r_0~ - 0.16 and r_0~ 0.364 ± 0.005 due to excitation at its $S_2 \leftarrow S_o$ and $S_1 \leftarrow S_o$ absorption bands, respectively. Accordingly, the relative variation of the ssFA of HL488 and both HL488-fluorescently labeled peptides with the solvent viscosity when the samples were excited at 335 nm (i.e. when performing time-resolved fluorescence measurements) was approximately half of the one obtained when λ_{exc}= 480 nm was used (i.e. when steady-state fluorescence measurements were carried out) (Figure 3.17 B). This value is comparable to the one measured by Johansson (Johansson, 1990) - r_0 = 0.373 ± 0.002 - for the fundamental anisotropies of several xanthene dyes in glycerol and propane-1,2-diol and by Rusinova and co-workers (Rusinova *et al.*, 2002), who measured A488 in a rigid environment (100% glycerol at -10 ºC) and obtained r_0 = 0.376 ± 0.003.

The fluorescence anisotropy decays obtained for the free probe in aliphatic alcohols were always mono-exponential (Figure 3.17 C) and the fitted rotational correlation times (Table 3.10) were linearly dependent on the solvent viscosity as expected (Figure 3.17 D). Assuming that the fluorophore has a spherical shape, the apparent hydrodynamic volume, V_h^{app}, of the dye can be calculated from its experimental rotational correlation time, ϕ, using Eq. 2.3. Accordingly, HL488 has a V_h^{app}~ 1.9 ± 0.2 nm^3 in this set of aliphatic alcohols.

- *Binary TFE/buffer mixtures*

A thorough solvatochromic and photophysical study of the free HL488 probe in binary mixtures of TFE/buffer was also carried out at 25 ºC. These were important control measurements for the subsequent experiments that were performed with both fluorescently-labelled CT peptides in equivalent binary solvent mixtures.

Upon increasing the TFE content of the binary solvent mixtures, both the absorption and fluorescence emission spectra of HL488 presented a net hypsochromic shift of approximately 10 nm (Figure 3.18 A and B, respectively). On the other hand, the free dye decayed once again monoexponentially in all the solvent mixtures studied and its fluorescence lifetime, τ, monotonically increased from 3.96 ns in buffer to 4.36 ns in TFE. An inflection point at ~ 75% TFE (vol/vol) was detected in both the variation of $\langle\lambda\rangle$ and τ with the TFE content of the binary mixture, as displayed in Figure 3.18 B and C. Again, a radiative constant k_F = (2.11 ± 0.08) ×10^8 s^{-1} (n= 18) was obtained by combining the quantum yield and lifetime measurements (Figure 3.18 D) in agreement with the previous study performed with the aliphatic alcohols.

The fluorescence anisotropy of the free HL488 dye decayed monoexponentially in all binary TFE/buffer mixtures studied. From the fitted rotational correlation times (Figure 3.19 A and Table 3.10), and taking into account the viscosity of the binary mixtures prepared (Figure 3.19 B), V_h^{app}= (1.06 ± 0.03) nm^3 (n= 8) was obtained for free HL488 from 0 to 60% TFE (vol/vol), which progressively increased to V_h^{app}~ 1.4 nm^3 in pure TFE. Altogether, the rotational diffusion data suggest that the conformation of the probe strongly depends on the solvent used, indicating that HL488 adopts a more compact conformation in the more hydrated solvent mixtures (TFE content < 60% (vol/vol)).

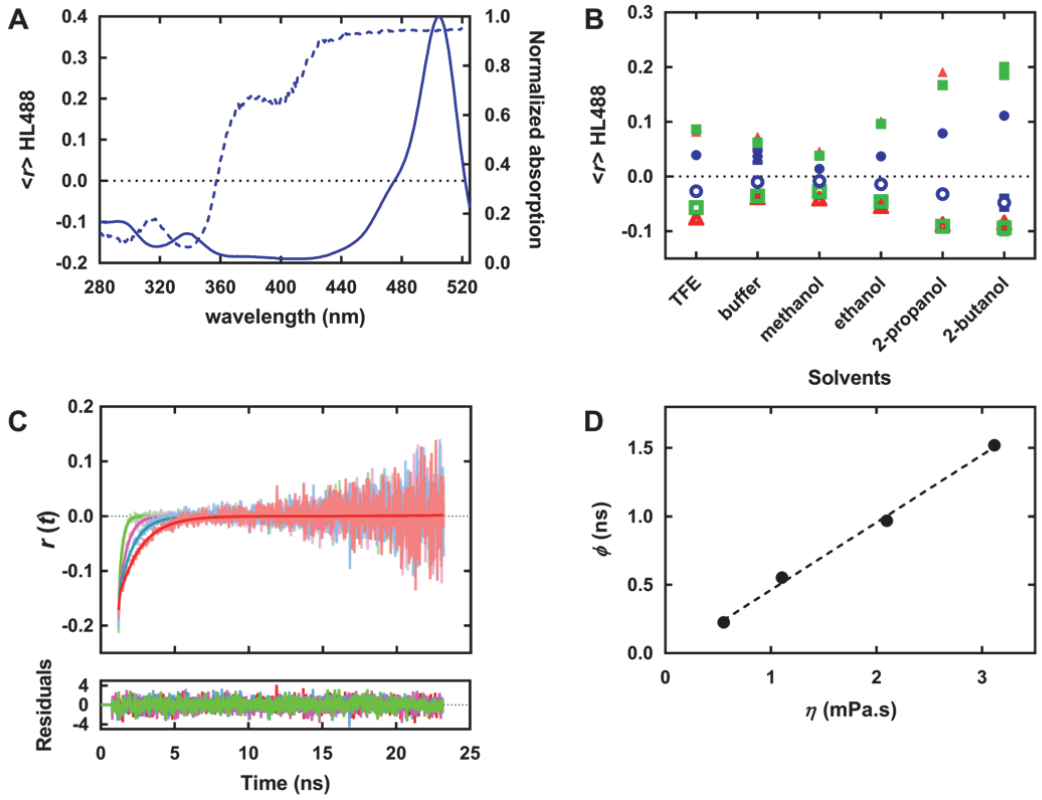

Figure 3.17 - Rotational dynamics of the free HL488 probe in homogeneous solution at 25 ºC. (**A**) Excitation anisotropy (λ_{em}= 525 nm; solid line) and absorption (dashed line) spectra for 1 μM free HL488 dye in glycerol (*T*= 8 ºC). The ssFA of the dye as a function of the excitation wavelength was calculated using Eq. 2.4. (**B**) The relative change in the ssFA of the free dye (blue circles), HL488-hCT (red triangles) and HL488-sCT (green squares) with the solvent viscosity when the samples are excited at 335 nm ($S_2 \leftarrow S_0$ transition, open symbols) is approximately half of the one obtained when λ_{exc}= 480 nm ($S_1 \leftarrow S_0$ transition, closed symbols). The concentration of HL488-CT used was 0.3 μM. (**C**) Nevertheless, the fluorescence anisotropy decays obtained for 1 μM free HL488 dye in methanol (green curve), ethanol (magenta curve), butanol (blue curve) and propanol (red curve), are well described by a monoexponential function (λ_{exc}= 325 nm; λ_{em}= 525 nm). The solid lines are the best fits of Eq. 3.25 to the experimental data (**D**) The rotational correlation time of free HL488 is linearly dependent on the viscosity of the aliphatic alcohol used (r^2= 0.9975). See Table 3.10 for additional experimental details and the obtained parameters.

Table 3.9 - Photophysical properties for the free HL488 probe in different solvents at 25 ºC. Maximum absorption wavelength, $\lambda_{\mathbf{max}}^{\mathbf{Abs}}$, intensity-averaged emission wavelength, $\langle\lambda\rangle$, quantum yield, Φ, ssFA $\langle r\rangle_{\mathbf{HL488}}^{\mathbf{480/525nm}}$ and long lifetime component, $\boldsymbol{\tau}$.The goodness-of-fit was judged by the $\boldsymbol{\chi_G^2}$. Values in square brackets are the errors of the recovered parameters estimated as the lower and upper bound of the joint confidence interval calculated for a 67% probability level.

Solvent	% TFE (vol/vol)	$\lambda_{\max}^{\mathrm{Abs}}$ (nm)	$\langle\lambda\rangle$ (nm)	Φ	$\langle r\rangle_{\mathrm{HL488}}^{480/525\mathrm{nm}}$	τ (ns)	χ_G^2
methanol	-	503	534.0	0.80	0.014 ± 0.002	4.07 [4.03;4.08]	1.07
ethanol	-	504	534.0	0.79	0.037 ± 0.004	3.89 [3.85;3.90]	1.11
2-propanol	-	504	533.0	0.76	0.079 ± 0.004	3.77 [3.77;3.78]	1.28
2-butanol	-	513	538.5	0.74	0.111 ± 0.007	3.72 [3.68;3.72][1]	1.03
TFE/buffer mixtures	0	501	534.1	0.84	0.014 ± 0.003	3.96 [3.92;3.97]	1.03
	5	501	534.2	0.86	0.018 ± 0.008	3.98 [3.95;3.99]	1.08
	15	501	533.8	0.86	0.028 ± 0.008	4.02 [3.98;4.03]	1.09
	20	500	533.1	0.83	0.028 ± 0.012	4.04 [4.00;4.05]	1.04
	25	499	532.9	0.85	0.026 ± 0.006	4.05 [4.01;4.06]	0.99
	40	498	531.3	0.84	0.026 ± 0.009	4.09 [4.05;4.10]	1.14
	50	496	530.5	0.86	0.024 ± 0.006	4.15 [4.11;4.16]	1.07
	60	496	529.8	0.87	0.036 ± 0.005	4.17 [4.14;4.18]	1.02
	70	494	528.7	0.97	0.030 ± 0.005	4.23 [4.19;4.24]	1.05
	75	496	529.1	0.93	0.034 ± 0.008	4.24 [4.20;4.25]	1.02
	80	494	528.4	0.81	0.034 ± 0.005	4.27 [4.23;4.28]	1.02
	90	494	526.7	0.91	0.037 ± 0.006	4.33 [4.29;4.34]	1.26
	100	492	525.7	0.86	0.052 ± 0.010	4.36 [4.32;4.37]	1.29
HFIP	-	488	517.8	0.89	0.018 ± 0.004	4.48 [4.44;4.49]	1.06

[1]Presented a double exponential decay, but the long lifetime component shown represented 99% of the decay.

Table 3.10 - Fluorescence anisotropy decay parameters for the free HL488 probe in different solvents at 25 ºC. Initial anisotropy, $r(0) = \beta$ and rotational correlation time, ϕ. The goodness-of-fit was judged by the χ^2_G. ssFA $\langle r \rangle^{335/525nm}_{HL488}$ Values in square brackets are the errors of the recovered parameters estimated as the lower and upper bound of the joint confidence interval calculated for a 67% probability level. The apparent hydrodynamic volume (V_h^{app}) calculated for the free dye using Eq. 2.3. n.d. Not determined.

Solvent	% TFE (vol/vol)	$r(0)$	ϕ (ns)	V_h^{app} (nm^3)	χ^2_G	$\langle r \rangle^{335/525nm}_{HL488}$
methanol	-	-0.137	0.23 [0.21;0.24]	1.7	1.05	-0.008 ± 0.004
ethanol	-	-0.143	0.55 [0.53;0.58]	2.1	1.11	-0.017 ± 0.003
2-propanol	-	-0.141	0.97 [0.94;1.01]	1.9	1.18	-0.031 ± 0.003
2-butanol	-	-0.145	1.52 [1.47;1.58]	2.0	1.17	-0.043 ± 0.003
TFE/buffer mixtures	0	-0.141	0.24 [0.22;0.25]	1.1	1.05	-0.012 ± 0.005
	5	-0.142	0.27 [0.26, 0.29]	1.1	1.05	-0.019 ± 0.005
	15	-0.144	0.31 [0.30;0.33]	1.0	1.11	-0.012 ± 0.005
	20	-0.143	0.37 [0.35;0.39]	1.1	1.08	-0.011 ± 0.004
	25	-0.143	0.39 [0.38;0.42]	1.1	1.13	-0.015 ± 0.004
	40	-0.141	0.46 [0.44;0.48]	1.1	1.06	-0.026 ± 0.004
	50	-0.13	0.49 [0.47;0.51]	1.1	1.16	-0.011 ± 0.004
	60	-0.141	0.49 [0.46;0.52]	1.1	1.10	-0.019 ± 0.005
	70	-0.146	0.53 [0.51;0.56]	1.2	1.11	-0.010 ± 0.005
	75	-0.145	0.51 [0.47;0.54]	1.2	1.02	-0.012 ± 0.002
	80	-0.141	0.55 [0.53;0.58]	1.3	1.13	-0.017 ± 0.004
	90	-0.142	0.55 [0.53;0.58]	1.4	1.18	-0.026 ± 0.005
	100	-0.149	0.57 [0.55;0.60]	1.4	1.10	-0.027 ± 0.006
HFIP	-	n.d.	n.d.	n.d.	n.d.	n.d.

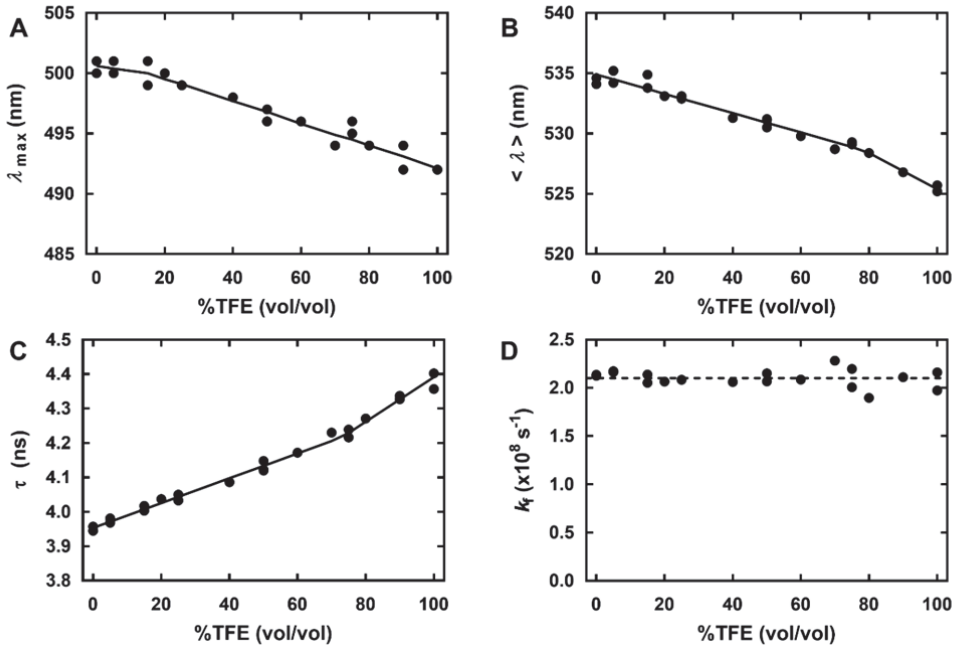

Figure 3.18 - Solvatochromic and photophysical studies of the free probe HL488 in binary mixtures of TFE/buffer at 25 ºC. Variation of the (**A**) maximum absorption wavelength, $\lambda_{\mathbf{max}}^{\mathbf{Abs}}$, (**B**) intensity-weighted average emission wavelength, $\langle\lambda\rangle$, and (**C**) fluorescence lifetime, τ, of 1 μM HL488 with the TFE content of the binary mixture. (**D**) The radiative constant of the free probe was found to be independent of the solvent composition of the sample, as it is exemplified here for the binary TFE/buffer mixtures studied ($\boldsymbol{k_F}$= (2.11 ± 0.08) ×10^8 s^{-1} (n= 18)).

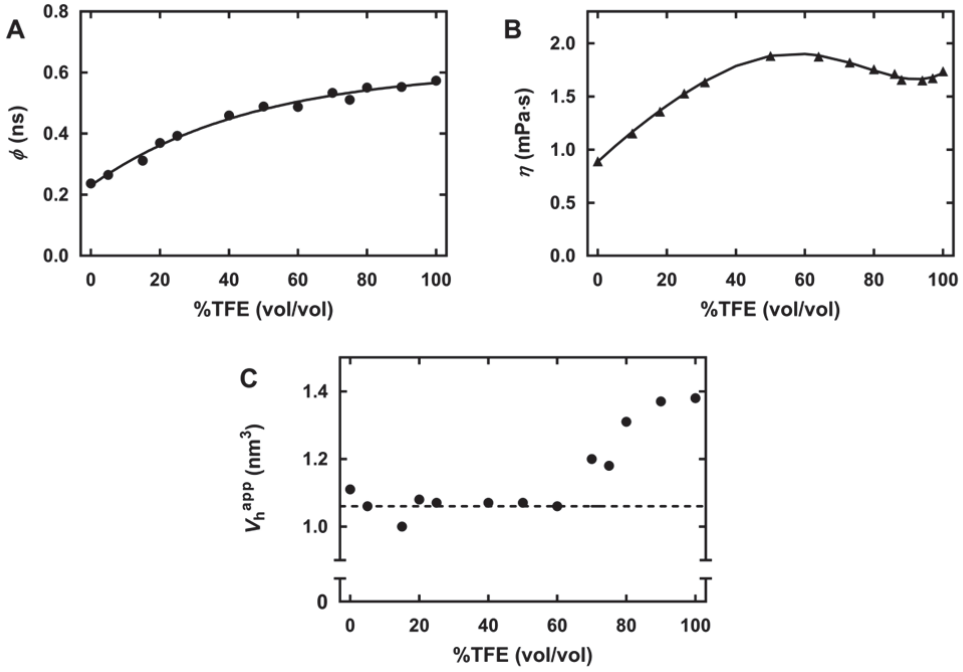

Figure 3.19 - Rotational dynamics of the free HL488 probe in binary TFE/buffer mixtures at 25 ºC. (**A**) Variation of the rotational correlation time for 1 μM free HL488 dye with the TFE content of the binary mixture. (**B**) Although the dynamic viscosity of these binary solvent mixtures does not vary monotonically with their TFE content (Table 3.5), (**C**) the apparent hydrodynamic volume calculated for the free dye using Eq. 2.3 was found to be essentially constant up to 60% TFE (vol/vol) $\boldsymbol{V_h^{app}}$ = (1.06 ± 0.03) nm^3 (n= 8)), and then progressively increased to $\boldsymbol{V_h^{app}}$ ~ 1.4 nm^3 in pure TFE.

3.4.1.2. **Characterization of HL488-labeled calcitonin peptides**

- *The unlabeled and fluorescently-labeled calcitonin peptides adopt a predominantly monomeric random coil conformation in aqueous solution*

During the course of this work, the methodology used to prepare the CT samples changed. At first, the adequate volume of the CT stock solution prepared in HFIP was directly injected into the working sample, i.e. in buffer, but this procedure caused multiple problems mainly related to the formation of non-fluorescent (dark states) peptide aggregates in solution (see section 3.6.1). Therefore, a new procedure was adopted that still involved the preparation of stock solutions of each peptide in HFIP, but now the organic solvent was evaporated using a light stream of nitrogen prior to resuspending the CT/ HL488-fluorescently labeled peptides in buffer/adequate solvent under study.

Using FCS measurements, we first established that upon using this new method of sample preparation the conjugated peptides are predominantly random coil monomers in buffer solution. This technique allowed measuring the translational diffusion coefficients of the conjugated peptides in buffer since this property is highly sensitive to the overall aggregation state of the fluorescently-labeled species (Garai *et al.*, 2007; Takahashi *et al.*, 2007; Ratha *et al.*, 2018). The representative AC curves for the free HL488 dye and both HL488-fluorescently labeled CT peptides that are displayed in Figure 3.20 A clearly show that their respective diffusion times allow distinguishing the 3D diffusion of the smaller fluorescent dye from the larger fluorescently-labeled peptides through the confocal volume. Using the diffusion times calculated from the AC curves, D_t = (1.34 $\pm$ 0.19) $\times 10^{-10}$ $m^2.s^{-1}$ (n= 19) and D_t = (1.46 $\pm$ 0.11) $\times 10^{-10}$ $m^2.s^{-1}$ (n= 11) were obtained for HL488-sCT and HL488-hCT in buffer solution at 25 ^oC, respectively (Eq. 3.38). These translational diffusion coefficients allowed concluding that both conjugated peptides adopt predominantly a random coil conformation and are essentially monomeric (seedless) in aqueous solution since they were very close to the values predicted using an empirical scale law for the dependence of the translational diffusion coefficient of random coil peptides/protein with its molecular weight (Figure 3.20 B).

Considering the molecular weights of HL488-sCT and HL488-hCT (Table 3.1) and using Eq. 3.40 and Eq. 3.41 obtained by Danielson and co-workers (Danielsson *et al.*, 2002), the CT peptides are expected to have a ca. $D_t = 1.61 \times 10^{-10}$ $m^2.s^{-1}$ in aqueous solution and $R_\mathrm{h} =$ 16.6 Å. From the experimental D_t values and using the Stokes-Einstein equation, one gets $R_\mathrm{h} =$ 18.3 Å and $R_\mathrm{h} =$ 16.8 Å for HL488-sCT and HL488-hCT, respectively. While the hydrodynamic radius obtained for the human variant is in good agreement to the predicted value for a monomeric random coiled peptide in solution, the value obtained for the salmon variant is ~2 Å larger than expected. This might indicate that sCT is not totally unstructured

in solution and that it acquires some residual (extended) structure that slows down its diffusion.

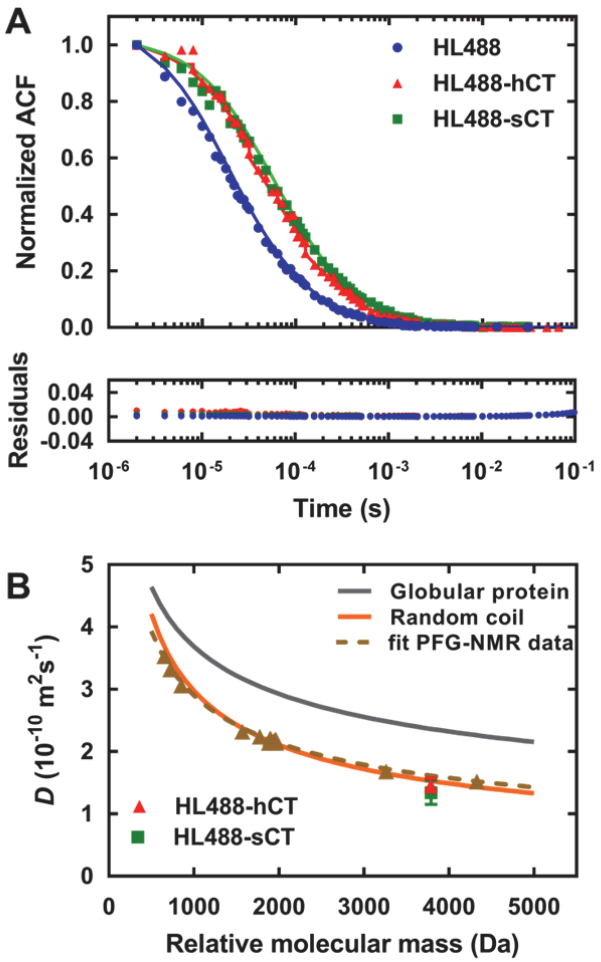

Figure 3.20 - FCS measurements show that the conjugated CT peptides adopt predominantly a random coil conformation in solution. (**A**) Representative normalized autocorrelation (AC) function curves obtained for 5 nM HL488 (blue circles), 30 nM HL488-hCT (red triangles) and HL488-sCT (green squares) in buffer using FCS. (**B**) The translational diffusion coefficients obtained from the analysis of the AC curves show that both fluorescently-labelled peptides essentially adopt a random coil conformation in buffer solution (the calculations were corrected for *T*= 25 ºC): $\boldsymbol{D_t}$= (1.34 ± 0.19) ×10^{-10} m^2s^{-1} for HL488-sCT (n= 19) (green squares) and $\boldsymbol{D_t}$= (1.46 ± 0.11) ×10^{-10} m^2s^{-1} for HL488-hCT (n= 11) (red triangles). The orange and grey lines describe the empirical power law $\boldsymbol{D_t = K\,MW^{-\varepsilon}}$ with $\varepsilon = 0.51$ and $\varepsilon = 0.33$ for random coil and globular peptides/proteins, respectively (see section 3.3.7.2 for more details). The brown triangles are the experimental values obtained for peptides ranging from 5 to 40 amino acid residues (Aβ(1-40) peptide with random coil conformation) determined with PFG-NMR (Danielsson *et al.*, 2002).

- Homogeneous solvents

We next sought to evaluate the ability of the covalently-linked HL488 dye to detect solvent-induced conformational transitions of the conjugated peptides. To this end, we took advantage of the previously pointed ability of aliphatic alcohols for mimicking proximity to

biological membranes and the known capacity of TFE in inducing partially folded intermediates of peptides/proteins (Luo and Baldwin, 1997; Buck, 1998; Gast *et al.*, 2001; Culik *et al.*, 2014; Gerig, 2015).

The spectral shifts presented by each fluorescently-labelled CT peptide in the chosen set of homogeneous solvents are summarized in Table 3.11 and Table 3.12 and closely reproduce the general trend already described for the free HL488 probe (Table 3.9). However, the fluorescence emission decay kinetics of both HL488-labelled peptides was now complex in the majority of the solvents studied (buffer, EtOH, PrOH and BuOH but not MeOH nor TFE) requiring 2 to 3 fluorescent lifetimes for an adequate fit of the multi-exponential decay law to the experimental time-resolved data. Nevertheless, the long fluorescence lifetime, τ_3, was always the dominant component being responsible in each case for more than 90% of the light emitted by the covalently linked fluorophore. The $\langle\tau\rangle_1$ of the conjugated peptides was always lower than the values obtained for the free dye, except in MeOH and TFE (Table 3.11 and Table 3.12). This indicates that the complex fluorescence decays presented by the fluorescently-labeled peptides were due to collisional quenching, probably due an intramolecular photon-induced electron transfer (PET) quenching mechanism by the side chains of some amino acid residues, as already described in the literature for similar fluorophores (Chen *et al.*, 2007, 2010; Ryan *et al.*, 2008). On the other hand, upon increasing the solvent viscosity, the interconversion between different peptide conformations slows down, increasing the probability of finding a static component in the detected fluorescence quenching. Therefore, the fluorescence properties of these conjugated peptides, particularly their fluorescence emission decay kinetics, are clearly controlled by their conformational dynamics in solution.

To gain more information about this topic, we next studied the influence of the solvent and temperature on the rotational depolarizing motions of the fluorophore covalently linked to each peptide variant by performing time-resolved fluorescence anisotropy measurements in the chosen set of aliphatic alcohols and TFE at RT and in TFE from 25 ºC to 60 ºC.

As it is exemplified in Figure 3.21 for HL488-hCT, the fluorescence emitted by both conjugated peptides was essentially fully depolarized at long times clearly indicating that no large peptide aggregates were present in the solvents tested. Furthermore, two correlation times were always required to describe the fluorescence anisotropy decays obtained for HL488-hCT and HL488-sCT in the chosen set of aliphatic alcohols and TFE at RT (Table 3.13 and Table 3.14) and in 100% TFE at different temperatures (Table S 3.1). The time-zero anisotropy was also always very close to the one measured for the free HL488 dye under the same experimental conditions ($r(0)$ ~ - 0.15 (Table 3.10)). This result indicates that essentially all the depolarization-inducing motions of the conjugated peptides were fully

captured in these time-resolved anisotropy measurements, i.e. there were no ultrafast motions of the covalently bound dye relative to the polypeptide chain that were undetected due to limitations linked to the time resolution of our instrumental setup.

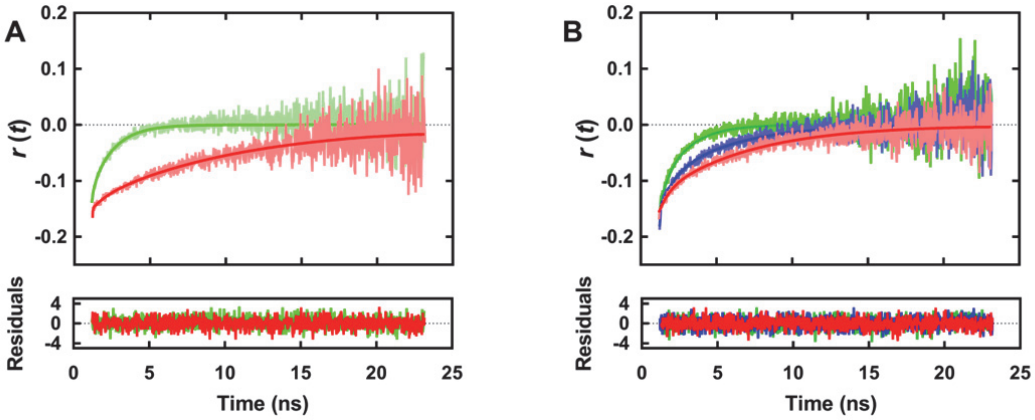

Figure 3.21 - Rotational dynamics of the HL488-hCT in homogeneous solution at 25 ºC. (**A**) Representative fluorescence anisotropy decays obtained for 0.8 μM HL488-hCT in ethanol (green) and 2-butanol (red) and (**B**) buffer (green), 50% TFE (vol/vol) (blue) and 100% TFE (vol/vol) (red) (λ_{exc}= 335 nm; λ_{em}= 525 nm; 24.4 ps/channel). The best fits of Eq. 3.25 to the experimental data (solid lines) required using two rotational correlation times, a short and a long one (ϕ_1 and ϕ_2, respectively) (see Table 3.13 for additional experimental details). The bottom panels correspond to the residuals of the fit.

Since the second rotational correlation time, ϕ_2, is always more than 4-fold longer than the first one, the total anisotropy decay can be approximated as the product of two independent depolarizing processes, reflecting two major molecular motions: (*i*) the short correlation time, ϕ_1 is assigned to the rapid restricted movements resulting from local motions experienced by the fluorescent probe covalently-linked to each CT peptide and/or due to the mobility of the peptide segment to which the fluorescent dye is attached, whereas (*ii*) the long correlation time, ϕ_2, is related to the global tumbling of the conjugated peptide in solution (Lipari and Szabo, 1980; Pastor *et al.*, 2007; Melo, Fedorov, *et al.*, 2014)

$$r(t) = r_{\text{fast}}(t) \cdot r_{\text{slow}}(t) \qquad \textbf{Eq. 3.69}$$

where

$$r_{\text{slow}}(t) = \exp(-t/\phi_{\text{global}}) \qquad \textbf{Eq. 3.70}$$

$$r_{\text{fast}}(t) = r(0)\left[\left(1 - {S_{\text{seg}}}^2\right) \cdot \exp(-t/\phi_{\text{seg}}) + {S_{\text{seg}}}^2\right] \qquad \textbf{Eq. 3.71}$$

Here, S_{seg} is the order parameter characterizing the restricted range of internal angular fluctuations of the protein segment containing the covalently bound HL488:

$$S_{\mathrm{seg}}{}^{2} = \beta_2/(\beta_1 + \beta_2) \qquad \textbf{Eq. 3.72}$$

The short and long rotational correlation times obtained from the fits (Table 3.13 and Table 3.14) in turn are related, respectively, to ϕ_{seg} and ϕ_{global} by:

$$\phi_1 = \left(\frac{1}{\phi_{\mathrm{seg}}} + \frac{1}{\phi_{\mathrm{global}}}\right)^{-1} \qquad \textbf{Eq. 3.73}$$

and

$$\phi_2 = \phi_{\mathrm{global}} \qquad \textbf{Eq. 3.74}$$

Both rotational correlation times were found to be linearly dependent on the solvent viscosity of the aliphatic/fluoroalcohol used at RT or of TFE at different temperatures, as it is shown in Figure 3.22 A and B for HL488-hCT and HL488-sCT, respectively. From the slope of these representations ($\phi_2 = \phi_{\mathrm{global}}$ *versus* η) and using Eq. 2.3, $V_{\mathrm{h}}^{\mathrm{app}}$= 13.5 nm^3 and $V_{\mathrm{h}}^{\mathrm{app}}$= 11.8 nm^3 was calculated for HL488-hCT and HL488-sCT at RT, respectively. Control far-UV CD measurements were performed with the unlabeled peptides and showed they have ~ 35-50% α-helix content in aliphatic/fluoroalcohols at RT. Specifically, the peptides have a high percentage of α-helical content in TFE, namely ~ 46% and ~ 51%, respectively (Table 3.13 and Table 3.14), and upon increasing the temperature from 25 to 60 ^{o}C, there was only a small decrease of 8 – 12% in the calculated helicity of the peptides (Figure S 3.2 and Table S 3.1). This reveals that both peptides retain a partially helical conformation even at high temperatures (in TFE) and overall they do not undergo any major conformational transition under all these experimental conditions. On the other hand, the segmental correlation time reflects the average time scale of the fast-localized motions of the covalently bound fluorescent dye. The range of angular displacement associated with these motions can be derived from the order parameter, S_{seg}, assuming a "wobbling-in-cone" model (Kinosita *et al.*, 1977; Lipari and Szabo, 1980; Czeslik *et al.*, 2003; Pastor *et al.*, 2007) in which the transition dipole moment of the dye is presumed to move freely within a cone with a fixed half-angle, θ_{seg}. In this framework, the half-angle of the cone within which the segment containing the covalently attached dye freely rotates can be calculated using:

$$\cos\theta_{\mathrm{seg}} = \frac{1}{2}\left[\sqrt{(8S_{\mathrm{seg}} + 1)} - 1\right] \qquad \textbf{Eq. 3.75}$$

Table 3.11 - Photophysical properties and fluorescence intensity decay parameters for HL488-hCT in different solvents at 25 ºC. Maximum absorption wavelength, λ_{max}^{Abs}, intensity-averaged emission wavelength, $\langle\lambda\rangle$, quantum yield, Φ, ssFA, $\langle r\rangle_{HL488}^{480/525nm}$ amplitude, α_i, and fluorescence lifetime, τ_i of the *i*th decay component, and fluorescence lifetime, $\langle\tau\rangle_1$. The goodness-of-fit was judged by the χ_G^2. Values in square brackets are the errors of the recovered parameters estimated as the lower and upper bound of the joint confidence interval calculated for a 67% probability level. n.d. – not determined.

Solvent	% TFE (vol/vol)	λ_{max}^{Abs} (nm)	$\langle\lambda\rangle$ (nm)	Φ	$\langle r\rangle_{HL488}^{480/525nm}$	α_1	τ_1(ns)	α_2	τ_2 (ns)	α_3	τ_3 (ns)	$\langle\tau\rangle_1$ (ns)	χ_G^2
methanol	-	504	537.0	0.79	0.046 ± 0.006	-	-	-	-	1.00	4.19 [4.16;4.22]	4.2	1.23
ethanol	-	506	537.2	0.76	0.101 ± 0.008	0.10	0.22 [0.18;0.26]	-	-	0.90	4.00 [3.97;4.02]	3.6	0.99
2-propanol	-	507	536.6	0.62	0.191 ± 0.007	0.11	0.47 [0.43;0.53]	-	-	0.89	3.89 [3.85;3.92]	3.5	1.03
2-butanol	-	517	547.0	0.67	0.187 ± 0.004	0.18	0.24 [0.23;0.26]	-	-	0.82	3.86 [3.82;3.87]	3.2	1.01
TFE/buffer mixtures	0	505	539.7	0.53	0.085 ± 0.004	0.19	0.15 [0.13;0.16]	0.14	1.48 [1.45;1.50]	0.67	3.91 [3.87;3.92]	2.8	1.16
	5	504	539.7	0.55	0.072 ± 0.011	0.15	0.19 [0.18;0.21]	0.15	1.76 [1.74;1.79]	0.69	4.01 [4.00;4.04]	3.1	1.03
	15	503	538.5	0.57	0.071 ± 0.008	0.12	0.26 [0.24;0.29]	0.14	2.22 [2.20;2.26]	0.74	4.13 [4.13;4.16]	3.4	0.99
	20	502	537.8	0.70	0.095 ± 0.006	0.11	0.95 [0.85;1.03]	-	-	0.89	4.09 [4.05;4.10]	3.8	1.14
	25	500	536.3	0.73	0.070 ± 0.006	0.08	0.53 [0.45;0.66]	-	-	0.88	4.03 [3.99;4.08]	3.7	1.29
	33	499	535.7	0.79	0.078 ± 0.003	0.07	0.77 [0.71;0.87]	-	-	0.93	4.11 [4.07;4.12]	3.9	1.10
	40	499	535.2	0.94	0.077 ± 0.004	0.05	0.31 [0.24;0.39]	-	-	0.95	4.20 [4.17;4.23]	4.0	1.06
	50	497	534.3	0.77	0.077 ± 0.005	0.05	0.45 [0.36;0.61]	-	-	0.95	4.21 [4.18;4.25]	3.8	1.24
	60	498	533.8	0.89	0.082 ± 0.005	-	-	-	-	1.00	4.22 [4.18;4.23]	4.2	1.29
	70	496	532.6	0.85	0.071 ± 0.004	0.06	0.30 [0.24;0.38]	-	-	0.94	4.33 [4.29;4.34]	4.1	1.02
	75	495	532.3	0.84	0.077 ± 0.005	0.03	0.40 [0.28;0.63]	-	-	0.97	4.35 [4.31;4.40]	4.2	1.12
	80	494	531.6	0.89	0.074 ± 0.007	-	-	-	-	1.00	4.39 [4.38;4.40]	4.4	1.24
	85	494	530.8	0.92	0.074 ± 0.003	-	-	-	-	1.00	4.44 [4.40;4.45]	4.4	1.11
	90	493	530.4	0.90	0.071 ± 0.005	-		-	-	1.00	4.48 [4.44;4.49]	4.5	1.19
	100	492	528.9	0.80	0.084 ± 0.004	-	-	-	-	1.00	4.59 [4.55;4.60]	4.6	1.10
HFIP	-	n.d.	n.d.	n.d.	n.d.	n.d.	n.d.	n.d.	n.d.	n.d.	n.d.	n.d.	n.d.

Table 3.12 - Photophysical properties and fluorescence intensity decay parameters for HL488-sCT in different solvents at 25 ºC. For further details, see the legend of Table 3.11.

Solvent	% TFE (vol/vol)	λ_{max}^{Abs} (nm)	$\langle\lambda\rangle$ (nm)	Φ	$\langle r\rangle_{HL488}^{480/525nm}$	α_1	τ_1(ns)	α_2	τ_2 (ns)	α_3	τ_3 (ns)	$\langle\tau\rangle_1$ (ns)	χ_G^2
methanol	-	504	536.7	0.78	0.038 ± 0.003	-	-	-	-	1.00	4.18 [4.14;4.19]	4.2	1.23
ethanol	-	507	537.3	0.71	0.096 ± 0.007	0.16	0.14 [0.13;0.16]	-	-	0.84	3.97 [3.94;3.98]	3.4	1.07
2-propanol	-	511	537.1	0.35	0.167 ± 0.006	0.19	0.16 [0.14;0.17]	0.08	1.24 [1.15;1.31]	0.73	3.85 [3.85;3.88]	3.0	1.18
2-butanol	-	518	546.4	0.25	0.193 ± 0.012	0.21	0.13 [0.11;0.22]	0.15	2.02 [1.67;2.49]	0.64	3.89 [3.83;3.98]	2.8	1.13
TFE/buffer mixtures	0	505	538.1	0.68	0.070 ± 0.003	0.08	0.27 [0.21;0.32]	0.08	1.66 [1.47;1.75]	0.84	3.93 [3.89;3.94]	3.5	1.06
	5	504	538.2	0.58	0.069 ± 0.006	0.11	0.64 [0.54;0.86]	-	-	0.89	3.91 [3.87;3.97]	3.6	1.24
	15	503	537.4	0.66	0.064 ± 0.008	0.08	0.68 [0.60;0.78]	-	-	0.92	4.03 [3.99;4.08]	3.8	1.28
	20	504	537.7	0.85	0.066 ± 0.006	0.09	0.16 [0.13;0.19]	-	-	0.91	4.18 [4.14;4.19]	3.8	1.28
	25	500	535.0	0.81	0.063 ± 0.004	-	-	-	-	1.00	4.13 [4.09;4.14]	4.0	1.27
	33	497	534.4	0.85	0.072 ± 0.005	-	-	-	-	1.00	4.14 [4.10;4.15]	4.1	1.20
	40	499	534.0	0.90	0.064 ± 0.005	-	-	-	-	1.00	4.17 [4.13;4.18]	4.2	1.08
	50	497	533.2	0.77	0.070 ± 0.003	-	-	-	-	1.00	4.23 [4.19;4.24]	4.2	1.06
	60	497	532.7	0.94	0.070 ± 0.003	-	-	-	-	1.00	4.26 [4.22;4.27]	4.3	1.28
	70	495	531.7	0.88	0.070 ± 0.003	-	-	-	-	1.00	4.31 [4.28;4.33]	4.3	1.00
	75	495	531.4	0.87	0.076 ± 0.003	-	-	-	-	1.00	4.33 [4.29;4.34]	4.3	1.02
	80	495	530.9	0.97	0.064 ± 0.004	-	-	-	-	1.00	4.38 [4.34;4.39]	4.4	1.09
	90	495	529.6	0.97	0.081 ± 0.006	-	-	-	-	1.00	4.45 [4.41;4.46]	4.5	1.04
	100	493	527.9	0.95	0.092 ± 0.006	-	-	-	-	1.00	4.54 [4.50;4.55]	4.5	1.02
HFIP	-	489	513.4	0.83	0.089 ± 0.004	-	-	-	-	1.00	4.63 [4.62;4.64]	4.6	1.13

Table 3.13 - Influence of solvent composition on the rotational dynamics of HL488-hCT at RT evaluated using time-resolved fluorescence anisotropy measurements at 25 ºC. amplitude, β_i and rotational correlation time, $\boldsymbol{\phi_i}$ of the *i*th decay component of the anisotropy decay, apparent hydrodynamic volume, $\boldsymbol{V_h^{app}}$, and semi-angle θ associated with the fast localized motions of the covalently-linked conjugated dye calculated according to the "wobbling-in-cone" model. $\boldsymbol{r(0)}$ is also presented. The goodness-of-fit was judged by the $\boldsymbol{\chi_G^2}$. Values in square brackets are the errors of the recovered parameters estimated as the lower and upper bound of the joint confidence interval calculated for a 67% probability level. The % helicity was determined with Eq. 3.13 from the data obtained by CD with 20 μM of unlabeled hCT. n.d. – not determined.

Solvent	% TFE (vol/vol)	β_1	ϕ_1 (ns)	β_2	ϕ_2 (ns)	$r(0)$	V_h^{app} (nm^3)	θ (degrees)	χ_G^2	$\langle r \rangle_{HL488}^{335/525nm}$	% helicity
methanol	-	-0.052	0.56 [0.51;0.64]	-0.087	2.16 [2.05;2.26]	-0.140	16.1	31.4	1.11	-0.041 ± 0.003	40.0
ethanol	-	-0.047	0.89 [0.79;1.00]	-0.106	4.25 [4.02;4.45]	-0.153	15.9	28.0	1.03	-0.055 ± 0.007	45.2
2-propanol	-	-0.018	0.96 [0.69;1.32]	-0.139	6.66 [6.45;6.98]	-0.157	13.1	16.1	1.14	-0.088 ± 0.003	43.2
2-butanol	-	-0.015	0.93 [0.63;1.32]	-0.133	9.84 [9.54;10.31]	-0.148	13.3	15.8	1.21	-0.085 ± 0.006	32.4
TFE/buffer mixtures	0	-0.032	0.44 [0.33;0.56]	-0.113	1.80 [1.71;1.91]	-0.145	8.41	23.1	1.06	-0.040 ± 0.007	4.7
	5	-0.039	0.40 [0.33;0.49]	-0.117	2.11 [2.02;2.21]	-0.156	8.46	24.8	1.07	-0.041 ± 0.004	5.5
	15	-0.040	0.54 [0.46;0.64]	-0.113	2.75 [2.61;2.89]	-0.153	8.80	25.4	1.02	-0.053 ± 0.002	9.3
	20	-0.045	0.90 [0.78;1.03]	-0.101	3.16 [3.03;3.34]	-0.146	9.25	28.0	1.16	-0.060 ± 0.004	15.0
	25	-0.042	0.71 [0.60;0.84]	-0.107	3.62 [3.48;3.80]	-0.149	9.98	27.3	1.10	-0.059 ± 0.003	23.5
	33	-0.045	0.87 [0.76;0.98]	-0.103	3.71 [3.55;3.88]	-0.148	9.13	27.7	1.20	-0.061 ± 0.004	23.3
	40	-0.050	1.13 [1.00;1.26]	-0.085	4.65 [4.46;4.92]	-0.135	10.31	29.3	1.02	-0.061 ± 0.006	24.5
	50	-0.045	0.85 [0.76;0.97]	-0.102	4.36 [4.18;4.56]	-0.148	9.36	27.0	1.09	-0.057 ± 0.003	29.1
	60	-0.049	0.89 [0.79;0.99]	-0.099	4.36 [4.13;4.57]	-0.148	9.49	29.1	1.06	-0.064 ± 0.003	29.6
	70	-0.045	0.76 [0.67;0.85]	-0.108	4.81 [4.61;4.99]	-0.153	10.79	27.2	1.20	-0.064 ± 0.003	32.9
	75	-0.040	0.84 [0.73;0.96]	-0.108	4.62 [4.42;4.84]	-0.148	10.61	25.8	1.08	-0.062 ± 0.003	46.1
	80	-0.044	0.73 [0.63;0.83]	-0.107	4.76 [4.56;4.94]	-0.151	11.28	27.1	1.09	-0.062 ± 0.003	38.8
	85	-0.044	0.80 [0.71;0.91]	-0.107	5.27 [5.11;5.47]	-0.151	12.85	27.2	1.20	-0.069 ± 0.004	n.d.
	90	-0.042	1.52 [1.38;1.73]	-0.088	6.11 [5.84;6.46]	-0.130	15.17	28.6	1.15	-0.061 ± 0.002	43.9
	100	-0.043	0.61 [0.52;0.71]	-0.115	6.49 [6.29;6.73]	-0.158	15.61	26.0	1.09	-0.074 ± 0.003	46.0
HFIP	-	n.d.	n.d.	n.d.	n.d.	n.d.	n.d.	n.d.	n.d.	n.d.	n.d.

Table 3.14 - Influence of solvent composition on the rotational dynamics of HL488-sCT at RT evaluated using time-resolved fluorescence anisotropy measurements. For further details, see the legend of Table 3.13.

Solvent	% TFE (vol/vol)	β_1	ϕ_1 (ns)	β_2	ϕ_2 (ns)	$r(0)$	V_h^{app} (nm^3)	θ (degrees)	χ^2_G	$\langle r \rangle_{HL488}^{335/525nm}$	% helicity
methanol	-	-0.059	0.34 [0.29;0.38]	-0.076	1.92 [1.82;2.05]	-0.135	14.4	34.6	1.09	-0.028 ± 0.003	47.7
ethanol	-	-0.068	0.80 [0.75;0.88]	-0.082	3.96 [3.75;4.18]	-0.150	14.8	37.3	1.08	-0.046 ± 0.008	49.0
2-propanol	-	-	-	-0.131	5.81 [5.65;6.17]	-0.131	11.3	-	1.24	-0.091 ± 0.007	50.0
2-butanol	-	-0.027	1.04 [0.84;1.31]	-0.127	9.12 [8.74;9.64]	-0.154	12.1	20.4	1.10	-0.094 ± 0.011	12.4
TFE/buffer mixtures	0	-0.051	0.38 [0.33;0.44]	-0.096	1.60 [1.53;1.71]	-0.147	7.5	30.0	1.08	-0.033 ± 0.003	8.8
	5	-0.058	0.50 [0.43;0.56]	-0.091	1.98 [1.85;2.11]	-0.148	7.9	32.3	1.02	-0.046 ± 0.005	12.5
	15	-0.073	0.77 [0.72;0.83]	-0.074	3.47 [3.25;3.67]	-0.148	9.9	37.6	1.07	-0.037 ± 0.004	26.5
	20	-0.059	0.47 [0.42;0.53]	-0.080	3.25 [3.08;3.47]	-0.139	9.5	34.1	1.15	-0.060 ± 0.004	15.0
	25	-0.065	0.50 [0.45;0.56]	-0.083	3.73 [3.53;3.98]	-0.148	10.1	35.1	1.15	-0.050 ± 0.002	49.7
	33	-0.073	0.69 [0.64;0.76]	-0.072	4.69 [4.40;4.96]	-0.145	11.6	38.0	1.10	-0.054 ± 0.002	23.3
	40	-0.066	0.70 [0.64;0.77]	-0.075	4.24 [4.02;4.52]	-0.141	9.8	36.3	1.20	-0.054 ± 0.004	24.5
	50	-0.066	0.73 [0.67;0.82]	-0.074	4.56 [4.28;4.82]	-0.141	10.0	36.4	1.18	-0.052 ± 0.005	48.5
	60	-0.075	0.75 [0.70;0.82]	-0.069	5.06 [4.80;5.36]	-0.144	11.0	38.8	1.17	-0.053 ± 0.003	29.6
	70	-0.076	0.73 [0.68;0.79]	-0.072	5.28 [5.01;5.63]	-0.148	11.8	38.5	1.06	-0.045 ± 0.003	32.9
	75	-0.070	0.78 [0.72;0.84]	-0.075	4.81 [4.55;5.08]	-0.145	11.1	36.9	1.12	-0.057 ± 0.002	49.2
	80	-0.075	0.72 [0.67;0.77]	-0.075	4.73 [4.47;5.05]	-0.150	11.2	37.8	1.05	-0.049 ± 0.002	38.8
	90	-0.073	0.73 [0.67;0.79]	-0.078	4.99 [4.67;5.23]	-0.151	12.4	37.0	1.00	-0.057 ± 0.003	43.9
	100	-0.070	0.81 [0.76;0.87]	-0.083	5.12 [4.90;5.42]	-0.153	12.3	35.7	1.07	-0.062 ± 0.004	51.3
HFIP	-	-0.063	0.90 [0.85;0.94]	-0.082	5.78 [5.55;6.01]	-0.146	14.5	34.5	1.1	-0.061 ± 0.002	n.d.

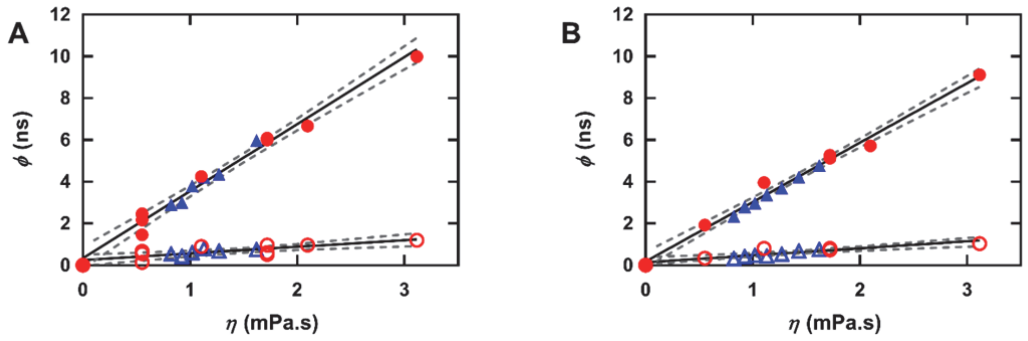

Figure 3.22 – The conformation adopted by the fluorescently-labelled calcitonins is essentially independent of the aliphatic alcohol/ % TFE used. Variation of the short (ϕ_1, open symbols) and long (ϕ_2, closed symbols) rotational correlation times obtained for (**A**) HL488-hCT and (**B**) HL488-sCT with the solvent viscosity. The rotational dynamics of the conjugated peptides solubilized in different aliphatic alcohols and TFE was studied at 25 ºC (red circles) or in 100% TFE at different temperatures (blue triangles) (parameters are present in Table 3.13, Table 3.14 and Table S 3.1). The dashed lines of each plot are the 95% confidence interval of the regression lines calculated from the sample data.

Interestingly, the rotational freedom of the fluorescent probe attached to each peptide was in general much more limited for HL488-hCT compared to HL488-sCT (Figure 3.23), although both CT peptides are conjugated to HL488 at their *N*-terminus and share a common disulfide bond between amino acid residues 1-7. In fact, although θ_{seg} is very similar for both conjugated peptides in a low viscosity solvent such as MeOH, the segmental dynamics of the *N*-terminus of HL488-hCT is in general much more sensitive to a change in the medium viscosity compared to HL488-sCT (Figure 3.23 A).

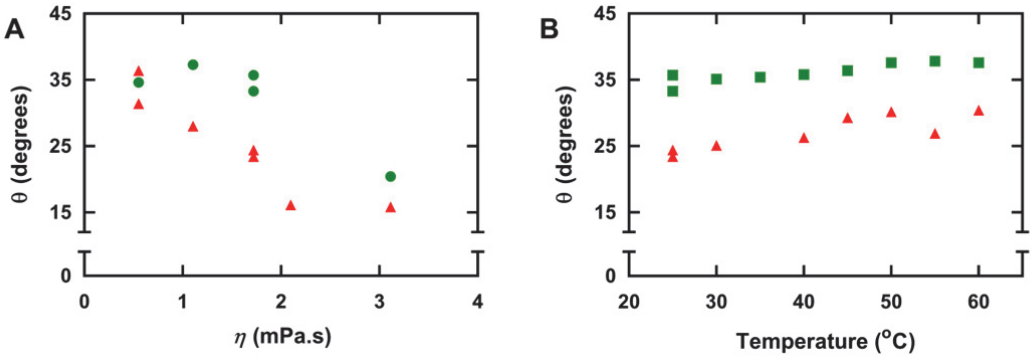

Figure 3.23 - The range of local motions available to the HL488 covalently-linked to calcitonin is wider for the salmon compared to the human variant. Variation of the semi-angle associated with the fast localized motions of the dye conjugated to hCT (red triangles) and sCT (green squares) calculated according to the "wobbling-in-cone" model with (**A**) the viscosity of pure solvents (MeOH, EtOH, PrOH, BuOH and TFE) at RT and (**B**) the temperature of pure TFE.

Using TFE as an example, an angle of θ_{seg} (HL488-hCT) ~ 23 – 26° and θ_{seg} (HL488-sCT) ~ 33 – 36° were obtained for each conjugated peptide in this solvent at RT, respectively (Table 3.13 and Table 3.14). When a high viscosity solvent such as BuOH is used, the amplitude of the segmental motions of both fluorescently-labeled peptides becomes much more restricted (θ_{seg} (HL488-hCT) ~ 16° and θ_{seg} (HL488-sCT) ~ 20°) and their rotational dynamics in solution is clearly dominated by the overall tumbling of the fluorescently-labeled peptides in solution (Figure 3.23 A). As expected, an increase in temperature produces a small increase in θ_{seg} for both conjugated peptides in TFE (Figure 3.23 B and Table S 3.1).

- *Binary TFE/buffer mixtures*

The secondary structure of both hCT and sCT changed upon increasing the TFE content of the binary TFE/buffer mixtures prepared as reported by far-UV CD measurements (Figure 3.24). The variation in the mean residue ellipticity at 222 nm of each CT variant with the TFE content of the binary mixtures allowed concluding that hCT underwent a two-step α-helical folding over the whole TFE/buffer range explored (inset of Figure 3.24 A), whereas sCT displayed a single conformational change, with the partially α-helical structure promoted in a single step at 0–25% TFE (inset of Figure 3.24 B), in agreement with the literature (Arvinte and Drake, 1993). The final helicity in pure TFE calculated for hCT was ~ 46% (Table 3.13) and for sCT ~ 51% (Table 3.14).

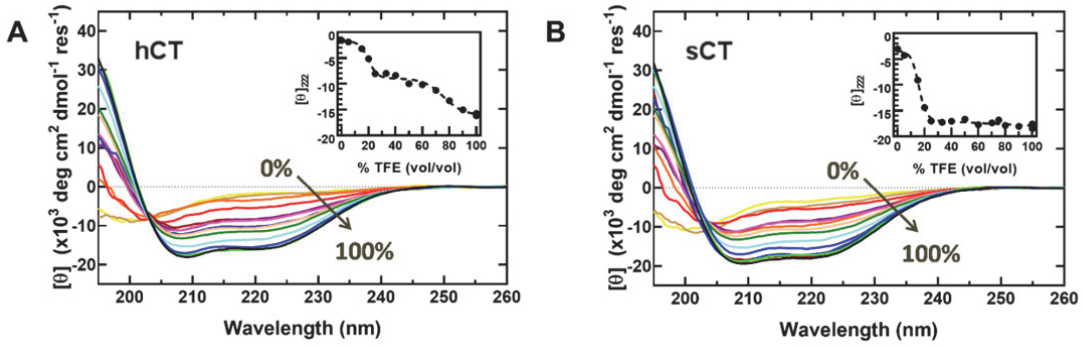

Figure 3.24 - TFE-induced secondary structural transitions for (A) hCT and (B) sCT at 25 ºC. Far-UV CD spectra for 20 μM of each CT variant in 0, 5, 15, 20, 25, 33, 40, 50, 60, 70, 75, 80, 90 and 100% (vol/vol) TFE. Insets: The mean residue ellipticity at 222 nm, $[\boldsymbol{\theta}]_{\mathbf{222\,nm}}$ (in units of 10^3 deg cm^2 dmol^{-1} res^{-1}) of each CT variant is plotted as a function of the TFE content of the binary mixture.

The spectral shifts of the covalently-bound dye were relatively insensitive to the solvent-induced conformational transitions of the peptides as both their maximum absorption wavelength, $\lambda_{\text{max}}^{\text{Abs}}$. and intensity-weighted average emission wavelength, $\langle\lambda\rangle$, steadily blue-shifted upon increasing the amount of organic cosolvent in solution (Figure S 3.3). Concomitantly, the fluorescence intensity decay kinetics of both peptides became

increasingly mono-exponential as the amount of buffer in the binary mixtures decreased (Table 3.11, Table 3.12 and Figure S 3.4) approaching the fluorescence lifetime measured for the free dye for %TFE > 40% (vol/vol) (Figure 3.25). Eventually, the establishment of hydrogen bonds between the dye and the fluoroalcohol and the solvent-induced conformational transition progressively shielded the fluorophore from contacting the polypeptide chain, reducing the probability of intramolecular quenching during the TFE-induced helix formation for each CT variant studied.

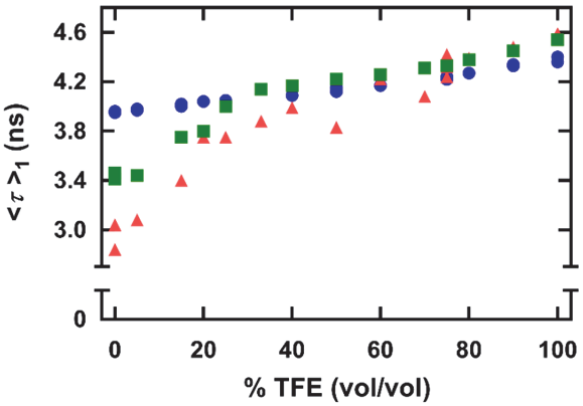

Figure 3.25 – Variation of the amplitude-weighted mean fluorescence lifetime of HL488-hCT and HL488-sCT in TFE/buffer binary mixtures. Free probe HL488 (blue circles), HL488-hCT (red triangles) and HL488-sCT (green squares).

As expected, the fluorescence anisotropy decays were good reporters of the coil-helix transition experienced by both CT peptides which is promoted by TFE, allowing to correlate the previously described changes in helical content with striking alterations in the rotational dynamics of the conjugated peptides in solution. While the short rotational correlation time of each fluorescently-labeled peptide was almost independent of the composition of the binary mixture used, the long rotational correlation time increased approximately 3-fold upon gradually changing the composition of the TFE/buffer binary mixtures from 0 to 100% TFE (Figure 3.26 A and B). The fluorescently-labeled CTs shared a first common transition whereupon their global rotational correlation times steadily increased from ϕ_2 ~1.6 – 1.8 ns in buffer to a final plateau value of ϕ_2= (4.8 $\pm$ 0.3) ns (n= 7) for HL488-sCT (Figure 3.26 B), between 33 and 100% (v/v) TFE) and an intermediate plateau level of ϕ_2= (4.5 $\pm$ 0.2) ns (n= 7) for HL488-hCT (Figure 3.26 A, between 40 and 80% (v/v) TFE). A second conformational change could also be detected for HL488-hCT upon changing the % of cosolvent from 80 to 100% TFE (v/v) since its global rotational correlation time further increased up to ϕ_2= (6.4 $\pm$ 0.3) ns (n= 3) at 100% TFE (vol/vol).

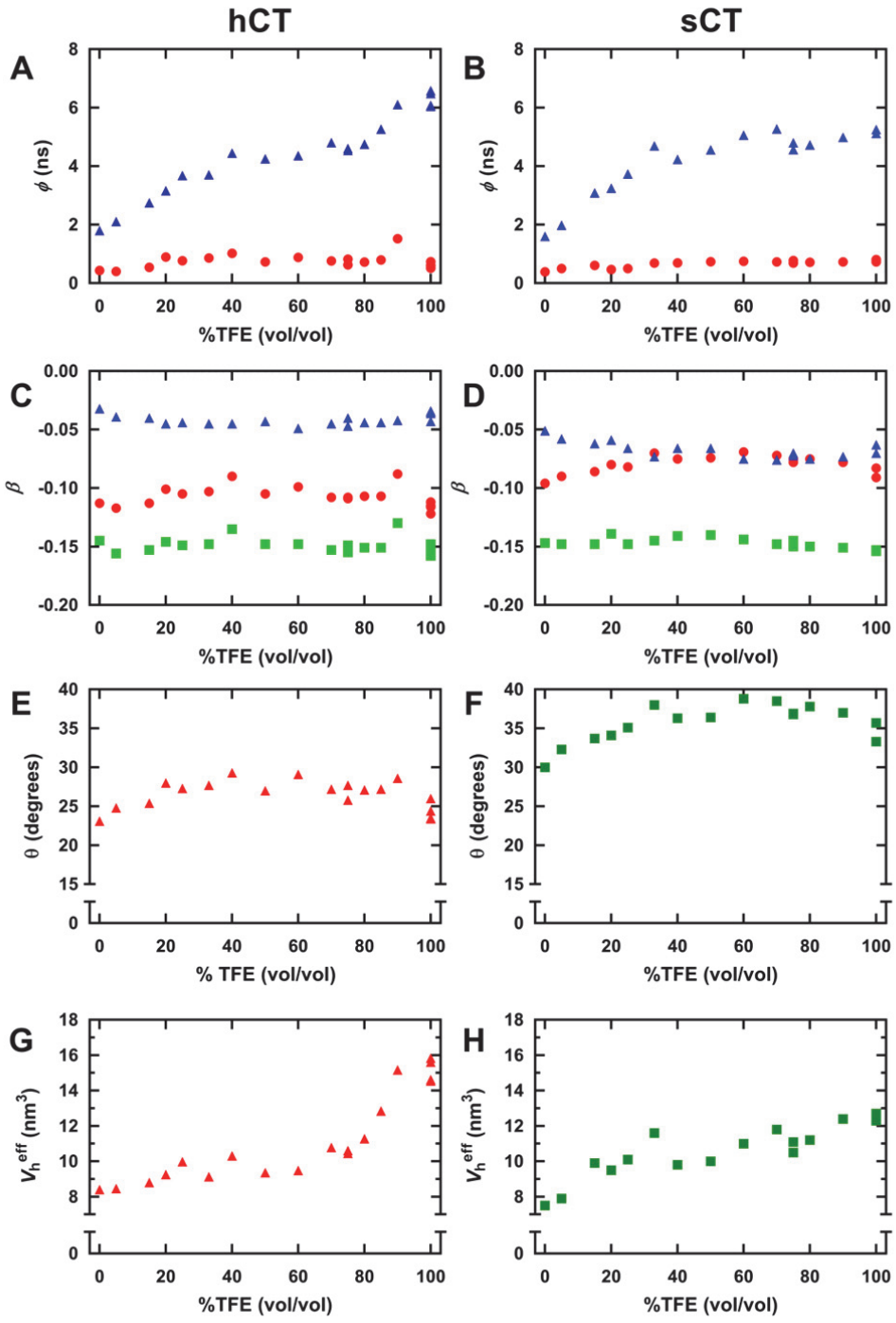

Figure 3.26 - TFE-induced structural transitions for HL488-hCT and HL488-sCT monitored at 25 ºC using time-resolved fluorescence anisotropy measurements. Variation of (**A** and **B**) the short (ϕ_1, blue triangles) and long (ϕ_2, red circles) rotational correlation times, (**C** and **D**) their respective amplitudes associated with the fast segmental motion of the dye covalently-linked to the peptides (β_1, blue triangle) and with the slow global tumbling of the conjugated peptide in solution (β_2, red circle), and of (**E** and **F**) the calculated $\boldsymbol{V_h^{app}}$ with the TFE content of the binary TFE/buffer mixture used. $\boldsymbol{r(0)}$ (green squares) are also plotted in panels **C** and **D**. (**G** and **H**) The "wobbling-in-cone" model was used to calculate the dependence of the semi-angle associated with the fast localized motions of the conjugated dye with the TFE content of the binary mixture. The measurements were performed with (**A**, **C**, **E** and **G**) HL488-hCT and (**B**, **D**, **F** and **H**) HL488-sCT.

Interestingly, the adoption of a partially helical conformation by each CT peptide had a minimal impact on the local/segmental rotational dynamics of the fluorescent dye covalently linked to each peptide as the semi-angle increased only ~5° during the first structural transition, reaching θ_{seg}= (27 ± 2)° (n= 13) and θ_{seg}= (37 ± 2)° (n= 11) for HL488-hCT and HL488-sCT, respectively (Figure 3.26 G and H).

In order to carry out a thermodynamic characterization of the TFE-induced folding of each peptide, a global analysis of the changes in their $[\theta]_{222\,nm}$,$\langle\tau\rangle_1$ and V_h^{app}, with the %TFE present in the binary mixture was performed as explained in detail in Section 3.3.8. A two-state model with a post-transition slope and a sequential three-state model adequately fitted the data obtained for sCT/HL488-sCT and hCT/HL488-hCT, respectively, as depicted in Figure 3.27 B and A, respectively. The spectroscopic parameters characteristic of each peptide conformer and the thermodynamic parameters recovered from these fittings are summarized in Table 3.15 and Table 3.16, respectively.

Table 3.15 - Spectroscopic parameters recovered from the global analysis of the TFE-induced structural transitions of sCT/HL488-sCT and hCT/HL488-hCT. A two-state model with a post-transition slope and a three-state model were fitted to the experimental data obtained for sCT/HL488-sCT and hCT/HL488-hCT, respectively. $\boldsymbol{S_U}$, $\boldsymbol{S_I}$ and $\boldsymbol{S_F}$ correspond to the spectroscopic signals characteristic of the unfolded, intermediate and folded CT states, respectively: $[\boldsymbol{\theta}]_{\mathbf{222nm}}$, mean residue ellipticity of each CT variant at 222 nm, $\langle\boldsymbol{\tau}\rangle_{\mathbf{1}}$mean fluorescence lifetime and $\boldsymbol{V_h^{app}}$, apparent hydrodynamic volume obtained from the time-resolved fluorescence intensity and anisotropy measurements performed with HL488-sCT/hCT. For more details, see Section 3.3.8.

System	Parameter	$[\theta]_{222\,nm}$ (10^3 deg cm^2 dmol^{-1} res^{-1})	$\langle\tau\rangle_1$ (ns)	V_h^{app} (nm^3)
sCT/HL488-sCT	S_U	- 3.4 ± 0.3	3.4 ± 0.2	7.6 ± 0.2
	S_F	-16.6 ± 0.4	3.9 ± 0.3	9.3 ± 0.4
hCT/HL488-hCT	S_U	- 1.7 ± 0.3	3.1 ± 0.3	8.7 ± 0.2
	S_I	-8.9 ± 0.3	4.0 ± 0.2	9.8 ± 0.3
	S_F	-16.1 ± 0.4	4.6 ± 0.2	15.2 ± 0.3

In summary, three different spectroscopic parameters provided a consistent picture of the mechanism of equilibrium TFE-induced folding of the two CT variants studied here. The unfolded state of hCT, at variance with the salmon variant, goes through an intermediate before reaching its partially folded state; in both cases a unique set of thermodynamic parameters successfully described the various transition curves monitored by different spectroscopic techniques.

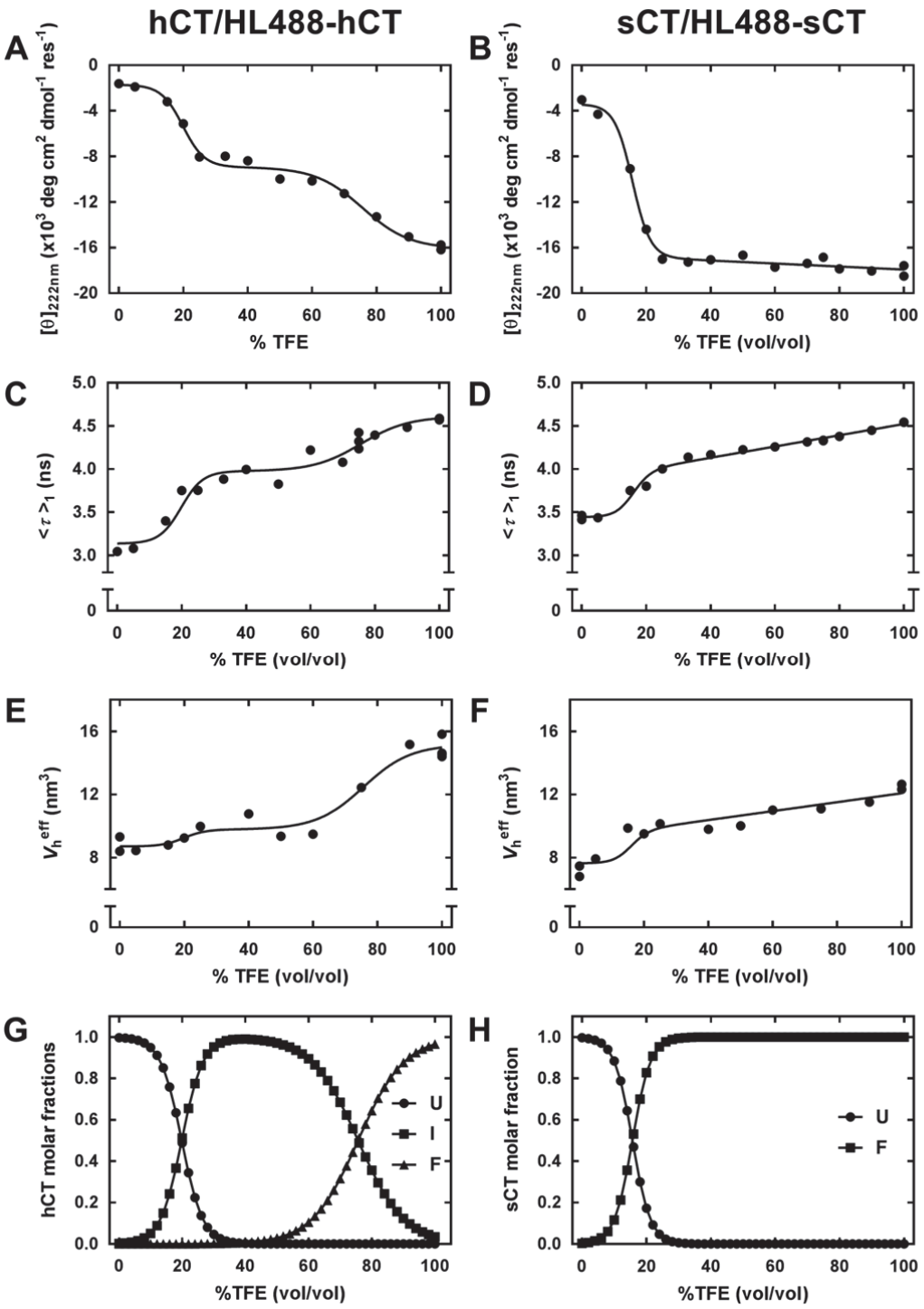

Figure 3.27 – Global analysis of the TFE-induced structural transitions at 25 ºC for hCT/HL488-hCT and sCT/HL488-sCT according to a three-state and a two-state model, respectively. The solid lines are the best global fit to the experimental data of (**A**, **C** and **E**) hCT/HLL488 (three-state model) and (**B**, **D** and **F**) sCT/HLL488-sCT (two-state model) (see section 3.3.8 for more details): (**A** and **B**) the mean residue ellipticity at 222 nm, $[\theta]_{222\,\mathrm{nm}}$, of each CT variant, (**C** and **D**) the amplitude-weighted mean fluorescence lifetime, $\langle\tau\rangle_1$ and (E and F) apparent hydrodynamic volume, V_h^{app} obtained for HL488-hCT and HL488-sCT as a function of the TFE content of the binary mixture. (**G**) The calculated fractions of unfolded (U), equilibrium intermediate (I) and final partial folded (**F**) hCT states and (**H**) unfolded (U) and folded (F) sCT states as a function of the TFE content of the binary mixture are also displayed. The global fitted parameters are summarized in Table 3.16.

Table 3.16 - Comparison of thermodynamic parameters for TFE-induced folding of sCT/HL488-sCT and hCT/HL488-hCT at 25 ^{0}C. A two-state model (1: U ↔ F) with a post-transition slope and a three-state model (1: U ↔ I and 2: I ↔ F) were fitted to the experimental data obtained for sCT/HL488-sCT and hCT/HL488-hCT, respectively. For more details, see Section 3.3.8.

System	$\Delta G_1^0(H_2O)$ (KJ·mol^{-1})	m_1 (x10^2 KJ·mol^{-1}·(%(v/v)$^{-1}$)	$\%TFE_{1/2}^1$ (%(v/v))	$\Delta G_2^0(H_2O)$ (KJ·mol^{-1})	m_2 (x10^2 KJ·mol^{-1}·(%(v/v)$^{-1}$)	$\%TFE_{1/2}^2$ (%(v/v))
sCT/ HL488-sCT	14.0	8.9 ± 0.1	15.7 ± 0.4	-	-	-
hCT/ HL488-hCT	14.7	7.4 ± 1.7	19.8 ± 0.8	26.3	3.4 ± 0.8	76 ± 2

3.4.1.3. **Discussion**

- *Spectroscopic and photophysical properties of free HL488*

In the first section of this chapter, we explored the use of HL488 as a sensor of the properties of its local environment, particularly of hydrogen bonding in the microenvironment immediately surrounding the fluorophore This preliminary fluorescence study was important to provide an interpretative framework for the spectroscopic data obtained subsequently with the fluorescently-labelled peptides in e.g. in interaction with lipid membranes.

Although the chemical structure of HL488 is not fully disclosed, the structure presented in Figure 3.9 C (adapted from (Jungbauer *et al.*, 2009)) suggests that HL488 belongs to the xanthene dyes family. The spectroscopic and photophysical properties of this family of fluorophores are well documented in the literature, particularly regarding the (*i*) effect of substituents on the xanthene π-system, and (*ii*) the influence of solvents, pH, temperature, dye concentration, oxygen, etc. on their spectral properties and fluorescence behavior (Martin, 1975; Arbeloa *et al.*, 1992; Klonis *et al.*, 1998) The observed variations in wavelength, fluorescence quantum yield and lifetimes were shown to result from a complex interplay between these intrinsic and external influences. Several factors have been discussed as possible explanations for this complex behavior namely the fact that xanthene dyes typically exist in solution in equilibrium between a variety of neutral and ionic forms, several can undergo a zwitterion ↔ lactone equilibrium in the ground state, some can interact to form ground state dimers and populate transient twisted intramolecular charge-transfer intermediate forms, to name a few (Zhang *et al.*, 2014).

As seen in Figure 3.16 and Table 3.9, the aliphatic alcohols caused batochromic (red) shifts in both the absorption and emission spectra of HL488 compared to water although hypsochromic effects were detected in both spectra when the solvents used were the fluoroalcohols TFE and HFIP. The shape of the absorption and emission specta (Figure 3.16) remained fairly invariant despite of the large blue/red-shifts observed, indicating that

the vibrational levels/molecular geometry of the ground and excited states of the dye remained similar (Martin, 1975). This indicates that there was not an excited state reaction that changed the fluorescent properties of the dye. The solvatochromic effects described above do not conform to the general solvent effects theory since they are not a merely consequence of a change in the polarity/polarizability of the environment of the fluorophore as there is not a good correlation between the observed Stokes shift and the orientation polarizability of the solvent (Lakowicz, 2006; Valeur and Berberan-Santos, 2012). Previously, Martin suggested that similar hypsochromic shifts detected in the emission spectra of fluorescein in alkaline solutions of TFE, water, MeOH and EtOH (among other solvents) correlated with the hydrogen-bonding power of the solvents and resulted from an increased stabilization of the ground-state compared to the excited state of the fluorophore due to hydrogen bonding formation between the oxygen atoms of the dye and the solvent (Martin, 1975).

Single exponential lifetimes were measured for HL488 in the set of homogeneous solvents studied providing further evidence that a single predominant species was present in solution in each case and exhibited only a minor variation over the set of solvents studied (Table 3.9). Since the intersystem crossing probability for this family of dyes is very low, the decrease in fluorescence lifetime along a series of homogeneous solvents is generally assigned to an increase in competitive nonradiative processes such as internal conversion (Arbeloa *et al.*, 1992; Magde *et al.*, 1999). Accordingly, the radiative constants calculated for HL488 in homogeneous solvents (k_f= (2.00 $\pm$ 0.06)$\times 10^8$ s^{-1}) and binary TFE/buffer mixtures (k_f= (2.11 $\pm$ 0.08)$\times 10^8$ s^{-1}) were almost a constant independent of the solvent used. These values are also in good agreement with recent determinations of k_f for ten rhodamine dyes in different solvents (2.3×10^8, 2.0×10^8, 2.2×10^8 and 2.0×10^8 s^{-1} for ethanol, water, acetonitrile, and dimethylformamide, respectively (Zhang *et al.*, 2014). A minor influence of oxygen quenching in the measured lifetimes cannot be discarded (particularly in water) since all time-resolved fluorescence measurements were performed with air-saturated solutions. This effect might explain why the empirical correlation established between the fluorescence lifetime of the free dye and the solvent acidity of the alcohol used (the higher the solvent hydrogen bond donating power, the slower the IC process) could not be extend to the measurement performed in aqueous solution (Figure 3.16 D).

The fluorescence anisotropy decays measured for free HL488 in aliphatic alcohols and in binary TFE/buffer mixtures clearly showed that the fluorescent dye displayed a larger apparent hydrodynamic volume in the less hydrated solvent mixtures used. This is in line with a MD study of A488 (a fluorescent dye that is structurally similar to HL488 since both belong to the xanthene dyes family) (Schröder *et al.*, 2005). The authors found that the average length of the dye in methanol (~1.5 nm) was larger than in water (~1.0 nm) and

considering that the headgroup of the dye is rather stiff, they assigned this difference to a change in length of the flexible linker of the dye. As displayed in Figure 3.9 C, HL488 also has a chain linker, presumably hydrophobic, between the carboxyphenyl group and the succinimidyl ester group. In addition to the dye conformation, thermally driven rotational diffusion is also governed by frictional coupling to their solvent environment. Therefore, a possible change in the rotational behavior of the dye/solvent system from the slip to a super-stick boundary condition due to possible strong hydrogen bonding between the functional groups of the probe and the alcoholic solvent molecules cannot be discarded (Dutt and Ghanty, 2003).

- *Conformational dynamics of HL488-labeled calcitonins in homogeneous solution*

Time-resolved fluorescence anisotropy measurements were performed with HL488-hCT and HL488-sCT to probe their rotational dynamics in solution. The small fluorophore is expected to minimally perturb the peptides since in both cases, HL488 was specifically attached at the *N*-terminus of the peptides, close to the intramolecular disulfide bond that is present in all CTs. The fluorescence anisotropy decays reflected two molecular processes in all cases: local internal/segmental fluctuations of the fluorescent dye, with a fast relaxation time ϕ_1, and overall rotational motion of the whole fluorescently-labelled molecule, with a relaxation time ϕ_2 much longer. The observation of a single long rotational time indicates a relatively compact hydrodynamic volume for the peptide that do not strongly deviates from a spherical shape. In fact, for a set of measurements performed in different aliphatic alcohols and TFE at RT, and in TFE within a temperature range of 25-60 ^{0}C, the long rotational time of the peptide was found to scale directly with the bulk solvent viscosity, revealing that under these experimental conditions the peptide backbone did not display a high flexibility. Complementary far-UV CD measurements showed that both peptides presented a high helical content in TFE at RT (~46% and ~51% of helical content, respectively). Interestingly, the apparent hydrodynamic volume obtained from the slope of ϕ_2 with the solvent viscosity was slightly higher for HL488-hCT compared to HL488-sCT ($V_{\mathrm{h}}^{\mathrm{app}}$= 13.5 nm^3 and $V_{\mathrm{h}}^{\mathrm{app}}$= 11.8 nm^3, respectively). Several biophysical studies have previously shown that the central region of both CT peptides adopt a helical conformation in organic solvents/SDS micelles, although with variable lengths, that is characterized by low mobility (Epand *et al.*, 1983, 1986; Orlowski *et al.*, 1987; Motta, Pastore, *et al.*, 1991; Arvinte and Drake, 1993; Siligardi *et al.*, 1994; Amodeo *et al.*, 1999). On the other hand, the C-terminal tails of both hormones (after their Pro residues (Figure 3.4 and Figure 3.5) are their most mobile regions, although they behave differently in each peptide. For hCT, the C-terminal tail is described in both NMR and MD studies to be mostly extended, showing almost no interaction with the central helix; on the other hand, the tail is always folded back

towards the helix in sCT, originating more compact conformations for this CT variant in solution (Amodeo *et al.*, 1999).

Although the overall conformational features of both peptides in this set of homogeneous solvents was very similar (except for the distinct conformational dynamics displayed by their C-terminal decapeptide), the θ values of the fast components (i.e. the cone half-angle explored by the fluorescent probe and proximal peptide segment according to a "wobbling-in-a-cone" model (Lipari and Szabo, 1980; Czeslik *et al.*, 2003) calculated for HL488-sCT was wider than for HL488-hCT in TFE at RT (θ_{seg}(HL488-sCT) ~ 33 -36^0 *versus* θ_{seg}(HL488-hCT) ~ 23 -26^0). In addition, θ_{seg}(HL488-hCT) was also found to be more sensitive than θ_{seg}(HL488-sCT) to the viscosity (Figure 3.23 A) and temperature (Figure 3.23 B) of the solution. Both these features imply that the local motion of the HL488 fluorophore is more hindered in hCT compared to sCT which may be due to the establishment of preferential interactions between the dye and the hCT peptide sequence; these would preclude large amplitude dye motions that contribute to the anisotropy decay of the fluorescently-labeled peptides in some of the solvents studied.

Finally, the solvent-induced conformational transitions of the CT peptides in binary TFE/buffer mixtures was also probed in detail using both time-resolved fluorescence intensity and anisotropy measurements, that were complemented with far-UV CD studies. The effects of fluoroalcohols on protein structure has been studied for decades (Buck, 1998). Disordered proteins and peptides generally undergo a gradual coil-to-helix transition as TFE is added to a solution, until reaching their maximally helical state by ~30-40% TFE. Fluroalcohols are also useful in stabilizing partially folded states of peptides/proteins, that otherwise would be impossible to study under equilibrium conditions. Although the precise mechanism of such conformational induction remains unclear, it is generally accepted upon that structure formation occurs due to enhanced intramolecular hydrogen-bonding capabilities of peptides located in TFE-rich environments. One view considers that TFE more favorably surrounds the protein than water, effectively leading to dehydration of the protein backbone which, consequently, leads to backbone-backbone hydrogen bond formation and hence promotes secondary structure stabilization (Luo and Baldwin, 1997; Gast *et al.*, 2001; Díaz *et al.*, 2002; Fioroni *et al.*, 2002; Eichenberger *et al.*, 2013). Other studies consider that instead of stabilizing the folded state, TFE acts to stabilize the unfolded state by structuring the solvent and, as a result, increasing the folded population. The bulky and hydrophobic CF_3 groups causes the clustering of TFE in water solutions (in micelle-like structures) as a tentative to shield these groups from direct contact with water. This clustering is maximal near 30% (v/v) TFE (Hong *et al.*, 1999; Gente and Mesa, 2000; Culik *et al.*, 2014).

Although there was a 100- fold difference in the concentration of the peptides used with each biophysical technique, the changes detected in the $[\theta]_{222\,\mathrm{nm}}$,$\langle\tau\rangle_1$ and $V_{\mathrm{h}}^{\mathrm{app}}$ with the %TFE present in the binary mixture were successfully globally analyzed using a single and a two-step α-helical folding transitions model for sCT and hCT, respectively, over the whole TFE/buffer range explored in this study (Figure 3.27). These results are in agreement with previously published studies (Amodeo *et al.*, 1999), and confirm that sCT adopts more readily an α-helical conformation in solution than hCT, probably due to the more amphipathic character of its α-helix. The site-specific labeling of the N-terminal amine group of the peptide allowed to detect with great spectroscopic sensitivity the ordering of the Cys1-Cys7 disulfide bond at low TFE concentration that has been previously described to correlate with the initiation of the α-helix (Arvinte and Drake, 1993). The transition from a random coil conformation to an increasingly longer α-helical structure is accompanied in both cases by an increase in the mean fluorescence lifetime of HL488-hCT/HL488-sCT due to a lower probability of intramolecular quenching of the fluorophore by the side chains of several amino acid residues due to a PET mechanism in a more extended peptide conformation (Chen *et al.*, 2007, 2010; Ryan *et al.*, 2008).

In conclusion, the combination of far-UV CD measurements with time-resolved fluorescence data proved to be a useful strategy to provide quantitative information about the conformational dynamics of human and salmon calcitonins and its dependency on the solvent. HL488 was therefore confirmed as a good fluorescent probe to monitor the overall rotational dynamics of peptides/proteins in solution.

3.4.2. Fibrillation kinetics of calcitonins

The main goals of this part of the work were to (i) define reproducible conditions to study the kinetics of CT amyloid fibril formation in aqueous solution using the extrinsic amyloid dye ThT, and then (ii) to test the role of accessory cellular components, like membranes, in the modulation of this process.

3.4.2.1. **Thioflavin T assays**

The fibrillation kinetic assays of amyloidogenic peptides/proteins are notorious for their low reproducibility which is often related with the formation of pre-aggregates (seeds) while preparing the samples. To avoid this problem, both the buffer solution and the ThT stock solution were always filtered prior to use. Also, the stock solutions of the peptides prepared in HFIP were always sonicated for 1 min in a bath sonicator to ensure dissociation of any pre-aggregated structures after defrosting. The systematic study performed by Giehm *et al.* in 2010, in which strategies to increase the reproducibility of protein fibrillation assays performed with a plate reader were suggested, was used here as a guide. The authors showed that these kinetics are critically dependent on shaking in various ways, namely the shaking mode (orbital *versus* linear), the ratio of the sample volume to well volume, and the addition of beads to increase the uniformity of shaking. In their case with α-synuclein, they found an optimum sample volume of 150 µL in a 96-well plate using 300 rpm orbital shaking and one 3- to 4-mm-diameter glass bead/well (Giehm and Otzen, 2010).

Here, we first tried to optimize the conditions to be used in order to have reproducible sigmoidal profiles for the fibrillations kinetics of hCT, while sCT should not produce any appreciable change in the fluorescence intensity of ThT over time. The extrinsic fluorescent probe Thioflavin T (ThT), one of the most accepted and widely used fluorescent dyes to detect amyloid fibril formation (Domanov and Kinnunen, 2008; Caillon *et al.*, 2013; Kegulian *et al.*, 2015; Martel *et al.*, 2017). ThT displays an enhanced fluorescence emission when bound to amyloid fibrils which is accompanied by a shift in its fluorescence emission maximum from 445 to 482 nm (Groenning, 2010). The basis for the change in its fluorescence properties arises from the fact that ThT functions as a molecular rotor (Stsiapura *et al.*, 2008). This dye is composed of two rings, a benzylamine and a benzathiole ring linked by a carbon bond (Kumar *et al.*, 2008; Stsiapura *et al.*, 2008; Biancalana and Koide, 2010; Groenning, 2010): when the dye is in aqueous solutions, the two rings rotate freely across the carbon bond that links them and this rotation quenches the excited state of the molecule. When bound to structures that limit this rotation (e.g. when intercalated between the β-strands present in an amyloid fibril), the fluorescence quantum yield of the probe pronouncedly increases since the loss of excitation by the non-radiative

decay pathway (rotation) is less available (Kumar *et al.*, 2008; Biancalana and Koide, 2010; Groenning, 2010). In addition, ThT does not affect the fibrillation kinetics of amyloidogenic peptides/proteins (or only to a limited extent) (Groenning, 2010).

Variable concentrations of both sCT and hCT, ranging from 1 to 20 μM of peptide, were used in each fibrillation assay with a constant molar ratio of 1:0.75 peptide:ThT. This guaranteed the same amount of ThT relatively to the peptide in order to avoid an excess of dye which could influence the evolution of amyloid fibril formation kinetics (Avidan-Shpalter and Gazit, 2006). The fluorescence intensity measurements of ThT were performed for several hours in a microplate reader, ranging from 20h to 60h depending on the fibrillation conditions. The number of measuring cycles was determined to cover the full kinetics of peptide fibrillation. Each measuring cycle comprises an initial phase of shaking (optional) and the period where the plate is scanned and the fluorescence intensity of ThT is measured. Depending on the duration of the cycle, the plate would remain at rest between cycles.

As it is described in detail in section 3.3.3, the fibrillation assays were first performed in the presence of 1% (v/v) HFIP. The operational conditions tested in several preliminary assays were the type of microplates, sample volumes (between 150 and 300 μL/well), number of beads/well and shaking profiles (orbital shaking at 600 rpm for 0, 30 or 300 s). The 96-well Greiner Bio-One non-binding black microplates were selected in these assays due to their non-binding surfaces which are achieved through a stable chemical modification to covalently link functional groups to the base polystyrene polymer (Greiner Catalog). These plates are supposed to diminish the peptide adsorption to the microplate. In the absence of agitation, the fibrillation kinetics of hCT took approximately 50 hours to be completed with a lot of variability between technical replicates (data not shown). Because of this, orbital shaking at 600 rpm was added to each measuring cycle. Some representative results are displayed in Figure 3.28.

The ThT traces of hCT show the typical sigmoidal fibril growth pattern characteristic of amyloids (Figure 3.28 A-C), whereas the fibrillation kinetics performed with sCT revealed no increase in the fluorescence intensity of ThT over time (Figure 3.28 D) indicating that no fibrils or aggregates are formed with this peptide, as expected (Andreotti *et al.*, 2011). Also, Figure 3.28 B shows that the use of 300 s instead of 30 s (Figure 3.28 A) of orbital shaking in each measuring cycle greatly accelerated the fibrillation kinetics of hCT performed with 150 μL total sample/well.

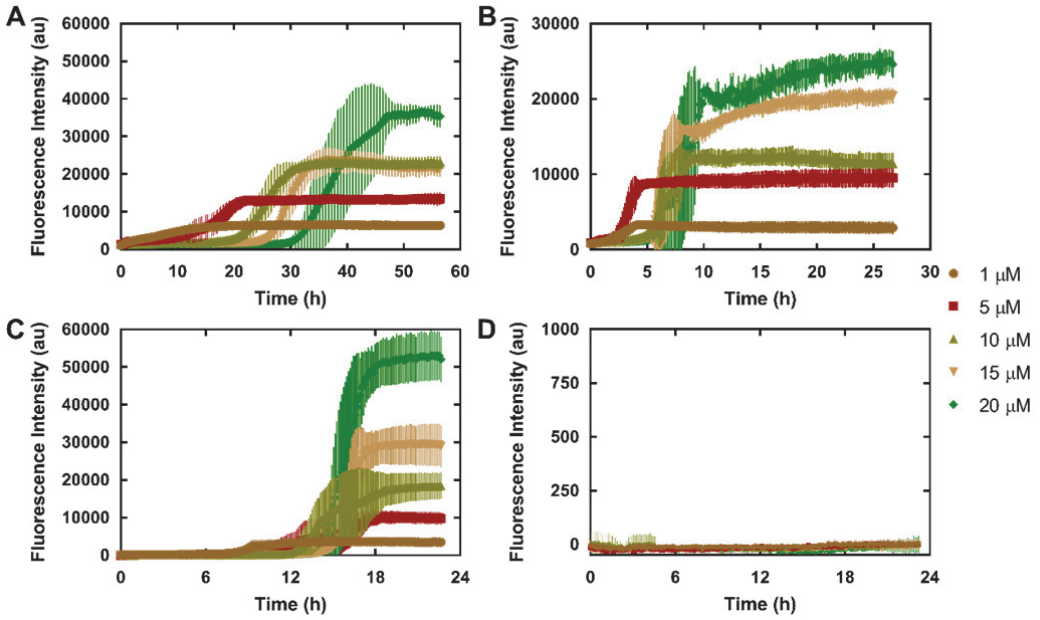

Figure 3.28 - Fibrillation kinetics of hCT are highly influenced by the conditions in which they are performed. Representative (**A,B,C**) hCT and (**D**) sCT fibrillation kinetics followed by measuring the fluorescence intensity of Thioflavin T (ThT) over time ($\boldsymbol{\lambda_{exc}}$= 440 nm, $\boldsymbol{\lambda_{em}}$= 480 nm) in a 96-well microplate. The kinetics were studied with concentrations ranging from 1 to 20 μM of peptide with a constant molar ratio of 1:0.75 peptide:ThT with (**A**) 150 μL of volume, 30s of orbital agitation, (**B**) 150 μL of volume, 300s of orbital agitation and (**C** and **D**) 300 μL of volume, 300s of orbital agitation. The assays were conducted (**A** and **B**) in the presence or (**C** and **D**) in the absence of 1% (v/v) HFIP. The curves represent the average ± SD of 4 or 5 technical replicates. The lag times ($\boldsymbol{\tau_{lag}}$) and apparent rate constant for the growth of fibrils ($\boldsymbol{k_{app}}$), were determined using Eq. 3.1 and the results are in Table 3.17. The ThT traces of hCT show the typical sigmoidal fibril growth pattern characteristic of amyloid formation for the higher concentrations of peptide used, while there was no significant increase in the fluorescence intensity of ThT measured for the samples with sCT.

Two degrees of variability were observed in these assays, namely intra-plate (technical replicates) and inter-plate ("biological" replicates) variability. Some technical replicates would present significant differences amongst themselves which could be identified and discarded. Comparisons between results from different microplates were more difficult due to the variability in the obtained lag times. Nevertheless, when all the replicates (technical and "biological") obtained in the presence of 1% (v/v) of HFIP were analyzed using Eq. 3.1 (Table 3.17) and represented together (Figure 3.29), some considerations could be taken. Although the average lag times and apparent rates of fibril formation have relative errors in the order of 40% (Table 3.17) a tendency for a direct relationship between the lag time of the kinetics and the peptide concentration used can be observed (Figure 3.29 A and C), which was a surprising and unexpected result. When the total sample volume used was doubled (from 150 to 300 μL/well), the lag time and the rate of fibril formation were found to be practically independent of the concentration of peptide used (Figure 3.29 E and F). A lower sample volume results in a higher degree of shaking compared to a higher sample

volume in the same size well and this may explain the difference between the obtained lag times (Giehm and Otzen, 2010).

Table 3.17 - Lag time, τ_{lag}, and apparent rate constant for the growth of fibrils, k_{app}, for the fibrillation kinetic assays of hCT performed in different conditions in the microplate reader. The fibrillation kinetic assays were followed using the fluorescence intensity of ThT or the ssFA of HL488. For additional details, see the legend of Figure 3.28, Figure 3.29 and Figure 3.30. The parameters were calculated according to Eq. 3.1. n is the number of replicates.

Volume *per* well / orbital shaking (Fluorophore)	Presence of HFIP	[hCT] (μM)	k_{app} (h^{-1})	τ_{lag} (h)	n
150 μL / 30s (ThT)	yes	1	1.3 ± 0.3	17.6 ± 7.0	10
		5	0.8 ± 0.2	19.7 ± 7.9	17
		10	0.8 ± 0.3	26.8 ± 6.6	15
		15	0.9 ± 0.2	28.7 ± 3.9	17
		20	0.8 ± 0.1	31.0 ± 5.7	11
150 μL / 300s (ThT)	yes	1	4.3 ± 3.2	1.8 ± 1.0	10
		5	4.3 ± 1.2	2.9 ± 0.6	20
		10	3.7 ± 1.0	6.3 ± 1.7	20
		15	4.9 ± 1.1	6.7 ± 2.4	20
		20	5.9 ± 2.0	8.1 ± 1.6	20
300 μL / 300s (ThT)	yes	1	1.4 ± 0.2	12.3 ± 3.9	9
		5	1.7 ± 0.6	9.0 ± 6.4	29
		10	1.8 ± 0.3	12.1 ± 3.8	31
		15	1.8 ± 0.4	11.3 ± 2.7	31
		20	2.1 ± 0.1	12.6 ± 3.2	30
300 μL / 300s (ThT)	no	1	2.8 ± 2.9	11.0 ± 5.4	27
		5	3.2 ± 1.5	11.6 ± 6.5	37
		10	2.7 ± 1.4	12.5 ± 7.1	26
		15	3.1 ± 1.3	14.0 ± 5.4	45
		20	2.6 ± 0.7	11.1 ± 4.3	49
300 μL / 300s (HL488 anisotropy) [1]	no	1	2.6 ± 0.8	3.7 ± 2.3	19
		5	6.8 ± 1.2	4.4 ± 3.0	19
		10	6.8 ± 2.2	7.2 ± 4.1	24
		15	7.5 ± 2.1	6.8 ± 2.5	24
		20	7.5 ± 2.3	7.6 ± 3.6	22

[1] The concentration of HL488-hCT used was 0.2 μM.

As this line of work continued, parallel partition studies of HL488-sCT towards POPC:POPS 80:20 LUVs revealed that the presence of a very small amount of HFIP in the solutions had a tremendous impact in the interaction kinetics of the fluorescently-labelled peptide with the liposomes (section 3.6.1). Therefore, the fibrillation studies of hCT/sCT were repeated but now using Method II of sample preparation, as described in detail in section 3.3.3.

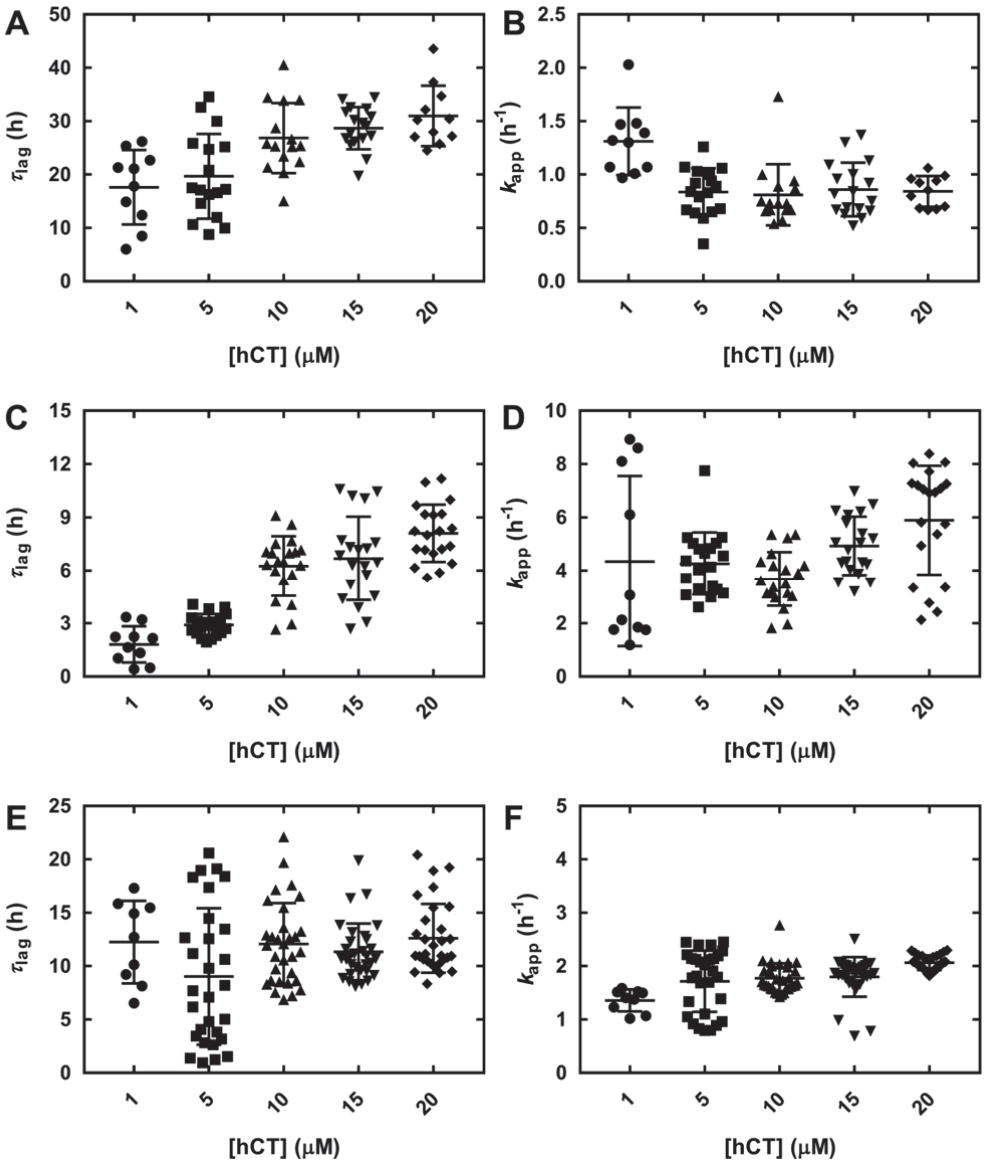

Figure 3.29 - hCT exhibits an abnormal relationship between initial concentration of peptide and lag time. The lag times ($\boldsymbol{\tau_{lag}}$; **A, C, E**) and apparent fibril growth rate, ($\boldsymbol{k_{app}}$; **B, D, F**), for the fibrillation kinetics of hCT performed with (**A** and **B**) 150 μL and 30s of orbital shaking before each cycle, (**C** and **D**) 150 μL and 300s of orbital shaking before each cycle and (**E** and **F**) 300 μL and 300s of orbital shaking before each cycle were calculated using to Eq. 3.1. All experiments were performed with a constant molar ratio of 1:0.75 peptide:ThT. For additional details, see the legend of Figure 3.28. For the lower sample volumes, there is a tendency for a direct relationship between the initial concentration of hCT and the lag time, which is much attenuated in a larger sample volume.

As can be seen in Figure 3.30 A, the lag times obtained in these conditions were very similar to the ones obtained in the presence of HFIP (Table 3.17 and Figure 3.29 A), suggesting that the presence of 1% (v/v) of this organic solvent does not impact significantly the fibrillation kinetics of the peptide. Still, the reproducibility of the assays remained a major issue.

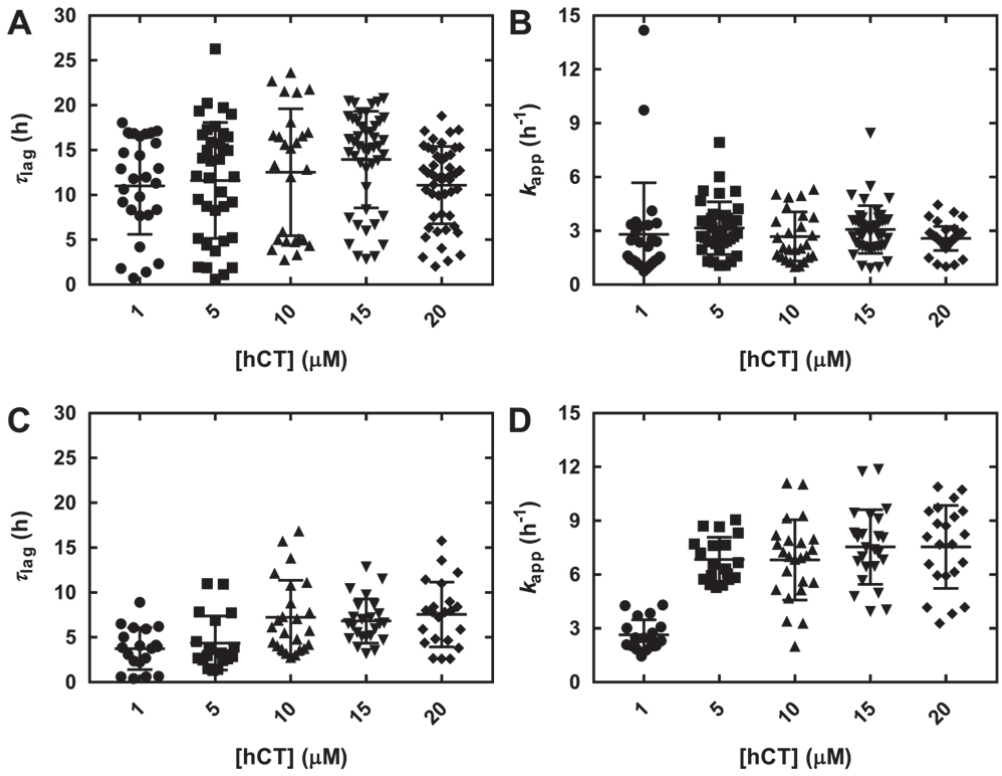

Figure 3.30 – The presence of HFIP does not cause the abnormal relationship between the initial concentration of peptide and lag time. The fibrillation kinetics of hCT with 300 μL of sample volume and 300s of orbital shaking before each cycle were repeated in the absence of HFIP. The lag times (**A, C**) and apparent fibril growth rate, k_{app} (**B, D**), were determined for the ThT kinetic assay (**A** and **B**) or anisotropy assay (**C** and **D**) using Eq. 3.1. The parameters obtained for these fits are presented in Table 3.17. The fibrillation was followed either using (**A** and **B**) a constant molar ratio of 1:0.75 peptide:ThT or (**C** and **D**) 0.2 μM HL488-hCT fixed for every concentration of peptide used.

3.4.2.2. Tracking the steady-state fluorescence anisotropy of fluorescently-labeled peptides

We next sought to characterize the fibril formation kinetics of hCT/sCT using a parameter other than the fluorescence intensity of ThT in order to shed some light about the intriguing relationship described above. Both peptides are labelled at their N-terminal to minimize both the interference with their fibrillation pathways and their interaction with negatively charged membranes In fact, it has been previously shown that FITC-labeled hCT at its single lysine residue, Lys18, and at the terminal group did not affect its progression into a fibrillated state (Arvinte et al, 1993). With this in mind, the assays were repeated in the presence of 0.2 μM

of the corresponding fluorescently-labeled peptide and its ssFA was monitored over time in a microplate reader. With 300 µL of sample volume and 300s of orbital shaking, the ssFA of HL488-hCT started to increase a few minutes after initializing the kinetics, reaching a plateau a few hours later; concomitantly, the fluorescence intensity of HL488-hCT decreased significantly (Figure 3.31 A, B, C). Both these changes suggest that we might be detecting an intermediate in the fibrillation pathway of hCT, probably an aggregate with a significant quenching of HL488-hCT fluorescence, which is not rich in β-sheet structure, by the absence of a parallel change in ThT fluorescent signal.

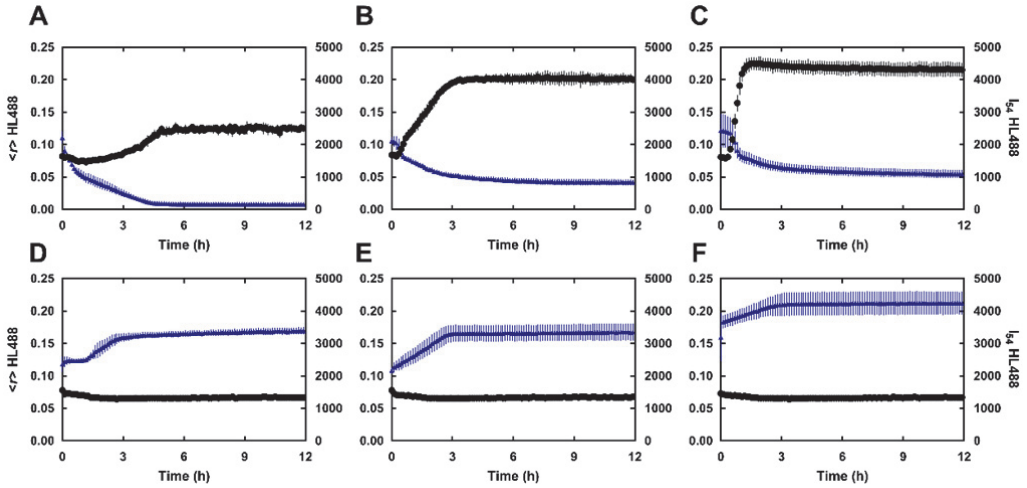

Figure 3.31 – Illustrative kinetic profiles for hCT and sCT aggregation studied using ssFA measurements of a fixed concentration of fluorescently-labeled peptide in the presence of HFIP. hCT and sCT fibrillation kinetics were monitored by measuring the changes in the ssFA of 0.2 µM tracer HL488-CT of the corresponding peptide added to each sample, $\langle r \rangle_{\mathbf{HL488}}^{\mathbf{485/520nm}}$ at 25 ºC (black curves, left axis). The kinetics exemplified of (**A, B, C**) hCT and (**D, E, F**) sCT were studied with concentrations of 1, 10 and 20 µM, respectively. The total fluorescence intensity (*I54,* blue curves, right axis) decreases over time for the hCT fibrillation kinetics and slightly increases over time in sCT assays. The assays were performed with 300 µL of sample volume and 300s of orbital agitation prior to the measurements. The curves represent the average ± SD of 4 or 5 technical replicates.

As for sCT, the ssFA of the tracer HL488-sCT remained essentially invariable during the experiment for the concentrations of peptide tested (Figure 3.31 D, E, F). When the shaking time of the assays was reduced to 30s/measuring cycle, the fibrillation kinetics of hCT were slower but their lag time was still shorter than the one observed using ThT under the same experimental conditions. These lag times were essentially independent of the peptide concentration used (data not shown).

At the end stage of the kinetics, each set of replicates was gathered for each peptide concentration studied and its fluorescence intensity decay kinetics was measured. The incorporation of the HL488-conjugated peptide into hCT aggregates/fibrils was accompanied by a pronounced decrease in its amplitude-weighted mean fluorescence

lifetime, which became lower than 2 ns, and much shorter than the values obtained for the equivalent sCT samples (Figure 3.31 and Table S 3.2). Under these conditions, ca 60-80% of the fluorescence emitted by the HL488-hCT is associated with the fast decay components, τ_1 0.2 ns and τ_2 1.4 ns (Table S 3.2). Altogether, the fluorescence data reveal a strong quenching of the HL488 fluorophore upon the incorporation of the tracer peptide into the hCT aggregates/amyloid fibrils when compared to the corresponding free monomeric fluorescently-labeled peptide in solution (Table 3.11) and the equivalent samples prepared with the non-amyloidogenic variant sCT.

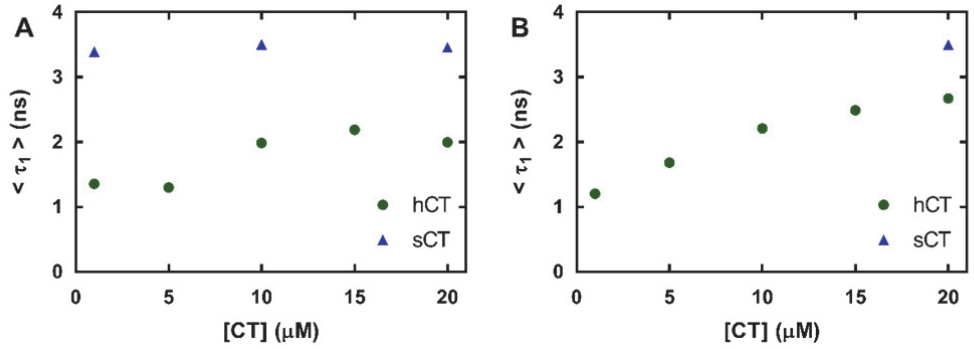

Figure 3.32 – The fluorescence of HL488-hCT is strongly quenched upon its incorporation in aggregates/fibrils. The amplitude-weighted average fluorescence lifetime of HL488-CT, $\langle\tau\rangle_1$,was determined for samples containing hCT (green circles) and sCT (blue triangles), which were gathered after the fibrillation kinetics performed in microplates. The fibrillation assays were performed (**A**) in the presence or (**B**) in the absence of HFIP. The results obtained are very similar and show an efficient dynamic quenching upon the incorporation of the HL488-hCT in hCT aggregates/fibrils, whereas for sCT the mean lifetimes are invariant compared to freshly prepared samples (Figure S 3.6 **C**). The results obtained for these analyses are in Table S 3.2.

More detailed information about the rotational dynamics of HL488-labeled peptides was obtained from the analysis of their fluorescence anisotropy decays (Figure 3.33). The fluorescence anisotropy decays of the tracer HL488-hCT peptide included in the 20 μM hCT sample required a very long rotational correlation time since its fluorescence anisotropy decay did not converge to zero at long times, at variance with the tracer HL488-sCT peptide in the samples prepared with 20 μM sCT which were completely depolarized at long times (Figure 3.33). It should be noted that very fast depolarizations are being lost in these measurements since the time-zero anisotropy recovered for 20 μM hCT with 0.2 μM of HL488-hCT was $r(0) =$ - 0.095 compared to $r(0) =$ - 0.141 for the free probe (Figure S 3.3 and Table 3.10).

There was not a significant difference in the results obtained in the presence or in the absence of HFIP for the amplitude-weighted average lifetimes of HL488-CT measured (Table S 3.2 and Figure 3.32) neither for the anisotropy decays (Figure S 3.3 and Figure 3.33).

Concluding, it was difficult to obtain reproducible assays and the obtained results seem to be in contrast to the available literature at the time. It would be interesting to further analyze the samples by other complementary biophysical and imaging techniques to the microplate assays, like CD or TEM.

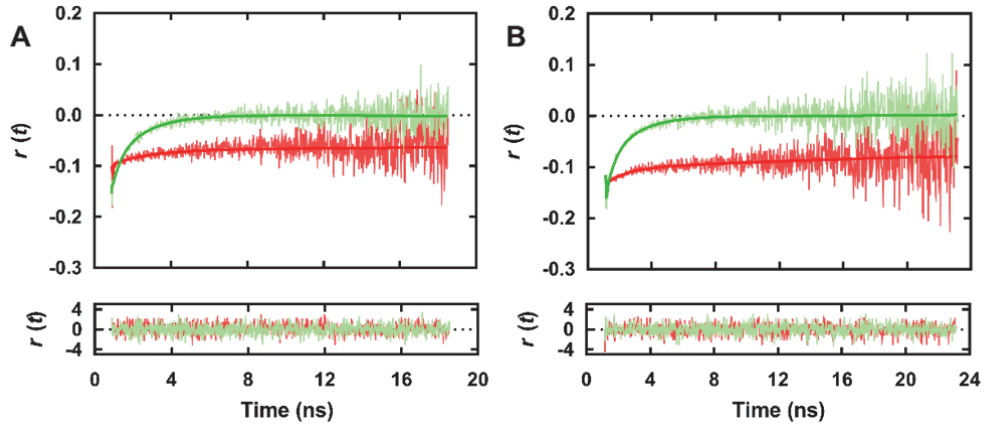

Figure 3.33 - The tracer amount of HL488-labeled hCT is efficiently incorporated into the hCT fibrils/aggregates formed. The fluorescence anisotropy decays of the samples obtained after at least 24h of incubation in the microplates anisotropy assay were measured. The green and red solid lines are the best fits of Eq. 3.25 to the experimental data obtained for 20 μM sCT (green curve) and 20 μM hCT (red curve) in the presence of 0.2 μM of the respective HL488-labelled peptide. The bottom panels correspond to the residuals of the fit. The parameters obtained for these fits are presented in Table S 3.3. (**A**) samples with HFIP (19.5 ps/channel) (**B**) samples without HFIP (24.4 ps/channel). The appearance of a long correlation time in the hCT samples is a clear evidence for the formation of large hCT aggregates (fibrils) in solution.

3.4.2.3. **Discussion**

The objective of this part of the work was to study and characterize the kinetics of CT amyloid fibril formation, using it as a model polypeptide to ultimately study the role of biological membranes in modulating this process. The idea was to gain an improved understanding of all steps of peptide aggregation, particularly the initial elusive stages involved in nucleation, through the application of a complementary set of advanced fluorescence methodologies.

The use of microplate readers to study the fibrillation kinetics of amyloidogenic peptides/proteins is very common (example for insulin: (Nielsen *et al.*, 2001); α-synuclein: (Giehm *et al.*, 2011) and IAPP: (Caillon *et al.*, 2013), as it allows testing different peptide concentrations and conditions at the same time in a fast and convenient manner, since the measurements are automatically performed over time. Nevertheless, the fibrillation process is highly dependent on shaking conditions, ratio of the sample volume to well volume, peptide concentration, the material of vessels in which the fibrillation is performed, among

other factors (Giehm and Otzen, 2010; Risør *et al.*, 2017). In spite our efforts, we were not able to obtain reproducible ThT-monitored fibrillation assays for hCT. The absence of agitation in our fibrillation studies resulted in very long lag times (in the order of 50h or more), making these a prohibitively/excessively slow aggregation process which severely hampered the performance of systematic studies. Giehm *et al.*, 2011 suggested that this very long kinetics can lead to problems related with slow competing processes such as evaporation, chemical modifications and photobleaching and therefore we introduced a shaking step in the fibrillation assays. However, there are also indications that the use of vigorous/extensive agitation might attenuate the effects of variable peptide/protein concentration, ionic strength or the effects of small molecules in the fibril formation process (Uversky *et al.*, 2001), making it more difficult to adequately interpret the results.

As presented in Table 3.17, the relative error obtained for the lag times was in general higher than the one for the apparent rate of hCT fibril growth, indicating that nucleation was the main determinant of the reproducibility of the assays. The nucleation process of the nucleation-dependent fibrillation is a stochastic event so the reproducibility of fibril formation assays will be dependent on the frequency of these events. Once the nucleus is formed, the elongation is expected to be more reproducible (Giehm and Otzen, 2010). Still, although the relative deviations in the average lag times and apparent rates of fibril formation were very high (Table 3.17), there was a clear indication of a direct relationship between the lag time of the kinetics and the peptide concentration used for some of the experimental conditions tested (Figure 3.29), which was a rather surprising and unexpected result. In fact, in a standard fibrillation pathway the lag phase usually becomes shorter upon increasing the protein/peptide concentration in solution since non-native intermolecular contacts are favored over native intramolecular contacts with the use of higher concentrations of proteins/peptides. These results are also at variance to what is described in the literature, with numerous studies of CT and IAPP as examples (Arvinte *et al.*, 1993; Avidan-Shpalter and Gazit, 2006; Yan *et al.*, 2006; Brender *et al.*, 2015). In the work performed by Avidan-Shpalter and Gazit the authors tested hCT concentrations ranging from 1 to 7 μM in 500 μL in 10 mM Tris buffer, pH 7.2, with the ThT concentration calculated to be 75% of the final peptide concentration. These are very similar conditions to the ones employed in our study, regarding the low ionic strength buffer, the relation between ThT and peptide concentration and the peptide concentration. They observed that the lag-phase decreased from ca. 240h to 20h upon increasing the concentration of peptide and concluded that the process could be explained by a heterogeneous nucleation mechanism. The kinetics observed in our work were much faster, although this might be related with the shaking, which is present in our assays and absent in theirs, as well as the different total volume used.

The use of the ssFA of a tracer amount of HL488-labeled peptides to monitor the fibril formation kinetics of hCT/sCT gave additional puzzling results because there was a large discrepancy between the lag times determined in these assays and the ones measured independently using the fluorescence intensity of ThT. The incorporation of the tracer HL488-hCT into larger aggregates/fibrils was clearly evident from the time-resolved fluorescence anisotropy decays obtained for the tracer peptide in the presence of 20 μM hCT (Figure 3.33), but not HL488-sCT/sCT. We hypothesized that we might be detecting intermediate species formed along the fibrillation pathway of hCT that have a large hydrodynamic volume but a low β-sheet content (and therefore the lack of parallel increase in ThT fluorescence intensity).

Altogether, our data suggest that the fibrillation kinetics of hCT in solution does not obey a standard mechanism. Interestingly, in 2017 Kamgar-Parsi and co-workers published results that shed some light in our data. They performed a systematic study on the effect of different experimental conditions on the fibrillation kinetics of CT peptides and reported a direct relationship between the aggregation lag time and the hCT concentration used in the assay, which persisted even with changes in buffer (sodium phosphate, pH7.4, Tris buffer, pH 7.4, and sodium bicarbonate buffer, pH 10), salt concentration (from 0 to 1 M of NaCl), temperature (25 and 37 ^{o}C) and others (e.g. agitation). Their results are explained in the basis that hCT monomers must suffer a structural conversion before they are incorporated into the fibrils. They propose the existence of two types of monomers, growth-competent and growth-incompetent. The formation of growth-incompetent aggregates is more likely in the presence of higher concentrations of peptide; these only slowly reverse to growth-competent monomers, also limiting the availability of these growth-competent monomers to allow the formation of mature fibrils (Kamgar-Parsi *et al.*, 2017). This proposed non-canonical model can explain the direct relationship between the lag time and the initial peptide concentration used in hCT fibrillation assays, which was also detected here under some experimental conditions; in addition, the intermediates detected in the ssFA kinetics might be related to the formation of these growth-incompetent aggregates. In this regard, it would be interesting to perform an assay where ThT intensity and HL488 anisotropy were measured in parallel, to relate the findings using both dyes in the same sample. Nevertheless, the formation of small amorphous aggregates due to the direct dissolution in buffer of the stock solution of peptide in HFIP cannot be completely disregarded as an important influence on the results obtained in our first set of experiments. It should be also emphasized that the method used by Kamgar-Parsi and co-workers to prepare the peptide samples was also different from ours. They synthesized the peptide ‘in-house’, dissolved it in HFIP, aliquoted and lyophilized it; just before the measurements, 300 μM intermediate

stock solutions were prepared in HCl (pH 4) at 4 ^{o}C, warmed up this stock to RT and prepared 100 µL total volume samples in uncoated Fisherbrand 96-well polystyrene plates.

In conclusion, at this point, further studies are warranted to clarify the fibrillation kinetics of hCT under different experimental conditions and to evaluate if the non-canonical fibrillation model recently proposed in the literature can adequately describe our data.

3.4.3. Interaction of calcitonin variants with liposomes

Lipid membranes, particularly those containing acidic phospholipids, are known to modulate the fibrillation pathway of amyloidogenic peptides as they usually cause an enhancement of amyloid fibril formation (Gorbenko and Kinnunen, 2006; Hebda and Miranker, 2009; Butterfield and Lashuel, 2010; Sheynis and Jelinek, 2010). Therefore, in parallel to the fibrillation studies of CTs in aqueous solution, the work progressed towards the characterization of CT interaction with liposomes prepared with a variable lipid composition. The first step of these studies involved measuring a membrane-water partition coefficient for the peptides since this parameter is proportional to the energetics of the peptide – lipid membrane interaction, which ultimately controls the surface concentration reached by the peptide in the liposomes.

3.4.3.1. **Calcitonin partition studies towards POPC:POPS LUVs**

- Intrinsic fluorescence properties of CTs

In a first set of experiments, we took advantage of the fact that both hCT and sCT are intrinsically fluorescent peptides (due to the presence of Y12 and Y22, respectively) to monitor the changes in the fluorescence properties of 10 µM of each CT variant upon its interaction with model lipid membranes (LUVs) composed of POPC:POPS 80:20. At this stage, the samples were prepared independently using Method I (i.e. by directly injecting an appropriate volume of the stock solution of the respective CT in HFIP to the different samples (see Section 3.3.3)). The absorption and fluorescence emission spectra of both CT variants did not undergo any significant spectral shifts upon the addition of increasing concentrations of LUVs, ranging from 0 to 1.5 mM accessible phospholipid (data not shown). On the other hand, the fluorescence intensity of sCT (Figure 3.34 A, red squares), but not of hCT (Figure 3.34 A, green triangles) progressively increased upon the addition of vesicles. The fluorescence quantum yield of sCT was approximately 1.3 times higher for the membrane-bound peptide as compared to the one in aqueous solution. This change probably reflects the burying of the tyrosine in the membrane. A similar behavior was found

for CTs in interaction with DMPG liposomes (Epand *et al.*, 1983) and hCT fibrillation has also been described to induce a strong increase in Y12 fluorescence (Arvinte *et al.*, 1993).

The interaction of each CT variant with liposomes was also studied by following the changes in the ssFA of the peptides with the lipid concentration. The variation in the ssFA of sCT was biphasic since it first increased until an accessible phospholipid concentration of 250 μM was reached and then decreased afterwards (Figure 3.34 B open red squares). In parallel, the ssFA of hCT steadily decreased upon increasing the lipid concentration in the sample. After correcting the experimental ssFAs for the scattering-induced depolarization of the radiation (as explained in Section 3.3.3.3), the corrected ssFAs of hCT were found to be essentially independent of the phospholipid concentration used ($\langle r \rangle_{Y12}$= 0.061 ± 0.010 (n= 8), (Figure 3.34 B closed green triangles)). On the other hand, the corrected ssFA of sCT increased hyperbolically with the lipid concentration and a K_p = (5.6 ± 1.1) x 10^5 and r_L = 0.114 ± 0.002 were obtained by fitting Eq. 3.6 to these experimental values (using *Q* = 1.3) (Figure 3.34 B closed red squares and red solid line). Altogether, these results imply that hCT, at variance with sCT, does not bind to POPC liposomes containing 20 mol% of POPS. However, since these analyses are strongly limited by the need to extensively correct the experimental data, we did not proceed with this methodology.

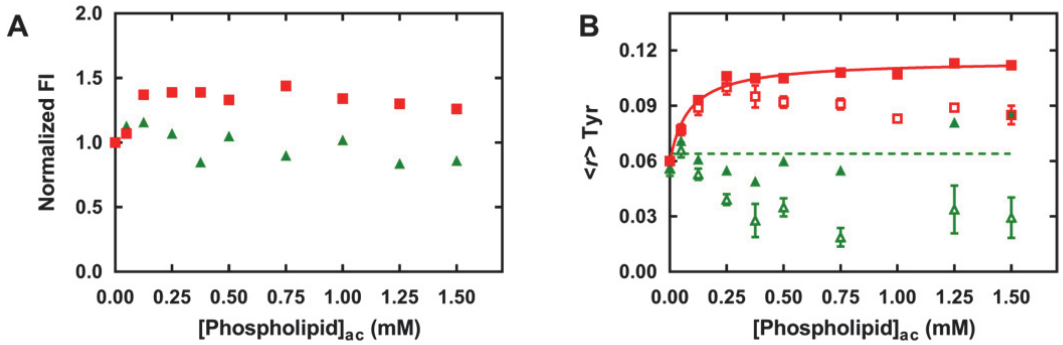

Figure 3.34 – sCT, but not hCT, interacts with POPC:POPS 80:20 LUVs. Variation of (**A**) the integrated fluorescence emission intensity and (**B**) ssFA, $\langle r \rangle_{Tyr}$, (λ_{exc}= 275 nm; λ_{em}= 300 nm), of 10 μM sCT (red squares) and hCT (green triangles) with the accessible phospholipid concentration. The ssFAs are uncorrected (open symbols) and corrected (closed symbols) for the scattering-induced depolarization of the radiation produced by the liposomes. The green dashed line is the mean corrected ssFA obtained for hCT: $\langle r \rangle_{Y12}$= 0.061 ± 0.010 (n= 8) and the red solid line is the best non-linear fit of Eq. 3.6 to the corrected ssFAs of sCT for K_p estimation. Method I was used to prepare the samples (section 3.3.3).

- Far-UV CD studies of CTs

The binding of each CT variant to lipid membranes was further characterized by measuring the far-UV CD spectra of either 20 μM hCT or sCT in buffer and in the presence of 1 and 4 mM of POPC:POPS 80:20 LUVs (Figure 3.35). As expected, both peptides are predominantly random coiled in buffer (Figure 3.35, red curves) (Epand *et al.*, 2004; Gaudiano *et al.*, 2005; Kamgar-Parsi *et al.*, 2017). Upon addition of liposomes, the far-UV CD spectra of hCT remained invariant, even in the presence of 4 mM of vesicles (Figure 3.34), confirming that the peptide does not interact with these lipid vesicles. On the other hand, the CD spectra obtained for sCT showed that the peptide underwent a random coil-to-helix transition in the presence of LUVs, a typical feature of IDPs (Abedini and Raleigh, 2009; Relini *et al.*, 2013) that has also been previously described for this peptide (Epand *et al.*, 2004), corroborating that the salmon variant binds to these lipid vesicles.

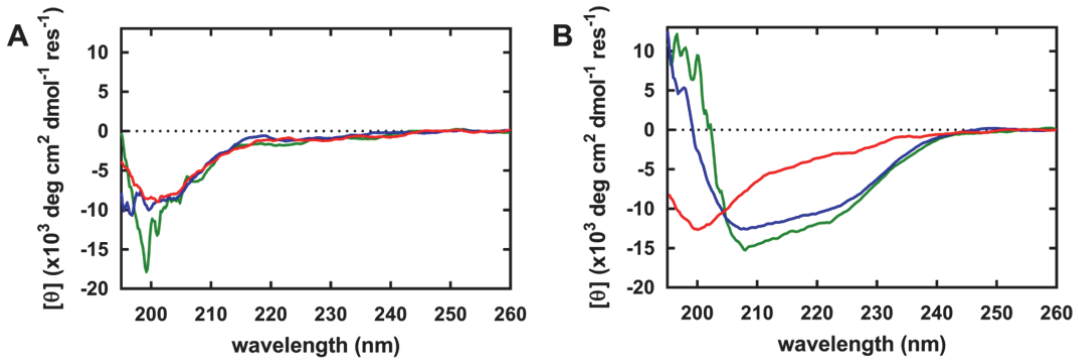

Figure 3.35 - CD spectra of sCT revealed the conversion of the peptide from random coil to α-helix in the presence of anionic lipid vesicles, a feature not observed for hCT. CD spectra were performed with 20 μM of each peptide in buffer (red line), 1 mM of LUVs (blue line) and 4 mM of LUVs (green line) of POPC:POPS 80:20 for (**A**) hCT and (**B**) sCT.

- Extrinsic fluorescence properties of HL488-CTs

The fluorescence properties of both HL488-fluorescently labelled CT variants, labeled at their N-terminal to minimize both the interference with their fibrillation pathways and their interaction with negatively charged membranes, were also exploited to characterize the binding of these conjugated peptides to anionic lipid vesicles. POPC liposomes were now prepared with 30 mol% of POPS to favor the electrostatic-mediated interactions between the cationic peptides and the acidic membranes. The emission properties of HL488-sCT were very good reporters of its binding to the negatively-charged liposomes. Upon increasing the lipid concentration, there was a progressive red-shift of its emission spectra from $\langle\lambda\rangle$ = ~ 539 nm to $\langle\lambda\rangle$ = 543 nm, that was accompanied by a progressive increase in the ssFA of HL488-sCT from $\langle r\rangle_{\mathrm{HL488-sCT}}$ = 0.068 ± 0.001 to 0.236 ± 0.014 (n= 2) in the

presence of 2 mM of accessible phospholipid. On the contrary, the fluorescence emission spectra of HL488-hCT (data not shown) and its ssFA were independent of the accessible phospholipid concentration present in each sample (0 – 2 mM) (Figure 3.36) $\langle r \rangle_{\mathrm{HL488-hCT}} =$ 0.079 ± 0.002 (n= 11)), even when POPC:POPS 50:50 LUVs were used ($\langle r \rangle_{\mathrm{HL488-hCT}} =$ (0.084 ± 0.003 (n= 11) (data not shown)). This conclusion was further confirmed by measuring the fluorescence anisotropy decays of HL488-hCT of these samples, in the absence and in the presence liposomes. Under all conditions studied, the anisotropy decays never displayed a limiting anisotropy characteristic of peptide binding to the lipid vesicles (data not shown). Altogether, the partition studies performed with the human and salmon CTs and the corresponding conjugated peptides using different spectroscopic techniques are in good agreement with each other, strongly indicating that the conjugated dye is not affecting the partition properties of hCT nor sCT towards the negatively-charged liposomes used.

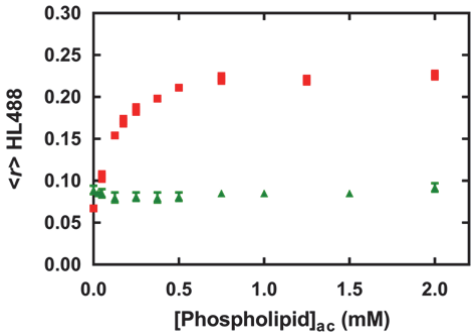

Figure 3.36 - The ssFA of the conjugated calcitonins are good reporters of their partition to anionic lipid vesicles. Variation of the ssFA, $\langle r \rangle_{\mathrm{HL488}}$, ($\lambda_{\mathrm{exc}}$ = 480 nm; λ_{em}= 525 nm), of 1 μM HL488-hCT (green triangles) and 0.2 μM HL488-sCT (red squares) with the accessible phospholipid concentration at RT. POPC:POPS 70:30 LUVs were used. Method II was used to prepare the samples (section 3.3.3).

3.4.3.2. HL488-hCT does not interact with liposomes prepared with a wide range of lipid compositions

Previous reports have described the interaction of hCT and sCT with liposomes prepared with more complex lipids/mixtures (Diociaiuti *et al.*, 2006; Sheynis and Jelinek, 2010). The inclusion of sphingolipids, cholesterol and other lipids in the lipid composition of the membrane affects not only the overall charge of the membrane but also the headgroup size of its constituent phospholipids which, in turn, can impact the membrane order and eventually promote the formation of nanodomains/patches with different lipid compositions, etc, (Caillon *et al.*, 2013). To test whether the lipid composition used in the preparation of the liposomes was the key factor controlling hCT binding to the lipid vesicles, we extended the partition studies performed with HL488-hCT towards liposomes prepared with lipid

compositions similar to the ones used in these reports: POPC:POPE:POPG 50:30:20, DOPC:Chol 75:25, DOPC:SM 75:25, DOPC:SM:Chol 65:25:10 and DOPC:Chol:GM1 50:46:4. As can be seen in Figure 3.37, the ssFA of HL488-hCT was independent of the phospholipid concentration used for all the lipid mixtures tested, either at 25 ºC or 37 ºC, and in a low (HEPES-KOH buffer, pH 7.4) or high ionic strength buffer (HEPES-KOH buffer, 150 mM NaCl, pH 7.4). We conclude that hCT/HL488-hCT did not display a high binding affinity towards any of the lipid compositions assayed and our studies were henceforth focused on sCT/HL488-sCT only.

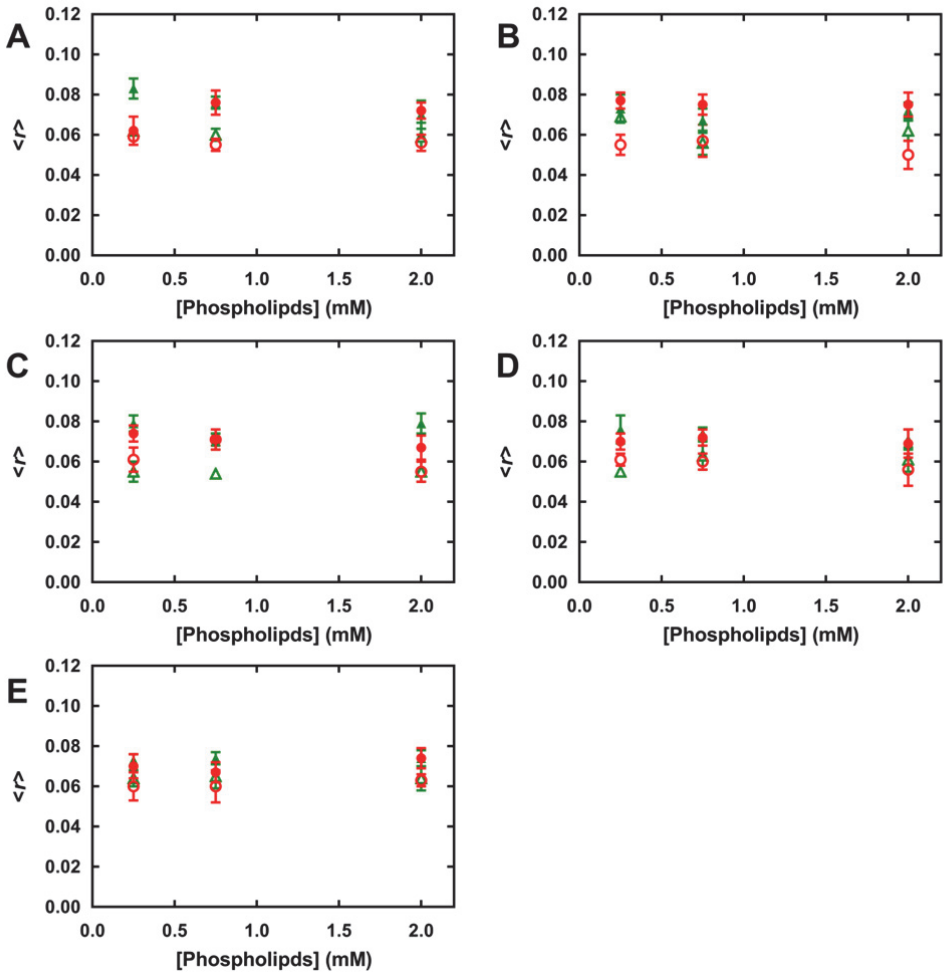

Figure 3.37 - HL488-hCT does not interact with LUVs composed of binary or ternary mixtures of phospholipids, sphingolipids and cholesterol. The ssFA, $\langle r \rangle_{\mathbf{HL488}}$, ($\lambda_{\mathbf{exc}}$ = 480 nm; $\lambda_{\mathbf{em}}$= 525 nm), of 2 μM HL488-hCT did not vary upon increasing the phospholipid concentration of (**A**) POPC:POPE:POPG 50:30:20, (**B**) DOPC:Chol 75:25, (**C**) DOPC:SM 75:25, (**D**) DOPC:SM:Chol 65:25:10 and (**E**) DOPC:Chol:GM1 50:46:4 either at 25 ºC (closed symbols) and 37 ºC (empty symbols), in a buffer with low (red symbols) or high (green symbols) ionic strengths. Method II was used to prepare the samples (section 3.3.3).The value obtained previously at 25 ºC in aqueous solution was $\langle r \rangle_{\mathbf{HL488}}$~ 0.08.

3.4.3.3. **sCT/HL488-sCT binding to liposomes is strongly electrostatic driven**

We next sought to characterize in more detail the influence of the anionic lipid content of the liposomes on the partition behavior of the fluorescently-labelled sCT variant. Partition studies of 0.2 μM HL488-sCT were therefore conducted with POPC liposomes including 0, 10, 20, 30 and 50 mol% of POPS. There was no spectroscopic evidence for HL488-sCT binding to the zwitterionic POPC liposomes (Figure 3.38 A and B, grey symbols). On the other hand, in the presence of anionic lipid membranes, a progressive red-shift in the maximum absorption (not shown) and intensity-weighted fluorescence emission wavelengths of HL488-sCT was detected upon increasing the phospholipid concentration (Figure 3.38 A); these spectral changes were always accompanied by an hyperbolical increase in the ssFA of the fluorescently-labelled peptide as a function of phospholipid concentration (Figure 3.38 B), providing evidence for HL488-sCT partition towards these lipid membranes. Moreover, both the spectral shifts ($\Delta\langle\lambda\rangle_{\max}^{\mathrm{Abs}}$ ~ 5 nm and $\Delta\langle\lambda\rangle_{\max}^{\mathrm{em}}$ ~ 4 nm, respectively) and the increase in the ssFA ($\Delta\langle r\rangle$ ~ 0.17) of HL488-sCT were more pronounced and leveled off at a lower accessible phospholipid concentration as the acidic phospholipid content of the liposomes increased from 10 to 50 mol% POPS. Parallel control measurements revealed that the amplitude-weighted mean lifetime, $\langle\tau\rangle_1$, of HL488-sCT did not vary upon its binding to POPC lipid vesicles containing either 20 (Figure 3.38 D) or 30 mol% of POPS (not shown). The fluorescence emission decay kinetics of 0.2 μM HL488-sCT was always adequately described by a tri-exponential function, typically with τ_1~ 0.22 ns, τ_2 ~ 1.54 ns and τ_3 ~ 4.08 ns and α_1 ~ 0.16, α_2 ~ 0.11 and α_3 ~ 0.73, respectively. The longest lifetime, τ_3 , was therefore always the dominant component of the fluorescence intensity decay, contributing with ~ 90% to the total fluorescence emission of the conjugated peptide.

Assuming a simple partition equilibrium of monomeric HL488-sCT towards the anionic membranes, the individual analysis of each partition curve of $\langle r\rangle$ *versus* $[L]_{ac}$ with Eq. 3.6 (*Q*= 1) yielded very similar r_L values for the membrane-bound conjugated peptide (r_L = 0.248 ± 0.018 (n= 8)). Therefore, this value was kept fixed in all the subsequent fits of the partition model to the data obtained with liposomes containing variable mol% of POPS. The partition coefficients measured for HL488-sCT, which are presented in Table 3.18, displayed an exponential dependence with the POPS content of the liposomes for a molar fraction of POPS higher than 10 mol% (Figure 3.38 C). This result confirms the importance of electrostatic interactions in HL488-sCT binding to the lipid membranes, as expected due to its net charge of +3. The K_p obtained for 10 mol% of POPS-containing liposomes indicates that HL488-sCT partition towards these liposomes is considerably weaker than

anticipated from the data obtained with the lipid membranes prepared with a higher content of anionic phospholipids.

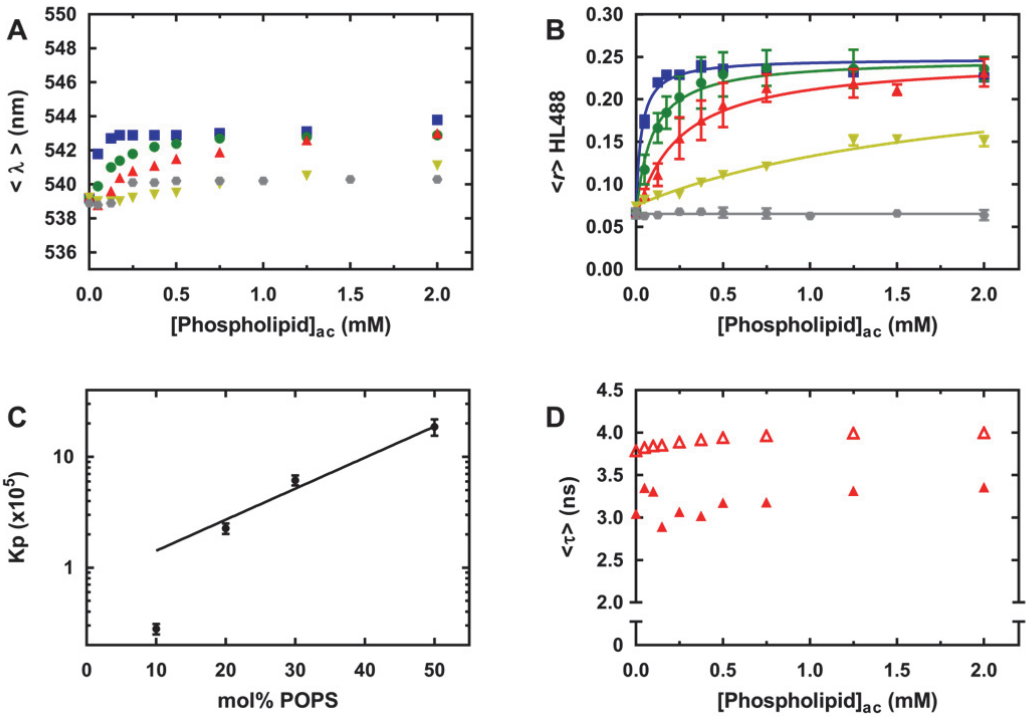

Figure 3.38 – The partition of HL488-sCT is controlled by the anionic lipid content of the liposomes. Variation of (**A**) the intensity-weighted emission wavelength, and (**B**) ssFA of 0.2 μM HL488-sCT with the accessible phospholipid concentration, providing evidence for HL488-sCT binding to the lipid membranes. The POPC liposomes contained 0 (grey diamonds), 10 (yellow inverted triangles), 20 (red triangles), 30 (green circles) and 50 mol% of POPS (blue squares). Solid lines in **B** are the best fits of Eq. 3.6, to the experimental data, except for POPC LUVs which is the average ± SD of ssFA. The fitted partition coefficients are presented in Table 3.18. (**C**) Dependence of the partition coefficient of HL488-sCT with the mol% of POPS included in the POPC LUVs. The results in **B** and **C** correspond to the average ± SD of: n= 1 POPC, n= 2 10 mol%, n= 4 20 mol%, n= 2 30 mol% and n= 1 50 mol% POPS. (**D**) The amplitude-average (filled triangles) and intensity-average (empty triangles) fluorescence lifetimes of 0.2 μM HL488-sCT are not significantly affected by the presence of POPC:POPS 80:20 LUVs. Method II was used to prepare the samples (section 3.3.3).

A complementary partition study of 20 μM sCT towards POPC liposomes containing 10, 20 and 30 mol% of POPS using far-UV CD measurements was also carried. As it is illustrated in Figure 3.39 A for POPC:POPS 80:20 LUVs, there is a progressive increase in the α-helical content of the peptide upon increasing the phospholipid concentration in solution, a clear evidence that sCT is partitioning towards the lipid membranes. The detection of an isodichroic point in the far-UV CD spectra of sCT at ~ 204 nm is a clear indication that only two species are present in solution, namely the membrane-bound and free peptide conformers.

The mean residue molar ellipticity of an amphipathic peptide at 222 nm can be used as a measurement of the extension of its membrane binding (Knight *et al.*, 2006). For 20 and 30 mol% of POPS, the individual analysis of each data set ($[\theta_{222\mathrm{nm}}]$ *versus* $[L]_{ac}$) according to a simple partition equilibrium (Eq. 3.6) resulted in similar values for $\Delta[\theta_{222\mathrm{nm}}]_{\max}$ ($\Delta[\theta_{222\mathrm{nm}}]_{\max}$ = -(14.88 ± 0.09) x 10^3 deg cm^2 dmol^{-1} res^{-1} (*n* = 2)). Therefore, this value was subsequently fixed in all the fits, including the one performed with the data obtained with POPC LUVs containing 10 mol% POPS; the fitted curves are shown in Figure 3.39 B, solid lines (Table 3.18). These results quantitatively confirm that the conjugation of sCT with the HL488 dye did not affect its membrane-binding properties since the K_p values obtained with the two complementary spectroscopic techniques (ssFA of HL488-sCT and CD measurements of sCT) are in good agreement (Table 3.18).

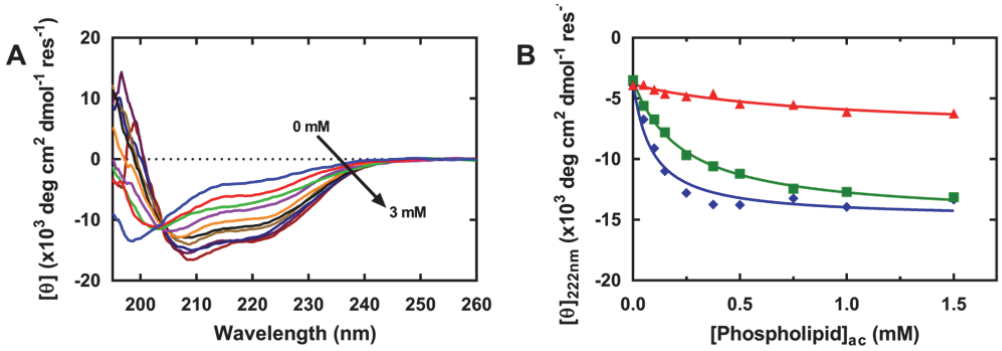

Figure 3.39 - sCT interacts with anionic phospholipids acquiring α-helical structure. (**A**) CD spectra of 20 μM sCT in the presence of different concentrations of 80:20 POPC:POPS LUVs (**B**) Comparison of the sCT $[\boldsymbol{\theta_{222\mathrm{nm}}}]$ (a local minima for α-helices) for LUVs containing different POPS content: 10 mol% (red triangles), 20 mol% (green squares) and 30 mol% (blue diamonds). Solid lines represent fits to the experimental data using Eq. 3.6. Calculated parameters are presented in Table 3.18.

Table 3.18 – The partition coefficients of sCT/HL488-sCT are critically dependent on the anionic lipid content of the liposomes. The partition coefficients, $\boldsymbol{K_p}$, of sCT were obtained from fitting Eq. 3.6 to the changes in its intrinsic ssFA ($\langle \boldsymbol{r} \rangle_{\mathbf{Y20}}$) and mean residue molar ellipticity at 222 nm ($[\boldsymbol{\theta_{222\mathrm{nm}}}]$), whereas for HL488-sCT extrinsic ssFA ($\langle \boldsymbol{r} \rangle_{\mathbf{HL488}}$) measurements were used. See Figure 3.34, Figure 3.38 and Figure 3.39 for more details.

mol% POPS	K_p (x10^5) ($\langle r \rangle_{\mathrm{Y20}}$) [1]	K_p (x10^5) ($\langle r \rangle_{\mathrm{HL488}}$) [2]	K_p (x10^5) ($\Delta[\theta_{222\mathrm{nm}}]$) [3]
10		0.28 ± 0.03	0.112 ± 0.014
20	5.50 ± 0.30	2.26 ± 0.24	2.42 ± 0.10
30		6.15 ± 0.63	6.49 ± 1.09
50		18.66 ± 3.16	

[1] using r_{L} = 0.11 ± 0.03 (*n* = 1)

[2] using r_{L} = 0.248 ± 0.018 (*n* = 8)

[3] using $\Delta[\theta_{222\mathrm{nm}}]_{\max}$ = -14.875 x 10^3 deg cm^2 dmol^{-1} res^{-1} (*n* = 2)

For 20 and 30 mol% of POPS-containing POPC LUVs, the CD spectra of sCT at the highest concentration of lipid used (3 mM) displayed the two canonical minima at 208 nm and 222 nm characteristic of an α-helical conformation. The % helicity estimated with Eq. 3.13 for the membrane-bound sCT was 38% and 39%, respectively, which corresponds to ca. 12 amino acid residues. This result matches the study of Epand and co-workers (Epand *et al.*, 1986) where the authors calculated that the secondary structure of sCT consisted of 40% α-helix in the presence of DMPG vesicles. Just for comparison, Morelli *et al*. concluded that this peptide would take up a helical structure 17 amino acids long (from residue 6 – 22) based on the structure determined for sCT in interaction with SDS micelles by NMR (Morelli *et al.*, 1992). It is not surprising that is slightly longer than the estimative made from our CD results for sCT in interaction with lipid membranes due to the higher curvature radius and charge density of the SDS micelles compared to the anionic LUVs used in this study.

3.4.3.4. Influence of the peptide concentration on HL488-sCT binding to liposomes

We next aimed to characterize the structural and dynamical features of putative oligomeric intermediate states triggered by the interaction of HL488-sCT with anionic lipid membranes within a wide range of L/P molar ratios. This can be of great interest since sCT has been used in the treatment of human diseases, as pointed in section 3.2.4, and has been previously shown to form annular pores in artificial membranes (Diociaiuti *et al.*, 2006, 2011). Using the same experimental design, the partition studies were repeated using higher concentrations of the fluorescently-labelled sCT. A fixed concentration of HL488-sCT of 2.0 μM and 5.0 μM was now added to an increasing concentration of POPC liposomes containing 20 mol% of POPS (0 – 2 mM of accessible phospholipid). As described before, each peptide-containing sample was prepared independently and UV-Vis absorption, steady-state and time-resolved fluorescence measurements were performed to detect and characterize in detail the possible intermediate species produced.

3.4.3.5. UV-Vis absorption spectra shows the formation of H-aggregates at a low Lipid/HL488-sCT ratio

The absorption spectra of both 2.0 μM and 5.0 μM HL488-sCT revealed a significant red-shift to ~509 - 511 nm with the addition of increasing concentrations of phospholipid, relatively to the spectra obtained in aqueous solution ($\lambda_{\max}^{\mathrm{Abs}}$ =504 nm). As described for 0.2 μM HL488-sCT samples, this reported the progressive binding of the conjugated peptide to the membrane surface of the negatively-charged lipid vesicles (data not shown). Simultaneously, there was a change in the shape of the absorption spectra of HL488-sCT,

particularly for the samples prepared with the highest concentration of conjugated peptide and low lipid concentrations (Figure 3.40 A): a “shoulder” appeared in the blue region of its absorption spectrum which was gradually lost upon increasing the lipid concentration (but never completely). These spectral alterations are characteristic of excitonic interactions between the chromophores due to their dimerization in the ground-state (Valdes-Aguilera and Neckers, 1989; Castro *et al.*, 2012). According to the exciton theory (Valdes-Aguilera and Neckers, 1989), the spectral alterations detected in the absorption spectra of HL488-sCT at low L/P molar ratio (low phospholipid concentration) reveal the formation of parallel aggregates (H-type) between the HL488 chromophores covalently linked to sCT. As expected, the intensity of the excitonic band was greater for the 5.0 μM than for the 2.0 μM HL488-sCT-containing samples (not shown).

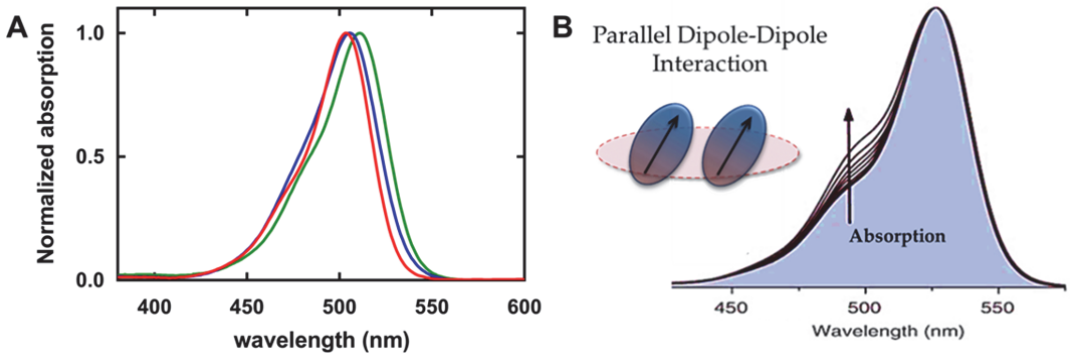

Figure 3.40 - The absorption spectra of 5.0 μM HL488-sCT in the presence of an increasing concentration of POPC:POPS 80:20 liposomes suggests the formation of H-type aggregates. (**A**) Upon increasing the accessible phospholipid concentration, the maximum absorption wavelength of HL488-sCT gradually red-shifted, alongside with a change in the shape of the absorption spectra at shorter wavelengths. Red, blue and green correspond to the measurement made in buffer, in the presence of 0.3 mM or 4 mM of POPC:POPS 80:20 LUVs, respectively. (**B**) Illustrative representation of the theoretical prediction for the impact of progressive H-type dimer formation on the absorption spectra of the chromophore upon increasing its concentration in solution. Method II was used to prepare the samples (section 3.3.3).

3.4.3.6. **The fluorescence of membrane-bound HL488-sCT oligomers is highly quenched**

Concomitantly, the fluorescence emission spectra of both 2.0 and 5.0 μM HL488-sCT also progressively red-shifted (not shown) upon their interaction with an increasing concentration of POPC:POPS 80:20 liposomes, as abovementioned for the 0.2 μM concentration. At the same time, the integrated areas calculated from the emission spectra obtained for each concentration of fluorescently-labeled sCT, normalized to its initial value in aqueous solution, presented a biphasic behavior (Figure 3.41 A): for 2.0 and 5.0 μM HL488-sCT, this parameter sharply decreased to a minimum value of ~60 and ~30% of their initial value in buffer solution, respectively, when low concentrations of phospholipid were added to the

solution (~0.5 mM accessible phospholipid concentration). Upon further increasing the phospholipid concentration, there was a progressive recovery of the integrated emission areas which would probably reach its initial value for even higher phospholipid concentrations. These results are in agreement with the formation of non-fluorescent (dark) H-aggregates at low lipid concentrations, as described above. Upon reaching a high local membrane surface concentration at a low L/P ratio, the fluorescently-labelled peptides interact with each other, resulting in a static quenching of their fluorescence intensity. The addition of higher liposome concentrations to the solution drives HL488-sCT partition to the membranes; however, the surface concentration of the membrane-bound peptides becomes increasingly diluted, promoting the disassembly of the membrane-bound peptide oligomers, and allowing HL488-sCT to partially recover its fluorescence intensity (Figure 3.41 A). The existence of a coupled HL488-sCT partition/oligomerization equilibria (Melo *et al.*, 2013) is also supported by the observation that the self-quenching of its fluorescence intensity is much more pronounced for 5.0 μM compared to 2.0 μM HL488-sCT-containing samples.

The fluorescence emission decay kinetics of both 2.0 and 5.0 μM HL488-sCT was also influenced by the lipid concentration used in the assay. The decays were always well described by a tri-exponential function, as for 0.2 μM concentration, but now the amplitude-weighted mean fluorescence lifetime of the conjugated peptide, decreased from 3.4 ns in buffer solution to ~ 2.5 and to ~ 2.2 ns for 2.0 and 5.0 μM HL488-sCT, respectively, at low lipid concentrations, and then tended to recover their original value upon increasing the lipid concentration (Figure 3.41 C). The main factor responsible for this biphasic effect was the parallel changes detected in the normalized pre-exponential factor of the longer lifetime component, α_3, which decreased from ~0.80 to ~0.60 and to ~0.50 for 2.0 and 5.0 μM HL488-sCT, respectively, at a low L/P ratio (Figure S 3.5 A and C). Simultaneously, the short and long lifetimes were essentially independent of the lipid concentration used (τ_1~ 0.2 ns and τ_3~ 4.0 ns, respectively), while the intermediate lifetime slightly decrease from τ_2 ~ 2.0 ns to ~ 1.0 ns at low lipid concentrations (Figure S 3.5 A and C). These results indicate that the membrane-bound HL488-sCT might be adopting a different conformation in the oligomers formed at a low L/P ratio which leads to changes on the HL488 environment/proximity to intramolecular quencher groups, and thus induced a variation on the relative contribution of each lifetime to the fluorescence intensity decay of HL488-sCT. Alternatively (and not mutually exclusive) there might be a dynamic contribution to the self-quenching of HL488-sCT fluorescence intensity when the conjugated peptide reaches a high membrane surface concentration. In sum, the results obtained so far indicate that the self-quenching of HL488-sCT fluorescence intensity detected at a low L/P ratio displays both static and dynamic components (Lakowicz, 2006).

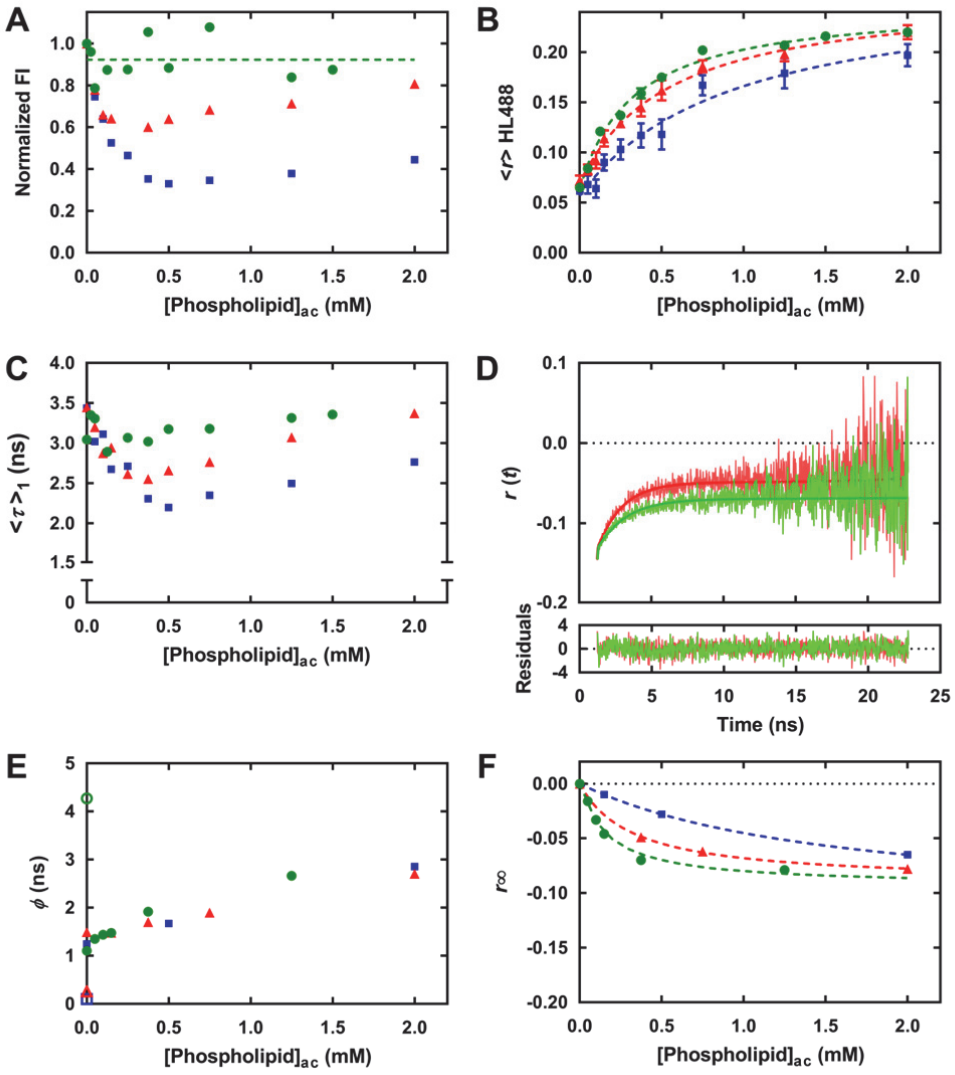

Figure 3.41 - The increase in the concentration of HL488-sCT reveals the formation of aggregates upon interaction with POPC:POPS 80:20 LUVs. Variation of the (**A**) fluorescence integrated emission area, normalized to its value in aqueous solution, ($\lambda_{exc} = 480$ nm, integrated area from 490-680 nm) (**B**) variation of ssFA, $\langle r \rangle_{HL488}^{480/525nm}$, (**C**) variation of amplitude-weighted mean fluorescence lifetime, $\langle \tau \rangle_1$ ($\lambda_{exc} = 335$ nm; $\lambda_{em} = 525$ nm), (**D**) fluorescence anisotropy decays of in the presence of 0.35 mM POPC:POPS 80:20 LUVs ($\lambda_{exc} = 335$ nm; $\lambda_{em} = 525$ nm), (**E**) Dependence of the rotational correlation times, ϕ_1 (open symbols) and ϕ_2(closed symbols), and (**F**) limiting anisotropy, r_∞, with the increasing concentration of accessible phospholipid for 0.2 μM (green), 2 μM (red) and 5 μM (blue) HL488-sCT. The solid lines in (**D**) are best fits of Eq. 3.26 to the experimental data. The bottom panel corresponds to the residuals of the fits. The results indicate the occurrence of static and dynamic quenching and suggest some depolarization by homo-FRET when higher concentrations of peptide are present.

Importantly, control experiments revealed that either concentration of the conjugated peptide was not able to induce the aggregation of the liposomes used because the light scattered by the liposomes showed an identical linear profile with the increasing lipid

concentration, in the absence and in the presence of the conjugated peptide (data not shown). Furthermore, an orthogonal control experiment was also performed by studying the variation of the fluorescence properties of HL488-sCT with its concentration in buffered solution. The integrated area of the fluorescence emission spectra of HL488-sCT varied linearly with the concentration of the conjugated peptide in solution, while the amplitude-weighted mean lifetime was fairly independent of the conjugated peptide concentration used (Figure S 3.6 B). Simultaneously, there was no evidence for peptide aggregation in aqueous solution since its ssFA remained essentially invariant with the increase in the labelled peptide concentration (Figure S 3.6). This study confirms that the addition of anionic lipid membranes is an absolute requirement for HL488-sCT to undergo a significant membrane-mediated aggregation at its surface which results in a pronounced self-quenching of its fluorescence emission at a low L/P ratio regime.

The ssFA for 2.0 and 5.0 μM HL488-sCT showed a hyperbolic increase upon rising the accessible phospholipid concentration in solution (Figure 3.41 B) documenting the progressive binding of the conjugated peptide to the anionic lipid membranes. If the interaction of the labeled peptide with the lipid membranes was described by a simple partitioning equilibrium, one would expect to obtain similar ssFA values for a fixed lipid concentration (Eq. 3.6), independently of the concentration of the conjugated peptide added to each sample. The experimental data does not comply with this prediction since the partition curves, particularly the ones obtained with 0.2 and 5.0 μM HL488-sCT, are not super-imposable (Figure 3.41 B). Since the majority of HL488-sCT oligomers are non-fluorescent (dark) complexes, the occurrence of significant intra-oligomeric homo-FRET, which would produce a strong depolarization of the emitted radiation (Davidson et al. 1998; Melo et al. 2014), can be ruled out as the factor responsible for this effect. In fact, no pronounced minima were detected in the variation of ssFA with [*L*] at low L/P ratios, at variance with a previous study performed with Alexa488-lysozyme (Melo et al. 2014). Most probably, the smaller overall increase in the ssFA of 5.0 μM compared to 0.2 μM HL488-sCT upon its membrane binding is due to a decrease in the average separation distance among the membrane-bound monomeric HL488-sCT, which results in some homo-FRET among these isolated fluorescent species.

The time-resolved fluorescence anisotropy measurements further corroborated this conclusion. One correlation time was used to describe the anisotropy decay curves obtained for all HL488-sCT concentrations in the presence of liposomes and a residual anisotropy value, was also included in these analyses since the fluorescence anisotropy decays of HL488-sCT did not converge to zero at longer times. This value reflects a restricted rotational motion of the fluorescently-labelled peptide upon binding to the anionic membrane. The depolarization of fluorescence comes from the local movement of the

labelled peptide exposed to the restrictions imposed by the lipid arrangement (fast timescale local motions), combined with the global rotation of the vesicle as a whole (slow timescale motion), which is in fact too slow to be significant during the time window defined by the excited-state lifetime of HL488-sCT (Zanin et al. 2013). As illustrate in Figure 3.41 D, the main effect on HL488-sCT anisotropy decays in interaction with 0.35 mM POPC:POPS 80:20 LUVs upon increasing its concentration from 0.2 to 2.0 μM was the obtention of a lower limiting anisotropy, r_∞, and not a much shorter rotational correlation time, which is the characteristic feature of strong intra-oligomeric homo-FRET (Yeow and Clayton, 2007; Bader *et al.*, 2011; Melo, Fedorov, *et al.*, 2014). In fact, whereas the progressive increase in the rotational correlation time of the conjugated peptide with the lipid concentration (which is reflecting its binding to the very large liposomes) was found to be essentially independent of the HL488-sCT concentration used in the assay (Figure 3.41 E), the limiting anisotropy values of the decays increased (to less negative values) for the highest concentration of HL488-sCT used (Figure 3.41 F).

3.4.3.7. **Discussion**

Quantitative evaluation of peptide binding to liposomes through the determination of their partition coefficients is the first key step in the elucidation of how anionic liposomes may influence the self-assembly mechanism of amyloidogenic peptides, in general, and of hCT and sCT, in particular. In fact, these equilibrium constants allow the calculation of the interfacial coverage of lipid vesicles with the peptide, which are often the critical parameter controlling the peptide membrane binding mode (peripheral *versus* partial insertion) and/or its membrane-bound conformation/oligomerization state. However, the majority of the spectroscopic binding studies performed with several CTs so far are essentially of a qualitative nature (Schmidt *et al.*, 1998; Wagner, Beck-Sickinger, *et al.*, 2004), and sometimes rely only on indirect evidences for the establishment of an association between the peptide and the lipid vesicles (e.g. Sheynis and Jelinek, 2010). Moreover, contradictory reports have also been published in some cases. For instance, hCT and its C-terminal fragment hCT(9-32) have been described to translocate the nasal epithelium (Schmidt *et al.*, 1998). Still, a solid-state NMR study surprisingly revealed that the fragment hCT(9-32), from L:P molar ratio between 20:1 and 200:1, is loosely associated with the phospholipid head groups at the surface of membranes composed of POPC:POPE:POPG (5:3:2), a phospholipid composition similar to the nasal epithelium (Wagner, Beck-Sickinger, *et al.*, 2004).

In the first part of this study, a complementary set of spectroscopic techniques (far-UV CD and steady-state and time-resolved fluorescence measurements) was therefore used to

quantitatively evaluate and compare the binding of unmodified and fluorescently-labelled CT variants to lipid membranes prepared with a variable anionic phospholipid content. Although the sCT solutions were 100-fold more concentrated in the CD compared to the fluorescence measurements made with the corresponding HL488-conjugated peptide, there was a very good quantitative agreement between the partition coefficients calculated from each data set (Table 3.18), ruling out that the possibility that the extrinsic fluorophore covalently-conjugated to the peptide might influence its behavior in relation to the lipid membranes.

Neither HL488-sCT (Figure 3.38) nor HL488-hCT (not shown) bound to zwitterionic POPC liposomes, as previously described for their interaction with 1,2-dimyristoyl-sn-glycero-3-phosphocholine (DMPC) liposomes (Epand *et al.*, 1983). However, whereas the partition of sCT/HL488-sCT was found to be strongly electrostatically-driven towards POPC liposomes containing more than 10 mol% of POPS (Figure 3.34 and Figure 3.38), there was no evidence for hCT/HL488-hCT binding to POPC:POPS lipid vesicles (Figure 3.34 and Figure 3.36) even when 50 mol% of POPS was included in the membranes (data not shown). This result is in general agreement with the study of Epand and collaborators (Epand *et al.*, 1983), where the authors describe that hCT was considerably less helical than sCT in the presence of DMPG liposomes: it was found that the propensity for the formation of α-helices – evaluated by the increase in the signal at 222 nm – was much less prominent in hCT ($[\theta]_{222\mathrm{nm}}$ = -2.24 x 10^3 deg cm^2 $dmol^{-1}$ res^{-1}) than for sCT and pCT ($[\theta]_{222\mathrm{nm}}$ = -12.35 x 10^3 and -8.13 x 10^3 deg $cm^2dmol^{-1}res^{-1}$, respectively). Still, channel formation was demonstrated for both sCT and hCT in black lipid membranes (BLM) made of DOPC:1,2-dioleoyl-sn-glycero-3-phosphoglycerol (DOPG) (85:15) (Stipani *et al.*, 2001). This discrepancy might be related with the method used to prepare the lipid membranes used in each case (see below). Overall, the distinct partition properties of sCT and hCT most probably reflect the different net charge of the peptides at pH 7.4, +3 and +1 for sCT and hCT, respectively, although the more pronounced spatial segregation of hydrophobic and hydrophilic groups in the AHs of sCT compared to hCT might also play a role (Figure 3.3). In fact, the extension of the AHs determined for each peptide in interaction with SDS micelles using NMR spectroscopy was quite different, namely between residues 9 and 16 for hCT (Motta *et al.*, 1998) and 6 and 22 for sCT (Morelli *et al.*, 1992).

Membrane binding of sCT was accompanied by a significant structural change according to the far-UV CD measurements. sCT assumes a random coil conformation with a far-UV CD minimum around 200 nm in aqueous solution, as it was previously described for hCT and sCT (Epand *et al.*, 2004; Gaudiano *et al.*, 2005; Kamgar-Parsi *et al.*, 2017) and other variants of this peptide (bCT, (Wang *et al.*, 2005b). The CD spectra changed, presenting two characteristic minima at 208 and 220 nm in the presence of a high concentration of POPC liposomes with more than 10 mol% of POPS, implying that the peptide adopts ~40%

of helical structure upon membrane binding in agreement with the literature (Epand *et al.*, 1986). Interestingly, the binding topology of the AH of eCT has been determined by performing NMR studies in oriented phospholipid bilayers of POPC:POPG 80:20 at 1 mol% peptide (Hashimoto *et al.*, 1999). As the amino acid sequence and biological activity of this CT variant resembles those of sCT, their membrane interactions are also expected to be similar. The authors found that the helix axis of the peptide lies in the plane of the lipid bilayer. This topology must favor the partially burying of the conjugated HL488 fluorophore at the membrane interface. From the maximal batochromatic spectral shift detected in the fluorescence emission spectra of HL488-sCT in interaction with anionic liposomes ($\Delta\langle\lambda\rangle$ ~ 4-5 nm), we estimated that the fluorophore is sensing a dielectric constant between the one of 2-propanol and 2-butanol (Table 3.12). The membrane anchoring of the fluorophore must also greatly impair the fast local/segmental motions of the conjugate dye since a single rotational correlation was necessary to describe the fluorescence anisotropy decay of HL488-sCT in the presence of increasing concentrations of POPC:POPS LUVS (Figure 3.41 E). The strong immobilization of the membrane-bound monomeric fluorescently-labeled peptide resulted in a pronounced increase in its ssFA (($\Delta\langle r\rangle$ ~ 0.17) (Figure 3.38), making this parameter an extremely faithful reporter of HL488-sCT binding to the liposomes.

The overall fluidity (ordered *versus* disordered), ganglioside and cholesterol content have all been shown to influence the fibrillation rates of amyloidogenic peptides and proteins and to be important factors in their anchoring to membranes (Kim *et al.*, 2006; Taylor and Hooper, 2006; Yanagisawa, 2015; Cebecauer *et al.*, 2017). Since Diociaiuti and collaborators (Diociaiuti *et al.*,2006) described that sCT forms annular oligomers in DPPC(1,2-dipalmitoyl-sn-glycero-3-phosphocholine):Chol:GM_1 (50:46:4) membranes and Sheynis and Jelinek (Sheynis and Jelinek, 2010) reported that cholesterol-containing membranes promoted the formation of an amyloid fibril network of hCT at the bilayer interface, more complex lipids/mixtures than POPC:POPS were also explored in this work. However, no evidence was found for HL488-hCT binding to POPC:POPE:POPG 50:30:20, DOPC:Chol 75:25, DOPC:SM 75:25, DOPC:SM:Chol 65:25:10 and DOPC:Chol:GM1 50:46:4 LUVs (Figure 3.37), even at 1 mM of accessible phospholipid concentration. These results led us to not further pursue the study of hCT/HL488-hCT and to focus instead on the characterization of the putative oligomeric species formed by sCT in lipid membranes.

The first indication for membrane-induced oligomerization of HL488-sCT came from the detection of a shoulder at low wavelengths in the normalized red-shifted absorption spectra obtained for 2 μM, and particularly 5 μM of HL488-sCT (compared to 0.2 μM HL488-sCT) in interaction with POPC:POPS 80:20 liposomes at low L/P ratio (high concentrations of conjugated peptide coupled to low phospholipid concentrations) (Figure 3.40 A). Exciton

theory predicts that additive interactions like van der Waals and/or hydrogen bonding can hold the dye ions together in solution and the excited-state levels of the monomer split in two upon dimerization. This phenomenon leads to distinct changes in the absorption spectrum as compared to the monomeric species and can be used to track the aggregation of labeled peptides/phospholipids in solution/liposomes (Bergström *et al.*, 2002). The changes in the absorption spectrum depend on the possible transitions from the ground state to either excited state, which are related with the geometry of the dimer: (a) for parallel dimers (H-type), the transition to the lower energy excited state is forbidden and the spectrum consists of a single band blue-shifted with respect to the monomer; (b) for head-to-tail dimers (J-type) the transition to the higher energy excited state is forbidden and the spectrum shows a single band red-shifted with respect to the monomer; (c) in dimers having intermediate geometries, both transitions are partially allowed and band splitting is observed.(Maiti *et al.*, 1998; Bergström *et al.*, 2002; Castro *et al.*, 2012) (Figure 3.42).

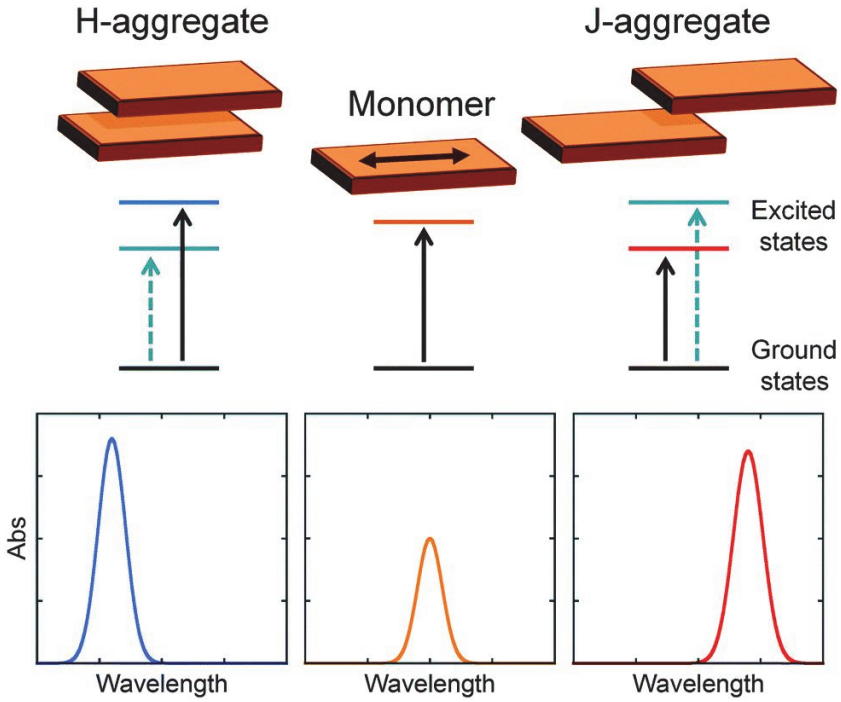

Figure 3.42 - Changes in the absorption spectra depending on the arrangements of H- and J-aggregates – exemplified for a dimer - of a π-conjugated molecule (monomer). When two dipoles are brought to close proximity side by side the energy of the individual molecules will split into two new states: One level is of lower and the other of higher energy than the monomer excited state. Parallel dipoles make up an overall higher dipole moment, i.e. stronger absorption, and the net result is a blue shift of absorption (hypsochromic). Similarly, for head-to-tail arrangement, the lower energy state has a larger transition dipole moment and the net effect is a red shift of absorption. The intermediate, oblique, orientation results in band split. Full arrows depict allowed (strong) transitions, and dashed arrows forbidden (or weak) ones. The double arrow represents the transition dipole for the monomer. Adapted from (Pescitelli *et al.*, 2014).

During the formation of H-type aggregates, like we detected in this study, the excited state of lower energy is better stabilized. Therefore, the transitions from the excited state to the ground state are very fast and happen mostly between the excitonic bands with vanishing dipole moments. As a result, most of the energy losses are non-radiative (e.g. thermal losses). Due to this reason the H-aggregates have very low florescence leading to the formation of non-fluorescent (dark) complexes, which are difficult to measure by regular techniques.

Accordingly, both the integrated emission area and amplitude-weighted mean fluorescence lifetime of both 2.0 and 5.0 μM HL488-sCT presented a biphasic behavior in the presence of POPC:POPS 80:20 liposomes: both parameters first decreased when low concentrations of phospholipid were added to the solution (~ 0.25 mM accessible phospholipid) and then progressively recovered upon further increase of the phospholipid concentration to values near the ones obtained in buffer (Figure 3.41 A and C, respectively). Upon reaching a high local membrane surface concentration (at low L/P ratio), the membrane-anchored peptides associate in-register, parallel to each other, in order for the chromophores to be able to interact with each other. Consequently, there is a strong static quenching of their fluorescence. Upon further increasing the liposome concentration in solution, the surface concentration of the membrane-bound peptides becomes progressively diluted on the liposome surface, effectively preventing their oligomerization (Figure 3.43), and the conjugated peptides partially recover their fluorescence intensity/lifetime

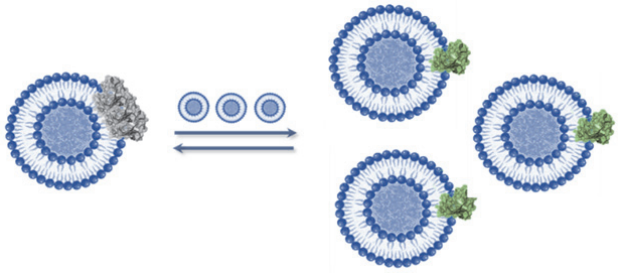

Figure 3.43 - Influence of the peptide/lipid molar ratio on oligomer formation. Upon increasing the phospholipid concentration, the surface concentration of membrane bound-peptide becomes more diluted preventing oligomerization on the membrane surface and recovering the fluorescence intensity.

It should be noted that the decrease in the steady-state fluorescence intensity of HL488-sCT relatively to its value in aqueous solution was much higher than the concomitant decrease detected in its amplitude-weighted mean lifetime. As already discussed, these results might indicate that some of the membrane-bound HL488-sCT participating in oligomer formation may be in a different conformation than their monomeric membrane-

bound counterparts, which leads to changes on the HL488 environment/proximity to intramolecular quencher groups, and thus inducing a variation on the relative contribution (normalized amplitude) of each lifetime to the fluorescence intensity decay of HL488-sCT. Eventually, there might also be a dynamic (diffusion-controlled) contribution to the self-quenching of HL488-sCT fluorescence intensity when the conjugated peptide reaches a high membrane surface concentration. Altogether, the steady-state and time-resolved fluorescence measurements of HL488-sCT at a low L/P ratio indicates that its self-quenching detected displays both static and dynamic components (Valeur and Berberan-Santos, 2012). Unfortunately, however, the fact that the majority of HL488-sCT membrane-bound oligomers are non-fluorescent prevented the application of a quantitative model describing the coupled partition/oligomerization of the conjugated peptide at the membrane surface at low L/P which would eventually allow us to retrieve information like the oligomer stoichiometry from the variation of their ssFA as function of accessible phospholipid concentration (Melo, Fedorov, *et al.*, 2014).

The work of Stipani and co-workers (Stipani *et al.*, 2001) was the earliest study describing that both sCT and hCT have channel-forming activity in BLMs prepared with a mixture of DOPC and DOPG (85:15). Their preliminary results with other calcitonins (eel and porcine) also showed this activity. No channel activity was found for hCT and sCT peptides in BLM of DOPC or PhC, corroborating other observations that there are no strong interactions between different CTs and zwitterionic lipids, such as DMPC, DPPC or SM (Epand *et al.*, 1983, 2004; Wagner, Van Mau, *et al.*, 2004; Gaudiano *et al.*, 2005). This work also underlined that if CTs indeed form a channel, it must aggregate into oligomers, since the α-helical portion of the CTs is not sufficiently long to span the lipid membrane (Stipani *et al.*, 2001). Later on, Diociaiuti and co-workers showed that sCT strongly interacts with raft-like liposomes (DPPC:Chol:GM1 50:46:4 mol%), formed annular oligomers (shown by negative contrast TEM) with a rich β-sheet structure and ion-channel activity, while it interacts only slightly with DPPC with no significant conformational modification (Diociaiuti *et al.*, 2006). The formation of these ion channels allowed calcium to cross the lipid membranes, which made the authors speculate if the formation of these channels could have a physiological significance in the role of CT in calcium homeostasis. This type of pores has been suggested to be formed by many other amyloid proteins reconstituted in liposomes and studied by atomic force microscopy (Quist *et al.*, 2005). One should be aware, however, that a direct comparison between these studies is not straightforward because very different peptide concentrations were used in these studies compared to our work: 5 μM (in our case) *versus* 1 mg of sCT – corresponds to approximately 290 μM (Diociaiuti *et al*., 2006) and 49 to 125 nM of hCT and sCT (Stipani *et al*., 2001). Given the very different techniques/model systems of membranes employed in these studies, one might speculate

that such a high concentration of peptide in Diociaiuti *et al*., 2006 was needed to form aggregates large enough to be seen in TEM. For Stipani *et al*., 2001, single-channel conductance measurements were performed in nanomolar regimes, since it is important that the peptides used form defined channels but do not act as detergents inducing lipid perturbation.

3.5. Conclusions

In summary, the solvatochromic study of HL488 revealed that the spectroscopic properties of this fluorophore do not conform to the general solvent effects theory since the hydrogen-bonding power of the solvents used strongly influenced the spectral shifts/photophysical properties of this fluorescent probe. Nevertheless, HL488 was confirmed to be a good fluorescence reporter of the overall rotational dynamics of peptides/proteins in solution. The combination of far-UV CD measurements with steady-state and time-resolved fluorescence data was found to be a useful approach that provided valuable information about the influence of the solvent on the conformational dynamics of fluorescently-labeled human and salmon calcitonins in solution.

Regarding the fibrillation kinetic studies of CTs, the preliminary data obtained for hCT in solution suggest that this process does not obey a standard mechanism. After improving the reproducibility of the microplate reader fibrillation assays, further studies are necessary to evaluate if the non-canonical fibrillation model recently proposed in the literature (Kamgar-Parsi *et al*., 2017) can be extended to our experimental conditions.

Finally, the partition studies confirmed the importance of electrostatic interactions in sCT/HL488-sCT binding to the lipid membranes, while no significant binding was observed for hCT/HL488-hCT using a wide range of lipid compositions. The study further established that the addition of anionic lipid membranes is an absolute requirement for HL488-sCT to undergo a significant membrane-mediated aggregation at the liposome surface. This results in a pronounced self-quenching of HL488-sCT fluorescence emission at a low L/P ratio regime, with both static and dynamic components. The formation of these dimers/oligomers might be related with the proposed ion channels observed by others regarding sCT (Stipani *et al.*, 2001; Diociaiuti *et al.*, 2006) and other amyloid proteins reconstituted in liposomes (Quist *et al.*, 2005).

3.6. Supplementary Information

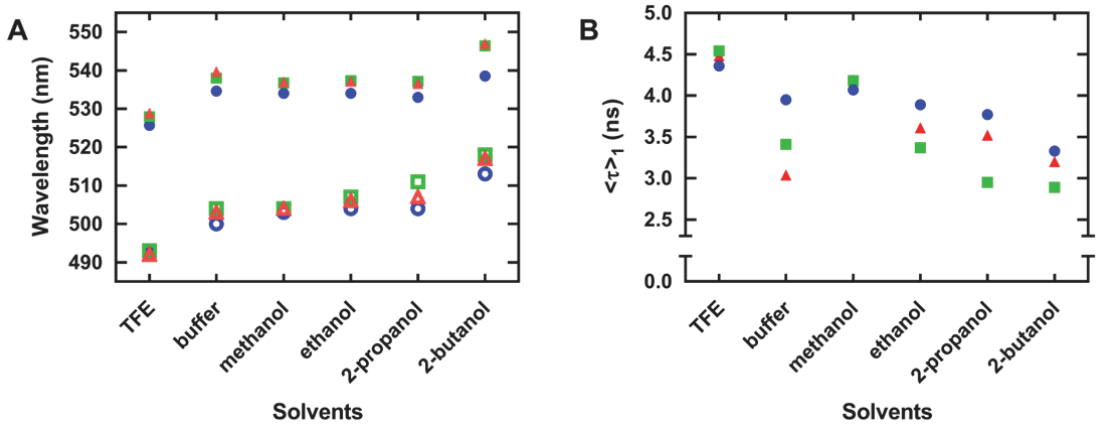

Figure S 3.1 - Solvatochromic and photophysical studies of the free probe HL488, HL488-hCT and HL488-sCT using pure solvents at 25 ºC. Variation of (**A**) the maximum absorption wavelength, λ_{max}^{Abs} (open symbols) and intensity-weighted average emission wavelength, $\langle\lambda\rangle$ (closed symbols), and of the (**B**) mean fluorescence lifetime, $\langle\tau\rangle_1$, with the solvent used for the free probe (blue circles), HL488-hCT (red triangles) and HL488-sCT (green squares), respectively.

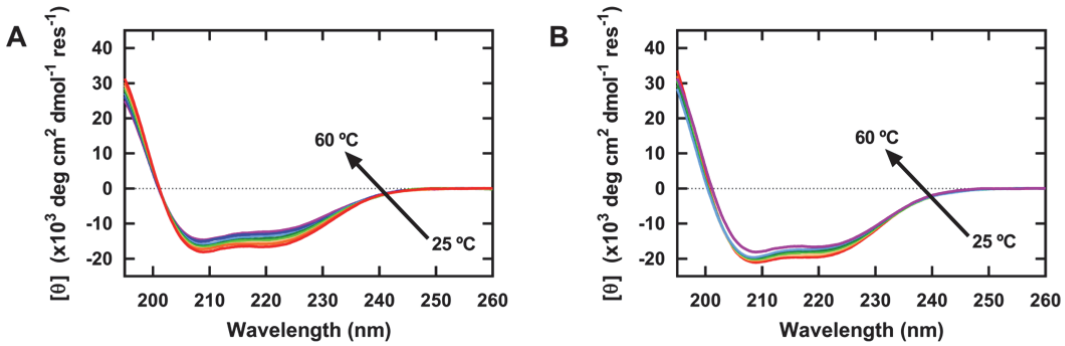

Figure S 3.2 - The secondary structure of hCT and sCT solubilized in 100% TFE is essentially independent of temperature. Far-UV CD spectra obtained for (**A**) hCT and (**B**) sCT at different temperatures. The helical content of the peptides changed from 47% to 35% and from 56% to 47% for hCT and sCT, respectively, upon increasing the temperature from 25 to 60 ^{o}C.

Table S 3.1 - Influence of temperature on the fluorescence intensity decay and rotational dynamics of HL488-hCT and HL488-sCT solubilized in TFE evaluated using time-resolved fluorescence intensity and anisotropy measurements. Fluorescence lifetime, τ amplitude, β_i and rotational correlation time, $\boldsymbol{\phi_i}$, of the *i*th decay component of the anisotropy decay, respectively, $\boldsymbol{r(0) = \beta_1 + \beta_2}$, apparent hydrodynamic volume, $\boldsymbol{V_h^{app}}$, and semi-angle, θ_{seg}, associated with the fast localized motions of the covalently-linked conjugated dye calculated according to the "wobbling-in-cone" model. The % helicity was determined with Eq. 3.13 from the data obtained by CD with 20 μM of unlabeled CT.

Peptide	Temperature (ºC)	τ (ns)	χ^2_G	β_1	ϕ_1 (ns)	β_2	ϕ_2 (ns)	$r(0)$	χ^2_G	V_h^{app} (nm^3)	θ_{seg} (degrees)	% helicity
hCT/ HL488-hCT	25	4.57 [4.53;4.58]	1.11	-0.043	0.61 [0.52;0.71]	-0.115	6.49 [6.29;6.73]	-0.158	1.09	14.6	23.4	47.5
	30	4.58 [4.54;4.59]	1.01	-0.039	0.75 [0.65;0.86]	-0.115	5.98 [5.79;6.20]	-0.154	1.01	15.6	25.1	45.3
	35	4.58 [4.54;4.59]	1.25	-0.044	0.69 [0.60;0.79]	-0.108	5.17 [5.005.36]	-0.152	1.00	15.4	27.0	43.7
	40	4.59 [4.55;4.60]	1.01	-0.042	0.67 [0.59;0.78]	-0.108	4.35 [4.22;4.52]	-0.150	1.05	14.9	26.3	42.5
	45	4.59 [4.55;4.61]	1.04	-0.049	0.79 [0.70;0.89]	-0.098	4.20 [4.02;4.40]	-0.147	1.00	16.4	29.3	40.9
	50	4.59 [4.55;4.61]	1.24	-0.054	0.60 [0.53;0.68]	-0.099	3.80 [3.68;3.94]	-0.153	1.07	16.7	30.2	38.7
	55	4.60 [4.56;4.61]	0.99	-0.043	0.43 [0.36;0.50]	-0.106	3.00 [2.91;3.11]	-0.149	0.94	14.8	26.9	37.3
	60	4.59 [4.55;4.60]	1.01	-0.053	0.55 [0.49;0.62]	-0.095	2.91 [2.76;3.05]	-0.147	1.05	16.3	30.4	35.3
sCT/ HL488-sCT	25	4.55 [4.51;4.56]	1.03	-0.063	0.73 [0.67;0.80]	-0.091	5.26 [5.04;5.56]	-0.154	1.08	12.7	33.3	55.5
	30	4.55 [4.51;4.56]	1.06	-0.067	0.76 [0.69;0.83]	-0.083	4.78 [4.52;5.05]	-0.150	1.13	12.4	35.1	53.9
	35	4.55 [4.51;4.57]	1.15	-0.068	0.67 [0.61;0.74]	-0.083	4.21 [3.98;4.45]	-0.151	1.18	12.6	35.4	53.1
	40	4.56 [4.52;4.57]	0.96	-0.069	0.53 [0.48;0.58]	-0.080	3.69 [3.45;3.94]	-0.149	1.03	12.6	35.8	51.6
	45	4.54 [4.50;4.57]	1.18	-0.072	0.43 [0.39;0.47]	-0.081	3.36 [3.18;3.56]	-0.153	1.01	13.1	36.4	50.6
	50	4.57 [4.53;4.59]	0.99	-0.072	0.47 [0.42;0.51]	-0.074	2.98 [2.86;3.15]	-0.146	1.05	13.1	37.6	48.9
	55	4.58 [4.54;4.59]	1.02	-0.076	0.44 [0.40;0.49]	-0.068	2.95 [2.76;3.15]	-0.144	1.01	13.8	37.8	47.5
	60	4.58 [4.54;4.59]	1.11	-0.072	0.32 [0.28;0.35]	-0.072	2.33 [2.21;2.46]	-0.144	1.05	13.1	37.6	47.5

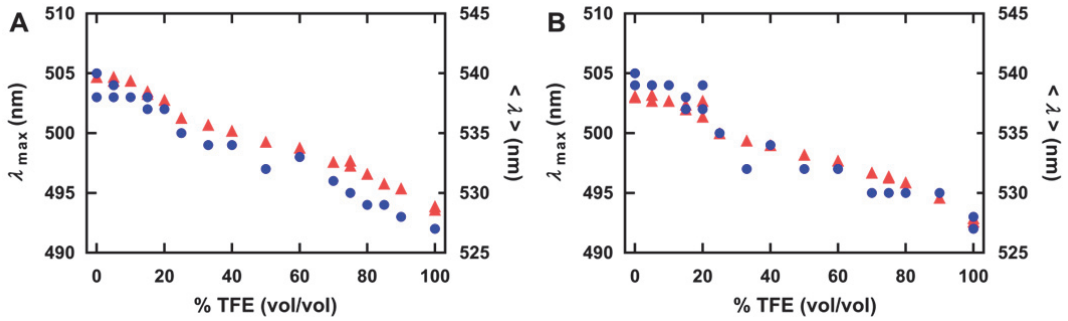

Figure S 3.3 - Solvatochromic study of HL488-hCT and HL488-sCT in binary TFE/buffer mixtures at 25 ºC. Variation of the maximum absorption wavelength, λ_{max}^{Abs} (red triangles, left axis) and intensity-weighted average emission wavelength, $\langle\lambda\rangle$ (blue circles, right axis) with the TFE content of the binary mixture for (**A**) HL488-hCT and (**B**) HL488-sCT.

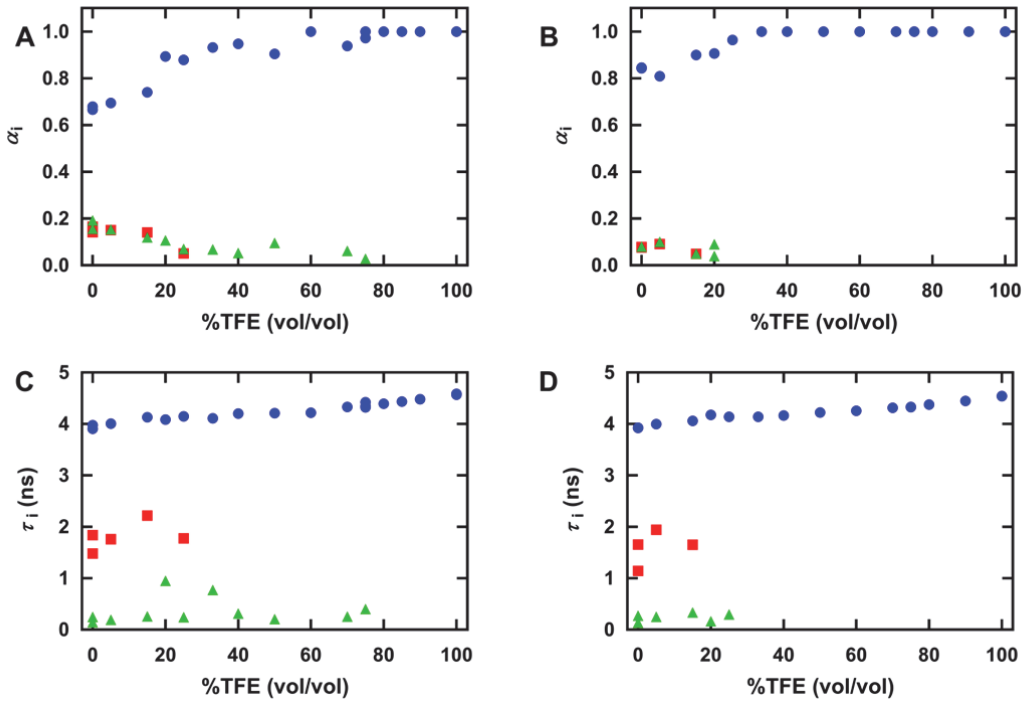

Figure S 3.4 - Influence of the TFE content on the fluorescence intensity decay parameters obtained for the CT conjugated peptides in TFE/buffer binary mixtures at 25 ºC. Variation of (**A** and **B**) the fractional amplitudes (α_1, green triangles; α_2, red squares and α_3, blue circles, respectively) and (**C** and **D**) lifetime components (τ_1, green triangles; τ_2, red squares and τ_3, blue circles, respectively) for (**A** and **C**) HL488-hCT and (**B** and **D**) HL488-sCT with the TFE content of the binary mixture at 25 °C (see Table 3.11 and Table 3.12 for more details).

Table S 3.2 – Influence of CT concentration on the fluorescence intensity decay parameters obtained for hCT and sCT samples containing 0.2 μM of the corresponding conjugated peptide at the end stage of their fibrillation kinetic assay. The fluorescence emission kinetics were measured using $\boldsymbol{\lambda_{exc}}$= 335 nm and $\boldsymbol{\lambda_{em}}$= 525 nm. $\boldsymbol{\alpha_i}$ normalized amplitudes; $\boldsymbol{\tau_i}$ fluorescence lifetimes; $\langle\boldsymbol{\tau}\rangle_{\mathbf{1}}$ and $\langle\boldsymbol{\tau}\rangle_{\mathbf{2}}$, amplitude-weighted and intensity-weighted mean fluorescence lifetimes, respectively. The goodness-of-fit was judged by the $\boldsymbol{\chi^2_G}$ value. Values in brackets are the errors of the recovered parameters estimated as the lower and upper bound of the joint confidence interval calculated for a 67% probability level.

[CT] (μM)		α_1	τ_1 (ns)	α_2	τ_2 (ns)	α_3	τ_3 (ns)	$\langle\tau\rangle_1$ (ns)	$\langle\tau\rangle_2$ (ns)	χ^2_G
with HFIP										
hCT	1	0.56	0.17 [0.17,0.18]	0.20	1.27 [1.24,1.29]	0.24	4.16 [4.16,4.19]	1.36	3.35	1.39
	5	0.38	0.25 [0.24,0.26]	0.40	1.24 [1.24,1.25]	0.22	3.26 [3.26,3.29]	1.30	2.26	1.13
	10	0.27	0.27 [0.27,0.29]	0.35	1.55 [1.53,1.57]	0.38	3.58 [3.57,3.59]	1.98	2.91	0.99
	15	0.25	0.28 [0.27,0.30]	0.31	1.65 [1.63,1.68]	0.44	3.68 [3.67,3.71]	2.19	3.09	1.12
	20	0.26	0.24 [0.23,0.25]	0.33	1.47 [1.47,1.49]	0.41	3.55 [3.52,3.61]	1.99	2.94	1.07
sCT	1	0.09	0.22 [0.19,0.25]	0.08	1.43 [1.37,1.51]	0.83	3.92 [3.91,3.95]	3.39	3.81	0.99
	10	0.07	0.33 [0.28,0.37]	0.10	2.05 [1.99,1.81]	0.83	3.95 [3.95,3.98]	3.50	3.81	1.03
	20	0.07	0.28 [0.24,0.31]	0.09	1.73 [1.63,1.81]	0.84	3.92 [3.88,3.95]	3.46	3.80	0.90
without HFIP										
hCT	1	0.53	0.38 [0.37,0.40]	0.29	2.16 [2.13,2.24]	0.17	6.43 [6.42,6.54]	1.96	4.42	1.26
	5	0.37	0.30 [0.29,0.31]	0.43	1.76 [1.73,1.77]	0.21	4.00 [4.00,4.03]	1.68	2.76	1.23
	10	0.27	0.304 [0.29,0.32]	0.35	1.80 [1.78,1.82]	0.38	3.897 [3.86,3.91]	2.21	3.17	1.19
	15	0.24	0.322 [0.30,0.34]	0.31	1.96 [1.94,2.00]	0.46	3.97 [3.97,4.00]	2.49	3.37	1.07
	20	0.19	0.34 [0.32,0.36]	0.28	1.84 [1.81,1.87]	0.53	3.94 [3.94,3.97]	2.67	3.45	1.17
sCT	20	0.08	0.33 [0.23,0.37]	0.17	2.00 [1.85,2.04]	0.82	4.00 [3.99,4.03]	3.50	3.85	1.08

Table S 3.3 - Fluorescence anisotropy decay parameters for 20 μM hCT and sCT samples containing 0.2 μM of the corresponding conjugated peptide at the end stage of their fibrillation kinetic assay. The anisotropy decays were measured using λ_{exc}= 335 nm and λ_{em}= 525 nm. β_i fractional amplitudes; ϕ_i, rotational correlation time; $r(0) = \beta_1 + \beta_2$. For additional details, see the legend of Figure 3.33.

[CT]	β_1	ϕ_1 (ns)	β_2	ϕ_2 (ns)	$r(0)$	χ^2_G
with HFIP						
hCT	-0.03	1.99 [1.49,2.26]	-0.07	240.6 [61.8,-]	-0.10	1.09
sCT	-0.05	0.37 [0.31,0.44]	-0.09	1.62 [1.54,1.71]	-0.14	0.98
without HFIP						
hCT	-0.03	1.36 [1.09,1.68]	-0.10	75.7 [61.2,99.7]	-0.13	1.11
sCT	-0.06	0.48 [0.41,0.55]	-0.09	1.9 [1.7,2.0]	-0.14	1.08

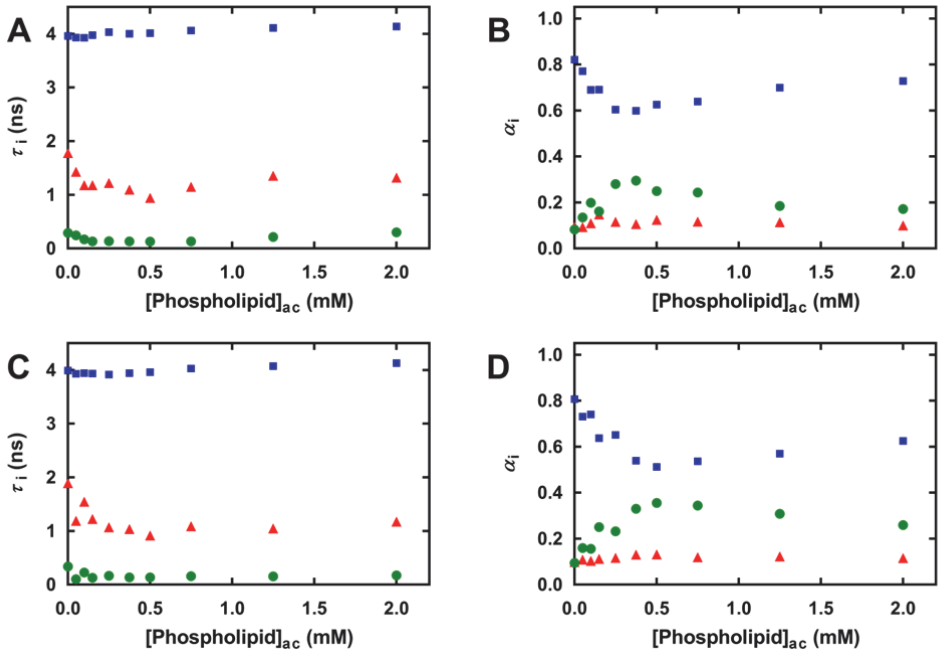

Figure S 3.5 - Changes in the time-resolved fluorescence emission components of HL488-sCT upon interaction with POPC:POPS 80:20 LUVs at 25 ºC. Variation of each lifetime component, τ_i (**A, C**) and the corresponding pre-exponential factors, α_i (**B, D**) obtained from the analysis of fluorescence emission decay kinetics in the presence of increasing accessible phospholipid concentrations for (**A** and **B**) 2.0 μM HL488-sCT and (**C** and **D**) 5.0 μM HL488-sCT.

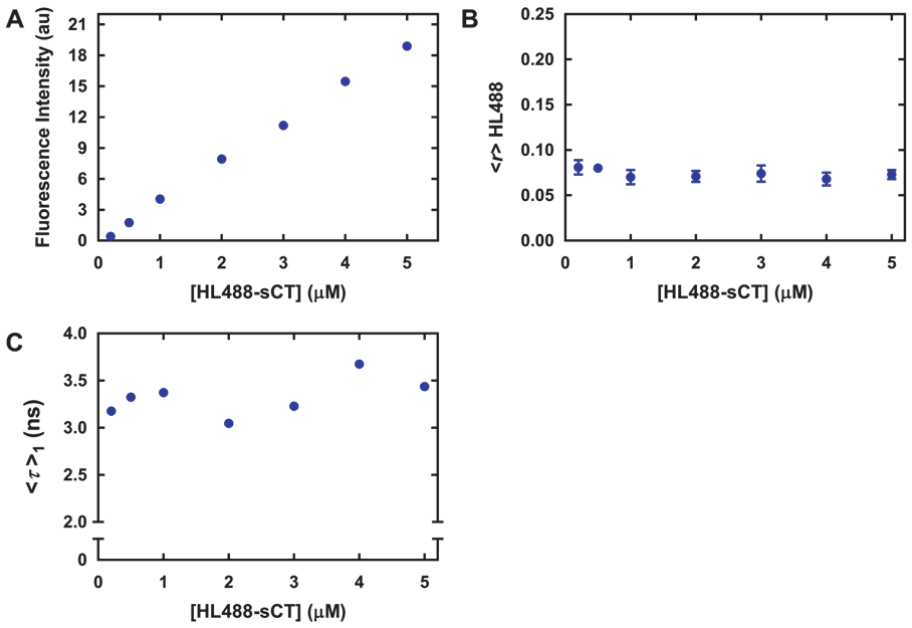

Figure S 3.6 - The fluorescence properties of HL488-sCT do not change significantly in buffer over the range of peptide concentrations used in the interaction studies of the conjugated peptide with LUVs prepared with variable lipid compositions. Variation of the (**A**) Fluorescence integrated emission area ($\lambda_{exc} = 480$ nm, integrated area from 490-680 nm) (**B**) variation of ssFA, $\langle r \rangle_{HL488}^{480/525nm}$ and (**C**) variation of amplitude-weighted mean fluorescence lifetime, $\langle \tau \rangle_1$ ($\lambda_{exc} = 335$ nm and $\lambda_{em} = 525$ nm) of increasing concentration of HL488-sCT in buffer. The fluorescence intensity of HL488-sCT increases linearly with the increase in the concentration. On the other hand, neither (**B**) $\langle r \rangle_{HL488}$ nor (**C**) $\langle \tau \rangle_1$ changed significantly with the increase in the labelled peptide concentration, revealing that there is not the formation of significant aggregates in buffer

3.6.1. The presence of a small amount of HFIP greatly influences the interaction kinetics of HL488-sCT with liposomes

The interaction of HL488-sCT/HL488-hCT with liposomes prepared with a variable lipid composition was studied in parallel to the CT fibrillation assays described in section 3.4.2. Control measurements showed that the method used to prepare the samples strongly impacted the interaction kinetics of HL488-sCT with POPC:POPS 80:20 LUVs, as illustrated in Figure S 3.7. The samples were prepared using either Method I or II, as described in Section 3.3.3. Briefly, an intermediate working peptide solution was prepared from the more concentrated stock solution in HFIP, either by directly injecting the appropriate amount of peptide in HFIP into a buffer solution (Method I) or by evaporating the organic solvent prior to the preparation of the intermediate peptide stock solution in buffer (Method II). The fluorescence intensity and ssFA of 0.2 μM HL488-sCT were then measured over time in the absence and in the presence of variable concentrations of lipid vesicles composed of POPC:POPS 80:20. When the samples were prepared in the presence of a small amount of HFIP (Method I), their fluorescence intensity and ssFA increased over time, particularly in the presence of high phospholipid concentrations: these samples took several hours to

reach a stable equilibrium value for their fluorescence intensity, and the sample containing 3 mM of total phospholipid did not reach a constant value at all even after an incubation time of 40 h (Figure S 3.7 A and B). On the other hand, when Method II was used to prepare the samples, both the fluorescence intensity and ssFA of 0.2 μM HL488-sCT proved to be constant over time for all the lipid concentrations tested (Figure S 3.7 C and D). These results led us to abandon Method I and to adopt Method II of sample preparation instead for the rest of the work developed.

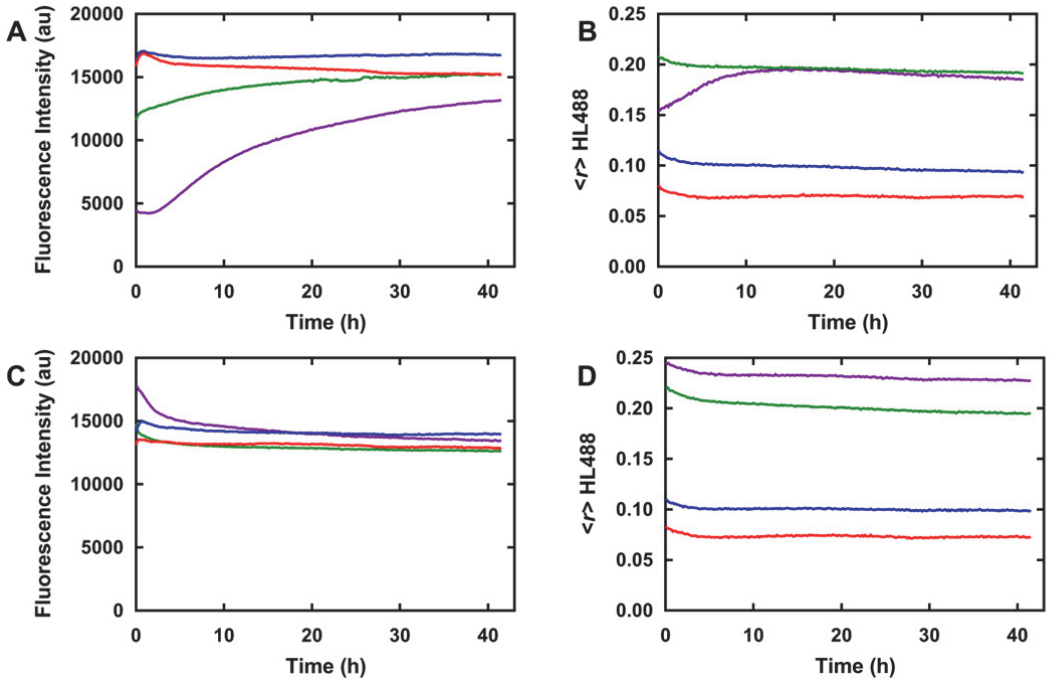

Figure S 3.7 - The method used to prepare the peptide samples strongly impacts the interactions kinetics of HL488-sCT with POPC:POPS 80:20 LUVs. Changes in (**A** and **C**) the total fluorescence intensity (*I54*) and (**B** and **D**) in the ssFA of 0.2 μM HL488-sCT, $\langle r \rangle_{\mathbf{HL488}}^{\mathbf{485/520nm}}$, over time at 25 ºC. The samples were prepared using (**A** and **B**) Method I or (**C** and **D**) Method II, as described in detail in section 3.3.3. The measurements were performed in the absence (red curve) or in the presence of 0.1 mM (blue curve), 1.0 mM (green curve) and 3 mM (purple curve) of POPC:POPS 80:20 LUVs using a microplate reader.

4. Islet Amyloid Polypeptide

4.1. Overview

Membrane-catalyzed amyloid fibril formation of human islet amyloid polypeptide (hIAPP) or amylin has been implicated as a mechanism by which hIAPP exerts its toxicity in type 2 diabetes. On the other hand, the membrane-bound aggregates of the rat variant of IAPP (rIAPP) are unable to progress into fibrillar structures since this is a non-amyloidogenic peptide. Here, we combined steady-state and time-resolved fluorescence measurements with fluorescence microscopy studies to comparatively examine how anionic lipid membranes control the self-assembly of these two peptides. Our studies confirmed that membrane-catalyzed fibrillation of hIAPP results in fibril growth into the solution. However, the membrane-mediated self-assembly of rIAPP is confined to the lipid bilayer. A direct correlation was established between the progressive membrane surface saturation with rIAPP and the ability of the peptide in reducing the average size of the anionic liposomes used in the assay. Furthermore, a time-resolved emission spectra (TRES) study of Laurdan revealed that membrane binding and oligomerization of rIAPP produced an increased rigidity and surface dehydration in the vicinity of the fluorescent probe that ultimately might be responsible for the ability of rIAPP to remodel the lipid membranes.

The experimental design was shared by me and Prof. Ana Coutinho, while the laboratory work and data analysis were performed by me with the following exceptions:

- all the time-resolved fluorescence measurements were performed by Dr. Aleksander Fedorov (CQFM/IBB, IST, UL, Portugal).
- the far-UV CD measurements were performed at Nuno C. Santos Lab (IMM, UL, Portugal) with the aid of Dr. André Faustino (both in laboratory work and data analysis), to whom we are much thankful;
- the TEM images were obtained at the Electron Microscopy Facility of Instituto Gulbenkian de Ciência (Oeiras, Portugal) with the support of M.Sc Ana Vinagre;
- the control experiments of TRES of Laurdan/POPC LUVs were performed by M.Sc Gustavo Scanavachi, from the Department of Applied Physics from the University of São Paulo (Brasil), to validate the script that he wrote in gnuplot® to analyze the data. He also wrote a script for the quantitative analysis of fibrillation kinetic assays.

Prof. Ana Coutinho and Prof. Manuel Prieto supervised the work.

4.2. Introduction

4.2.1. IAPP and Type 2 diabetes mellitus

The β-cells found within the islets of Langerhans of the pancreas are the most well-known site for the production of IAPP. The discovery of this peptide hormone, also called amylin, was made here, in the form of amyloid fibrils observed in patients with T2DM and in diabetic cats (Westermark *et al.*, 1986, 1987). IAPP is also expressed in the δ-cells in rat and mouse, in the gastrointestinal tract of rat, mouse, cat and human, and in sensory neurons in rats (Westermark *et al.*, 2011). This 37-amino acid peptide hormone is generated by proteolysis of an inactive 67 amino acid long pro-peptide and is processed and co-secreted with insulin in those cells (Bharadwaj *et al.*, 2018). IAPP has an effect on insulin secretion dependent on its concentration. A low IAPP concentration increases the basal insulin release and a higher concentration inhibits the secretion of insulin induced by glucose. IAPP also inhibits glucagon release, inhibits gastric emptying similar to glucagon-like peptide and decreases food intake; interestingly, it also inhibits bone resorption (Suckale and Solimena, 2010; Wielinga *et al.*, 2010; Bharadwaj *et al.*, 2018). Although IAPP is a hormone, specific receptors for this peptide have not been found. Only some specific binding sites have been identified in the brain and in the renal cortex (Westermark *et al.*, 2011; Caillon *et al.*, 2013).

The human peptide is mainly stored in the halo region of β-cell insulin granules, along with C-peptide and other components. The intragranular pH has been estimated to be 5-6, favorable for the basic hIAPP to remain soluble; these are also the optimal conditions for the crystallization of zinc-insulin hexamers, the known way for insulin to be stored (Hutton, 1982; Suckale and Solimena, 2010; Nanga *et al.*, 2011; Caillon *et al.*, 2015). IAPP is probably protected from aggregation by interaction with other components, including insulin, which has been found to effectively inhibit IAPP fibril formation (Westermark *et al.*, 1996). IAPP is than released to the extracellular compartment, which has a pH of 7.4 (Caillon *et al.*, 2015). This feature is important regarding the charge of the peptide, its aggregation and the interaction with membranes.

Regarding the relation of IAPP and T2DM, there seems to be a loop in cause-effect consequences. Insulin resistance is a pathological condition in which cells fail to respond normally to insulin, verified in metabolic syndrome, obesity or even pregnancy (Hull *et al.*, 2004). In a normal situation, the organism response to the release of insulin is the cellular uptake of glucose from the bloodstream to be used as a energy source and a concomitant inhibition of the use of stored lipids. Here, the concentration of glucose in the blood decreases within normal ranges. The resistance to insulin by cells leads to a high blood glucose level that in turn stimulates β-cells of the pancreas to increase the production of insulin, and so on. This contributes to the development of T2DM. Since to an increased

production of insulin in humans is associated an increased production of human IAPP (hIAPP), this may favor the interaction between different monomers and, eventually, the induction of fibrillation (Mulder *et al.*, 1996; Westermark *et al.*, 2011). hIAPP and insulin ratio was found to be 1:100 in healthy individuals, while it increases to 1:20 in T2DM (Caillon *et al.*, 2015; Ke *et al.*, 2017). The misfolding or abnormal accumulation of IAPP in the pancreas contribute to the death of insulin-producing pancreatic islet β-cells (Sparr *et al.*, 2004). hIAPP amyloid deposits are found in more than 95% of T2DM patients. Whether islet amyloidosis is the cause or the consequence of the disease it is still unclear (Singh *et al.*, 2015). Despite of extensive research, the exact toxic mechanism by which hIAPP fibrillation contributes to the disruption of β-cells is still unknown and numerous efforts are underway to try to understand its aggregation pathway (Zhao *et al.*, 2014).

There has also been evidence that links T2DM and neurodegenerative diseases. Recently, several studies in AD animal models have shown that diet or chemically induced impairments in insulin signaling promoted AD pathology, synaptic degeneration and neuronal dysfunction, with neuroinflammatory and oxidative stress mechanisms pointed as possible underlying mechanisms (Bharadwaj *et al.*, 2018).

4.2.2. Structural and conformational features of IAPP

IAPP has a disulfide bond between cysteines 2 and 7 and is C-terminally amidated, pre-requisites for full biological activity (Westermark *et al.*, 2011). All species have a tyrosine residue in position 37, useful for intrinsic fluorescence studies of these peptides (Figure 4.1 A). hIAPP and the non-amyloidogenic rat variant (rIAPP) are soluble and unstructured in solution, being classified as IDPs. The majority of structural information of the supposedly IAPP monomers is acquired using CD shortly after sample preparation for the case of hIAPP (Jayasinghe and Langen, 2005; Knight *et al.,* 2006; Abedini *et al*., 2007; Engel, 2009; Caillon *et al*., 2013). This variant will usually aggregate in a manner of minutes to hours depending on the concentration and physiological buffer it is dissolved (Caillon *et al*., 2013; Li *et al.,* 2016). The aggregation of hIAPP is believed to occur in a stepwise manner, with the monomeric peptide forming increasingly complex structures such as oligomers, protofibrils and eventually amyloid fibrils; at some point along this pathway, the structure formed is cytotoxic to the pancreatic β-cell.

The use of fragments or short peptides as models for studying the structure or amyloid formation emerged has a result of the high complexity of studying the full polypeptides and the molecular basis of their assembly processes (briefly reviewed in (Gazit, 2005)). It was also necessary to take into account that the synthesis of large aggregation-prone peptides was a complicated and expensive process. Examples of this strategy started in 1990, when

Westermark and co-workers showed that a fragment of 10 residues from IAPP formed fibrils similar to the full-length peptide (Westermark *et al.*, 1990). The sequence of hIAPP has been extensively studied either using the full-length peptide or fragments (Table 4.1). These studied allowed the identification of three main parts in the sequence: i) from amino acid 1 to 19, is the N-terminal region responsible for the binding and possible insertion into membranes; ii) the region 20-29 is considered essential for amyloid fibril formation and iii) region 30 to 37 favors fibrils formation.

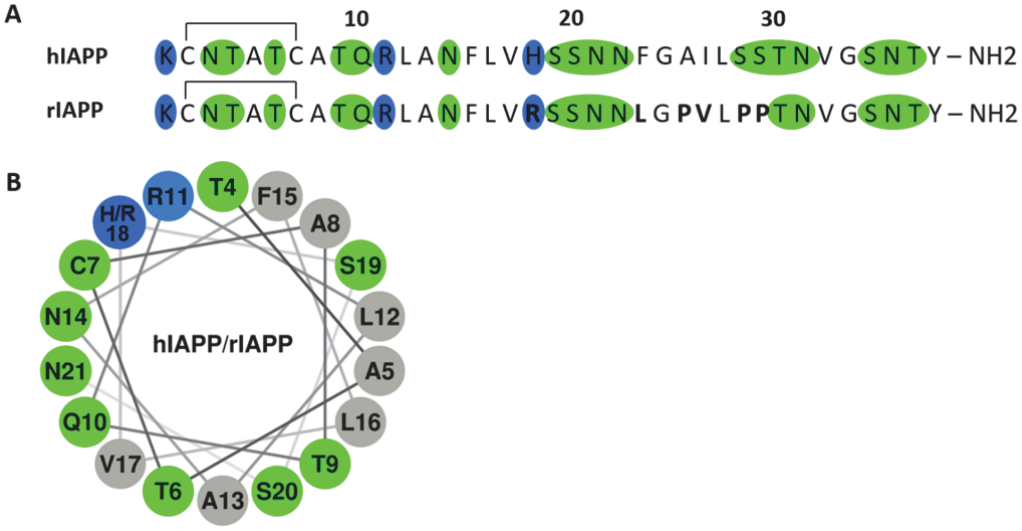

Figure 4.1 - Comparison between the (A) primary sequences and (B) helical wheels of human (hIAPP) and rat (rIAPP) IAPP. (A) IAPP contains a disulfide bridge between Cys2 and Cys7 and a C-terminal amidated residue. The six different residues between hIAPP and rIAPP are indicated with bold lettering. **(B)** The N-terminal of these peptides can form an amphipathic helix as illustrated by the helical wheel from residues 4 to 21 (the only different amino acid for the two sequences is in position 18, which changes from a His in hIAPP to Arg in rIAPP, both of which are positively charged at physiologic pH). Residues in blue and green are, respectively, positively charged and polar (solvent/headgroup accessible) and grey residues are hydrophobic (tailgroup accessible).

The first region includes about half of the amino acids of the peptide and is considerable conserved among all the species; with the most common substitution being the change of His in position 18 to an Arg. In fact, most of the positive charge of these peptides is within these first 19 residues. The N-terminal of hIAPP is *per se* positively charged both at pH 5 and 7.4 as well as the side chains of the basic amino acids Lys1 and Arg11; His18 at a neutral pH will be essentially unprotonated while in an acidic pH will be protonated. rIAPP has an Arg in position 18, making it more positive than hIAPP at physiological pH. Nevertheless, it was found that hIAPP binds more to negatively charged membranes than rIAPP (Knight and Miranker, 2004; Sparr *et al.*, 2004) so although the charge is undoubtedly important to the binding to membranes (Jayasinghe and Langen, 2005), this interaction is not exclusively electrostatic (Cao *et al.*, 2013). Examples of this are studies performed with zwitterionic lipids, such as DOPC/DPPC (Bag *et al.*, 2013), DMPC/1,2-dihexanoyl-sn-

glycero-3-phosphocholine (DHPC) bicelles (Caillon *et al.*, 2013) and POPC (Martel *et al.*, 2017). A study performed with monolayers with hIAPP fragments revealed that the N-terminal of the peptide, rather than the 20-29 amyloidogenic region, is important for the interaction and insertion of the peptide in the membrane (Engel *et al.*, 2006). The study reveals that 20-29 region remains available for fibril formation when monomeric hIAPP inserts the membrane via its N-terminal, an aspect also observed by others (Kurganov *et al.*, 2004; Engel *et al.*, 2006).

Table 4.1 – Characteristic features of different hIAPP segments. Adapted from (Ahmad *et al.*, 2011)**.**

Segment	Residues	Remarks
1-37	KCNTATCATQRLANFLVHSSNNFGAILSSTNVGSNTY	Mature polypeptide
1-13	KCNTATCATQRLA	Unable to form fibril
1-19	KCNTATCATQRLANFLVHS	Essential for membrane interaction
8-20	ATQRLANFLVHSS	Able to form fibrils
11-20	RLANFLVHSS	Amyloidogenic (in vitro)
12-17	LANFLV	Aggregation enhancer
14-20	NFLVHSS	Amyloidogenic (in vitro)
14-18	NFLVH	Possibly important for π-stacking
15-20	FLVHSS	Aggregation enhancer
15-19	FLVHS	Possibly important for π-stacking
17-37	VHSSNNFGAILSSTNVGSNTY	Amyloidogenic (in vitro)
20-37	SNNFGAILSSTNVGSNTY	Forms a contiguous β-sheet
20-29	SNNFGAILSS	Intrinsically amyloidogenic domain
20-25	SNNFGA	Inhibitors of amyloid formation
22-27	NFGAIL	Minimum amyloid forming fragment
23-27	FGAIL	Minimal requirement for aggregation
24-37	GAILSSTNVGSNTY	Amyloidogenic (in vitro)
24-29	GAILSS	Inhibitors of amyloid formation
30-37	TNVGSNTY	Amyloidogenic (in vitro)

Although IAPP is considerably conserved among different mammalian species, there are considerable differences in the middle segment of the peptide, influencing its fibrillogenic behavior (Westermark *et al.*, 1990). The inability of rIAPP to form β-sheet aggregates may be related with the presence of three proline residues within the segment 20-29 of the peptide which tend to disrupt secondary structure (Jayasinghe and Langen, 2007). Proline disrupts the hydrogen bonding and intra-molecular β-sheet formation, hampering the formation of amyloid fibrils by rIAPP (Raleigh *et al.*, 2017). While hIAPP segment 20-29 is intrinsically amyloidogenic in vitro, the rat/mouse segment is not (Goldsbury *et al.*, 2000; Westermark, 2011). A triple proline substitution in hIAPP reduced significantly its aggregation but it was still detected (Abedini and Raleigh, 2006)

Region 30 to 37 is again considerable conserved amongst species. The presence of the C-terminal it is not determinant for fibrillation but the interactions that it makes may modulate the kinetics of amyloid formation (Nanga *et al.*, 2011). The non-amidated version of the peptide fibrillates at a slower pace than the amidated one, as well as some other mutations outside the core region of the peptide were seen to influence the fibrillation rate.

4.2.2.1. **Conformational properties of membrane-bound IAPPs**

Upon interacting with membranes, both hIAPP and rIAPP tend to adopt a helical conformation. In fact, an NMR study of recombinant wild-type rIAPP revealed that part of the chain, from residues 5 to 19, already shows α-helical propensity in solution (Williamson and Miranker, 2007). Depending on the charge of the lipid and the L/P, this conformation can be more or less stable and in the case of hIAPP, evolve to a β-sheet rich structure. The α-helical intermediate found for hIAPP has been considered an on-pathway intermediate for amyloid formation (Jayasinghe and Langen, 2005; Hebda and Miranker, 2009; Butterfield and Lashuel, 2010; Li *et al*., 2016). Although the transition from a random coil to the α-helix is important, is not synonym of formation of β-sheet, as seen with rIAPP. Forming a β-sheet is conditioned by other factors such as the natural propensity for the sequences to adopt β-sheet structures, the interaction among peptides, and the disposition of the peptides in the membrane, among others.

Both SDS (Nanga *et al.*, 2011) (Figure 4.2 c) and dodecylphosphocholine (DPC) micelles (Nanga *et al.*, 2008, 2009) were used to increase the helical content of IAPP or IAPP fragments (from residue 1-19) and with this determine their structure bound to membrane mimetics; it was found that these scaffolds gave rise to structures stable for days which were, consequently, easier to study (Caillon *et al.*, 2013).

The high resolution structure solved by NMR for hIAPP in the presence of SDS micelles at pH 7.3 revealed that hIAPP has an overall kinked helix motif, with an N-terminal helix from Cys7–Val17 separated from the other helix, from Asn21–Ser28, by a turn comprising residues His18–Ser20 and with a short 3_{10}-helix from residues Gly33 to Asn35 (Figure 4.2 a, blue helices). The region constrained by the disulfide bridge is partially unstructured and pointing away from the hydrophobic side of the N-terminal helix (Nanga *et al.*, 2011). When compared to a previous structure for the non-amidated and consequently negatively charged peptide where the last 3_{10}-helix was not found (Patil *et al.*, 2009), the authors claim that the lack of the amide group made the interaction with the head group of SDS unfavorable. Furthermore, it also lacks the favorable hydrogen bonding interactions between the uncharged and biologically relevant C-terminal of the peptide. A paramagnetic quenching experiment using manganese chloride revealed that the side chains of residues in the first helical region, as well as some residues in the C-terminal were most likely

embedded into the head group region of SDS. Tyr37 is one of these residues, although to a less extent than the helical region (Nanga *et al.*, 2011). The authors also suggest that the existence of the kink is not enforced by the binding to the membrane since a different group presented earlier a similar description for the structure of the peptide in fluorinated organic solvents, e.g. HFIP (Cort *et al.*, 2009).

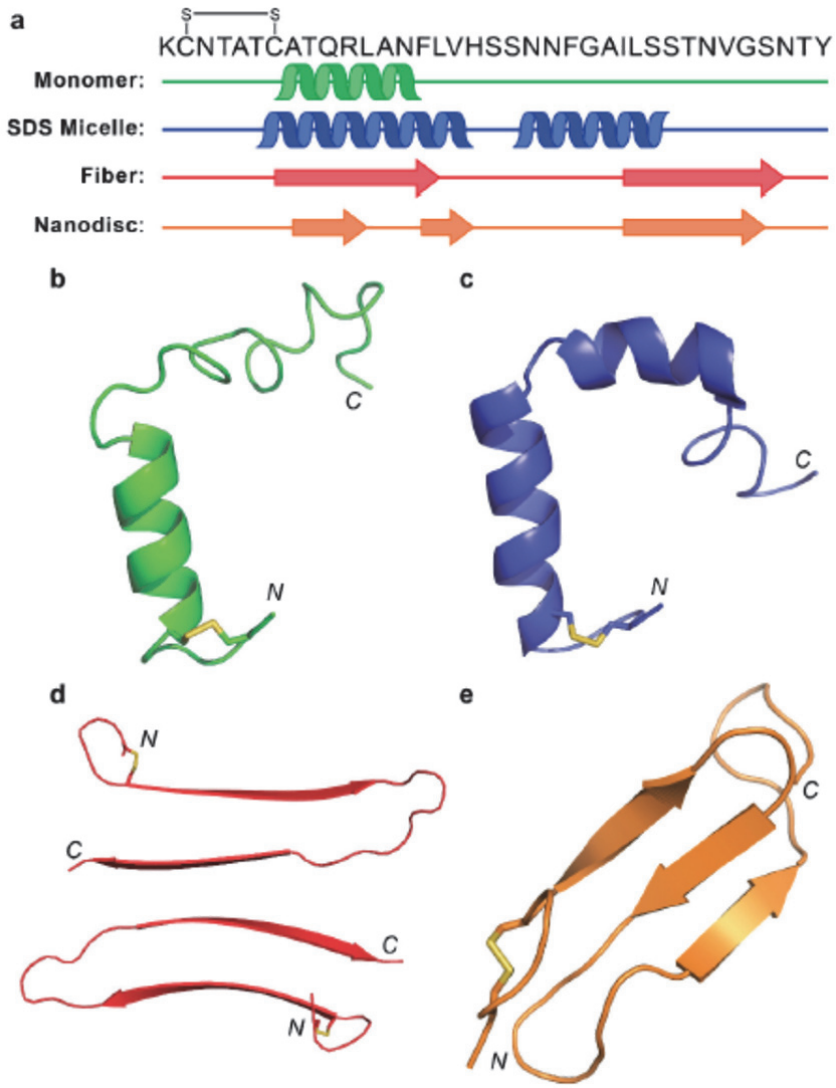

Figure 4.2 - Comparison of hIAPP known structures and models. (a) Models of hIAPP suggest the folding of part of the sequence of the monomeric subunit, although it seems to be highly dependent on the sample preparation and membrane scaffold used for the determination. **(b)** Monomeric hIAPP prepared at pH 5.3 demonstrates a partial α-helix spanning from C7 to F15 (PDB: 5MGQ) (Camargo, Tripsianes, *et al.*, 2017). (**c**) Monomeric hIAPP stabilized by SDS micelles adopts a similar N-terminal helix and a second helical region near the C-terminus (PDB: 2L86) (Nanga *et al.*, 2011). (**d**) The morphology of hIAPP fibers shows two β-hairpins interacting through their C-terminal β-strands (Luca *et al.*, 2007). (**e**) The folded hIAPP monomer interacting with the surface of nanodisc-1 possesses three antiparallel β -strands (Camargo, Korshavn, *et al.*, 2017). Adapted from (Camargo, Korshavn, *et al.*, 2017).

Another 3D model of the α-helical structure of hIAPP bound to LUVs prepared with 80:20 POPS:POPC in 10 mM phosphate buffer, pH 7, was determined employing a combination of site-directed spin labeling, electron paramagnetic resonance (EPR) spectroscopy, and molecular modeling (Apostolidou *et al.*, 2008). The authors found that the membrane-bound hIAPP has a central helical region from residue 9 to residue 22, with disordered N- and C-terminal region. This structure leaves much of the highly amyloidogenic stretch from residue 20 to residue 29 exposed for misfolding and β-sheet formation. Again, the 3_{10}-helix was not found in this conditions.

A very recent study determined the structure of hIAPP bound to nanodiscs (90:10 DMPC:DMPG) by NMR, conducted at 35 °C and pH 5.3. Overall, the simulated structural model represents a consistently folded hIAPP monomeric subunit with three antiparallel β-strands observed for Ala8-Leu12, Phe15-His18, and Ile26-Ser29 with flexible loops connecting them (Figure 4.2 e). The results suggested that the folded structure sits close to the bilayer surface with its β-sheet structure nearly perpendicular to the bilayer (Camargo, Korshavn, *et al.*, 2017). The observed flexibility and solvent accessibility of the nucleating region of hIAPP (from residues Asn22 to Leu27, the domain NFGAIL) suggest its availability to interact with other membrane-associated or soluble hIAPP species to promote the formation of higher ordered species, previously pointed by Westermark (Westermark *et al.*, 1990). Using MD simulations, they also determined that the helical *N*-terminus was strongly associated with the membrane while unstructured C-terminus was solvent exposed (Camargo, Korshavn, *et al.*, 2017).

The structure of rIAPP in DPC micelles is dominated by an N-terminal bent towards the hydrophobic face of the amphipathic helical region, spanning from residues Ala5 to Ser23, and a disordered *C*-terminus. A distortion in the helix is seen in residues 18 and 19, giving a more disordered helix from residues 20 to 23. After the prolines in positions 25, 28 and 29, from residue 30 onwards the C-terminal residues are in an extended and disordered conformation. This *C*-terminus does not seem to interact with any other part of the rIAPP molecule by the absence of long or medium-range characteristic signals (Nanga *et al.*, 2009). In fact, the paramagnetic quenching experiment revealed that the full region from Gly 24 to Tyr 37 is mainly extended out of the micelle. It also showed that most of the residues in rIAPP are bound to the surface of the micelle and do not penetrate deeply into the micelle, opposite to what was seen for hIAPP (Nanga *et al.*, 2011) and $hIAPP_{1-19}$ (Nanga *et al.*, 2008). Nevertheless, a prediction of the membrane-associated conformation of hIAPP and rIAPP made by Monte Carlo simulations to zwitterionic lipids (Figure 4.3 (Bag *et al.*, 2013)) points for rIAPP being weakly associated with the membrane, without a significant insertion, while hIAPP insertion is unfavorable.

The extent of insertion into the membranes seems to be very dependent on the techniques used and the lipids tested, with inconsistent reports throughout the literature. $hIAPP_{1-19}$ and $rIAPP_{1-19}$ differ only in residue 18 but they bind membranes in different orientations (Nanga et al., 2008) and these differences can correlate with the difference in their potential for membrane disruption.

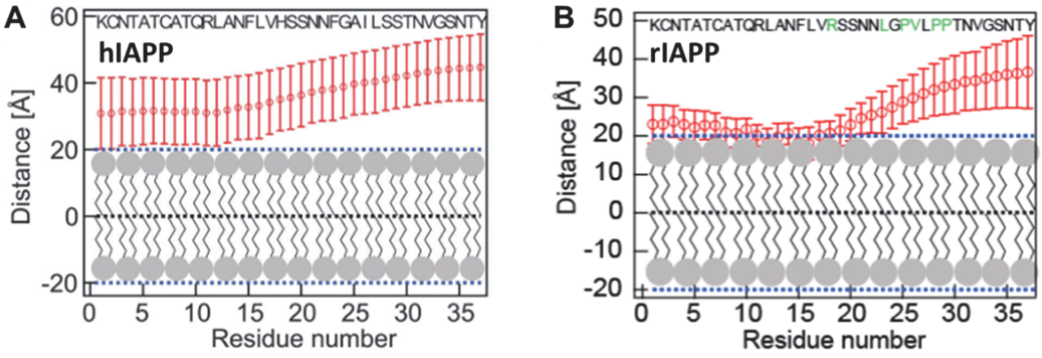

Figure 4.3 - MCPep predictions of membrane association of (A) hIAPP and (B) rIAPP. In MCpep simulation, membrane midplane is taken a reference distance. The bilayer thickness is assumed to be 40 Å. The distance of the individual amino acids from the membrane midplane is used to predict the favorable position and association of the peptide under consideration. The predicted orientation of hIAPP over a membrane shows peptide insertion to be unfavorable and the C-terminal to be away from the membrane, while the simulation for rIAPP predicts weak membrane association without significant insertion. In the sequence of rIAPP the amino acids different from hIAPP are in green. Adapted from (Bag *et al.*, 2013)

The presence of a short 3_{10}-helix from residues Gly33 to Asn35 in hIAPP as compared to the completely disordered structure in rIAPP is also debatable, but may have an impact in the different propensities for self-association of the peptides. A large contribution to energy of self-association is lost if rIAPP is unable to form ordered structures, whereas the presence of the 3_{10}-helix in hIAPP provides an additional ordered interaction surface. Short helices are conformationally flexible and convert with ease between α-helical and 3_{10}-helix. Particularly, 3_{10} helices are more prone to partially unfold than a α -helix conformation and are also more prone to undergo a helix-to-β sheet transition since the Φ/Ψ torsion angles are relatively similar (Harrison *et al.*, 2007; Nanga *et al.*, 2011).

4.2.2.2. **Structure of amyloid hIAPP fibrils**

The supramolecular organization of hIAPP fibrils was elucidated by Luca and co-workers (Luca *et al.*, 2007). They showed that the core of IAPP protofilaments that constitute the fibrils are stabilized by both hydrophobic and polar side chains interactions (Figure 4.2 d). There are interactions between the hydrophobic side chains of residues 23-27 with 15-17 and 32, and the polar side chains of residues 28-31 within one molecular layer may interact

with the same residues in the other molecular layer. Previous studies pointed for an antiparallel β-sheet formed by residues 24 to 29 and 32 to 37 and a β-turn at residue 20 which allowed the 18-23 region to extend the β-sheet (Jaikaran and Clark, 2001). Regions from 12-17, 22-27 and 31-37 were also proposed to form antiparallel β-sheets with regions 18-21 and 28-30 forming the β-turns (Kajava *et al.*, 2005), revealing a very good agreement between the proposed models for the amyloid fibrils formed by IAPP.

4.2.3. Influence of lipids in IAPP fibrillation

IAPP fibrillation is deeply influenced by the presence of lipids and several in vitro studies reveal not only they can serve as sites for nucleation/accumulation of fibrillar aggregates but also targets of the structures formed during the aggregation process (Knight and Miranker, 2004; Gorbenko and Kinnunen, 2006; Jayasinghe and Langen, 2007; Caillon *et al.*, 2015).

Several studies found that IAPP binding to membranes containing anionic lipids led to its conversion into an α-helical form and to eventual formation of β-sheets and fibrillation (Jayasinghe and Langen, 2005; Apostolidou *et al.*, 2008; Knight *et al.*, 2008), leading both to a decrease in the lag time when compared to the process in solution and an increase in the rate of fibrils growth. Fibrillation studies of IAPP induced by liposomes prepared with DOPC/DOPG (Knight and Miranker, 2004; Jha, Udgaonkar, *et al.*, 2009) only DOPG (Knight *et al.*, 2008) or DOPC/1,2-dioleoyl-sn-glycero-3-phosphoserine (DOPS) (Engel *et al.*, 2008) exhibited a sigmoidal profile, showing that the free energy contribution of the lipid bilayer to the transition state of fibril formation is determined by increasing the local peptide concentration. It should be noted, however, that the in vivo deposits of hIAPP occur extracellularly and PG does not exist in the outer leaflets of plasma membranes of mammalian cells (Wakabayashi and Matsuzaki, 2009). This indicates that amyloidogenesis must be induced by lipids with different characteristics and/or attributes, and not just the negative charge. Nevertheless, hIAPP aggregation acceleration was also observed with relative physiological concentrations of PS, namely 1-10 mol%PS (Jayasinghe and Langen, 2005). This PS content is within the determined from membranes of pancreatic islets of rodents (4-14% PS). PS is more common on the cytosolic face of the plasma membrane and is less concentrated on the extracellular surface although it has been suggested that hIAPP could have access to both sites (Rustenbeck *et al.*, 1994). Some studies with higher amounts of mol%PS, e.g. 30%, are also found in literature, that resembles the total amount of negatively charged lipids (Engel *et al.*, 2006), where the authors see an induced fibrillation (Sparr *et al.*, 2004; Engel *et al.*, 2008; Khemtémourian *et al.*, 2011; Caillon *et al.*, 2013).

In this respect, the formation of amyloid fibrils by hIAPP is also possibly mediated by gangliosides in lipid rafts on live cell membranes. There was the observation of hIAPP amyloid deposits on cell membranes and amyloid fibrils accumulated in domains enriched in gangliosides and Chol, in a concentration-dependent manner, leading to cell death. The depletion of these molecules significantly reduced the amount of hIAPP accumulated (Wakabayashi and Matsuzaki, 2009).

More recently, two studies have extensively and systematically investigated the interaction of hIAPP with several model systems/membrane compositions, comparing an array of different conditions usually found in the literature. Caillon and co-workers (Caillon *et al*., 2013) studied the interaction of hIAPP with 16 different membrane model systems, including detergent micelles, bicelles, small and large unilamellar vesicles (SUVs and LUVs, respectively) by CD spectroscopy, ThT assays and EM. The general conclusions of this study were that (i) SDS and DPC micelles stabilize the α-helical conformation of IAPP and do not induce IAPP fibril formation; (ii) the headgroup of the lipid has a strong influence on the kinetics of amyloid formation while (iii) the degree of unsaturation of the lipid chains has a little effect. Contrary to some reports (Wakabayashi and Matsuzaki, 2009), the addition of SM did not show any effect of IAPP-fibril morphology neither on the fibril formation kinetics; concerning cholesterol, membranes containing this sterol seemed to retard IAPP fibril formation, whereas a previous report showed that a mixture of DOPC:DPPC:Chol accelerated hIAPP aggregation (Jha, Udgaonkar, *et al.*, 2009). On the other hand, Zhang and collaborators (Zhang *et al.*, 2017) characterized IAPP interaction and amyloid formation in the presence of LUVS prepared with 33 different membrane compositions (by varying the type and amount of anionic lipids, the zwitterionic lipid, the inclusion of Chol or SM), under variable buffer and salt conditions, using ThT, FRET and IAPP-induced membrane leakage assays. This study showed that increasing the concentration of anionic lipids from 8 to 25 mol% reduced the lag time of hIAPP fibril formation by 5-fold. The effects of cholesterol on amyloid formation were masked when more than 25 mol% of POPS was added to the system. The presence of SM had a similar effect in the leakage experiments: SM decreased the IAPP-induced membrane leakage in the absence of anionic lipids but had no effect in the presence of 10 mol% of POPS. IAPP amyloid formation in the presence of membranes was independent of the choice of zwitterionic lipids. In contrast, the extent of leakage was dependent on the lipid chosen since lipids that form more ordered membranes led to lesser leakage. This data may support the idea that hIAPP needs to insert into the membrane to promote leakage. The presence of salts speeds up the aggregation of IAPP in solution while delaying it in the presence of negatively-charged vesicles, by decreasing electrostatic interactions. In the first case this decrease is favorable, as interactions between hIAPP peptides are favored while in the latter case the interaction of the peptide with the

membrane is diminished, and consequently amyloid formation is delayed. The FRET and dextran leakage experiments performed favor the hypothesis for the formation of pores (Zhang *et al.*, 2017).

A recent study pointed that between freshly dissolved hIAPP, oligomeric hIAPP and mature hIAPP amyloid fibrils, the first enhanced membrane fluidity and caused losses in cell viability, although all of them revealed to be toxic to pancreatic β-cells (Pilkington *et al.*, 2016). Lipids isolated from the rat insulinoma-derived INS-1E β-cell line were used to make vesicles and study their influence in hIAPP aggregation. The authors found similar effects on the kinetic of fibril formation of hIAPP as compared to the use of a complex anionic model vesicles, made up of DOPC, DOPG, DPPC, 1,2-Dipalmitoyl-sn-glycero-3-phosphoglycerol (DPPG) and Chol, larger than the one seen for a simple DOPC:DOPG 7:3 model (Seeliger *et al.*, 2012). On the other hand, Cao and Co-workers studied both hIAPP and rIAPP, as well as a series of mutated forms of hIAPP and showed that none of the 8 peptides studied except for hIAPP induced cytotoxicity towards INS-1 β cells, over a concentration range of 15-60 μM of peptide, while all of them induced leakage of pure or 25% anionic membrane vesicles in L:P ratios of 10:1 to 200:1, with more or less strength (Cao *et al.*, 2013). They found a multistep process for the hIAPP-induced leakage that correlates in time with the fibrillation of the peptide, showing that additional damage might come from the formation of fibrils, in agreement with other works (Engel *et al.*, 2008). Also, the leakage induced by the variety of peptides studied was not accompanied by any significant and detectable α-helical or β-sheet structure, a surprising conclusion taking into account other reports where for similar buffer conditions i.e. high ionic strength, the peptides assumed α-helical conformations, with more or less expression. The major difference relied on the lipid to peptide ratio, since the one used by that authors was 6.7 and normally one finds a ratio of 20 or above (Cao *et al.*, 2013).

In vitro experiments with 1-stearoyl-2-oleoyl-sn-glycero-3-phosphocholine (SOPC) and POPG supported lipid bilayers (SLBs) confirmed that negatively charged lipids facilitate the formation of amyloids by hIAPP (Domanov and Kinnunen, 2008). A confocal microscopy study of Sparr and co-workers showed that hIAPP aggregated and extracted lipids from the membrane in the presence of POPC GUVs. The emerging fibril incorporated part of those lipids, in a detergent-like mechanism (Sparr *et al.*, 2004), similar to the observed by others (Domanov and Kinnunen, 2008). Several authors used neutron reflectometry to study the influence of peptides in the membranes. Accordingly, if any of the peptides studied incorporated into, associated with or altered the structure of the lipid membrane layer, the scattering length density (SLD) distribution would change. Junghans and co-workers (Junghans *et al.*, 2016) demonstrated that hIAPP removes DOPG lipids from a bilayer and the amount of lipid removed was linear with respect to the peptide concentration. 5 μM of

hIAPP was capable of disrupting the structure of the DOPG bilayer and the resulting structures had peptide and lipids, although in an unknown proportion. The interactions between membrane and peptide were shown not to be solely dependent on headgroup charge as hIAPP had little or no effect on bilayers composed of DPPG and mixed 80:20 mol% DPPC:DPPG bilayers. Also, it had no effect on bilayers composed of saturated-acyl chains like zwitterionic DPPC. rIAPP had no effect on any of the above membrane formulations.

4.2.4. Objectives and chapter organization

The main goal of this chapter was to use a multi-probe fluorescence approach to provide a comparative molecular description of the membrane-induced aggregation of hIAPP and rIAPP. Both unconjugated and tracer amounts of bright fluorescently-labeled-Atto488 peptides were used in these studies. The versatility of fluorescence spectroscopy was expected to provide an array of parameters that could be used as sensitive reporters of distinct aspects related to the mechanism of action of hIAPP/rIAPP at the membrane level, e.g. their membrane binding and location, rotational dynamics and self-assembly state.

Specifically, we sought to: (i) study and compare the interaction of rIAPP and hIAPP with POPC LUVs prepared with a variable POPS content, (ii) gain detailed structural and dynamic information about the membrane-induced oligomerization/ amyloid fiber formation pathways of each IAPP variant in interaction with POPS LUVs, (iii) establish a correlation between the surface coverage of the liposomes and the membrane-perturbing activity of each IAPP variant, and (iv) clarify the interplay between the membrane-induced self-assembly of hIAPP/rIAPP and their membrane remodeling properties which ultimately are expected to control their cytotoxic effects.

Complementary far-UV CD studies were used to characterize the conformational transitions undergone by hIAPP/rIAPP in interaction with the lipid membranes and TEM was combined with FAIM studies to confirm the formation of amyloid fibrils by hIAPP under specific experimental conditions. Finally, DLS measurements reported about the impact of membrane surface crowding with rIAPP on the average size of the liposome population.

4.3. Materials and Methods

4.3.1. Reagents

Synthetic unlabeled full-length human and rat islet amyloid polypeptide variants (hIAPP and rIAPP, respectively) were purchased from Bachem (Bubendorf, Switzerland). Both peptides have the naturally occurring free *N*-terminus, an amidated *C*-terminus and a disulfide bond between Cys2 and Cys7 residues. Fluorescently-labeled human and rat IAPP incorporating Atto488 (Atto488-hIAPP and Atto488-rIAPP, respectively), were custom synthesized by Bachem. Fluorophore attachment to the *N*-terminus lysine residue of acetylated IAPP peptides was performed via conjugation to their ε-amine group by the manufacturer (Figure 4.4). The relative molecular mass and peptide purity was evaluated by the manufacturer using MS and RP-HPLC, respectively (Table 4.2). The purity was reported as >95% for all peptide batches used in this work. The peptide content of unlabeled hIAPP and rIAPP batches was ~80% from the manufacturer as obtained by amino acid analysis and this was taken into account in the calculation of the final peptide concentration of each sample. The lyophilized peptides were kept frozen at -20°C and used without additional purification.

Table 4.2 – Chemical properties of the synthetic unlabeled full-length human and rat IAPP variants (hIAPP and rIAPP, respectively) and the correspondingly fluorescently-conjugated peptides. All peptides were obtained from Bachem as trifluoroacetate salts.

Peptide	Catalog No.	Molecular weight (g mol^{-1})			
		Theoretical [1]	Determined by MS	Purity [1]	Net Charge at pH 7.0 [2]
hIAPP	H-7905	3903.3	3903.9	> 95%	3.0
rIAPP	H-9475	3920.5	3920.6	> 95%	3.9
Atto488-hIAPP	custom synthesis	3945.37+dye	3945.37+dye	>95%	1.0
Atto488-rIAPP	custom synthesis	3962.48+dye	3961.57+dye	>96%	1.9

[1] determined by % peak area in RP-HPLC analysis

[2]. calculated using Bachem Peptide Calculator (http://www.bachem.com/service-support/peptide-calculator/ [accessed on May 2018]

POPC, POPS and 1,2-dioleoyl-*sn*-glycero-3-phosphoethanolamine-*N*-(lissamine rhodamine B sulfonyl) (Rhod-PE) were obtained from Avanti Polar Lipids. The chemical structures of both phospholipids and Rhod-PE are presented in Figure 3.8 and Figure 4.5, respectively.

Figure 4.4 - Sequence of fluorescently-labeled IAPPs with Atto488. Human (top) and rat (bottom) IAPPs were labeled by the manufacturer in their Lys1. The *N*-terminus was also acetylated to improve labeling efficiency (according to manufacturer indications). A disulfide bridge is present in both peptides between Cys2 and Cys7 and the peptides have an amidated *C*-terminus. Amino acids colored are: basic (blue), polar (green) and hydrophobic (black).

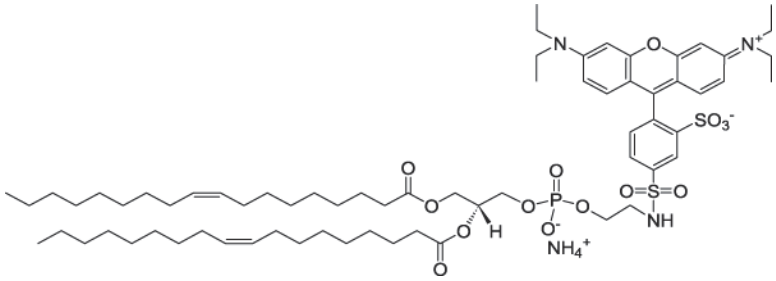

Figure 4.5 - Molecular structure of Rhod-PE. Adapted from avantilipids.com [accessed May 2018].

The free fluorescent dyes Atto 488 NHS ester (Atto488) (Figure 4.6 A) and Thioflavin T (ThT) (Figure 3.9 E) were obtained from Merck KgaA. The fluorescent dyes A488, fluorescein (Figure 3.9 A and B, respectively) and 6-dodecanoyl-2-dimethylaminonaphthalene (Laurdan) (Figure 4.6 B) were obtained from Thermo Fisher Scientific. Additional information for these fluorescent probes is summarized in Table 3.2 and Table 4.3. Other common reagents can be found in Section 3.3.1.

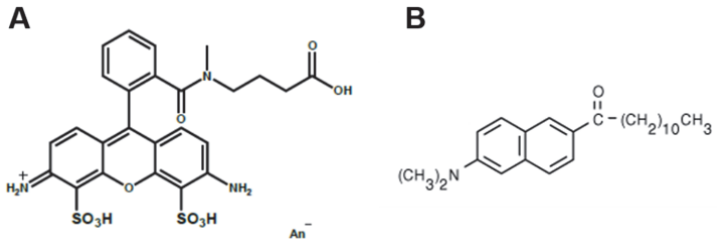

Figure 4.6 - Fluorescent probes used throughout this chapter. (A) Atto488 and (**B**) laurdan. The chemical structures were obtained from the internet site of the respective manufacturer [accessed on May 2018].

Table 4.3 – Additional information for the fluorescent probes and fluorescently-labeled lipid used in this section of the work.

Fluorescent probe/labeled lipid	Catalog number	Molecular weight (g mol^{-1})	Solvent of the stock solution	Spectrophotometric quantification	
				λ (nm)	ε x 10^4 ($M^{-1}cm^{-1}$)
Atto488	41698	981	20 mM HEPES-KOH, 1 mM EDTA, pH 7.4	501	9.0 [1]
Laurdan	D250	353.55	Chloroform	364	2.0 [2]
Rhod-PE	810150	1301.72	Chloroform	559	9.5 [3]

[1] *Merck KgaA* Catalog

[2] Haugland, 2005

[3] Castro *et al.*, 2012

4.3.2. Preparation of IAPP samples

The stock solutions of the unlabeled IAPP peptides were prepared by directly dissolving 1 mg of each lyophilized powder in HFIP to a final concentration of 0.82 mM to break any preformed aggregates (preexisting seeds or nuclei) (Jha, Sellin, *et al.*, 2009; Amaro *et al.*, 2013; Rolinski *et al.*, 2015); smaller amounts of each fluorescently-labeled IAPP variant were used to obtain stock solutions at a final concentration ranging from 0.025 to 0.1 mM. The working peptide samples were prepared immediately prior to the experiments by adding the appropriate volume of each peptide stock solution to LPB Eppendorfs® and subsequently evaporating the organic solvent with a nitrogen flow. The peptide film was then resuspended in the appropriate volume of buffer and sonicated for approximately 1 min in a bath sonicator to ensure complete solubilization of the peptide prior to performing the experiments according to the procedures listed below. The main buffer system used in this work was 20 mM HEPES-KOH, 1 mM EDTA, pH 7.4 (working buffer). The buffer solution was prepared using ultrapure water produced using a Milli-Q system (>18 MΩ·cm) (Q-Gard® 1, Millipore, MA, USA) and was always filtered with 0.22 μm cellulose acetate filters (Millipore) prior to use. The exception were the samples prepared for the CD studies where 5 mM HEPES-NaOH, 1 mM EDTA buffer, pH 7.4 was used instead to minimize interferences with the measurements. The final concentration of the fluorescently-labeled peptides was evaluated spectrophotometrically using the molar absorption coefficient indicated in Table 4.3.

4.3.2.1. **IAPP fibrillation kinetics**

The kinetics of IAPP amyloid fibril formation was first measured in aqueous solution by monitoring the changes over time of either (i) the steady-state fluorescence anisotropy

(ssFA) of its intrinsically fluorescent amino acid residue, Y37, (ii) the increased fluorescence emission intensity of the amyloid specific dye ThT upon its binding to the IAPP amyloid fibrils, and/or (iii) the ssFA of a tracer amount of Atto488-labelled IAPP in the presence of an excess of the correspondingly unlabeled peptide. Samples were prepared either with 8 or 24 μM of hIAPP/rIAPP in the working buffer in the absence or in the presence of 30 μM of ThT for type (i) and type (ii) assays, respectively. For type (iii) assays, the tracer Atto488-conjugated peptide corresponded to 1.25 mol% of the total peptide present in the sample. The fibrillation kinetic assays were then repeated in the presence of 100 or 500 μM POPS LUVs to study the influence of the lipid concentration on the self-assembly kinetics of IAPP.

Each peptide sample was introduced in a 0.5 x 0.5 cm quartz fluorescence cuvette that was maintained under quiescent conditions at RT. At each time point, the cuvette was mixed manually by inversion prior to performing the fluorescence intensity/ssFA measurements of the sample. Occasionally, the fluorescence emission spectrum of the fluorescent probe under study (Y37, ThT or Atto488) were acquired at the initial and end stages of the kinetics (0h and usually 24h incubation, respectively). Complementary time-resolved fluorescence intensity and anisotropy measurements were also performed at the end stage of the kinetics for type (i) and type (iii) assays. In some control type (i) experiments, 30 μM ThT was added to each peptide solution only after 24h incubation of the sample to independently confirm amyloid fibril formation. Adequate blank controls (samples without peptide) were prepared in each case and the corresponding signals were always subtracted from the peptide-containing samples. These controls were particularly important when the fluorescence assays were performed with the cationic ThT dye in the presence of anionic liposomes due to ThT binding to the lipid membranes. The excitation and emission wavelengths used for these measurements are summarized in Table 4.4.

The conformational changes undergone by the peptide in the absence and in the presence of lipid in type (i) assays were also studied using CD spectroscopy; the measurements were performed immediately after preparing the samples and at the end stage of the kinetics (at 0 and 24h incubation time, respectively). The concomitant morphological alterations of representative samples were also characterized using negative staining transmission electron microscopy (TEM) for type (i) assays or fluorescence anisotropy imaging microscopy (FAIM) for type (iii) assays (of the samples with unlabeled IAPP with 1.25 mol% of the corresponding Atto488-conjugated peptide).

Data analysis

For a quantitative description and easy comparison of the kinetic curves obtained under distinct experimental conditions, ThT fluorescence intensity or the ssFA of IAPP

(Y37)/Atto488-conjugated peptide were plotted as a function of time and analyzed as previously described in Section 3.3.3.2. Briefly, an empirical sigmoidal curve described by the following equation was fitted to the experimental data sets using Gnuplot version 5.2:

$$Y = Y_{\mathrm{i}} + \frac{Y_{\mathrm{f}}}{1 + e^{-[(t-t_{\mathrm{m}})/\tau_{\mathrm{g}}]}} \qquad \textbf{Eq. 4.1}$$

where Y is the fluorescence parameter under study measured at time t and t_{m} is the time at which 50% of maximal fluorescence intensity/ssFA is reached. The initial and final baselines, Y_{i} and Y_{f}, respectively, were calculated by calculating the average of the appropriate intensities recorded before and after the elongation phase, respectively. The apparent rate constant for the growth/elongation of fibrils, k_{app}, is given by $1/\tau_{\mathrm{g}}$ and the lag time, τ_{lag}, is calculated as $t_{\mathrm{m}} - 2\,\tau_{\mathrm{g}}$ as illustrated in Figure 3.10.

4.3.3. Preparation of Atto488 in glycerol

For the measurement of the steady-state excitation anisotropy spectrum of Atto488 the stock solution of the free dye was prepared in ethanol. A very small amount of Atto488 in ethanol was then dissolved in a previously gravimetrically prepared glycerol solution to an approximate final concentration of 1 μM. The solution was left stirring overnight at RT to complete homogeneity before performing the measurement.

4.3.4. Preparation of large unilamellar vesicles

Large unilamellar vesicles (LUVs) were prepared by extrusion through 100 nm pore diameter polycarbonate membranes as previously described in Section 3.3.2. The lipid compositions prepared were POPC, POPC:POPS 50:50 or POPS in the working buffer. The POPC LUVs used for the validation of the implemented analysis of time-dependent fluorescence shift (TDFS) measurements of Laurdan (Section 4.3.8.2) were made in 10 mM HEPES, pH 7.0 with 150 mM NaCl and 0.2 mM EDTA. The exact concentration of phospholipid stock solutions was determined by phosphate analysis (McClare, 1971). For the FRET and Laurdan experiments, LUVs containing the adequate fluorescent lipid probe were prepared by co-solubilization with POPC or POPS at the desired molar ratio prior to solvent evaporation (1:400 for Rhod-PE and 1:100 for Laurdan, respectively). The stock solutions of Rhod-PE and Laurdan were prepared in chloroform and quantified spectrophotometrically using the molar absorption coefficient presented in Table 4.3.

4.3.5. Influence of membrane composition and L/P ratio on IAPP interaction with liposomes

The membrane partition eventually coupled to IAPP self-assembly of each IAPP variant with liposomes prepared with a variable lipid composition (POPC, POPC/POPS and POPS) was studied by monitoring the changes in the intrinsic steady-state fluorescence properties of IAPP and/or of a tracer amount of Atto488-conjugated IAPP (mixed peptide samples) upon increasing the total phospholipid concentration in solution. A constant concentration of 8 or 24 μM of both IAPP peptides was added to LUVs suspensions prepared independently ranging from 0 to 0.5 mM total phospholipid concentration. For 24 μM hIAPP a single control experiment with POPS until 4 mM total phospholipid concentration was made (Figure S 4.2). The mixed peptide samples contained 1.25 mol% of the corresponding Atto488-conjugated peptide and their interaction with lipid membranes was studied using only POPS LUVs. Control assays with 0.3 μM Atto488-conjugated IAPP only were also performed in this case. After an incubation time of 30min at RT, the ssFA was measured using the experimental conditions described in Table 4.4. Occasionally the fluorescence emission spectra of the fluorescent probe under study (Y37 or Atto488) were also acquired. In the case of the presence of the tracer amount of labeled peptide, both the signal from Y37 and Atto488 were measured, except for 0.3 μM Atto488-IAPP alone, where the intensity of Y37 is too low to be measured. The overall time of these measurements was always kept below the lag time of the corresponding IAPP fibrillation kinetics in solution.

4.3.6. FRET-based binding assay of rIAPP to POPS LUVs

4.3.6.1. Principles

Förster resonance energy transfer (FRET) is a non-radiative long-range dipole-dipole energy transfer mechanism that occurs between a donor molecule (D) in the excited state to an acceptor molecule (A) in the ground state. The acceptor, which becomes excited upon the energy transfer, may be fluorescent or not - in the latter case the energy gets dissipated as heat. FRET can occur between different (D ≠ A) or identical (D = A) molecules; the first case is described as hetero-FRET whereas the latter case is referred to as homo-FRET (Valeur and Berberan-Santos, 2012). FRET occurs without the emission of photons and does not require molecular contact between the D and A molecules but it is highly dependent on the distance, r, between the D-A pair. FRET is therefore often referred as a "spectroscopic ruler" because it occurs within 1 to 10 nm length scale (Lakowicz, 2006). In practice, FRET length depends on the critical distance or Förster radius, R_0, defined as the distance at which FRET within a given pair is 50% efficient, i.e. the distance at which energy

transfer and spontaneous decay of the excited donor are equally probable for a given single D-A pair. The Förster radius is characteristic of each donor-acceptor pair in a given environment and can be calculated from the spectroscopic properties of the D and A using (Lakowicz, 2006; Valeur and Berberan-Santos, 2012):

$$R_0{}^6 = \frac{9000(\ln 10)\, k^2 \Phi_D}{128\pi^5 N_A n^4} J(\lambda) \qquad \textbf{Eq. 4.2}$$

where Φ_D is the quantum yield of the donor in the absence of energy transfer, N_A is the Avogadro number, n is the refraction index of the medium and k^2 is the orientational factor. This factor is dependent on the mutual orientation of the donor and acceptor transition moments, and is usually assumed to be $2/3$ (Lakowicz, 2006), a value adequate for the dynamic random averaging of the donor and acceptor transition moments during the excited-state lifetime of the donor (isotropic dynamic averaging limit). $J(\lambda)$ is the overlap integral that reflects the degree of spectral overlap between the donor fluorescence emission and the acceptor absorption spectra:

$$J\,(\lambda) = \int_0^\infty F_D(\lambda)\, \varepsilon_A(\lambda)\, \lambda^4\, \mathrm{d}\lambda \qquad \textbf{Eq. 4.3}$$

Here, $F_D(\lambda)$ is the corrected fluorescence emission spectrum of the donor with the total intensity normalized to unity area ($\int_0^\infty F_D(\lambda)\, \mathrm{d}\lambda = 1$) and $\varepsilon_A(\lambda)$ is the molar absorption coefficient of the acceptor at wavelength λ. Hence, for R_0 in Å, λ in nm, $\varepsilon_A(\lambda)$ in $M^{-1}cm^{-1}$ (overlap integral in units of $M^{-1}\,cm^{-1}\,nm^4$), Eq. 4.2 becomes:

$$R_0 = 0.2108 \left[k^2 \Phi_D\, n^{-4} \int_0^\infty F_D(\lambda)\, \varepsilon_A(\lambda)\, \lambda^4\, \mathrm{d}\lambda \right]^{1/6} \qquad \textbf{Eq. 4.4}$$

Single distance between donor and acceptor

The rate of energy transfer from a donor to an acceptor $k_T(r)$ is given by:

$$k_T(r) = \frac{1}{\tau_D} \left(\frac{R_0}{r}\right)^6 \qquad \textbf{Eq. 4.5}$$

τ_D is the fluorescence lifetime of the donor in the absence of energy transfer, r is the donor to acceptor distance and R_0 is the Förster radius. The FRET efficiency, E, is defined as the fraction of photons absorbed by the donor that are successfully transferred to the acceptor. This fraction is given by:

$$E = \frac{k_T(r)}{k_T(r) + 1/\tau_D} \qquad \textbf{Eq. 4.6}$$

Taking into account Eq. 4.5, Eq. 4.6 can be rewritten as:

$$E = \frac{1}{1 + \left(\frac{r}{R_0}\right)^6} \leftrightarrow E = \frac{{R_0}^6}{{R_0}^6 + r^6} \qquad \textbf{Eq. 4.7}$$

The inverse sixth power dependence of E with r and R_0 explains why FRET is most sensitive to donor-acceptor distances when this parameter is comparable to the Förster critical radius. In fact, the energy transfer efficiency depends so strongly on the distance that FRET measurements are only reliable within the distance range $0.5R_0 < r < 2R_0$, as E varies steeply between 98.5 to 1.5% within this interval (Loura *et al.*, 2011 Shrestha *et al.*, 2015). The experimental evaluation of FRET efficiencies can be made using the fluorescence intensities of the D in the absence, I_{D}, and in the presence, I_{DA}, of A or the respective lifetimes under the same conditions (i.e. τ_{D} and τ_{DA}, respectively) (Shrestha *et al.*, 2015):

$$E = 1 - \frac{I_{\mathrm{DA}}}{I_{\mathrm{D}}} = 1 - \frac{\tau_{\mathrm{DA}}}{\tau_{\mathrm{D}}} \qquad \textbf{Eq. 4.8}$$

In case the decay of the donor fluorophore is complex and adequately described by a multiexponential function, Eq. 4.9 should be used instead:

$$E = 1 - \frac{\langle\tau\rangle_1^{\mathrm{DA}}}{\langle\tau\rangle_1^{\mathrm{D}}} \qquad \textbf{Eq. 4.9}$$

where $\langle\tau\rangle_1^{\mathrm{D}}$ and $\langle\tau\rangle_1^{\mathrm{DA}}$ are the amplitude-weighted mean fluorescence lifetimes of the donor in the absence and in the presence of the acceptor, respectively. It should be noted that the calculation of FRET efficiencies using fluorescence lifetimes instead of fluorescence intensities is much less prone to errors as lifetimes are independent of the concentration of fluorophores. The only available experimental readout for detecting homo-FRET is the fluorescence anisotropy of the sample because in this case the successive reversible FRET steps among the fluorophores lead to a strong depolarization of the fluorescence emitted without any concomitant variation of its fluorescence intensity or lifetime (Jameson and Ross, 2010; van Ham *et al.*, 2010; Bader *et al.*, 2011; Melo, Loura, *et al.*, 2014).

FRET in two dimensions (2D-FRET)

FRET measurements can be used to evaluate the binding of a fluorescently-labeled peptide/protein (D) to an ensemble of lipid vesicles, each containing a randomly-distributed population of acceptors (e.g. a fluorescently-labelled phospholipid at its headgroup). The rational of these experiments is that when the tracer fluorescently-labelled peptide remains free in solution, it cannot undergo efficient Förster energy transfer to the membrane-embedded acceptor as the average D-A distance is > $2\mathrm{R}_0$. However, upon progressive

recruitment of the D into the lipid vesicles driven by e.g. an increase in the total peptide concentration added to the liposome suspension, the membrane-bound fluorescently-labeled peptide (D) can now efficiently transfer energy to two planes of 2D-randomly distributed acceptor phospholipids, resulting in a decrease in the mean fluorescence lifetime of the donor and, consequently, in an increase in the overall energy transfer efficiency of the system. Ultimately, the overall FRET efficiency of the system is independent of the donor concentration used but extremely dependent on the membrane surface density of the acceptor and the transverse distances of closest approach, h_i, between each donor population/acceptor-containing plane (Figure 4.7) (Loura *et al.*, 2009; Loura and Prieto, 2011; Melo, Loura, *et al.*, 2014).

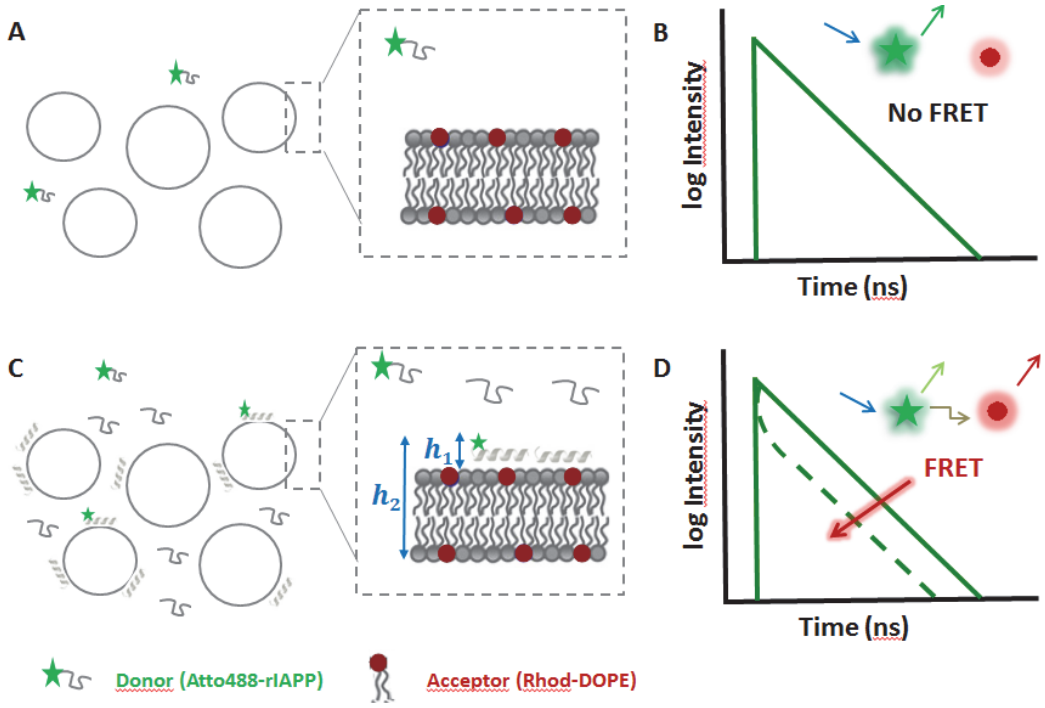

Figure 4.7 - Schematic illustration of the FRET-based binding assay of rIAPP to POPS liposomes. (A) At a very low concentration of Atto488-rIAPP (donor, D), the conjugated peptide remains predominantly free in solution. These free Ds are too distant from the membrane-embedded acceptors (Rhod-DOPE, A) and therefore cannot undergo FRET, **(B)** presenting a characteristic long mean fluorescence lifetime. **(C)** Upon increasing the concentration of the unlabeled rIAPP added to each sample, Atto488-rIAPP is progressively recruited to the lipid bilayers due to rIAPP partition coupled to its oligomerization on the anionic liposome surface. In parallel, the fraction of free donors in solution gradually decreases. **(D)** The mean fluorescence lifetime of the membrane-bound conjugated peptide becomes shorter due to efficient 2D-FRET between the membrane-bound Atto488-rIAPP (D) and the fluorescently-labelled phospholipids (A) present at each acceptor plane. The overall energy transfer efficiency of the system progressively increases towards a limiting value when full membrane coverage of the lipid vesicles by the peptide is reached. Adapted from Stachowiak *et al.*, 2012.

Experimental measurements

FRET experiments were performed using Atto488 as a donor and Rhod-PE as the acceptor. Increasing concentrations of rIAPP, ranging from 1.6 to 24 μM of peptide with 0.1 μM of Atto488-rIAPP fixed, giving a labeling percentage between 5% and 0.33%, respectively, were investigated in the presence of 100 and 500 μM of POPS LUVs, in the absence or in the presence of the acceptor, Rhod-PE (1:400 molar ratio). Steady-state and time-resolved measurements were performed with the wavelengths summarized in Table 4.4. Control experiments of the increasing concentrations of rIAPP with the fixed amount of labeled peptide in buffer were performed. FRET efficiencies were calculated using the fluorescence lifetimes (Eq. 4.9).

4.3.7. DLS measurements of the influence of rIAPP binding to POPS LUVS

4.3.7.1. Principles

Dynamic Light Scattering (DLS), also known as photon correlation spectroscopy or *quasi*-elastic light scattering, is a powerful tool for studying the diffusion behavior of particles in solution (Lomakin *et al.*, 2005). This technique is particularly suitable to characterize the size distribution and polydispersity of a sample. DLS is based on determining the rate at which intensity of scattered light fluctuates upon the movement of particles diffusing by random Brownian motion. If the particles are small compared to the wavelength ($\sim \lambda/10$), the scattered light carries the same energy to the incident light, is equal in all directions and it is not angle-dependent – Rayleigh scattering. The intensity of light scattered is proportional to the 6th power of the diameter of the particles ($I \propto d^6$) and inversely proportional to the 4th power of the incident laser wavelength ($I \propto 1/\lambda^4$). When the size of the particles exceed this threshold, the Rayleigh theory is replaced by the anisotropic Mie scattering (inelastic scattering) and the scattered light becomes angle dependent and does not have the same energy to the incident light. Larger particles mostly scatter in the forward direction (Bhattacharjee, 2016; Malvern Instruments, 2017). Scattering of particles with nearly the same size of the incident laser wavelength results in a plot of intensity as a function of scattering angle that forms a complex function of maxima and minima. Mie theory is the only one that explains correctly this complex function and will give the correct answer over all wavelengths, sizes and angles, and is used in the Malvern software for the conversion of intensity distribution into volume (Malvern Instruments, 2017).

In a DLS instrument, the incident laser light is scattered in all directions upon encountering the randomly diffusing particles in solution. The scattered light from these continuously mobile particles will either result in mutually destructive phases and cancel out, or in

mutually constructive phases to produce a detectable signal, and hence the intensity of scattered light fluctuates over time. Analogously to FCS, these intensity fluctuations are recorded in a DLS instrument by a detector, a digital autocorrelator, that correlates the intensity of the scattered light with respect to time (ns-μs), giving a normalized intensity correlation function which is usually denoted as $G'_2(\tau)$ (second-order correlation function):

$$G'_2(\tau) = \frac{\langle I(t) \cdot I(t+\tau) \rangle}{\langle I(t) \rangle^2} \quad \textbf{Eq. 4.10}$$

where τ is the lag time between two time-points. The motion of particles relative to each other is correlated by means of a normalized electric field correlation function, $G'_1(\tau)$, also known as the first-order correlation function (Lomakin *et* al., 2005; Stetefeld *et al*, 2016):

$$G'_1(\tau) = \frac{\langle E(t) \cdot E(t+\tau) \rangle}{\langle E(t) \rangle^2} \quad \textbf{Eq. 4.11}$$

where $E(t)$ and $E(t+\tau)$ represent the scattered electric fields at times t and $t+\tau$. The autocorrelation (AC) functions $G'_1(\tau)$ and $G'_2(\tau)$ can be coupled to each other by means of the Siegert relation (Lomakin *et* al., 2005; Stetefeld *et al*, 2016):

$$G'_2(\tau) = 1 + b\,|G'_1(\tau)|^2 \quad \textbf{Eq. 4.12}$$

where b is an instrumental factor dependent on the detector area and optical alignment. Briefly, for a *monodisperse population* of particles undergoing random motion, $G'_1(\tau)$ decays monoexponentially with a decay constant Γ:

$$G'_1(\tau) = \exp(-\Gamma\tau) \quad \textbf{Eq. 4.13}$$

This decay constant, in turn, is directly related to the translational diffusion coefficient of the particles, D_t, according to the following equation:

$$\Gamma = -D_t q^2 \quad \textbf{Eq. 4.14}$$

where the scattering vector, q ,given by:

$$q = \frac{4\pi n_0}{\lambda_0} \sin(\theta/2) \quad \textbf{Eq. 4.15}$$

n_0 is the refractive index of the solvent, λ_0 is the wavelength of incident light and θ is the scattering angle. Eq. 4.12 can be re-written as:

$$G'_2(\tau) = 1 + b\ \exp(-2D_t q^2 t) \quad \textbf{Eq. 4.16}$$

allowing to establish a direct relationship between the fluctuations in the light scattered by an homogeneous population of particles and their random motion in solution. Information about the size of the macromolecules/nanoparticles is contained in this analysis because

large particles diffuse slowly, resulting in similar positions at different time points, compared to small particles which diffuse must faster and do not remain at the same position for long. It should be noted that in the case of a polydisperse system, $G'_1(\tau)$ is no longer a monoexponential function and an intensity-weighted integral over a distribution of decay rates, $G_{\mathrm{p}}(\Gamma)$, must be considered (Lomakin *et* al., 2005; Stetefeld *et al*, 2016):

$$G'_1(\tau) = \int_o^{\infty} G_{\mathrm{p}}(\Gamma) \cdot \exp(-\Gamma\tau)\ d\Gamma \qquad \textbf{Eq. 4.17}$$

Finally, in modern DLS instruments, a correlogram is generated where a raw correlation function, RCF, is plotted against the delay time, τ (Bhattacharjee, 2016):

$$\mathrm{RCF} = G'_2(\tau) - 1 = b\ \exp(-2D_{\mathrm{t}}q^2t) \qquad \textbf{Eq. 4.18}$$

In a DLS experiment, the diameter that is obtained is the hydrodynamic diameter, D_h, of a sphere that has the same D_t as the particle being studied. The size of a particle is calculated from the translational diffusion coefficient by using the Stokes-Einstein equation (Einstein, 1905)

$$D_h = \frac{k_B T}{3\pi\eta D_t} \qquad \textbf{Eq. 4.19}$$

where k_B the Boltzmann constant, T is the absolute temperature and η is the viscosity of the medium. This equation reveals that DLS measurements are very sensitive to solvent viscosity and temperature, parameters which are given as input to the measurement/analysis software. The AC functions of the scattered light are analyzed according to two different mathematical algorithms, the cumulants analysis or the CONTIN (Bhattacharjee, 2016; Stetefeld *et al*., 2016). In the first, the initial part to the AC is fitted with a single exponential decay to retrieve the z-average size and the polydispersity index (PdI), which can be used as a rule of thumb for assessing the suitability of a sample to be analyzed by DLS. The PdI typically depicts the intensity of light scattered by various fractions of the particles differing in their sizes and is calculated by (width/mean)^2 for each peak (Bhattacharjee, 2016;). Samples with PdI values ≤ 0.1 are considered highly monodisperse, 0.1 < PdI < 0.4 are moderately polydisperse while samples with PdI > 0.4 are highly polydisperse and might not be suitable for DLS analysis.

Although less sensitive to noisy data, the cumulants analysis it is unsuitable for samples that are not highly monodisperse. The CONTIN uses a modified version of a non-monomodal distribution method where the AC function is fitted against longer times and provides a size distribution analysis with average size and width for every peak. For highly monodisperse samples, both algorithms should yield similar results.

DLS is a non-invasive technique that requires small amounts of samples for analysis and is particularly useful to check for aggregation of biomolecular preparations in a fast, precise and reproducible manner (Lorber *et al.*, 2012). Modern DLS instruments have non-invasive backscatter detection (NIBS) (Bhattacharjee, 2016; Malvern Instruments, 2017). The detectors are avalanche photodiodes are placed at an angle of 173º relatively to the laser beam (backscatter detection) and the optics are not in contact with the sample being known as non-invasive. The NIBS excludes excess scattered light as it increases the illuminated area in the sample as compared to the 90 ºC arrangement. This setup helps to detect scattered light by smaller particles which have lower intensity signals and since the incident beam does not go through the entire sample, it also reduces the effect where the scattered light from one particle is scattered by other particles, known as multiple scattering, so higher concentrated samples can be measured. Automated focusing lens determine the illuminated area, i.e. in the middle of the cuvette or closer to the wall, depending on the intensity of the scattered light (Bhattacharjee, 2016; Malvern Instruments, 2017). This arrangement also reduces the contribution of dust particles or larger aggregates, which mainly scatter in the forward direction (Mie scattering). Even with this setup, larger aggregates must be prevented by cleaning the cuvette and filtering the samples whenever possible before the measurements.

DLS can be used as a routine technique to determine the size of fairly monodisperse solutions. Although it is possible, DLS is less suitable for determining the molecular weight than static light scattering and/or analytical ultracentrifuge, as it is not a reliable and reproducible method. DLS is also dependent on the concentration of the samples and restricted to transparent sample preparation. Although the use of fluorescent samples is discouraged because of the possible absorption of the scattering laser by the molecules (Bhattacharjee, 2016), a recent study performed measurements with carboxylated polystyrene particles with 105 nm doped with different fluorescence dyes (DY555 or DY680) concentrations, ranging from 0.1 to 1 mM). The results revealed no significant influence of absorbing and emitting dyes in the particle size or size distribution, even at such high concentrations (Geißler *et al.*, 2015).

4.3.7.2. **Experimental measurements**

The impact of the interaction of rIAPP with negatively charged membranes (POPS LUVs) were evaluated using DLS. Increasing concentrations of rIAPP, ranging from 1.6 to 24 μM of total peptide, were added to 100 or 500 μM of POPS LUVs. Control experiments in the absence of peptide were also made. After an incubation period of at least 30 minutes at RT, DLS measurements were carried out on a Malvern Zetasizer Nano ZS (Malvern

Instruments, UK) with 173º backward scattering, equipped with a He-Ne laser (632.8 nm). Prior to each measurement set, the sample was equilibrated for 2 min at 25 ºC in the sample holder. Each sample was measured 20 times with a single run per measurement and a detection period of 15 seconds per run, to ensure that every single measurement run is recorded. Solvent viscosity and temperature were given as input to the measurement/analysis software: n_0 = 1.330 and η = 0.8872 cP.

The data obtained for POPS LUVs in the presence of variable concentrations of rIAPP was statistically analyzed intra-group (of 20 measurements) by average and standard deviation, discarding outliers. Each experiment was repeated at least three times. Presented values are mean ± standard deviation.

Data analysis

The normalized intensity AC curves were analyzed using the CONTIN method to obtain the translational diffusion coefficients, D_{t}, of the particles under investigation. This method provides a distribution of diffusion behavior and hence a distribution of hydrodynamic diameter, D_h. The results are presented as an intensity-weighted distribution. As an example, the following equation describes the intensity distribution for a solution containing N_a and N_b molecules with size a and b, respectively:

$$\%\, I_{\mathrm{a}} = \frac{N_a \cdot a^6}{N_a \cdot a^6 + N_b \cdot b^6} \times 100 \qquad \textbf{Eq. 4.20}$$

where the $\%\, I_{\mathrm{a}}$ is represents the intensity-weighted distribution for particles with size a.

4.3.8. Impact of rIAPP binding to the membranes in the interfacial properties of POPS LUVs

4.3.8.1. Principles

Generalized polarization (GP) of Laurdan

Laurdan is a fluorescent membrane probe that has been widely used to assess membrane order/hydration of both model systems of membranes and cell membranes (Demchenko *et al.*, 2012) (Demchenko *et al*., 2015) The dipole moment of Laurdan increases by 13 D upon excitation (Cwiklik *et al*., 2011), and therefore its fluorescence emission properties are extremely dependent on the polarity and viscosity of the solvent used. This is a consequence of solvent dipole reorientation around the fluorescent dye during its excited state lifetime. Briefly, the solvent cage surrounding a molecule in its ground state is optimized to minimize the overall energy of the system; upon light absorption, there is an

ultrafast redistribution of its electronic cloud (change in dipole moment), while the solvent nuclei retain the spatial arrangement characteristic of the ground state (the so-called Franck-Codon state is reached). The solvent shell needs then to reorient around the excited fluorophore for the system to reach an energetically favorable solvent-relaxed S_1 state, a process that is called solvent relaxation (SR) (Valeur and Berberan-Santos, 2012). When SR occurs on a time scale similar to the fluorescence lifetime of the fluorophore, emission from the excited states between the Franck-Codon and full solvent-relaxed equilibrated states can occur and therefore there will be a time-dependent fluorescence shift (TDFS) of the emission spectra of Laurdan (Figure 4.8) (Pokorna *et al*., 2013).

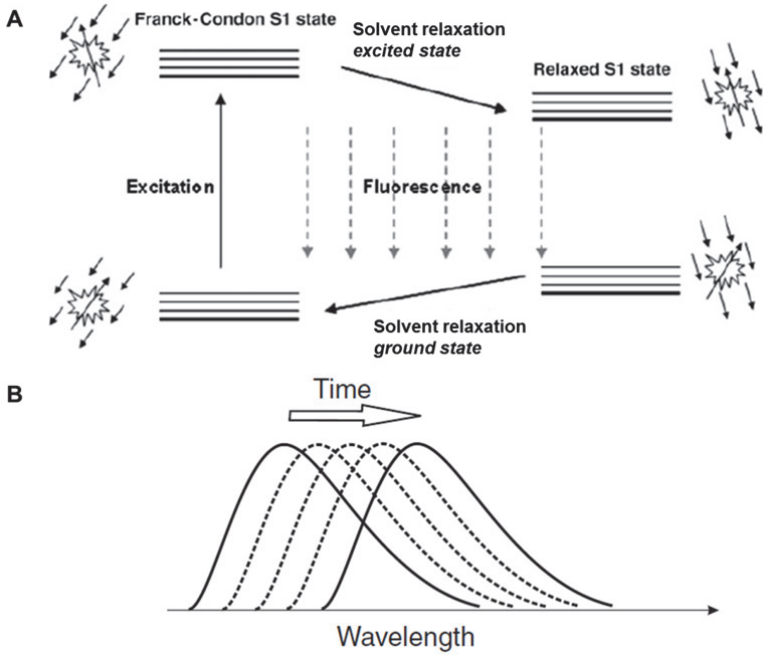

Figure 4.8 - Schematic representation of the solvent relaxation process. (**A**) The dipoles of the fluorophore and the solvent molecules are arranged in a way to minimize the free energy of the system in the ground state. Upon light absorption, there is an ultrafast redistribution of the dipole moment of the fluorophore, while the solvent dipoles remain equal to the ground-state order – Franck-Condon S1 state. The consequent reorientation of the solvent molecules is called solvent relaxation, which leaves the dipoles of the solvent oriented so as to lower the free energy of the system. When fluorescence lifetime of a fluorophore and the solvent relaxation occur in similar timescales, emission from the excited states between the Franck-Condon and the relaxed S1 state is observed. (**B**) There will be a time-dependent fluorescence shift (TDFS) of the emission spectra of Laurdan. Adapted from Valeur and Berberan-Santos, 2012 and Pokorna *et al*., 2013.

Laurdan can present a large Stokes shift of up to 7 400 cm^{-1} in lipid bilayers (Parasassi et al., 1990). This has been used by Gratton and co-workers to define an empirical ratiometric parameter, the so-called generalized polarization function, *GP*:

$$GP = \frac{I_{440} - I_{490}}{I_{440} + I_{490}} \qquad \textbf{Eq. 4.21}$$

where $\boldsymbol{I_{440}}$ and $\boldsymbol{I_{490}}$ are the fluorescence intensities at the specified wavelengths. The *GP* values of Laurdan are high when no solvent relaxation occurs, and since the main solvent dipoles surrounding Laurdan in phospholipid membranes are water molecules, a high *GP* value reports a low water content/mobility at the membrane interface region. On the other hand, if the membrane interface is highly hydrated, the emission spectrum of Laurdan strongly shifts to the red and a low *GP* value is recorded (Figure 4.9) (Owen *et al*., 2012; Pokorna *et al*., 2013). As the transition from a liquid crystalline to a gel phase is accompanied by an increased molecular packing of the phospholipids, which decreases both the water penetration and dynamics at the interface region, the steady-state *GP* parameter has been mostly used as a reporter of membrane order/lipid packing (Yu *et al.*, 1996; Bagatolli and Gratton, 2000; Harris *et al.*, 2002).

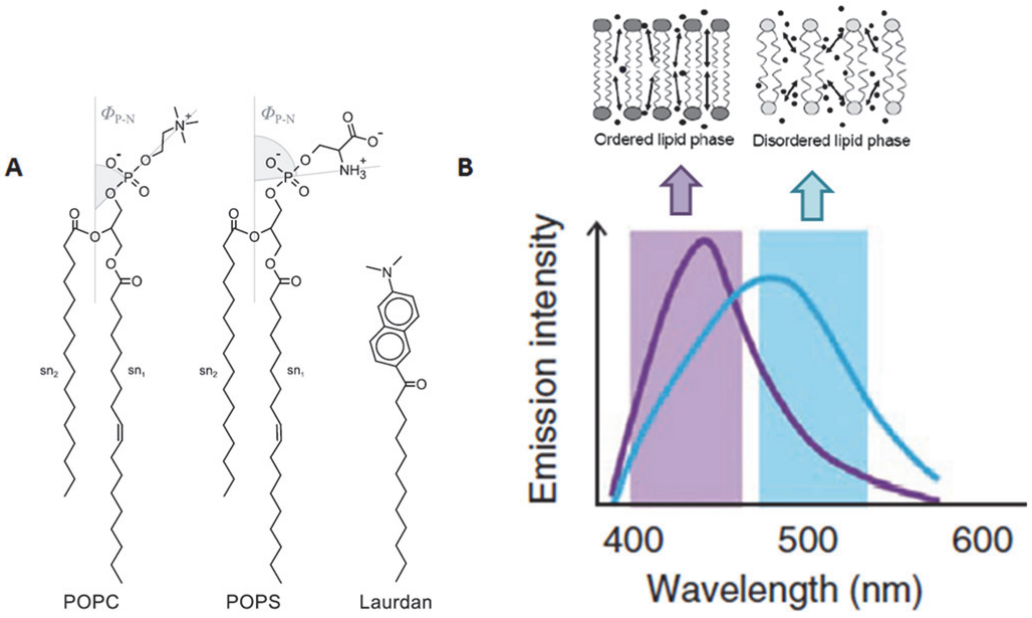

Figure 4.9 - Laurdan is a commonly used fluorescent membrane polarity probe. (A) Estimated location of Laurdan in lipid membranes: the fluorescence properties of Laurdan reflect predominantly the mobility of the hydrated *sn*-1 carbonyl groups of a phospholipid bilayer in the liquid crystalline phase and not its extent of hydration. Adapted from (Jurkiewicz, Cwiklik, Vojtíšková, *et al.*, 2012) **(B)** Schematic representation of the fluorescence properties of Laurdan: the dye fluoresces with a peak emission around 450 nm (violet) when residing in a ordered lipid phase and ~490-500 nm in a disordered lipid phase (blue). Adapted from (Owen *et al.*, 2012).

Time-resolved emission spectra and time-dependent fluorescence shifts

One of the methods often used to get a more detailed picture about the rate and extent of SR in membranes is the reconstruction of the time-resolved emission spectra (TRES) of a

membrane polarity probe, in our case Laurdan. Briefly, a set of fluorescence intensity decays are measured at different emission wavelengths, $\boldsymbol{I_{exp}(\lambda, t)}$, encompassing the entire steady-state emission spectrum of the probe. Using an iterative reconvolution fitting procedure of the real fluorescence decays, $\boldsymbol{I(\lambda, t)}$, with their respective instrument response function, $\boldsymbol{IRF(\lambda, t)}$, as previously described in detail in section 3.3.6.2:

$$I_{\mathrm{calc}}(\lambda, t) = I\,(\lambda, t) \otimes IRF(\lambda, t) \qquad \textbf{Eq. 4.22}$$

it is possible to parametrize $\boldsymbol{I(\lambda, t)}$,:

$$I(\lambda, t) = \sum_{i=1}^{n} \propto_{i\lambda} \cdot \exp(-t/\tau_{i\lambda}) \qquad \textbf{Eq. 4.23}$$

It should be noted that no physical meaning can be assigned to the parameters used to empirically describe the decays, i.e. the pre-exponentials, $\propto_{\boldsymbol{i\lambda}}$, and fluorescence lifetimes, $\boldsymbol{\tau_{i\lambda,}}$. It is also worth noticing that the intensity decays are wavelength-dependent because of the time needed for the fluorophore to go from its Franck-Condon excited state to its fully relaxed excited state. Since there are no fluorophores in the more relaxed excited states until some solvent relaxation has occurred, there will be a rise in intensity at longer wavelengths which is frequently associated with a negative pre-exponential factor that is recovered from the analysis of the time-resolved data. The fluorescence decays measured at different wavelengths, $\boldsymbol{I(\lambda, t)}$, are then normalized using the fluorescence intensities obtained from a corrected steady-state emission spectrum of Laurdan, $\boldsymbol{SS_0(\lambda)}$, in order to reconstruct $\boldsymbol{TRES(\lambda, t)}$:

$$TRES(\lambda, t) = \frac{I(t, \lambda).SS_0(\lambda)}{\int_0^{\infty} I(t, \lambda)\, dt} \qquad \textbf{Eq. 4.24}$$

The raw time-dependent emission spectra can finally be converted from a wavelength, $\boldsymbol{TRES(\lambda, t)}$, to a wavenumber scale, $\boldsymbol{TRES(\nu, t)}$, using (Lakowicz, 2006; Valeur and Beberan-Santos, 2012):

$$TRES(\nu, t) = TRES(\lambda, t).\lambda^2 \qquad \textbf{Eq. 4.25}$$

The spectra in the wavenumber domain are then fitted to a log-normal line shape function, $\boldsymbol{F(\upsilon, t)}$,

$$F(\upsilon; t) = h\begin{cases}\exp[-\ln(2)\,\{\ln(1+\alpha)/\gamma\}^2]: & \alpha > -1 \\ 0 \qquad\qquad\qquad\qquad\quad : & \alpha \leq -1\end{cases} \qquad \textbf{Eq. 4.26}$$

with

$$\alpha \equiv 2\gamma\,(\nu - \nu_{\mathrm{P}})/\Delta \qquad \textbf{Eq. 4.27}$$

The four parameters, i.e. the peak height, $\boldsymbol{h}$, the peak frequency, $\boldsymbol{\nu_{\mathrm{P}}}$, the asymmetry parameter, $\boldsymbol{\gamma}$, and the width parameter, $\boldsymbol{\Delta}$, are adjusted in a nonlinear least-squares fitting procedure for each time point $\boldsymbol{t}$. From these, one can finally evaluate the time-dependent shift of the peak maxima, $\nu(t)$, of the reconstructed $\boldsymbol{TRES}(\nu,\boldsymbol{t})$: the *overall shift in the spectra*, $\boldsymbol{\Delta\nu}$, is proportional to the difference of energies between the Franck-Condon state and the fully relaxed stated of Laurdan, and therefore reflects the degree of hydration (local polarity) at the membrane location of the extrinsic fluorescent probe (Horng *et al*., 1995):

$$\Delta\upsilon = \upsilon_{(0)} - \upsilon_{(\infty)} \qquad \textbf{Eq. 4.28}$$

where $\boldsymbol{\upsilon_{(0)}}$ is the position of TRES maximum at *t*= 0 which can be estimated using the method of Fee and Maroncelli (Fee and Maroncelli, 1994) and $\boldsymbol{\upsilon_{(\infty)}}$ is the position of TRES at the fully relaxed state. The *kinetics of these spectral shifts* (*relaxation curve*) depends on the interaction of the dye with its surroundings and the reorientation (mobility) of the polar solvent molecules in the immediate vicinity of the probe. Different probes can be used to measure local polarity and mobility at different depths depending on their insertion in the lipid bilayers.

Finally, the fitted spectra to the reconstructed TRES in the wavenumber domain can also be used to calculate their full width at half-maximum, FWHM($\boldsymbol{t}$):

$$\mathrm{FWHM}(t) = \Delta(\mathrm{t})\left(\frac{\sinh(\gamma(t))}{\gamma(t)}\right) \qquad \textbf{Eq. 4.29}$$

The evolution of FWHM($\boldsymbol{t}$) accounts for the changes in broadness of $\boldsymbol{TRES}(\nu,\boldsymbol{t})$ over time and usually goes through a maximum during the dipolar relaxation process. These features give information about the environmental heterogeneity of the fluorophores emitting at a specific time $\boldsymbol{t}$, i.e. it is informative on the heterogeneity of the solvent shell surrounding each individual fluorophore in a sample which ultimately is responsible for the non-uniform distribution of the individual dipolar relaxation phenomena. The time at which the time-course of FWHM reaches its maximum is a good estimate of the average time taken by the system to complete the dipolar relaxation process (Pokorna *et al*., 2013; Amaro *et al*., 2017). Altogether, the parameters obtained from a detailed analysis of TRES give powerful information about the local polarity (hydration level) and lipid packing around Laurdan and will be extremely sensitive to changes in these membrane properties caused by the interaction of peptides with the lipid bilayer (Amaro *et al*., 2014).

4.3.8.2. **Experimental measurements**

Generalized polarization (GP) of Laurdan

The same experimental design as described in section 4.3.7.2 was also used here to evaluate the influence of rIAPP binding on the interfacial membrane properties of POPS lipid vesicles. Increasing concentrations of rIAPP, ranging from 1.6 to 24 μM of peptide were added either to 100 or 500 μM of POPS LUVs labeled with Laurdan (the fluorescent probe to lipid molar ratio used was 1:100). The shift in the steady-state emission spectra of Laurdan, which reflect changes in the hydration/lipid packing of its environment, were quantified by calculating the generalized polarization (*GP*) function of Laurdan (Eq. 4.21) after correcting its emission spectra for the transmissitivity and sensitivity bias of the monochromators and PMT incorporated in the SLM 8100 spectrofluorometer. An adequate blank was always taken into account in these calculations.

Time-resolved emission spectra and time-dependent fluorescence shift

The TRES of Laurdan give quantitative information regarding the energy loss during the relaxation of the solvent around Laurdan and can be used to infer about changes in mobility (lipid packing) and/or hydration of the microenvironment of Laurdan. The TRES of 100 μM of POPS LUVs labeled with Laurdan (1:100) in the absence and in the presence of 12 μM of rIAPP were reconstructed as described in detail in the section above. For validating the complex TDFS data treatment performed according to the literature (Horng *et al.,* 1995; Pokorna *et al*., 2013), control reconstructed TRES of Laurdan were also made for POPC LUVs at 23 ºC and 37 ºC. These results are presented in detail in section 4.7. Briefly, fluorescence intensity decays of Laurdan were recorded at a series of wavelengths encompassing its steady-state emission spectrum (from 400 to 500 nm, with a step of 10 nm) using the TCSPC technique (λ_{exc}= 335 nm). The data were collected in a multichannel analyzer with a time window of 1024 channels, at typically 16 ps/channel (λ_{em}: 400 – 450 nm), 24.4 ps/channel (λ_{em}: 460 - 490 nm) and 39.9 ps/channel (λ_{em}: 500 – 540 nm); usually up to 50 000 and 20 000 counts were accumulated in the peak channel of the IRF and decay curves, respectively. To minimize photobleaching problems, each sample was sub-divided in small volumes to perform a subset of the fluorescence intensity decays described above.

Data analysis

Each fluorescence intensity decay was fitted to a multiexponential function (Eq. 4.23) by iteratively convoluting this empirical function with the respective instrumental response function (Eq. 4.22) using the TRFA Data Processing Package version 1.4 (Scientific

Software Technologies Centre, Belarusian State University) software, as described in detail in section 3.3.6.2. The fitted decays together with the corrected steady-state emission spectrum of Laurdan were used for obtaining the TRES using the spectral reconstruction method described above (Eq. 4.24). The fitting of the time-resolved spectra in the wavenumber domain to a log-normal line shape function was performed using a routine implemented using the Gnuplot software.

4.3.9. UV-Vis absorption spectroscopy

UV-visible absorption measurements were carried out at RT using a Shimadzu MPC-3100 spectrophotometer or using a double-beam V-660 Jasco spectrophotometer, essentially as described in section 2.3.2.

4.3.10. Circular dichroism spectroscopy

CD measurements were carried out accordingly to the conditions previously described in section 3.3.5.2. The samples analyzed were 8 and 24 μM of hIAPP and rIAPP, in the absence and in the presence of 100 and 500 μM of POPS LUVs. The spectra were obtained either immediately after preparing the samples (0h) or after an incubation period of at least 24h in 5 mM HEPES-KOH, 1 mM EDTA, pH 7.4 buffer in quiescent conditions. The helical content of each peptide (% helicity) was calculated on the basis of the Eq. 3.13 and Eq. 3.14, considering the $[\theta]_{222\mathrm{nm,max}}$ of a 37-residue peptide to be − 35 027 deg·cm^2·dmol^{-1}·res^{-1}.

4.3.11. Fluorescence spectroscopy

4.3.11.1. Steady-state fluorescence measurements

Intrinsic fluorescence measurements of the unlabeled IAPP peptides were performed using the HORIBA Jobin Yvon Fluorolog-3-21 spectrofluorometer essentially as described in section 3.3.6.1. Fluorescence measurements of the free dyes and *N*-terminally Atto488-labeled peptides were either performed on the HORIBA spectrofluorometer or using an SLM AMINCO 8100 spectrofluorometer, as described in 3.3.6.1. Unless otherwise stated, the excitation and emission wavelengths employed in the experiments are presented in Table 4.4. Changes in the fluorescence emission spectra were evaluated by determining the intensity average emission wavelength, $\langle\lambda\rangle$, according to equation Eq. 3.17. The steady-state fluorescence anisotropy measurements, $\langle r\rangle$, as defined by Eq. 2.4, were also performed as described above in section 3.3.6.1.

Table 4.4 - Excitation and emission wavelengths used in the steady-state and time-resolved fluorescence measurements performed throughout this chapter.

Fluorescent dye	Fluorescence emission spectra		Steady-state anisotropy measurements		Time-resolved fluorescence measurements	
	λ_{exc} (nm)	λ_{em} (nm)	λ_{exc} (nm)	λ_{em} (nm)	λ_{exc} (nm)	λ_{em} (nm)
Y37	275	280 – 400	282	320	282	320
Atto488	480	490 – 600*	500	525	310	525
Laurdan	370	385 – 600	-	-	335	400-540
Thioflavin T	450	470 – 600	-	-	-	-

* In the FRET experiments, the fluorescence emission spectra were measured between 490 and 680 nm.

4.3.11.2. **Time-resolved fluorescence measurements**

Fluorescence intensity and anisotropy decays were performed and analyzed as described in section 3.3.6.2. The excitation and emission wavelengths employed in the experiments are presented in Table 4.4.

4.3.12. Fluorescence microscopy

4.3.12.1. **CLSM experimental measurements**

Confocal microscopy images were acquired using a Leica SP5 TCS confocal inverted microscope (Leica Microsystems CMS GmbH, Manheim, Germany). The samples imaged were 8 and 24 μM of hIAPP or rIAPP, in absence and in the presence of 100 and 500 μM of POPS LUVs either (i) in the presence of a trace amount of the corresponding Atto488-labeled peptide or (ii) fluorescently-stained with ThT. The samples were placed in 8-well Ibidi chambers at *T*= 21 ± 1 ºC. Excitation lines provided by an Ar laser were focused into the sample by the 10x air objective (NA= 0.4). The 458 and 488 nm Ar laser lines were used to excite the samples stained with ThT and Atto488, respectively. The emission was collected between 470 and 600 nm and between 500 and 600 nm, for the ThT- and Atto488-containing samples, respectively, after passing through a dichroic mirror. A 53.1 μm diameter pinhole placed in front of the image plane blocked out-of-focus signals.

4.3.12.2. **FAIM experimental measurements**

The samples imaged by fluorescence anisotropy microscopy were (i) a control sample of free Atto488 dye, (ii) 0.3 μM of Atto-hIAPP or Atto-rIAPP freshly prepared, and (iii) 8 and 24 μM of hIAPP or rIAPP, in absence and in the presence of 100 and 500 μM of POPS LUVs

in the presence of a trace amount of the corresponding Atto488-labeled peptide after at least a 24h incubation period under quiescent conditions (see section 4.3.2.1). The implementation and calibration of the FAIM setup used in these measurements is described in detail in Chapter 2. Here, the Ti:sapphire laser was tuned at 780 nm, the objective used was 10x objective and the G-factor was calculated daily using a reference solution of A488 dye.

4.3.13. Transmission Electron Microscopy (TEM)

Principles

TEM is an imaging technique that allows the visualization of fibrils in the nanometer range. It is a relatively quick assay that provides qualitative (formation or not of fibrils, appearance and abundance) and quantitative data (e.g. length of filaments). The visualization of samples by TEM is preceded by a step of negative staining to provide a contrast and preserve the morphology. Usually, a metallic salt is used, such as uranyl acetate or phosphotungtic acid. The stain coats the sample creating a layer of electron-dense material. The electron beam used in TEM passes through the sample and is absorbed by the metallic stain, rendering the sample lighter and the surrounding darker. This technique it is not capable of confirming the presence of β-sheet structures and another technique may be required for this (Gras *et al*., 2011).

Experimental procedures

TEM images were measured at the Electron Microscopy Facility of Instituto Gulbenkian Ciência (IGC). Copper 100 mesh grids coated with 1% (w/v) formvar (®Agar Scientific) in chloroform (VWR) and carbon were glow-discharged during 30s using a plasma cleaner and a current of 30 mA before applying the sample. Samples analyzed by TEM were treated after at least 24h incubation by the negative stain technique: they were absorbed to the clean side of a carbon film on mica, stained with neutral phosphotungstic acid (PTA, Fluka Analytical) buffered to pH 7 and transferred to the grid. 10 µL of each sample was allowed to adsorb to the grid for 2 min. The sample was blotted and rinsed with Millipore water using No. 1 Whatman filter paper. Immediately after blotting, freshly filtered 2% PTA was applied for 2 min and then blotted. The images were taken under low dose conditions (<10 e^-/A_2) at magnifications ranging from 12000 to 30000 times on a Hitachi H-7650 scanning Transmission Electron Microscope operated at 120kV equipped with a XR41M mid mount AMT digital camera for data acquisition. The microscope is housed in a dedicated room with temperature and humidity control.

4.4. Results and discussion

4.4.1. hIAPP, but not rIAPP, readily fibrillates in aqueous solution

At the onset of this study, it was fundamental to characterize the fibrillation kinetics of hIAPP in aqueous buffer at RT under the experimental conditions employed in this study since it is known that the self-assembly of amyloidogenic peptides/proteins is critically dependent on a wide range of parameters (e.g. buffer, temperature, stirring conditions, etc. (Giehm and Otzen, 2010; Caillon *et al.*, 2013; Risør *et al.*, 2017). rIAPP was used here as a control because it is a non-amyloidogenic IAPP variant (Moriarty and Raleigh, 1999; Nath *et al.*, 2011; Westermark *et al.*, 2011). Intrinsic fluorophores have previously been used as tools to reveal conformational changes upon protein aggregation (Padrick and Miranker, 2001, 2002; Maji *et al.*, 2005; Rolinski *et al.*, 2010; Amaro *et al.*, 2013). Therefore, we first took advantage of the fact that both rIAPP and hIAPP are intrinsically fluorescent peptides due to the presence of Y37 at the C-terminus of each sequence to monitor the changes in the steady-state fluorescence anisotropy (ssFA) of 8 and 24 μM rIAPP and hIAPP over time. Considering that hIAPP fibrillation is highly dependent on peptide concentration (Padrick and Miranker, 2002; Knight *et al.*, 2006; Domanov and Kinnunen, 2008), these concentrations were chosen in line with recent publications (Kegulian *et al.*, 2015; Pilkington *et al.*, 2016; Martel *et al.*, 2017). To maximize the reproducibility of these assays it is extremely important to guarantee that the experiments start with essentially monomeric peptides as it is well known that the presence of preformed aggregates can seed their fibrillation in solution. Therefore, the previously described method II used in the preparation of CT (Chapter 0, section 3.3.3) solutions was also employed here (Jha, Sellin, *et al.*, 2009; Rolinski *et al.*, 2010; Amaro *et al.*, 2011, 2013). In short, after evaporating a small volume of each peptide stock solution in HFIP, the peptide films were resuspended in buffer and sonicated for a brief period of ca. 1 min.

The ssFA of the peptides at the beginning of their incubation was essentially independent of the peptide variant and concentration used ($\langle r \rangle_{Y37}$= 0.040 $\pm$ 0.011 (n= 4) (Table 4.5)) ruling out the presence of large peptide aggregates in solution. This parameter remained essentially invariant over a 24h-incubation period for both concentrations of rIAPP tested (exemplified in Figure 4.10 A for 24 μM rIAPP (red symbols)) and 8 μM hIAPP (Table 4.5). However, 24 μM hIAPP showed a sigmoid kinetic profile characteristic of the fibrillation of amyloidogenic peptides (Engel *et al.*, 2008; Kegulian *et al.*, 2015) as its ssFA sharply increased from $\langle r \rangle_{Y37}$ = 0.041 ± 0.006 in the lag phase to $\langle r \rangle_{Y37}$= 0.142 ± 0.011 in the plateau phase (Figure 4.10 A, green symbols). Clearly, the presence of a significant amount of aggregated seeds formed during the evaporation of the organic solvent can be ruled out

because classical fibrillation profiles were obtained with a long lag phase followed by a rapid peptide aggregation.

Table 4.5 - Influence of peptide and lipid concentration on the fibrillation kinetics of rIAPP and hIAPP. The steady-state fluorescence anisotropy of Y37, $\langle r \rangle_{\mathbf{Y37}}$, was measured at the beginning (*t*= 0h) and end stage (*t*= 24h) of the fibrillation kinetics of each peptide variant in the absence and in the presence of variable concentrations of POPS LUVs (average ± SD of *n* independent experiments).

Sample	[Peptide] (μM)	[LUVs] (μM)	Time (h)	$\langle r \rangle_{\mathrm{Y37}}$
rIAPP	8	0	0	0.043 ± 0.015 (n= 5)
			24	0.034 ± 0.015 (n= 4)
		100	0	0.103 ± 0.022 (n= 7)
			24	0.094 ± 0.024 (n= 7)
		500	0	0.080 ± 0.023 (n= 5)
			24	0.079 ± 0.023 (n= 4)
	24	0	0	0.025 ± 0.010 (n= 4)
			24	0.024 ± 0.007 (n= 4)
		100	0	0.062 ± 0.008 (n= 3)
			24	0.056 ± 0.014 (n= 3)
		500	0	0.081 ± 0.033 (n= 3)
			24	0.076 ± 0.039 (n= 3)
hIAPP	8	0	0	0.051 ± 0.015 (n= 6)
			24	0.057 ± 0.026 (n= 5)
		100	0	0.104 ± 0.011 (n= 6)
			24	0.226 ± 0.014 (n= 5)
		500	0	0.102 ± 0.021 (n= 6)
			24	0.186 ± 0.026 (n= 5)
	24	0	0	0.039 ± 0.005 (n= 6)
			24	0.195 ± 0.025 (n= 5)
		100	0	0.080 ± 0.010 (n= 4)
			24	0.209 ± 0.020 (n= 5)
		500	0	0.091 ± 0.024 (n= 5)
			24	0.191 ± 0.041 (n= 4)

The ssFA reached at the end stage was found to be slightly variable among different fibrillation runs (Table 4.5). This is probably due to small variations in the initial peptide concentration and/or on the overall amount of peptide converted to fibrils due to the intrinsic stochastic nature of amyloid fibril formation. At the plateau stage of the kinetics, a small blue shift of approximately 2 nm was also detected in the emission spectra of 24 μM hIAPP but

not rIAPP that was accompanied by a slight increase in the fluorescence intensity of its Y37 residue, as it is illustrated in Figure 4.11 A, most likely reflecting the burying of the tyrosine residue in the amyloid fibrils (Padrick and Miranker, 2001; Bhattacharya and Mukhopadhyay, 2015).

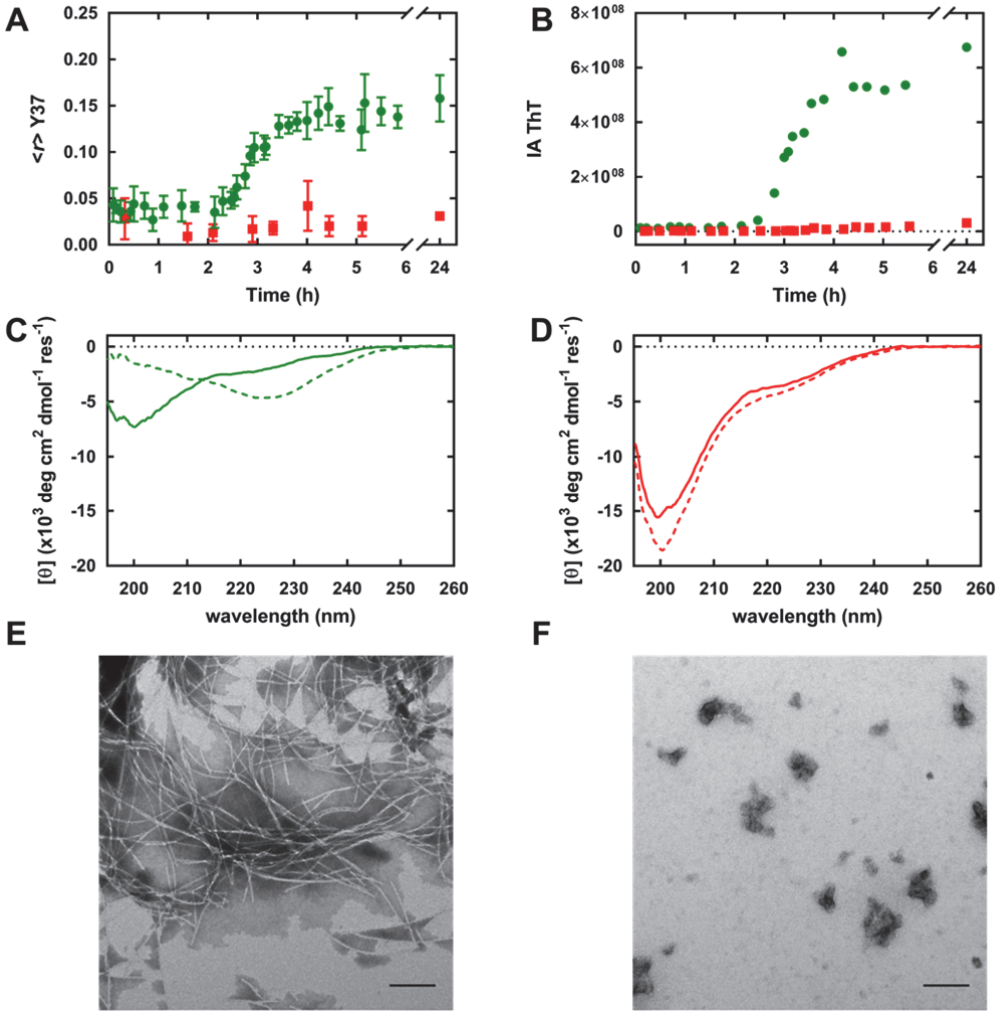

Figure 4.10 - hIAPP, but not rIAPP, readily fibrillates in aqueous solution. Representative fibrillation kinetics of 24 μM hIAPP (green circles) and rIAPP (red squares) in buffered solution; the kinetics was tracked by monitoring the changes over time of (**A**) the steady-state fluorescence anisotropy of Y37, $\langle r \rangle_{Y37}^{282/320nm}$ and (**B**) the fluorescence intensity of 30 μM ThT (integrated area from 470-600 nm, IA (λ_{exc}= 440 nm)). In both cases, hIAPP, but not rIAPP, displayed characteristic sigmoidal fibrillation kinetics. The concomitant secondary conformational and morphological changes that occurred in each sample were further characterized using (**C** and **D**) CD and (**E** and **F**) TEM. The CD spectra were obtained for 24 μM (**C**) hIAPP and (**D**) rIAPP freshly dissolved (solid line) and after a 24 h incubation (dashed lined). hIAPP undergoes a pronounced conformational change from a more disordered structure at time 0h to a structure enriched in β-sheet at 24h, while rIAPP remains a random coil in solution even after a 24h incubation period. Representative negative stain TEM images of 24 μM (**E**) hIAPP and (**F**) rIAPP. After 24h of incubation, samples were stained with 2% PTA. Individual fibrils can be clearly identified in E (Scale bar 200 nm). The incubations in **A**, **B**, **E** and **F** were performed in 20 mM HEPES-KOH, 1 mM EDTA, pH 7.4 buffer, while the incubations in **C** and **D** were performed in 5 mM HEPES-NaOH, 1mM EDTA, pH 7.4, at RT. Samples were left to incubate under quiescent conditions except for the samples used in the fluorescence studies which were homogenized by inversion just prior to measuring each time point of the kinetics.

Finally, more detailed information about the rotational dynamics of the peptides at the end stage of the kinetics was also obtained from the analysis of their fluorescence anisotropy decays in aqueous solution. As it is shown in Figure 4.11 B, the fluorescence anisotropy decay of 24 μM hIAPP does not fully depolarize during its excited-state lifetime of ~1 ns (Table 4.6) at variance with rIAPP, confirming the formation of large peptide aggregates in solution. Whereas a single short rotational correlation time of ϕ_1~ 0.3 ns was measured for rIAPP, an additional longer rotational correlation time was needed to adequately describe the fluorescence anisotropy decay of hIAPP (ϕ_2~ 9 ns, Table 4.7).

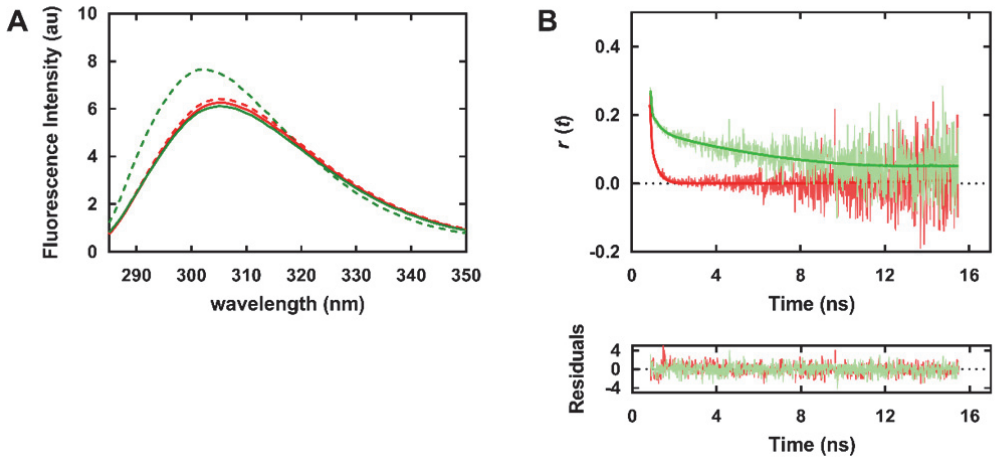

Figure 4.11 – The intrinsic fluorescence properties of IAPP can be used to monitor its fibrillation kinetics in solution. (A) Representative fluorescence emission spectra obtained for 24 μM hIAPP (green lines) and rIAPP (red lines) immediately after preparing the samples (solid lines) and after 24h of incubation (dashed lines) under quiescent conditions (λ_{exc}= 275 nm). hIAPP fibrillation is accompanied by a ~2 nm blue-shift in Y37 emission spectra and an increase in its fluorescence quantum yield. (**B**) Time-resolved fluorescence anisotropy decays obtained for 24 μM hIAPP (green curve) and rIAPP (red curve) after ~6h of incubation (at the point where the plateau of the fibrillation kinetics was detected) (λ_{exc}= 282 nm; λ_{em}= 320 nm; 16.3 ps/channel). The solid lines are the best fits of Eq. 3.25 to the experimental data and the obtained parameters are present in Table 4.7. See the legend of Figure 4.10 for additional experimental details. The formation of large aggregates (fibrillar structures) was evident for hIAPP since it was unable to depolarize the fluorescence emission from Y37 during the time window defined by its fluorescence excited-state lifetime.

A more quantitative analysis of the fibrillation kinetics of hIAPP confirmed the importance of sample agitation during these measurements. The kinetics obtained in this chapter were performed individually in 0.5 x 0.5 cm fluorescence cuvettes under essentially quiescent conditions. Yet, at each time point the sample was homogenized manually by inversion before performing the fluorescence measurements. When the fluorescence signal was measured every 10 - 20 min (e.g. Figure 4.10 A), a lag time (τ_{lag}) of 2.2 ± 0.5 h and an apparent elongation rate, k_{app}= 2.8 ± 0.9 h^{-1} were obtained for 24 μM hIAPP (n= 3) from the fitting of Eq. 4.1 to the experimental data. Some control measurements, however, needed a less detailed characterization of the kinetics and therefore the fluorescence properties of the

sample were measured only sporadically (typically two or three times during the first 5h of the incubation period and then at the end of the kinetics, *t*= 24h). In these cases, the ssFA of the sample remained essentially invariant during the first stage of the measurements implying a longer lag time for the kinetics; nevertheless the final values obtained for the ssFA of hIAPP at the end of each run were very similar, independently of the total amount of sample agitation ($\langle r \rangle_{Y37}$= 0.195 $\pm$ 0.025, *t*= 24h, n= 5, Table 4.5). This result is comparable to the data obtained by Padrick and Miranker while studying the fibrillation kinetics of hIAPP using 25 μM of IAPP, 3% (v/v) HFIP, 100 mM KCl, 50 mM potassium phosphate (pH 7.4) $\langle r \rangle_{Y37}$= 0.235, (Padrick and Miranker, 2001). Altogether, these results confirm that amyloid fibril formation by hIAPP is a process highly dependent on the environmental conditions (Caillon *et al.*, 2013); this observation can also justify the differences between results found in the literature. Kinunnen and co-workers (Kinnunen *et al.*, 2015) showed that the elongation of fibrils had already started after 2h when assaying 2 μM IAPP with 10 μM ThT in a total volume of 200 mL of 20 mM HEPES, 0.1 mM EDTA, pH 7.0, using a microplate reader. On the other hand, Caillon and co-workers reported a τ_{lag} of 9.7 h for 10 μM of peptide in 200 μL with 10 μM ThT in 10 mM Tris/HCl, 100 mM NaCl, pH 7.4 (Caillon *et al.*, 2013). Different preparation of samples, buffers, temperatures and even the vessels where the fibrillation is performed affects the fibrillation.

Table 4.6 - Fluorescence intensity decay parameters obtained for 24 μM rIAPP and hIAPP at pH 7.4 and RT after ~6h of incubation (at the point where the plateau was observed). The normalized amplitudes, α_i, fluorescence lifetimes, τ_i, amplitude-weighted and intensity-weighted mean fluorescence lifetimes, $\langle \boldsymbol{\tau} \rangle_{\mathbf{1}}$ and $\langle \boldsymbol{\tau} \rangle_{\mathbf{2}}$, respectively, of IAPP Y37 residue are presented (λ_{exc} = 282 nm; λ_{em} = 320 nm). For additional details, see the legend of Figure 4.11. Values in square brackets are the errors of the recovered parameters estimated as the lower and upper bound of the joint confidence interval calculated for a 67% probability level. The goodness-of-fit was judged by the χ_G^2 value.

Sample	α_1	τ_1 (ns)	α_2	τ_2 (ns)	α_3	τ_3 (ns)	$\langle \tau \rangle_1$ (ns)	$\langle \tau \rangle_2$ (ns)	χ_G^2
rIAPP	0.30	0.36 [0.35,0.37]	0.62	1.24 1.24,1.25]	0.09	2.54 2.54,2.56]	1.10	1.42	1.00
hIAPP	0.51	0.18 [0.18,0.19]	0.39	0.97 0.97,0.97]	0.10	2.94 2.94,2.96]	0.77	1.64	1.13

The fluorescence properties of 30 μM of ThT were used to follow the fibrillation kinetics of 8 and 24 μM rIAPP and hIAPP in aqueous solution at RT. As it is exemplified in Figure 4.10 B (green symbols), the sigmoid profile obtained for the increase in the integrated fluorescence intensity of ThT over time in the presence of 24 μM hIAPP was very similar to the one obtained when following the intrinsic ssFA of hIAPP (τ_{lag}= 2.5 h and k_{app}= 3.4 h^{-1} in this case), confirming that the peptide aggregates previously detected have an amyloid character. As expected, the fluorescence properties of the dye remained invariant in the

presence of both concentrations tested of the non-amyloidogenic peptide rIAPP (Figure 4.10 B, 24 μM rIAPP, red symbols and 8 μM rIAPP (data not shown)) and 8 μM hIAPP (Figure 4.15 C).

Table 4.7 - Fluorescence anisotropy decay parameters obtained for 24 μM rIAPP and hIAPP at pH 7.4 and RT after ~6h of incubation (at the point where the plateau was observed). The amplitudes, β_i, and rotational correlation times, ϕ_i, are presented. $r(0) = \beta_1 + \beta_2$ ($\lambda_{exc} = 282$ nm; $\lambda_{em} = 320$ nm). Values in square brackets are the errors of the recovered parameters estimated as the lower and upper bound of the joint confidence interval calculated for a 67% probability level. The goodness-of-fit was judged by the χ^2_G value.

Sample	β_1	ϕ_1 (ns)	β_2	ϕ_2 (ns)	$r(0)$	χ^2_G	$\langle r \rangle_{exp}$
rIAPP	0.125	0.27 [0.25,0.29]	-	-	0.125	1.13	0.031 ± 0.003
hIAPP	0.057	0.33 [0.25,0.43]	0.153	9.02 [7.82,10.62]	0.210	1.25	0.204 ± 0.004

Finally, the conformational and morphological changes of both peptide solutions were also monitored using far-UV CD measurements (Figure 4.10 C-D) and TEM (Figure 4.10 E-F and Figure S 4.4 B-E). Figure 4.10 C-D shows that both 24 μM hIAPP and rIAPP display a predominantly random coil conformation in aqueous solution immediately after sample preparation as their CD spectra peaks with negative ellipticity at ~200 nm, in agreement with data from literature obtained both at low (Brender, Hartman, *et al.*, 2008; Khemtémourian *et al.*, 2011; Kegulian *et al.*, 2015) and high ionic strength media (Knight *et al.*, 2006; Li *et al.*, 2016; Martel *et al.*, 2017). The CD spectra of 24 μM hIAPP, but not rIAPP progressed from a random coil at 0 h to a β-sheet enriched structure after 24 h of incubation, as evidenced by the typical β-sheet CD spectra obtained (Figure 4.10 C and D, red and green line, respectively). Also, it is in close agreement to other reports found in literature that also show this temporal evolution (Khemtémourian *et al.*, 2011; Li *et al.*, 2016). TEM images confirmed the formation of very long filaments at the end stage of the kinetics of 24 μM hIAPP, with widths around 7 to 10 nm (Figure 4.10 E and Figure S 4.4 E). The widths of the detected hIAPP filaments are comparable to the ones described previously (Goldsbury *et al.*, 1997; Luca *et al.*, 2007). The wider filaments seen in some micrographs probably arise from bundling up together two or three of the thinner ones. For 8 μM hIAPP, TEM micrographs revealed the presence of a much lower amount of shorter peptide filaments with morphological characteristics otherwise very similar to the ones obtained with 24 μM hIAPP (Figure S 4.4 D). It seems that the amount of fibrillar material produced in these samples was not sufficient to be detected neither by CD measurements nor by an increase in ThT fluorescence intensity (Figure 4.15 C). The incubation of similar concentrations of rIAPP only produced some amorphous round structures as exemplified in Figure 4.10 F and Figure S 4.4 B and C. The amorphous aggregates detected for rIAPP did

not bind ThT and were β-sheet free as determined by CD, confirming that they do not correspond to amyloid fibrils. Martell and co-workers have also previously detected the formation of rIAPP aggregates of small size by DLS and reported "rare amorphous aggregates" by TEM for 28 μM of peptide incubated for 16h, in a pH 7.4 100 mM HEPES buffer with 150 mM NaCl (Martel *et al.*, 2017).

In summary, these results confirmed that hIAPP, but not rIAPP, readily form amyloid fibrils in aqueous solution when incubated at high concentrations for 24 h at RT under essentially quiescent conditions. Furthermore, the ssFA of Y37 was confirmed to be a useful parameter that can be used to monitor this process without introducing any perturbation on the system under study.

4.4.2. Atto488-hIAPP is a good reporter of hIAPP fibrillation in solution

In the previous section it was shown that the intrinsic fluorescence properties of IAPP peptides can be used to track their fibrillation in solution. However, these measurements present several drawbacks: (*i*) the absorption and fluorescence emission of Y37 occurs in the UV range of the electromagnetic spectrum, where in most cases the residual fluorescent impurities of a sample also absorb radiation and light scattering effects become important; (*ii*) tyrosine residues have low molar absorption coefficients and fluorescence quantum yields which limits the intrinsic sensitivity of these fluorescence assays, and (*iii*) the fluorescence properties of tyrosine residues are not suitable for some fluorescence aplications (eg. FAIM, FRET). We therefore sought to explore the use of IAPP peptides conjugated to the very bright fluorescent dye Atto488 as reporters of their self-assembly, first in aqueous solution and then in the presence of lipid vesicles. This dye has excellent water solubility, high fluorescence quantum yield and photostability, and is highly suitable for single-molecule fluorescence measurements and high-resolution microscopy studies (Atto-TEC catalogue). The fluorophore was covalently attached to the *N*-terminal residue of IAPP peptides (Figure 4.4). This position is expected to cause minimal interference on the fibrillation pathway of the peptide, since it has been found that the amyloidogenic-prone region of hIAPP is located near its C-terminal, from residue 22 to 27, residues NFGAIL (Table 4.1 (Ahmad *et al.*, 2011)). Also, a very small amount (typically 1.25%) of the Atto488-fluorescently-labelled peptide relatively to the total concentration of IAPP variant was included in each mixed peptide sample to minimize their possible influence on the process under study and minimize the occurrence of homo-FRET that would strongly depolarize the fluorescence emitted by the probe.

The fibrillation kinetics of 24 μM hIAPP and rIAPP with a tracer amount of the corresponding Atto488-labelled peptide was again studied in aqueous solution at RT by simultaneously

recording the changes in the ssFA of Y37 (Figure 4.12 A, closed symbols) and of the Atto488-conjugated peptide (Figure 4.12 A, open symbols). For hIAPP, both signals presented an overlapping sigmoidal profile over time, with a τ_{lag}= 2.1 ± 0.9 h and an apparent elongation rate, k_{app}= 3.5 ± 0.4 h^{-1} (n= 2), revealing that the concentration of tracer peptide used had a minimal impact on amyloid fiber formation by hIAPP. On the other hand, the ssFA of both rIAPP/Atto488-rIAPP remained invariant under the same incubation conditions, as expected. The fluorescence emission spectra of the fluorophore covalently-linked to hIAPP, but not rIAPP, underwent a ~3 nm red-shift and a significant decrease in its fluorescence intensity upon hIAPP fibrillation in solution (Figure 4.12 B).

The fluorophore Atto488 had to be excited near its $S_2 \leftarrow S_0$ instead of $S_1 \leftarrow S_0$ absorption band, similarly to what happened previously for HL488 (section 3.3.6.2). The experimentally determined fluorescence lifetime of the free dye is coherent with the one provided by the manufacturer ($\langle\tau\rangle_1$ = 4.1 ns, Haugland, 2005) which shows no sign of influence of the selection of absorption band (Figure S 4.1). Similarly, the fluorescence intensity of Atto488-rIAPP decayed almost mono-exponentially in the mixed peptide samples, with a dominant long fluorescence lifetime of ~4 ns ($\langle\tau\rangle_2$~ 4.0 ns), parallel to what was measured for 0.3 μM Atto488-rIAPP and Atto488-hIAPP (Table 4.8). However, the incorporation of the Atto488-conjugated peptide in hIAPP amyloid fibrils was accompanied by a pronounced decrease in its intensity-weighted mean fluorescence lifetime, which became $\langle\tau\rangle_2$~ 2.3 ns (Table 4.8). Under these conditions, ~40% of the fluorescence emitted by the sample was associated to the fast decay components of τ_1~ 0.3 ns and τ_1~ 1.2 ns (Table 4.8). Altogether, the fluorescence data reveal a strong quenching of the Atto488 fluorophore upon the incorporation of the tracer peptide into the hIAPP amyloid fibrils when compared to the corresponding free monomeric peptide in solution.

We next sought to obtain more detailed information about the rotational dynamics of the Atto488-labeled peptides by performing time-resolved fluorescence anisotropy measurements. As it is illustrated in Figure 4.12 C, the anisotropy decays obtained for the Atto488-labelled peptides are inverted relatively to the usual situation as their fluorescence anisotropy have an initial negative *r*(0) value that eventually decays to 0 at long times. From the anisotropy excitation spectrum obtained for the free dye Atto488 in glycerol at T= 8 °C, i.e. under experimental conditions that minimize fluorescence depolarization due to the rotational dynamics of the fluorophore in solution, we obtained $\langle r\rangle_{\mathrm{Atto488}}^{310\mathrm{nm}}$= -0.125 (Figure S 4.1), indicating that the absorption and emission transition dipole moments of Atto488 must be just about perpendicular to each other at this excitation wavelength. On the other hand, the ssFA of the dye was invariant within the range from 440 to 520 nm, $\langle r\rangle_{\mathrm{Atto488}}^{440-520\ \mathrm{nm}}$= 0.367

± 0.002 ($S_1 \leftarrow S_0$ absorption band) (Figure S 4.1) close to the maximum expected value for collinear absorption and emission transition dipole moments (Eq. 2.1).

Table 4.8 - Fluorescence intensity decay parameters of obtained for Atto488-conjugated peptides of the mixed peptide samples at pH 7.4 and RT after ~6h of incubation (when the plateau was observed). The normalized amplitudes, α_i, fluorescence lifetimes, τ_i, amplitude-weighted and intensity-weighted mean fluorescence lifetimes, $\langle \boldsymbol{\tau} \rangle_{\mathbf{1}}$ and $\langle \boldsymbol{\tau} \rangle_{\mathbf{2}}$, respectively, are presented ($\lambda_{\mathbf{exc}} = 310$ nm; $\lambda_{\mathbf{em}} = 525$ nm). The samples correspond to 24 μM rIAPP/hIAPP with 1.25% of the corresponding Atto488-fluorescently labeled peptide. For additional details, see the legend of Figure 4.12. Values in square brackets are the errors of the recovered parameters estimated as the lower and upper bound of the joint confidence interval calculated for a 67% probability level. The goodness-of-fit was judged by the $\boldsymbol{\chi^2_G}$ value.

Sample	[IAPP] (μM)	α_1	τ_1 (ns)	α_2	τ_2 (ns)	α_3	τ_3 (ns)	$\langle\tau\rangle_1$ (ns)	$\langle\tau\rangle_2$(ns)	χ^2_G
rIAPP	0[1]	-	-	0.08	1.40 [1.30,1.58]	0.93	4.10 [4.06,4.11]	3.89	4.02	1.11
	24	-	-	0.06	0.80 [0.71,1.01]	0.94	4.04 [4.01,4.07]	3.86	4.00	1.03
hIAPP	0[1]	-	-	0.07	0.78 [0.72,0.95]	0.93	3.98 [3.94,3.99]	3.76	3.93	1.20
	24	0.36	0.26 [0.25,0.27]	0.39	1.17 [1.17,1.18]	0.26	3.16 [3.15,3.18]	1.35	2.29	1.20

[1] The concentration of Atto488-IAPP used was 0.3 μM.

For the fluorescence anisotropy decay measured with the free Atto488, an $r(0)$= -0.128 and a rotational correlation time of ϕ_1= 0.16 ns [0.15;0.18] was obtained (Figure S 4.1 B). The initial anisotropy for both tracer Atto488-fluorescently labeled peptides in the mixed peptide solutions obtained at the end stage of the fibrillation kinetics were $r(0)$ < -0.125 (Figure 4.12 C and Table 4.9), revealing that probably there are very fast segmental/librational motions of the covalently-conjugated fluorophores which are below the time resolution of our instrumental setup. Atto488-rIAPP completely depolarized its fluorescence emission within the time window available to the measurement of its anisotropy decay, with a rotational correlation time of ϕ_1= 1.0 ± 0.1 ns and $r(0)$= – 0.098 ± 0.004 (*n* = 6), indicating that no large fluorescent species were assembled in solution. The anisotropy decay obtained for Atto488-hIAPP did not converge to zero at long times which is consistent with a very restricted rotational mobility of the fluorescently-labeled peptide upon its incorporation in the hIAPP fibrillar structures (Figure 4.12 and Table 4.9).

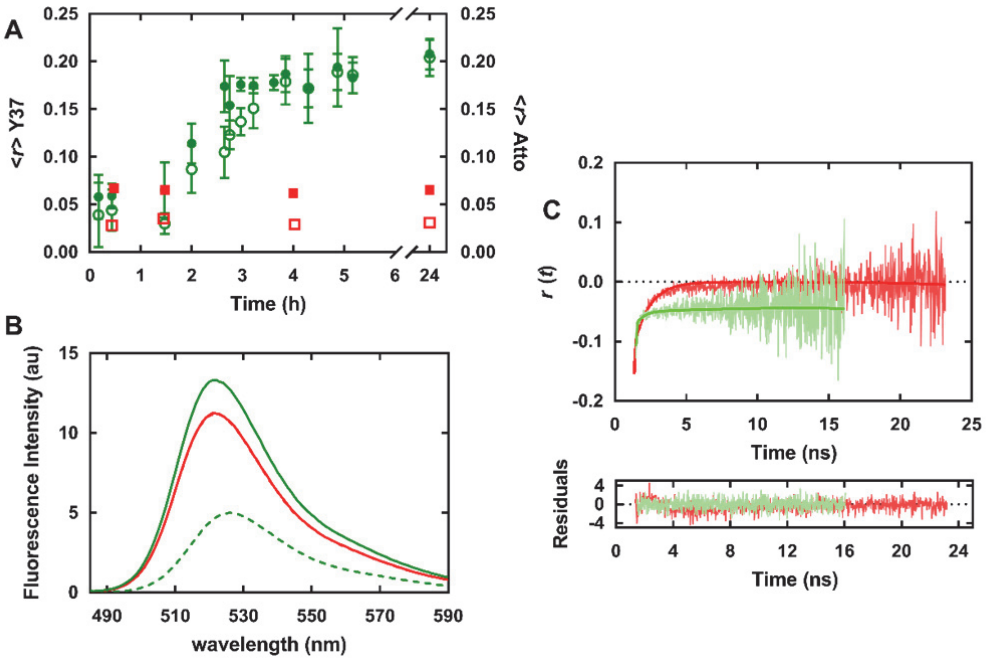

Figure 4.12 - The presence of a tracer amount of Atto488-labeled peptide does not affect the fibrillation ability of hIAPP in solution. (**A**) Representative fibrillation kinetics of 24 μM hIAPP (green circles) and rIAPP (red squares) in the presence of 1.25% (0.3 μM) of the respective Atto488-labelled peptide. The $\langle r \rangle_{\mathrm{Y37}}^{282/320\mathrm{nm}}$ (open symbols, left axis) and of the covalently-bound Atto488, $\langle r \rangle_{\mathrm{Atto488}}^{500/525\mathrm{nm}}$ (closed symbols, right axis), were measured in turn for the same sample over time. Both signals were able to detect the fibrillation of hIAPP in solution, reaching identical plateau values of $\langle r \rangle_{\mathrm{Y37}} \sim \langle r \rangle_{\mathrm{Atto488}} \sim 0.20$. For rIAPP, both fluorescence anisotropies remained essentially invariant over time ($\langle r \rangle_{\mathrm{Y37}}$ = 0.031 ± 0.003; $\langle r \rangle_{\mathrm{Atto488}}$ = 0.065 ± 0.002). (**B**) Representative fluorescence emission spectra of 24 μM hIAPP (green lines) and rIAPP (red lines) in the presence of 1.25% of the respective Atto488-labelled peptide measured immediately after preparing the samples (solid lines) and after 24h of incubation (dashed lines) under quiescent conditions (λ_{exc}= 480 nm). The emission spectra of the covalently-linked fluorophore undergo a decrease in fluorescence intensity and a ~3 nm red-shift upon hIAPP fibrillation in solution (Table 4.10). The spectra of rIAPP for 0h and 24h are overlapped. (**C**) The fluorescence anisotropy decays of these samples were also measured, after ~6h of incubation (when the plateau was observed). The green and red solid lines are the best fits of Eq. 3.25 to the experimental data obtained for 24 μM hIAPP (green curve, 16.3 ps/channel) and rIAPP (red curve, 24.4 ps/channel). For additional details, see the legend of Table 4.9. The appearance of a long correlation time in the first case is a clear evidence for the formation of large hIAPP aggregates (fibrils) in solution.

In conclusion, the control fibrillation kinetics performed with hIAPP in aqueous solution at RT revealed a safe time frame of at least ~2 h before the onset of amyloid fibril formation, particularly for the experiments conducted with 24 μM of hIAPP. When the peptide samples were left undisturbed, the lag time of the fibrillation kinetics was longer than 2h, and the spectroscopic measurements could be performed during an extended period of time without expecting any major interference from the self-assembly of hIAPP in solution.

Table 4.9 - Fluorescence anisotropy decay parameters of obtained for Atto488-conjugated peptides of the mixed peptide samples at pH 7.4 and RT after ~6h of incubation (when the plateau was observed). The fractional amplitudes, β_i, and rotational correlation times, ϕ_i, are presented. $r(0) = \beta_1 + \beta_2$ ($\lambda_{exc} = 310$ nm; $\lambda_{em} = 525$ nm). The samples correspond to 24 μM rIAPP/hIAPP with 1.25% of the corresponding Atto488-fluorescently labeled peptide. For additional details, see the legend of Figure 4.12. Values in square brackets are the errors of the recovered parameters estimated as the lower and upper bound of the joint confidence interval calculated for a 67% probability level. The goodness-of-fit was judged by the χ^2_G value.

Sample	[IAPP] (μM)	β_1	ϕ_1 (ns)	β_2	ϕ_2 (ns)	$r(0)$	χ^2_G
hIAPP	0[1]	-0.101	0.79 [0.74;0.84]	-	-	-0.101	1.13
	24	-0.019	0.54 [0.34,0.93]	-0.050	66.14 [36.13,-]	-0.068	1.12
rIAPP	0[1]	-0.091	0.96 [0.90,1.03]	-	-	-0.091	1.20
	24	-0.098	1.10 [1.04,1.19]	-	-	-0.098	1.34

[1] The concentration of Atto488-IAPP used was 0.3 μM.

4.4.3. FAIM maps of Atto-hIAPP reveal hIAPP aggregation in solution

The presence of a tracer amount of the Atto488-fluorescently labeled peptide allowed using FAIM to visualize the possible fibrillar structures formed upon incubating the mixed peptide samples for 24h under quiescent conditions at RT. The implementation and calibration of the 2PE FAIM setup is described in detail in Chapter 2. As it is mentioned there, it is necessary to determine the *G*-factor of the apparatus on a daily basis. This correction factor accounts for the difference in the sensibility of the two photomultipliers (PTMs), as well as for very small variations in the position of the polarization beam splitter cube (PBS), since it is necessary to remove it periodically from the setup. The free dye A488 was used here for this purpose and a *G*-factor ~ 0.60 ± 0.03 (*n*= 5) was obtained for the set of measurements described in this Chapter. The 2PE ssFA maps for both free dyes A488 and Atto488 used for calibration and validation of the system are presented in Figure S 4.3 and the data summarized in Table S 4.1.The ssFA measured in a spectrofluorometer for 0.3 μM Atto488-rIAPP, either alone in buffer or in the presence of 8 or 24 μM of the corresponding unlabeled peptide, was approximately $\langle r \rangle_{\text{exp}}^{\text{1PE}}$ = 0.063 ± 0.002 (*n*= 3) (Table 4.10). The matching CLSM images of these samples did not reveal any aggregates, and accordingly the corresponding 2PE FA maps originated histograms that were well fitted by a single Gaussian distribution centered at $\langle r \rangle_{\text{exp}}^{\text{2PE}}$ = 0.140 ± 0.025 (*n*= 3) Figure 4.13 A, C and E Table 4.10). These results reinforce the conclusion that rIAPP is unable to fibrillate in aqueous solution, being essentially monomeric even when high concentrations of unlabeled peptide are added to the solution. Regarding the amyloidogenic hIAPP variant studied, the ssFA measured for 0.3 μM Atto488-hIAPP in a spectrofluorometer was $\langle r \rangle_{\text{exp}}^{\text{1PE}}$= 0.065 ±

0.006 (Table 4.10). The histogram obtained from its 2PE FA map was again well described by a single Gaussian peak, $\langle r \rangle_{\mathrm{exp}}^{\mathrm{2PE}}$= 0.15 ± 0.10 (Table 4.10).

Interestingly, although the 1PE ssFA of 0.3 μM Atto488-hIAPP in the presence of 8 μM hIAPP did not provide any evidence for the formation of amyloid fibrils ($\langle r \rangle_{\mathrm{exp}}^{\mathrm{1PE}}$ = 0.067 ± 0.003 (Table 4.10)), occasionally some fluorescent aggregates could be detected in the sample using CLSM (Figure 4.13 D, left panel). The histograms obtained from the 2PE FA map calculated for these peptide assemblies were monodistributed and, as it is exemplified in Figure 4.13 D, right panel, centered at much larger values compared to the equivalent rIAPP sample (Figure 4.13 C, right panel: $\langle r \rangle_{\mathrm{exp}}^{\mathrm{2PE}}$ = 0.323 ± 0.036 (Table 4.10). This is in agreement with the TEM micrographs obtained at the end stage of the fibrillation kinetics of hIAPP samples prepared with the same concentration (Figure S 4.4 D) and the observation that these assays were in general less reproducible than the ones carried out with 24 μM of hIAPP. When 0.3 μM Atto488-hIAPP was mixed with 24 μM hIAPP, the 1PE ssFA of the sample was always much higher than in the previous situation ($\langle r \rangle_{\mathrm{exp}}^{\mathrm{1PE}}$ = 0.243 ± 0.005, Table 4.10), clearly showing the ability of Att0488-hIAPP to incorporate into hIAPP amyloid fibrils as discussed in the previous section. The CLSM images obtained for these samples at the plateau stage of their fibrillation kinetics clearly revealed the formation of an extensive network of peptide aggregates (Figure 4.13.F, left panel) that resulted in a 2PE FA map with very high ssFA values; the corresponding histogram was again well described by a single Gaussian function but that was now centered at an even higher value $\langle r \rangle_{\mathrm{exp}}^{\mathrm{2PE}}$ = 0.386 ± 0.056 (Table 4.10). It should be stressed that the optical resolution (< 200 nm) of fluorescence microscopy (FAIM: Figure 4.13) is below TEM resolution (TEM: Figure S 4.4). Most likely, the μm-long peptide aggregates detected with CLSM (Figure 4.13 D and F) correspond to large bundles of hIAPP amyloid fibrils

Globally, these results confirm that FAIM can be an efficient tool to detect and characterize the heterogeneous aggregates formed along the fibrillation pathway of an amyloidogenic protein/peptide, usefully complementing the ensemble-average measurements performed in a conventional spectrofluorometer/ plate reader.

Note that, despite the fact that for the labeled peptides alone presented the larger discrepancy between the value converted from 1PE measurements in the spectrofluorometer and the 2PE value obtained in the microscope, the current setup is able to distinguish between free dye, free labeled peptide in solution, larger concentrations of peptide with a tracer amount of labeled peptide, in solution and in fibrillar/agregated structures, found for hIAPP. This is a major achievement considering the technical limitations that still limit the implemented FAIM setup.

Table 4.10 - Monitorization of the influence of peptide and lipid concentration on the fibrillation kinetics of rIAPP and hIAPP using a tracer amount of the corresponding Atto488-fluorescently-labelled peptide. The fluorescence properties of Atto488 were measured at the beginning (*t*= 0 h) and end stage (*t*= 24 h) of the fibrillation kinetics of each peptide variant in the absence and in the presence of variable concentrations of POPS LUV. For additional experimental details see the legend of Figure 4.13, Figure 4.21 and Figure 4.22. n.d., not determined.

Sample	[IAPP] (μM)	[POPS] (μM)	$\langle\lambda\rangle_{0h}$ (nm) [1]	$\Delta\langle\lambda\rangle$ (nm) [2]	$\langle r\rangle_{Atto488}^{24h}$		
					Spectrofluorometer		Microscope
					$\langle r\rangle_{exp}^{1PE}$	$\langle r\rangle_{calc}^{2PE}$ [3]	$\langle r\rangle_{image}^{2PE}$ [4]
Atto488 -rIAPP	0.3	0	531.8	n.d.	0.064 ± 0.006 (n= 3)	0.092	0.15 ± 0.05 (n= 15 875)
rIAPP	8 [5]	0	529.9	0	0.065 ± 0.002	0.093	0.16 ± 0.06 (n= 15 875)
		100	530.4	n.d.	0.146 ± 0.009	n.d.	n.d.
		500	530.7	n.d.	0.157 ± 0.009	n.d.	n.d.
	24 [5]	0	531.7	0	0.061 ± 0.001	0.087	0.11 ± 0.07 (n= 15 875)
		100	531.7	n.d.	0.060 ± 0.001	0.086	0.12 ± 0.08 (n= 15 875)
		500	532.3	n.d.	0.187 ± 0.002	0.267	0.32 ± 0.09 (n= 15 843)
Atto488 -hIAPP	0.3	0	531.8	n.d.	0.065 ± 0.006 (n= 3)	0.093	0.15 ± 0.10 (n= 15 851)
hIAPP	8 [5]	0	531.7	0	0.067 ± 0.003	0.096	0.32 ± 0.04 (n= 3 854)
		100	532.9	2.4	0.226 ± 0.006	0.323	0.36 ± 0.07 (n= 2 016)
		500	532.7	3.3	0.209 ± 0.005	0.298	0.31 ± 0.06 (n= 1 940)
	24 [5]	0	531.8	3.4	0.243 ± 0.005	0.347	0.39 ± 0.06 (n= 5 240)
		100	534.6	3.0	0.198 ± 0.002	0.283	0.31 ± 0.05 (n= 5 279)
		500	533.3	3.3	0.191 ± 0.005	0.273	0.31 ± 0.06 (n= 5 634)

[1] intensity-weighted average emission wavelength from freshly prepared samples

[2] $\Delta\langle\lambda\rangle = \langle\lambda\rangle_{24h} - \langle\lambda\rangle_{0h}$

[3] The ssFAs measured in the spectrofluorometer (λ_{exc}= 500 nm, λ_{em}= 525 nm) were converted to the expected values if 2PE instead of 1PE was used. The conversion factor used was 1.428.

[4] Gaussian fit (average ± SD) to the histograms obtained from the FA maps calculated on a pixel-by-pixel basis from a 127x125 pixels image. The number of pixels *n* used for each 2PE anisotropy determination is indicated for each sample. The FAIM measurements were performed using the objective 10x, NA 0.4.

[5] The concentration of the tracer peptide was kept at 1.25% of the total peptide concentration used in the sample.

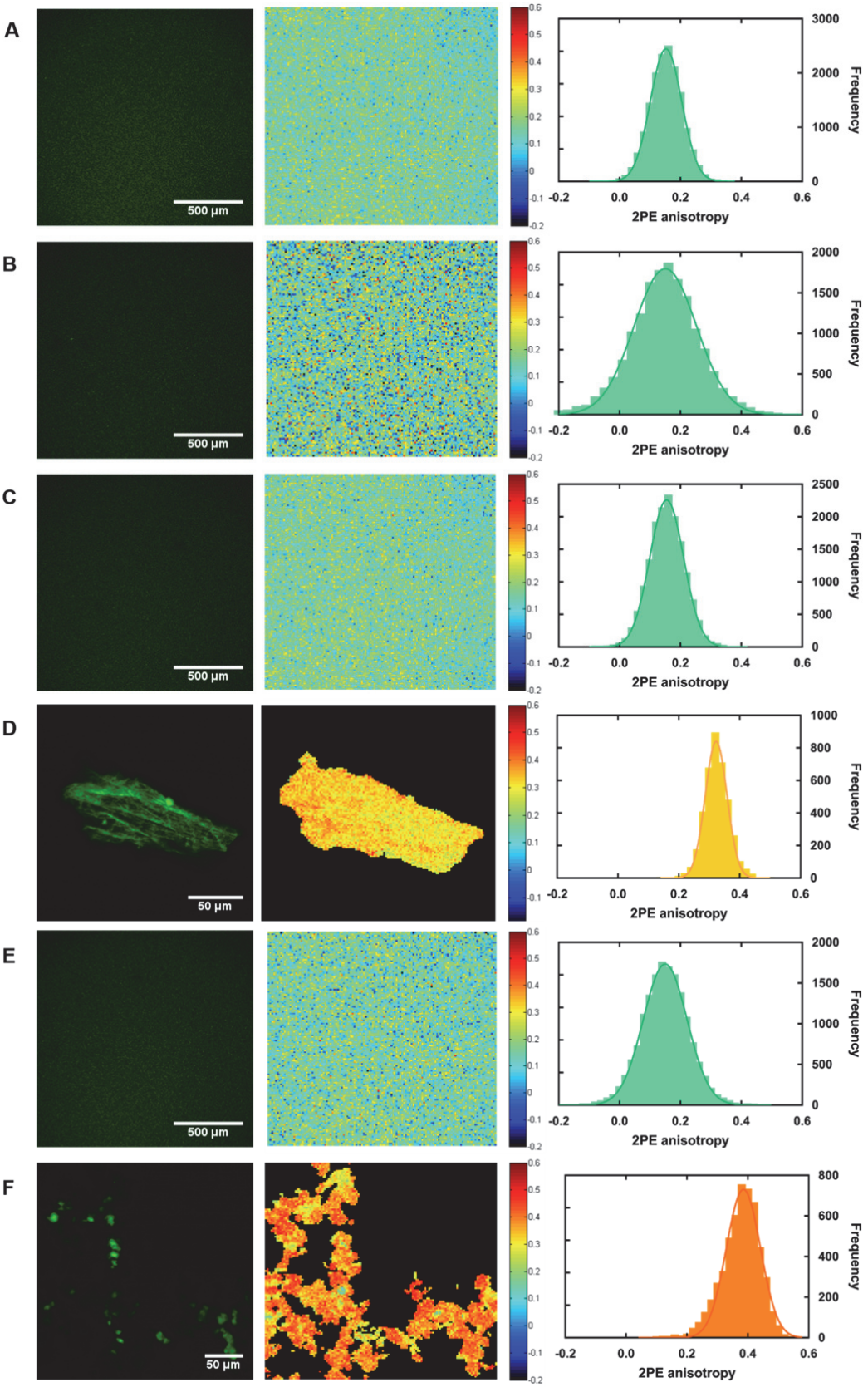
A
500 µm
0.6
0.5
0.4
0.3
0.2
0.1
0
-0.1
-0.2
3000
2000
1000
0
Frequency
-0.2
0.0
0.2
0.4
0.6
2PE anisotropy
B
500 µm
2000
1500
1000
500
0
Frequency
-0.2
0.0
0.2
0.4
0.6
2PE anisotropy
C
500 µm
2500
2000
1500
1000
500
0
Frequency
-0.2
0.0
0.2
0.4
0.6
2PE anisotropy
D
50 µm
1000
800
600
400
200
0
Frequency
-0.2
0.0
0.2
0.4
0.6
2PE anisotropy
E
500 µm
2000
1500
1000
500
0
Frequency
-0.2
0.0
0.2
0.4
0.6
2PE anisotropy
F
50 µm
800
600
400
200
0
Frequency
-0.2
0.0
0.2
0.4
0.6
2PE anisotropy

4.4.4. The membrane-mediated fibrillation of hIAPP is strongly enhanced by low concentrations of anionic liposomes

The presence of membranes is known to strongly influence the fibrillation of amyloidogenic peptides. Particularly, anionic liposomes have been implicated in the enhancement of amyloid fibril formation by amyloidogenic proteins and peptides, including hIAPP. (Gorbenko and Kinnunen, 2006; Hebda and Miranker, 2009; Butterfield and Lashuel, 2010; Sheynis and Jelinek, 2010). Therefore, we first assessed the influence of anionic phospholipid content of liposomes on the fibril-forming properties of hIAPP by monitoring the changes in its ssFA (Y37) under the experimental conditions employed in this study. The non-amyloidogenic rat variant of IAPP was again used as a control as it allows distinguishing the effects produced by the membrane-binding properties of each peptide from the ones resulting from their fibril-forming propensity. 24 μM rIAPP or hIAPP were incubated with variable total phospholipid concentrations of LUVs prepared with 100 mol% POPC, 50:50 mol% POPC:POPS or 100 mol% POPS and the intrinsic ssFA of rIAPP/hIAPP was measured after 30 minutes of incubation. As shown in Figure 4.14 A, the intrinsic ssFA of both rIAPP and hIAPP remained essentially invariant in the presence of 100% POPC LUVs indicating that there was no significant binding of either peptide to the lipid vesicles, at least within the time frame/ concentration range of phospholipid concentrations used. The addition of increasing concentrations of 50:50 POPC:POPS or POPS LUVs to rIAPP induced a monotonous although small increase in its ssFA, from $\langle r \rangle_{\mathrm{Y37}}$ ~ 0.04 to $\langle r \rangle_{\mathrm{Y37}}$ ~ 0.09 (Figure 4.14 B and C). Interestingly, when the experiments were repeated with hIAPP, biphasic profiles were now obtained for $\langle r \rangle_{\mathrm{Y37}}$ as a function of total lipid concentration (Figure 4.14 B and C).

Figure 4.13 - The tracer Atto488-labeled hIAPP is efficiently incorporated into hIAPP aggregates. Representative CLSM image (left panels, $\boldsymbol{\lambda_{exc}}$= 488 nm, $\boldsymbol{\lambda_{em}}$= 500-600 nm), 2PE ssFA maps (middle panels; $\boldsymbol{\lambda_{exc}^{2PE}}$ = 780 nm, emission selected with 500-550 band pass filter) and histograms (right panels) obtained for (**A**, **C** and **E**) Atto488-labelled rIAPP and (**B**, **D** and **F**) Atto488-labelled hIAPP: (**A** and **B**) in the absence (0.3 μM, freshly prepared solutions), and in the presence of (**C** and **D**) 8 μM or (**E** and **F**) 24 μM of the respective unlabeled peptide (after at least 24h incubation at RT). In these last cases, the concentration of the tracer peptide was kept at 1.25% of the total peptide concentration used in the sample. The 10x air objective was used in all the measurements. The image processing of the raw data was performed using a MATLAB script as previously described (Chapter 2) giving directly the 2PE FA false-color maps (middle panels) and the data for obtaining the histograms (right panels). A Gaussian distribution was successfully fitted to each of these histograms using GraphPad Prism 7 (full curves). The average and standard deviation of these fits and the number of pixels processed in the data treatment are presented in Table 4.10. The presence of large peptide aggregates presenting a high 2P FA was only detected for the Atto488-labelled hIAPP in the presence of a large excess of unlabeled hIAPP.

Up to 100 – 200 μM of total phospholipid, the ssFAs of hIAPP progressively increased with the concentration of lipid and the values measured were much higher than the ones obtained with the equivalent rIAPP samples; upon further increasing the liposome concentration added to the solution, the ssFA of hIAPP gradually decreased, converging to the values measured for rIAPP at identical high lipid concentrations.

Altogether, these results confirmed that electrostatic interactions are the major driving force governing hIAPP and rIAPP binding to lipid membranes consistent with their predicted net charges of +3 and +3.9 at pH 7.0 (Table 4.2) (in addition to their N-terminal amine group, the basic residues present in hIAPP and rIAPP are Lys1 and Arg11 and Lys1, Arg11 and Arg18, respectively). In fact, it has already been shown that the highly cationic N-terminal segments of these peptides are responsible for their partitioning to anionic liposomes (Williamson and Miranker, 2007; Patil *et al.*, 2009).

Furthermore, the data also strongly suggest that low but not high concentrations of anionic liposomes accelerate hIAPP fibrillation kinetics since only in the first case the ssFA of hIAPP approached the typical plateau values measured at the end stage of hIAPP fibrillation in solution (particularly when 100 mol% POPS LUVs were used, Table 4.5).

The alternative explanation that the second stage of the biphasic profiles were due to an experimental artefact, namely liposome-induced depolarization of the emitted radiation due to scattering effects, was ruled out by extending the lipid concentrations used in the assay. As it is shown in Figure S 4.2, this effect only became important at much higher total lipid concentrations ($[L]_t$> 1 mM).

In order to gain further information about this catalytic effect induced by the presence of the anionic lipid membranes, complementary kinetic assays were used to investigate how the anionic phospholipid content of liposomes modulated hIAPP fibrillation in solution. The experiments were carried out with 8 and 24 μM of rIAPP and hIAPP, in the presence of either 100 μM or 500 μM POPS LUVs. This liposome composition was chosen because the biphasic behavior described above was much more noticeable when 100 mol% POPS instead 50:50 mol% POPC:POPS LUVs were used (Figure 4.14 B and C). On the other hand, these lipid concentrations were selected because a maximum increase in the ssFA of hIAPP was detected for 100 μM POPS LUVs, whereas very similar values were obtained for the ssFA of both peptides in the presence of 500 μM POPS LUVs (Figure 4.14 C). Similarly to what was previously performed for IAPP peptides in solution, the temporal dependence of both the ssFA (Y37) of the peptides and fluorescence intensity of the amyloidophilic fluorescent dye ThT were monitored in independent experiments, as it is exemplified for hIAPP in Figure 4.15 A-D. The changes in the secondary structure and morphology of both peptides were also evaluated at the onset (*t*= 0 h) and end stage (*t*= 24 h) of each kinetics

by performing far-UV CD (Figure 4.16) and TEM measurements (Figure 4.15 E-H and Figure S 4.4)

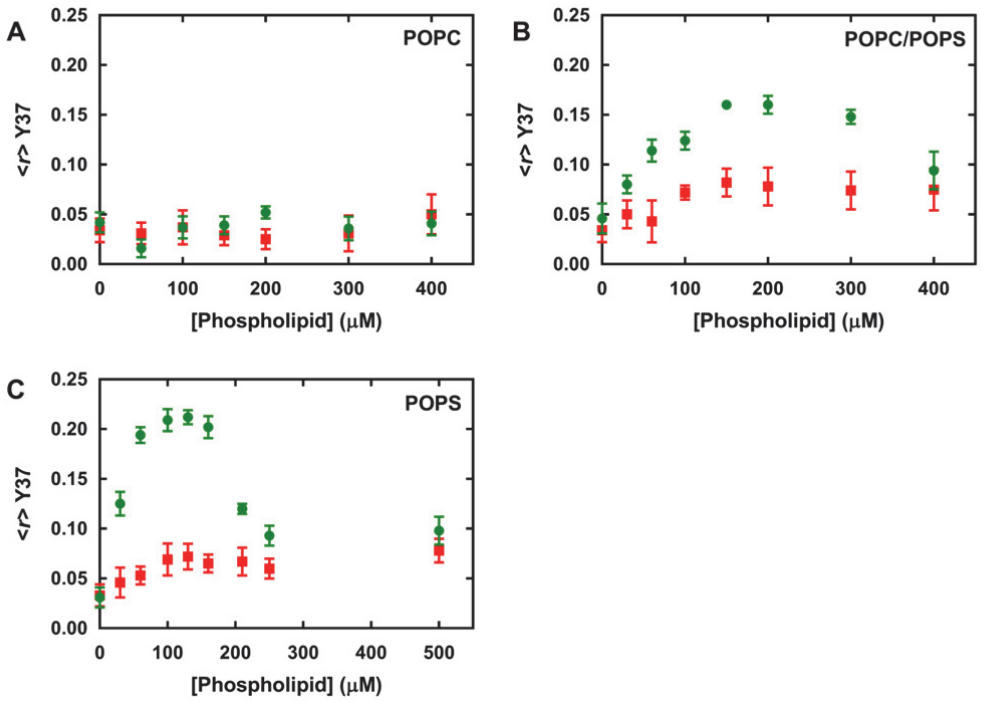

Figure 4.14 - The anionic phospholipid content of liposomes controls the membrane-mediated hIAPP fibrillation. The interaction of 24 μM hIAPP (green circles) and rIAPP (red squares) with variable total lipid concentrations of **(A)** POPC, **(B)** POPC:POPS 50:50 and **(C)** POPS LUVs was monitored using the ssFA of their Y37 residue, $\langle r \rangle_{\mathrm{Y37}}^{282/320\mathrm{nm}}$. The ssFA changes were biphasic for hIAPP only in the presence of POPS-containing liposomes. For rIAPP, a monotonous increase from $\langle r \rangle_{\mathrm{Y37}}$ ~ 0.04 in buffer to $\langle r \rangle_{\mathrm{Y37}}$ ~ 0.09 was detected upon increasing the concentration of anionic liposomes, irrespectively of their POPS content (50 or 100 mol%).

For both 8 and 24 μM of rIAPP, the addition of either 100 or 500 μM POPS LUVs to the solution produced an almost instantaneous yet minor increase in its ssFA slightly from $\langle r \rangle_{\mathrm{Y37}}$ ~ 0.04 ± 0.01 to $\langle r \rangle_{\mathrm{Y37}}$ ~ 0.09 ± 0.01 that remained stable over 24 h (Table 4.5). This was not accompanied by any significant development of ThT signal (data not shown). Concomitantly, the peptide underwent a structural transition from predominantly random coil to α-helix upon membrane binding to the POPS LUVs, as revealed by the negative peaks at 208 and 222 nm in their CD spectra, that did not evolve over time (Figure 4.16 A-D). The fact that the CD spectra of rIAPP under these conditions present a slightly more intense minimum at 208 nm instead at 222 nm indicates that there might be a short polyproline II helix in rIAPP as suggested by Jayasinghe and Langen, 2005 (Jayasinghe and Langen, 2005) The detection of an isodichroic point at 203-204 nm in the CD spectra confirms that the rat variant of IAPP is undergoing a two-state conformational transition between a

predominantly random coil in aqueous solution to membrane-bound helical states. It is also interesting to note that the α-helical content derived from the CD spectra for rIAPP bound to the liposomes indicates that an increase in peptide concentration from 8 to 24 μM resulted in less membrane-bound peptide in the presence of 100 μM compared to 500 μM POPS LUVs, from 46.2% to 37.5% (Figure 4.16 A and C and Table 4.11).

Finally, the TEM images obtained for rIAPP after incubation for 24 h in the presence of POPS LUVs confirmed that no fibrillation occurred in these samples as expected for this control non-amyloidogenic peptide (Figure S 4.4).

Table 4.11 - Estimated % of helicity for rIAPP samples. Calculated according to Eq. 3.13 and assuming $[\boldsymbol{\theta}]_{\mathbf{222nm,max}}$ of a 37-residue peptide is − 35 027 deg·cm^2·dmol^{-1}·res^{-1}.

Sample	[IAPP] (μM)	[POPS] (μM)	$[\boldsymbol{\theta}]_{222nm}$ (x10^3 $\mathbf{deg{\cdot}cm^2{\cdot}dmol^{-1}{\cdot}res^{-1}}$)	% **helicity**
rIAPP	8	0	-4.32	12.3
		100	-16.17	46.2
		500	-17.07	48.7
	24	0	-3.60	10.3
		100	-13.15	37.5
		500	-16.41	46.9

Regarding 8 μM of hIAPP in buffer, and as already described, both fluorescence readouts remained constant over time, ruling out any extensive fibrillation of hIAPP at this peptide concentration even after 24 h incubation under quiescent conditions (Figure 4.15 A and C and Table 4.5). However, both 100 and 500 μM POPS LUVs were able to catalyze the formation of amyloid fibrils as revealed by the simultaneous small increases in the ssFA of the peptide (Figure 4.15 A and Table 4.5), and in ThT fluorescence intensity (Figure 4.15 C). These kinetics, however, had a long lag time as these changes were only detected when the samples were incubated for longer than 4 h. In spite of the low S/N ratio, it was also clearly evident that the CD spectra obtained for 8 μM hIAPP in the presence of both concentrations of POPS liposomes changed over time from a predominantly α-helical conformation (freshly prepared samples) to a β-sheet enriched structure (after 24h incubation) (Figure 4.16 E and F). These results were confirmed by the TEM images obtained for these samples which revealed the presence of a small amount of long straight fibrils, which sometimes seem to be adherent to the surface of intact liposomes (Figure 4.15 E and G and Figure S 4.4).

The influence of the L/P ratio on the fibrillation kinetics of hIAPP was much clearer when the assays above were repeated with a 3-fold higher concentration of peptide. As shown in

Figure 4.15 B (red triangles), the addition of 100 μM POPS LUVs to 24 μM hIAPP produced a very fast increase of its intrinsic ssFA over time. The ThT fluorescence assay demonstrated that under these experimental conditions the peptide had a strong ability to form amyloid-like structures at the end stage of this kinetics (Figure 4.15 D, red triangles), which was confirmed by both CD (Figure 4.16 H) and TEM (Figure 4.15 F and Figure S 4.4) measurements.

A quantitative analysis of the sigmoidal kinetics obtained revealed that this small concentration of liposomes both greatly decreased the τ_{lag}= 0.32 ± 0.02 h and increased the apparent rate constant for the growth/elongation of hIAPP fibrils to k_{app} 27.4 ± 4.6 h^{-1} (*n*= 2) compared to the peptide fibrillation kinetics in solution (Figure 4.15 B, green circles). This indicates that this lipid concentration greatly accelerates the nucleation step for hIAPP fibril formation as well as speeding elongation rate. The opposite effects were obtained when 24 μM hIAPP was incubated with 500 μM instead of 100 μM POPS LUVs as an apparent slowdown of the fibrillation kinetics of the peptide could be detected in this case (Figure 4.15 B, blue squares). Although the CD spectra revealed that at the onset of the peptide-membrane interaction 24 μM hIAPP was predominantly α-helical (Figure 4.16 G), a large amount of fibrillar material was produced at the end of the incubation as shown by the obtained TEM images (Figure 4.15 H and Figure S 4.4 K). Accordingly, these fibrillar structures were found to enhance ThT fluorescence intensity (Figure 4.15 D, blue squares) and displayed a characteristic β-sheet CD spectrum (Figure 4.16 H).

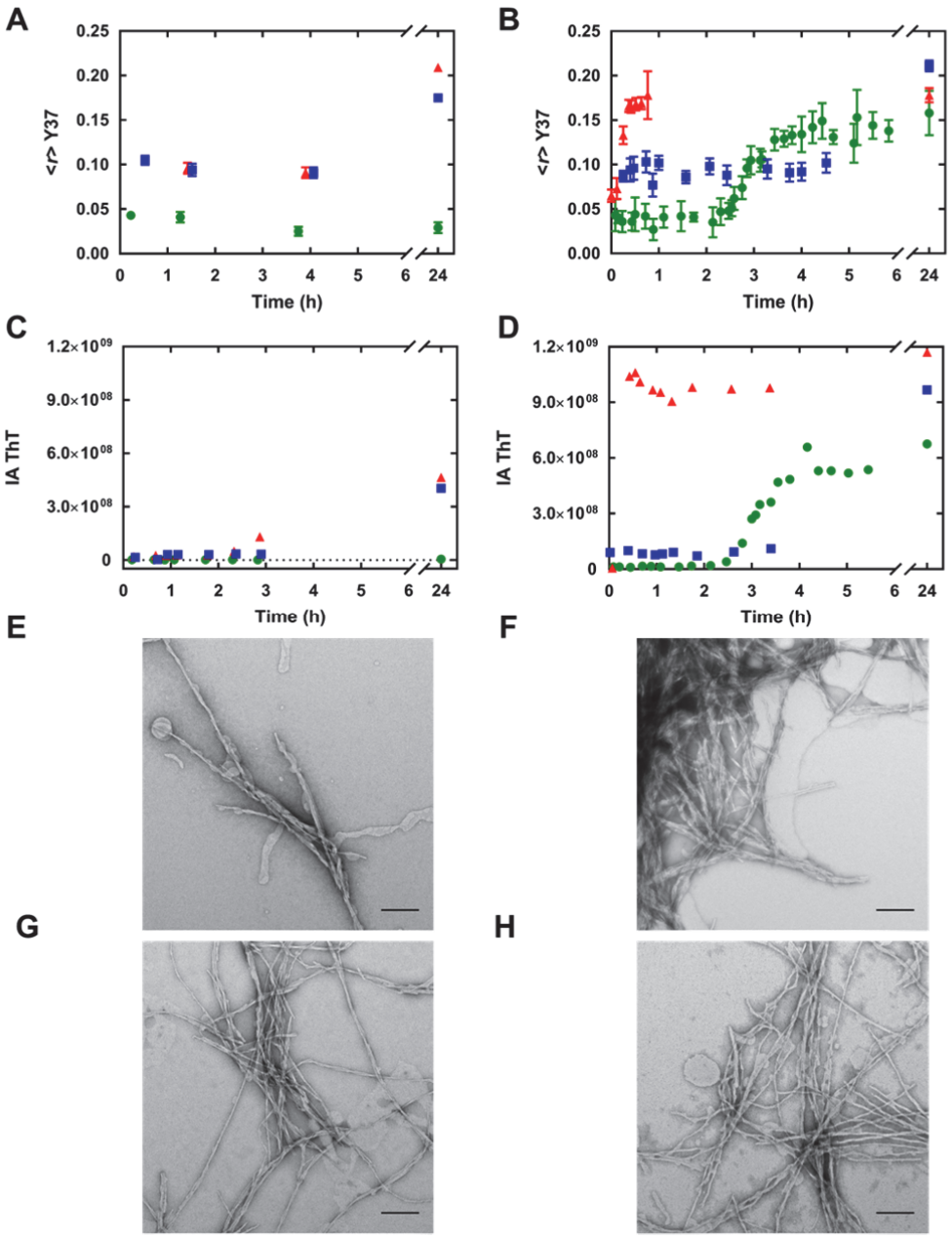

Figure 4.15 – The catalysis of hIAPP fibrillation by anionic lipid vesicles critically depends on the total peptide and lipid concentrations used. The fibrillation kinetics of (**A** and **C**) 8 µM and (B and **D**) 24 µM hIAPP were tracked by monitoring the changes over time of (**A** and **B**) the intrinsic fluorescence properties of each peptide due to its Y37 residue $\langle r \rangle_{Y37}^{282/320nm}$, and (**C** and **D**) the fluorescence intensity of 30 µM ThT (integrated area from 470-600 nm, IA (λ_{exc}= 440 nm)). Each set of kinetic studies were performed in buffer (green circles, control) and in the presence of 100 µM (red triangles) or 500 µM POPS LUVs (blue squares). There is a strong correlation between the sharp increase detected in ssFA of Y37 and the fluorescence intensity of ThT for samples prepared using the same experimental conditions, confirming that both signals can be used to monitor hIAPP fibrillation. The fibrillation of 8 µM hIAPP requires a long incubation time of the sample, independently of the experimental conditions used. For 24 µM hIAPP, 100 µM but not 500 µM POPS LUVs readily accelerates the fibrillation kinetics of the peptide. Representative negative stain TEM images of (**E** and **G**) 8 µM and (**F** and **H**) 24 µM hIAPP in the presence of (**E** and **F**) 100 µM and (**G** and **H**) 500 µM POPS LUVs. After 24h of incubation, samples were stained with 2% PTA. Individual fibrils can be easily identified in the images. Magnifications of 12 000x were used for A and B, 20 000x for C, 10 000x for D. Scale bars are 200 nm.

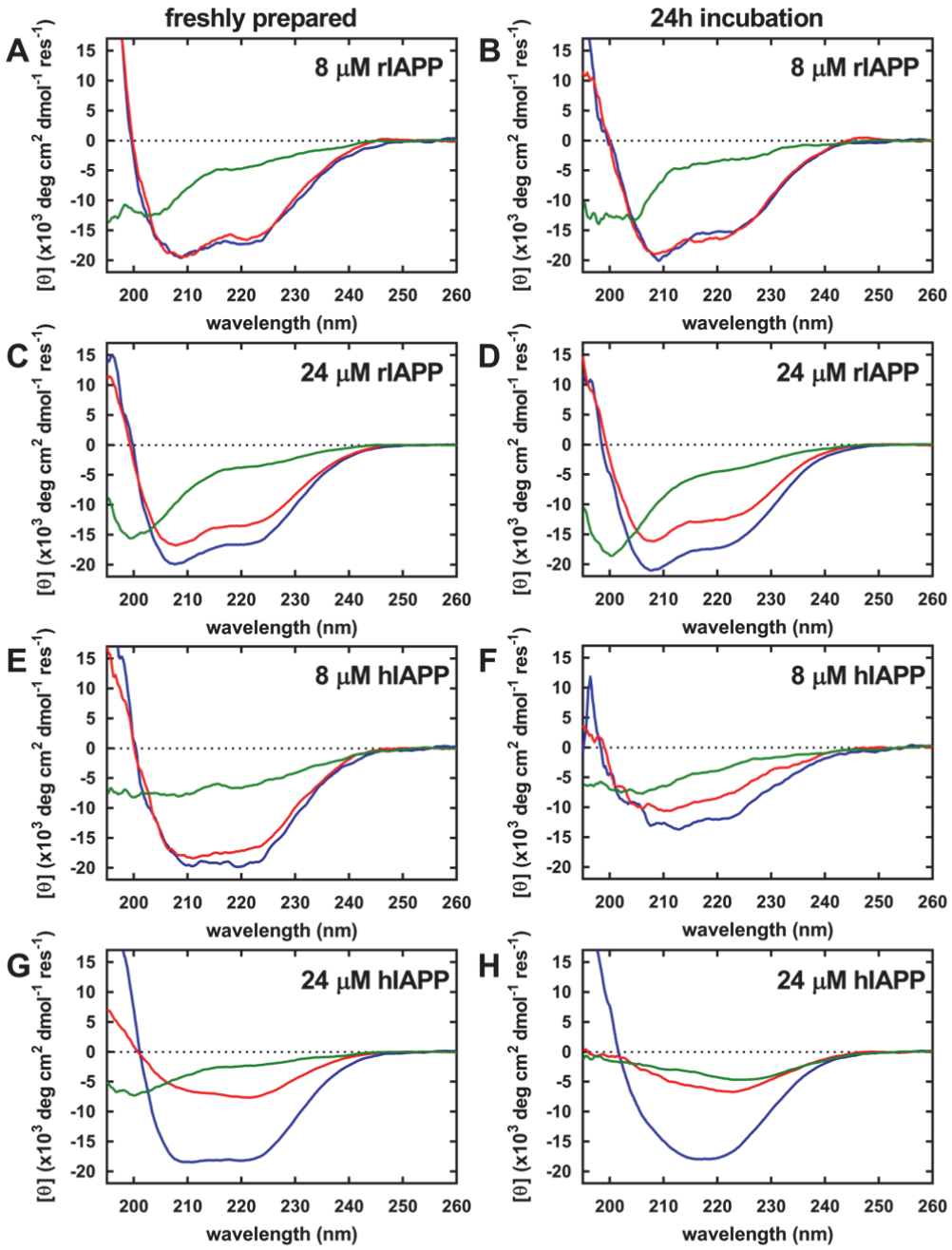

Figure 4.16 - Influence of lipid concentration on the secondary conformational changes undergone by rIAPP and hIAPP. The CD spectra were obtained for (**A - D**) rIAPP and (**E - H**) hIAPP. The samples were prepared in the absence (green lines) and in the presence of 100 μM (red lines) or 500 μM of POPS LUVs (blue lines) and (**A, C, E** and **G**) measured immediately or (**B, D, F** and **H**) after 24 h under quiescent conditions at RT.

4.4.5. The binding of each Atto488-fluorescently labeled IAPP variant to the anionic liposomes is strongly driven by the membrane-induced oligomerization of the corresponding unlabeled peptide

Similarly to the experiments performed with the unlabeled peptides, the interaction of different concentrations of rIAPP/hIAPP with POPS LUVS was again investigated but now using the fluorescence signal from a tracer amount of the correspondingly Atto488-labeled peptide as the reporter of the interaction under study. First, the interaction of 0.3 μM of Atto488-hIAPP/rIAPP with increasing concentrations of the anionic liposomes was measured by following the changes in its fluorescence properties. Surprisingly, its fluorescence emission properties (spectral shape and fluorescence intensity (data not shown) and ssFA (Figure 4.17 A and B, green circles) remained essentially invariant for both fluorescently-labelled peptides within the concentration range 0 – 500 μM of POPS, an indication that their membrane-binding properties were greatly affected by covalently-linking the Atto488 fluorophore at the *N*-terminal residue of each peptide. It can also not be discarded the possibility that the binding of the labeled peptide to the membrane leads to a conformation that completely quenches the fluorescence of the peptide. Unfortunately, the use of such low peptide concentration prevented measuring the signal from the *C*-terminal Y37 residue of each peptide which would allow testing this hypothesis in an independent fashion.

Secondly, when the same experiments were repeated with mixed peptide samples (8 μM rIAPP/hIAPP with 1.25% of the corresponding tracer peptide), the ssFA of the conjugated peptides was now found to increase hyperbolically with the lipid concentration, rising from $\langle r \rangle_{\mathrm{Atto488}}$~ 0.06 in aqueous solution to a plateau level $\langle r \rangle_{\mathrm{Atto488}}$~ 0.15 at high phospholipid concentrations (Figure 4.17 A and B, red triangles).

The intrinsic ssFA of rIAPP/hIAPP measured for the same samples confirmed that indeed both rIAPP and hIAPP were binding to the lipid bilayers as the usual small $\Delta \langle r \rangle_{\mathrm{Y37}}$ ~ 0.04 - 0.05 was detected (Figure 4.17 C and D, red triangles), with no concomitant detection of hIAPP fibrillation. Accordingly, the fluorescence intensity of both tracer peptides in the presence of the liposomes decreased 10 – 20% relatively to the signal obtained in buffer (data not shown) which was accompanied by a minimal spectral red-shift of 0.5 – 1.0 nm (Table 4.10.)

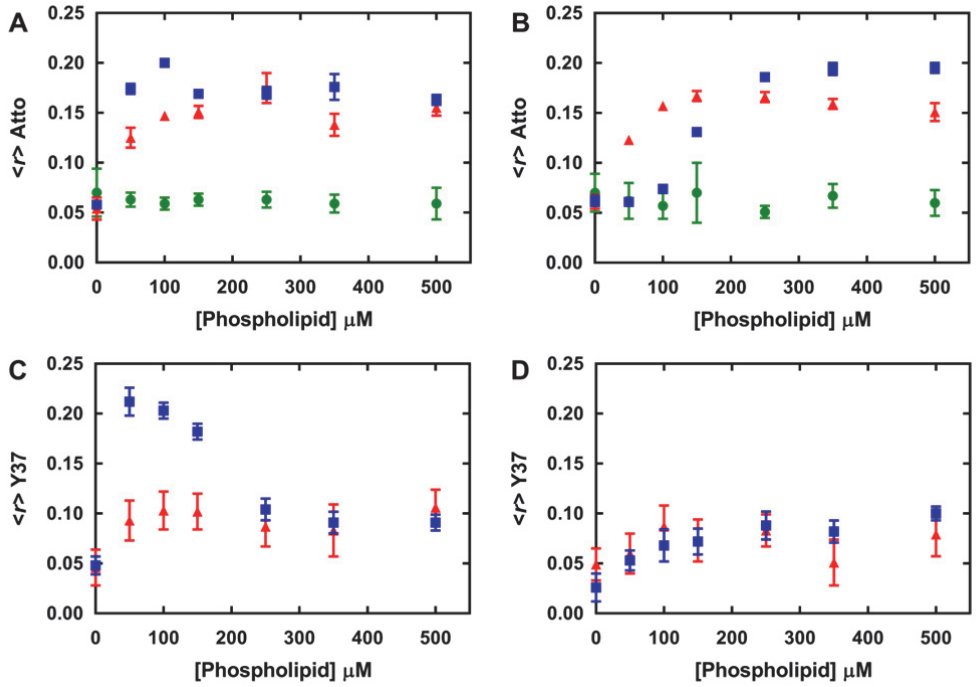

Figure 4.17 - The ssFA of the tracer peptide displays a complex behavior in the presence of anionic lipid membranes. The interaction of (**A**) Atto488-hIAPP and (**B**) Atto488-rIAPP in the absence (0.3 μM, green circles) and in the presence of 8 μM (red triangles, 0.1 μM of labeled peptide) and 24 μM (blue squares) of the respective unlabeled peptide with POPS LUVs was monitored by measuring in parallel the changes in the ssFA (**A** and **B**) of the tracer peptide, $\langle r \rangle_{\mathbf{Atto488}}^{\mathbf{500/525nm}}$ and (**C** and **D**) of Y37, $\langle r \rangle_{\mathbf{Y37}}^{\mathbf{282/320nm}}$. Although the results obtained for ssFA of Y37 in the presence of a tracer amount of 1.25% fluorescently-labelled peptide are in agreement with the ones obtained previously with solely the unlabeled peptide (Figure 4.14) the changes in the ssFA of Atto488 display a more intricate behavior, suggesting that crowding of the membrane surface is controlling rIAPP binding to the anionic lipid membranes (see the text for further discussion). Some error bars are smaller than the size of the symbol.

Finally, a 3-fold increase in the concentration of the unlabeled peptide (24 μM rIAPP/hIAPP with 1.25% of the corresponding tracer peptide) unexpectedly yielded yet a different behavior of $\langle r \rangle_{\mathrm{Atto488}}$ as a function of lipid concentration. Whereas the ssFA of Atto488-hIAPP again increased with the lipid concentration used (Figure 4.17 A, blue squares), it now reached a maximum of $\langle r \rangle_{\mathrm{Atto488}}$~ 0.20 at $[L]_t$= 100 μM that slowly converged to a plateau level of $\langle r \rangle_{\mathrm{Atto488}}$~ 0.15 upon increasing the lipid concentration in solution, i.e. gradually approaching the values obtained with the lower peptide concentration. The emission spectra of the samples that presented the highest ssFA displayed a more pronounced red-shift of ca. 3 – 3.5 nm (Table 4.10), as illustrated in Figure 4.18 A and C, which was now accompanied by a strong quenching of their fluorescence intensity (Figure 4.18 D, closed circles). Parallel measurements of the ssFA-Y37 confirmed that these alterations in the fluorescence emission properties of the tracer peptide were due to an extensive membrane-mediated fibrillation of hIAPP at the lowest concentrations of POPS used ([POPS]< 250 μM), as discussed above (Figure 4.17 C, blue squares).

If the mixed peptide samples were prepared using the rat variant instead of hIAPP (24 μM rIAPP with 1.25% of Atto488-rIAPP), a surprising sigmoid increase in the ssFA with the lipid concentration was now found, reaching $\langle r \rangle_{\mathrm{Atto488}}$= 0.20 at the highest lipid concentrations used (Figure 4.17 B, blue squares). Concomitantly, the fluorescence intensity of the tracer peptide progressively decreased up to ~ 80% of its value in buffer (Figure 4.18 D, open triangles), while its emission spectra only slightly red-shifted in the presence of the membranes (Figure 4.18 B and C and Table 4.10). Curiously, when the experimental readout used was $\langle r \rangle_{\mathrm{Y37}}$, the usual binding curve of rIAPP to the lipid membranes was now obtained (Figure 4.17 D, blue squares), with no signs of any sigmoid effect.

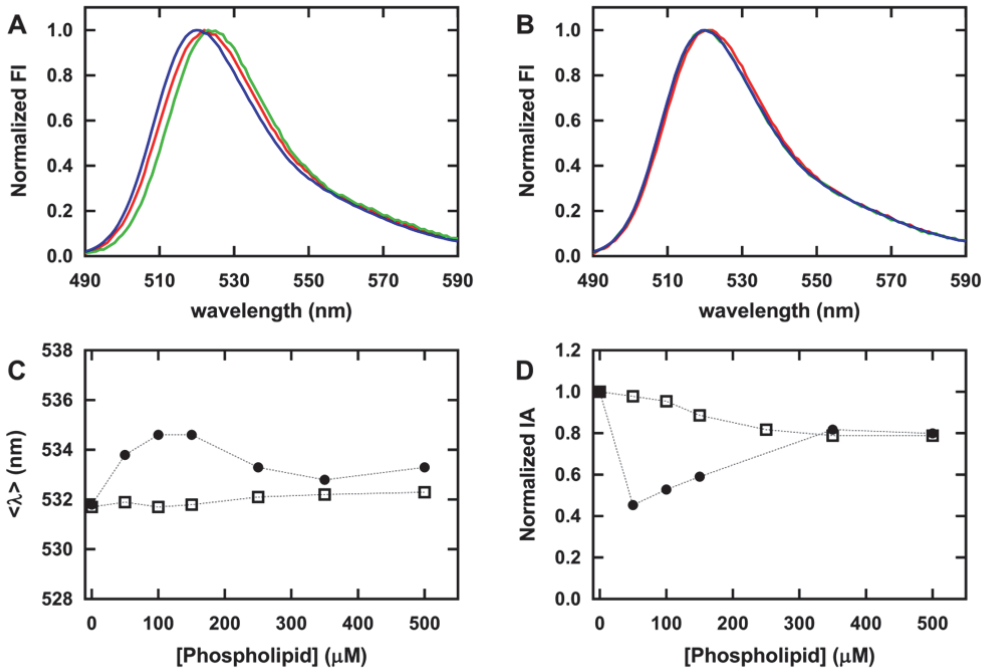

Figure 4.18 – Variation of the fluorescence properties of the tracer peptide in the presence of an excess of unlabeled peptide and POPS LUVs. Representative fluorescence emission spectra of 0.3 μM (**A**) Atto488-hIAPP and (**B**) Atto488-rIAPP, with 24 μM of the corresponding unlabeled peptide, in the absence (blue curves) or presence of 100 μM (green curve) and 500 μM (red curve) POPS LUVs (λ_{exc}= 480 nm). Influence of lipid concentration on (**C**) the intensity-weighted average emission wavelength $\langle \lambda \rangle$, and (**D**) normalized integrated area, IA, of Atto488-rIAPP (open triangles) and Atto488-hIAPP (closed circles).

These interesting results suggest that although the tracer Atto488-conjugated peptides binds weakly to POPS LUVs, the presence of large concentrations of the corresponding unlabeled peptide in the sample can prompt their recruitment to the anionic lipid membranes. To shed light on the mechanism responsible for this effect, the order of addition of the unlabeled peptide and fluorescently-labeled peptide to the liposomes was tested. In the first case, 0.3 μM Atto488-rIAPP was first incubated in buffer or in the presence of 100 μM and 500 μM POPS LUVs for approximately 1 h. As it is shown in Figure 4.19 A, the ssFA of all samples was very low and approximately constant over 1 h, $\langle r \rangle_{\mathrm{Atto488}}$~ 0.065 ± 0.003. At the indicated time point (arrow), 8 μM of unlabeled rIAPP was added to each sample which was then mixed by inversion of the respective cuvette. The ssFA of the tracer peptide increased rapidly over time until reaching an approximate constant value of $\langle r \rangle_{\mathrm{Atto488}}$~ 0.153 ± 0.002 only in the presence of POPS LUVs. The reverse experiment was also performed whereupon 8 μM of unlabeled rIAPP was now first incubated alone in buffer or in the presence of 100 μM and 500 μM POPS LUVs for approximately 1 h. The corresponding ssFA were $\langle r \rangle_{\mathrm{Y37}}^{\mathrm{buffer}}$= 0.030 ± 0.006, $\langle r \rangle_{\mathrm{Y37}}^{100\ \mu\mathrm{M}}$= 0.078 ± 0.009 and $\langle r \rangle_{\mathrm{Y37}}^{500\ \mu\mathrm{M}}$ = 0.093 ± 0.002, respectively (Figure 4.19 B, open symbols). The slightly higher value obtained for the ssFA in the presence of liposomes confirms the interaction between rIAPP and the lipid membranes. At approximately 1h (arrow), 0.3 μM Atto488-rIAPP was then added to each cuvette. After mixing by inversion, again the presence of POPS LUVs was found necessary for the ssFA of the tracer peptide to increase up to $\langle r \rangle_{\mathrm{Atto488}}^{100\ \mu\mathrm{M}}$= 0.149 ± 0.003 and $\langle r \rangle_{\mathrm{Atto488}}^{500\ \mu\mathrm{M}}$= 0.152 ± 0.002, respectively; meanwhile $\langle r \rangle_{\mathrm{Atto488}}^{\mathrm{buffer}}$= 0.064 ± 0.002 did not vary over time (Figure 4.19 B, closed symbols). In parallel, the intrinsic ssFA of rIAPP of each sample did not change from the previous measured value.

In summary, the data indicate that POPS LUVs are an absolute requirement for the interaction between the unlabeled rIAPP and Atto488-rIAPP, which must therefore occur on the lipid vesicles. The simplest model that explains this situation considers that the electrostatic-driven membrane partitioning of rIAPP to 100 mol% POPS LUVs is so strong that a very high surface concentration of the peptide is reached at the lipid concentrations used here, ultimately triggering the oligomerization of the membrane-bound peptides. The coupled rIAPP partition/oligomerization equilibria must be very dynamic, allowing for the recruitment and trapping of the much weaker membrane-binding tracer peptide in the membrane-bound rIAPP oligomers formed under these experimental conditions. The alternative pathway involving direct binding of the fluorescently-labeled peptides from the aqueous solution to the membrane-bound oligomeric rIAPP intermediates seems less probable since in this case no signs of membrane saturation would be expected in the ssFA

measurements of this fluorescently-labeled peptide at variance with our experimental data (Figure 4.17 B) (see discussion below).

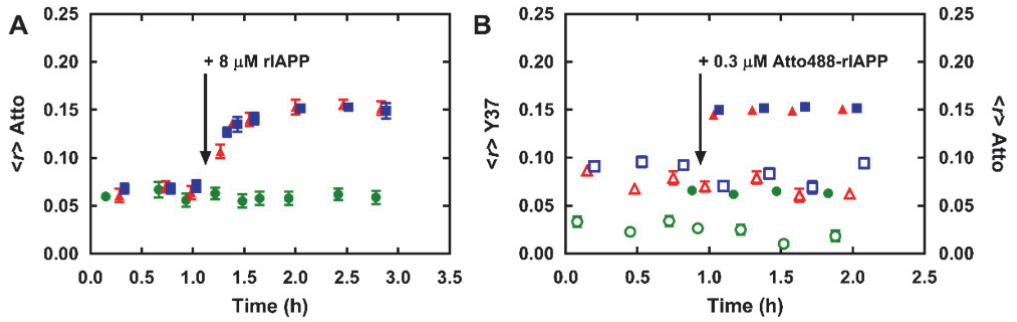

Figure 4.19 – Atto488-rIAPP is efficiently pulled to anionic lipid membranes in the presence of a high concentration of unlabeled peptide. Two sets of experiments were performed to show that the fluorescently-labeled rIAPP is drawn into the membrane by a large concentration of unlabeled peptide. (**A**) In the first case, 0.3 μM Atto488-rIAPP was first incubated in the absence (green circles) or in the presence of 100 μM (red triangles) or 500 μM (blue squares) POPS LUVs for approximately 1h. At that point, 8 μM of rIAPP was added to the solution (arrow). (**B**) In the second case, the order of addition was reversed as 0.3 μM Atto488-rIAPP was only added to the samples (arrow) after pre-incubating 8 μM of rIAPP in the absence (green circles) or in the presence of 100 μM (red triangles) or 500 μM (blue squares) POPS LUVs for ~1h. In both cases, the changes in the $\langle r \rangle_{\mathrm{Atto488}}^{500/525\mathrm{nm}}$ (closed symbols) were monitored over time. In (B), $\langle r \rangle_{\mathrm{Y37}}^{282/320\mathrm{nm}}$ (open symbols, left axis) was also measured in turn for the same sample over time. The ssFA of Atto488-rIAPP increased from $\langle r \rangle_{\mathrm{Atto488}}$~0.06 to ~0.15 in the presence of POPS LUVs only when 8 μM of unlabeled rIAPP was also present in the sample, independently of the order of addition.

Another intriguing result was the pronounced sigmoid profile obtained when studying the interaction between 24 μM rIAPP with 1.25% of the corresponding tracer peptide and 100 μM POPS LUVs. To investigate whether the incubation time of the samples was playing a role on these data due to e.g. the transient formation of membrane-bound dark (non-fluorescent) state, the interacting kinetics of the mixed peptide samples with 100 μM and 500 μM POPS LUVs was studied. Control measurements in buffer were also performed. As it is shown in Figure 4.20 the interaction of either Atto488-conjugated peptide with the anionic membranes was again confirmed to be fast when a large concentration of the corresponding unlabeled peptide was simultaneously present in solution since the ssFAs obtained for each tracer peptide at the first time point of the kinetics remained essentially constant over the first 4 - 5 h of the measurements. Since this is a temporal window much larger than the average time required to perform the measurements presented in each panel of Figure 4.17 (usually ~ 30 min – 1h), this first hypothesis was therefore ruled out. In fact, the only samples that significantly changed their $\langle r \rangle_{\mathrm{Atto488}}$ after 24 h of incubation were the ones prepared with hIAPP, which was expected considering the amyloidogenic properties of this peptide variant. In this case, the addition of lipid vesicles to the mixed

peptide samples containing 8 μM hIAPP clearly resulted in two stages of increased anisotropy, as this parameter first rose very fast to $\langle r \rangle_{\mathrm{Atto488}}$~ 0.15 in the presence of the membranes, followed by a transition into a maximum value of $\langle r \rangle_{\mathrm{Atto488}}$~ 0.20 at the end stage of the kinetics (Figure 4.20 B). The lower value must be reporting the membrane-induced oligomerization of the helical intermediates formed along the interaction pathway of hIAPP with membranes, whereas the highest value measured after 24h incubation is clearly associated with amyloid fibril formation.

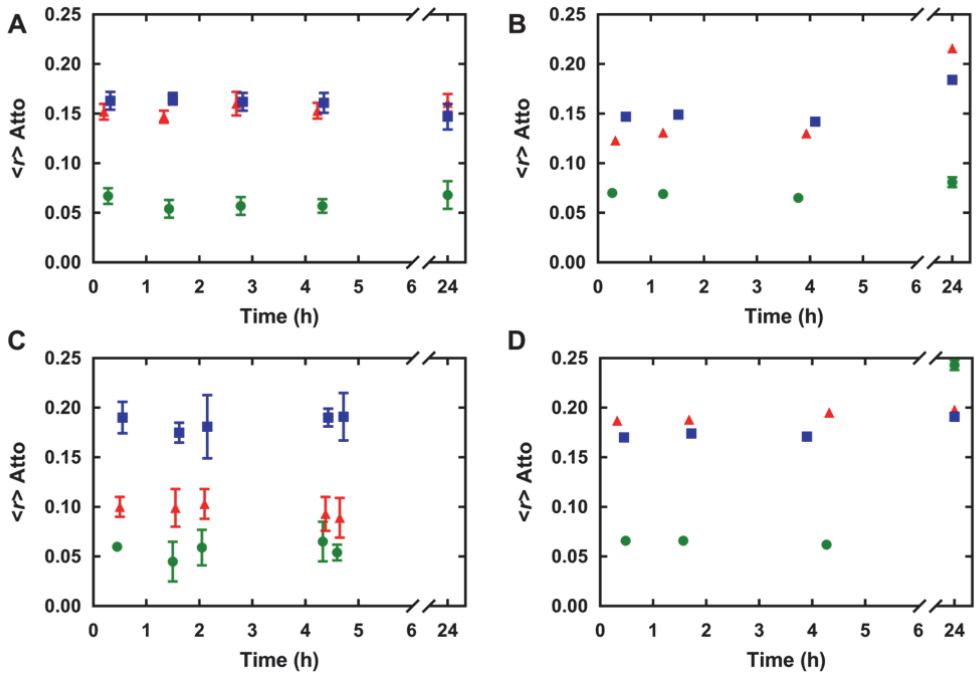

Figure 4.20 – Kinetics of membrane interaction of hIAPP and rIAPP monitored by the steady-state fluorescence anisotropy of a tracer amount of Atto488-labelled peptide. The interaction of each IAPP variant with POPS LUVs was monitored by measuring the changes in the ssFA of Atto488 of a tracer amount (1.25%) of Atto488-labelled peptide, $\langle r \rangle_{\mathrm{Atto488}}^{500/525\mathrm{nm}}$, over time in the presence of (**A** and **B**) 8 μM and (**C** and **D**) 24 μM of (**A** and **C**) rIAPP or (**B** and **D**) hIAPP. The samples were prepared in the absence (green circles) or in the presence of 100 μM POPS LUVs (red triangles) and 500 μM POPS LUVs (blue squares).

The CLSM images obtained for the mixed hIAPP samples after 24 h incubation under quiescent conditions confirmed these conclusions as they showed the formation of large mixed peptide-membrane aggregates, particularly when the samples were prepared with 24 μM hIAPP (Figure 4.21, left panels). The corresponding 2PE FA maps originated histograms that were well described by a single Guassian function that was always centered at very high $\langle r \rangle_{\mathrm{exp}}^{\mathrm{2PE}}$ values (Table 4.10). In contrast, the CLSM images of the tracer peptide and 24 μM rIAPP in buffer and in the presence of 100 μM or 500 μM POPS LUVs

always revealed homogeneous solutions, at least within the resolution of this technique (Figure 4.22, left panels).

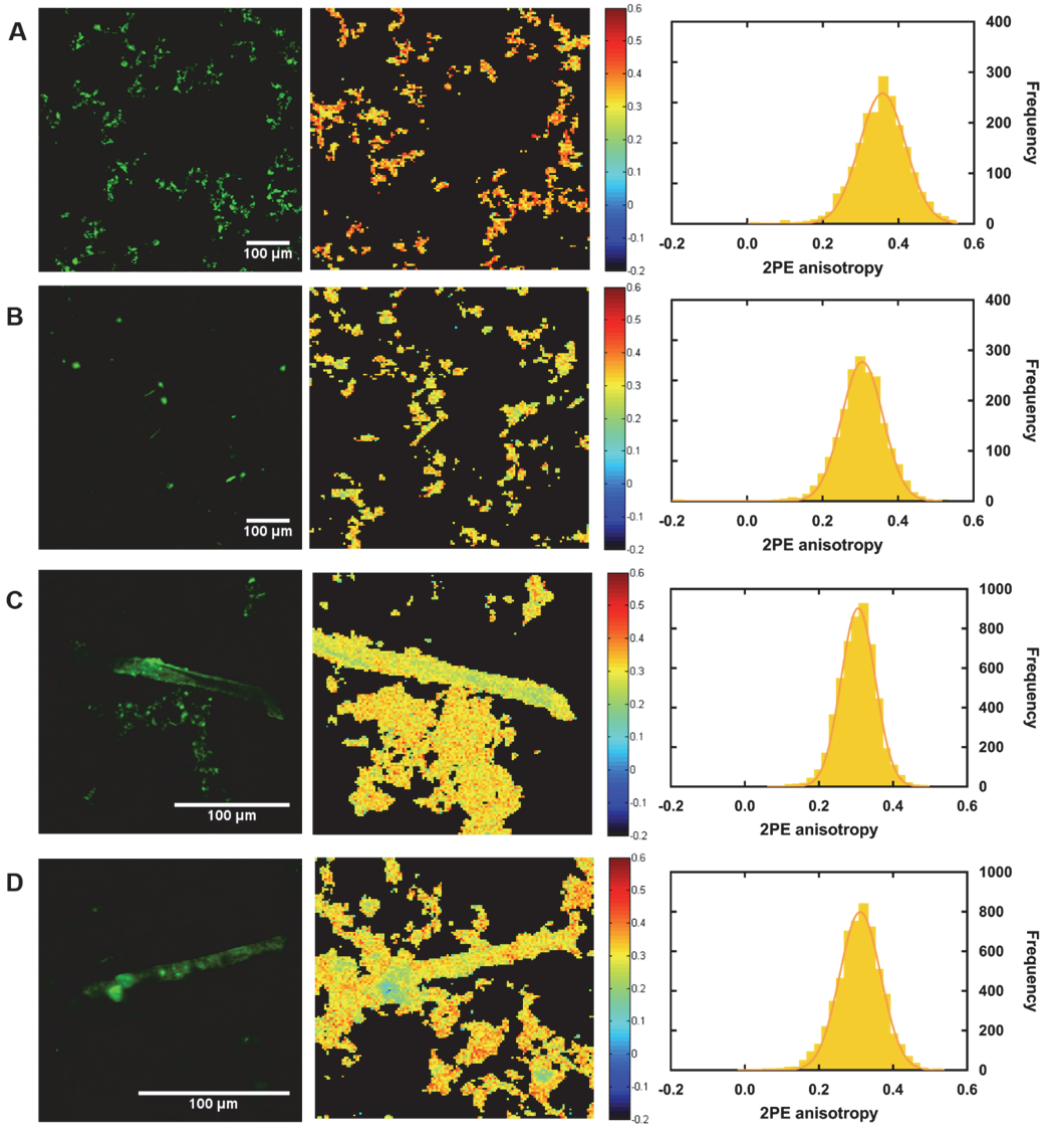

Figure 4.21 - POPS LUVs induces the formation of hIAPP aggregates as revealed by FAIM. Representative CLSM image (left panels; λ_{exc}= 488 nm, λ_{em}= 500-600 nm). 2PE FA maps (middle panels; λ_{exc}^{2PE} = 780 nm, emission selected with 500-550 nm band pass filter) and histograms (right panels) obtained for (**A** and **B**) 8 µM and (**C** and **D**) 24 µM hIAPP with 1.25% of the tracer Atto488-hIAPP in the presence of (**A** and **C**) 100 µM and (**B** and **D**) 500 µM POPS LUVs after incubating the samples for 24h at RT. The 10x air objective was used in all the measurements. The image processing of the raw data was performed using a MATLAB script as previously described (Chapter **2**) giving directly the 2PE FA false-color maps (middle panels) and the data for obtaining the histograms (right panels). A Gaussian distribution was successfully fitted to each of these histograms using GraphPad Prism 7 (full curves). The average and standard deviation of these fits and the number of pixels processed in the data treatment are presented in Table 4.10. The presence of large peptide aggregates presenting a high 2P FA could be easily detected in the samples.

In agreement with the ensemble-measurements performed with the spectrofluorometer, the 2PE ssFA of Atto488-rIAPP/24 μM rIAPP increased in the presence of 500 μM POPS LUVs, a result that was explained by the recruitment of Atto488-rIAPP to the lipid membranes being triggered by the concomitant membrane-induced oligomerization of the unlabeled peptide (Figure 4.22 C and Table 4.10). On the other hand, the histograms retrieved from the 2PE FA maps obtained for the tracer peptide/24 μM rIAPP samples in buffer and in the presence of 100 μM POPS LUVs were very similar (Figure 4.22 A and B and Table 4.10), further hinting that Atto488-rIAPP does not bind significantly to the lipid membranes under these experimental conditions.

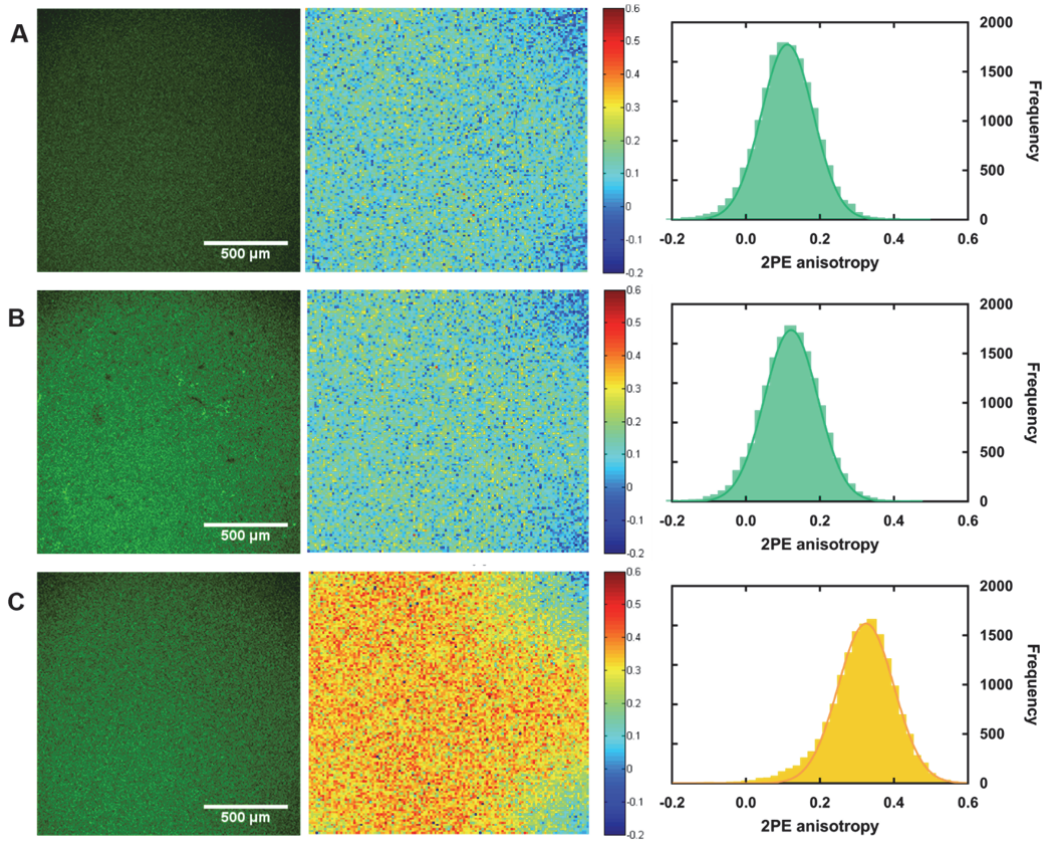

Figure 4.22 - The increase in the FA of 24 μM rIAPP detected in the presence of 500 μM POPS LUVs was not accompanied by the formation of any large lipid-peptide mixed aggregates. Representative CLSM image ((left panels; λ_{exc}= 488 nm, λ_{em}= 500-600 nm), 2PE FA maps (middle panels; λ_{exc}^{2PE} = 780 nm, emission selected with 500-550 band pass filter) and histograms (right panels) obtained for 24 μM of rIAPP with 1% of Atto488-labelled rIAPP in (**A**) the absence and in the presence of (**B**) 100 μM and (**C**) 500 μM POPS LUVs after incubating the samples for 24h at RT. The 10x air objective was used in all the measurements. The image processing of the raw data was performed using a MATLAB script as previously described (Chapter **2**) giving directly the 2PE FA false-color maps (middle panels) and the data for obtaining the histograms (right panels). A Gaussian distribution was successfully fitted to each of these histograms using GraphPad Prism 7 (full curves). The average and standard deviation of these fits and the number of pixels processed in the data treatment are presented in Table 4.10.

4.4.6. Membrane saturation controls rIAPP binding to POPS LUVs

To help dissecting the mechanism responsible for the pronounced sigmoid profile obtained when studying the interaction of the tracer peptide Atto488-rIAPP with 100 μM POPS LUVs in the presence of a high concentration of rIAPP, we next investigated in more detail the influence of the L/P ratio on these results. Towards this goal, the reverse experimental design was now used, i.e. both steady-state and time-resolved FA measurements of the tracer peptide Atto488-rIAPP were performed in buffer and in the presence of fixed concentrations of anionic liposomes (100 μM and 500 μM POPS LUVs) upon varying the total rIAPP concentration in solution. The ssFA of the tracer peptide Atto488-rIAPP was found to be independent of the concentration of unlabeled peptide added to the aqueous solution within the concentration range 1.6 - 24 μM, as shown in Figure 4.23 ($\langle r \rangle_{\text{Atto488}}$= 0.065 ± 0.009 (*n*= 19), green circles), and in agreement with the data presented in Figure 4.20 A and C.

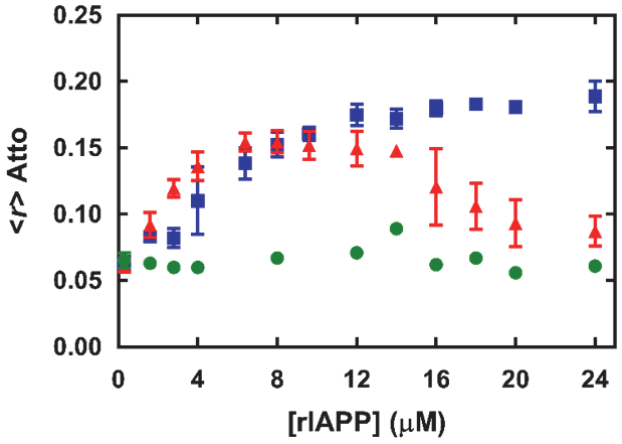

Figure 4.23 – Membrane surface crowding controls rIAPP binding to POPS LUVs. The interaction of variable concentrations of rIAPP with 100 μM (red triangles) and 500 μM (blue squares) POPS LUVs was monitored by measuring the changes in the ssFA of 1.25% tracer Atto488-rIAPP added to each sample, $\langle r \rangle_{\text{Atto488}}^{500/525\text{nm}}$ at RT. As a control, the same measurements were also performed in buffer (green circles). A biphasic change in the fluorescence anisotropy of Atto488-rIAPP was detected in the presence of 100 μM but not 500 μM POPS LUVS suggesting that the anionic liposomes reach saturation with membrane-bound [rIAPP] ~8 – 12 μM only in the first case.

As illustrated in Figure 4.24 A, the corresponding time-resolved data confirmed that rIAPP did not self-assemble in buffer since the fluorescence anisotropy decays obtained from these samples completely overlapped, fully depolarizing the emitted radiation within the time scale of the experiment ($\langle \tau \rangle_2$ = 4.02 ± 0.01 ns (*n*= 6) (Table S 4.2)). A single rotational correlation time of ϕ_1= 0.99 ± 0.07 (*n*= 6) for Atto488-rIAPP in buffer solution was needed to adequately fit the data, although the fact that $r(0)$= -0.098 ± 0.004 (*n*= 6) < $\langle r \rangle_{\text{Atto488}}^{310\text{ nm}}$= -0.125 clearly indicates that there is a small contribution of a fast depolarizing component that that was not captured within the time window of these measurements (Table 4.12).

Similar $r(0)$ values were consistently obtained also in the presence of liposomes: $r(0) =$ -0.101 ± 0.006 (*n* = 13) and $r(0) =$ -0.096 ± 0.009 (*n* = 11) for 100 μM and 500 μM of POPS LUVs, respectively (Table 4.12).

When the same set of measurements were repeated in the presence of 500 μM, the ssFA of Atto488-rIAPP was now found to steadily increase with the total concentration of the unlabeled peptide until reaching a plateau value of $\langle r \rangle_{\mathrm{Atto488}}$= 0.180 $\pm$ 0.006 (*n*= 17) (Figure 4.23, blue squares), Since the corresponding fluorescence intensity decays of the conjugated peptide were almost monoexponential with a constant mean fluorescence lifetime of $\langle \tau \rangle_2$ = 3.93 $\pm$ 0.03 ns (*n*= 12) (Table S 4.2), one can safely conclude that there was a progressive increase in the hydrodynamic volume of the emitting species upon increasing the concentration of unlabeled peptide added to the sample, reflecting the progressive association of the peptide to the very large anionic liposomes. The representative fluorescence anisotropy decays presented in Figure 4.24 C further corroborate this conclusion as it is clearly discernible that the decays displayed an increasing limiting anisotropy that converged to r_∞= -0.046 $\pm$ 0.004 (*n*= 6) at the highest concentrations of the unlabeled peptide used, while the rotational correlation time plateaued at ϕ_1= 1.3 $\pm$ 0.1 (*n*= 6) (Table 4.12 and Figure S 4.5 E). If the interaction of the tracer peptide with the lipid membranes was described by a simple partitioning equilibrium, one would expect to obtain a constant ssFA for a fixed lipid concentration Eq. 3.6, independently of the concentration of unlabeled peptide added to each sample. The experimental data does not comply with this prediction, strongly supporting the existence of coupled rIAPP partition/oligomerization equilibria that pulls the conjugated peptide to the lipid bilayers, as discussed above. Therefore, the changes detected in ϕ_1 and r_∞ may not only be reflecting the progressive binding of the Atto488-fluorescently labeled peptide to the anionic liposomes but also its steady incorporation into the membrane-bound oligomers formed by the unlabeled peptide.

Interestingly, a 5-fold decrease in the concentration of POPS LUVs added to the peptide solutions (from 500 to 100 μM) only produced a significant impact on the ssFA of the tracer peptide for [rIAPP] $\leq$ 8 – 12 μM, as from these peptide concentrations onwards the fluorescence anisotropy of Atto488-rIAPP progressively decreased instead of reaching a plateau value as described earlier for the assays performed with 500 μM POPS LUVs (Figure 4.23, red triangles *versus* blue squares).

The occurrence of homo-FRET could be a possible explanation for these data because the Förster radius, R_0, estimated for the Atto488-Atto488 pair by the company ATTO-TEC is 5.0 nm (catalogue Atto). However, the concentration of the tracer fluorescent peptide was kept constant at an intentionally very low value of 1.25% to avoid this possibility.

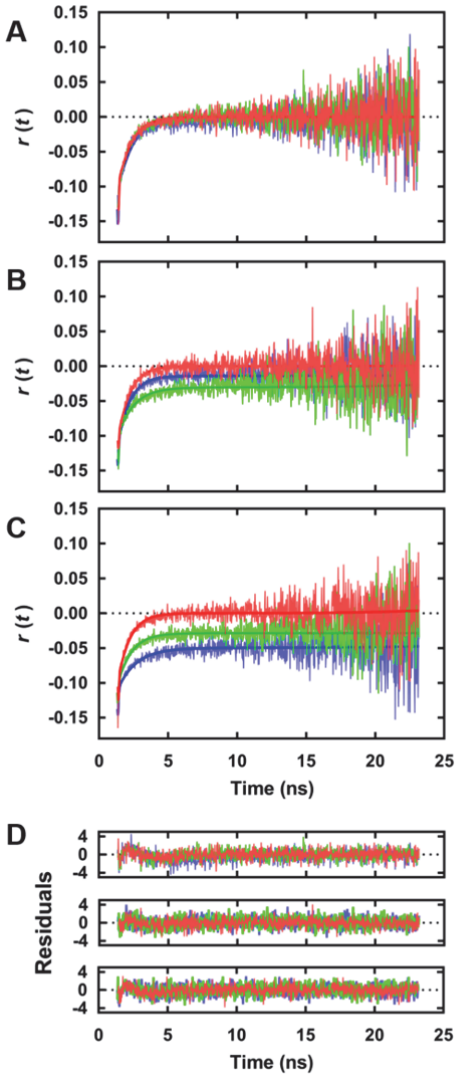

Figure 4.24 – Illustrative fluorescence anisotropy decays of the tracer Atto488-rIAPP obtained with variable total concentrations of rIAPP in the absence and in the presence of POPS LUVs. The time-resolved fluorescence anisotropy of 0.3 μM Atto488-rIAPP (red), 8 μM rIAPP with 1.25% Atto488-rIAPP (green) and 24 μM with 1.25% Atto488-rIAPP (blue) was measured (**A**) in buffer and in the presence of (**B**) 100 μM an (**C**) 500 μM POPS LUVs ($\lambda_{exc} = 310$ nm; $\lambda_{em} = 525$ nm). Solid lines are the best fits of Eq. 3.25 to the experimental data. The parameters obtained for the fits are present in Table 4.12. Figure D corresponds to the residuals of the fit for **A** (top panel), **B** (middle panel) and **C** (bottom panel). For additional details, see the legend of Figure 4.23. The time scale was 24.4 ps/channel for all decays.

The fluorescence anisotropy decays of these samples further helped to rule out homo-FRET as the reason for this behavior. They revealed that the changes in the ssFA of Atto488-rIAPP detected at high concentrations of rIAPP resulted from a progressive convergence of both the limiting anisotropy, r_∞, and rotational correlation time, ϕ_1, of Atto488-rIAPP towards the values typical obtained for the free peptide in buffer (Table 4.12 and Figure S 4.5 C). A constant mean fluorescence lifetime of $\langle\tau\rangle_2$= 3.96 ± 0.04 ns (*n*= 13) was again obtained for this set of samples (Table S 4.2).

Table 4.12 - Fluorescence anisotropy decay parameters obtained for 1.25% tracer Atto488-rIAPP in the presence of variable concentrations rIAPP and POPS LUVs. The fractional amplitudes, β_i, and rotational correlation times, ϕ_i, are presented ($\lambda_{exc} = 310$ nm; $\lambda_{em} = 525$ nm). $r(0) = \beta_1 + r_\infty$. For additional experimental details, see the legend of Figure 4.23 and Figure 4.24. The corresponding steady-state values are also presented. Values in square brackets are the errors of the recovered parameters estimated as the lower and upper bound of the joint confidence interval calculated for a 67% probability level. The goodness-of-fit was judged by the χ_G^2 value.

Sample	[rIAPP] (μM)	β_1	ϕ_1(ns)	r_∞	$r(0)$	χ_G^2	$\langle r \rangle_{\text{Atto488}}^{500/525\text{nm}}$
buffer	0 [1]	-0.09	0.96 [0.90,1.03]	-	-0.09	1.20	0.059 ± 0.008
	8.0	-0.10	0.93 [0.88,0.99]	-	-0.10	1.21	0.054 ± 0.011
	12	-0.10	0.94 [0.88,1.00]	-	-0.10	1.25	0.071 ± 0.009
	16	-0.10	0.98 [0.92,1.04]	-	-0.10	1.10	0.062 ± 0.003
	20	-0.10	1.02 [0.96,1.08]	-	-0.10	1.26	0.056 ± 0.010
	24	-0.10	1.12 [1.04,1.19]	-	-0.10	1.34	0.062 ± 0.005
100 μM LUVs	0 [1]	-0.09	0.84 [0.78,0.90]	-	-0.09	1.22	0.060 ± 0.006
	1.6	-0.07	1.04 [0.96,1.12]	-0.02	-0.09	1.18	0.087 ± 0.009
	2.8	-0.07	1.08 [0.99,1.17]	-0.03	-0.10	1.19	0.114 ± 0.007
	4.0	-0.07	1.09 [0.99,1.20]	-0.04	-0.10	1.16	0.144 ± 0.013
	6.4	-0.06	1.28 [1.19,1.40]	-0.03	-0.09	1.17	0.161 ± 0.006
	8.0	-0.07	1.21 [1.11,1.32]	-0.04	-0.10	1.07	0.158 ± 0.001
	9.6	-0.07	1.13 [1.05,1.21]	-0.03	-0.10	1.09	0.151 ± 0.005
	12	-0.07	1.16 [1.09,1.24]	-0.03	-0.10	1.09	0.136 ± 0.007
	14	-0.07	1.11 [1.02,1.21]	-0.04	-0.11	1.10	0.146 ± 0.010
	16	-0.09	0.91 [0.85,0.99]	-0.02	-0.10	1.11	0.100 ± 0.009
	18	-0.09	0.92 [0.86,1.01]	-0.03	-0.11	1.25	0.102 ± 0.007
	20	-0.09	0.88 [0.82,0.93]	-0.01	-0.10	1.12	0.073 ± 0.002
	24	-0.09	0.83 [0.78,0.89]	-0.01	-0.11	1.10	0.074 ± 0.003
500 μM LUVs	0 [1]	-0.09	0.86 [0.80,0.94]	-	-0.09	1.20	0.059 ± 0.007
	2.8	-0.07	0.96 [0.87,1.06]	-0.01	-0.08	1.18	0.077 ± 0.023
	4.0	-0.07	1.05 [0.97,1.14]	-0.03	-0.10	1.15	0.132 ± 0.016
	6.4	-0.07	1.03 [0.95,1.11]	-0.02	-0.09	1.14	0.130 ± 0.011
	8.0	-0.06	1.16 [1.07,1.25]	-0.03	-0.09	1.16	0.142 ± 0.005
	9.6	-0.06	1.16 [1.08,1.28]	-0.03	-0.10	1.19	0.157 ± 0.007
	12	-0.06	1.32 [1.20,1.44]	-0.05	-0.10	1.10	0.183 ± 0.005
	14	-0.06	1.21 [1.09,1.33]	-0.04	-0.10	1.25	0.167 ± 0.005
	16	-0.06	1.25 [1.13,1.37]	-0.05	-0.11	1.11	0.186 ± 0.007
	18	-0.06	1.28 [1.18,1.42]	-0.04	-0.10	1.21	0.181 ± 0.009
	20	-0.06	1.49 [1.39,1.64]	-0.05	-0.11	1.13	0.180 ± 0.010
	24	-0.06	1.33 [1.22,1.47]	-0.05	-0.11	1.16	0.174 ± 0.006

[1] The concentration of Atto488-rIAPP used was 0.3 μM.

Altogether, the fluorescence anisotropy data suggest that for 100 μM POPS LUVs the limiting factor controlling the ssFA of Atto488-rIAPP is the progressive saturation of the anionic lipid membranes with rIAPP. Upon increasing the total concentration of unlabeled peptide, the partitioning of Atto488-rIAPP (displaying low affinity/weak binding) and unlabeled peptide (exhibiting high affinity/strong binding) towards the very low concentration of POPS LUVs used becomes increasingly competitive; as the available membrane surface area decreases, more and more Atto488-rIAPP remains free in solution as it is outcompeted by rIAPP for membrane binding; as a result, an efficient integration of Atto488-rIAPP into the membrane-bound rIAPP oligomers becomes increasingly less probable, ultimately resulting in a progressive decrease in the ssFA of the tracer peptide for [rIAPP] $\geq$ 8 – 12 μM.

4.4.7. An independent FRET binding assay confirms that membrane surface crowding limits rIAPP binding to POPS LUVs

To independently test whether membrane saturation was the limiting factor controlling Atto488-rIAPP binding to low concentrations of POPS LUVs, a FRET binding assay was also carried out. The rationale of this experiment is explained in detail in section 4.3.6. Briefly, a constant concentration of 0.1 μM Atto488-rIAPP (donor, D) was added to either 100 μM or 500 μM POPS LUVs which were either unlabeled (D samples) or contained the fluorescently-labeled phospholipid Rhod-DOPE (acceptor, A) at a molar ratio of 1:400 in their composition (DA samples). A typical set of fluorescence emission spectra obtained in the FRET assay is shown in Figure 4.25 A. The fluorescence emission spectrum displayed by 0.1 μM Atto488-rIAPP in the presence of 12 μM rIAPP and 100 μM of unlabeled POPS LUVs had a maximum emission wavelength at around 525 nm (Figure 4.25 A, blue spectrum). The same concentration of Rhod-DOPE-containing LUVs (1:400) exhibited a peak at around 590 nm but with a very low fluorescence intensity, indicating that direct excitation of the acceptor Rhod-DOPE at 480 nm is minimal (Figure 4.25 A black spectrum). Finally, the emission spectra of 0.1 μM Atto488-rIAPP/12 μM rIAPP in the presence of the same concentration of Rhod-DOPE-containing LUVs (1:400) also exhibited a peak at 525 nm, although with a lower fluorescence intensity, and displayed a small increase in the fluorescence intensity at 590 nm when compared to the control donor sample (Figure 4.25 A, blue spectrum). The decrease in the fluorescence intensity of the donor with a concomitant increase in the fluorescence intensity of the acceptor reveals the occurrence of FRET, and therefore is reporting Atto488-rIAPP binding to the liposomes (Figure 4.25 A). Although the fluorescence intensities from a spectral region where only D emits (in this case, 500 – 550 nm) can be used to compute FRET efficiencies (Eq. 4.8), these calculations are more error-prone than the ones performed with the amplitude-weighted

mean fluorescence lifetime, $\langle\tau\rangle_1$ (Eq. 4.9), as this last parameter is independent of the concentration of the fluorophore at variance with the fluorescence intensity of a sample.

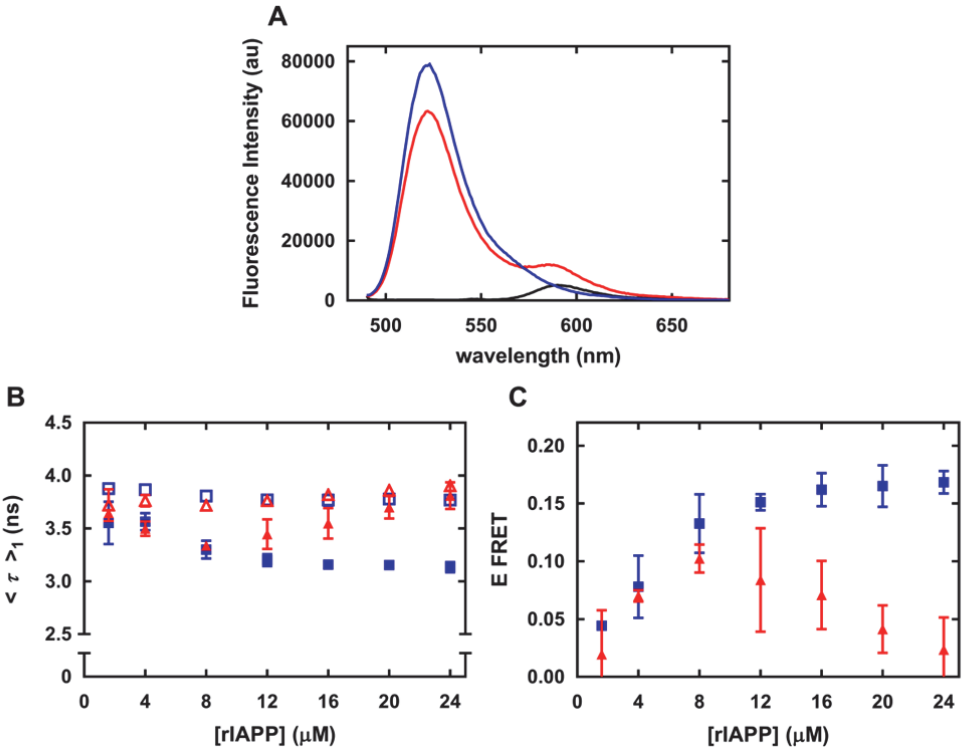

Figure 4.25 – FRET measurements further corroborate that membrane surface crowding controls rIAPP binding to POPS LUVs. A FRET assay was used to independently evaluate the binding of Atto488-rIAPP to POPS LUVs. The concentration of the tracer Atto488-rIAPP (donor) was kept constant at 0.1 μM in all samples. The FRET acceptors were POPS LUVs fluorescently-labeled with Rhod-DOPE (1:400). (**A**) Illustrative emission spectra obtained for the tracer Atto488-rIAPP and 12 μM of rIAPP in the presence of 100 μM of unlabeled POPS LUVs (D, blue) or POPS LUVs Rhod-DOPE (DA, red). The emission spectrum of 100 μM of Rhod-DOPE-containing POPS LUVs (A, black) is also displayed (λ_{exc} = 480 nm). (**B**) The concomitant variations in the amplitude-weighted average lifetime of Atto488-rIAPP, $\langle\boldsymbol{\tau}\rangle_{\mathbf{1}}$, are presented for samples prepared in the absence (empty symbols, POPS LUVs) and in the presence of acceptor (filled symbols, 1:400 Rhod-DOPE POPS LUVs). (**C**) Variation of the overall FRET efficiency, E FRET, calculated according to Eq. 4.9, as a function of the concentration of rIAPP in solution obtained for the samples prepared in the presence of lipid: 100 μM (red triangles) or 500 μM (blue squares) total lipid.

The fluorescence intensity decays of Atto488-rIAPP were measured in the presence and in the absence of acceptors (Figure 4.25 B and C, open and closed symbols, respectively) for 100 μM and 500 μM POPS LUVs (Figure 4.25 B, triangles and squares, respectively). For the samples in the absence of acceptors, unlabeled POPS LUVs were used. The $\langle\tau\rangle_1$ of the tracer peptide was confirmed to be essentially independent of the concentration of unlabeled peptide added to each sample in the presence of either 100 μM or 500 μM POPS LUVs (Figure 4.25 B, open symbols). However, when 500 μM Rhod-DOPE- containing LUVs were used, $\langle\tau\rangle_1$ progressively decreased upon increasing the concentration of rIAPP

(Figure 4.25 B, blue closed squares). The corresponding energy transfer efficiency, *E*, calculated using Eq. 4.9, presented a hyperbolical variance with [rIAPP] (Figure 4.25 C, blue closed squares), confirming the progressive recruitment of Atto488-rIAPP to the lipid membranes upon augmenting the concentration of unlabeled peptide. The energy transfer efficiency computed from the time-resolved data leveled off at *E*~ 0.15 at the highest concentrations of unlabeled peptide used; however, it is not possible to retrieve the transverse distance of closest approach between the covalently-linked Atto488 fluorophore and the acceptor phospholipids without characterizing the expected heterogeneity in the donor population (i.e. the probable presence of distinct membrane-bound peptide populations with variable oligomerization stoichiometries).

A 5-fold decrease in the concentration of acceptor-containing LUVs produced a biphasic variation in the mean fluorescence lifetime of the donor, as it first decreased down to $\langle\tau\rangle_1$~ 3.3 ns at ~12 μM of rIAPP and then progressively recuperated the value measured upon addition of the unlabeled lipid vesicles (Figure 4.25 B, red closed triangles). Consequently, the energy transfer efficiency peaked at ~12 μM of rIAPP and then progressively approached zero Figure 4.25 C, red closed triangles). These results are again explained by the model previously discussed: up to 12 μM of rIAPP, increasing the concentration of unlabeled peptide added to the samples caused a progressive recruitment and trapping of the donor, Atto488-rIAPP to the lipid vesicles; these membrane-bound Atto488-rIAPP molecules could now efficiently transfer energy to the randomly-distributed membrane-bound acceptors. Upon reaching membrane saturation, further increasing the concentration of rIAPP in the samples progressively prevented Atto488-rIAPP binding to the lipid vesicles due to a competition effect, as discussed above. Since these measurements were performed in macroscopic (bulk) conditions (cuvette measurements), the increase in the concentration of free fluorescently-labeled peptide concomitantly caused a decrease in the overall energy transfer calculated for the system since these FRET donors cannot undergo efficient Förster energy transfer due to the very large average donor-acceptor distance (> $2R_0$ (Loura and Prieto, 2011). Once more, this set of results reinforces the conclusion that 100 μM POPS LUVs become saturated with peptide concentrations around 8-12 μM of rIAPP and this is reason behind the sigmoid behavior detected for the ssFA of Atto488-rIAPP (Figure 4.17 B).It should be mentioned that control measurements of the ssFA of the tracer peptide were also made for each sample used in the FRET experiments, and they displayed a similar behavior to the one described above (Figure S 4.6).

So far, our focus has been on the membrane-induced conformational and oligomerization changes produced on rIAPP and hIAPP that help explaining their catalytic effect on amyloid fiber formation in the case of hIAPP. The next set of experiments was directed on

evaluating the impact of hIAPP and rIAPP interaction with the anionic liposomes on their morphology, membrane surface hydration and lipid mobility at the glycerol level.

4.4.8. Progressive surface saturation with rIAPP induces membrane remodeling of POPS LUVs

Dynamic light scattering (DLS) measurements were first performed with 100 μM and 500 μM of POPS extruded lipid vesicles in the presence of the increasing concentration of rIAPP (Figure 4.26). For both lipid concentrations tested, the intensity-weighted distribution of liposome sizes were unimodal in the absence of peptide, representing a uniform population of LUVS with a hydrodynamic diameter centered at D_h= 130.9 ± 3.6 nm (n=8, 4 independent experiments of each concentration of LUVs), as it is exemplified in Figure 4.26 A (top panel). Upon increasing the concentration of rIAPP added to 100 μM POPS LUVs, this peak progressively moved to lower values although always contributing over 98% to the light-scattered intensity detected, as it is exemplified in Figure 4.26 A (medium and bottom panels: addition of 4 μM and 15 μM rIAPP, respectively). As depicted in Figure 4.26 B, the progressive saturation of POPS LUVs with rIAPP caused a gradual shift in their apparent hydrodynamic diameter. Concomitantly, two other peaks could be identified in the size distribution histograms corresponding to additional populations of lipid vesicles in these peptide-containing samples with a smaller and much larger apparent hydrodynamic volume, respectively. The contribution of these populations to the histograms obtained were variable but became increasingly significant for [rIAPP]> 12 μM as revealed by the parallel increase in the polydispersion index (PdI) of the samples (Figure 4.26 B).

The DLS data obtained when the same concentrations of rIAPP were added to 500 μM instead of 100 μM POPS LUVs revealed that rIAPP binding to the anionic lipid membranes had now a minor impact on the morphology of the liposome population. Figure 4.26 C shows that in this case the apparent hydrodynamic diameter of the LUVs corresponding to the dominant peak detected in the histograms (responsible for over 99% of the sample intensity) remained essentially independent of the peptide concentration added to the sample (D_h= 133.4 ± 1.8 nm). Simultaneously a very slight increase in PdI with the peptide concentration used could be detected, although never exceeding 0.2.

Altogether, the data indicates that the binding of the slightly cationic peptide rIAPP to the anionic liposomes does not have the ability to cross-bridge the vesicles due to the establishment of electrostatic interactions. On the contrary, the gradual saturation of these anionic lipid membranes with rIAPP caused a progressive remodeling of the liposomes leading to a population of smaller lipid vesicles; therefore, this process must be

accompanied by the expulsion of some lipids, eventually through peptide-induced tubulation of the lipid vesicles as recently described in the literature for α-synuclein and apolipoproteins (Varkey *et al.*, 2010), temporin B (Kinnunen *et al.*, 2015) and hIAPP and rIAPP (Domanov and Kinnunen, 2008; Kegulian *et al.*, 2015; Kinnunen *et al.*, 2015).

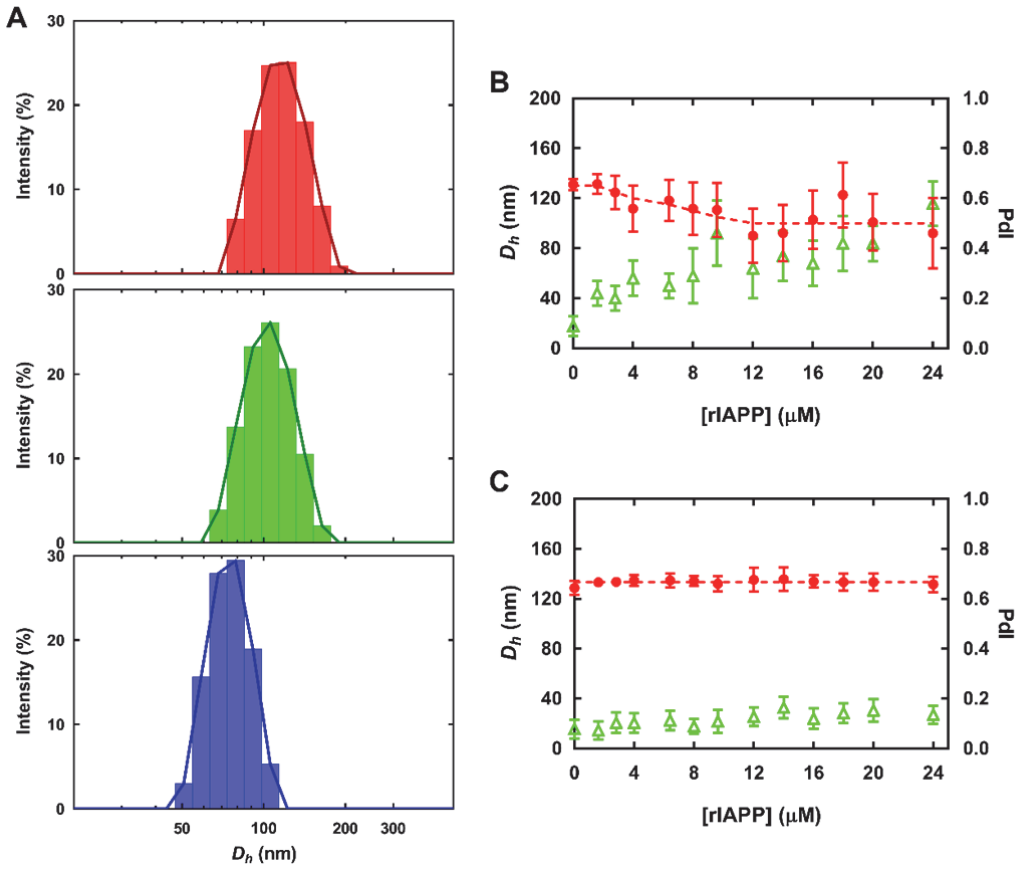

Figure 4.26 – Saturating concentrations of rIAPP are able to induce the remodeling of anionic liposomes. Dynamic Light Scattering (DLS) measurements were performed to evaluate the impact of rIAPP binding to POPS LUVs. (**A**) Representative histograms obtained for 100 μM of POPS LUVs in the absence (top panel), and in the presence of 4 μM (middle panel) and 12 μM rIAPP (bottom panel), after incubation of the samples for ca. 30 min. (**B** and **C**) Evolution of the apparent average hydrodynamic diameter (red circles, left axis) and polydispersity index of the liposome population (PdI, open green triangles, right axis) upon titration of (**B**) 100 μM or (**C**) 500 μM POPS LUVs with rIAPP. For 100 μM LUVs, the progressive saturation of the membrane surface with rIAPP may lead to an induced curvature in the liposomes with the exclusion of some lipids, leading to a population of smaller liposomes. In the full range of concentrations, two other populations appear with variable contribution in every measurement (except for POPS LUVs alone), one smaller and one higher, with very variable sizes. The peak shown here is the one with a higher contribution to the overall intensity. Results shown are the average of 18 to 20 runs (mean ± SD). Dashed lines are just a guide to the eye.

We attempted to perform a similar set of DLS measurements using the same concentration range of hIAPP and POPS LUVs. However, due to the amyloidogenic character of this peptide, the membrane-catalyzed fibril formation seemed to completely destroy the

liposomes as these DLS measurements were highly irreproducible, always giving a PdI of 1 or near 1.

4.4.9. Membrane binding and oligomerization of rIAPP produces surface dehydration and decreased mobility of the interface region of POPS LUVs

Finally, the impact of rIAPP binding on the membrane surface properties of POPS LUVs was also studied using Laurdan, a widely employed polarity-sensitive membrane probe (Parasassi *et al.*, 1990; Harris *et al.*, 2002; Sanchez *et al.*, 2007). As explained in detail in 4.3.8, the dipole moment of Laurdan increases upon its excitation, causing a re-organization of its surrounding polar moieties. Computer simulations and fluorescence quenching methods have shown that this this dye is stably located at the glycerol level of a phospholipid bilayer (Jurkiewicz *et al.*, 2005; Barucha-Kraszewska *et al.*, 2010) and therefore its fluorescence emission spectra provide site-specific information about the interfacial properties of the lipid bilayers (Figure 4.9). Since at this bilayer depth the water molecules are bound to the phospholipids, solvent relaxation (SR) ultimately reflects the motion of the whole hydrated phospholipid moieties around the excited state of Laurdan (Jurkiewicz, Cwiklik, Jungwirth, *et al.*, 2012). Representative normalized and corrected fluorescence emission spectra of Laurdan are shown in Figure 4.27 A. The addition of 12 μM rIAPP to POPS LUVs had a different impact on the fluorescence emission properties of this membrane probe depending on the total concentration of POPS: a significant blue-shift in the emission spectrum of Laurdan was detected for 100 μM (Figure 4.27 A, red line) but not 500 μM of Laurdan-containing POPS LUVs (Figure 4.27 A, blue line) as compared to the emission properties of the membrane-embedded probe in a peptide-free sample (Figure 4.27 A, black line).

This spectral shift in the fluorescence emission of Laurdan was quantified by calculating the generalized polarization, *GP*, of the membrane probe (Eq. 4.21). The *GP* obtained for POPS liposomes in the low ionic strength buffer used was *GP*= -0.066 $\pm$ 0.007, as expected for fluid lipid bilayers (Owen *et al*., 2012) (Figure 4.27 B). The addition of 1.6 up to 24 μM rIAPP to 500 μM Laurdan-containing POPS LUVs had a residual influence on the *GP* of Laurdan (Figure 4.27 B, blue squares); however, the same range of peptide concentrations produced a steady increase in this parameter up to *GP*= 0.159 for 24 μM rIAPP in the presence of 100 μM Laurdan-containing POPS LUVs (Figure 4.27 B, red triangles). It can therefore be concluded that rIAPP binding to this low concentration of anionic liposomes produced significant changes in the interfacial properties of POPS LUVs, namely a decrease in the mobility of the phospholipids at the glycerol level and/or an increased dehydration of the membrane surface.

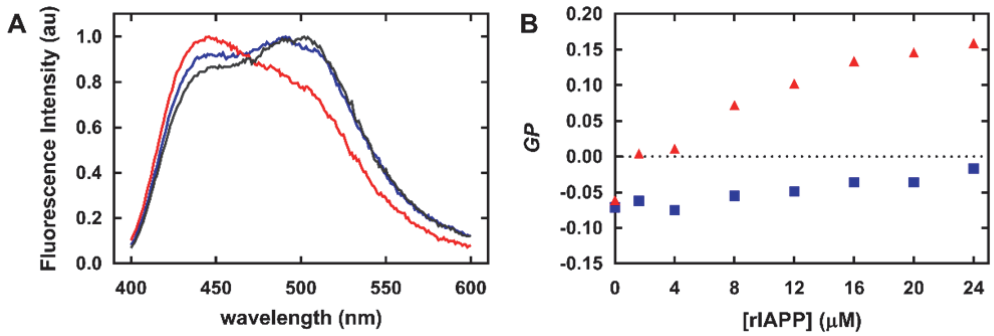

Figure 4.27 – Progressive membrane saturation with rIAPP affects the interfacial properties of POPS LUVs. (**A**) Illustrative normalized and corrected emission spectra (λ_{exc} = 370 nm) obtained for 100 μM (red line) and 500 μM Laurdan-containing POPS LUVs (1:100) (blue line) in the presence of 12 μM rIAPP. The emission spectrum of Laurdan obtained for a peptide-free sample is also shown (100 μM POPS LUVs, black line). The spectral shifts detected for Laurdan reflect peptide-induced changes in membrane properties (hydration and/or mobility) of its immediate environment. (**B**) Effect of increasing concentrations of rIAPP on the generalized polarization, GP (Eq. 4.21), of Laurdan for 100 μM (red triangles) and 500 μM of Laurdan-containing POPS LUVs (1:100) (blue squares).

A more detailed analysis of the emission properties of Laurdan was carried out by reconstructing the time-resolved emission spectra (TRES) of this membrane probe in the absence and in the presence of 12 μM rIAPP. These reconstructed spectra can then be used to examine the effects of membrane saturation with rIAPP on the time-dependent fluorescence shifts (TDFS) of Laurdan, ultimately allowing to disentangle the relative contribution of the peptide-induced changes in local membrane hydration/ lipid mobility, as it is described in detail in section 4.3.8 (Figure 4.28). Both the implemented TRES and TDFS analyses were first validated by using the changes with temperature of the emission properties of Laurdan in POPC LUVs as the testing system. As it is detailed in Section 4.7.1, the results obtained were in excellent agreement with the data gathered from the literature (Table S 4.3), confirming the quality of the time-resolved fluorescence measurements performed in this work.

The primary data required for reconstructing the TRES of Laurdan is a set of fluorescence intensity decays of this membrane probe measured at different emission wavelengths (typically using a 10 nm step), and comprising all of its emission spectrum. As it is illustrated in Figure 4.28 A, the intensity decays of Laurdan are much faster at short compared to long emission wavelengths; in addition, a characteristic rise time can be detected in the fluorescence decays of Laurdan for $\lambda_{em} \geq 470$ nm, revealing the progressive formation of more solvent-relaxed species. In fact, the intensity decays of Laurdan are wavelength-dependent because of the time needed for the hydrated phospholipids to adjust to the increase in the dipole moment of the probe upon Laurdan excitation; this causes the fluorophore molecules to gradually change from their Franck-Condon state to a more solvent-relaxed stated. Until some SR has occurred, there are no molecules in the relaxed

state. So typically there is a rise in intensity at long wavelengths, which is associated with a negative pre-exponential factor that is recovered from the multi-exponential analysis of the fluorescence intensity decays, reflecting the formation of these more solvent relaxed states (Lakowicz, 2006). The SR decay rate of each sample reveals the collective (ensemble average) relaxation of the dye environment: there is a pronounced time-dependent red-shift of the Laurdan emission spectra because the fluorophores that emit at earlier times tend to have shorter emission wavelengths, whereas the ones that emit at longer times tend to have longer emission wavelengths (Figure 4.28 B) (Lakowicz, 2006). It should be noted that TRES are often represented as a function of wavenumber instead of wavelength because the former are directly proportional to the energy of the emitted photons.

A detailed analysis of the reconstructed TRES allows gathering additional information about the characteristics of SR of Laurdan in the absence and in the presence of 12 μM rIAPP. Assuming that the membrane composition does not significantly impact on Laurdan membrane location, two main parameters describing local polarity and mobility of the probed system can be derived from the analysis of TRES. The first one is the overall emission spectral shift, $\Delta\nu = \nu(0) - \nu(\infty)$ (Eq. 4.28), which directly reflects the polarity of the dye microenvironment (Pokorna *et al.*, 2013). Apart from the extent of membrane hydration, i.e. phospholipid hydration at the glycerol level of the bilayer, the polar residues of the peptide might also influence this parameter (Macháň *et al.*, 2014). This parameter can be calculated form the relaxation curve of Laurdan once the position of TRES maximum at t = 0, $\nu(0)$, is known. The value obtained for Laurdan using the method of Fee and Maroncelli (Fee and Maroncelli, 1994) was $\nu(0)$ = 23 800 cm^{-1} (Jurkiewicz, Cwiklik, Vojtíšková, *et al.*, 2012). Accordingly, the total amount of spectral shift obtained for Laurdan embedded in POPS LUVs was $\Delta\nu_{POPS}$ = 4 277 cm^{-1}, which is comparable to $\Delta\nu_{POPC}$ = 4 048 cm^{-1} obtained for the control zwitterionic liposomes (Figure 4.28 C and Table 4.13 and Table S 4.3) indicating that the interface of the anionic liposomes is slightly more hydrated compared to the zwitterionic lipid vesicles; in addition to the different chemical structure of the zwitterionic and anionic phospholipid head groups, the composition of the buffer, namely its ionic strength may also play a role here (Jurkiewicz, Cwiklik, Vojtíšková, *et al.*, 2012; Javanainen *et al.*, 2017). Jurkiewicz and co-workers present a value of $\Delta\nu$ = 4 100 cm^{-1} for POPC:POPS 80:20 in water (Jurkiewicz, Cwiklik, Vojtíšková, *et al.*, 2012).

The kinetics of the relaxation curve depicting the time-dependent Stokes shift of Laurdan after addition of rIAPP was slower in comparison to the one obtained for the control samples (Figure 4.28 C, red and black curves, respectively), revealing that the mobility of the phospholipid interface region was clearly decreased in the presence of 12 μM rIAPP. The percentage of the relaxation process that was faster than the resolution of the

instrumentation used, calculated as $(\upsilon_e(0) - \upsilon_m(0))/\,\upsilon_e(0) - \upsilon(\infty)$, where e and m index $\upsilon(0)$ values obtained from the time-zero spectrum estimation and from TRES reconstruction, respectively (Jurkiewicz, Cwiklik, Vojtíšková, *et al.*, 2012) was estimated to be ~ 20% for the sample in the presence of rIAPP and ~ 22% for LUVs alone. Assuming that both relaxation processes were essentially completed within the experimental time window, a $\Delta\nu_{POPS/rIAPP}$= 4 041 cm^{-1} < $\Delta\nu_{POPS}$ = 4 277 cm^{-1} was obtained for each of the samples studied (Table 4.13).

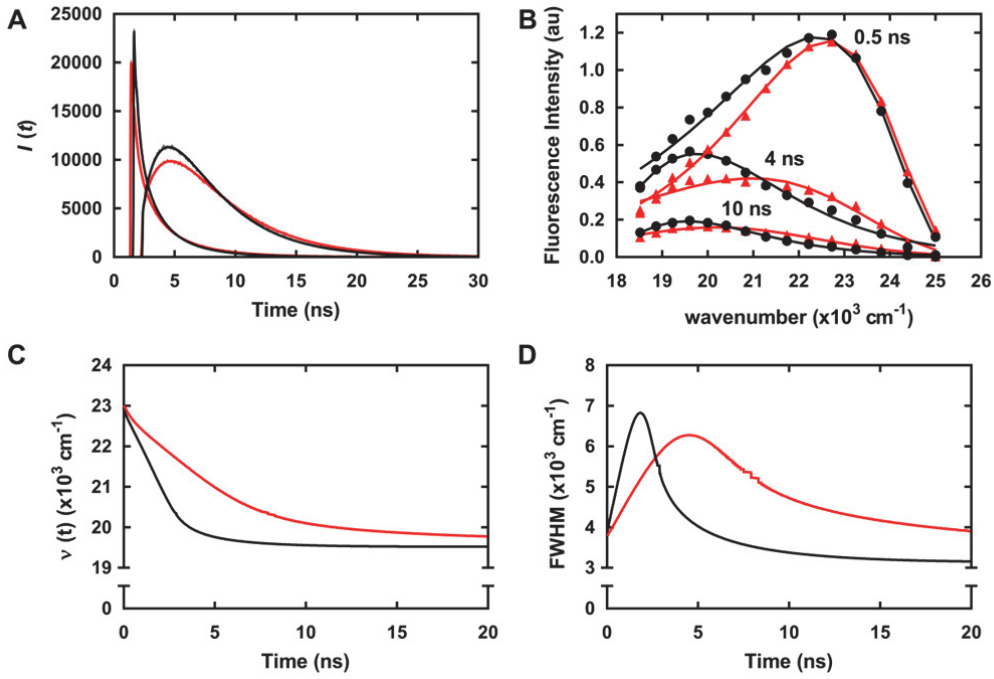

Figure 4.28 - Membrane crowding of POPS LUVs with rIAPP causes both an increased rigidity and decreased interfacial hydration as revealed by the membrane polarity probe Laurdan. (**A**) Illustrative fluorescence intensity decays of Laurdan, $\boldsymbol{I(t)}$, in the absence (black line) and in the presence of 12 μM rIAPP (red line) at RT (λ_{exc} = 340 nm; λ_{em} = 400 nm for the faster decays and λ_{em} = 540 nm for the slower decays). The intensity decays are wavelength-dependent because of solvent relaxation during the excited-state lifetime of the fluorescent polarity probe. (**B**) Reconstructed TRES obtained for Laurdan after correcting for their relative contribution to the steady-state emission spectrum (Eq. 4.24): t = 0.5, 4 and 10 ns, respectively. Fitting the calculated TRES provides information about the time course of (**C**) the position of the spectra maxima and (**D**) full width at half-maximum (FWHM) in the absence (black line) and in the presence of 12 μM rIAPP (red line). 100 μM POPS LUVs were used in the assays with a probe:lipid molar ratio used of 1:100.

This result shows that saturation of the membrane interface with rIAPP produced a slightly more dehydrated environment compared to POPS LUVs alone which might result from the peptide-induced ejection of water molecules around the fluorescent label upon its binding to the lipid bilayers.

Table 4.13 – Impact of rIAPP on the generalized polarization, *GP*, polarity, Δν, and mobility, time at maximum FWHM, detected by Laurdan incorporated in POPS LUVs at RT (*T*= 23 °C). 12 μM rIAPP were added to 100 μM POPS LUVs prepared with a Laurdan:lipid molar ratio used of 1:100. The total amount of fluorescence shift (Δν) is calculated according to Eq. 4.28 considering that $\nu(\mathbf{0})$= 23 800 cm^{-1} (Jurkiewicz, Cwiklik, *et al.,* 2012). FWHM is calculated according to Eq. 4.29.

Sample	[rIAPP] (μM)	*GP*	Δν (cm^{-1})	Time at max FWHM (ns)
POPS	0	- 0.061	4 277	1.82
POPS	12	0.102	4 041	4.52

The second parameter of interest is obtained from the time evolution of the broadness of the TRES of Laurdan, here recorded as the spectral full width at half maximum (FWHM). The FWHM curves shown in Figure 4.28 D for the sample without addition of rIAPP (black curve) and following the addition of 12 μM rIAPP (red curve) initially increase until reaching a maximum, which is followed by an exponential decrease. These features confirm that the entire dipolar relaxation phenomenon was essentially captured during the time-frame of the measurement; however, two important effects were apparent in these profiles. First, significant differences were observed in the shape of the curves as the width of the FWHM profile for the peptide-containing sample was much larger than the one obtained for the control sample. This reveals that the heterogeneity of the probe environment increases significantly in the presence of the peptide compared to the control anionic liposomes. In addition, their maxima shifted from 1.82 ns to 4.52 ns upon adding 12 μM rIAPP to POPS LUVs (Table 4.13), indicating that the local membrane dynamics was clearly affected by the peptide-membrane interactions. This result gives further evidence for a reduced mobility of the lipid acyl groups in the vicinity of the probe upon the addition of rIAPP. Possibly, the establishment of hydrogen bonds between the polar groups of the helical peptides and the lipid acyl groups might be also contributing for the decreased rotational and translational mobility of the phospholipids (Macháň *et al.*, 2014). Finally, it should be noted that the DLS data obtained for 12 μM rIAPP/100 μM POPS LUVs revealed an essentially monodisperse population of liposomes, with the major peak contributing over 98% to the light-scattered intensity by the sample, albeit with a smaller average hydrodynamic diameter than the control lipid vesicles (Figure 4.26). This result guarantees that at this L/P ratio, the peptide did not induce a full disintegration of the anionic liposomes into smaller vesicles, a process that could invalidate the interpretation of the TDFS data.

In summary, our TDFS measurements revealed that Laurdan sensed increased membrane dehydration and decreased mobility of the phospholipid interface region caused by surface saturation of the anionic liposomes with rIAPP; both changes in the interfacial membrane properties of the lipid vesicles account for the concomitant increase detected in the *GP* value of Laurdan (Figure 4.27 and Table 4.13).

4.5. Discussion

A multi-probe fluorescence approach was used in this study to investigate the influence of anionic liposomes on the self-assembly mechanism of hIAPP and rIAPP. The objective was to advance our understanding about the molecular factors that tune the membrane-induced aggregation of these peptides and ultimately regulate the catalytic/inhibitory effect exerted by the negatively-charged lipid membranes on hIAPP fibrillation. In particular, using a complementary set of biophysical techniques, including steady-state and time-resolved fluorescence intensity and anisotropy measurements, we aimed to elucidate the structural and dynamic features of the oligomeric intermediate states formed during the early stages of these aggregation pathways. We intended to establish a correlation between the population of these intermediate species and the consequent peptide-induced changes on the morphology and membrane surface properties of the lipid vesicles.

The combined use of unlabeled IAPP variants and custom-synthesized fluorescently-labelled peptides allowed us to obtain site-specific information regarding the conformational/oligomerization changes undergone by rIAPP and hIAPP along their self-assembly pathways in the absence and in presence of anionic lipid vesicles. Both IAPP variants are intrinsically fluorescent as they share a common aromatic tyrosine residue at their *C*-terminal residue (Y37) (Figure 4.1). On the other hand, the bright Atto488 fluorophore was covalently linked to the opposite end of these molecules, namely at the ε-amine group of the *N*-terminal lysine residue of each IAPP variant (Figure 4.4). This position was elected to minimize the degree of possible perturbation introduced on the fibrillation pathway of hIAPP since it has been proposed that the *N*-terminal segment containing the disulfide bond occupies a peripheral position in hIAPP protofilaments, whereas the C-terminal region of IAPP is directly involved in fibril formation (Kajava *et al.*, 2005; Ahmad *et al.*, 2011; Bedrood *et al.*, 2012). An analogous labelling strategy has previously been employed without detection of any significant effects on the self-assembly properties of hIAPP (Knight and Miranker, 2004; Yan *et al.*, 2006; Bag *et al.*, 2013). In a first set of experiments, we confirmed that the method used to prepare the peptide samples was very reproducible yielding essentially monomeric forms for both unlabeled and Atto488-fluorescently IAPP variants, even when the final peptide concentration in solution was increased up to 24 μM (Figure 4.10 and Figure 4.12). The ssFA measured for Atto488-hIAPP and Atto488-rIAPP was $\langle r \rangle_{\mathrm{Atto488-hIAPP}} \sim \langle r \rangle_{\mathrm{Atto488-rIAPP}} = 0.064$ (Table 4.10) in agreement with the values measured previously for the monomeric rhodamine-labeled form of the peptide ($\langle r \rangle_{\mathrm{TAMRA-hIAPP}} = 0.106 \pm 0.005$ (Knight and Miranker, 2004) and for Alexa568-hIAPP in buffer ($\langle r \rangle_{\mathrm{Alexa568-hIAPP}} = 0.083 \pm 0.005$ immediately after dilution (Domanov and Kinnunen, 2008). It should be noted that in both cases the dyes were

covalently linked to the *N*-terminus of the peptides, and according to the Perrin equation (Eq. 2.2), the mean fluorescence lifetime of each dye, in addition to the hydrodynamic properties displayed by each conjugated peptide, also influences its ssFA (Lakowicz, 2006).

These preliminary studies were fundamental to identify the spectroscopic fingerprints of each fluorescent probe that accompanied hIAPP fibrillation in solution. It was found that the intrinsic ssFA of hIAPP was a good reporter of this process since it pronouncedly increased from $\langle r \rangle_{\mathrm{Y37}}$~ 0.04 up to $\langle r \rangle_{\mathrm{Y37}}$~ 0.19 – 0.21 at the end stage of the fibril formation kinetics (Figure 4.12 and Table 4.10). Concomitantly, there was a slight increase in the intrinsic fluorescence intensity of hIAPP that was accompanied by a 2-nm blue-shift in its emission spectra (Figure 4.11). These spectroscopic changes reflect the burying of the tyrosine residues at the core of hIAPP fibrils formed, in agreement with the work of Padrick (Padrick and Miranker, 2001). On the other hand, the ssFA of a trace amount of Atto488-hIAPP also allowed tracking the fibril formation kinetics of hIAPP in solution as typically this parameter underwent a sigmoidal increase from $\langle r \rangle_{\mathrm{Atto488}}$~ 0.06 up to $\langle r \rangle_{\mathrm{Atto488}}$ < ~ 0.20 upon fibril formation (Figure 4.12 A and Table 4.10), accurately reporting the formation of very large self-assembled species that almost did not depolarize the fluorescence emitted by the probe during its excited-state lifetime (Figure 4.12 C and Table 4.9). The covalently-linked fluorescent probe introduced no significant perturbation on hIAPP fibrillation kinetics as revealed by the overlapping sigmoid kinetics obtained for $\langle r \rangle_{\mathrm{Y37}}$ and $\langle r \rangle_{\mathrm{Atto488}}$ *versus* time (Figure 4.12 A). Interestingly, the obtention of large amounts of hIAPP mature fibrils with a cross-β conformation also impacted the emission properties of the extrinsic probe Atto488 since there was a simultaneous pronounced decrease in its fluorescence intensity and mean fluorescence lifetime that was accompanied by a 3-nm red shift in its emission spectra (Figure 4.12 B and Table 4.10). Eventually, the assembly of several hIAPP protofilaments into mature fibers must be responsible for these spectroscopic changes since the covalently-linked dye to the *N*-terminal residue of the peptide is expected to be excluded from the fibril core (Kajava *et al.*, 2005; Ahmad *et al.*, 2011; Bedrood *et al.*, 2012). Nevertheless, hIAPP fibrils have been shown to have multiple filaments attached (Kajava *et al.*, 2005; Luca *et al.*, 2007; Patil *et al.*, 2011; Martel *et al.*, 2017), similar to the ones observed here using TEM (Figure 4.10 E and Figure S 4.4), and in coherence with the secondary nucleation mechanism proposed for hIAPP (Padrick and Miranker, 2002), where the formation of new fibrils can be catalyzed on the surfaces of preformed fibrils.

Finally, these initial studies were also essential to characterize the influence of the reaction conditions on the concentration-dependent fibrillation kinetics of hIAPP. The extent of sample stirring experienced by each sample was found to be an important parameter that strongly modulated the length of the initial lag phase of this nucleated polymerization process (Figure 4.12 and Figure 4.15), as expected. A quantitative analysis of the data

allowed concluding that even for the highest concentration of hIAPP tested (i.e., 24 μM) there was a safe time frame of at least 2h before the onset of the growth phase of the kinetics whereupon the elongation of the critical nuclei formed in the first stage of the kinetics occurred.

Subsequently, a second set of experiments was performed to clarify the influence of both the anionic lipid content of the liposomes and L/P ratio on the membrane-catalyzed fibrillation of hIAPP under the experimental conditions used in this study. The use of rIAPP as a control peptide is mechanistically informative because previous studies have shown that only the aggregation of hIAPP, but not rIAPP, in the presence of lipid membranes is accompanied by an α-helical to β-sheet conformational transition (Jayasinghe and Langen, 2005; Knight *et al.*, 2006). Although rIAPP is 84% identical to hIAPP (Westermark *et al.*, 2011), this is a non-amyloidogenic variant. This has been ascribed to the presence of three proline residues in positions 25, 28 and 29 (Westermark *et al.*, 1990; Moriarty and Raleigh, 1999; Nilsson and Raleigh, 1999; Azriel and Gazit, 2001; Jaikaran *et al.*, 2001). In fact, Pro residues are known to be strong β-sheet breakers, by disrupting the hydrogen bonding and intra-molecular β-sheet formation, hampering the formation of amyloid fibrils by rIAPP (Moriarty and Raleigh, 1999; Raleigh *et al.*, 2017).

Therefore, the combined use of the unlabeled peptide and of its Atto488-conjugated derivative in these experiments is expected to help distinguishing the changes produced on their fluorescence properties that are associated with the intermediate stages of membrane binding/oligomerization of the peptides from the ones related to the final cooperative conversion of these intermediate oligomeric species into β-sheet fibers.

Globally, our studies confirmed that both factors, i.e. the anionic content of the liposomes (Figure 4.14) and the L/P ratio used (Figure 4.15 and Figure 4.17), significantly modulate the kinetics of membrane-induced hIAPP in agreement with published data (Knight and Miranker, 2004; Jayasinghe and Langen, 2005; Caillon *et al.*, 2013; Zhang *et al.*, 2017). Knight and Miranker performed one of the earliest systematic studies on this topic (Knight and Miranker, 2004). Using DOPS or DOPG mixtures the authors found that (*i*) for 10 μM hIAPP and pure DOPG vesicles, there was an ideal lipid concentration (~125 μM) corresponding to a minimum in the mid-transition for the fiber formation process, and (*ii*) depending on the lipid concentration being above or below this value, there was either a minimum of the mid-transition time for variable DOPG content in the membrane composition, or no minimum was observed (i.e. the mid-transition time decreased continuously with increasing DOPG content). These observations were interpreted as being the result of a balance between increasing overall peptide binding as the PG content of the

lipid vesicles was augmented and increasing hIAPP dilution on the membrane surface as the total lipid concentration was increased for a specific lipid composition studied.

Around the same time, Jayasinghe and Lange obtained similar results using POPS as the anionic lipid as they detected the appearance of an optimal POPS concentration for acceleration of hIAPP fibrillation, which was also found to be sensitive to the ionic strength of the buffer (Jayasinghe and Langen, 2005).

Although the variation in the intrinsic ssFA of hIAPP allowed to easily detect the membrane-induced fibrillation of this peptide (Figure 4.15 A and B), as corroborated by complementary ThT-binding experiments (Figure 4.15 C and D), far-UV CD measurements (Figure 4.16) and TEM studies (Figure 4.15 E-H and Figure S 4.4), this parameter was much less sensitive in reporting the coupled membrane binding/oligomerization of both unlabeled IAPP variants to the anionic lipid membranes. In fact, these coupled equilibria were accompanied by only a relatively modest change in this parameter, $\Delta\langle r\rangle_{\mathrm{Y37}}$~ 0.05 (Figure 4.14 and Figure 4.17 C and D).

The possible adoption by these peptides of a membrane-bound conformation that keeps their C-terminal extended away from the surface as suggested by the group of Miranker (Knight *et al.*, 2006) is a likely justification for these experimental results.

There is considerable evidence from NMR, EPR spectroscopy and MD studies that support this proposal. As before mentioned (Section 4.2.2), Apostolidou and co-workers found that the membrane-bound hIAPP has a central helical region from residue 9 to residue 22, with disordered N- and C-terminal region. This structure leaves much of the highly amyloidogenic stretch from residue 20 to residue 29 exposed for misfolding and β-sheet formation (Apostolidou *et al.*, 2008). The high resolution structure solved by NMR for hIAPP in the presence of SDS micelles at pH 7.3 (Nanga *et al*., 2011) showed similar results, with an overall kinked helix motif, with residues 7 – 17 and 21 – 28 in a helical conformation, and with a 3_{10}-helix comprising of residues Gly33-Asn35 at its C-terminus. They also referred to the importance of this short 3_{10}-helix, compared to the completely disordered structure in rIAPP (Nanga *et al.*, 2009), that may have an impact in the different propensities for self-association of the peptides. Still, the previous determined structure (Apostolidou *et al.*, 2008) did not possess this 3_{10}-helix. The recently suggested structure of hIAPP bound to nanodiscs (90:10 DMPC:DMPG) by NMR, conducted at 35 °C and pH 5.3, consists of a folded hIAPP monomeric subunit with three antiparallel β-strands observed for Ala8-Leu12, Phe15-His18, and Ile26-Ser29 with flexible loops connecting them. Using MD simulations, they also determined that the helical N-terminus was strongly associated with the membrane while unstructured C-terminus was solvent exposed (Camargo, Korshavn, *et al.*, 2017). Even though the exact secondary structure appears to depend on peptide

preparation, membrane scaffold and technique used, all models tend to reinforce the proposal of Miranker of a peptide C-terminal extended away from the surface of membranes.

We therefore sought to use the Atto488-labeled peptides as an alternative to better characterize, at the molecular level, the complex fibrillation pathway undergone by hIAPP/rIAPP after binding to the membranes. However, it was found that the chemical conjugation of the Atto488 fluorophore to these peptides greatly impacted their membrane binding properties (Figure 4.17 A and B, green circles). The membrane partitioning of both cationic IAPP variants is known to be strongly electrostatically driven (Ahmad *et al.*, 2011; Caillon *et al.*, 2015). The *N*-terminal segments of both peptides bear positive charges and therefore these regions are largely responsible for their binding to membranes, particularly when the lipid membranes contain an anionic phospholipid in their lipid composition (Zhao *et al.*, 2004; Engel *et al.*, 2006; Gorbenko and Kinnunen, 2006; Martel *et al.*, 2017). Due to economic reasons, the manufacturer recommended the fluorophore Atto488 to be attached to the ε-amine of the *N*-terminal lysine residue of each acetylated IAPP variant. This chemical modification is expected to produce an overall decrease of 2 units in the net charge of each peptide. The acetylation introduced to prevent *N*-terminal degradation, a common practice in peptide synthesis as refered by the peptide manufacturers, removes its positive charge. The labeling performed in the Lys1 residue removes the positive charge of this amino acid. These changes in the peptide net charge on conjugation with the Atto488-label must greatly reduce their affinity towards the anionic lipid membranes (Figure 4.29 B), and consequently their ssFA remained essentially invariant within the lipid concentration range explored (0 – 500 μM, Figure 4.17 A and B, green circles) even when 100 mol% POPS vesicles were used. A recent study using a C-terminal Rhodamine-labeled IAPP did not find any binding when measuring the diffusion times by FCS of 100 nM of peptide towards ~1 μM POPC:POPG:Cholesterol, 1:1:1 mol/mol vesicles with ~ 45-50 nm in PBS, pH 7.4 at RT (Rawat, Maity, *et al.*, 2018)

The repetition of these measurements with 8 or 24 μM rIAPP/ hIAPP of unlabeled peptide with a trace amount of 1.25 mol% of the corresponding conjugated peptide revealed a complex behavior for the ssFA of the tracer peptide, which critically depended on both the total phospholipid (Figure 4.14) and peptide concentration used in the experiments (Figure 4.17).

Previously, Miranker and collaborators have shown that hIAPP precursors transiently adopt an α-helical state upon association with membranes prior to their conversion into a β-sheet-rich mature amyloid fibrils (Knight *et al.*, 2006), also observed by others (Jayasinghe and Langen, 2005; Apostolidou *et al.*, 2008; Knight *et al.*, 2008).

Based on their CD study of hIAPP and rIAPP in interaction with DOPG vesicles, the authors proposed a general four-step mechanism to explain the helical acceleration of hIAPP amyloid formation in vitro: (*i*) coupled binding of monomeric, random-coil IAPP to lipid and folding into α-helix is governed by a partitioning equilibrium; (*ii*) aggregation of membrane-bound helical states is nucleated by formation of low-order aggregates; (*iii*) propagation of existing aggregates by addition of monomer is energetically more favorable than nucleation of new aggregates, and (*iv*) α-helical aggregates of hIAPP, but not rIAPP, cooperatively convert to β-sheet (Knight *et al.*, 2006). Membrane insertion cannot easily occur for IAPP without oligomerization, as the charged arginine (Arg11) in the middle of the AH cannot be buried in the membrane without a major distortion of the bilayer (Nanga *et al.*, 2009). Accordingly, we propose that peptide conjugation with Atto488 greatly affected its membrane binding properties but not their ability to integrate the transiently-populated oligomeric helical species formed along the membrane-induced self-assembly pathway of rIAPP/hIAPP (Figure 4.29 C).

The surprising results obtained for the variation of the ssFA of the tracer peptide with the total phospholipid and peptide concentration can then be explained by considering the cooperative partition of both rIAPP and hIAPP to the anionic lipid membranes (Knight *et al.*, 2006). At low lipid concentrations, while the majority of the peptide might still remain free in solution, simultaneously, high membrane surface concentrations of each peptide are reached, triggering their self-assembly in the lipid vesicles, since there are very few liposomes in solution. Upon increasing the total lipid concentration in solution, the molar fraction of membrane-bound peptide progressively increases but the peptide becomes increasingly diluted on the membrane surface, driving its dissociation (Butterfield and Lashuel, 2010; Melo *et al.*, 2011, 2013). Therefore, we propose that in the mixed peptide samples, the membrane-induced oligomerization of the unlabeled peptide is able to recruit the weakly membrane-bound Atto488-labeled peptides into the intermediate membrane-bound aggregated helical states, causing a pronounced increase in the ssFA of the tracer conjugated peptides (Figure 4.29 C).

An alternative pathway that would allow direct recruitment of the fluorescently-labeled peptides from the aqueous solution into the membrane oligomeric species, bypassing the transient formation of membrane-bound helical Atto488-rIAPP molecules, does not seem probable because no signs of membrane saturation would then be expected at low lipid concentrations at variance with our experimental data (Figure 4.17) (see discussion below).

Moreover, the lateral aggregation of IAPP peptides on the membranes is believed to be mediated by favorable coiled-coil interactions among leucine and valine residues located on

the hydrophobic face of the AH (Knight *et al.*, 2006) which, are not exposed to the aqueous solution.

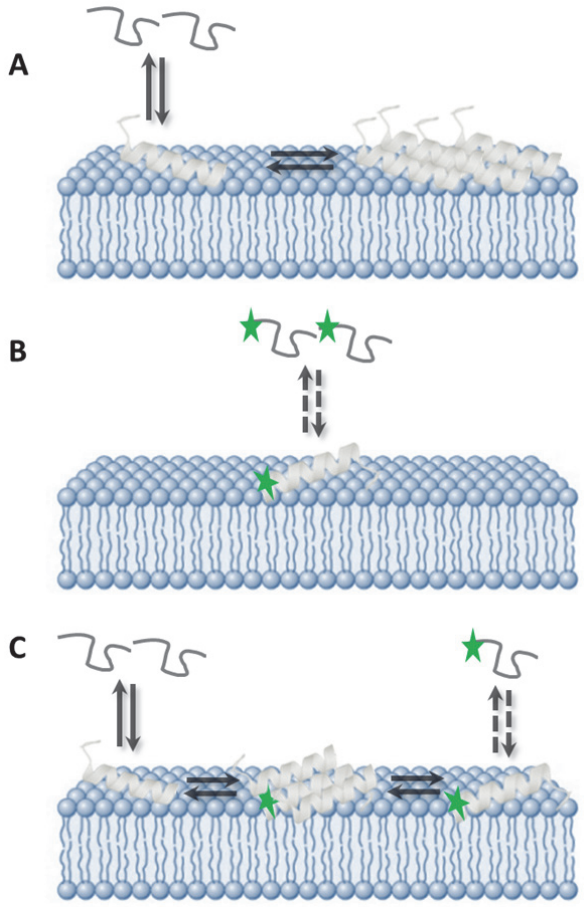

Figure 4.29 - Models of interaction of IAPP peptides with membranes. Aqueous-phase hIAPP and rIAPP are predominantly random coil in solution, with a minor tendency to transiently sample α-helical states. (**A**) At low (hIAPP and rIAPP) and high (rIAPP) concentrations, the unlabeled peptides interact with membranes and acquire α-helical conformations. However, (**B**) the fluorescently labeled peptide in its *N*-terminal is unable to bind strongly to the membranes and remains mostly in solution. In the presence of unlabeled peptide (**C**), the membrane-induced oligomerization of the unlabeled peptide is able to recruit the weakly membrane-bound Atto488-labeled peptides into the intermediate membrane-bound aggregated helical states. Scheme not made to scale.

Lastly, it is also important to stress that the fluorescence properties of the tracer amount of the Atto488-fluorescently labeled peptides were once again extremely sensitive to the final stage of the membrane-induced fibrillation of hIAPP, since a ~3-nm red-shift in their fluorescence emission spectra accompanied by strong fluorescence quenching were only detected when significant membrane-induced amyloid fiber formation occurred concomitantly (Figure 4.18 C and D). Hence, the use of the tracer Atto488-hIAPP further allowed easily distinguishing the experimental conditions that only produced a coupled

membrane partition/oligomerization of hIAPP from the ones that enabled further cooperative conversion of the α-helical aggregates of hIAPP into β-sheet-rich fibrils. We therefore conclude that the conjugated peptides used here are extremely good reporters of the membrane-induced oligomerization of rIAPP/hIAPP.

It can be argued that if a cooperative mechanism (membrane-induced oligomerization) is involved in the recruitment of the tracer peptide to the membranes, one should expect a sigmoidal relationship for the variation of the ssFA of Atto488-hIAPP with phospholipid concentration, particularly at the lowest peptide concentration used ([IAPP]= 8 μM). This was not the case either for hIAPP or rIAAP (Figure 4.17 A and B, red triangles). Eventually, either the initial membrane-induced oligomeric species have a low stoichiometry or the intrinsic partition coefficient of the peptides to POPS vesicles in a low ionic strength buffer is so high that a significant membrane-induced oligomerization of either peptide is always present in our samples. Additional tests of our model would require repeating these experiments but now using either (*i*) an even lower concentration of hIAPP/rIAPP in the mixed peptide samples prepared in the presence of variable phospholipid concentrations, or (*ii*) a wider phospholipid concentration range to examine whether upon further increasing the lipid concentration in solution the ssFA of the tracer peptide starts to decrease towards to the values obtained for the free conjugated peptide in solution due to progressive dissociation of the membrane-bound oligomeric species. It would also be interesting to compare the results obtained for hIAPP and rIAPP in these experiments because their self-assembly in the membrane is expected to be different. The high resolution structure solved by NMR for rIAPP in interaction with dodecylphosphocholine (DPC) micelles (Nanga *et al.*, 2009) shows that the *N*-terminal segment of rIAPP is a stable helix (segment 5 – 17) which is bound to the surface of the membrane but its C-terminal region is completely disordered and mobile. Has previously discussed, hIAPP in the presence of SDS micelles (Nanga *et al.*, 2011) has the 3_{10}-helix in the C-terminal, although the existence of this short helix might depend on the membrane scaffold used. Nevertheless, for rIAPP, the presence of the prolines greatly inhibits the tendency in forming larger membrane-bound aggregates with a β-sheet structure (Brender *et al.*, 2012). In addition, the membrane binding topology of these peptides may also play a role in their oligomerization propensity. Although rIAPP and hIAPP adopt similar α-helical folds at their N-terminal, it has been suggested that the basic amino acid residue placed in the middle of each peptide (His18 for hIAPP and Arg18 for rIAPP) controls the penetration depth of the peptide at the membrane surface: a deprotonated state for His18 in hIAPP compared to a protonated Arg18 residue in rIAPP moves the peptide away from the membrane surface, driving its oligomerization (Brender *et al.*, 2012). A prediction from Monte Carlo simulation (using the MCpep server) of the orientation of hIAPP over a membrane shows that peptide insertion is energetically

unfavorable (Bag *et al.*, 2013); residues in the N-terminal, from Lys1 to Phe15, are expected to be much closer to the membrane than the rest of the sequence. In summary, the lesser degree of structure in the C-termini of rIAPP and its shallower location in the membranes are both important structural features likely to impact on its early aggregation prone tendency and membrane-disruption potential.

The ssFA studies performed with unlabeled rIAPP containing a trace amount of the Atto488-fluorescently labeled peptide clearly showed that rIAPP binding to the POPS vesicles reached a saturation point depending on the total peptide concentration used. When the samples were prepared with a low L/P ratio (24 μM of rIAPP and [POPS] ≤ 100 μM (Figure 4.17 B, blue squares) or [rIAPP] ≥ 10 – 12 μM with 100 μM POPS (Figure 4.23, red triangles), the ssFA of Atto488-rIAPP was much lower than the value expected if all the fluorescently-labeled peptide was membrane-bound. These results were explained by considering that, at these low phospholipid concentrations, the membrane surface area available for peptide binding is limited and the competition between rIAPP and Atto488-rIAPP for membrane binding becomes important. Under these experimental conditions, rIAPP binding to POPS vesicles is much stronger compared to Atto488-rIAPP, as discussed above, ultimately leading to full coverage of the membrane vesicles by the unlabeled peptide. Ultimately, this prevents further membrane partitioning of the weaker membrane-binding tracer peptide, and consequently its incorporation into the intermediate oligomeric helical species formed at the membrane surface is hindered. Upon increasing the phospholipid concentration to 500 μM, the crowding of the membrane surface with rIAPP decreases, allowing for Atto488-rIAPP binding to the lipid membranes. This interpretation of the data was fully corroborated by performing complementary time-resolved fluorescence anisotropy studies (Figure 4.24) and an independent FRET binding assay of Atto488-rIAPP to the lipid membranes (Figure 4.25). The far-UV CD spectra obtained for rIAPP also gives further support to this model since the CD spectra revealed that an increase in peptide concentration from 8 to 24 μM rIAPP resulted in less membrane-bound peptide in the presence of 100 μM but not 500 μM POPS LUVs (Figure 4.16 B and D). These results are also in line with the suggestion of Knight and Miranker (2006) that the high density and amphipathicity of IAPP helices indicate that the membrane-induced helical intermediate states are ordered parallel bundles stabilized by favorable coiled-coil interactions mediated by residues 12, 16, 23, and 26 (Knight *et al.*, 2006).

Assuming that only the outer layer of the liposomes is available for establishing interactions with the peptides, the accessible lipid concentration is approximately half of the total lipid concentration present in each sample, so for 100 μM of POPS LUVs, this would correspond to $[L]_{ac}$=50 μM. Bearing in mind that the saturation point is attained using 10 – 12 μM rIAPP

and further considering that all peptide is bound to the lipid vesicles under these conditions, the membrane saturation was reached at a L_{ac}/P molar ratio ~ 4.2 – 5. Taking into account an area per lipid of 0.627 nm^2 for POPS (Pan *et al.*, 2014) the 4.2 – 5 available phospholipids/peptide would account for an accessible phospholipid are per peptide of ~ 2.6 - 3.1 nm^2. This calculation is close to the estimated surface area occupied by each rIAPP molecule assuming that the peptide adopts an α-helical conformation similar to the one presented by rIAPP in interaction with DPC micelles (Nanga *et al.*, 2009). As it is shown in Figure 4.30, the expected surface area occupied by the peptide is ~ 2.6 nm^2, assuming that the length and diameter of the α-helix from residues Ala5 to Leu23 and Phe15 to Val17 are 2.27 nm and 1.15 nm, respectively. The disordered C-terminal of the peptide was ignored in these calculations, as it is impossible to predict the behavior of this segment. If equivalent calculations are now performed with 500 μM of POPS LUVs (which correspond to $[L]_{ac}$ = 250 μM) and 24 μM rIAPP (the highest concentration of rIAPP used in our studies), one obtains a L_{ac}/P molar ratio ~ 10.4 > 4.2 – 5, justifying why membrane saturation with rIAPP was never reached when this concentration of POPS LUVs was used in the experiments. These calculations required several approximations, including i) that the lipid vesicles are assumed to keep their morphology and integrity (which is only partially true given the difference seen in our DLS studies (Figure 4.26) although the difference might not be significant for these calculations), ii) complete partition of the peptides to the POPS membranes was considered, iii) peptide packing problems on the membrane surface were disregarded, iv) possible conformational changes of the membrane-bound peptides upon their oligomerization were ignored, etc. Still, a good quantitative agreement between the experimental and calculated saturation points was found nevertheless.

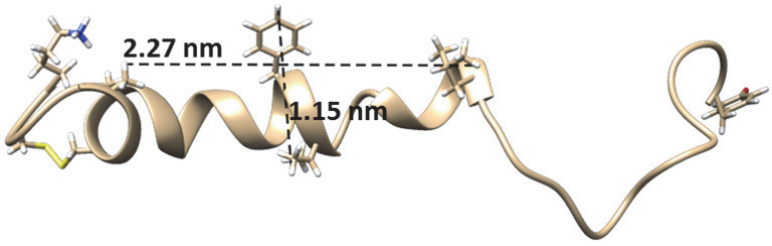

Figure 4.30 - Proposed structure of rIAPP with DPC micelles determined with NMR (Nanga et al., 2009). The helix formed from residues A5 to L23 has ~ 2.27 nm of length and 1.15 nm of width, assuming Phe15 and Val17 to be in opposite sides of the helix, giving an ~ 2.6 nm^2 of area occupied in the membrane. The disordered C-terminal of the peptide was ignored for these calculations, as it is impossible to predict the behavior of this segment. These calculations were made with one chain of the PDB structure 2KJ7 using UCSF Chimera 1.8.1.

On the other hand, the characterization by TEM of the hIAPP samples incubated in the presence of variable concentrations of POPS LUVs clearly confirmed that the membrane-induced hIAPP fibril growth was not restricted by the amount of membrane surface area

available, at variance with rIAPP. The intermediate membrane-bound oligomeric species of hIAPP grew by addition of monomers, extending away from the membrane surface and ultimately disintegrating the vesicles, with the incorporation of phospholipids in the fibrils (Figure 4.15 E-H and Figure S 4.4). This also prevented the use of DLS to track the hIAPP-induced changes in the morphology of POPS vesicles (data not shown). Previous reports using fluorescence microscopy have already described that amyloid fibrils of hIAPP obtained in vitro in the presence of zwitterionic giant unilamellar vesicles (Sparr *et al.*, 2004), symmetric supported lipid bilayers composed of DOPG, but not DPPG (Junghans *et al.*, 2016) and mixed lipid (SOPC:POPG 80:20) SLBs (Domanov and Kinnunen, 2008) incorporated phospholipids. In the latter case, hIAPP fibers grew from apparently unstructured membrane-associated peptide aggregates, preceding their wrapping with lipid. Our studies are in agreement with these observations, implying that the formation of fibrils by hIAPP in the presence of membranes in our conditions reveal a detergent-like mechanism (Figure 4.31).

The final set of experiments performed in this study aimed to establish a correlation between the progressive membrane surface saturation with rIAPP and the peptide-induced changes on the morphology and membrane surface properties of the POPS vesicles. One of the cellular mechanisms that contribute to recognition and generation of membrane curvature is wedge-like AH insertion (Figure 4.32 A, Zeno and Stachowiak, 2018). In fact, one of the most common motifs found in membrane-remodeling proteins and peptides are the presence of AHs.

In most cases, membrane binding triggers a conformational change in peptides as they undergo a transition from a disordered to an α-helical bound state. At this point, the hydrophobic face of the AH is buried in contact with the hydrophobic membrane interior and its polar face is exposed to the hydrophilic lipid head groups and aqueous solution. Often, when these AHs or AHs-containing proteins bind to the lipid membranes, shape changes can be directly observed as vesiculation and tubulation through electron or fluorescence microscopy imaging. Examples of this membrane remodeling include α-synuclein and apolipoproteins (Varkey *et al.*, 2010), temporin B (Kinnunen *et al.*, 2015) and hIAPP and rIAPP (Domanov and Kinnunen, 2008; Kegulian *et al.*, 2015; Kinnunen *et al.*, 2015).

The previously observed membrane remodeling occurred only above a certain peptide to lipid ratio, implying the need of a threshold local protein concentration on the membrane surface for curvature induction. Macromolecular crowding has been proposed as an additional non-specific mechanism capable of generating membrane curvature (Stachowiak *et al.*, 2012). Membrane surface crowding by structured (Stachowiak *et al.*, 2012) as well intrinsically disordered proteins (Busch *et al.*, 2015) attached to the liposomes via His6-tag

binding to Ni-NTA lipids was found to be capable of inducing membrane curvature. This concept is illustrated in (Figure 4.32 B). When the density of proteins on one membrane surface is higher than the density on the opponent membrane, the membranes take a curved shape, owing to the difference in steric pressure on the two membrane sides. The repulsive steric forces caused by membrane surface crowding can therefore be released through membrane deformation. Using transgenic mice, Boassa and co-workers revealed the pathological implication of this mechanism, where overexpressed α-synuclein remodeled membranous organelle system into highly curved structures at presynaptic termini (Boassa *et al.*, 2013).

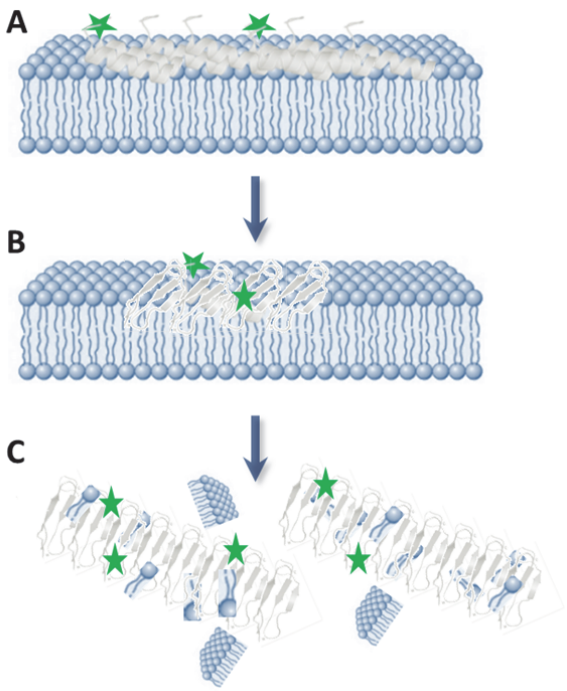

Figure 4.31 – hIAPP solubilizes vesicles with a *detergent-like* mechanism. (**A**) In the presence of higher concentrations of hIAPP, local concentration and orientation of the α-helical conformations catalyze the change to (**B**) β-sheets and to the formation of amyloid fibrils. (**C**) Ultimately, either intermediate or final species destroy the membrane, in a *detergent-like* mechanism. Scheme not made to scale.

Our work provides clear evidence that crowding effects, in addition to the AH insertion mechanism, are both important contributors to the rIAPP ability in inducing membrane remodeling. The gradual increase in membrane surface coverage with rIAPP affects the balance of steric pressure between the opposing membrane leaflets; this, in turn, drives the formation of membrane tubules and vesiculation, as recently described for hIAPP and rIAPP

(Kegulian *et al.*, 2015), ultimately resulting in the formation of smaller vesicles as detected by our DLS measurements (Figure 4.26).

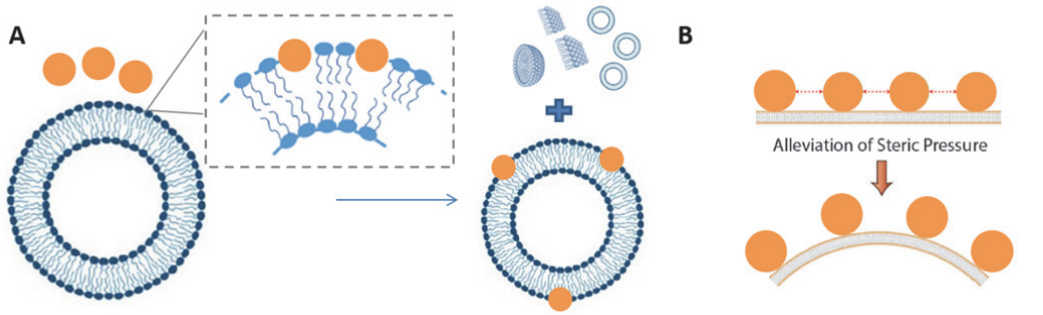

Figure 4.32 - rIAPP effect in the membranes is a combination of wedge-like and crowding effects. (**A**) By interacting with the membranes and acquiring an α-helical conformation (orange circles) the peptide acts as a 'wedge' on the membrane surface inducing curvature effects and causing tubulation, vesiculation and/or formation of lipid-peptide complexes, leading to the formation of smaller vesicles. (**B**) The crowding on the membrane surface leads to the bending of the membrane via steric pressure. Scheme not done by scale. Adapted from Zeno and Stachowiak, 2018.

Recent reports in the literature highlight the ability of hIAPP and rIAPP in inducing membrane remodeling. Domanov and Kinnunen (Domanov and Kinnunen, 2008) time-lapse fluorescence microscopy first demonstrated that hIAPP has the ability to induce a fast and extensive transformation of SLBs composed of SOPC:POPG 80:20. In particular, lipid vesicles and tubes were expelled from the SLBs during the first hour after IAPP addition. Later on, Kinnunen and co-workers extended these studies and showed by fluorescence microscopy that hIAPP, rIAPP and the antimicrobial peptide temporin B caused the expulsion of numerous lipid tubules from supported lipid membranes of POPC. The fact that both amyloidogenic (hIAPP) and non-amyloidogenic (rIAPP and temporin B) peptides had the same effect reveals that this phenomenon is not associated with the amyloid formation. Interestingly, these effects were detected even when anionic phospholipids were absent from the membrane composition of SLBs (Kinnunen *et al.*, 2015). More recently, Kegulian and co-workers have shown that treatment of liposomes prepared with variable lipid compositions with human and rat IAPP were capable of inducing the formation of various highly curved structures, such as tubules or smaller vesicles. This membrane-remodeling process was assigned to membrane curvature induced by IAPP, which was considered to be mediated by the wedging of membrane-inserting AHs (Kegulian *et al.*, 2015). Although it also occurred with zwitterionic SLBs (Kinnunen *et al.*, 2015), membrane remodeling is mostly observed in the presence of negatively charged lipids. Changes in the cellular membrane composition that increases negative charge density due to e.g. altered lipid or fatty acid metabolism could be a risk factor for membrane disruption. The fact that either monomers, oligomers and/or fibrils have been seen to interact with cellular membranes

differing widely in their lipid compositions might suggest a combined effect of multiple mechanisms for membrane disruption in disease pathology, has can also be concluded for the different mechanisms described in literature for in vitro effects, i.e. detergent-like mechanisms, pore-like formation and carpeting model (Press-Sandler and Miller, 2018; Rawat, Langen, *et al.*, 2018).

Finally, the rIAPP-induced perturbation of the interfacial properties of POPS vesicles was also studied using the widely used membrane-polarity probe Laurdan (Parasassi *et al.*, 1998; Harris *et al.*, 2002; Sanchez *et al.*, 2007; Owen *et al.*, 2012; Amaro *et al.*, 2017). Upon varying the concentration of rIAPP added to 100 μM POPS LUVs from 1.6 up to 24 μM, the generalized polarization, *GP*, of Laurdan was found to steadily increase from *GP* = -0.061 up to *GP* = 0.159 (Figure 4.27 B, red triangles); the equivalent experiment performed with 500 μM Laurdan-containing POPS LUVs only produced a modest change on the *GP* of Laurdan (Figure 4.27 B, blue squares). It was concluded that the progressive surface membrane crowding with rIAPP produced a gradual decrease in the mobility of the phospholipids at the glycerol level and/or an increased dehydration of the membrane surface.

A more in-depth analysis of the time-resolved emission properties of Laurdan yields independent information on polarity and mobility at the *sn*-1 carbonyls level, in contrast to *GP* (Sheynis *et al.*, 2003; Jurkiewicz *et al.*, 2005; Jesenska *et al.*, 2009; Pokorna *et al.*, 2013; Amaro *et al.*, 2014, 2017). Accordingly, under membrane saturation conditions (12 μM rIAPP/100 μM POPS (Figure 4.28)), the analysis of Laurdan TDFS measurements revealed that the intercalation of rIAPP increased membrane dehydration and slowed down the mobility of the phospholipid interface region. A note of caution should be made here; upon peptide insertion, $\Delta\nu$ does not necessarily describe the interfacial membrane hydration exclusively, since it can also be affected by the presence of the peptide in the vicinity of the probe, as pointed in Macháň *et al.*, 2014. It is interesting to compare our results with this recent study of Hof and collaborators where the authors established a correlation between the changes in acyl group mobility of POPC LUVs at the glycerol level with the preferential orientation adopted by a set of five different membrane active peptides. A comparison of TDFS of Laurdan produced by LAH_4 at basic pH (a model α-helical peptide), alamethicin, LW21 and LAT revealed that the incorporation of these transmembrane peptides decreased the degree of lipid mobility at the glycerol level, as revealed by an increase in the relaxation time, while the probed polarity was unchanged or increased. On the other hand, peripheral binding of the α-helical peptide LAH_4 at pH 4.5 did not influence the polarity and mobility on the glycerol level of the bilayer, indicating that in this case the acyl groups, about 1 nm below the external interface of the bilayer, were not sensing the peripherally bound peptide.

These results suggested that the *GP* value of Laurdan in the cases examined were more sensitive to mobility than polarity at the glycerol level of lipid bilayers and revealed that a more deeper penetration depth of the membrane active peptide at the membrane interface strongly influenced the mobility sensed by Laurdan at the phospholipid acyl groups level.

A MCPep simulation performed by Bag predicted that rIAPP would associate weakly with a membrane, with amino acids close to the phospholipids heads and practically no insertion in the membrane, in contrast with the observed for mellitine, which was predicted to completely insert into the membrane, but somehow more favorable than the prediction made for hIAPP, in which the amino acids are displayed further away from the membrane surface (Bag *et al.*, 2013). The presence of rIAPP near the glycerol and headgroup regions of the long-chain lipids DMPG and DMPC has been previously experimentally reported using NMR (Smith *et al.*, 2009). However, one should bear in mind that the effects exerted by cationic amphipathic peptides are expected to be amplified in the presence of anionic liposomes, particularly when using a low ionic strength buffer (20 mM HEPES-KOH, pH 7.4 with 1 mM EDTA). In this respect, the group of Martin Hof has also studied the interactions of monovalent cations with mixed negatively charged lipid bilayers (80:20 POPC:POPS LUVs) (Jurkiewicz, Cwiklik, Vojtíšková, *et al.*, 2012). In this case, time-resolved fluorescence solvent relaxation showed significant decrease both in mobility and hydration of the lipid carbonyls probed by Laurdan upon addition of 1 M of the monovalent cations. Complementary MD simulations allowed obtaining a detailed molecular picture of the effects exercised by these ions: it showed deep penetration of the cations down to the glycerol level of the lipid bilayer where they paired with oxygen atoms of the carbonyl groups. Moreover, the cations bridged neighboring lipids forming clusters up to 4 lipid molecules, which decreased the area per lipid, thickened the membrane and hindered lipid dynamics. A similar compression of the POPS bilayer upon extensive binding of the cationic rIAPP might be responsible for the dehydration of the interface region and a hindered dynamics at the glycerol level observed in the TDFS studies performed here. In this regard, membrane intercalation and/or partial charge compensation that accompanies the binding of the cationic peptide to the lipid vesicles might contribute to compact the anionic phospholipids and induce local curvature effects on the membranes. Eventually, these peptide-induced perturbations of the interfacial region of the anionic liposomes give rise to the progressive size reduction in the liposome population upon gradual coverage of the membrane surface (Figure 4.26). In order to release the extra surface pressure caused by progressive saturation of the membranes with rIAPP, some phospholipids must have been expelled from the liposomes, leading to a reduction of their apparent hydrodynamic diameter, as discussed above.

Being a hormone involved in regulatory processes regarding food intake and glucose levels, there should be specific receptors for IAPP, although only specific binding sites have been discovered in the brain and renal cortex. This is due to the novel discovery of receptor activity-modifying proteins (RAMPs), which have the ability to dimerize with the calcitonin receptors and change their affinity, leading to the formation of receptors with enhanced affinity for IAPP. These have been demonstrated in a β-cell line (Martinez *et al.*, 2000). The adoption of α-helical conformations is common to most of IAPP variants, including human, rat, chicken, salmon and cat (Williamson and Miranker, 2007) and it might be important for IAPP hormonal activity. Taking into account the structural resemblances between the members of the calcitonin family, IAPP has also been showed to bind CGRP receptors (Hay, 2017).

The fact that both amyloidogenic and non-amyloidogenic peptides can have a remodeling/disruptive effect towards membranes reveals that this phenomenon is not exclusively associated with the amyloid formation, but might consist on a more general effect of crowding and interaction of α-helices with membranes. This has been previously referred when peptides/peptide fragments or proteins that do not typically aggregate, were able to cause membrane leakage or remodeling.

Differences in membrane binding were also seen to be associated with differences in toxicity. hIAPP and $hIAPP_{1-19}$ have a high potential to disrupt both artificial membranes and islet cells and were seen to be buried in the micelles (Brender, Lee, *et al.*, 2008; Nanga *et al.*, 2008, 2011) even though the peptide $hIAPP_{1-19}$ is unable to form fibrils. $rIAPP_{1-19}$ is significantly less toxic than the human homologous, although the only difference is residue 18; $rIAPP_{1-19}$ binds only to the surface, similarly to the full-length rIAPP (Nanga *et al.*, 2008, 2009; Smith *et al.*, 2009) and is only capable of disrupting membranes in low L/P ratios that probably favor membrane insertion and peptide oligomerization (Knight *et al.*, 2006). rIAPP has little effect on the order of the acyl chains and the lipid headgroup, indicating that the peptide binds superficially at the top of the lipid bilayer by an electrostatic interaction with the lipid headgroup.

Similar conclusions were drawn by Martel and co-workers which studied both the full-length IAPP peptides and fragments corresponding to the N- and C-terminal of IAPP. The hIAPP 1-20 fragment, responsible for the binding to the membranes and lacking the amyloidogenic segment, showed a higher capacity for permeating membranes than the full hIAPP (Martel *et al.*, 2017). Brender and co-workers defend a similar hypothesis, when stated that amyloid fibril formation and membrane disruption (cytotoxicity) are induced by different regions of IAPP (Brender, Lee, *et al.*, 2008).

Nevertheless, Cao and Co-workers studied both hIAPP and rIAPP, as well as a series of mutated forms of hIAPP and showed that none of the 8 peptides studied except for hIAPP induced cytotoxicity towards INS-1 β cells, over a concentration range of 15-60 μM of peptide, while all of them induced leakage of pure or 25% anionic membrane vesicles in L/P ratios of 10:1 to 200:1, with more or less strength (Cao *et al.*, 2013). They found a multistep process for the hIAPP-induced leakage that correlates in time with the fibrillation of the peptide, showing that additional damage might come from the formation of fibrils, in agreement with other works (Engel *et al.*, 2008). Also, the leakage induced by the variety of peptides studied was not accompanied by any significant and detectable α-helical or β-sheet structure, a conclusion surprising taking into account other reports where for similar buffer conditions i.e. high ionic strength, the peptides assumed α-helical conformations, in higher or lower extent. The major difference relies on the L/P ratio, since the one used by those authors was 6.7 and normally one finds a ratio of 20 or above (Cao *et al.*, 2013).

The effects observed here regarding the remodeling or the complete disruption of membranes might only be related with devastating consequences in a disease scenario, namely in Type 2 diabetes mellitus. This disease can lead to a chronic oxidative stress to cells which causes impairments in the normal function of cells, in the fatty acid metabolism, increased blood glucose levels, amongst others. Mitochondrial membranes were seen to be particularly prone to disruption (Gurlo *et al*., 2010) and both rIAPP and hIAPP have been seen to interact with the inner mitochondrial membrane in mouse pancreatic islet β-cells and in cells from a human insulinoma (Kegulian *et al.*, 2015). The curvature of mitochondrial cristae as well as the negative charge contributes to this binding. The impairment of these membranes may lead to the release of the mitochondria content that promotes further apoptosis. One consequence of apoptosis is the increase of cardiolipin in the outer membrane of mitochondria, which leads to an increase in the anionic content of the membrane and consequently an increase of the interaction of the positively charged peptides with it. Increased blood glucose has also been seen to increase the anionic phospholipid content of β-cell membranes (Farese *et al.*, 1986; Rustenbeck *et al.*, 1994). Mitochondrial dysfunction has been pointed as one cause for IAPP cytotoxicity and a consequence of concentration-dependent formation of non-amyloid, α-helical intermediates (Magzoub and Miranker, 2012). Other study showed that α-helical hIAPP oligomers permeabilize pancreatic β-cell membranes and cause those cells to lose their normal morphology and viability (Bram *et al.*, 2014).

Nonspecific detergent-like mechanism, presumably caused by hIAPP oligomers, has been seen in time-lapse AFM studies, both on zwitterionic lipid raft membranes (DOPC:DPPC:Chol 1:2:1) in 10 mM NaH_2PO_4, 100 mM NaCl, 5 mM $MgCl_2$, pH 7.4 (Weise *et al.*, 2010) and mica-supported anionic lipid bilayers (POPC:POPG 3:1 covered in 10 mM

Tris-HCl, pH 7.4, at low and high ionic strength) (Green *et al.*, 2004) and suggested that lipid loss rather than the formation of discrete protein pores renders the membrane leaky. Extractions of lipids from the bilayer by sub-micromolar hIAPP concentrations resulted directly in the increase in membrane fluidity and not necessarily their collapsing, although a cytotoxicity assay in SH-SY5Y cell line suggested that the membrane destabilization is cytotoxic (Bag *et al.*, 2013). Freshly dissolved hIAPP added to dispersed mouse and human islet cells was seen to induce the formation of abnormal vesicle-like membrane structures in association with vacuolization and cell death, that occurred via both apoptosis and necrosis (Janson *et al.*, 1999). In a cellular environment, hIAPP has been observed to cause morphological changes in cellular membranes, including disruption, blebbing or vesicle budding (Hiddinga and Eberhardt, 1999; Saafi *et al.*, 2001; Engel *et al.*, 2008).

4.6. Conclusions

In summary, our results confirmed that hIAPP, but not rIAPP, readily form amyloid fibrils in aqueous solution when incubated at high concentrations for 24h at RT under essentially quiescent conditions. Furthermore, the ssFA of Y37 was confirmed to be a useful parameter that can be used to monitor this process without introducing any perturbation on the system under study. The steady-state fluorescence anisotropy measurements with spatial resolution by making use of a fluorescence laser scanning microscope can be an efficient tool to detect and characterize the heterogeneous aggregates formed along the fibrillation pathway of an amyloidogenic protein/peptide, usefully complementing the ensemble-average measurements performed in a conventional spectrofluorometer/ plate reader. The FAIM measurements performed here allowed distinguishing samples containing the free Atto488 dye, free Atto488-rIAPP and Atto488-hIAPP peptides and large networks of fibrillar hIAPP which was a major achievement considering the technical limitations that still constrain the implemented FAIM setup. Our studies confirmed that membrane-catalyzed fibrillation of hIAPP results in fibril growth into the solution, with the total disruption of vesicles in a detergent-like mechanism, while the membrane-mediated self-assembly of rIAPP is confined to the lipid bilayer. We found that progressive membrane saturation with rIAPP correlated with its ability in reducing the average size of anionic liposomes. The time-resolved emission spectra study of Laurdan revealed that membrane binding and oligomerization of rIAPP produced an increased surface dehydration and decrease mobility in the vicinity of the probe that ultimately might be responsible for rIAPP ability in remodeling the lipid membranes.

4.7. Supplementary Information

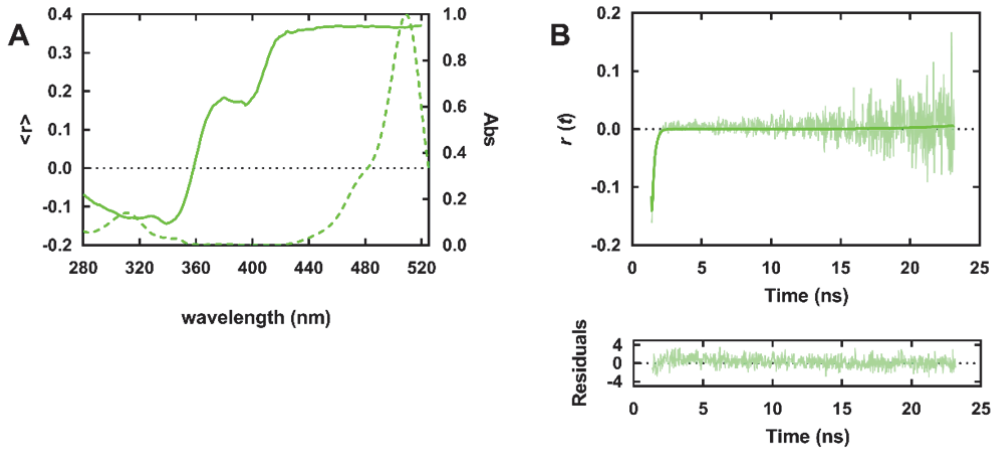

Figure S 4.1 – Fluorescence anisotropy properties of free Atto488 dye. (**A**) Excitation anisotropy spectrum (λ_{em}= 525 nm; solid line) and absorption spectra (dashed line) for 1 μM free Atto488 dye in glycerol (*T*= 8 ºC). The ssFA of the dye as a function of the excitation wavelength was calculated using Eq. 2.4. (**B**) Time-resolved fluorescence anisotropy decay of Atto488 in buffer at RT (λ_{exc} = 310 nm; λ_{em} = 525 nm). The dark green solid line represents the best fit of Eq. 3.19 to the raw data (light green line): $r(0)$= -0.128 and ϕ = 0.16 ns [0.15;0.18]. The residuals of the fit are plotted on the bottom panel. The time scale was 24.4 ps/channel. The fluorescence lifetime measured for the free dye was ~ 4 ns, close to the value reported by the manufacturer.

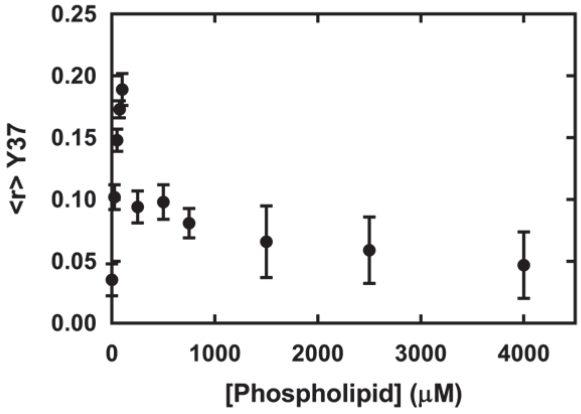

Figure S 4.2 - Variation of the steady-state fluorescence anisotropy of Y37, $\langle r \rangle_{Y37}$, from 24 μM hIAPP with the concentration of POPS LUVs (λ_{exc}= 282 nm; λ_{em}= 320 nm).

Table S 4.1 – Calibration of the FAIM setup. The steady-state fluorescence anisotropy, $\langle r \rangle_{\text{free dye}}$, measured in a conventional spectrofluorometer and using the implemented FAIM setup are presented.

Sample	$< r >_{\text{free dye}}$		
	Spectrofluorometer		Microscope
	$\langle r \rangle_{\text{exp}}^{\text{1PE}}$	$\langle r \rangle_{\text{calc}}^{\text{2PE}}$ [1]	$\langle r \rangle_{\text{image}}^{\text{2PE}}$ [2]
Alexa488	0.013 ± 0.005	0.019	0.037 ± 0.064 (*n*= 15 875)
Atto488	0.022 ± 0.009	0.031	0.047 ± 0.074 (*n*= 15 875)

[1] The ssFAs obtained in the spectrofluorometer (λ_{exc}= 500 nm, λ_{em}= 525 nm) were converted to the expected values if 2PE instead of 1PE was used. The conversion factor used was 1.428.

[2] Gaussian fit (average ± SD) to the histograms obtained from the FA maps calculated on a pixel-by-pixel basis from a 127x125 pixels image. The number of pixels *n* used for each 2PE anisotropy determination is indicated for each sample. The FAIM measurements were performed using the objective 10x, NA 0.4.

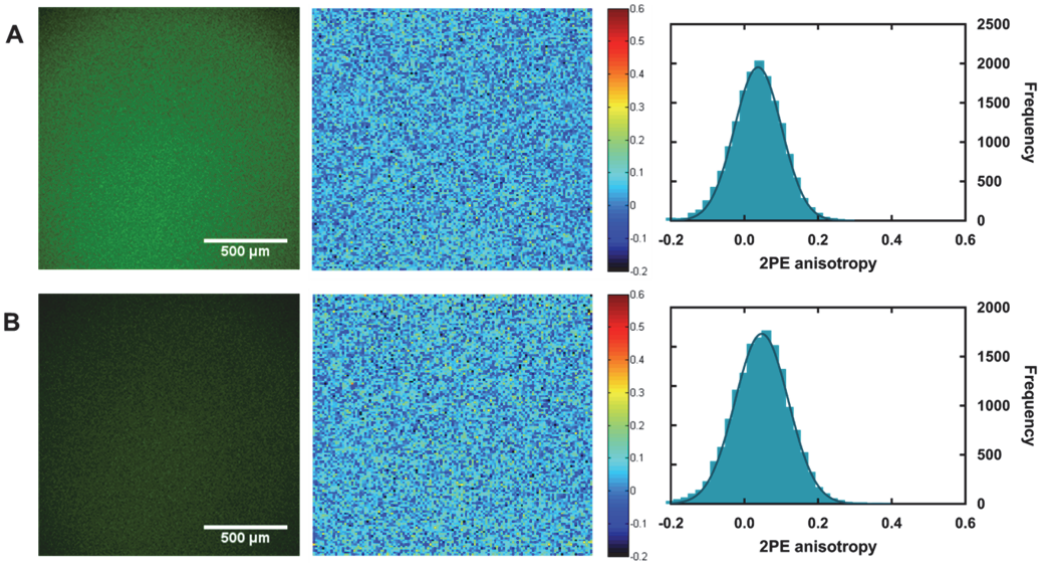

Figure S 4.3 - Validation of the fluorescence anisotropy imaging (FAIM) setup. Representative CLSM images (left panels; λ_{exc}= 488 nm, λ_{em}= 500-600 nm), 2PE FA maps (middle panels; $\lambda_{\text{exc}}^{\text{2PE}}$ = 780 nm, emission selected with 500-550 band pass filter) and histograms (right panels) obtained for the free dyes A488 and Atto488 in water at RT. The 10x air objective was used in all the measurements. The pixel-by-pixel calculated FA is represented in a false color scale from blue (-0.2) to red (0.6). A Gaussian distribution was successfully fitted to these histograms using GraphPad Prism 7 (full curves); the average ± SD of these fits and the number of pixels processed are summarized in Table S 4.1. Image processing for obtaining the histograms was performed using a MATLAB script as described in Chapter **2**.

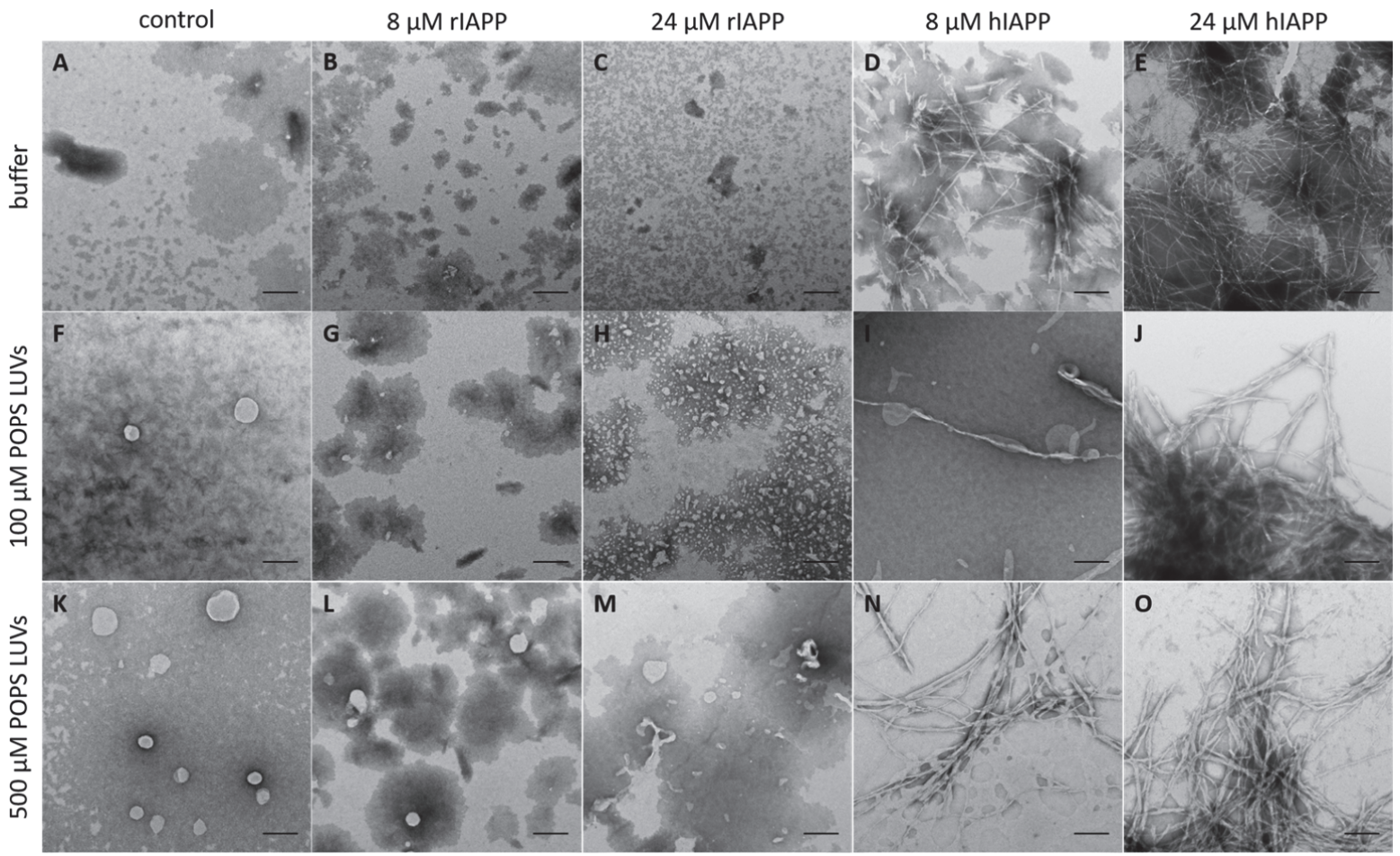

Figure S 4.4 - hIAPP, but not rIAPP, readily fibrillates after 24h of incubation in the absence and in the presence of negatively charged POPS LUVs. Representative negative stained TEM images of (**B, C, G, H, L** and **M**) rIAPP and (**D, E, I, J, N** and **O**) hIAPP (**B** – **E**) in the absence and in the presence of (**G** – **J**) 100 and (**L** – **O**) 500 µM POPS LUVs, respectively. After 24h of incubation, each sample was stained with 2% PTA. The (**A**) buffer and (**F**) 100 and (**K**) 500 µM POPS LUVs were also imaged as a control. Individual fibrils can only be easily identified in samples containing either 8 µM (**D**, **I**, **N**) or 24 µM hIAPP (**E**, **J**, **O**) independently of the addition of anionic liposomes. Images were obtained with a magnifications of 20 000x. Scale bars are 200 nm.

Table S 4.2 - Fluorescence intensity decay parameters obtained for 1.25 % tracer Atto488-rIAPP in the presence of variable concentrations rIAPP and POPS LUVs. The normalized amplitudes, α_i, fluorescence lifetimes, τ_i, amplitude-weighted and intensity-weighted mean fluorescence lifetimes, $\langle\boldsymbol{\tau}\rangle_{\mathbf{1}}$ and $\langle\boldsymbol{\tau}\rangle_{\mathbf{2}}$ respectively, are presented ($\lambda_{\mathbf{exc}} = 310$ nm; $\lambda_{\mathbf{em}} = 525$ nm). For additional experimental details, see the legend of Figure 4.23. Values in square brackets are the errors of the recovered parameters estimated as the lower and upper bound of the joint confidence interval calculated for a 67% probability level. The goodness-of-fit was judged by the $\boldsymbol{\chi^2_G}$ value.

Sample	[rIAPP] (μM)	α_1	τ_1 (ns)	α_2	τ_2 (ns)	$\langle\tau\rangle_1$ (ns)	$\langle\tau\rangle_2$ (ns)	χ^2_G
buffer	0 [1]	0.07	1.40 [1.30,1.58]	0.93	4.10 [4.06,4.11]	3.89	4.02	1.11
	8	0.06	0.78 [0.65,0.94]	0.94	4.04 [4.00,4.11]	3.85	4.00	1.12
	12	0.06	0.56 [0.48,0.64]	0.94	4.05 [4.01,4.08]	3.83	4.02	1.07
	16	0.05	1.10 [1.00,1.22]	0.95	4.07 [4.04,4.08]	3.91	4.03	1.02
	20	0.05	0.70 [0.55,0.92]	0.95	4.05 [4.01,4.10]	3.89	4.02	1.05
	24	0.06	0.80 [0.71,1.01]	0.94	4.04 [4.01,4.07]	3.86	4.00	1.03
100 μM LUVs	0 [1]	0.07	1.23 [1.16,1.36]	0.93	4.08 [4.04,4.09]	3.88	4.01	1.26
	1.6	0.13	1.25 [1.20,1.31]	0.87	4.10 [4.08,4.11]	3.72	3.97	1.21
	2.8	0.10	0.61 [0.57,0.70]	0.90	3.96 [3.93,4.03]	3.62	3.91	1.25
	4.0	0.10	0.94 [0.90,1.08]	0.90	3.98 [3.95,4.03]	3.68	3.91	1.09
	6.4	0.11	0.93 [0.90,1.00]	0.89	4.00 [3.96,4.07]	3.67	3.91	1.17
	8.0	0.10	1.09 [1.04,1.18]	0.90	4.02 [3.98,4.05]	3.74	3.94	1.25
	9.6	0.09	1.04 [1.01,1.13]	0.91	3.99 [3.95,4.06]	3.73	3.92	1.14
	12	0.09	1.28 [1.21,1.40]	0.91	4.02 [3.98,4.05]	3.77	3.93	1.02
	14	0.09	1.30 [1.24,1.40]	0.91	4.02 [3.98,4.03]	3.78	3.94	1.08
	16	0.07	1.28 [1.18,1.39]	0.93	4.06 [4.02,4.07]	3.87	4.00	0.97
	18	0.08	1.72 [1.57,1.81]	0.92	4.07 [4.03,4.08]	3.89	3.99	0.95
	20	0.06	1.56 [1.46,1.70]	0.94	4.08 [4.04,4.09]	3.92	4.01	1.07
	24	0.06	1.33 [1.18,1.49]	0.94	4.07 [4.04,4.08]	3.90	4.01	1.09
500 μM LUVs	0 [1]	0.09	1.04 [0.95,1.12]	0.91	4.04 [4.04,4.05]	3.77	3.97	1.21
	2.8	0.16	0.63 [0.60,0.68]	0.84	4.02 [3.99,4.03]	3.49	3.97	1.18
	4.0	0.10	1.37 [1.28,1.47]	0.90	4.06 [4.03,4.07]	3.79	3.96	1.03
	6.4	0.11	0.96 [0.91,1.00]	0.89	4.04 [4.00,4.05]	3.71	3.95	1.06
	8.0	0.11	1.44 [1.36,1.50]	0.89	4.07 [4.03,4.10]	3.77	3.95	1.19
	9.6	0.10	1.14 [1.09,1.30]	0.90	4.01 [3.98,4.08]	3.73	3.93	1.13
	12	0.11	1.40 [1.32,1.47]	0.89	4.03 [4.02,4.06]	3.74	3.92	1.15
	14	0.10	1.07 [1.00,1.17]	0.90	4.00 [3.96,4.07]	3.70	3.91	1.24
	16	0.10	1.20 [1.11,1.29]	0.90	3.99 [3.96,4.06]	3.72	3.90	1.11
	18	0.10	1.13 [1.08,1.32]	0.90	3.98 [3.95,4.05]	3.70	3.90	1.26
	20	0.11	1.33 [1.27,1.45]	0.89	4.01 [3.97,4.08]	3.72	3.90	1.09
	24	0.11	1.35 [1.28,1.46]	0.89	4.03 [4.03,4.04]	3.74	3.93	0.98

[1] The concentration of Atto488-rIAPP used was 0.3 μM

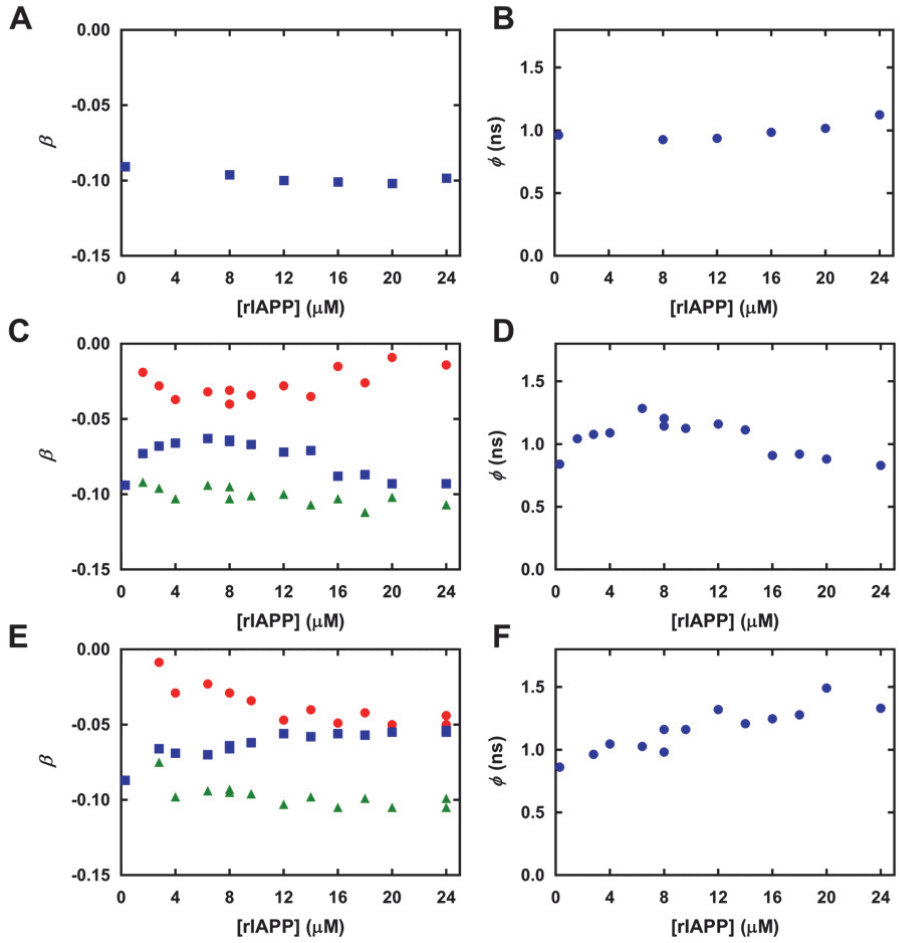

Figure S 4.5 - Influence of total rlAPP concentration on the fitted fluorescence anisotropy decay parameters obtained for the tracer Atto488-rlAPP in the absence and in the presence of POPS LUVs. Variation of the (**A**, **C** and **E**) pre-exponential β_1 (blue squares), limiting anisotropy r_∞ (red circles) and $r(0) = \beta_1 + r_\infty$ (green triangles) and (**B**, **D** and **F**) rotational correlation time ϕ_1 obtained for 1% Atto488-rlAPP as a function of total rlAPP concentrations (**A** and **B**) in buffer and in the presence of (**C** and **D**) 100 μM or (**E** and **F**) 500 μM POPS LUVs. For additional details, see the legend of Figure 4.23 and Table 4.12.

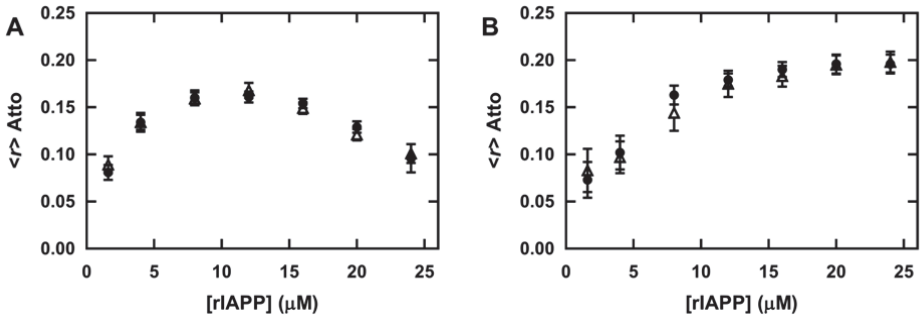

Figure S 4.6 - The mol% of fluorescently-labeled peptide used in the FRET assay does not influence rlAPP binding to POPS LUVs. The interaction of variable concentrations of rlAPP with (**A**) 100 μM and (**B**) 500 μM POPS LUVs at RT was monitored by measuring the changes in the ssFA of 0.1 μM tracer Atto488-rlAPP added to each sample, $\langle r \rangle_{\mathrm{Atto488}}^{500/525\mathrm{nm}}$. The mol% of fluorescently-labelled peptide in the sample ranged from ~6 mol% to 0.4 mol% when the unlabeled peptide concentration was varied from 1.6 up to 24 μM, respectively. The liposomes used were either unlabeled (D, closed circles) or contained Rhod-PE at 1:400 (DA, open circles).

4.7.1. Time-dependent fluorescence shift (TDFS) measurements of Laurdan – validation of the implemented analysis

Laurdan is an extrinsic fluorescent membrane polarity-sensitive dye that was used in section 4.3.8 to evaluate the impact of rIAPP binding on the interfacial membrane properties of POPS vesicles, namely to detect possible peptide-induced perturbations on the dynamics (lipid packing) and polarity in the immediate vicinity of the fluorophore. The use of Laurdan to study the temperature dependence of the local polarity (interfacial hydration) and mobility of the hydrated phospholipids of a well-defined system (large unilamellar vesicles of POPC) was used here as a reference (Amaro *et al*., 2017) in order to test the implemented analysis of TDFS according to the methodology described in the literature (Horng *et al*., 1995; Pokorna *et al*., 2013). The increase in membrane fluidity caused by an increase in temperature was easily detected from measuring the generalized polarization (*GP*) of Laurdan, which changed from *GP* = - 0.180 to *GP* = - 0.370 at 21 and 37 ºC, respectively, in good agreement with the literature (Table S 4.3).

To get a more detailed picture of the dipolar relaxation of the system, a set of fluorescence intensity decays was measured for Laurdan at different emission wavelengths (from 400 to 540 nm, with a 10-nm step) encompassing its steady-state emission spectrum at the chosen temperatures, namely *T*= 23 and *T*= 37 ºC. As it is illustrated in Figure S 4.7 A for *T*= 23 ºC, the fluorescence emission decays of Laurdan were significantly slower at longer emission wavelengths and a characteristic rise time could be detected for $\lambda \geq 470$ nm. These features arise because the system needs time to relax from its Franck-Codon state, which is reached immediately upon excitation, to the equilibrated solvent-relaxed first singlet excited state. Since the photons with a higher energy (i.e. close to the Franck-Codon state of the fluorophore) are emitted early on, there is a pronounced time-dependent red-shift of the emission spectra of Laurdan (Figure S 4.7B). After converting the data to the wavenumber domain, the analysis of the reconstructed TRES allowed obtaining a more detailed description of the dipolar relaxation of the system at the two temperatures studied by considering the time course of the position of their peak maximum and FWHM (Figure S 4.7 C and D, respectively. As it is summarized in Table S 4.3 an excellent agreement between this work and the literature (Amaro *et al*.., 2017) was also found for the total amount of fluorescence shift, $\Delta\nu$, and the time at which the spectral half width reaches its maximum value at both temperatures, validating the time-resolved fluorescence measurements as well as the implemented analysis of TDFS according to the methodology described in the literature (Horng *et al.,* 1995; Pokorna *et al*., 2013).

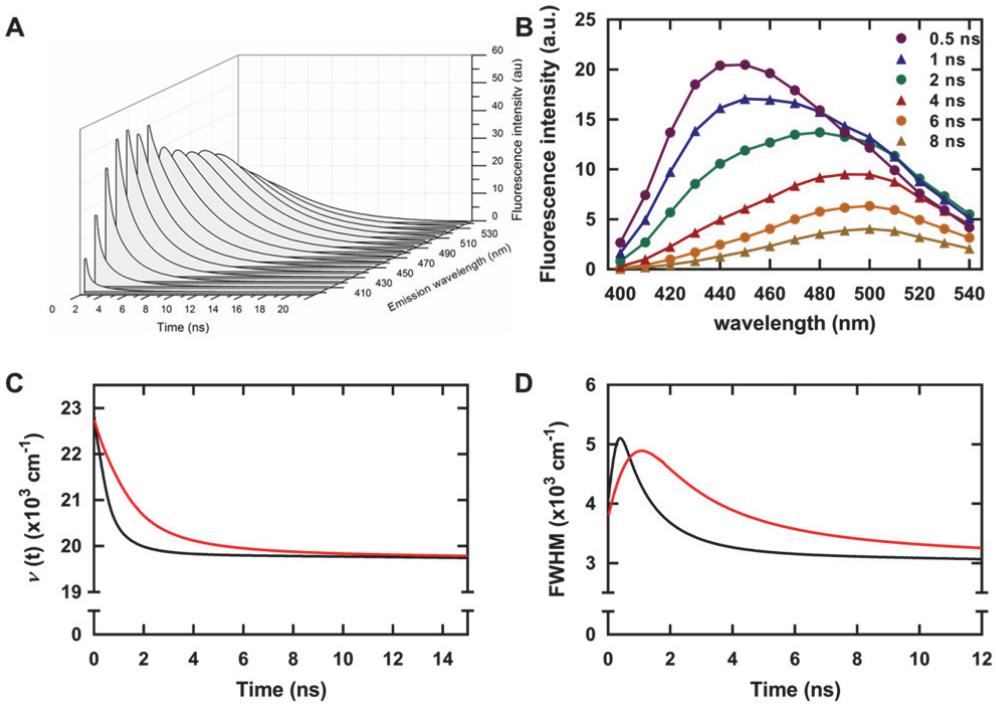

Figure S 4.7 - Temperature dependence of the local polarity and mobility experienced by Laurdan incorporated in POPC large unilamellar vesicles. (A) Illustrative fluorescence intensity decays and **(B)** reconstructed time-resolved emission spectra (TRES) obtained for Laurdan at T= 23 ^{o}C after correcting for their relative contribution to the steady-state emission spectrum of the fluorescent probe (Eq. 4.24) t= 0.5, 1, 2, 4, 6 and 8 ns, respectively. **(C)** Position of the spectra maxima and **(D)** full width at half maximum (FWHM) as a function of temperature (T= 23 ^{o}C, red line; T= 37 ^{o}C, black line) after transforming the TRES of Laurdan to the wavenumber domain (Eq. 4.25). The buffer was 10 mM HEPES, pH 7.0 with 150 mM NaCl and 0.2 mM EDTA and the probe:lipid molar ratio used was 1:100.

Table S 4.3 - Effect of temperature on the *GP* values and time-dependence of TRES parameters for Laurdan incorporated in POPC LUVs. The probe:lipid molar ratio used was 1:100.

Parameter	T= 23 ^{o}C		T= 37 ^{o}C	
	This work	Reference [1]	This work	Reference [1]
GP	- 0.180	- 0.177 ± 0.004	- 0.370	- 0.360 ± 0.003
$\Delta\nu$ (cm^{-1}) [2]	4 048	4 095 ± 50	4 099	4 078 ± 50
Time at maximum FWHM (ns)	1.08	1.06 ± 0.05	0.39	0.32 ± 0.05

[1] Amaro. *et al*. (2017)

[2] total amount of fluorescence shift calculated according to Eq. 4.26, Eq. 4.27 and Eq. 4.28.

5. Conclusions and perspectives

The pathological conversion of native soluble peptides and proteins into β-sheet-rich amyloid fibrils is the culprit of a series of human diseases. Several biological factors, including the biological membranes, are able to influence this process but the underlying molecular mechanisms are far from being completely understood. The lipid membranes have a dual role, not only facilitating this process but also being the target of the reactive intermediates formed along the fibrillation pathways of the amyloidogenic peptides/proteins. Major efforts have been made to detect and characterize these species since they are challenging to study due to both their metastable character and low abundance. In this context, the main goal of this work was to combine complementary biophysical and fluorescence spectroscopy/microscopy approaches to understand the effect of lipid membranes in modulating the conversion of soluble peptides into oligomeric intermediates/amyloid fibrils. More specifically, we aimed (i) to gain detailed structural and dynamic information about the membrane-induced oligomerization/ amyloid fiber formation pathways of model amyloidogenic polypeptides, and (ii) to evaluate the ability of the intermediate species formed along these pathways in perturbing the membrane organization. To this end, we chose to use human calcitonin (hCT) and islet amyloid polypeptide (hIAPP) as model amyloidogenic peptides. Importantly, both peptides have variants that are non-amyloidogenic (salmon CT (sCT) and rat IAPP (rIAPP), respectively) that can be used as controls since their self-assembly does not progress into the formation of amyloid fibrils.

CTs and IAPPs belong to the same superfamily of peptides, the calcitonin peptide family, which makes them structurally related peptide hormones (section 3.2.1). This allowed the use of similar experimental strategies to study the influence of anionic lipid membranes on their self-assembly pathways. Among other characteristics, these polypeptides have a single tyrosine residue in their sequence (Y12 in hCT and Y22 in sCT - Figure 3.3 – and Y37 in hIAPP and rIAPP - Figure 4.1). The intrinsic fluorescence properties of tyrosine were successfully used to report the binding of the peptides to lipid vesicles (Figure 3.34 and Figure 4.14) and the fibrillation of the hIAPP/rIAPP in solution and in the presence of membranes (Figure 4.15). However, tyrosine residues characteristically present a low fluorescence quantum yield which strongly limits the sensitivity of the fluorescence assays performed; on the other hand, their maximal emission wavelength typically is $\lambda_{\max}^{\mathrm{em}}$~ 305 nm, which makes the fluorescence measurements highly prone to scatter–induced artefacts (for example, the ssFA of both CTs needed to be extensively corrected in the presence of high concentrations of large unilamellar vesicles (LUVs) (Figure 3.34). Although it is certainly advantageous to study the peptides without any chemical modifications, their fluorescent-labeling with highly photostable fluorescent dyes that present a high quantum yield opens a

variety of possibilities regarding the application of advanced fluorescence techniques, namely time-resolved fluorescence anisotropy measurements, FCS and FAIM, to the characterization of their rotational and diffusion properties in solution.

Both CT and IAPP peptides were therefore fluorescently-labeled at their N-terminal residues in an attempt to minimize the possible interference with both the amyloid process and their interaction with negatively charged lipid membranes. In fact, both hormones have a disulfide bridge from residue 1 (CT) or 2 (IAPP) to 7 that constrains the N-terminal movements. The central and C-terminal regions of both peptides have also been found to be involved in the fibrillation pathway, as explained in detail in sections 3.2.7 (hCT) and 4.2.2.2 (hIAPP). Moreover, previous works have been successful in studying these and related peptides in terms of fibrillation assays and binding to the membranes (Knight and Miranker, 2004; Domanov and Kinnunen, 2008; Amaro *et al.*, 2016).

Due to mainly economic reasons, human and salmon calcitonins were conjugated to HiLyte^{TM} Fluor 488 at their *N*-terminus (HL488-hCT and HL488-sCT, respectively), whereas Atto488 was covalently-linked to the N-terminal lysine residue of acetylated IAPP peptides via conjugation to their ε-amine group (Atto488-hIAPP and Atto488-rIAPP, respectively). In both cases, tracer amounts of the fluorescently-labeled peptides were found to successfully incorporate the aggregates/amyloid fibrils formed by the bulk unmodified peptide present in the assay (Figure 3.33 and Figure 4.12). However, whereas HL488-hCT and HL488-sCT presented similar membrane binding properties to the corresponding unmodified peptides (Figure 3.34 and Figure 3.36), the N-terminal-labeling of IAPPs with the Atto488 dye greatly affected their membrane binding affinity (Figure 4.14 and Figure 4.17). The labeling of the CTs with HL488 did not affect their charge net charge at neutral pH (Table 3.1) while the labeling of IAPPs with Atto488 altered their net charge by a factor of -2 (Table 4.2), due to the acetylation of their *N*-terminus and the labeling is the positively charged side chain of the amino acid lysine. The presence of the fluorescent dye in the N-terminal of IAPP might have interfered with the binding of the peptide to lipid vesicles. Despite this observation, the use of tracer amounts of these conjugated peptides was found to be a very useful tool to detect the membrane-induced fibrillation of hIAPP (Figure 4.21) and oligomerization of rIAPP (Figure 4.23), allowing to successfully distinguish both situations.

The development of a reproducible procedure for the preparation of monomeric aqueous solutions of the fluorescently-labelled CT peptides was a major bottleneck in the development of the project, as described in section 3.6.1 (Figure S 3.7). The final procedure adopted included the preparation of stock solutions of each peptide in HFIP, evaporation of the organic solvent with a light stream of nitrogen and resuspension of the conjugated peptide in buffer/ adequate solvent, in agreement with (Rolinski *et al.*, 2010; Amaro *et al.*, 2011, 2013). The implementation of this method of sample preparation greatly increased the experimental pace of the second part of the thesis work described in Chapter 4.

Another experimental problem faced in the early development of the project was the establishment of a reproducible microplate reader assay for the fibrillation studies performed with CTs in solution. As described in detail in section 3.4.2 some parameters were varied (e.g. time of agitation and volume of the sample) in an attempt to improve the reproducibility of these assays without great success. Still, our data hinted that the fibrillation kinetics of hCT in solution did not follow a standard mechanism under the experimental conditions tested, since there was a direct relationship between the lag time of the kinetics and the peptide concentration used in the assay (Figure 3.29), in contrast to some literature available for hCT (Arvinte *et al.*, 1993; Avidan-Shpalter and Gazit, 2006) and the general notion of fibrillation kinetics (Munishkina *et al.*, 2004). This behavior was not directly related to the presence/absence of HFIP in the final peptide solution since there was not a significant effect in the lag times of the fibrillation kinetics upon eliminating the organic solvent from the solution (Figure 3.29, Figure 3.30 and Table 3.17).

Later on, similar results were published by Kamgar-Parsi and co-workers in 2017; these were explained on the basis that hCT monomers must suffer a structural conversion before they are incorporated into the fibrils. The authors proposed the existence of two types of monomers, growth-competent and growth-incompetent, respectively. The formation of growth-incompetent aggregates is more likely in the presence of higher concentrations of peptide and they only slowly reverse to growth-competent monomers, also limiting the availability of these growth-competent monomers to allow the formation of mature fibrils (Kamgar-Parsi *et al.*, 2017). The results obtained by these authors can in part explain the observed results in our experiments. Not only the direct relationship between the peptide initial concentration and the lag time can be justified by the formation of these growth-incompetent aggregates, but the immediate increase in the ssFA of the conjugated peptide might be revealing the formation of intermediates along the fibrillation pathway of hCT (Figure 3.31). In fact, the ssFA of a fluorescently-labeled peptide is usually a much more sensitive reporter of the increase in size of the fluorescent species compared to the changes in their secondary structure over time. At this point, additional studies are needed to clarify the fibrillation kinetics of hCT under different experimental conditions and to evaluate if the non-canonical fibrillation model recently proposed in the literature can adequately describe our data. In this regard, it would be interesting to perform assays where the ThT fluorescence intensity and the ssFA of a tracer amount of HL488-hCT were measured in parallel during the fibrillation kinetics of variable concentration of hCT to relate the information given by each fluorescent dye simultaneously present in the same sample.

On the other hand, the fibrillation mechanism of hIAPP was found to have the canonical inverse relationship between the lag time of the assay and the concentration of peptide (Figure 4.15), in agreement with previous results (Yan *et al.*, 2006; Brender *et al.*, 2015). This fibrillation was accelerated in the presence of low concentrations of negatively charged vesicles (Figure 4.15 and Figure 4.20). The implementation of FAIM (Chapter 2) allowed for

the measurement of ssFA of rIAPP and hIAPP samples with spatial resolution. This was fundamental to identify the formation of fibrils (Figure 4.13 D) in a situation where the bulk, steady-state fluorescence measurements did not indicate the formation of larger aggregates (Figure 4.20 A). It was also possible to see the difference between the final stage obtained for 24 μM of rIAPP and hIAPP in the presence of lipids, showing that the high values of ssFA in the case hIAPP indicated the presence of aggregates/fibrils (Figure 4.21 D) while for rIAPP reported only the binding of the peptide to the LUVs, without any larger structures visible (Figure 4.22 C).

The experimental data strongly supports the existence of a coupled sCT and rIAPP partition/oligomerization equilibria that pulls the conjugated peptide to the lipid bilayers that leads to the formation of oligomers/aggregates at low L/P (Figure 3.41 and Figure 4.23). In the case of HL488-sCT, this resulted in a pronounced self-quenching of its fluorescence emission at a low L/P ratio regime, with both static and dynamic components. The formation of these dimers/oligomers might be related with the proposed ion channels observed by others regarding sCT (Stipani *et al.*, 2001; Diociaiuti *et al.*, 2006) and to other amyloid proteins reconstituted in liposomes (Quist *et al.*, 2005). Regarding IAPP, our studies confirmed that, under our experimental conditions, the hIAPP fibrils formed upon the interaction with membranes grow into the solution and disrupt totally the lipid vesicles, in a detergent-like mechanism (Figure 4.15) while the oligomerization of rIAPP is restricted to the lipid bilayer (Figure 4.23). We found that progressive membrane saturation with rIAPP correlated with its ability in reducing the average size of anionic liposomes. The time-resolved emission spectra study of Laurdan revealed that membrane binding and oligomerization of rIAPP produced an increased surface dehydration and decrease mobility in the vicinity of the probe that ultimately might be responsible for rIAPP ability in remodeling the lipid membranes. We think that a similar approach as the one taken for rIAPP (a combination of FRET and DLS assays, with a time-resolved emission spectra study of Laurdan) would bring extremely valuable information regarding the relationship between liposome coverage by sCT and the perturbation effects exerted by the peptide on the interfacial membrane properties. Likewise, leakage experiments would be a valuable complement to the work performed so far with both CT and IAPP. These experiments should allow us to establish a correlation between the surface coverage of the lipid vesicles by the peptide and their ability to permeabilize the vesicles through a pore mechanism and/or a more general membrane disruption mechanism. The next logical step would be to characterize the interaction of sCT/rIAPP with more complex lipid compositions and test whether the effects observed upon the interaction of rIAPP with POPS LUVs also occurred when smaller amounts of negatively charged lipid were used and/or different lipid compositions were tested, e.g. including sterols, sphingolipids, gangliosides, among others.

In sum, we have shown that, although incapable of forming fibrils, the non-amyloidogenic peptides sCT and rIAPP form intermediates upon their interaction with lipid vesicles, depending on the concentration of peptide and lipid in the system. Critical peptide concentrations lead to the aggregation of the fluorescently-labeled monomeric peptides at the lipid surface of the negatively-charged vesicles which are non-fluorescent. The identification of this type of oligomeric intermediates might have an important role in the fibrillation kinetics mediated by membranes and/or contribute directly or indirectly to the cellular toxicity observed in vivo.

6. References

Abedini A, and Raleigh DP (2009) A critical assessment of the role of helical intermediates in amyloid formation by natively unfolded proteins and polypeptides. *Protein Eng Des Sel* **22**:453–9.

Abedini A, and Raleigh DP (2006) Destabilization of human IAPP amyloid fibrils by proline mutations outside of the putative amyloidogenic domain: Is there a critical amyloidogenic domain in human IAPP? *J Mol Biol* **355**:274–281.

Ahmad E, Ahmad A, Singh S, Arshad M, Khan AH, and Khan RH (2011) A mechanistic approach for islet amyloid polypeptide aggregation to develop anti-amyloidogenic agents for type-2 diabetes. *Biochimie* **93**:793–805.

Ahmed M, Davis J, Aucoin D, Sato T, Ahuja S, Aimoto S, Elliott JI, Van Nostrand WE, and Smith SO (2010) Structural conversion of neurotoxic amyloid-beta(1-42) oligomers to fibrils. *Nat Struct Mol Biol* **17**:561–7.

Aisenbrey C, Borowik T, Byström R, Bokvist M, Lindström F, Misiak H, Sani M-A, and Gröbner G (2008) How is protein aggregation in amyloidogenic diseases modulated by biological membranes? *Eur Biophys J* **37**:247–55.

Al-Soufi W, Reija B, Felekyan S, Seidel CAM, and Novo M (2008) Dynamics of supramolecular association monitored by fluorescence correlation spectroscopy. *ChemPhysChem* **9**:1819–1827.

Alexandrescu AT (2005) Amyloid accomplices and enforcers. *Protein Sci* **14**:1–12.

Amaro M, Birch DJS, and Rolinski OJ (2011) Beta-amyloid oligomerisation monitored by intrinsic tyrosine fluorescence. *Phys Chem Chem Phys* **13**:6434–6441.

Amaro M, Kubiak-Ossowska K, Birch DJS, and Rolinski OJ (2013) Initial stages of beta-amyloid $A\beta_{1-40}$ and $A\beta_{1-42}$ oligomerization observed using fluorescence decay and molecular dynamics analyses of tyrosine. *Methods Appl Fluoresc* **1**:015006.

Amaro M, Reina F, Hof M, Eggeling C, and Sezgin E (2017) Laurdan and Di-4-ANEPPDHQ probe different properties of the membrane. *J Phys D Appl Phys* **50**:aa5dbc.

Amaro M, Šachl R, Aydogan G, Mikhalyov II, Vácha R, and Hof M (2016) GM1Ganglioside Inhibits β-Amyloid Oligomerization Induced by Sphingomyelin. *Angew Chemie - Int Ed* **55**:9411–9415.

Amaro M, Šachl R, Coutinho A, Prieto M, and Hof M (2014) Biophysical Review Time-Resolved Fluorescence in Lipid Bilayers : Selected Applications and. *Biophys J* **107**:2751–2760.

Amodeo P, Motta A, Strazzullo G, and Morelli MAC (1999) Conformational flexibility in calcitonin: The dynamic properties of human and salmon calcitonin in solution. *J Biomol NMR* **13**:161–174.

Andreotti G, Méndez BL, Amodeo P, Morelli MAC, Nakamuta H, and Motta A (2006) Structural determinants of salmon calcitonin bioactivity: the role of the Leu-based amphipathic alpha-helix. *J Biol Chem* **281**:24193–203.

Andreotti G, and Motta A (2004) Modulating calcitonin fibrillogenesis: an antiparallel alpha-helical dimer inhibits fibrillation of salmon calcitonin. *J Biol Chem* **279**:6364–70.

Andreotti G, Vitale RM, Avidan-Shpalter C, Amodeo P, Gazit E, and Motta A (2011) Converting the highly amyloidogenic human calcitonin into a powerful fibril inhibitor by three-dimensional structure homology with a non-amyloidogenic analogue. *J Biol Chem* **286**:2707–18.

Apostolidou M, Jayasinghe SA, and Langen R (2008) Structure of α-helical membrane-bound human islet amyloid polypeptide and its implications for membrane-mediated misfolding. *J Biol Chem* **283**:17205–17210.

Arbeloa TL, Arbeloa FL, Bartolomé PH, Arbeloa IL, López Arbeloa T, López Arbeloa F, Hernández Bartolomé P, and López Arbeloa I (1992) On the mechanism of radiationless deactivation of rhodamines. *Chem Phys* **160**:123–130.

Arosio P, Knowles TPJ, and Linse S (2015) On the lag phase in amyloid fibril formation. *Phys Chem Chem Phys* **17**:7606–7618.

Arvinte T, Cudd A, and Drake AF (1993) The structure and mechanism of formation of human calcitonin fibrils. *J Biol Chem* **268**:6415–22.

Arvinte T, and Drake AF (1993) Comparative study of human and salmon calcitonin secondary

structure in solutions with low dielectric constants. *J Biol Chem* **268**:6408–14.

Aso Y, Shiraki K, and Takagi M (2007) Systematic Analysis of Aggregates from 38 Kinds of Non Disease-Related Proteins: Identifying the Intrinsic Propensity of Polypeptides to Form Amyloid Fibrils. *Biosci Biotechnol Biochem* **71**:1313–1321.

Avidan-Shpalter C, and Gazit E (2006) The early stages of amyloid formation: biophysical and structural characterization of human calcitonin pre-fibrillar assemblies. *Amyloid* **13**:216–25.

Azria M (1989) *The Calcitonin: Physiology and Pharmacology* (Karger ed).

Azriel R, and Gazit E (2001) Analysis of the minimal amyloid-forming fragment of the islet amyloid polypeptide. An experimental support for the key role of the phenylalanine residue in amyloid formation. *J Biol Chem* **276**:34156–61.

Bacia K, and Schwille P (2007) Practical guidelines for dual-color fluorescence cross-correlation spectroscopy. *Nat Protoc* **2**:2842–2856.

Bader AN, Hoetzl S, Hofman EG, Voortman J, van Bergen en Henegouwen PMP, van Meer G, and Gerritsen HC (2011) Homo-FRET imaging as a tool to quantify protein and lipid clustering. *Chemphyschem* **12**:475–83.

Bader AN, Hofman EG, van Bergen En Henegouwen PMP, and Gerritsen HC (2007) Imaging of protein cluster sizes by means of confocal time-gated fluorescence anisotropy microscopy. *Opt Express* **15**:6934–45.

Bag N, Ali A, Chauhan VS, Wohland T, and Mishra A (2013) Membrane destabilization by monomeric hIAPP observed by imaging fluorescence correlation spectroscopy. *Chem Commun (Camb)* **49**:9155–9157.

Bagatolli LA, and Gratton E (2000) Two photon fluorescence microscopy of coexisting lipid domains in giant unilamellar vesicles of binary phospholipid mixtures. *Biophys J* **78**:290–305.

Balbirnie M, Grothe R, and Eisenberg D (2001) An amyloid-forming peptide from the yeast prion Sup35 reveals a dehydrated beta-sheet structure for amyloid. *Proc Natl Acad Sci* **98**:2375–80.

Barucha-Kraszewska J, Kraszewski S, Jurkiewicz P, Ramseyer C, and Hof M (2010) Numerical studies of the membrane fluorescent dyes dynamics in ground and excited states. *Biochim Biophys Acta - Biomembr* **1798**:1724–1734.

Barwell J, Gingell JJ, Watkins H a., Archbold JK, Poyner DR, and Hay DL (2012) Calcitonin and calcitonin receptor-like receptors: Common themes with family B GPCRs? *Br J Pharmacol* **166**:51–65.

Bauer HH, Aebi U, Haner M, Hermann R, Muller M, and Merkle HP (1995) Architecture and polymorphism of fibrillar supramolecular assemblies produced by in vitro aggregation of human calcitonin.

Bedrood S, Li Y, Isas JM, Hegde BG, Baxa U, Haworth IS, and Langen R (2012) Fibril structure of human islet amyloid polypeptide. *J Biol Chem* **287**:5235–5241.

Bellotti V, and Chiti F (2008) Amyloidogenesis in its biological environment: challenging a fundamental issue in protein misfolding diseases. *Curr Opin Struct Biol* **18**:771–9.

Bergström F, Mikhalyov II, Hägglöf P, Wortmann R, Ny T, and Johansson LB-Å (2002) Dimers of dipyrrometheneboron difluoride (BODIPY) with light spectroscopic applications in chemistry and biology. *J Am Chem Soc* **124**:196–204.

Bergwitz C, Gardella TJ, Flannery MR, Potts JTJ, Kronenberg HM, Goldring SR, and Juppner H (1996) Full Activation of Chimeric Receptors by Hybrids between Parathyroid Hormone and. *J Biol Chem* **271**:26469–26472.

Berthelot K, Cullin C, and Lecomte S (2013) What does make an amyloid toxic: Morphology, structure or interaction with membrane? *Biochimie* **95**:12–19.

Bertolani A, Pizzi A, Pirrie L, Gazzera L, Morra G, Meli M, Colombo G, Genoni A, Cavallo G, Terraneo G, and Metrangolo P (2017) Crystal Structure of the DFNKF Segment of Human Calcitonin Unveils Aromatic Interactions between Phenylalanines. *Chem - A Eur J* **23**:1985.

Betaneli V, and Schwille P (2013) Fluorescence Correlation Spectroscopy to Examine Protein–Lipid Interactions in Membranes, in *Lipid-Protein Interactions: Methods and Protocols* (Nielsen SB, Otzen DE, and Kleinschmidt JH eds) pp 253–278.

Bharadwaj P, Solomon T, Malajczuk CJ, Mancera RL, Howard M, Arrigan DWM, Newsholme P, and Martins RN (2018) Role of the cell membrane interface in modulating production and uptake of Alzheimer's beta amyloid protein. *Biochim Biophys Acta - Biomembr* **1860**:1639–1651.

Bhattacharjee S (2016) DLS and zeta potential - What they are and what they are not? *J Control Release* **235**:337–351.

Bhattacharya M, and Mukhopadhyay S (2015) Studying Protein Misfolding and Aggregation by Fluorescence Spectroscopy, in *Reviews in Fluorescence* (Geddes CD ed) pp 1–27.

Biancalana M, and Koide S (2010) Molecular mechanism of Thioflavin-T binding to amyloid fibrils. *Biochim Biophys Acta* **1804**:1405–12.

Birch DJS (2001) Multiphoton excited fluorescence spectroscopy of biomolecular systems. *Spectrochim Acta - Part A Mol Biomol Spectrosc* **57**:2313–2336.

Blackley HK, Sanders GH, Davies MC, Roberts CJ, Tendler SJ, and Wilkinson MJ (2000) In-situ atomic force microscopy study of beta-amyloid fibrillization. *J Mol Biol* **298**:833–40.

Boassa D, Berlanga ML, Yang MA, Terada M, Hu J, Bushong EA, Hwang M, Masliah E, George JM, and Ellisman MH (2013) Mapping the Subcellular Distribution of -Synuclein in Neurons using Genetically Encoded Probes for Correlated Light and Electron Microscopy: Implications for Parkinson's Disease Pathogenesis. *J Neurosci* **33**:2605–2615.

Boehm K, Guddorf J, Albers A, Kamiyama T, Fetzner S, and Hinz HJ (2008) Thermodynamic analysis of denaturant-induced unfolding of HodC69S protein supports a three-state mechanism. *Biochemistry* **47**:7116–7126.

Bram Y, Frydman-Marom A, Yanai I, Gilead S, Shaltiel-Karyo R, Amdursky N, and Gazit E (2014) Apoptosis induced by islet amyloid polypeptide soluble oligomers is neutralized by diabetes-associated specific antibodies. *Sci Rep* **4**:1–9.

Breimer LH, MacIntyre I, and Zaidi M (1988) Peptides from the calcitonin genes: molecular genetics, structure and function. *Biochem J* **255**:377–90.

Brender JR, Hartman K, Reid KR, Kennedy RT, and Ramamoorthy A (2008) A Single Mutation in the Nonamyloidogenic Region of Islet Amyloid Polypeptide Greatly Reduces Toxicity. *Biochemistry* 12680–12688.

Brender JR, Krishnamoorthy J, Sciacca MFM, Vivekanandan S, D'Urso L, Chen J, La Rosa C, and Ramamoorthy A (2015) Probing the sources of the apparent irreproducibility of amyloid formation: Drastic changes in kinetics and a switch in mechanism due to micellelike oligomer formation at critical concentrations of IAPP. *J Phys Chem B* **119**:2886–2896.

Brender JR, Lee EL, Cavitt MA, Gafni A, Steel DG, and Ramamoorthy A (2008) Amyloid fiber formation and membrane disruption are separate processes localized in two distinct regions of IAPP, the type-2-diabetes-related peptide. *J Am Chem Soc* **130**:6424–6429.

Brender JR, Salamekh S, and Ramamoorthy A (2012) Membrane disruption and early events in the aggregation of the diabetes related peptide IAPP from a molecular perspective. *Acc Chem Res* **45**:454–462.

Brewer HBJ, and Ronan R (1970) Bovine parathyroid hormone: amino acid sequence. *Proc Natl Acad Sci* **67**:1862–1869.

Briggs R, Kennelly SP, and O'Neil D (2016) Drug treatments in Alzheimer's disease. *Clin Med (Northfield Il)* **16**:247–253.

Brown EM (2013) Role of the calcium-sensing receptor in extracellular calcium homeostasis. *Best Pract Res Clin Endocrinol Metab* **27**:333–343.

Buck M (1998) Trifluoroethanol and colleagues: Cosolvents come of age. Recent studies with peptides and proteins. *Q Rev Biophys* **31**:297–355.

Bulseco DA, and Wolf DE (2007) Fluorescence Correlation Spectroscopy: Molecular Complexing in

Solution and in Living Cells. *Methods Cell Biol* **81**:525–559.

Busch DJ, Houser JR, Hayden CC, Sherman MB, Lafer EM, and Stachowiak JC (2015) Intrinsically disordered proteins drive membrane curvature. *Nat Commun* **6**:1–11.

Butterfield SM, and Lashuel H a (2010) Amyloidogenic protein-membrane interactions: mechanistic insight from model systems. *Angew Chem Int Ed Engl* **49**:5628–54.

Byfield PGH, Turner K, Galante L, Gudmundsson T V., and MacIntyre I (1969) The Isolation of Human Calcitonin. *Proc Natl Acad Sci* 13–14.

Caillon L, Hoffmann ARF, Botz A, and Khemtemourian L (2015) Molecular structure, membrane interactions, and toxicity of the islet amyloid polypeptide in type 2 diabetes mellitus. *J Diabetes Res* **2016**:1–13.

Caillon L, Lequin O, and Khemtemourian L (2013) Evaluation of membrane models and their composition for islet amyloid polypeptide-membrane aggregation. *Biochim Biophys Acta* **1828**:2091–8.

Camargo DCR, Korshavn KJ, Jussupow A, Raltchev K, Goricanec D, Fleisch M, Sarkar R, Xue K, Aichler M, Mettenleiter G, Walch AK, Camilloni C, Hagn F, Reif B, and Ramamoorthy A (2017) Stabilization and structural analysis of a membrane-associated hIAPP aggregation intermediate. *Elife* **6**:1–22.

Camargo DCR, Tripsianes K, Buday K, Franko A, Göbl C, Hartlmüller C, Sarkar R, Aichler M, Mettenleiter G, Schulz M, Böddrich A, Erck C, Martens H, Walch AK, Madl T, Wanker EE, Conrad M, De Angelis MH, and Reif B (2017) The redox environment triggers conformational changes and aggregation of hIAPP in Type II Diabetes. *Sci Rep* **7**:1–11.

Cameron WD, Bui C V, Hutchinson A, Loppnau P, Gräslund S, and Rocheleau J V (2016) Apollo-NADP+: A spectrally tunable family of genetically encoded sensors for NADP+. *Nat Methods* **13**:352–358.

Canosa J, Rodrıguez A, and Tojo J (1998) Dynamic Viscosities of (Methyl Acetate or Methanol) with (Ethanol ,1-Propanol ,2-Propanol ,1-Butanol , and 2-Butanol) at 298.15 K. *J Chem Eng Data* **43**:417–421.

Cao P, Abedini A, Wang H, Tu L-H, Zhang X, Schmidt AM, and Raleigh DP (2013) Islet amyloid polypeptide toxicity and membrane interactions. *Proc Natl Acad Sci* **110**:19279–19284.

Cao Z, Huang CC, and Tan W (2006) Nuclease resistance of telomere-like oligonucleotides monitored in live cells by fluorescence anisotropy imaging. *Anal Chem* **78**:1478–1484.

Castanho MARB, Santos NC, and Loura LMS (1997) Separating the turbidity spectra of vesicles from the absorption spectra of membrane probes and other chromophores. *Eur Biophys J* **26**:253–259.

Castro BM, de Almeida RFM, Fedorov A, and Prieto M (2012) The photophysics of a Rhodamine head labeled phospholipid in the identification and characterization of membrane lipid phases. *Chem Phys Lipids* **165**:311–9.

Catalán J (2009) Toward a Generalized Treatment of the Solvent Effect Based on Four Empirical Scales : Dipolarity (SdP, a New Scale), Polarizability (SP), Acidity (SA), and Basicity (SB) of the Medium. *J Phys Chem B* **113**:5951–5960.

Catalán J, and Díaz C (1999) Extending the Solvent Acidiy Scale to Highly Acidic Organic Solvents: The Unique Photophysical Behaviour of 3,6-Diethyltetrazine. *European J Org Chem* **4**:885–891.

Catalán J, Díaz C, López V, Pérez P, De Paz J-LG, and Rodríguez JG (1996) A Generalized Solvent Basicity Scale: The Solvatochromism of 5-Nitroindoline and Its Homomorph 1-Methyl-5-nitroindoline. *Liebigs Ann* **11**:1785–1794.

Catalán J, López V, and Pérez P (1995) Solvent dipolarity/polarizability (SPP) of alcoholic solvents. *Liebigs Ann* **5**:793–795.

Catalán J, López V, Pérez P, Martin-Villamil R, and Rodríguez JG (1995) Progress towards a generalized solvent polarity scale: The solvatochromism of 2-(dimethylamino)-7-nitrofluorene and its homomorph 2-fluoro-7-nitrofluorene. *Liebigs Ann* **2**:241–252.

Cebecauer M, Hof M, and Amaro M (2017) Impact of GM1 on Membrane-Mediated

Aggregation/Oligomerization of β-Amyloid: Unifying View. *Biophys J* **113**:1194–1199.

Chan FTS, Kaminski CF, and Schierle GSK (2011) HomoFRET fluorescence anisotropy imaging as a tool to study molecular self-assembly in live cells. *ChemPhysChem* **12**:500–509.

Chang CL, Roh J, and Hsu SYT (2004) Intermedin, a novel calcitonin family peptide that exists in teleosts as well as in mammals: A comparison with other calcitonin/intermedin family peptides in vertebrates. *Peptides* **25**:1633–1642.

Chen H, Ahsan SS, Santiago-Berrios MB, Abruña HD, and Webb WW (2010) Mechanisms of quenching of Alexa fluorophores by natural amino acids. *J Am Chem Soc* **132**:7244–5.

Chen H, Rhoades E, Butler JS, Loh SN, and Webb WW (2007) Dynamics of equilibrium structural fluctuations of apomyoglobin measured by fluorescence correlation spectroscopy. *Proc Natl Acad Sci* **104**:10459–64.

Chesnut CH, Azria M, Silverman S, Engelhardt M, Olson M, and Mindeholm L (2008) Salmon calcitonin: A review of current and future therapeutic indications. *Osteoporos Int* **19**:479–491.

Chimon S, Shaibat MA, Jones CR, Calero DC, Aizezi B, and Ishii Y (2007) Evidence of fibril-like β-sheet structures in a neurotoxic amyloid intermediate of Alzheimer's β-amyloid. *Nat Struct Mol Biol* **14**:1157–64.

Chiti F, and Dobson CM (2009) Amyloid formation by globular proteins under native conditions. *Nat Chem Biol* **5**:15–22.

Chiti F, and Dobson CM (2017) Protein Misfolding, Amyloid Formation, and Human Disease: A Summary of Progress Over the Last Decade. *Annu Rev Biochem* **86**:27–68.

Chiti F, and Dobson CM (2006) Protein misfolding, functional amyloid, and human disease. *Annu Rev Biochem* **75**:333–66.

Chiti F, Webster P, Taddei N, Clark A, Stefani M, Ramponi G, and Dobson CM (1999) Designing conditions for in vitro formation of amyloid protofilaments and fibrils. *Proc Natl Acad Sci* **96**:3590–3594.

Cleary JP, Walsh DM, Hofmeister JJ, Shankar GM, Kuskowski MA, Selkoe DJ, and Ashe KH (2005) Natural oligomers of the amyloid-beta protein specifically disrupt cognitive function. *Nat Neurosci* **8**:79–84.

Conway KA, Lee SJ, Rochet JC, Ding TT, Williamson RE, and Lansbury PT (2000) Acceleration of oligomerization, not fibrillization, is a shared property of both alpha-synuclein mutations linked to early-onset Parkinson's disease: implications for pathogenesis and therapy. *Proc Natl Acad Sci U S A* **97**:571–6.

Cope SM, Shinde S, Best RB, Ghirlanda G, and Vaiana SM (2013) Cyclic N-terminal loop of amylin forms non amyloid fibers. *Biophys J* **105**:1661–9.

Copp DH, and Cheney B (1962) Calcitonin - a hormone from the Para-thyroid which Lowers the Calcium-level of the Blood. *Nature* **193**:381.

Cort JR, Liu Z, Lee GM, Huggins KNL, Janes S, Prickett K, and Andersen NH (2009) Solution state structures of human pancreatic amylin and pramlintide. *Protein Eng Des Sel* **22**:497–513.

Creighton TE (1999) *Encyclopedia of molecular biology* (Creighton TE ed).

Culik RM, Abaskharon RM, Pazos IM, and Gai F (2014) Experimental validation of the role of trifluoroethanol as a nanocrowder. *J Phys Chem B* **118**:11455–11461.

Czeslik C, Royer C, Hazlett T, and Mantulin W (2003) Reorientational dynamics of enzymes adsorbed on quartz: a temperature-dependent time-resolved TIRF anisotropy study. *Biophys J* **84**:2533–41.

Danielsson J, Jarvet J, Damberg P, and Gräaslund A (2002) Translational diffusion measured by PFG-NMR on full length and fragments of the Alzheimer Aβ(1-40) peptide. Determination of hydrodynamic radii of random coil peptides of varying length. *Magn Reson Chem* **40**:S89–S97.

Davey RA, and Findlay DM (2013) Calcitonin: Physiology or fantasy? *J Bone Miner Res* **28**:973–979.

Demchenko AP, Duportail G, Oncul S, Klymchenko AS, and Mely Y (2012) Introduction to

Fluorescence Probing of Biological Membranes, in *Methods in Membrane Lipids* (Owen DM ed) pp 19–44.

Devauges V, Marquer C, Lécart S, Cossec J-C, Potier M-C, Fort E, Suhling K, and Lévêque-Fort S (2012) Homodimerization of Amyloid Precursor Protein at the Plasma Membrane: A homoFRET Study by Time-Resolved Fluorescence Anisotropy Imaging. *PLoS One* **7**:e44434.

Devauges V, Matthews DR, Aluko J, Nedbal J, Levitt JA, Poland SP, Coban O, Weitsman G, Monypenny J, Ng T, and Ameer-Beg SM (2014) Steady-state acceptor fluorescence anisotropy imaging under evanescent excitation for visualisation of FRET at the plasma membrane. *PLoS One* **9**.

Díaz MD, Fioroni M, Burger K, and Berger S (2002) Evidence of complete hydrophobic coating of bombesin by trifluoroethanol in aqueous solution: An NMR spectroscopic and molecular dynamics study. *Chem - A Eur J* **8**:1663–1669.

Diociaiuti M, Gaudiano MC, and Malchiodi-Albedi F (2011) The slowly aggregating salmon Calcitonin: a useful tool for the study of the amyloid oligomers structure and activity. *Int J Mol Sci* **12**:9277–95.

Diociaiuti M, Polzi LZ, Valvo L, Malchiodi-Albedi F, Bombelli C, and Gaudiano MC (2006) Calcitonin forms oligomeric pore-like structures in lipid membranes. *Biophys J* **91**:2275–81.

Dobson CM (1999) Protein misfolding, evolution and disease. *Trends Biochem Sci* **24**:329–32.

Domanov YA, and Kinnunen PKJ (2006) Antimicrobial peptides temporins B and L induce formation of tubular lipid protrusions from supported phospholipid bilayers. *Biophys J* **91**:4427–4439.

Domanov YA, and Kinnunen PKJ (2008) Islet Amyloid Polypeptide Forms Rigid Lipid–Protein Amyloid Fibrils on Supported Phospholipid Bilayers. *J Mol Biol* **376**:42–54.

Dubach JM, Vinegoni C, Mazitschek R, Fumene Feruglio P, Cameron LA, and Weissleder R (2014) In vivo imaging of specific drug-target binding at subcellular resolution. *Nat Commun* **5**:1–9.

Dumoulin M, Canet D, Last AM, Pardon E, Archer DB, Muyldermans S, Wyns L, Matagne A, Robinson C V, Redfield C, and Dobson CM (2005) Reduced global cooperativity is a common feature underlying the amyloidogenicity of pathogenic lysozyme mutations. *J Mol Biol* **346**:773–88.

Dutt GB, and Ghanty TK (2003) Rotational dynamics of nondipolar probes in ethanols: How does the strength of the solute-solvent hydrogen bond impede molecular rotation? *J Chem Phys* **119**:4768–4774.

Eichenberger AP, Van Gunsteren WF, and Smith LJ (2013) Structure of hen egg-white lysozyme solvated in TFE/water: A molecular dynamics simulation study based on NMR data. *J Biomol NMR* **55**:339–353.

Einstein A (1905) Über die von der molekularkinetischen Theorie der Wärme geforderte Bewegung von in ruhenden Flüssigkeiten suspendierten Teilchen. *Ann Phys* **322**:549–560.

Engel MFM, Khemtemourian L, Kleijer CC, Meeldijk HJD, Jacobs J, Verkleij AJ, de Kruijff B, Killian JA, and Höppener JWM (2008) Membrane damage by human islet amyloid polypeptide through fibril growth at the membrane. *Proc Natl Acad Sci* **105**:6033–8.

Engel MFM, Yigittop H, Elgersma RC, Rijkers DTS, Liskamp RMJ, de Kruijff B, Höppener JWM, and Killian JA (2006) Islet amyloid polypeptide inserts into phospholipid monolayers as monomer. *J Mol Biol* **356**:783–9.

Epand RF, Orlowski RC, and Epand RM (2004) The biological potency of a series of analogues of human calcitonin correlates with their interactions with phospholipids. *Biopolymers* **76**:258–65.

Epand RM, Epand RF, and Orlowski RC (1988) Biologically active calcitonin analogs which have minimal interactions with phospholipids. *Biochem Biophys Res Commun* **152**:203–207.

Epand RM, Epand RF, and Orlowski RC (1985) Presence of an amphipathic helical segment and its relationship to biological potency of calcitonin analogs. *Int J Pept Protein Res* **25**:105–111.

Epand RM, Epand RF, Orlowski RC, Schlueter RJ, Boni LT, and Hui SW (1983) Amphipathic helix and its relationship to the interaction of calcitonin with phospholipids. *Biochemistry* **22**:5074–84.

Epand RM, Epand RF, Orlowski RC, Seyler JK, and Colescott RL (1986) Conformational flexibility and biological activity of salmon calcitonin. *Biochemistry* **25**:1964–1968.

Exley C, House E, Collingwood JF, Davidson MR, Cannon D, and Donald AM (2010) Spherulites of amyloid-beta42 in vitro and in Alzheimer's disease. *J Alzheimers Dis* **20**:1159–65.

Farese R V, Dimarco PE, Barnes DE, Sabir MA, Larson RE, Davis JS, and Morrison AD (1986) Rapid Glucose-Dependent Increases in Phosphatidic-Acid and Phosphoinositides in Rat Pancreatic-Islets. *Endocrinology* **118**:1498–1503.

Fattore A Del, Teti A, and Rucci N (2008) Osteoclast receptors and signaling. *Arch Biochem Biophys* **473**:147–160.

Fee RS, and Maroncelli M (1994) Estimating the Time-Zero Spectrum in Time- Resolved Emission Measurements of Solvation Dynamics. *Chem Phys* **183**:235.

Fernandes F, Coutinho A, Prieto M, and Loura LMS (2015) Electrostatically driven lipid-protein interaction: Answers from FRET. *Biochim Biophys Acta - Biomembr* **1848**:1837–1848.

Feyen JHM, Gamse R, Cardinaux F, Bruns C, Azria M, and Trechsel U (1992) N-terminal truncation of salmon calcitonin leads to calcitonin antagonists: Structure activity relationship of N-terminally truncated salmon calcitonin fragments in vitro and in vivo. *Biochem Biophys Res Commun* **187**:8–13.

Findlay DM, Michelangeli VP, Martin TJ, Orlowski RC, and Seyler JK (1985) Conformational requirements for activity of salmon calcitonin. *Endocrinology* **117**:801–805.

Fioroni M, Diaz MD, Burger K, and Berger S (2002) Solvation phenomena of a tetrapeptide in water/trifluoroethanol and water/ethanol mixtures: A diffusion NMR, intermolecular NOE, and molecular dynamics study. *J Am Chem Soc* **124**:7737–7744.

Fitzpatrick AWP, Debelouchina GT, Bayro MJ, Clare DK, Caporini MA, Bajaj VS, Jaroniec CP, Wang L, Ladizhansky V, Müller SA, MacPhee CE, Waudby CA, Mott HR, Simone A De, Knowles TPJ, Saibil HR, Vendruscolo M, Orlova E V, Griffin RG, and Dobson CM (2013) Atomic structure and hierarchical assembly of a cross-β amyloid fibril - Supplementary Info. *Proc Natl Acad Sci* **5590**:5468–5473.

Foderà V, Cataldo S, Librizzi F, Pignataro B, Spiccia P, and Leone M (2009) Self-organization pathways and spatial heterogeneity in insulin amyloid fibril formation. *J Phys Chem B* **113**:10830–7.

Fowler SB, Poon S, Muff R, Chiti F, Dobson CM, and Zurdo J (2005) Rational design of aggregation-resistant bioactive peptides: reengineering human calcitonin. *Proc Natl Acad Sci* **102**:10105–10.

Fuertes G, García-Sáez AJ, Esteban-Martín S, Giménez D, Sánchez-Muñoz OL, Schwille P, and Salgado J (2010) Pores formed by Baxα5 relax to a smaller size and keep at equilibrium. *Biophys J* **99**:2917–25.

Galdiero S, Falanga A, Cantisani M, Vitiello M, Morelli G, and Galdiero M (2013) Peptide-lipid interactions: Experiments and applications. *Int J Mol Sci* **14**:18758–18789.

Garai K, Sureka R, and Maiti S (2007) Detecting amyloid-beta aggregation with fiber-based fluorescence correlation spectroscopy. *Biophys J* **92**:L55–L57.

García-Sáez AJ, and Schwille P (2010) Surface analysis of membrane dynamics. *Biochim Biophys Acta* **1798**:766–76.

Gast K, Siemer A, Zirwer D, and Damaschun G (2001) Fluoroalcohol-induced structural changes of proteins: Some aspects of cosolvent-protein interactions. *Eur Biophys J* **30**:273–283.

Gaudiano MC, Colone M, Bombelli C, Chistolini P, Valvo L, and Diociaiuti M (2005) Early stages of salmon calcitonin aggregation: effect induced by ageing and oxidation processes in water and in the presence of model membranes. *Biochim Biophys Acta* **1750**:134–145.

Gazit E (2005) Mechanisms of amyloid fibril self-assembly and inhibition: Model short peptides as a key research tool. *FEBS J* **272**:5971–5978.

Gehne S, Sydow K, Dathe M, and Kumke MU (2013) Characterization of cell-penetrating lipopeptide micelles by spectroscopic methods. *J Phys Chem B* **117**:14215–14225.

Gellermann GP, Appel TR, Tannert A, Radestock A, Hortschansky P, Schroeckh V, Leisner C, Lütkepohl T, Shtrasburg S, Röcken C, Pras M, Linke RP, Diekmann S, and Fändrich M (2005) Raft lipids as common components of human extracellular amyloid fibrils. *Proc Natl Acad Sci* **102**:6297–302.

Gendron P-O, Avaltroni F, and Wilkinson KJ (2008) Diffusion coefficients of several rhodamine derivatives as determined by pulsed field gradient-nuclear magnetic resonance and fluorescence correlation spectroscopy. *J Fluoresc* **18**:1093–1101.

Gente G, and Mesa C La (2000) Water—Trifluoroethanol Mixtures: Some Physicochemical Properties. *J Solution Chem* **29**:1159–1172.

Gerig JT (2015) Further Efforts Toward a Molecular Dynamics Force Field for Simulations of Peptides in 40% Trifluoroethanol-Water. *J Phys Chem B* **119**:5163–5175.

Ghosh S, Saha S, Goswami D, Bilgrami S, and Mayor S (2012) *Dynamic imaging of homo-FRET in live cells by fluorescence anisotropy microscopy*, 1st ed.

Giehm L, Lorenzen N, and Otzen DE (2011) Assays for α-synuclein aggregation. *Methods* **53**:295–305.

Giehm L, and Otzen DE (2010) Strategies to increase the reproducibility of protein fibrillization in plate reader assays. *Anal Biochem* **400**:270–281.

Gilani AG, Paktinat N, and Moghadam M (2011) Relative permittivity data of binary mixtures containing 2-butanol, 2-butanone, and cyclohexane. *J Chem Thermodyn* **43**:569–575.

Goldsbury C, Goldie K, Pellaud J, Seelig J, Frey P, Müller SA, Kistler J, Cooper GJS, and Aebi U (2000) Amyloid fibril formation from full-length and fragments of amylin. *J Struct Biol* **130**:352–362.

Goldsbury CS, Cooper GJS, Goldie KN, Müller SA, Saafi EL, Gruijters WTM, Misur MP, Engel A, Aebi U, and Kistler J (1997) Polymorphic fibrillar assembly of human amylin. *J Struct Biol* **119**:17–27.

Goldschmidt L, Teng PK, Riek R, and Eisenberg D (2010) Identifying the amylome, proteins capable of forming amyloid-like fibrils. *Proc Natl Acad Sci* **107**:3487–3492.

Gorbenko GP, and Kinnunen PKJ (2006) The role of lipid-protein interactions in amyloid-type protein fibril formation. *Chem Phys Lipids* **141**:72–82.

Green FR, Lynch B, and Kaiser ET (1987) Biological and physical properties of a model calcitonin containing a glutamate residue interrupting the hydrophobic face of the idealized amphiphilic alpha-helical region. *Proc Natl Acad Sci U S A* **84**:8340–8344.

Green JD, Kreplak L, Goldsbury C, Li Blatter X, Stolz M, Cooper GJS, Seelig A, Kistler J, and Aebi U (2004) Atomic force microscopy reveals defects within mica supported lipid bilayers induced by the amyloidogenic human amylin peptide. *J Mol Biol* **342**:877–887.

Greenfield NJ (2007a) Determination of the folding of proteins as a function of denaturants, osmolytes or ligands using circular dichroism. *Nat Protoc* **1**:2733–2741.

Greenfield NJ (2007b) Using circular dichroism spectra to estimate protein secondary structure. *Nat Protoc* **1**:2876–2890.

Groenning M (2010) Binding mode of Thioflavin T and other molecular probes in the context of amyloid fibrils-current status. *J Chem Biol* **3**:1–18.

Hamada D, and Dobson CM (2002) A kinetic study of beta-lactoglobulin amyloid fibril formation promoted by urea. *Protein Sci* **11**:2417–26.

Hammer ND, Wang X, McGuffie BA, and Chapman MR (2008) Amyloids: friend or foe? *J Alzheimer's Dis* **13**:407–419.

Harding SE (1997) The intrinsic viscosity of biological macromolecules. Progress in measurement, interpretation and application to structure in dilute solution. *Prog Biophys Mol Biol* **68**:207–262.

Harris FM, Best KB, and Bell JD (2002) Use of laurdan fluorescence intensity and polarization to distinguish between changes in membrane fluidity and phospholipid order. *Biochim Biophys Acta - Biomembr* **1565**:123–128.

Harrison RS, Sharpe PC, and Fairlie DP (2007) Amyloid peptides and proteins in review. *Rev Physiol Biochem Pharmacol* **159**:1–77.

Hashimoto Y, Toma K, Nishikido J, Yamamoto K, Haneda K, Inazu T, Valentine KG, and Opella SJ (1999) Effects of glycosylation on the structure and dynamics of eel calcitonin in micelles and lipid bilayers determined by nuclear magnetic resonance spectroscopy. *Biochemistry* **38**:8377–8384.

Haspel N, Zanuy D, Ma B, Wolfson H, and Nussinov R (2005) A comparative study of amyloid fibril formation by residues 15-19 of the human calcitonin hormone: a single beta-sheet model with a small hydrophobic core. *J Mol Biol* **345**:1213–27.

Haugland RP (2005) *The Handbook. A Guide to Fluorescent Probes and Labeling Technologies*, 10th ed.

Haustein E, and Schwille P (2007) Fluorescence correlation spectroscopy: novel variations of an established technique. *Annu Rev Biophys Biomol Struct* **36**:151–69.

Hay DL (2017) Amylin. *Headache* **57**:89–96.

Hebda JA, and Miranker AD (2009) The interplay of catalysis and toxicity by amyloid intermediates on lipid bilayers: insights from type II diabetes. *Annu Rev Biophys* **38**:125–52.

Hedde PN, Ranjit S, and Gratton E (2015) 3D fluorescence anisotropy imaging using selective plane illumination microscopy. *Opt Express* **23**:22308.

Hell SW (2003) Toward fluorescence nanoscopy. *Nat Biotechnol* **21**:1347–1355.

Hess ST, and Webb WW (2002) Focal volume optics and experimental artifacts in confocal fluorescence correlation spectroscopy. *Biophys J* **83**:2300–2317.

Hiddinga HJ, and Eberhardt NL (1999) Intracellular amyloidogenesis by human islet amyloid polypeptide induces apoptosis in COS-1 cells. *Am J Pathol* **154**:1077–1088.

Hilton JM, Dowton M, Houssami S, and Sexton PM (2000) Identification of key components in the irreversibility of salmon calcitonin binding to calcitonin receptors. *J Endocrinol* **166**:213–226.

Hirsch PF, and Baruch H (2003) Is calcitonin an important physiological substance? *Endocrine* **21**:201–208.

Hong DP, Hoshino M, Kuboi R, and Goto Y (1999) Clustering of fluorine-substituted alcohols as a factor responsible for their marked effects on proteins and peptides. *J Am Chem Soc* **121**:8427–8433.

Honig S, Rajapakse CS, and Chang G (2013) Current treatment approaches to osteoporosis - 2013. *Bull Hosp Jt Dis* **71**:184–8.

Houssami S, Findlay DM, Brady CL, Martin TJ, Epand RM, Moore EE, Murayama E, Tamura T, Orlowski RC, and Sexton PM (1995) Divergent structural requirements exist for calcitonin receptor binding specificity and adenylate cyclase activation. *Mol Pharmacol* **47**:798–809.

Huang R, Vivekanandan S, Brender JR, Abe Y, Naito A, and Ramamoorthy A (2012) NMR characterization of monomeric and oligomeric conformations of human calcitonin and its interaction with EGCG. *J Mol Biol* **416**:108–120.

Hull RL, Westermark GT, Westermark P, and Kahn SE (2004) Islet amyloid: A critical entity in the pathogenesis of type 2 diabetes. *J Clin Endocrinol Metab* **89**:3629–3643.

Hutton JC (1982) The internal pH and membrane potential of the insulin-secretory granule. *Biochem J* **204**:171–8.

Iconomidou V a, Leontis A, Hoenger A, and Hamodrakas SJ (2013) Identification of a novel “aggregation-prone’/’amyloidogenic determinant” peptide in the sequence of the highly amyloidogenic human calcitonin. *FEBS Lett* **587**:569–74.

Inoue S (2008) In situ Abeta pores in AD brain are cylindrical assembly of Abeta protofilaments. *Amyloid* **15**:223–233.

Itoh-Watanabe H, Kamihira-Ishijima M, Kawamura I, Kondoh M, Nakakoshi M, Sato M, and Naito A (2013) Characterization of the spherical intermediates and fibril formation of hCT in HEPES solution using solid-state 13C-NMR and transmission electron microscopy. *Phys Chem Chem Phys*

15:16956–64.

Jacobs JW, Lund PK, Potts JT, Bell NH, and Habener JF (1981) Procalcitonin is a glycoprotein. *J Biol Chem* **256**:2803–2807.

Jaikaran ETAS, and Clark A (2001) Islet amyloid and type 2 diabetes: from molecular misfolding to islet pathophysiology. *Biochim Biophys Acta* **1537**:179–203.

Jaikaran ETAS, Higham CE, Serpell LC, Zurdo J, Gross M, Clark A, and Fraser PE (2001) Identification of a novel human islet amyloid polypeptide β-sheet domain and factors influencing fibrillogenesis. *J Mol Biol* **308**:515–525.

Jameson DM, and Ross JA (2010) Fluorescence polarization/anisotropy in diagnostics and imaging. *Chem Rev* **110**:2685–708.

Janson J, Ashley RH, Harrison D, McIntyre S, and Butler PC (1999) The mechanism of islet amyloid polypeptide toxicity is membrane disruption by intermediate-sized toxic amyloid particles. *Diabetes* **48**:491–498.

Javanainen M, Melcrová A, Magarkar A, Jurkiewicz P, Hof M, Jungwirth P, and Martinez-Seara H (2017) Two cations, two mechanisms: Interactions of sodium and calcium with zwitterionic lipid membranes. *Chem Commun* **53**:5380–5383.

Jayasinghe SA, and Langen R (2005) Lipid membranes modulate the structure of islet amyloid polypeptide. *Biochemistry* **44**:12113–9.

Jayasinghe SA, and Langen R (2007) Membrane interaction of islet amyloid polypeptide. *Biochim Biophys Acta* **1768**:2002–9.

Jesenska A, Sýkora J, Olżyńska A, Brezovský J, Zdráhal Z, Damborský J, and Hof M (2009) Nanosecond time-dependent stokes shift at the tunnel mouth of haloalkane dehalogenases. *J Am Chem Soc* **131**:494–501.

Jeworrek C, Hollmann O, Steitz R, Winter R, and Czeslik C (2009) Interaction of IAPP and insulin with model interfaces studied using neutron reflectometry. *Biophys J* **96**:1115–1123.

Jha A, Udgaonkar JB, and Krishnamoorthy G (2009) Characterization of the Heterogeneity and Specificity of Interpolypeptide Interactions in Amyloid Protofibrils by Measurement of Site-Specific Fluorescence Anisotropy Decay Kinetics. *J Mol Biol* **393**:735–752.

Jha S, Sellin D, Seidel R, and Winter R (2009) Amyloidogenic Propensities and Conformational Properties of ProIAPP and IAPP in the Presence of Lipid Bilayer Membranes. *J Mol Biol* **389**:907–920.

Johansson LB-Å (1990) Limiting fluorescence anisotropies of perylene and xanthene derivatives. *J Chem Soc Faraday Trans* **86**:2103–2107.

Jungbauer LM, Yu C, Laxton KJ, and LaDu MJ (2009) Preparation of fluorescently-labeled amyloid-beta peptide assemblies: the effect of fluorophore conjugation on structure and function. *J Mol Recognit* **22**:403–13.

Junghans A, Watkins EB, Majewski J, Miranker AD, and Stroe I (2016) Influence of the Human and Rat Islet Amyloid Polypeptides on Structure of Phospholipid Bilayers: Neutron Reflectometry and Fluorescence Microscopy Studies. *Langmuir* **32**:4382–4391.

Jurkiewicz P, Cwiklik L, Jungwirth P, and Hof M (2012) Lipid hydration and mobility: An interplay between fluorescence solvent relaxation experiments and molecular dynamics simulations. *Biochimie* **94**:26–32.

Jurkiewicz P, Cwiklik L, Vojtíšková A, Jungwirth P, and Hof M (2012) Structure, dynamics, and hydration of POPC/POPS bilayers suspended in NaCl, KCl, and CsCl solutions. *Biochim Biophys Acta - Biomembr* **1818**:609–616.

Jurkiewicz P, Sýkora J, Olżyńska A, Humpolíčková J, and Hof M (2005) Solvent relaxation in phospholipid bilayers: Principles and recent applications. *J Fluoresc* **15**:883–894.

Kajava A V, Aebi U, and Steven AC (2005) The parallel superpleated beta-structure as a model for amyloid fibrils of human amylin. *J Mol Biol* **348**:247–252.

Kakio A, Nishimoto S, Kozutsumi Y, and Matsuzaki K (2003) Formation of a membrane-active form of amyloid beta-protein in raft-like model membranes. *Biochem Biophys Res Commun* **303**:514–8.

Kamgar-Parsi K, Hong L, Naito A, Brooks CL, and Ramamoorthy A (2017) Growth-incompetent monomers of human calcitonin lead to a noncanonical direct relationship between peptide concentration and aggregation lag time. *J Biol Chem* **292**:14963–14976.

Kamihira-Ishijima M, Naito A, Tuzi S, Nosaka AY, and Saitô H (2000) Conformational transitions and fibrillation mechanism of human calcitonin as studied by high-resolution solid-state 13C NMR. *Protein Sci* **9**:867–77.

Kamihira-Ishijima M, Oshiro Y, Tuzi S, Nosaka AY, Saitô H, and Naito A (2003) Effect of electrostatic interaction on fibril formation of human calcitonin as studied by high resolution solid state 13C NMR. *J Biol Chem* **278**:2859–65.

Kanaori K, and Nosaka AY (1996) Characterization of Human Calcitonin Fibrillation in Aqueous Urea Solution By H-1 Nmr Spectroscopy. *Biochemistry* **35**:12671–12676.

Kanaori K, and Nosaka AY (1995) Study of Human Calcitonin Fibrillation by Proton Nuclear Magnetic Resonance Spectroscopy. *Biochemistry* **34**:12138–12143.

Kapurniotu A (2004) Contribution of conformationally constrained calcitonin (Ct) analogs to the understanding of the structural and conformational requirements of calcitonin bioactivity and to the design of potent agonists. *Curr Med Chem* **11**:2845–2865.

Kazantzis A, Waldner M, Taylor JW, and Kapurniotu A (2002) Conformationally constrained human calcitonin (hCt) analogues reveal a critical role of sequence 17-21 for the oligomerization state and bioactivity of hCt. *Eur J Biochem* **269**:780–791.

Ke PC, Sani M-A, Ding F, Kakinen A, Javed I, Separovic F, Davis TP, and Mezzenga R (2017) Implications of peptide assemblies in amyloid diseases. *Chem Soc Rev* **46**:6492–6531.

Kegulian NC, Sankhagowit S, Apostolidou M, Jayasinghe SA, Malmstadt N, Butler PC, and Langen R (2015) Membrane curvature-sensing and curvature-inducing activity of islet amyloid polypeptide and its implications for membrane disruption. *J Biol Chem* **290**:25782–25793.

Kelly JW (1998) The alternative conformations of amyloidogenic proteins and their multi-step assembly pathways. *Curr Opin Struct Biol* **8**:101–6.

Kelly SM, Jess TJ, and Price NC (2005) How to study proteins by circular dichroism. *Biochim Biophys Acta* **1751**:119–39.

Kelly SM, and Price NC (2000) The Use of Circular Dichroism in the Investigation of Protein Structure and Function. *Curr Protein Pept Sci* **1**:349–384.

Khemtémourian L, Doménech E, Doux JPF, Koorengevel MC, and Killian JA (2011) Low pH Acts as Inhibitor of Membrane Damage Induced by Human Islet Amyloid Polypeptide. *J Am Chem Soc* **133**:15598–15604.

Khurana R, Agarwal A, Bajpai VK, Verma N, Sharma AK, Gupta RP, and Madhusudan KP (2004) Unraveling the Amyloid Associated with Human Medullary Thyroid Carcinoma. *Endocrinology* **145**:5465–5470.

Kim S Il, Yi JS, and Ko YG (2006) Amyloid β oligomerization is induced by brain lipid rafts. *J Cell Biochem* **99**:878–889.

Kinnunen PKJ (2009) Amyloid Formation on Lipid Membrane Surfaces. *Open Biol J* **2**:163–175.

Kinnunen PKJ, Domanov YA, Mattila JP, and Varis T (2015) Formation of lipid/peptide tubules by IAPP and temporin B on supported lipidmembranes. *Soft Matter* **11**:9188–9200.

Kinosita K, Kawato S, and Ikegami a (1977) A theory of fluorescence polarization decay in membranes. *Biophys J* **20**:289–305.

Klein TR, Kirsch D, Kaufmann R, and Riesner D (1998) Prion rods contain small amounts of two host sphingolipids as revealed by thin-layer chromatography and mass spectrometry. *Biol Chem* **379**:655–66.

Klonis N, Clayton AHA, Voss EW, and Sawyer WH (1998) Spectral properties of fluorescein in

solvent-water mixtures: Applications as a probe of hydrogen bonding environments in biological systems. *Photochem Photobiol* **67**:500–510.

Knight JD, Hebda JA, and Miranker AD (2006) Conserved and cooperative assemble of membrane-bound alfa-helical states of islet amyloid polypeptide. *Biochemistry* **45**:9496–9508.

Knight JD, and Miranker AD (2004) Phospholipid catalysis of diabetic amyloid assembly. *J Mol Biol* **341**:1175–1187.

Knight JD, Williamson JA, and Miranker AD (2008) Interaction of membrane-bound islet amyloid polypeptide with soluble and crystalline insulin. *Protein Sci* **17**:1850–1856.

Knowles TPJ, Vendruscolo M, and Dobson CM (2014) The amyloid state and its association with protein misfolding diseases. *Nat Rev Mol Cell Biol* **15**:384–396.

Knowles TPJ, Waudby CA, Devlin GL, Cohen SIA, Aguzzi A, Vendruscolo M, Terentjev EM, Welland ME, and Dobson CM (2009) An Analytical Solution to the Kinetics of Breakable Filament Assembly The growth kinetics of amyloid fibrils and related self-assembly phenomena are revealed by analytical theory. *Science (80-)* **326**:1533–1537.

Koshioka M, Sasaki K, and Masuhara H (1995) Time-Dependent Fluorescence Depolarization Analysis in Three-Dimensional Microspectroscopy. *Appl Spectrosc* **49**:224–228.

Krebs MRH, Macphee CE, Miller AF, Dunlop IE, Dobson CM, and Donald AM (2004) The formation of spherulites by amyloid fibrils of bovine insulin. *Proc Natl Acad Sci* **101**:14420–4.

Kumar S, Singh AK, Krishnamoorthy G, and Swaminathan R (2008) Thioflavin T displays enhanced fluorescence selectively inside anionic micelles and mammalian cells. *J Fluoresc* **18**:1199–205.

Kurganov B, Doh M, and Arispe N (2004) Aggregation of liposomes induced by the toxic peptides Alzheimer's Abetas, human amylin and prion (106-126): facilitation by membrane-bound GM1 ganglioside. *Peptides* **25**:217–32.

Kyle RA (2001) Historical Review - Amyloidosis: a convoluted story. *Br J Haematol* **114**:529–538.

Lakowicz JR (2006) *Principles of Fluorescence Spectroscopy, 3rd Edition. Springer Science, New York.*

Latypov RF, Harvey TS, Liu D, Bondarenko P V, Kohno T, Fachini RA, Rosenfeld RD, Ketchem RR, Brems DN, and Raibekas AA (2007) Biophysical Characterization of Structural Properties and Folding of Interleukin-1 Receptor Antagonist. *J Mol Biol* **368**:1187–1201.

Lee R van der, Buljan M, Lang B, Weatheritt RJ, Daughdrill GW, Dunker AK, Fuxreiter M, Gough J, Gsponer J, Jones DT, Kim PM, Kriwacki RW, Oldfield CJ, Pappu R V, Tompa P, Uversky VN, Wright PE, and Babu MM (2014) Classification of intrinsically disordered regions and proteins. *Chem Rev* **114**:6589–6631.

Leung BO, and Chou KC (2011) Review of super - Resolution fluorescence microscopy for biology. *Appl Spectrosc* **65**:967–980.

Levitt JA, Matthews DR, Ameer-Beg SM, and Suhling K (2009) Fluorescence lifetime and polarization-resolved imaging in cell biology. *Curr Opin Biotechnol* **20**:28–36.

Li W, Wang Y, Shao H, He Y, and Ma H (2007) Probing Rotation Dynamics of Biomolecules Using Polarization Based Fluorescence Microscopy. *Microsc Res Tech* **70**:390–395.

Li X, Jiang G, Wu D, Wang X, and Zeng B (2009) Construction of a Recombinant Eukaryotic Expression Plasmid Containing Human Calcitonin Gene and Its Expression in NIH3T3 Cells. *J Biomed Biotechnol* **2009**:1–7.

Li Y, Wang L, Lu T, Wei Y, and Li F (2016) The effects of chondroitin sulfate and serum albumin on the fibrillation of human islet amyloid polypeptide at phospholipid membranes. *Phys Chem Chem Phys* **18**:12000–12008.

Lidke KA, Rieger B, Lidke DS, and Jovin TM (2005) The role of photon statistics in fluorescence anisotropy imaging. *IEEE Trans Image Process* **14**:1237–1245.

Lin H, Bhatia R, and Lal R (2001) Amyloid β protein forms ion channels: implications for Alzheimer's disease pathophysiology. *FASEB J* **15**:2433–2444.

Lipari G, and Szabo A (1980) Effect of librational motion on fluorescence depolarization and nuclear magnetic resonance relaxation in macromolecules and membranes. *Biophys J* **30**:489–506.

Lomakin A, Teplow DB, and Benedek GB (2005) Quasielastic Light Scattering for Protein Assembly Studies, in *Methods in Molecular Biology* pp 153–174.

Loman A (2010) Molecular Sizing using Fluorescence Correlation Spectroscopy. Dissertation Division of Mathematics and Natural Sciences, Georg-August-Universität Göttingen.

Lopes DHJ, Chapeaurouge A, Manderson GA, Johansson JS, and Ferreira ST (2004) Redesigning the Folding Energetics of a Model Three-helix Bundle Protein by Site-directed Mutagenesis. *J Biol Chem* **279**:10991–10996.

Lopez D, and Koch G (2017) Exploring functional membrane microdomains in bacteria: an overview. *Curr Opin Microbiol* **36**:76–84.

Lorber B, Fischer F, Bailly M, Roy H, and Kern D (2012) Protein analysis by dynamic light scattering: Methods and techniques for students. *Biochem Mol Biol Educ* **40**:372–382.

Loura LMS, and Prieto M (2011) FRET in Membrane Biophysics: An Overview. *Front Physiol* **2**:82.

Loura LMS, Prieto M, and Fernandes F (2009) Quantification of protein–lipid selectivity using FRET. *Eur Biophys J* **39**:565–578.

Luca S, Yau WM, Leapman R, and Tycko R (2007) Peptide conformation and supramolecular organization in amylin fibrils: Constraints from solid-state NMR. *Biochemistry* **46**:13505–13522.

Lundberg KM, Stenland CJ, Cohen FE, Prusiner SB, and Millhauser GL (1997) Kinetics and mechanism of amyloid formation by the prion protein H1 peptide as determined by time-dependent ESR. *Chem Biol* **4**:345–55.

Luo P, and Baldwin RL (1997) Mechanism of helix induction by trifluoroethanol: A framework for extrapolating the helix-forming properties of peptides from trifluoroethanol/water mixtures back to water. *Biochemistry* **36**:8413–8421.

Macháň R, Jurkiewicz P, Olżyńska A, Olšinová M, Cebecauer M, Marquette A, Bechinger B, and Hof M (2014) Peripheral and integral membrane binding of peptides characterized by time-dependent fluorescence shifts: Focus on antimicrobial peptide LAH4. *Langmuir* **30**:6171–6179.

Magde D, Rojas GE, and Seybold PG (1999) Solvent Dependence of the fluorescence lifetime of xanthene dyes. *Photochem Photobiol* **70**:737–744.

Magzoub M, and Miranker AD (2012) Concentration-dependent transitions govern the subcellular localization of islet amyloid polypeptide. *FASEB J* **26**:1228–1238.

Maier R, Kamber B, Riniker B, and Rittel W (1976) Analogues of human calcitonin. IV. Influence of leucine substitutions in positions 12, 16 and 19 on hypocalcaemic activity in the rat. *Clin Endocrinol* **5**:327S–332S.

Maiti NC, Mazumdar S, and Periasamy N (1998) J- and H-Aggregates of Porphyrin−Surfactant Complexes: Time-Resolved Fluorescence and Other Spectroscopic Studies †. *J Phys Chem B* **102**:1528–1538.

Maji SK, Amsden JJ, Rothschild KJ, Condron MM, and Teplow DB (2005) Conformational dynamics of amyloid β-protein assembly probed using intrinsic fluorescence. *Biochemistry* **44**:13365–13376.

Maji SK, Perrin MH, Sawaya MR, Jessberger S, Vadodaria K, Rissman RA, Singru PS, Nilsson KPR, Simon R, Schubert D, Eisenberg D, Rivier J, Sawchenko P, Vale W, and Riek R (2009) Functional amyloids as natural storage of peptide hormones in pituitary secretory granules. *Science (80-)* **325**:328–332.

Malvern Instruments (2017) *Dynamic Light Scattering: An Introduction in 30 Minutes*.

Mark JE (2007) *Physical Properties of Polymers Handbook. Springer US, New York, United States of America*.

Martel A, Antony L, Gerelli Y, Porcar L, Fluitt A, Hoffmann K, Kiesel I, Vivaudou M, Fragneto G, and De Pablo JJ (2017) Membrane Permeation versus Amyloidogenicity: A Multitechnique Study of Islet Amyloid Polypeptide Interaction with Model Membranes. *J Am Chem Soc* **139**:137–148.

Martin MM (1975) Hydrogen bond effects on radiationless electronic transitions in xanthene dyes. *Chem Phys Lett* **35**:105–111.

Martinez A, Kapas S, Miller M-J, Ward Y, and Cuttitta F (2000) Coexpression of Receptors for Adrenomedullin ,. **141**:406–411.

Martins IC, Kuperstein I, Wilkinson H, Maes E, Vanbrabant M, Jonckheere W, Van Gelder P, Hartmann D, D'Hooge R, De Strooper B, Schymkowitz J, and Rousseau F (2008) Lipids revert inert Aβ amyloid fibrils to neurotoxic protofibrils that affect learning in mice. *EMBO J* **27**:224–233.

Mayer LD, Hope MJ, and Cullis PR (1986) Vesicles of variable sizes produced by a rapid extrusion procedure. *Biochim Biophys Acta* **858**:161–8.

McClare CW (1971) An accurate and convenient organic phosphorus assay. *Anal Biochem* **39**:527–530.

Meadows RP, Nikonowicz EP, Jones CR, Bastian JW, Gorenstein DG, and Bastian JW (1991) Two-Dimensional NMR and Structure Determination of Salmon Calcitonin in Methanol. *Biochemistry* **30**:1247–1254.

Melo AM, Fedorov A, Prieto M, and Coutinho A (2014) Exploring homo-FRET to quantify the oligomer stoichiometry of membrane-bound proteins involved in a cooperative partition equilibrium. *Phys Chem Chem Phys* **16**:18105–18117.

Melo AM, Loura LMS, Fernandes F, Villalaín J, Prieto M, and Coutinho A (2014) Electrostatically driven lipid–lysozyme mixed fibers display a multilamellar structure without amyloid features. *Soft Matter* **10**:840.

Melo AM, Prieto M, and Coutinho A (2011) The effect of variable liposome brightness on quantifying lipid-protein interactions using fluorescence correlation spectroscopy. *Biochim Biophys Acta* **1808**:2559–68.

Melo AM, Ricardo JC, Fedorov A, Prieto M, and Coutinho A (2013) Fluorescence detection of lipid-induced oligomeric intermediates involved in lysozyme "amyloid-like" fiber formation driven by anionic membranes. *J Phys Chem B* **117**:2906–17.

Merle M, Lefevre G, and Milhaud G (1979) Predicted secondary structure of calcitonin in relation to the biological activity. *Biochem Biophys Res Commun* **87**:455–460.

Meyer J-P, Pelton JT, Hoflack J, and Saudek V (1991) Solution structure of salmon calcitonin. *Biopolymers* **31**:233–241.

Moe GR, and Kaiser ET (1985) Design, synthesis, and characterization of a model peptide having potent calcitonin-like biological activity: implications for calcitonin structure/activity. *Biochemistry* **24**:1971–1976.

Moe GR, Miller RJ, and Kaiser ET (1983) Design of a peptide hormone: Synthesis and characterization of a model peptide with calcitonin-like activity. *J Am Chem Soc* **105**:4100–4102.

Morelli MAC, Pastore A, and Motta A (1992) Dynamic properties of salmon calcitonin bound to sodium dodecyl sulfate micelles: A restrained molecular dynamics study from NMR data. *J Biomol NMR* **2**:335–348.

Moriarty DF, and Raleigh DP (1999) Effects of sequential proline substitutions on amyloid formation by human amylin20-29. *Biochemistry* **38**:1811–1818.

Moriarty DF, Vagts S, and Raleigh DP (1998) A role for the C-terminus of calcitonin in aggregation and gel formation: a comparative study of C-terminal fragments of human and salmon calcitonin. *Biochem Biophys Res Commun* **245**:344–348.

Motta A, Andreotti G, Amodeo P, Strazzullo G, and Morelli MAC (1998) Solution structure of human calcitonin in membrane-mimetic environment: the role of the amphipathic helix. *Proteins* **32**:314–23.

Motta A, Morelli MAC, Goud N, and Temussi PA (1989) Sequential 1H NMR assignment and secondary structure determination of salmon calcitonin in solution. *Biochemistry* **28**:7996–8002.

Motta A, Pastore A, Goud NA, and Morelli MAC (1991) Solution Conformation of Salmon Calcitonin in Sodium Dodecyl Sulfate Micelles As Determined by Two-Dimensional NMR and Distance Geometry Calculations. *Biochemistry* **30**:10444–10450.

Motta A, Temussi PA, Wünsch E, Bovermann G, Wunsch E, and Bovermann G (1991) A 1H NMR Study of Human Calcitonin in Solution. *Biochemistry* **30**:2364–2371.

Mouritsen OG, and Zuckermann MJ (2004) What's so special about cholesterol? *Lipids* **39**:1101–13.

Mulder H, Ahrén B, and Sundler F (1996) Islet amyloid polypeptide and insulin gene expression are regulated in parallel by glucose in vivo in rats. *Am J Physiol* **271**:E1008-14.

Munishkina LA, Cooper EM, Uversky VN, and Fink AL (2004) The effect of macromolecular crowding on protein aggregation and amyloid fibril formation. *J Mol Recognit* **17**:456–64.

Munishkina LA, Phelan C, Uversky VN, and Fink AL (2003) Conformational behavior and aggregation of α-synuclein in organic solvents: Modeling the effects of membranes. *Biochemistry* **42**:2720–2730.

Murphy DB (2001) *Fundamentals of Light Microscopy and Electronic Imaging*.

Naito A, Kamihira-Ishijima M, Inoue R, and Saitô H (2004) Structural diversity of amyloid fibril formed in human calcitonin as revealed by site-directed 13C solid-state NMR spectroscopy. *Magn Reson Chem* **42**:247–57.

Nakamuta H, Orlowski RC, and Epand RM (1990) Evidence for calcitonin receptor heterogeneity: binding studies with nonhelical analogs. *Endocrinology* **127**:163–169.

Nanga RPR, Brender JR, Vivekanandan S, and Ramamoorthy A (2011) Structure and membrane orientation of IAPP in its natively amidated form at physiological pH in a membrane environment. *Biochim Biophys Acta - Biomembr* **1808**:2337–2342.

Nanga RPR, Brender JR, Xu J, Hartman K, Subramanian V, and Ramamoorthy A (2009) Three-dimensional structure and orientation of rat islet amyloid polypeptide protein in a membrane environment by solution NMR spectroscopy. *J Am Chem Soc* **131**:8252–8261.

Nanga RPR, Brender JR, Xu J, Veglia G, and Ramamoorthy A (2008) Structures of Rat and Human Islet Amyloid Polypeptide IAPP1− 19 in Micelles by NMR Spectroscopy. *Biochemistry* **47**:12689–12697.

Naot D, and Cornish J (2008) The role of peptides and receptors of the calcitonin family in the regulation of bone metabolism. *Bone* **43**:813–8.

Nath A, Miranker AD, and Rhoades E (2011) A membrane-bound antiparallel dimer of rat islet amyloid polypeptide. *Angew Chemie - Int Ed* **50**:10859–10862.

Nath A, and Rhoades E (2013) A flash in the pan: dissecting dynamic amyloid intermediates using fluorescence. *FEBS Lett* **587**:1096–105.

Neher R, Riniker B, Maier R, Byfield PGH, Gudmundsson T V, and MacIntyre I (1968) Human Calcitonin. *Nature* **220**:984–986.

Nelson DL, and Cox MM (2005) *Principles of Biochemistry*, 4th ed. (W. H. Freeman and Company ed).

Nelson R, Sawaya MR, Balbirnie M, Madsen AØ, Riekel C, Grothe R, and Eisenberg D (2005) Structure of the cross-beta spine of amyloid-like fibrils. *Nature* **435**:773–8.

Niall HD, Keutmann HT, Copp DH, and Potts JTJ (1969) Amino Acid Sequence of Salmon Ultimobranchial Calcitonin. *Proc Natl Acad Sci* **64**:771–778.

Nielsen L, Khurana R, Coats A, Frokjaer S, Brange J, Vyas S, Uversky VN, and Fink AL (2001) Effect of environmental factors on the kinetics of insulin fibril formation: Elucidation of the molecular mechanism. *Biochemistry* **40**:6036–6046.

Nielsen SB, and Otzen DE (2010) Impact of the antimicrobial peptide Novicidin on membrane structure and integrity. *J Colloid Interface Sci* **345**:248–256.

Nilsson MR, and Raleigh DP (1999) Analysis of amylin cleavage products provides new insights into the amyloidogenic region of human amylin. *J Mol Biol* **294**:1375–1385.

Noronha M, Lima JC, Paci E, Santos H, and Maçanita AL (2007) Tracking local conformational changes of ribonuclease A using picosecond time-resolved fluorescence of the six tyrosine residues. *Biophys J* **92**:4401–14.

Ogawa K, Nishimura S, Doi M, Kyogoku Y, Hayashi M, and Kobayashi Y (1994) Conformational analysis of elcatonin in solution. *Eur J Biochem* **222**:659–666.

Ogawa K, Nishimura S, Doi M, Takashima H, Nishi Y, Yoshida T, Ohkubo T, and Kobayashi Y (2006) Conformational analysis of human calcitonin in solution. *J Pept Sci* **12**:51–7.

Ono K, Condron MM, and Teplow DB (2009) Structure-neurotoxicity relationships of amyloid beta-protein oligomers. *Proc Natl Acad Sci* **106**:14745–14750.

Orlowski RC, Epand RM, and Stafford AR (1987) Biologically potent analogues of salmon calcitonin which do not contain an N-terminal disulfide-bridged ring structure. *Eur J Biochem* **162**:399–402.

Owen DM, Rentero C, Magenau A, Abu-Siniyeh A, and Gaus K (2012) Quantitative imaging of membrane lipid order in cells and organisms. *Nat Protoc* **7**:24–35.

Padrick SB, and Miranker AD (2002) Islet amyloid: Phase partitioning and secondary nucleation are central to the mechanism of fibrillogenesis. *Biochemistry* **41**:4694–4703.

Padrick SB, and Miranker AD (2001) Islet amyloid polypeptide: Identification of long-range contacts and local order on the fibrillogenesis pathway. *J Mol Biol* **308**:783–794.

Palepu R, and Clarke J (1989) Viscosities and densities of 2,2,2-trifluoroethanol + water at various temperatures. *Thermochim Acta* **156**:359–363.

Pan J, Cheng X, Monticelli L, Heberle FA, Kučerka N, Tieleman DP, and Katsaras J (2014) The molecular structure of a phosphatidylserine bilayer determined by scattering and molecular dynamics simulations. *Soft Matter* **10**:3716–3725.

Parasassi T, De Stasio G, D'Ubaldo A, and Gratton E (1990) Phase fluctuation in phospholipid membranes revealed by Laurdan fluorescence. *Biophys J* **57**:1179–1186.

Parasassi T, Krasnowska EK, Bagatolli LA, and Gratton E (1998) LAURDAN and PRODAN as polarity-sensitive fluorescent membrane probes. *J Fluoresc* **8**:365–373.

Pastor I, Ferrer ML, Lillo MP, Gómez J, and Mateo CR (2007) Structure and dynamics of lysozyme encapsulated in a silica sol-gel matrix. *J Phys Chem B* **111**:11603–10.

Patil SM, Mehta A, Jha S, and Alexandrescu AT (2011) Heterogeneous amylin fibril growth mechanisms imaged by total internal reflection fluorescence microscopy. *Biochemistry* **50**:2808–19.

Patil SM, Xu S, Sheftic SR, and Alexandrescu AT (2009) Dynamic α-helix structure of micelle-bound human amylin. *J Biol Chem* **284**:11982–11991.

Pescitelli G, Di Bari L, and Berova N (2014) Application of electronic circular dichroism in the study of supramolecular systems. *Chem Soc Rev* **43**:5211–5233.

Pilkington EH, Gurzov EN, Kakinen A, Litwak SA, Stanley WJ, Davis TP, and Ke PC (2016) Pancreatic β-Cell Membrane Fluidity and Toxicity Induced by Human Islet Amyloid Polypeptide Species. *Sci Rep* **6**:1–10.

Poirier MA, Li H, Macosko J, Cai S, Amzel M, and Ross CA (2002) Huntingtin spheroids and protofibrils as precursors in polyglutamine fibrilization. *J Biol Chem* **277**:41032–41037.

Pokorna S, Olźyńska A, Jurkiewicz P, and Hof M (2013) Imaging Molecular Order in Cell Membranes by Polarization-Resolved Fluorescence Microscopy, in *Springer Series on Fluorescence* (Brasselet S, Ferrand P, and Kress A eds) pp 141–160.

Potts JTJ, Reisfeld RA, Hirsch PF, Wasthedt AB, Voelkel EF, and Munson PL (1967) Purification of Porcine Thyrocalcitonin. *Proc Natl Acad Sci* **58**:328–335.

Press-Sandler O, and Miller Y (2018) Molecular mechanisms of membrane-associated amyloid aggregation: Computational perspective and challenges. *Biochim Biophys Acta - Biomembr* **1860**:1889–1905.

Quist A, Doudevski I, Lin H, Azimova R, Ng D, Frangione B, Kagan B, Ghiso J, and Lal R (2005) Amyloid ion channels: a common structural link for protein-misfolding disease. *Proc Natl Acad Sci* **102**:10427–32.

Raffen R, Dieckman LJ, Szpunar M, Wunschl C, Pokkuluri PR, Dave P, Wilkins Stevens P, Cai X, Schiffer M, and Stevens FJ (1999) Physicochemical consequences of amino acid variations that

contribute to fibril formation by immunoglobulin light chains. *Protein Sci* **8**:509–17.

Raleigh DP, Zhang X, Hastoy B, and Clark A (2017) The β-cell assassin: IAPP cytotoxicity. *J Mol Endocrinol* **59**:R121–R140.

Ranjbar B, and Gill P (2009) Circular dichroism techniques: biomolecular and nanostructural analyses- a review. *Chem Biol Drug Des* **74**:101–20.

Rao J, Bhattacharya D, Banerjee B, Sarin A, and Shivashankar G V. (2007) Trichostatin-A induces differential changes in histone protein dynamics and expression in HeLa cells. *Biochem Biophys Res Commun* **363**:263–268.

Ratha BN, Kim M, Sahoo B, Garai K, Lee DK, and Bhunia A (2018) Insulin–eukaryotic model membrane interaction: Mechanistic insight of insulin fibrillation and membrane disruption. *Biochim Biophys Acta - Biomembr* **1860**:1917–1926.

Rawat A, Langen R, and Varkey J (2018) Membranes as modulators of amyloid protein misfolding and target of toxicity. *Biochim Biophys Acta - Biomembr* **1860**:1863–1875.

Rawat A, Maity BK, Chandra B, and Maiti S (2018) Aggregation-induced conformation changes dictate islet amyloid polypeptide (IAPP) membrane affinity. *Biochim Biophys Acta - Biomembr* **1860**:1734–1740.

Reches M, Porat Y, and Gazit E (2002) Amyloid fibril formation by pentapeptide and tetrapeptide fragments of human calcitonin. *J Biol Chem* **277**:35475–80.

Relini A, Marano N, and Gliozzi A (2013) Misfolding of Amyloidogenic Proteins and Their Interactions with Membranes. *Biomolecules* **4**:20–55.

Relini A, Torrassa S, Rolandi R, Gliozzi A, Rosano C, Canale C, Bolognesi M, Plakoutsi G, Bucciantini M, Chiti F, and Stefani M (2004) Monitoring the process of HypF fibrillization and liposome permeabilization by protofibrils. *J Mol Biol* **338**:943–57.

Renz M (2013) Fluorescence microscopy-A historical and technical perspective. *Cytom Part A* **83**:767–779.

Rigoldi F, Metrangolo P, Redaelli A, and Gautieri A (2017) Nanostructure and stability of calcitonin amyloids. *J Biol Chem* **292**:7348–7357.

Risør MW, Juhl DW, Bjerring M, Mathiesen J, Enghild JJ, Nielsen NC, and Otzen DE (2017) Critical Influence of Cosolutes and Surfaces on the Assembly of Serpin-Derived Amyloid Fibrils. *Biophys J* **113**:580–596.

Rochet JC, and Lansbury PT (2000) Amyloid fibrillogenesis: themes and variations. *Curr Opin Struct Biol* **10**:60–8.

Rolinski OJ, Amaro M, and Birch DJS (2010) Early detection of amyloid aggregation using intrinsic fluorescence. *Biosens Bioelectron* **25**:2249–2252.

Rolinski OJ, Wellbrock T, Birch DJS, and Vyshemirsky V (2015) Tyrosine Photophysics during the Early Stages of β-Amyloid Aggregation Leading to Alzheimer's. *J Phys Chem Lett* **6**:3116–3120.

Rosenfeld MG, Mermod JJ, Amara SG, Swanson LW, Sawchenko PE, Rivier J, Vale WW, and Evans RM (1983) Production of a novel neuropeptide encoded by the calcitonin gene via tissue-specific RNA processing. *Nature* **304**:129–135.

Roy M, Chen H, and Sippel RS (2013) Current Understanding and Management of Medullary Thyroid Cancer. *Oncologist* **12**:991–998.

Rusinova E, Tretyachenko-Ladokhina V, Vele OE, Senear DF, and Alexander Ross JB (2002) Alexa and Oregon Green dyes as fluorescence anisotropy probes for measuring protein-protein and protein-nucleic acid interactions. *Anal Biochem* **308**:18–25.

Rustenbeck I, Matthies A, and Lenzen S (1994) Lipid composition of glucose-stimulated pancreatic islets and insulin-secreting tumor cells. *Lipids* **29**:685–92.

Rusu L, Gambhir A, McLaughlin S, and Rädler J (2004) Fluorescence correlation spectroscopy studies of peptide and protein binding phospholipid vesicles. *Biophys J* **87**:1044–1053.

Ryan TM, Howlett GJ, and Bailey MF (2008) Fluorescence detection of a lipid-induced tetrameric

intermediate in amyloid fibril formation by apolipoprotein C-II. *J Biol Chem* **283**:35118–28.

Saafi EL, Konarkowska B, Zhang S, Kistler J, and Cooper GJS (2001) Ultrastructural evidence that apoptosis is the mechanism by which human amylin evokes death in RINm5F pancreatic islet β-cells. *Cell Biol Int* **25**:339–350.

Sahoo B, Nag S, Sengupta P, and Maiti S (2009) On the stability of the soluble amyloid aggregates. *Biophys J* **97**:1454–1460.

Sanchez SA, Tricerri MA, Gunther G, and Gratton E (2007) Laurdan Generalized Polarization: from cuvette to microscope. *Mod Res Educ Top Microsc* **2**:1007–1014.

Sanderson MJ, Smith I, Parker I, and Bootman MD (2014) Fluorescence microscopy. *Cold Spring Harb Protoc* **2014**:1042–1065.

Schmidt M, Sachse C, Richter W, Xu C, Fandrich M, and Grigorieff N (2009) Comparison of Alzheimer A (1-40) and A (1-42) amyloid fibrils reveals similar protofilament structures. *Proc Natl Acad Sci* **106**:19813–19818.

Schmidt MC, Rothen-Rutishauser B, Rist B, Beck-Sickinger AG, Wunderli-Allenspach H, Rubas W, Sadée W, and Merkle HP (1998) Translocation of human calcitonin in respiratory nasal epithelium is associated with self-assembly in lipid membrane. *Biochemistry* **37**:16582–90.

Schneider M, Walta S, Cadek C, Richtering W, and Willbold D (2017) Fluorescence correlation spectroscopy reveals a cooperative unfolding of monomeric amyloid-β 42 with a low Gibbs free energy. *Sci Rep* **7**:1–8.

Schröder GF, Alexiev U, and Grubmüller H (2005) Simulation of fluorescence anisotropy experiments: probing protein dynamics. *Biophys J* **89**:3757–70.

Seelig J (2004) Thermodynamics of lipid-peptide interactions. *Biochim Biophys Acta* **1666**:40–50.

Seeliger J, Weise K, Opitz N, and Winter R (2012) The effect of Aβ on IAPP aggregation in the presence of an isolated β-cell membrane. *J Mol Biol* **421**:348–363.

Sexton PM, Poyner DR, Simms J, Christopoulos A, and Hay DL (2009) Modulating receptor function through RAMPs: can they represent drug targets in themselves? *Drug Discov Today* **14**:413–419.

Sharma P, Varma R, Sarasij RC, Ira, Gousset K, Krishnamoorthy G, Rao M, and Mayor S (2004) Nanoscale Organization of Multiple GPI-Anchored Proteins in Living Cell Membranes. *Cell* **116**:577–589.

Sheynis T, and Jelinek R (2010) Lipid-induced calcitonin fibrillation blocks membrane interactions of a peptide antibiotic. *J Phys Chem B* **114**:15530–15535.

Sheynis T, Sykora J, Benda A, Kolusheva S, Hof M, and Jelinek R (2003) Bilayer localization of membrane-active peptides studied in biomimetic vesicles by visible and fluorescence spectroscopies. *Eur J Biochem* **270**:4478–4487.

Shtainfeld A, Sheynis T, and Jelinek R (2010) Specific mutations alter fibrillation kinetics, fiber morphologies, and membrane interactions of pentapeptides derived from human calcitonin. *Biochemistry* **49**:5299–307.

Sieber P, Riniker B, Brugger M, Kamber B, and Rittel W (1970) Menschliches Calcitonin. VI. Die Synthese von Calcitonin M. *Helv Chim Acta* **53**:2135–2150.

Siegel J, Suhling K, Lévêque-Fort S, Webb SED, Davis DM, Phillips D, Sabharwal Y, and French PMW (2003) Wide-field time-resolved fluorescence anisotropy imaging (TR-FAIM): Imaging the rotational mobility of a fluorophore. *Rev Sci Instrum* **74**:182–192.

Siligardi G, Samori B, Melandri S, Visconti M, and Drake AF (1994) Correlations between biological activities and conformational properties for human, salmon, eel, porcine calcitonins and Elcatonin elucidated by CD spectroscopy. *Eur J Biochem* **221**:1117–1125.

Simons K, and Ikonen E (1997) Functional rafts in cell membranes. *Nature* **387**:569–72.

Simons K, and Sampaio JL (2011) Membrane organization and lipid rafts. *Cold Spring Harb Perspect Biol* **3**:a004697.

Singh S, Trikha S, Bhowmick DC, Sarkar AA, and Jeremic AM (2015) Lipids in Protein Misfolding.

855:95–116.

Sipe JD, Benson MD, Buxbaum JN, Ikeda S-I, Merlini G, Saraiva MJM, and Westermark P (2010) Amyloid fibril protein nomenclature: 2010 recommendations from the nomenclature committee of the International Society of Amyloidosis. *Amyloid* **17**:101–4.

Smith PES, Brender JR, and Ramamoorthy A (2009) Induction of Negative Curvature as a Mechanism of Cell Toxicity by Amyloidogenic Peptides : The Case of Islet Amyloid Polypeptide. *J Am Chem Soc* 4470–4478.

Sparr E, Engel MFM, Sakharov D V, Sprong M, Jacobs J, De Kruijff B, Höppener JWM, and Killian JA (2004) Islet amyloid polypeptide-induced membrane leakage involves uptake of lipids by forming amyloid fibers. *FEBS Lett* **577**:117–120.

Stachowiak JC, Schmid EM, Ryan CJ, Ann HS, Sasaki DY, Sherman MB, Geissler PL, Fletcher DA, and Hayden CC (2012) Membrane bending by protein-protein crowding. *Nat Cell Biol* **14**:944–949.

Stefani M (2012) Structural features and cytotoxicity of amyloid oligomers: implications in Alzheimer's disease and other diseases with amyloid deposits. *Prog Neurobiol* **99**:226–45.

Stipani V, Gallucci E, Micelli S, Picciarelli V, and Benz R (2001) Channel formation by salmon and human calcitonin in black lipid membranes. *Biophys J* **81**:3332–8.

Stroop SD, Kuestner RE, Serwold TF, Chen L, and Moore EE (1995) Chimeric human calcitonin and glucagon receptors reveal two dissociable calcitonin interaction sites. *Biochemistry* **34**:1050–1057.

Stroop SD, Nakamuta H, Kuestner RE, Moore EE, and Epand RM (1996) Determinants for calcitonin analog interaction with the calcitonin receptor N-terminus and transmembrane-loop regions. *Endocrinology* **137**:4752–4756.

Stsiapura VI, Maskevich AA, Kuzmitsky V a, Uversky VN, Kuznetsova IM, and Turoverov KK (2008) Thioflavin T as a molecular rotor: fluorescent properties of thioflavin T in solvents with different viscosity. *J Phys Chem B* **112**:15893–902.

Suckale J, and Solimena M (2010) The insulin secretory granule as a signaling hub. *Trends Endocrinol Metab* **21**:599–609.

Suhling K, Levitt J, and Chung P-H (2014) Time-Resolved Anisotropy Imaging, in *Fluorescence Spectroscopy and Microscopy* (Engelborghs Y, and Visser AJWG eds) pp 503–519.

Takahashi Y, Okamoto Y, Popiel HA, Fujikake N, Toda T, Kinjo M, and Nagai Y (2007) Detection of polyglutamine protein oligomers in cells by fluorescence correlation spectroscopy. *J Biol Chem* **282**:24039–24048.

Taylor DR, and Hooper NM (2006) The prion protein and lipid rafts (Review). *Mol Membr Biol* **23**:89–99.

Tong J, Borbat PP, Freed JH, and Shin Y-K (2009) A scissors mechanism for stimulation of SNARE-mediated lipid mixing by cholesterol. *Proc Natl Acad Sci* **106**:5141–6.

Turoverov KK, Kuznetsova IM, and Uversky VN (2010) The protein kingdom extended: Ordered and intrinsically disordered proteins, their folding, supramolecular complex formation, and aggregation. *Prog Biophys Mol Biol* **102**:73–84.

Twery MJ, Seitz PK, Nickols GA, Cooper GW, Gallagher JP, and Orlowski RC (1988) Analogue separates biological effects of salmon calcitonin on brain and renal cortical membranes. *Eur J Pharmacol* **155**:285–292.

Tycko R (2011) Solid State NMR Studies of Amyloid Fibril Structure. *Annu Rev Phys Chem* **62**:279–299.

Uversky VN (2013) Unusual biophysics of intrinsically disordered proteins. *Biochim Biophys Acta - Proteins Proteomics* **1834**:932–951.

Uversky VN, Li J, and Fink AL (2001) Pesticides directly accelerate the rate of alpha-synuclein fibril formation : a possible factor in Parkinson ' s disease. *FEBS Lett* **500**:105–108.

Valdes-Aguilera O, and Neckers DC (1989) Aggregation Phenomena in Xanthene Dyes. *Acc Chem Res* **22**:171–177.

Valera E, and Masliah E (2016) Therapeutic approaches in Parkinson's disease and related disorders. *J Neurochem* **139**:346–352.

Valera E, Spencer B, and Masliah E (2016) Immunotherapeutic Approaches Targeting Amyloid-β, α-Synuclein, and Tau for the Treatment of Neurodegenerative Disorders. *Neurotherapeutics* **13**:179–189.

Valeur B, and Berberan-Santos MN (2012) *Molecular Fluorescence: Principles and Applications*.

van Ham TJ, Esposito A, Kumita JR, Hsu S-TD, Schierle GSK, Kaminski CF, Dobson CM, Nollen E a a, and Bertoncini CW (2010) Towards multiparametric fluorescent imaging of amyloid formation: studies of a YFP model of alpha-synuclein aggregation. *J Mol Biol* **395**:627–42.

Varkey J, Isas JM, Mizuno N, Jensen MB, Bhatia VK, Jao CC, Petrlova J, Voss JC, Stamou DG, Steven AC, and Langen R (2010) Membrane curvature induction and tubulation are common features of synucleins and apolipoproteins. *J Biol Chem* **285**:32486–32493.

Wagner K, Beck-Sickinger AG, and Huster D (2004) Structural Investigations of a Human Calcitonin-Derived Carrier Peptide in a Membrane Environment by Solid-State NMR. *Biochemistry* 12459–12468.

Wagner K, Van Mau N, Boichot S, Kajava A V, Krauss U, Le Grimellec C, Beck-Sickinger AG, and Heitz F (2004) Interactions of the human calcitonin fragment 9-32 with phospholipids: a monolayer study. *Biophys J* **87**:386–95.

Wakabayashi M, and Matsuzaki K (2009) Ganglioside-induced amyloid formation by human islet amyloid polypeptide in lipid rafts. *FEBS Lett* **583**:2854–8.

Wang SS-S, Good T a, and Rymer DL (2005a) The influence of phospholipid membranes on bovine calcitonin peptide's secondary structure and induced neurotoxic effects. *Int J Biochem Cell Biol* **37**:1656–69.

Wang SS-S, Good TA, and Rymer DL (2005b) The influence of phospholipid membranes on bovine calcitonin secondary structure and amyloid formation. *Protein Sci* **14**:1419–1428.

Warren SC, Margineanu A, Katan M, Dunsby C, and French PMW (2015) Homo-FRET based biosensors and their application to multiplexed imaging of signalling events in live cells. *Int J Mol Sci* **16**:14695–14716.

Weise K, Radovan D, Gohlke A, Opitz N, and Winter R (2010) Interaction of hIAPP with model raft membranes and pancreatic β-cells: cytotoxicity of hIAPP oligomers. *ChemBioChem* **11**:1280–1290.

Westermark P (2011) Amyloid in the islets of Langerhans: thoughts and some historical aspects. *Ups J Med Sci* **116**:81–9.

Westermark P, Andersson A, and Westermark GT (2011) Islet Amyloid Polypeptide, Islet Amyloid, and Diabetes Mellitus. *Physiol Rev* **91**:795–826.

Westermark P, Engström U, Johnson KH, Westermark GT, and Betsholtz C (1990) Islet amyloid polypeptide: pinpointing amino acid residues linked to amyloid fibril formation. *Proc Natl Acad Sci U S A* **87**:5036–40.

Westermark P, Li ZC, Westermark GT, Leckström A, and Steiner DF (1996) Effects of beta cell granule components on human islet amyloid polypeptide fibril formation. *FEBS Lett* **379**:203–6.

Westermark P, Wernstedt C, Wilander E, Hayden DW, O'Brien TD, and Johnson KH (1987) Amyloid fibrils in human insulinoma and islets of Langerhans of the diabetic cat are derived from a neuropeptide-like protein also present in normal islet cells. *Proc Natl Acad Sci U S A* **84**:3881–5.

Westermark P, Wernstedt C, Wilander E, and Sletten K (1986) A novel peptide in the calcitonin gene related peptide family as an amyloid fibril protein in the endocrine pancreas. *Biochem Biophys Res Commun* **140**:827–31.

Whitmore L, and Wallace BA (2008) Protein secondary structure analyses from circular dichroism spectroscopy: Methods and reference databases. *Biopolymers* **89**:392–400.

Widengren J, Mets U, and Rigler R (1995) Fluorescence Correlation Spectroscopy of Triplet-States in Solution - a Theoretical and Experimental-Study. *J Phys Chem* **99**:13368–13379.

Widengren J, and Rigler R (1998) Fluorescence Correlation Spectroscopy as a tool to investigate chemical reactions in solutions and on cell surfaces. *Cell Mol Biol* **44**:857–879.

Wielinga PY, Löwenstein C, Muff S, Munz M, Woods SC, and Lutz TA (2010) Central amylin acts as an adiposity signal to control body weight and energy expenditure. *Physiol Behav* **101**:45–52.

Williams TL, and Serpell LC (2011) Membrane and surface interactions of Alzheimer's Aβ peptide - Insights into the mechanism of cytotoxicity. *FEBS J* **278**:3905–3917.

Williamson JA, and Miranker AD (2007) Direct detection of transient alpha-helical states in islet amyloid polypeptide. *Protein Sci* **16**:110–7.

Wimalawansa SJ (1997) Amylin, calcitonin gene-related peptide, calcitonin, and adrenomedullin: a peptide superfamily. *Crit Rev Neurobiol* **11**:167–239.

Yan L-M, Tatarek-Nossol M, Velkova A, Kazantzis A, and Kapurniotu A (2006) Design of a mimic of nonamyloidogenic and bioactive human islet amyloid polypeptide (IAPP) as nanomolar affinity inhibitor of IAPP cytotoxic fibrillogenesis. *Proc Natl Acad Sci* **103**:2046–51.

Yanagisawa K (2015) GM1 ganglioside and Alzheimer's disease. *Glycoconj J* **32**:87–91.

Yandek LE, Pokorny A, Florén A, Knoelke K, Langel Ü, and Almeida PFF (2007) Mechanism of the cell-penetrating peptide transportan 10 permeation of lipid bilayers. *Biophys J* **92**:2434–2444.

Yeow EKL, and Clayton AHA (2007) Enumeration of oligomerization states of membrane proteins in living cells by homo-FRET spectroscopy and microscopy: Theory and application. *Biophys J* **92**:3098–3104.

Yi H-S, Choi B, and Lee S (2011) Molecular Understanding and Assessment of Hypoparathyroidism. *Endocrinol Metab* **26**:25–32.

Yoshiike Y, Kayed R, Milton SC, Takashima A, and Glabe CG (2007) Pore-forming proteins share structural and functional homology with amyloid oligomers. *Neuromolecular Med* **9**:270–275.

Yu WM, So PT, C. French T, and Gratton E (1996) Fluorescence generalized polarization of cell-membranes - a 2-photon scanning microscopy approach. *Biophys J* **70**:626–636.

Zaidi M, Inzerillo a M, Moonga BS, Bevis PJR, and Huang CL-H (2002) Forty years of calcitonin--where are we now? A tribute to the work of Iain Macintyre, FRS. *Bone* **30**:655–63.

Zhang X, St Clair JR, London E, and Raleigh DP (2017) Islet amyloid polypeptide membrane interactions: Effects of membrane composition. *Biochemistry* **56**:376–390.

Zhang XF, Zhang Y, and Liu L (2014) Fluorescence lifetimes and quantum yields of ten rhodamine derivatives: Structural effect on emission mechanism in different solvents. *J Lumin* **145**:448–453.

Zhao H, Tuominen EKJ, and Kinnunen PKJ (2004) Formation of amyloid fibers triggered by phosphatidylserine-containing membranes. *Biochemistry* **43**:10302–7.

Zhao J, Hu R, Sciacca MFM, Brender JR, Chen H, Ramamoorthy A, and Zheng J (2014) Non-selective ion channel activity of polymorphic human islet amyloid polypeptide (amylin) double channels. *Phys Chem Chem Phys* **16**:2368–2377.